FACULDADE DE ENGENHARIA DA UNIVERSIDADE DO PORTO

Conception and Development of a Battery Composite Enclosure for a Motorcycle

Hélder Filipe Ventura da Cunha

Master in Mechanical Engineering

FEUP Supervisor: Prof.José Joaquim da Mota Machado

FEUP Co-supervisor: Prof. Ana Rosanete Lourenço Reis

Adamastor Supervisor: Eng. Frederico Tomé Ribeiro

November 7, 2025

© Hélder Cunha, 2025

Resumo

A crescente procura por soluções de mobilidade sustentáveis e de baixas emissões tem impulsionado avanços tecnológicos significativos na mobilidade elétrica, estendendo-se não apenas aos automóveis, mas também aos motociclos. Neste contexto, o sistema de bateria assume um papel central, dado o seu carácter crítico e a elevada sensibilidade em termos de segurança. O design, o desempenho e os mecanismos de proteção associados ao sistema de bateria estabelecem fatores determinantes para assegurar a fiabilidade, a segurança e a eficiência do veículo. Nos últimos anos, a aplicação de materiais compósitos em estruturas de baterias tem-se revelado uma solução promissora, oferecendo elevado desempenho mecânico, redução de peso e maior versatilidade no design estrutural.

A presente dissertação centra-se no desenvolvimento e implementação de uma metodologia para o design e fabrico de invólucros de bateria em material compósito destinadas a motociclos elétricos, tendo em consideração os requisitos funcionais, bem como as normas de segurança e homologação aplicáveis a estes sistemas, especificamente UN ECE R136 e UL 94. O trabalho foi desenvolvido na empresa Adamastor, especializada na produção de supercarros em materiais compósito, e em colaboração com dois fabricantes de motociclos elétricos, a Stark Future e a Famel.

O primeiro estudo incidiu na avaliação do potencial de um invólucro de bateria em compósito de fibra de carbono destinado aos modelos de motociclos Stark VARG EX/MX. Através de simulações por elementos finitos e de um processo de otimização do empilhamento de lâminas recorrendo aos softwares Altair HyperMesh ® e OptiStruct ®, foi obtido um design estruturalmente eficiente e leve, evidenciando uma potencial redução de peso de sensivelmente 30% face ao invólucro de liga de magnésio existente, mantendo simultaneamente elevada rigidez e integridade mecânica.

O segundo estudo centrou-se no desenvolvimento de um invólucro de bateria amovível destinado ao futuro modelo elétrico Famel E-XF. Foi definida e aplicada uma metodologia abrangente, contemplando as etapas de design conceptual, validação numérica mecânica e térmica, processos de otimização, fabrico do protótipo e realização de ensaios experimentais. A validação mecânica, baseada nos procedimentos de ensaio descritos na norma UN ECE R136, foi realizada através de análises explícitas dinâmicas por elementos finitos, com o objetivo de avaliar a integridade estrutural do design em material compósito reforçado com estruturas de favo de alumínio. Adicionalmente, foram realizadas análises térmicas transientes para avaliar o comportamento de transferência de calor, verificando-se a necessidade de integração de soluções adicionais de gestão térmica.

Foi produzido com sucesso um protótipo à escala real em material compósito de fibra de carbono, recorrendo a um processo de fabrico em *prepreg* e posterior cura em autoclave. Ensaios experimentais de inflamabilidade, realizados de acordo com a norma UL 94 HB, tanto para o laminado como para materiais comparativos, confirmaram o seu comportamento retardante à chama. O protótipo resultante evidenciou uma redução de peso estimada em aproximadamente 60% face ao design anterior do invólucro da Famel, mantendo conformidade com os requisitos de segurança

e desempenho mecânico.

Em síntese, a presente dissertação fornece uma metodologia abrangente para o design, análise e validação de invólucros de bateria em material compósito para motociclos elétricos. Os resultados demonstram a viabilidade e o potencial destas tecnologias no desenvolvimento de soluções de mobilidade elétrica mais leves, seguras e eficientes, estabelecendo uma base sólida para futuros desenvolvimentos e aplicações industriais.

Palavras-chave: Materiais compósitos; Invólucro de bateria; Motas elétricas; Otimização; Análise por elementos finitos; Processo prepreg-autoclave; Ensaio à chama UL 94; Protótipo.

Abstract

The growing demand for sustainable and low-emission mobility solutions has driven major technological advancements in electric mobility, extending beyond automobiles to include motorcycles. Within this context, the battery system plays a pivotal role as one of the most critical and safety-sensitive components of an electric motorcycle. Its design, performance, and protection are central to ensuring safety, reliability, and efficiency. In recent years, the use of composite materials for battery enclosures has emerged as a promising solution, offering high mechanical performance, reduced weight, and increased design flexibility.

This dissertation focuses on the development and implementation of a methodology for the design and manufacture of composite battery enclosures for electric motorcycles, addressing both functional requirements and the safety and homologation standards applicable to these systems (UN ECE R136 and UL 94). The work was carried out at Adamastor, a company specialised in composite supercar manufacturing, and was developed in collaboration with two electric motorcycle manufacturers: Stark Future and Famel.

The first study evaluated the potential of a carbon fibre composite battery enclosure for the Stark VARG EX/MX motorcycles. Through finite element simulations and composite layup optimisation using Altair HyperMesh and OptiStruct, a lightweight and structurally efficient design was achieved, demonstrating a potential weight reduction of approximately 30% compared with the existing magnesium alloy enclosure while improving stiffness and mechanical integrity.

The second study focused on the development of a removable battery enclosure for the upcoming Famel E-XF electric motorcycle. A complete methodology was defined, covering conceptual design, numerical mechanical and thermal validation, optimisation, prototype manufacturing, and experimental testing. The mechanical validation, following the test procedures described in UN ECE R136, employed explicit dynamic finite element analyses to evaluate the structural integrity of the composite and honeycomb-reinforced design. Thermal transient analyses were performed to assess heat transfer behaviour, revealing the need for additional thermal management solutions.

A full-scale carbon fibre composite prototype was successfully produced using a prepreg and autoclave manufacturing process. Experimental flammability testing of the laminate and comparable materials, conducted according to the UL 94 HB standard, confirmed their flame-retardant performance. The resulting prototype achieved a weight reduction of approximately 60% compared to Famel's previous enclosure design while maintaining compliance with safety and mechanical performance requirements.

Overall, this work provides a comprehensive framework for the design, analysis, and validation of composite battery enclosures for electric motorcycles. It demonstrates the feasibility and potential of composite technologies in advancing lightweight, safe, and efficient electric mobility solutions, establishing a foundation for future product development and industrial implementation.

Keywords: Composite materials; Battery enclosure; Electric motorcycles; Optimisation; Finite element analysis; Prepreg-Autoclave Process; UL 94 flammability test; Prototype.

Agradecimentos

Em primeiro lugar, gostaria de expressar o meu sincero agradecimento a todos os membros da Adamastor pela ajuda indispensável prestada ao longo do projeto, bem como pela maneira como me receberam e integraram na equipa. Em particular, gostaria de expressar o meu agradecimento ao Eng. Frederico Ribeiro pelo apoio constante, pela disponibilidade e pelo conhecimento transmitido, incansavelmente, ao longo de um projeto que superou diversas etapas e desafios.

Agradeço aos meus orientadores da FEUP, Professores José Machado e Ana Reis, pela disponibilidade, orientação e pelos contributos essenciais ao desenvolvimento deste trabalho. Expresso também o meu agradecimento à FEUP e ao Projeto Hi-rEV – Recuperação do Setor de Componentes Automóveis, por tornarem possível a concretização deste trabalho. Estendo, igualmente, o meu agradecimento ao INEGI, pela disponibilidade e pelo apoio prestado na realização dos testes de resistência à chama.

À minha namorada, Beatriz, pelo amor, pela presença constante e pela força que me transmitiu em todos os momentos, especialmente nos mais difíceis. Obrigado por acreditares em mim, por me inspirares a dar sempre o meu melhor e por estares sempre ao meu lado, és essencial para o meu sucesso.

Aos meus amigos, pela amizade e companheirismo que tornaram esta fase da minha vida mais leve e memorável.

Por último, e com especial significado, expresso o meu mais profundo agradecimento aos meus pais, por toda a dedicação e pelos sacrifícios que me permitiram chegar até aqui. Dedico-lhes esta dissertação, pois sem eles, nada disto teria sido possível.

Hélder Filipe Cunha

"It always seems impossible until it's done"

Nelson Mandela

AI Tools Recognition The author acknowledges the use of ChatGPT (https://chatgpt.com/) as a tool for improving the clarity and quality of the academic language in this thesis. The final text has been carefully revised to align with the author's own writing style and intended meaning.

Contents

1 Introduction **1**
- 1.1 Objectives and Motivation . . . 1
- 1.2 Intervenient Companies . . . 2
  - 1.2.1 Adamastor . . . 2
  - 1.2.2 Famel . . . 3
  - 1.2.3 Stark Future . . . 3
- 1.3 Methodology . . . 4
- 1.4 Project Timeline . . . 5
- 1.5 Structure of the Dissertation . . . 7

2 State of the art **9**
- 2.1 Electric Mobility . . . 9
- 2.2 Benchmarking . . . 11
- 2.3 Composite Materials . . . 12
  - 2.3.1 Reinforcements . . . 14
  - 2.3.2 Matrix . . . 16
  - 2.3.3 Comparison of Properties . . . 16
  - 2.3.4 Prepreg-Autoclave Manufacturing Process . . . 17
- 2.4 Review of Relevant Literature and Key Insights . . . 21
  - 2.4.1 Weight Saving . . . 22
  - 2.4.2 Impact Resistance . . . 23
  - 2.4.3 Thermal Management . . . 23
  - 2.4.4 Fire Safety . . . 23
  - 2.4.5 Optimisation . . . 24
- 2.5 Regulations and Standards . . . 24
  - 2.5.1 UN ECE R136 . . . 25
  - 2.5.2 UL 94 Standard for Safety of Flammability . . . 26
- 2.6 Composite Mechanics . . . 27
  - 2.6.1 Classical Lamination Theory . . . 27
  - 2.6.2 Failure Criteria . . . 30
- 2.7 Finite Element Method . . . 33
  - 2.7.1 Linear Static Analysis . . . 34
  - 2.7.2 Nonlinear Static Analysis . . . 35
  - 2.7.3 Linear Steady State Heat Transfer Analysis . . . 36
  - 2.7.4 Linear Transient Heat Transfer Analysis . . . 38
- 2.8 Dynamic Explicit Analysis . . . 39
  - 2.8.1 Time Discretisation . . . 39
  - 2.8.2 Central Difference Integration . . . 41

2.8.3 Stability Condition . . . 43
2.8.4 Mass Scaling and Hourglass Control . . . 45
2.9 Composite Numerical Modeling in Altair OptiStruct® . . . 46
2.10 OptiStruct Composite Optimisation . . . 48
2.10.1 Optimisation-Assisted Composite Design . . . 48
2.10.2 Optimisation . . . 49
2.10.3 Methodology . . . 50

3 Preliminary Analysis of the Stark VARG EX/MX Battery Enclosure 54
3.1 Context and Motivation . . . 54
3.1.1 Initial Circumstances . . . 54
3.1.2 Stark Future VARG EX/MX Battery . . . 55
3.1.3 Collaboration Objectives . . . 56
3.1.4 Initial Design Strategies . . . 57
3.2 Reverse Engineering of the Battery Design . . . 58
3.2.1 Battery Cells and Capacity . . . 59
3.2.2 Creation of the geometry . . . 60
3.3 Structural Simulations . . . 62
3.3.1 Simulation Setup . . . 62
3.3.2 Simulation Procedure and Results . . . 68
3.4 Composite Lay-up Optimisation . . . 70
3.5 Free Size Optimisation . . . 70
3.5.1 Parameters . . . 70
3.5.2 Result . . . 72
3.6 Size Optimisation . . . 74
3.6.1 Parameters . . . 74
3.6.2 Results . . . 75
3.7 Final Considerations . . . 80

4 Design of the Famel E-XF Battery Enclosure Prototype 81
4.1 Context and Objectives . . . 81
4.1.1 Famel E-XF Battery . . . 82
4.2 Methodology . . . 83
4.3 Initial Design . . . 87
4.3.1 Carbon Fibre Pre-preg Material . . . 88
4.3.2 Honeycomb Material . . . 89
4.3.3 Design . . . 91

5 Mechanical Validation of the Enclosure Design in FEA 93
5.1 Methodology . . . 93
5.1.1 Mechanical Drop Test . . . 93
5.1.2 Mechanical Shock Test . . . 95
5.1.3 Limitations and Considerations . . . 96
5.1.4 Unwritten Work . . . 98
5.2 Numerical Modelling . . . 98
5.2.1 Geometry . . . 98
5.2.2 Mesh . . . 100
5.2.3 Laminate . . . 106
5.2.4 Honeycomb Structure . . . 108

5.2.5 Connectors . . . 111
5.2.6 Battery Model . . . 112
5.2.7 Contact Definition . . . 115
5.2.8 Drop Test Boundary Conditions and Loads . . . 117
5.2.9 Drop Test Explicit Analysis Parameters . . . 118
5.2.10 Mechanical Shock Test Boundary Conditions and Loads . . . 120
5.2.11 Mechanical Shock Test Analysis Parameters . . . 121
5.3 Computation and Energy Checks . . . 122
5.4 Result Analysis Methodology . . . 123
5.5 Drop Test Analysis Results . . . 125
5.5.1 Drop Orientation n°1 . . . 125
5.5.2 Drop Orientation n°2 . . . 131
5.5.3 Drop Orientation n°3 . . . 134
5.5.4 Drop Orientation n°4 . . . 137
5.5.5 Drop Orientation n°5 . . . 142
5.5.6 Drop Orientation n°6 . . . 147
5.5.7 Drop Orientation n°7 . . . 149
5.5.8 Conclusion of Drop Test Simulations . . . 154
5.6 Shock Test Analysis Results . . . 154
5.6.1 **Y+** and **Y+** Shock Analyses . . . 155
5.6.2 **X** and **Z** Shock Analyses . . . 160

6 Thermal Validation of the Enclosure Design in FEA 162
6.1 Methodology . . . 162
6.2 Limitations and Considerations . . . 164
6.3 Numerical Modelling . . . 165
6.3.1 Geometry . . . 165
6.3.2 Mesh . . . 166
6.3.3 Carbon Fibre Composite Material . . . 169
6.3.4 Honeycomb Structure Material . . . 171
6.3.5 Thermal Contact . . . 173
6.3.6 Convection . . . 174
6.3.7 Heat Flux Load . . . 180
6.3.8 Linear Transient Heat Transfer Analyses Parameters . . . 181
6.4 Thermal Analysis Results . . . 181
6.4.1 Battery Heating + Free Convection . . . 182
6.4.2 Battery Heating + Forced Convection . . . 185
6.4.3 Result Takeaways . . . 187

7 Design Validation of the Enclosure 190
7.1 Internal laminate study . . . 190
7.1.1 Methodology . . . 190
7.1.2 Result study . . . 191
7.2 Enclosure Handle Validation . . . 194
7.2.1 Handle Design . . . 194
7.2.2 Handle FEA Validation Setup . . . 195
7.2.3 Analysis Results . . . 201
7.2.4 Handle Validation Conclusion . . . 205

8 Optimised Design of the Prototype Enclosure 206
8.1 Review of the Critical Areas of Design . . . 206
8.2 Optimised Design . . . 209

9 Production of the Enclosure Prototype 214
9.1 Design for Production . . . 215
9.1.1 Design changes . . . 215
9.1.2 Final Design . . . 218
9.1.3 Design Details . . . 222
9.2 Moulds . . . 227
9.2.1 Design . . . 227
9.2.2 Preparation of Stock . . . 231
9.2.3 CNC Machining . . . 233
9.2.4 Preparation . . . 236
9.3 3D Printing . . . 238
9.4 Lamination Process . . . 239
9.4.1 Preparation and Process Definition . . . 240
9.4.2 First Lamination . . . 245
9.4.3 First Autoclave Cycle . . . 250
9.4.4 Second Lamination . . . 252
9.4.5 Second Autoclave Cycle . . . 253
9.4.6 Demoulding and Finishing . . . 254

10 Carbon Fibre Composite Material Flammability Testing 257
10.1 Specimen Production . . . 257
10.2 UL 94 Horizontal Burning Test . . . 262
10.2.1 Description and Preliminary Measures . . . 262
10.2.2 Results . . . 264

11 Conclusion 267
11.1 Project Overview and Reflections . . . 267
11.2 Future Work . . . 268

References 270

A Molicel Lithium-ion Battery Cells 279
A.1 INR-21700-P42A . . . 280
A.2 INR-21700-P45B . . . 281
A.3 INR-21700-P50B . . . 282

B Toray Carbon Fibre Composite Pre-pregs 283
B.1 Toray E731 pre-preg . . . 284
B.2 Toray E745 pre-preg . . . 288
B.3 Toray E750 pre-preg . . . 289
B.4 Toray TC346 pre-preg . . . 290

C Easy Composites 6.4 mm cell Aluminium Honeycomb 308

D SikaPower®-740 (ADEKIT A140-1 / H9940-1) Epoxy Adhesive 311

E Machining Setup Sheet **317**
E.1 Bottom Mould 318
E.2 Top Mould 320

F Nesting and Ply Report **321**

List of Figures

1.1 Adamastor Furia . . . 2
1.2 Famel E-XF Classic and Café Racer . . . 3
1.3 Stark VARG MX . . . 4
1.4 Project timeline . . . 7

2.1 Passenger Car Registrations in Portugal by Energy Type, January 2025 (Adapted from [6]) . . . 10
2.2 Basic building blocks in fibre-reinforced composites (Adapted from [12]) . . . 13
2.3 Schematic representation of typical 2D woven fabric structures (Adapted from [14]). 14
2.4 Flow chart of the typical production technology of thermosetting resin composites (Adapted from [21]) . . . 18
2.5 Carbon fibre prepreg cloth . . . 19
2.6 Vacuum Bagging process [22] . . . 20
2.7 Autoclave process [13, 14] . . . 20
2.8 Horizontal burning test for HB classification [38] . . . 27
2.9 Classical Lamination Theory laminate system (Adapted from [41]) . . . 28
2.10 In-plane, bending, and twisting loads applied on a laminate [12]. . . . 30
2.11 Finite element discretisation of a 3D domain into 4 node tetrahedral elements [46] 34
2.12 Applicability of implicit and explicit analyses (Adapted from [55]) . . . 41
2.13 First and second-order solid elements common in HyperMesh® . . . 44
2.14 First and second-order quadrilateral shell elements (QUAD4 and QUAD8 in HyperMesh®) 45
2.15 First and second-order triangular shell elements (TRIA3 and TRIA6 in HyperMesh®) 45
2.16 Ply stacking sequence with respect to the element normal [57] . . . 47
2.17 Alignment of elements according to the laminate main direction, before and after orientation [57] . . . 48
2.18 a) Traditional Design b) Optimisation-driven design (Adapted from [41]) . . . 49
2.19 Visual representation of convergence (Adapted from [59]) . . . 50
2.20 Free-size ply shape generation (Adapted from [41]) . . . 51
2.21 Altair's three-step optimisation methodology [41] . . . 53

3.1 Stark Future VARG EX and its Battery [1] . . . 55
3.2 Stark Future battery "honeycomb" structure (From the YouTube video [60]) . . . 56
3.3 Outline of the geometry of the Stark VARG battery enclosure with a zoomed inset on the "honeycomb" geometry . . . 61
3.4 Outside and inside views of the CAD model of the half enclosure . . . 61
3.5 CAD model of the full enclosure . . . 62
3.6 Two-dimensional external surface of the battery half-enclosure after topology alterations in HyperMesh® . . . 63

3.7 Discretised enclosure model in HyperMesh® . . . 64
3.8 Laminate definition in HyperMesh® . . . 65
3.9 Constrained boundary conditions highlighted in HyperMesh® . . . 66
3.10 Mechanical Shock procedure for electric vehicles [65] . . . 66
3.11 Three subcase loading conditions . . . 67
3.12 Tsai–Wu failure index contour plots, Load Subcase 1 (Analysis 1 on the left, Analysis 2 on the right) . . . 69
3.13 Tsai–Wu failure index contour plots, Load Subcase 2 (Analysis 1 on the left, Analysis 2 on the right) . . . 69
3.14 Tsai–Wu failure index contour plots, Load Subcase 3 (Analysis 1 on the left, Analysis 2 on the right) . . . 70
3.15 Free size optimisation objective function convergence plot . . . 72
3.16 Thickness distribution after free-size optimisation . . . 73
3.17 Resulting ply shapes after free-size optimisation . . . 74
3.18 Size optimisation objective function convergence plot . . . 75
3.19 Mass constraint convergence plot . . . 76
3.20 Element thickness plot after size optimisation . . . 77
3.21 Element thickness plot after size optimisation, by orientation . . . 77
3.22 Ply shapes resulting from size optimisation . . . 78
3.23 Tsai-Wu failure index contour plot result of the optimised design . . . 79

4.1 Enclosure geometry, as shared by Famel (Dimensions in mm) . . . 82
4.2 Structure of the Numerical Validation part of the work . . . 84
4.3 Structure of the Production and Experimental part of the work . . . 86
4.4 Reverse-engineered CAD geometry of the enclosure provided . . . 87
4.5 Initial Enclosure Prototype Design CAD Model . . . 91

5.1 7 orientation drop test procedure highlighted in zones of contact . . . 94
5.2 Coordinate system considered for the testing simulation procedure . . . 96
5.3 Surface topology alterations by edge suppression in the enclosure model (suppressed edges in blue) . . . 99
5.4 Fillet defeature process to honeycomb core geometry . . . 100
5.5 Criterion Levels in HyperMesh® [70] . . . 101
5.6 Components discretised with shell elements . . . 102
5.7 Components discretised with solid elements . . . 102
5.8 Details in the external enclosure mesh . . . 103
5.9 Quality metrics of exterior shell mesh . . . 104
5.10 Quality Index of exterior shell mesh . . . 104
5.11 Quality Index of interior shell mesh . . . 105
5.12 Quality metrics of honeycomb core solid mesh . . . 105
5.13 Element normals of the enclosure model . . . 106
5.14 Material orientation of the enclosure model . . . 107
5.15 Laminate in HyperMesh® . . . 108
5.16 Reference directions of honeycomb structures [73] . . . 109
5.17 Honeycomb Dimensions . . . 110
5.18 Honeycomb structures and its material coordinate system in purple . . . 110
5.19 Connectors in the HyperMesh® enclosure model . . . 112
5.20 Rectangular cuboid and its principal Cartesian system . . . 113
5.21 `CONM2`, `RBE3` element and respective axis system (Drop test orientation nº1) . . . 114

5.22 RBE3 elements for drop test orientation n°4 and 5 . . . 115
5.23 Wall model with `RBE2` element in green . . . 116
5.24 Contact surfaces in HyperMesh® . . . 116
5.25 Resultant velocity direction in each drop test orientation . . . 118
5.26 Acceleration shock defined . . . 120
5.27 `TABLED1` curve in HyperMesh® . . . 121
5.28 Drop n°1 explicit simulation energy plot . . . 125
5.29 Drop n°1 contact progression . . . 127
5.30 Internal displacement progression . . . 128
5.31 Peak internal displacement by components . . . 129
5.32 Peak stress state in composite components . . . 129
5.33 Peak stress and strain state in honeycomb structure . . . 130
5.34 Drop n°2 explicit simulation energy graph . . . 132
5.35 Drop n°2 shock wave progression . . . 133
5.36 Drop n°3 explicit simulation energy graph . . . 134
5.37 Drop n°3 contact zone . . . 135
5.38 Drop n°3 external laminate stress state . . . 135
5.39 Drop n°3 honeycomb structure deformation . . . 136
5.40 Drop n°3 internal laminate deformation . . . 136
5.41 Drop n°4 explicit simulation energy graph . . . 137
5.42 Drop n°4 shock wave . . . 138
5.43 Drop n°4 element strain . . . 139
5.44 Drop n°4 contact zone . . . 139
5.45 Drop n°4 external laminate stress . . . 140
5.46 Drop n°4 honeycomb structure strain . . . 140
5.47 Drop n°4 honeycomb structure stress (Filtered in red for $\sigma_{VM} > 5$ MPa) . . . 141
5.48 Drop n°4 internal laminate stress . . . 141
5.49 Drop n°5 explicit simulation energy graph . . . 142
5.50 Drop n°5 high element strain . . . 143
5.51 Drop n°5 enclosure vertex deformation . . . 143
5.52 Drop n°5 ill-deformed elements at the edge of the honeycomb structure . . . 143
5.53 Drop n°5 contact zone . . . 144
5.54 Drop n°5 external laminate strain . . . 144
5.55 Drop n°5 external laminate stress . . . 145
5.56 Drop n°5 internal surface stress . . . 145
5.57 Drop n°5 inferior honeycomb strain . . . 146
5.58 Drop n°5 inferior honeycomb stress . . . 146
5.59 Drop n°6 explicit simulation energy graph . . . 147
5.60 Drop n°6 external laminate stress . . . 148
5.61 Drop n°7 explicit simulation energy graph . . . 149
5.62 Drop n°7 enclosure vertex deformation . . . 150
5.63 Drop n°7 external laminate strain . . . 150
5.64 Drop n°7 peak contact zone . . . 151
5.65 Drop n°7 first and last contact instances . . . 151
5.66 Drop n°7 external laminate stress . . . 152
5.67 Drop n°7 superior honeycomb strain . . . 152
5.68 Drop n°7 superior honeycomb stress (Filtered in red for $\sigma_{VM} > 5$ MPa) . . . 153
5.69 Drop n°7 internal surface stress . . . 153

5.70 **Y+** shock explicit simulation energy graph . . . 155
5.71 **Y-** shock explicit simulation energy graph . . . 156
5.72 Nodal displacement at instant of peak deformation (**Y+** simulation to the left and **Y-** to the right) . . . 157
5.73 Nodal displacement in honeycomb cores at instant of peak deformation (**Y+** simulation to the left and **Y-** to the right) . . . 157
5.74 P_1 principal stress in honeycomb cores at instant of peak deformation, filtered in red for $\sigma_{VM} > 1.6$ MPa (**Y+** simulation to the left and **Y-** to the right) . . . 158
5.75 P_1 principal stress in internal laminate at instant of peak deformation (**Y+** simulation to the left and **Y-** to the right) . . . 158
5.76 P_1 principal stress in external laminate at instant of peak deformation (**Y+** simulation to the left and **Y-** to the right) . . . 159
5.77 **X** shock explicit simulation energy graph . . . 160
5.78 **Z** shock explicit simulation energy graph . . . 161

6.1 Solid CAD enclosure model for thermal analysis in SolidWorks® (Section view) . 165
6.2 3D topology visualisation tool applied to the model . . . 166
6.3 Laminate components discretised with solid elements . . . 167
6.4 Honeycomb components discretised with solid elements . . . 167
6.5 Jacobian matrix mesh quality metric (elements under 0.6 isolated to the right) . . 168
6.6 Aspect ratio mesh quality metric (elements over 5 isolated to the right) . . . 168
6.7 `MAT5` materials created for the carbon fibre laminate material of the model enclosure 171
6.8 Unit cell of a hexagonal honeycomb with non-uniform thickness cell walls, dimensions and axis orientation (Adapted from [32]) . . . 172
6.9 Honeycomb structures and global axis system in HyperMesh® . . . 173
6.10 Visualisation of the thermal contact in HyperMesh® . . . 173
6.11 Free convection zones considered, colour-coded . . . 175
6.12 Forced convection zones considered, colour-coded with air direction identified . . 178
6.13 Heat flux load visualisation in HyperMesh® . . . 180
6.14 Temperature evolution of key points of the enclosure . . . 182
6.15 Temperature contour plot of the enclosure at timestep $t = 6.0 \times 10^4$ ms (60 seconds) 182
6.16 Temperature contour plot of the enclosure at the final timestep $t = 1.8 \times 10^6$ ms (30 minutes) . . . 183
6.17 Element fluxes contour plot of the enclosure at the final timestep $t = 1.8 \times 10^6$ ms (30 minutes) . . . 185
6.18 Temperature evolution of key points of the enclosure . . . 185
6.19 Temperature contour plot of the enclosure at timestep $t = 9.0 \times 10^4$ ms (90 seconds) 186
6.20 Temperature contour plot of the enclosure at the final timestep $t = 1.8 \times 10^6$ ms (30 minutes) . . . 186
6.21 Element fluxes contour plot of the enclosure at the final timestep $t = 1.8 \times 10^6$ ms (30 minutes) . . . 187
6.22 Temperature contour plot of aluminium enclosure model at the final timestep $t = 1.8 \times 10^6$ ms (30 minutes) . . . 188

7.1 Deformation contour of the enclosure components, 6-ply, 8-ply and 4-ply internal laminates, from left to right, respectively . . . 192
7.2 P_1 principal stress contour of the internal laminate, 6-ply, 8-ply and 4-ply internal laminates, from left to right, respectively . . . 192

7.3 Maximum shear stress contour of the internal laminate, 6-ply, 8-ply and 4-ply internal laminates, from left to right, respectively . . . 193
7.4 Simple handle CAD design in SolidWorks ® . . . 195
7.5 Discretised handle geometry . . . 196
7.6 Nodal density around hole geometry . . . 196
7.7 Quality Index (Q.I.) plot of handle mesh . . . 197
7.8 Jacobian matrix plot of handle mesh . . . 197
7.9 Aspect ratio plot of handle mesh . . . 197
7.10 Handle laminate in HyperMesh®. . . . 198
7.11 Schematic representation of the loads and boundary conditions applied . . . 199
7.12 Close up of the boundary conditions in the handle clearance hole . . . 199
7.13 Distributed load and symmetry boundary conditions applied to the model . . . 200
7.14 Deformation behaviour of the handle under analysis (Scale:2.0) . . . 201
7.15 Displacement contour of the handle under analysis . . . 201
7.16 P_1 (major) principal strain countour plot of the model under analysis . . . 202
7.17 Tsai-Wu composite failure index contour plot of the handle under analysis . . . 202
7.18 Composite bond failure index contour plot results . . . 202
7.19 Maximum P_1 principal composite stress contour plot results . . . 203
7.20 Maximum shear stress contour plot results . . . 204
7.21 Maximum $1Z$ interlaminar shear stress contour plot results . . . 204
7.22 Maximum $2Z$ interlaminar shear stress contour plot results . . . 205

8.1 Filtered contour plots results from drop test orientation nº4 . . . 207
8.2 Filtered contour plots results from drop test orientation nº5 . . . 207
8.3 Filtered contour plots results from drop test orientation nº7 . . . 208
8.4 Maximum shear stress filtered contour plot results from drop test orientation nº3 . 208
8.5 Outline of reinforcements defined for the optimised enclosure design . . . 209
8.6 Optimised enclosure prototype design with the reinforcement integrated into it, along with the honeycomb structures . . . 210
8.7 Top reinforcement CAD model . . . 211
8.8 Bottom reinforcement CAD model . . . 212
8.9 Illustration of the integration of the reinforcements into the external enclosure laminate . . . 212

9.1 Battery provided by Famel for dimensional verification . . . 216
9.2 Exploded view of the final enclosure prototype design . . . 218
9.3 Enclosure lid in SolidWorks® . . . 219
9.4 3D-printed core in SolidWorks® . . . 219
9.5 Top honeycomb structure in SolidWorks® . . . 219
9.6 Bottom reinforcement SolidWorks® CAD model . . . 220
9.7 SolidWorks® CAD model of the bottom laminate of the enclosure . . . 220
9.8 Assembled enclosure prototype CAD model with global dimensions . . . 221
9.9 Sectional view of the assembled enclosure prototype showing internal dimensions 221
9.10 Adhesive flange feature for connection between the top and bottom parts of the enclosure . . . 223
9.11 Laminate design detail nº1 . . . 225
9.12 Laminate design detail nº2 . . . 225
9.13 bigHead® components integration into composite laminates [103] . . . 226
9.14 Laminate design detail nº3 . . . 226

9.15 bigHead® design and application guidance [104] . . . 227
9.16 Mould designs in SolidWorks®, stock dimensions in wireframe representation . . 228
9.17 Features in the design of the bottom half-mould . . . 229
9.18 Features in the design of the bottom half-mould (assembled) . . . 229
9.19 Hole positioning feature in the top mould . . . 230
9.20 Features in the handle mould . . . 230
9.21 Draft angle analysis on the three mould designs . . . 231
9.22 Epoxy tooling board stock optimisation . . . 232
9.23 Epoxy adhesive application to the epoxy blocks . . . 232
9.24 Stock vacuum bagging process . . . 233
9.25 Bottom half-mould at the end of CAM simulation . . . 234
9.26 Top mould at the end of CAM simulation . . . 234
9.27 Details from the CAM machining program . . . 235
9.28 CNC machining of the bottom half-moulds . . . 235
9.29 Moulds after machining . . . 236
9.30 Close-up views of the moulds after machining . . . 236
9.31 Bottom half-moulds after application of mould sealer . . . 237
9.32 Top mould insert positioning solution . . . 238
9.33 Cores and reinforcement after additive manufacturing . . . 238
9.34 Sanded printed cores . . . 239
9.35 Nesting layout for the bottom component . . . 240
9.36 “Horizontal” ply configuration . . . 241
9.37 “Vertical” ply configuration . . . 242
9.38 Layup sequence of the top laminate . . . 242
9.39 Ply shape templates for the bottom laminate . . . 244
9.40 Cut plies from the “Horizontal” configuration . . . 244
9.41 Prepared honeycomb panels . . . 244
9.42 Moulds and prepreg materials ready for manufacturing . . . 245
9.43 First plies conformed to the bottom mould after debulking . . . 246
9.44 Mould during the second debulking process . . . 246
9.45 Bottom mould with reinforcement positioned . . . 247
9.46 Prepreg cuts for conformation on the top mould . . . 247
9.47 Lamination details in the top mould . . . 248
9.48 Application of release film and breather cloth in the vacuum bagging process . . 249
9.49 Vacuum bagging detail in the top mould . . . 249
9.50 Vacuum gauge during the “drop test” procedure . . . 250
9.51 Moulds in the autoclave before the first autoclave cycle . . . 250
9.52 Autoclave process readings . . . 251
9.53 First autoclave cycle . . . 251
9.54 Details of manufacturing of the top enclosure component . . . 252
9.55 Additional manufacturing details . . . 253
9.56 Second autoclave cure process . . . 253
9.57 Second autoclave cycle . . . 254
9.58 Second autoclave cure process . . . 255
9.59 Enclosure after removal of excess material . . . 255
9.60 Enclosure components after trimming process . . . 256
9.61 Enclosure weight measurement . . . 256

10.1 Lamination of plies for specimen production . . . 258

10.2 Vacuum bagging of specimen laminates . . . 258
10.3 Specimen laminates inside the autoclave before cure . . . 259
10.4 Cured specimen laminates . . . 259
10.5 Specimen preparation . . . 260
10.6 UL chamber used during testing . . . 262
10.7 Specimen during testing conditions, exposed to the flame . . . 264
10.8 Specimen during testing conditions, flame removed . . . 264
10.9 Specimen after testing . . . 266

A.1 Product data sheet of Molicel INR-21700-P42A [107] . . . 280
A.2 Product data sheet of Molicel INR-21700-P45B [108] . . . 281
A.3 Product data sheet of Molicel INR-21700-P50B [109] . . . 282

B.1 Page 1 of Toray's E731 pre-preg datasheet [66] . . . 284
B.2 Page 2 of Toray's E731 pre-preg datasheet [66] . . . 285
B.3 Page 3 of Toray's E731 pre-preg datasheet [66] . . . 286
B.4 Page 4 of Toray's E731 pre-preg datasheet [66] . . . 287
B.5 Page 5 of Toray's E731 pre-preg datasheet [66] . . . 288
B.6 Page 1 of Toray's E745 pre-preg datasheet [68] . . . 289
B.7 Page 2 of Toray's E745 pre-preg datasheet [68] . . . 290
B.8 Page 3 of Toray's E745 pre-preg datasheet [68] . . . 291
B.9 Page 4 of Toray's E745 pre-preg datasheet [68] . . . 292
B.10 Page 5 of Toray's E745 pre-preg datasheet [68] . . . 293
B.11 Page 1 of Toray's E750 pre-preg datasheet [67] . . . 294
B.12 Page 2 of Toray's E750 pre-preg datasheet [67] . . . 295
B.13 Page 3 of Toray's E750 pre-preg datasheet [67] . . . 296
B.14 Page 4 of Toray's E750 pre-preg datasheet [67] . . . 297
B.15 Page 5 of Toray's E750 pre-preg datasheet [67] . . . 298
B.16 Page 6 of Toray's E750 pre-preg datasheet [67] . . . 299
B.17 Page 7 of Toray's E750 pre-preg datasheet [67] . . . 300
B.18 Page 1 of Toray's TC346 pre-preg datasheet [63] . . . 301
B.19 Page 2 of Toray's TC346 pre-preg datasheet [63] . . . 302
B.20 Page 3 of Toray's TC346 pre-preg datasheet [63] . . . 303
B.21 Page 4 of Toray's TC346 pre-preg datasheet [63] . . . 304
B.22 Page 5 of Toray's TC346 pre-preg datasheet [63] . . . 305
B.23 Page 6 of Toray's TC346 pre-preg datasheet [63] . . . 306
B.24 Page 7 of Toray's TC346 pre-preg datasheet [63] . . . 307

C.1 Page 1 of Aluminium Honeycomb datasheet . . . 309
C.2 Page 2 of Aluminium Honeycomb datasheet . . . 310

D.1 Page 1 of SikaPower®-740 datasheet . . . 312
D.2 Page 2 of SikaPower®-740 datasheet . . . 313
D.3 Page 3 of SikaPower®-740 datasheet . . . 314
D.4 Page 4 of SikaPower®-740 datasheet . . . 315
D.5 Page 5 of SikaPower®-740 datasheet . . . 316

E.1 Page 1 of bottom mould CNC machining setup sheet . . . 318
E.2 Page 2 of bottom mould CNC machining setup sheet . . . 319
E.3 Top mould CNC machining setup sheet . . . 320

F.1 Nesting report page 1 322
F.2 Nesting report page 2 323
F.3 Nesting report page 3 324
F.4 Nesting report page 4 325
F.5 Nesting report page 5 326
F.6 Nesting report page 6 327

List of Tables

2.1 Specification comparison of the Famel E-XF motorcycle and other direct competitors 11
2.2 Specifications of electric motorcycles currently in production 12
2.3 Properties of epoxy-matrix fibre-reinforced composites, comparison of different unidirectional (UD) pre-pregs with UD layup [11, 18–20] 17
2.4 Heat Transfer and Structural Analysis Analogy [49] 37

3.1 Unit system chosen for finite element analysis 63
3.2 Analysis 1 mesh statistics 64
3.3 Analysis 2 (Fillet) mesh statistics 64
3.4 Properties of Toray 346 Intermediate Modulus 6K Carbon 200gsm 2x2 Twill 42% RC prepreg composite material [63, 64] 65
3.5 Results from initial linear static FEA for three load cases, comparing the baseline design (Analysis 1) and a filleted version (Analysis 2) 68
3.6 Laminate input for optimisation 71
3.7 Free size optimisation input parameters 71
3.8 Laminate after free size optimisation 73
3.9 Size optimisation input parameters 75
3.10 Laminate after size optimisation 76
3.11 Comparison of results between the optimised and original design 78

4.1 Properties of E731-00 HS2238 Carbon TR30S T 245gsm 2 x 2 Twill 3K 42% RC prepreg composite material [64, 66] 89
4.2 Properties of 6.4mm Cell 3003 Aluminium Series Honeycomb from Easy Composites 90

5.1 7 orientation drop test procedure description 95
5.2 Unit system chosen for finite element analysis 99
5.3 Mesh Statistics 103
5.4 Laminate specifications for the enclosure model 107
5.5 Drop test explicit dynamic analysis settings 119
5.6 Mechanical shock test explicit dynamic analysis settings 121
5.7 Maximum meaningful values of stress and strain state, by component (Orientation n°1) 131
5.8 Maximum meaningful values of stress and strain state, by component (Orientation n°2) 134
5.9 Maximum meaningful values of stress and strain state, by component (Orientation n°3) 137
5.10 Maximum meaningful values of stress and strain state, by component (Orientation n°4) 142

5.11 Maximum meaningful values of stress and strain state, by component (Orientation nº5) . . . 147
5.12 Maximum meaningful values of stress and strain state, by component (Orientation nº6) . . . 149
5.13 Maximum meaningful values of stress and strain state, by component (Orientation nº7) . . . 154
5.14 Maximum meaningful values of stress and strain state, by component (Mechanical Shock **Y+**) . . . 159
5.15 Maximum meaningful values of stress and strain state, by component (Mechanical Shock **Y-**) . . . 160

6.1 Thermal model mesh Statistics . . . 167
6.2 Battery Heating + Free Convection analysis settings . . . 181

7.1 Energy absorption metrics for different internal laminates . . . 191
7.2 Comparison of post-processing results of different internal laminates . . . 193
7.3 Comparison of the resulting enclosure mass for different internal laminates . . . 194
7.4 Handle model mesh Statistics . . . 196
7.5 Handle laminate specifications . . . 198

9.1 Bottom half-mould CNC machining statistics . . . 233
9.2 Top mould CNC machining statistics . . . 234

10.1 E731 prepreg specimens dimensions and mean ply thickness . . . 261
10.2 Specimen measurements made by Inegi . . . 263
10.3 Horizontal burning test results . . . 265

List of Acronyms

GT	Grand Tourer
UN ECE	United Nations Economic Commission for Europe
UL	Underwriters Laboratories
HB	Horizontal Burning
BEV	Battery Electric Vehicle
EV	Electric Vehicle
ICE	Internal Combustion Engine
R&D	Research and Development
PHEV	Plug-in Hybrid Electric Vehicle
HEV	Hybrid Electric Vehicle
CAGR	Compound Annual Growth Rate
FRC	Fiber-Reinforced Composite
PMC	Polymeric Matrix Composite
PEEK	Polyether ether ketone
UD	Unidirectional
CNC	Computer Numerical Control
REESS	Rechargeable Electrical Energy Storage System
CLT	Classical Lamination Theory
2D	Two-dimensional
3D	Three-dimensional
FPF	First Ply Failure
LPF	Last Ply Failure
FEM	Finite Element Method
FEA	Finite Element Analysis
CAD	Computer-Aided Design
CAE	Computer-Aided Engineering

Chapter 1

Introduction

1.1 Objectives and Motivation

In recent years, the global mobility sector has undergone a profound transformation driven by the urgent need to reduce greenhouse gas emissions and transition towards sustainable transport solutions. This shift has stimulated rapid technological progress in electric mobility, not only in the automotive industry but also in the field of two-wheeled vehicles. The transition from fossil fuels to fully electric propulsion systems has emerged as the central pathway toward achieving cleaner and more efficient mobility.

The interest in electric motorcycles has been steadily increasing, with manufacturers introducing new and progressively more refined models every year. These vehicles combine performance, efficiency, and reduced environmental impact, positioning themselves as viable and attractive alternatives to conventional combustion motorcycles.

At the core of this transition lies the battery system, the most critical component of an electric motorcycle. Batteries determine key performance aspects such as range, weight distribution, and overall efficiency, while also influencing vehicle safety and longevity. Given their structural and functional relevance, the battery enclosures that house these systems play a crucial role. Beyond providing mechanical protection, they must integrate multiple functions, including electrical connectivity, thermal management, mechanical fixation, and environmental shielding, all while contributing to the aesthetic and structural integrity of the motorcycle. Moreover, these components are subject to stringent safety regulations, ensuring safety in electric motorcycles.

In parallel, the past decade has seen a growing emphasis on composite materials, whose superior strength-to-weight ratio and design flexibility make them attractive for applications where both performance and efficiency are critical. The convergence of these two areas, electric mobility and advanced composites, opens new possibilities for the development of composite battery enclosures, offering significant benefits in terms of weight reduction, enhanced mechanical performance, improved safety, and greater design freedom.

The present project is positioned within this context, focusing on the design and development of composite battery enclosures for electric motorcycles. Its main objective is to establish and

apply a methodology that ensures these enclosures fulfil all their structural, functional, and safety requirements, while adhering to the homologation standards imposed on such critical components. Beyond the conceptual and computational stages, this work aims to extend the methodology to practical implementation, encompassing design, optimisation, prototyping, and experimental validation, thereby demonstrating a complete workflow for the development of a composite battery enclosure from concept to prototype testing.

1.2 Intervenient Companies

The present work was carried out at Adamastor and developed in collaboration with Famel and Stark Future, within separate projects dedicated to the products of each company.

1.2.1 Adamastor

Adamastor is a Portuguese low-volume supercar manufacturer based in Perafita, the host company for this dissertation project. Focused on innovation, technology, and engineering, its activities account for several in-house projects encompassing all stages of development, from concept to the final product, integrating areas of engineering, design, and manufacturing.

Founded in 2010 from the collaboration of automobile enthusiasts, the current team of 14 professionals holds extensive experience in composite materials and the automobile industry, particularly in motorsports, ranging from GT racing to the pinnacle of Formula 1. Adamastor revealed its first prototype in 2012, and in 2017 launched its first model, the Adamastor P003RL, a lightweight, track-focused road car with 80% of its components sourced nationally.

In 2024, Adamastor revealed its most ambitious project to date with the unveiling of the Adamastor Furia, the first Portuguese supercar. Furia is a mid-engined, carbon fibre composite monocoque performance-oriented supercar powered by a Ford Performance bi-turbo V6 producing over 650 horsepower. It features a cutting-edge aerodynamic design and patented suspension geometry. Beyond producing a supercar, the team aims to expand its activities and enroll the Furia in motorsport, specifically in the 24h Series and Le Mans, in the GT category.

Figure 1.1: Adamastor Furia

Alongside the development of the Furia, Adamastor provides advanced engineering solutions for other companies, particularly in the field of composite material components, where this dissertation finds its place.

1.2.2 Famel

Famel is a historic Portuguese motorcycle manufacturer, originally founded in Águeda in the late 1940s by three partners with the initial purpose of producing moped and bicycle rims. In 1952, the company expanded its activity to the manufacture of mopeds, producing over thirty different models until its closure in 1994. Throughout its history, Famel used engines from several manufacturers, most notably Zündapp.

Its first model, the Utilitária (1952), marked the beginning of its production line, while the Famel Electric (1994), an electric scooter, was its last. Among its most iconic creations was the Foguete (1957), and particularly the XF-17, launched in 1975, which became one of the most popular motorcycles in Portugal during the 1980s and 1990s.

After the company's insolvency in 2002, the Famel brand remained dormant until 2014, when its revival was announced through an electric mobility project. This initiative evolved into the development of a new model inspired by the legendary XF-17, now featuring full electric propulsion. Currently based in Guimarães, Famel is preparing for the commercial launch of its new electric motorcycle, the Famel E-XF, in the near future.

Figure 1.2: Famel E-XF Classic and Café Racer

1.2.3 Stark Future

Stark Future is a company founded in 2020, headquartered in Barcelona, dedicated to the design and manufacture of high-performance electric motorcycles. The company was established with the ambition of accelerating the transition toward sustainable, zero-emission motorcycling by combining cutting-edge electric propulsion technology with advanced engineering and design [1].

Its first and flagship product, the Stark VARG, was unveiled in late 2021 and quickly gained international attention for redefining electric motocross performance. The motorcycle delivers power comparable to, or exceeding, that of traditional combustion-engine motocross bikes, while

offering significantly reduced noise, zero emissions, and minimal maintenance requirements. Designed and developed entirely in-house, the VARG integrates a lightweight carbon and aluminium chassis, advanced battery systems, and a fully customisable power delivery through an intuitive digital interface [1].

Stark Future positions itself as a technology-driven company focused on innovation, performance, and sustainability. Its engineering philosophy prioritises high power-to-weight ratios, efficiency, and rider experience, aiming to demonstrate that electric technology can not only match but surpass conventional motorcycling performance. Through its pioneering approach, Stark Future represents a new benchmark in the electrification of off-road and high-performance motorcycles [1].

Figure 1.3: Stark VARG MX

1.3 Methodology

The main objective of this work is to establish a methodology for the design and development of a composite battery enclosure for an electric motorcycle, one capable of fulfilling all its functional, structural, and safety requirements, while complying with the applicable homologation standards. Beyond its formulation, this methodology is also intended to be implemented in practice, following each stage through to the fabrication of a real composite prototype.

The foundation for defining this methodology was twofold. Firstly, it was based on the requirements and specifications defined by each collaborating company, including the dimensional, mechanical, thermal, and weight constraints derived from both the battery system and the motorcycle architecture. Secondly, the methodology was guided by the safety and homologation regulations governing the approval and commercialisation of batteries and related components for electric motorcycles in Europe. These regulations impose stringent standards on mechanical integrity, thermal behaviour, and fire resistance, providing not only legal but also performance benchmarks for design. The consulted standards include UN ECE R100.03, UN ECE R136, and the UL 94 Standard for Flammability of Plastic Materials.

From these foundations, a comprehensive and sequential methodology was developed, encompassing the conceptual design, numerical validation through mechanical and thermal finite

element analyses, design optimisation, prototype manufacturing using composite fabrication techniques, and experimental validation through laboratory testing. This framework establishes a robust and systematic approach that ensures the reliability, performance, and safety of the developed enclosure.

The dissertation is structured around two distinct case studies, developed in collaboration with two different companies: Famel and Stark Future. Both aimed to apply the proposed methodology, though each followed a different trajectory.

Initially, the project was conceived exclusively in collaboration with Famel. However, due to misalignment between the project's timeline and the stage of development of Famel's motorcycle and battery system, an alternative collaboration was pursued with Stark Future. While the partnership with Stark Future began promisingly, it was discontinued at an early stage, before the complete implementation of the design and validation process could take place. Nevertheless, the work conducted, including reverse engineering of the existing Stark VARG enclosure, structural finite element simulations, composite lay-up optimisation, and thermal analyses using the Altair HyperWorks® suite, provided valuable insights and technical experience. Despite being limited in scope, this preliminary study proved instrumental for the development of the subsequent Famel project.

The second case study, developed for Famel, followed the intended methodological framework more closely. It involved the reverse engineering of the initial design, mechanical and thermal finite element validations in accordance with both regulatory and design requirements, design optimisations, prototype fabrication through composite manufacturing processes, and the planning and execution of experimental testing, including UL 94 flammability tests and mechanical tests inspired by the UN ECE R136 procedures.

For the computational and design work, SolidWorks® was employed for CAD modelling, Altair HyperMesh® / OptiStruct® for finite element analysis and composite lay-up optimisation, and Autodesk Fusion® for defining and programming machining operations.

The details of each stage of this methodology, as well as the results obtained, are presented in the subsequent chapters, within the context of each case study.

1.4 Project Timeline

This section presents the sequence of activities carried out over the 37 weeks allocated for the completion of this dissertation project, distinguishing between the periods dedicated to the Stark Future and Famel collaborations. It is important to note that the project experienced several setbacks and changes in direction, which required continuous adaptation and iterative decision-making to ensure progress toward the defined objectives.

The initial phase, spanning weeks 1 to 6, was dedicated to research and literature review. During the first four weeks, the focus remained on the Famel project, as the collaboration change had not yet been initiated. In week 5, the first meeting with Stark Future took place, and from that point onward, the project focus shifted entirely to this new collaboration.

Between weeks 7 and 11, the work concentrated on the Stark Future enclosure study, including the reverse engineering of the existing enclosure geometry, structural and thermal finite element analyses, and composite lay-up optimisation for a carbon fibre reinforced enclosure design.

From weeks 12 to 17, the project was temporarily without an active industrial partner, as Stark Future had quietly discontinued its participation. During this period, efforts focused on the writing of the dissertation and exploring the possibility of effectively starting the collaboration with Famel.

The Famel project was formally resumed between weeks 18 and 21, with tasks centred on the reverse engineering of the enclosure geometry and mechanical validation through finite element simulations. Weeks 22 and 23 were dedicated to the thermal analysis of the composite enclosure design.

From weeks 23 to 28, the work focused on a redesign phase, including the optimisation of the enclosure, dimensional adjustments due to updates in Famel's battery system, and the preparation of the final geometry for production. This period also included the design of the production moulds.

Between weeks 28 and 34, the focus shifted to prototype manufacturing preparation, including the machining and finishing of the moulds, 3D printing of core components, and the definition of the lay-up plan and ply nesting for lamination. During this phase, UL 94 HB flammability test specimens were also fabricated.

On the 3rd of September (week 30), the UL 94 HB flammability testing was conducted at INEGI's Flame Testing Laboratory.

The prototype fabrication took place over three consecutive days between weeks 34 and 35, using prepreg hand lamination and autoclave curing.

Finally, weeks 36 and 37 were dedicated to the writing, refinement, and completion of the dissertation document.

The overall sequence of tasks described above is summarised in the Gantt chart presented in Figure 1.4.

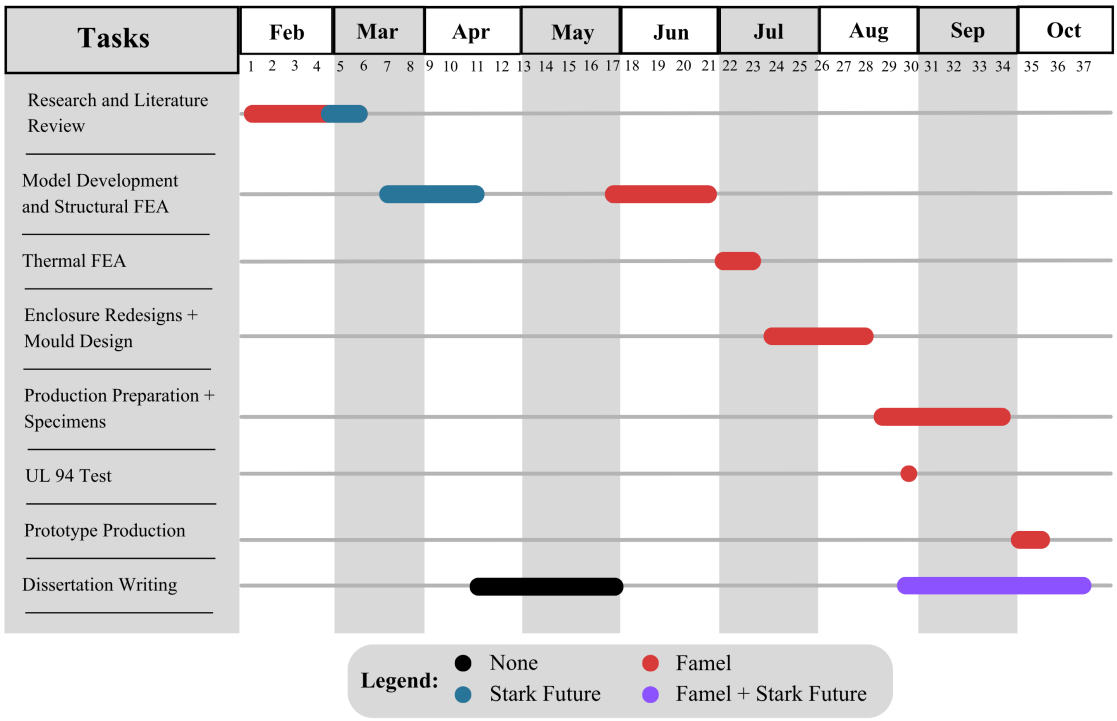

Figure 1.4: Project timeline

1.5 Structure of the Dissertation

The dissertation is organised into several chapters, each addressing a specific stage of the project.

Chapter 2 presents the state of the art, where the concepts necessary to understand the scope of this work are introduced fully. It begins with a review of the current state of electric mobility and a benchmarking of the motorcycle models considered in this project. This is followed by an overview of composite materials and a review of relevant literature, as well as the presentation of the regulations and standards that guided the work. The chapter concludes with an explanation of the finite element methods used, static, explicit dynamic, and thermal, and a discussion on composite modelling and lay-up optimisation within Altair OptiStruct® and HyperMesh®.

Chapter 3 concerns the Stark Future project, providing a detailed description of the work carried out in reverse engineering, structural finite element analyses, and composite lay-up optimisation of a carbon fibre enclosure design. The chapter concludes with the main findings and insights obtained from this preliminary study.

Chapter 4 introduces the Famel collaboration and the design of the E-XF battery enclosure prototype. It explains the development context and the methodology employed for the design and preparation of the prototype.

Chapter 5 addresses the mechanical validation of the Famel enclosure design in accordance with the mechanical testing procedures defined by the UN ECE R136 regulation. The validation

strategy is outlined, the finite element models are described, and the results are analysed and discussed.

Chapter 6 presents the thermal finite element study of the Famel composite enclosure design. The model setup, methodology, and results are discussed, providing insights into the thermal behaviour of the component.

Chapter 7 focuses on two complementary design validation studies: the optimisation of the internal laminate to enhance its efficiency, and the mechanical validation of a carbon fibre composite handle design under simulated loading conditions.

Chapter 8 explores an optimised design concept for the composite battery enclosure, with a focus on improving its mechanical integrity and ensuring greater protection of the battery system.

Chapter 9 details the production-related stages, including the final redesign of the enclosure to meet manufacturing constraints, the design and machining of the moulds, the 3D printing of core components, the definition of ply and nesting strategies, and the full prepreg lay-up and autoclave curing process used to manufacture the prototype.

Finally, Chapter 10 presents the manufacturing of composite specimens and their UL 94 flammability testing. The procedures, conditions, and results are discussed, assessing the flame-retardant behaviour of the developed composite materials.

Chapter 2

State of the art

2.1 Electric Mobility

Mobility is an essential aspect of the modern, ever more connected world, encompassing personal transportation, public transit, logistics, and infrastructure. The way society thinks about mobility has significantly changed with the advancement of technology and the shift in mentality with regard to the environmental consequences of human activity [2].

The emerging solution to sustainable transportation has been in the development of battery electric vehicles (BEVs). Electric vehicles (EVs) are, in their concept, not a recent phenomenon; they had an early appearance and decline in the late 19th and early 20th century, when the automobile was in its infancy. Through the course of the 1960s to 1990s, a series of regulatory incentives and environmental policies with origin in the United States (Zero-Emission Vehicle Program) and later in Europe sparked institutional and private Research and Development (R&D) programs in EV technology [3]. Although a significant push for the adoption and democratization of EVs was made, with the implementation of several pilot and demonstration projects with subsidies incentives in Europe (Rugen Island, Mendriso, La Rochelle, and others) and the arrival of electric vehicles such as the *Peugeot 106 Électrique*, *Renault Clio Électrique* and *Honda EV Plus*, the public interest in EVs remained very low [4]. A key reason for the disappointment in the mass commercialization of battery electric vehicles (BEVs) was the limited technological progress achieved during the 1990s, particularly in battery development and the consequent high price and low range. During this period, electric vehicles were primarily equipped with lead-acid batteries, which resulted in a short lifespan and limited range. Towards the end of the decade, research and development shifted focus to nickel-metal hydride and lithium-ion batteries, but these remained expensive due to low production volumes [3]. Come the mid 2000s, concerns about climate change and the search for more sustainable technologies motivated stricter emissions targets and a new wave of development, especially concerning battery technology with the collaboration of battery suppliers and manufacturers in Japan, such as *Toyota* and *Panasonic* or *Honda* and its *Blue Energy Venture*. In addition to technology advancements, government funding and incentives like American government investments, European Commission R&D programs, Japan subsidies

for the purchase of BEVs and tax exemptions stimulated research, charging infrastructure. As a result, sales of EVs started to represent a small part of automotive sales in the 2010s.

Electric vehicles (EVs) have gained a significant market share in recent years, with a notable growth in the last five years, sparked, in part, by the entry of competitive brands from China. This expansion includes various electrically powered vehicles, from electric cars to buses, scooters, and bicycles [5]. Several factors reinforce this increase in mobility electrification, such as government policies and incentives, technological advancements, improved charging infrastructure, and growing customer demands [2].

As of January 2025, battery electric vehicles (BEVs) account for 22.4% of the passenger car registrations in Portugal, a substantial increase from 5.2% in 2020. Together, battery electric vehicles (BEVs), Plug-in Hybrid Electric Vehicles (PHEVs), and Hybrid Electric Vehicles (HEVs) now account for more than half of the registrations. The pie chart in Figure 2.1 illustrates this distribution [6].

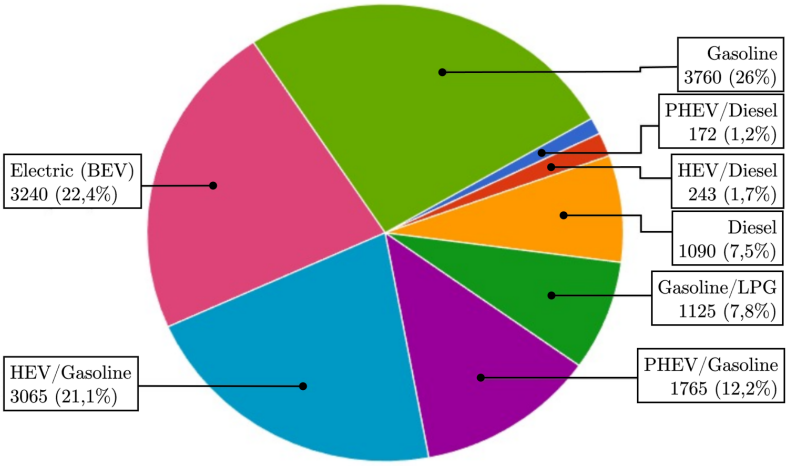

Figure 2.1: Passenger Car Registrations in Portugal by Energy Type, January 2025 (Adapted from [6])

The future of electric mobility is promising. Europe is one of the leaders in the race for the transition to zero-emission transportation, and in Portugal, the adoption of EVs is expected to grow significantly, driven by the goal of achieving carbon neutrality by 2050 [7]. Projections indicate that the global electric mobility market is expected to grow at a Compound Annual Growth Rate (CAGR) of 20% between 2024 and 2032 [2].

Motorcycles and small two-wheelers such as mopeds represent a growing portion of the mobility market, as seen, there is a trend towards mobility electrification, with potential for an increasing demand in electric motorcycles, scooters, mopeds and e-bikes. Over the last year in Portugal, a total of 46540 motorcycles, scooters and mopeds were registered, 1066 of these were electric [8]. Though they represent a small portion of registrations in Portugal, other countries such as Italy are particularly fond of electric motorcycles and lead in registrations in Europe with 11 400 registrations in 2022 [9].

In other parts of the world, the Asia-Pacific region is a major market for electric two-wheel mobility, in particular in the electric scooter and moped section. Countries such as Taiwan, Singapore, Indonesia are pioneers in the adoption of large-scale solutions for personal electric mobility via the usage of electric scooters. One example is Gogoro, a Taiwanese company, revolutionized urban mobility with their widespread battery swapping system, enabling users with an electric mobility experience without the usual range limitation. The establishment of a widespread network of battery swap stations can meet the battery needs of EMVs anytime, anywhere, through the change of a depleted battery with a charged one at a station [10].

Portugal and Europe may follow these trends in two-wheel electric mobility, making electric motorcycles a viable mobility choice. Electric two-wheel mobility can be attractive in the particular conditions that medium to large cities offer, and the way of life of its inhabitants. Low- distance commutes with busy traffic conditions (slow speed, congestion, lack of parking) and numerous charging opportunities combined with the low cost of running and low maintenance inherent to electric two-wheelers make them an attractive transport solution in urban environments.

2.2 Benchmarking

To contextualise the development of the present project, a benchmarking study was conducted to compare the Famel E-XF and Stark VARG MX motorcycles with other electric two-wheelers currently available on the market. The main specifications of competing models are summarised in Tables 2.1 and 2.2.

Table 2.1: Specification comparison of the Famel E-XF motorcycle and other direct competitors

Model	Famel E-XF	Maeving RM1	Super Soco TC Max	Horwin CR6
Style	**Café Racer**	Café Racer	Café Racer	Café Racer
Equivalent	**125 cc**	125 cc	125 cc	125 cc
Rated Power	**-**	3.0 kW/4 hp	-	-
Max. Power	**5 kW/6.7 hp**	4.4 kW/5.9 hp	5.1 kW/6.9 hp	5.3 kW/7.1 hp
Range	**Up to 120 km**	Up to 130 km	Up to 100 km	Up to 120 km
Battery	**2 × Li-ion** **1.8 kWh/37.5 Ah** **(48 V)**	2 × Li-ion 2 kWh/42 Ah (50.4 V)	Li-ion 3.24 kWh/45 Ah (72 V)	2 × Li-ion 3.8 kWh/53 Ah (72 V)
Removable Batteries	**Yes**	Yes	Yes	No
Max. Speed	**>100 km/h**	72.5 km/h	95 km/h	95 km/h
Charge Time	**≈ 5h**	4h Fast Charging	5h Fast Charging	3h for 0-80%
Weight	**-**	124 kg	101 kg	134 kg W/O Battery
Base Price	**6 500 €**	7 250 €	4 499 €	6 990 €

The Famel E-XF, a 125 cc equivalent café racer, positions itself in the same segment as models such as the Maeving RM1, Super Soco TC Max, and Horwin CR6. In comparison, the E-XF presents competitive performance values, with a peak power of 5 kW and a top speed exceeding 100 km/h. Its dual 1.8 kWh removable battery configuration allows for a range above 120 km, comparable to or slightly higher than most direct competitors. The charging time of approximately

five hours is consistent with others in its class, while its projected base price of 6 500 € places it within the middle range of the segment. As the E-XF is still under development, these values may vary in the production version. It is also important to note that range and charging times should be interpreted as indicative, as manufacturers often use different testing methodologies.

Table 2.2: Specifications of electric motorcycles currently in production

Model	**Gogoro 2 series**	**Super Soco CPx Pro**	**Famel E-XF**	**Stark VARG MX**	**Energica Ego+/RS**
Style	Scooter	Scooter	**Café Racer**	**Motocross**	Sportbike
Equivalent	125 cc	125 cc	**125 cc**	**125 cc**	1000 cc
Rated Power	7kW/9.4 hp	7kW/9.4 hp	**-**	**45 kW/60 hp**	110 kW/147 hp
Max. Power	-	8kW/10.9 hp	**5 kW/6.7 hp**	**60 kW/80 hp**	126 kW/169 hp
Range	Up to 170 km	Up to 100 km	**> 120 km**	**-**	246 km
Battery	2 × Li-ion 1.74 kWh/36.25 Ah (48 V)	2 × Li-ion 5.4 kWh/90 Ah (60 V)	**2 × Li-ion** **1.8 kWh/37.5 Ah** **(48 V)**	**Li-ion** **7.2 kWh/20 Ah** **(360 V)**	Lithium Polymer 21.5 kWh/72 Ah (300 V)
Removable Batteries	Yes	Yes	**Yes**	**No**	No
Max. Speed	90 km/h	105 km/h	**>100 km/h**	**≈ 170 km/h**	240 km/h (Limited)
Charge Time	-	3.5h Fast Charging	**≈ 5h**	**2h Fast Charging**	40 min for 0-80% Fast Charging
Weight	122 kg	143 kg	**-**	**118 kg**	260 kg
Base Price	-	5 099 €	**6 500 €**	**12 490 €**	33 174 €

The Stark VARG MX, on the other hand, represents a high-performance electric motocross motorcycle. With a peak power output of 60 kW and a weight of 118 kg, it far exceeds the specifications of other 125 cc-equivalent models and almost competes with high-end electric motorcycles such as the Energica Ego+/RS. Its 7.2 kWh lithium-ion battery and fast-charging capability provide exceptional power-to-weight performance and short turnaround times.

Overall, the benchmarking confirms that both motorcycles occupy distinct but strategically relevant positions in the electric mobility market. The Famel E-XF targets the accessible, urban commuter segment, prioritising practicality and retro-styled design, while the Stark VARG MX demonstrates the potential of electric propulsion in high-performance, off-road applications.

2.3 Composite Materials

This section delves into fundamental concepts about fibre-reinforced polymer composites, as they are the subject of this project. Other types of composites will not be addressed.

Composite materials are defined as materials formed by the heterogeneous combination of at least two distinct constituents, with an interface between them. They leverage the synergetic properties of their constituents to achieve superior overall performance compared to their individual components [11]. The constituents of a composite system can be categorised into two primary groups based on their function: **matrix** and **reinforcement**. Additional secondary constituents, such as coupling agents, coatings and fillers, may also be present. Furthermore, a third parameter should be considered due to its crucial importance to the system: **the fibre-matrix interface**.

The creation of a composite structure begins with the arrangement of a large number of fibres within a thin matrix layer to form a *lamina* (ply), typically ranging in thickness from 0.1 to 1

mm. In the case of continuous fibre laminas, fibre orientation can be unidirectional, bidirectional, or multidirectional. Bi- or multidirectional fibre arrangements are achieved through weaving, knitting, or other textile-based processes.

An unidirectional lamina exhibits high strength and stiffness along the fibre direction but significantly lower properties in the transverse direction. In bidirectional lamina, these properties can be tailored by adjusting the fibre distribution in both directions, enabling the design of balanced laminas. Discontinuous fibre composites, a different type of fibre-reinforced polymer, offer the possibility of unidirectional or random orientation, with lower strength and modulus than continuous fibre composites, however random fibres can provide isotropic in-plane properties.

To achieve the required thickness for supporting specific loads or maintaining defined deflections, multiple laminas are stacked in a prescribed sequence with varying fibre orientations and then consolidated to form a *laminate* [12].

Figure 2.2 illustrates the previously discussed concepts related to composites.

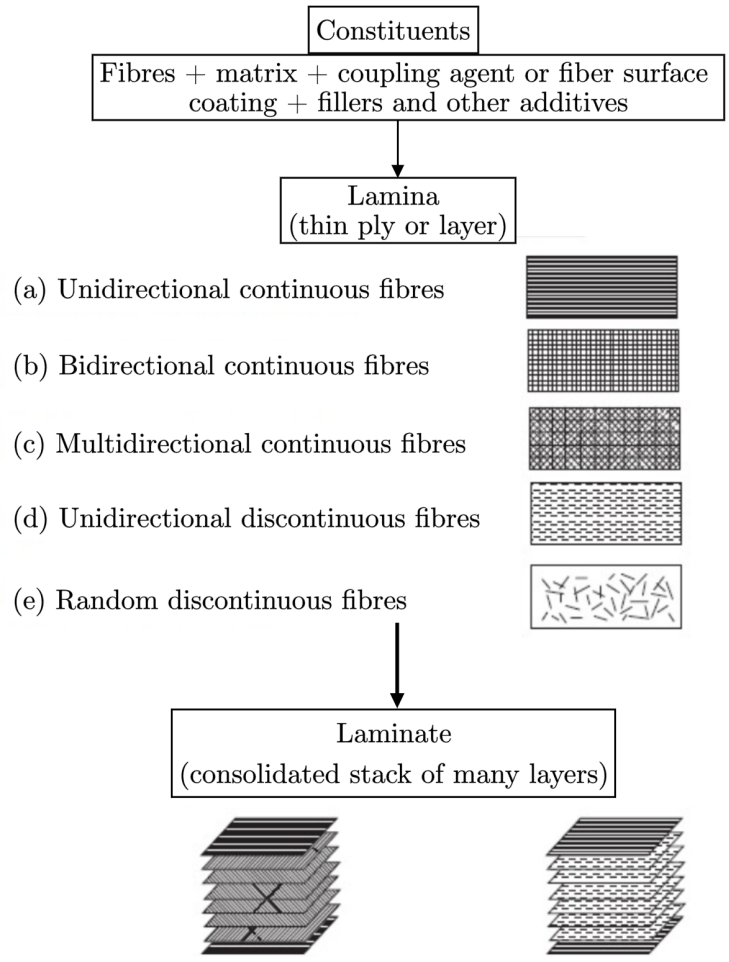

Figure 2.2: Basic building blocks in fibre-reinforced composites (Adapted from [12])

2.3.1 Reinforcements

Reinforcements, in the form of fibres, are the primary component of a fibre-reinforced composite. They occupy a significant mass fraction of the material and play the main role within the system. Fibres bear the majority of the load, provide the material with its structural properties, strength, and stiffness, and impart the required thermal and electrical characteristics. The appropriate selection of fibre type, volume fraction, orientation, and length is crucial, as it directly influences density, tensile and compressive modulus and strength, cost, thermal and electrical conductivities, and fatigue behaviour [11, 12].

Fibre reinforcements can be unidirectional or arranged into a connected structure known as fabric or cloth. Fabric architectures include woven (plain, twill, satin; Figure 2.3), 3D, nonwoven, knitted, and braided structures, each influencing the composite's properties. Woven fabrics provide stability and strength, while 3D constructions enhance through-the-thickness reinforcement. Nonwoven and stitched fabrics offer flexibility, whereas knitted and braided fabrics enable complex preforms but may reduce in-plane strength [13].

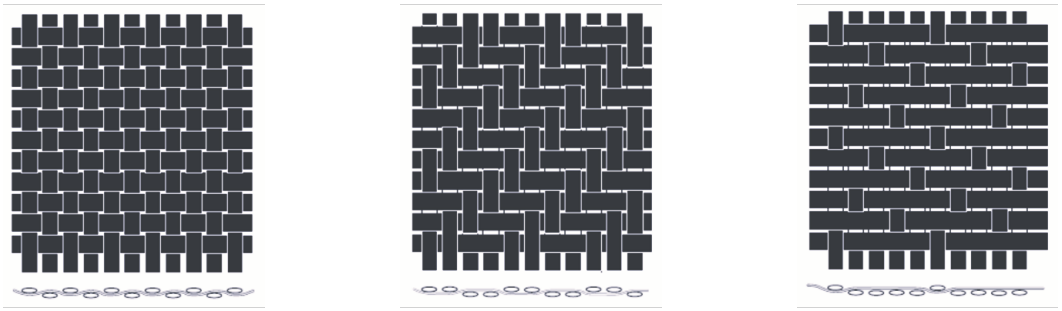

(a) Plain Weave (b) Twill Weave (c) Satin Weave

Figure 2.3: Schematic representation of typical 2D woven fabric structures (Adapted from [14]).

2.3.1.1 Glass Fibres

Glass fibres are the most commonly used reinforcement for polymeric matrix composites. The principal advantages of glass fibres include low cost, high tensile strength, excellent chemical resistance, and superior insulating properties. However, they also present certain drawbacks, such as a relatively low tensile modulus, high density, susceptibility to abrasion during handling, relatively low fatigue resistance, and high hardness [12].

The two most common types of glass fibres used in the industry are E-glass and S-glass [11].

2.3.1.2 Carbon Fibres

Carbon fibres come with distinct mechanical properties and prices depending on factors such as precursor material, manufacturing process, and fibre modulus classification, all of which influence their performance. They can be categorized into two categories depending on their carbon content: carbon fibres with carbon content between 80 % and 95%, and graphite fibres, with content

exceeding to 95 % [11]. Carbon fibres are available in a range of tensile modulus values and can be broadly classified as ultra-high modulus (>500 GPa), high modulus (>300 GPa), intermediate modulus (>200 GPa), low modulus (100 GPa), and high-strength (>4 GPa) carbon fibres [15].

Generally, low-modulus fibres exhibit lower density, reduced cost, higher tensile and compressive strengths, and greater tensile strain-to-failure compared to high-modulus fibres. Carbon fibres offer several advantages, including exceptionally high tensile strength-to-weight and tensile modulus-to-weight ratios, a very low coefficient of linear thermal expansion, high fatigue strength, and excellent thermal conductivity. Their superior structural properties relative to weight make them attractive for high-performance applications. However, they also have drawbacks, such as low strain-to-failure, low impact resistance, relatively high cost, and high electrical conductivity, which can cause "shorting" in unprotected electrical systems [12].

Carbon fibres are produced from two primary types of precursors: PAN and pitch, each influencing their final characteristics [12].

2.3.1.3 Aramid Fibres

Aramid fibres are synthetic, aromatic polyamides arranged in a cristalline structure, Kevlar®[1] is one of the most widely used aramid fibres in practical applications [11]. Aramid fibres possess the highest tensile strength-to-weight ratio and the lowest density among common reinforcing fibres. They also offer excellent impact resistance, unlike glass and carbon fibres, along with good fatigue resistance, outstanding chemical resistance, low thermal conductivity and expansion, and effective damping properties. Nonetheless, the main disadvantages of aramid fibre-reinforced composites include their low compressive strength and difficulty in cutting or machining [12]. Due to their unique properties, aramid fibre reinforced composites are utilized in a wide range of applications, including aerospace engineering (such as aircraft structures), body armor, bulletproof vests, automotive brake systems, and marine structures [16].

2.3.1.4 Natural Fibres

Natural fibres commonly used in composite material applications are plant-derived, with flax being the most widely utilized natural fibre in composites.

Recently, natural fibre-reinforced polymers have gained increasing attention due to environmental concerns and their inherent advantages [17]. These benefits include low cost, biodegradability, ease of production, very low density, and competitive specific mechanical properties compared to E-glass fibres [11, 12]. An additional advantage of flax and other natural fibres is their vibration damping capability, which has led to applications in hybrid laminates combining flax layers with carbon fibre composites [17, 18]

Nevertheless, natural fibres present significative limitations: moisture absorption, reduced durability and poor bonding with certain matrices [17]. These characteristics can restrict their application under specific conditions.

[1] Kevlar®is a DuPont trademark

2.3.2 Matrix

Reinforcements alone are of little use unless they are bonded together to form of a structural element. The matrix acts as the binder material, typically composed of polymers (plastics). It transfers loads to the reinforcement, provides toughness to the composite, protects it from external conditions, and maintains the shape and surface appearance of the composite system [11, 13]. While the matrix is not the main load-bearing material in a composite system, its correct selection has a profound effect on the composite's overall quality. The matrix plays a crucial role in determining the compressive, shear properties of the material, as well as its fatigue behaviour.

Polymer matrices are divided into two groups, thermoplastics and thermoset resins. This classification arises from the differences in their molecular structure, which influence both their properties in liquid (plastic) and solid states. In thermoplastic polymers, individual molecules are not chemically bonded, in the solid state, they are held together by weak intermolecular forces. Consequently, thermoplastics can be heat-softened, melted and reshaped. In contrast, thermoset polymers form permanent cross-links, creating a rigid three-dimensional network. Once these cross-links are formed during the curing reaction, the thermoset polymer cannot be remelted through the application of heat [12].

Common thermoplastics include polyamide, polyethylene, polypropylene, PEEK (polyether ether ketone) and polycarbonate [13]. Thermoplastic matrices have gained attention due to their recyclability and advancements in high-temperature-resistant formulations. Compared to thermosets, they offer superior impact resistance, greater toughness, and lower density. However, their application can be limited by reduced mechanical performance at high temperatures, lower rigidity, and challenges in achieving proper impregnation with reinforcements. The latter is particularly critical, as fibre-matrix interaction is essential for optimal mechanical performance [12]. Recent advancements in thermoplastic polymers have greatly contributed to enhance the applicability of thermoplastic-matrix composites.

Thermoset matrices are the most widely used in fibre-reinforced composites due to their high rigidity, mechanical strength, thermal and dimensional stability, and chemical resistance. They also exhibit lower creep and stress relaxation while being easier to process. However, their brittleness, poor impact resistance, and limited recyclability are notable drawbacks [12]. Extensive knowledge has been accumulated on thermoset resins and their interaction with fibre reinforcements, making them a well-established choice for high-performance composite applications where structural integrity and long-term stability are necessary.

2.3.3 Comparison of Properties

Table 2.3 compares several mechanical properties of composites made from epoxy-matrix prepregs reinforced with different fibres. The fibres, layup, and loading direction are all unidirectional. It is important to emphasise that the values presented in the table are representative of the specific laminates described. The properties of a composite material are influenced by multiple factors, including layup configuration, loading direction, fabric architecture, and manufacturing process.

Table 2.3: Properties of epoxy-matrix fibre-reinforced composites, comparison of different unidirectional (UD) pre-pregs with UD layup [11, 18–20]

Epoxy laminate fibre	Young's modulus E (GPa)	Tensile strength σ_r (MPa)	Specific mass ρ (g/cm^3)	Max. service temperature T_{max} (°C)	Fibre volume fraction (%)	Cost (€ / kg)
E-Glass	35-45	300-1100	1.60-1.95	170-190	30-60	22.3-31.6
High-strength carbon fibre	129-154	1740-2170	1.55-1.58	140-220	65-75	34.4-38.2
Interm. modulus carbon fibre	170	2400	1.50-1.70	120-200	60	-
Aramid	60-80	1100-1380	1.38	140-220	45-50	43.9-72.3
Flax	35	387	1.30	-	-	-

2.3.4 Prepreg-Autoclave Manufacturing Process

In terms of manufacturing processes, and to maintain conciseness, only the prepreg–autoclave manufacturing process will be mentioned. This process constitutes a fundamental aspect of the present work, as Chapter 9 is entirely dedicated to the manufacturing methodology of the composite prepreg battery enclosure prototype.

The flow chart presented in Figure 2.4 outlines the typical sequence of operations for manufacturing a composite component using manually laid-up prepreg material and cured in an autoclave, directly formed in a mould without the need for a master.

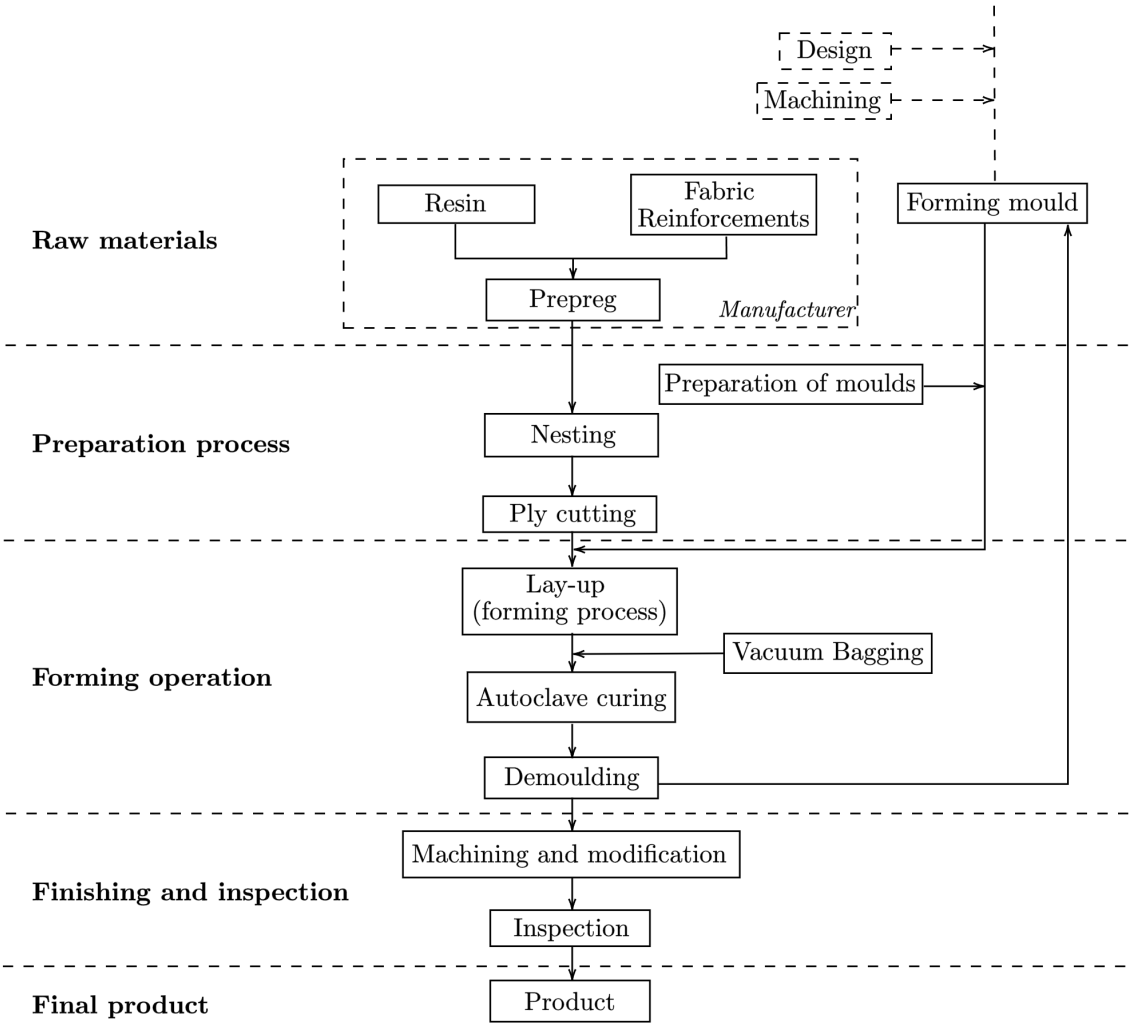

Figure 2.4: Flow chart of the typical production technology of thermosetting resin composites (Adapted from [21])

The process begins with the required materials: the composite material, composed of a polymer matrix (resin) and reinforcing fibres, and the forming mould (or moulds). The combination of resin and reinforcement can be achieved through different approaches. In the prepreg–autoclave process, the reinforcement fibres are pre-impregnated with a controlled amount of resin by the material supplier, producing intermediate materials known as *prepregs* (pre-impregnated fabrics). These prepregs are manufactured under controlled temperature and pressure conditions, or using solvent techniques, with a pre-catalysed resin system. The curing agent (hardener) within the resin remains largely inactive at ambient temperature, allowing the prepreg to retain a practical shelf life of several weeks once defrosted. To ensure long-term storage stability, prepregs are kept frozen at low temperatures (typically around $-18°C$). When required for manufacturing, they are thawed and handled under controlled conditions. In terms of supply form, prepregs are generally delivered and used as rolls, ready for manual layup [22]. Figure 2.5 shows a carbon fibre prepreg cloth.

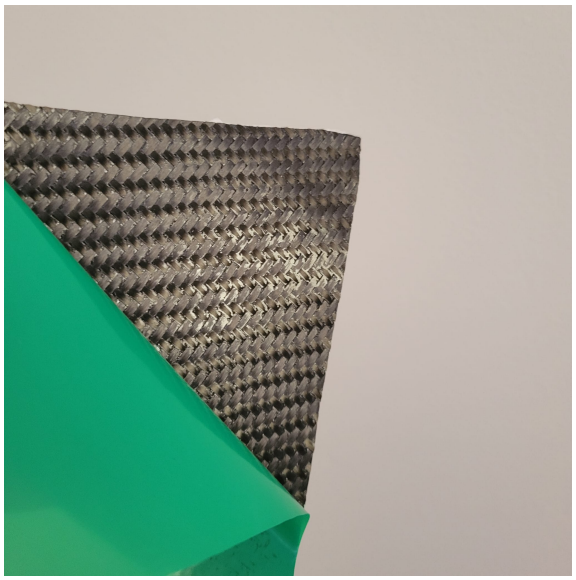

Figure 2.5: Carbon fibre prepreg cloth

In the manufacturing process, moulds are components that contain the negative geometry of the composite part to be produced. The creation of these moulds can follow two main approaches: directly designing and machining the mould, or first designing a *master* with the positive geometry of the desired component, from which the moulds are subsequently taken.

In the case of a *direct mould*, the mould is manufactured from high-temperature epoxy tooling blocks or boards, which are precisely CNC-machined to the required geometry. The machined surface is then finely sanded, sealed with multiple layers of surface sealant, and coated with a release agent. This preparation ensures a smooth, dimensionally accurate mould surface that prevents adhesion to the composite part and allows for repeated use. The quality of the mould (and of the master, when applicable) is therefore crucial, as the surface finish and dimensional accuracy of the final composite component are directly dependent on it.

Before production, the required ply shapes, ply count, and fibre orientations of the composite laminate are defined. These plies are then digitally arranged in an optimised layout to minimise material waste, through a process known as *nesting*. The nesting layout is subsequently used to cut the prepreg sheets, typically with a numerically controlled (CNC) cutting machine to ensure precision and repeatability.

The prepared prepreg plies are then laid up, either manually or with automated layup equipment, directly onto the mould surface following the prescribed stacking sequence. After layup, the laminate undergoes a process known as *vacuum bagging*, where a flexible plastic film is sealed around the laminate and attached to the mould. Air is extracted from within the bag using a vacuum pump, applying up to one atmosphere of pressure on the laminate to achieve initial consolidation. This process is illustrated in Figure 2.6 [22].

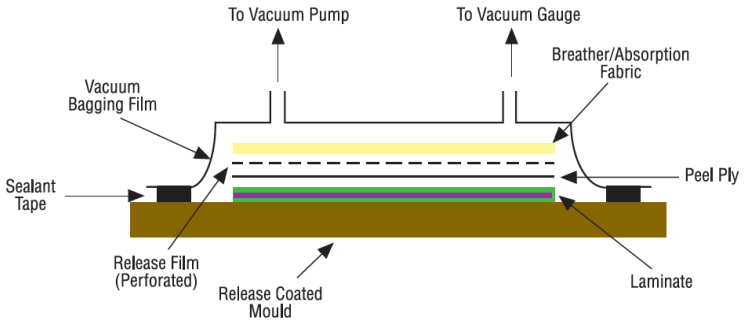

Figure 2.6: Vacuum Bagging process [22]

The application of vacuum removes entrapped air within the laminate, thereby reducing void content and air-induced defects. It also applies a uniform pressure that improves ply consolidation and ensures the laminate conforms more accurately to the mould geometry. This results in superior surface finish and enhanced mechanical properties. Plastic *release films* are placed directly on the laminate to prevent adhesion between the cured resin and the *breather cloth* during curing. The breather cloth provides air evacuation paths within the vacuum bag and contributes to uniform pressure distribution across the laminate.

Following vacuum bagging, the composite laminate is heated, typically between 120–180 °C, allowing the resin to first reflow and subsequently cure. Additional pressure is provided by an autoclave, essentially a pressurised oven, which applies high pressure and controlled temperature to the laminate [22]. The application of autoclave pressure ensures optimal consolidation, minimising porosity and maximising the mechanical performance of the cured part. Figure 2.7 illustrates the autoclave process and a representative cure cycle in terms of temperature, pressure, and vacuum.

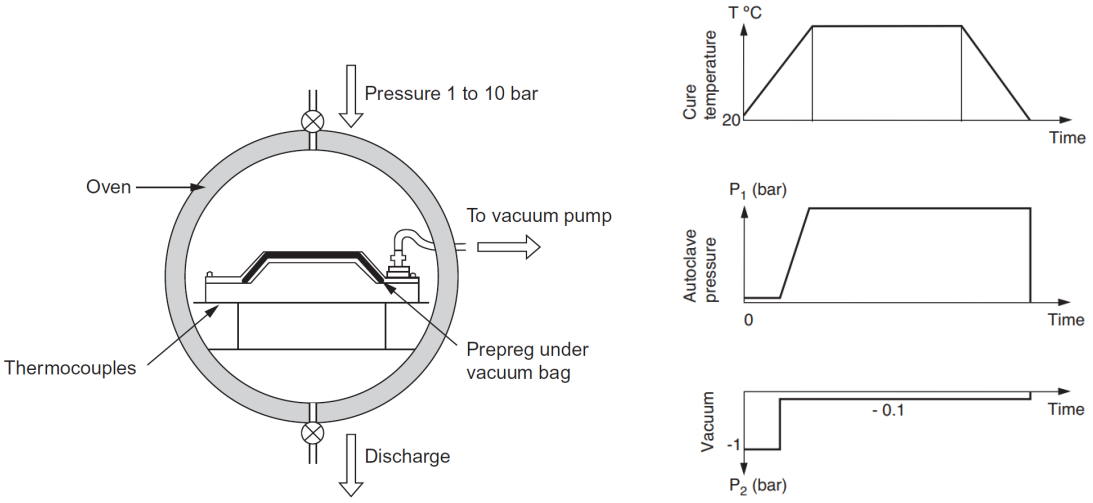

(a) Schematic representation (b) Cure cycle

Figure 2.7: Autoclave process [13, 14]

After curing, the component is demoulded, inspected to verify both external and internal quality, and subsequently machined to remove excess material or incorporate final features, resulting in the finished part.

2.4 Review of Relevant Literature and Key Insights

This section presents a review of relevant academic and technical literature related to the development of composite battery enclosures. It begins with an overview, based on the literature, of the main functions of battery enclosures and of the benefits and challenges associated with employing composite materials in their construction. The purpose of this review is not only to summarise previous research but also to extract practical insights that directly inform the design choices and methodologies adopted in the present work. The discussion is structured into five thematic areas: Weight Saving, Impact Resistance, Thermal Management, Fire Safety, and Optimisation, each addressing a key aspect of the multifunctional performance required for composite enclosures. Within each theme, the consulted studies are briefly described, highlighting their objectives and main findings, followed by a concise reflection on the specific knowledge or design considerations derived for the current project.

Lithium-ion (Li-ion) batteries are the foundation of modern electric vehicles, offering high energy density, long cycle life, and relatively low self-discharge rates compared to other battery technologies. Li-ion batteries have been and are still the subject of intensive research and development; the advancements in technology in this field have been instrumental in the rise of electric vehicles and will remain crucial for the transition to zero-emission transportation [23, 24].

Battery housings, or enclosures, are protective structures surrounding key battery components, including cells, cables, and electronics. Their primary functions are to safeguard these components from external conditions and to facilitate secure placement and mounting within the vehicle. These components are engineered with several factors in mind [23–28]:

- **Structural Support**: Provides mechanical stability, keeping the battery pack secured and preventing excessive movement or vibration;
- **Impact/Crash protection**: Acts as a protective barrier, preventing cell puncture or deformation in the event of an impact or crash;
- **Thermal Management**: Regulates battery temperature and may incorporate cooling or heat dissipation systems;
- **Sealing and Environmental protection**: Shields components from external contaminants such as dust, dirt and water while ensuring corrosion resistance;
- **Electrical and Electromagnetic insulation**: Provides adequate grounding, short circuit prevention, and reduces electromagnetic interference with other vehicle electronics;

- **Modularity and Serviceability**: Some designs may provide easy battery replacement or maintenance.

Battery enclosures can be made from metals such as steel or aluminium, non-metallic materials like polymers or composites, or a combination of both [25]. Composite-based battery enclosure solutions in particular have recently been the subject of interest [24]. Composite materials offer several characteristics that make them well-suited for battery enclosure applications. They exhibit excellent structural integrity with a remarkable strength-to-weight ratio, especially when reinforced with carbon or glass fibres [25, 29].

Composites also possess high fatigue resistance, allowing well-designed battery enclosures to withstand prolonged cyclic loading. Furthermore, fibre-reinforced polymers are relatively inert to environmental degradation and thus show potential as corrosion-resistant materials, a crucial factor since batteries can release moisture and corrosive substances [25, 29].

Another key characteristic of composite materials is their relatively low thermal conductivity when compared to metals. For instance, carbon fibre-reinforced plastics exhibit a thermal conductivity approximately 200 times lower than aluminium. While this property can be beneficial for reducing heat transfer between components and assisting targeted thermal management strategies, it can also pose challenges when simple or passive cooling methods are required. The inherently low heat dissipation capacity of composite materials often necessitates the adoption of more complex, active thermal management systems to maintain safe operating temperatures within the battery pack [25, 27].

Moreover, the inherent electrical conductivity of carbon fibre composites provides an additional advantage, as it allows for effective electrical grounding and integration of conductive pathways within the battery system architecture.

The studies by Azzopardi et al., "Recent Advances in Battery Pack Polymer Composites" [25], and Kaleg et al., "Addressing Fire Safety, Ground Impact Resistance, and Thermal Management in Composite EV Battery Enclosures: A Review" [23], were foundational to this work. Both serve as comprehensive overviews of composite battery enclosures and established the basis for understanding enclosure design, performance requirements, and multifunctional characteristics.

2.4.1 Weight Saving

Weight reduction is generally the primary motivation for adopting composite materials in automotive structures. Both industry practice and academic research show that the drive toward lightweighting remains the foremost rationale for the substitution of metals with composites in battery enclosure applications.

In this context, the study by Schludi et al., "*Lightweight and Safe Composite Battery Housings*" [27], served as a key reference. The work presents a lightweight composite battery enclosure designed for the automotive industry, reviewing its mechanical behaviour, modularity, and fire and thermal performance. According to Schludi et al., composite battery enclosures can achieve up to 40% mass reduction relative to metallic equivalents while retaining comparable stiffness and

strength. Such reductions directly enhance vehicle range and energy efficiency, which are critical for electric mobility. Their study also inspired aspects of the present work's design approach, particularly the use of honeycomb sandwich cores.

2.4.2 Impact Resistance

Regarding impact resistance, various studies have demonstrated that the introduction of thin-walled energy-absorbing structures, such as honeycombs, can significantly enhance crash performance. The review by Kaleg et al. [23] provided an extensive overview of such strategies, presenting literature examples that explore crash absorption through engineered cellular and sandwich structures.

Furthermore, the study by Wang et al., "Design Optimization of a Novel Negative Poisson's Ratio Non-Module Battery Pack System Considering Crashworthiness and Heat Dissipation" [30], provided a concrete example of this approach. The authors developed a battery enclosure incorporating negative-Poisson-ratio tubular honeycomb structures designed to absorb impact energy during side-pole collisions. Their methodology, which employed explicit dynamic analysis, reinforced the decision to adopt explicit simulations in the development methodology defined for this work.

2.4.3 Thermal Management

Thermal management represents one of the most critical aspects in the design of safe and reliable composite battery enclosures. Wang et al. [30] also addressed this challenge by integrating an active heat dissipation system within their crash-absorbing structure, employing a water-cooled radiator to dissipate heat through external airflow. This innovative approach demonstrated the potential of multifunctional structural elements that combine mechanical protection and thermal regulation.

The review studies by Azzopardi et al. [25], Kaleg et al. [23], and Schludi et al. [27] provide comprehensive discussions on heat generation, battery operating temperature ranges, and thermal runaway mechanisms. For instance, Azzopardi et al. [25] report optimal lithium-ion battery operating temperatures between 25–40 °C, while Schludi et al. [27] identify an acceptable range of 10–40 °C. These works also classify Battery Thermal Management Systems (BTMS) as passive, active, or hybrid, presenting both simulation and real-world solutions. Collectively, they formed the conceptual foundation for understanding and addressing thermal management challenges in composite enclosures for this project.

2.4.4 Fire Safety

It is important to distinguish between flammability and flame resistance: the former describes how easily a material ignites and sustains combustion, while the latter refers to its capacity to resist ignition and prevent flame spread [31].

Schludi et al. [27] investigated the fire resistance of composite materials, particularly in sandwich configurations incorporating additive-modified resins for enhanced fire performance. Similarly, Azzopardi et al. [25] and Kaleg et al. [23] discussed the incorporation of flame-retardant additives and their influence on both mechanical and thermal properties. Their analyses also emphasise the importance of fire testing standards such as UL 94, commonly used to classify the flammability of polymer composites. These insights were instrumental in establishing fire safety as a central design consideration in the present work, highlighting the balance between mechanical performance and fire resistance in composite enclosures.

Furthermore, the study by Lu and Chen, "*Thermal Transport and Fire Retardance Properties of Cellular Aluminium Alloys*" [32], revealed that closed-cell aluminium alloy foams exhibit exceptional fire resistance, in addition to high specific stiffness and energy absorption capability. This finding motivated the inclusion of aluminium honeycomb structures in the current enclosure design, serving both impact absorption and fire protection purposes.

2.4.5 Optimisation

Although properties such as flame retardancy, crashworthiness, and heat dissipation have been studied individually, the integration of these aspects within a single composite system remains relatively underexplored [23].

The review by Nikbakt et al., "*A Review on Optimization of Composite Structures Part I: Laminated Composites*" [33], provided an essential theoretical framework for understanding optimisation techniques applicable to composite laminates. This work clarified the various objectives, constraints, and computational approaches that can be employed to tailor composite performance.

More concretely, Wang et al. [30] implemented a multi-objective optimisation strategy in their composite battery enclosure design, balancing crashworthiness with thermal performance. Complementary studies by Shui et al., "Design Optimization of Battery Pack Enclosure for Electric Vehicle" [34], and Zhang et al., "Multi-Objective Optimization of Lithium-Ion Battery Pack Casing for Electric Vehicles: Key Role of Materials Design and Their Influence" [35], further demonstrated how numerical optimisation can guide the development of a battery enclosure design.

Together, these references shaped the direction of the present work. They demonstrated the benefits and paved the way for the adoption of composite optimisation strategies applied in this study. The route ultimately chosen was also defined based on Adamastor's expertise in composite modelling and design using the Altair HyperWorks® environment.

2.5 Regulations and Standards

This section outlines the main regulations and standards considered throughout the project. The focus is placed on the **UN ECE R136** regulation, which defines the safety requirements for rechargeable energy storage systems (REESS) in electric vehicles, and on the **UL 94** flammability test, which classifies the fire behaviour of polymeric materials. Both frameworks were used as guiding

references to ensure that the developed battery enclosure concept adheres to recognised safety and performance criteria.

2.5.1 UN ECE R136

The UN ECE R136 (*Uniform provisions concerning the approval of vehicles of category L with regard to specific requirements for the electric power train*) governs the homologation of electric motorcycles and their battery systems. The regulation is divided into two parts: Part I addresses the electric power train; Part II covers the rechargeable electrical energy storage system (REESS). In the context of battery enclosure design, Part II is the most relevant [36].

In homologation testing under R136, the battery system, and by extension the enclosure protecting it, must be subjected to rigorous electrical, thermal, vibration and mechanical abuse conditions. The intent is to ensure safe operation in real-world use and in fault or accident conditions. Test categories include [36, 37]:

- **Voltage protection tests:** Verification of safe behaviour under extreme states of charge (over-discharge / over-charge).
- **Current protection tests:** Assessment of system integrity under excessive current draw or external short-circuit conditions.
- **High-temperature tests:** Exposure to elevated ambient temperatures or thermal cycling to verify operational safety.
- **Vibration tests:** Application of vibration profiles representative of motorcycle operation to evaluate potential structural, electrical, or thermal failures.
- **Mechanical drop test for removable REESS:** The REESS assembly (including its enclosure) is subjected to a controlled drop event to simulate real-world accidental drops or impact conditions.
- **Mechanical shock:** The battery system must withstand acceleration and deceleration loads, in lateral, frontal, and vertical directions, representative of a two-wheeler operating environment.
- **Fire resistance test:** The most severe test involves exposing the battery to open flames by placing it above a tank of burning gasoline. The exposure continues for a defined period, after which the system is monitored until it cools to ambient temperature or for a minimum of three hours. Compliance is achieved if no explosion occurs during or after the exposure.
- **External short-circuit, over-charge, over-discharge, over-temperature, and over-current protection tests:** Verification that the complete system, including its enclosure, supports safe behaviour under all fault conditions.

Once all required tests are successfully completed under R136, the battery pack and its protective enclosure may receive approval, allowing the homologation mark to be applied. This certifies that the design fulfils the regulatory safety requirements for category L electric vehicles.

In the context of this work, which focuses on the design and development of the battery enclosure, the information available regarding the internal components and configuration of the REESS was limited. Consequently, the regulation was adopted primarily as a guiding framework to ensure that the design meets the relevant safety intentions. A comprehensive simulation of all R136 test conditions was not feasible; therefore, the regulation was selectively interpreted to prioritise and simulate the most representative and technically achievable tests within the available resources and data.

2.5.2 UL 94 Standard for Safety of Flammability

The *UL 94, Standard for Safety of Flammability of Plastic Materials for Parts in Devices and Appliances* establishes the testing framework used to evaluate the flammability of polymeric materials. It serves as the basis for assessing the fire retardancy of plastics to certify their safety in both critical and everyday applications. For composite materials, it is regarded as the benchmark reference for evaluating fire behaviour, being widely applied in certification processes across industries such as aerospace and other high-performance sectors.

The standard defines several test procedures to classify materials according to their burning characteristics, the most common being the vertical (V) and horizontal burning (HB) tests. As the HB test plays a relevant role in this dissertation, a concise description is provided below. For full technical specifications, refer to the UL 94 standard [38]. The following summary is based on the 2001 edition.

In the horizontal burning (HB) test, three specimens are tested in a horizontal position and exposed to a 20 mm blue flame applied to one end at a 45° angle. Each specimen, measuring 125 ±5 mm in length and 13.0 ±0.5 mm in width, is marked with two reference lines at 25 ±1 mm and 100 ±1 mm from the ignited end. The burner is positioned so that the flame impinges 6 ±1 mm into the free end of the specimen for 30 ±1 s, or until the combustion front reaches the 25 mm mark. Timing begins once the flame front reaches this mark. If burning continues after flame removal, the time for the combustion front to travel from 25 mm to 100 mm and the damaged length, L, are recorded. Tests are conducted at 15–35°C and 45–75% relative humidity, with specimens preconditioned according to ASTM D618 (ISO 291) at 23 ±2°C and 50 ±5% relative humidity for at least 48 hours. The linear burning rate, V, in mm/min, is determined for each specimen using:

$$V = 60\frac{L}{t} \tag{2.1}$$

where L is the damaged length in millimetres, and t is the time in seconds. If the flame front passes the 100 mm mark, L is taken as 75 mm.

A material is classified as HB if:

- Its burning rate does not exceed 40 mm/min over a 75 mm span for specimens 3.0–13 mm thick; or
- Its burning rate does not exceed 75 mm/min for specimens thinner than 3.0 mm; or
- It ceases to burn before reaching the 100 mm reference mark.

If one of the three initial specimens fails to comply, a second set of three is tested, and all must meet the criteria for the material to be classified as HB at that thickness. Figure 2.8 schematically illustrates the HB test setup.

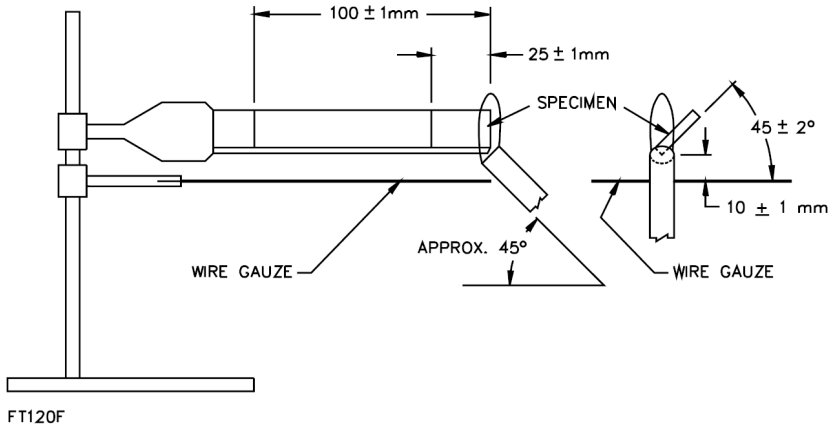

Figure 2.8: Horizontal burning test for HB classification [38]

It is important to note that UL 94 ratings are thickness-dependent. A resin that achieves HB classification at 1.5 mm thickness may fail at 0.74 mm. While some materials maintain consistent performance across thicknesses, this behaviour is not guaranteed [31].

2.6 Composite Mechanics

2.6.1 Classical Lamination Theory

Laminated composite parts are generally modelled as orthotropic or transversely isotropic materials, thus their mechanical stress-strain relationship differs from isotropic materials. Classical Lamination Theory (CLT) aims to characterize the strains and stresses in each ply of an orthotropic, laminated structure. A complicated three-dimensional elasticity problem is reduced to a solvable two-dimensional mechanics problem through effective and reasonably accurate simplifying assumptions [39]. The basic assumptions of the theory are [12, 40]:

- The plate consists of orthotropic, linear elastic, laminas (plies) bonded together, with the principal material axes of the orthotropic lamina oriented along arbitrary directions with respect to the x-y axes;
- Plane stress state ($\sigma_3 = \tau_{23} = \tau_{31} = 0$);

- Displacements and strains are small and linearly distributed in the thickness direction;
- A perfect interlaminar bond exists between various laminae.

The coordinate and laminate system is considered as represented in Figure 2.9. The coordinate system defines the x-y plane at the middle surface of the laminate, with the z-axis being the thickness direction, the first ply is defined as the most negative ply, by convention.

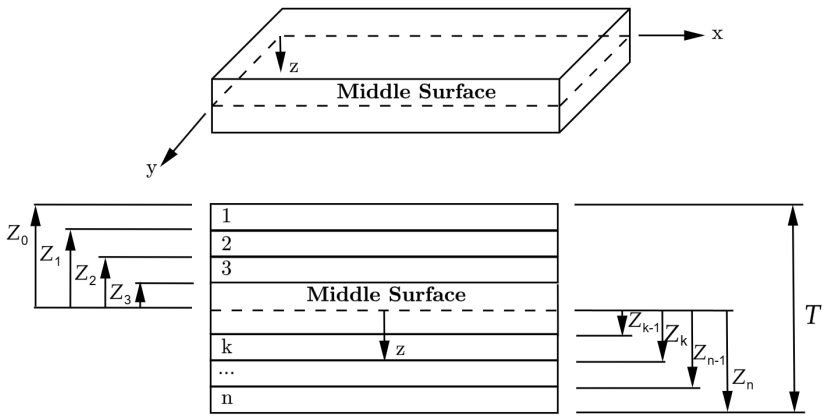

Figure 2.9: Classical Lamination Theory laminate system (Adapted from [41])

The deformations for each lamina (ply) k are defined as [12]:

$$\left\{\varepsilon\right\}^{(k)} = \begin{Bmatrix} \varepsilon^0_{xx} \\ \varepsilon^0_{yy} \\ \gamma^0_{xy} \end{Bmatrix}^{(k)} + z \begin{Bmatrix} k_{xx} \\ k_{yy} \\ k_{xy} \end{Bmatrix}^{(k)} \tag{2.2}$$

where,

$\varepsilon^0_{xx}, \varepsilon^0_{yy}$: midplane normal strains in the laminate;

γ^0_{xy}: midplane shear strains in the laminate;

k_{xx}, k_{yy}: bending curvatures of the laminate;

k_{xy}: twisting curvature of the laminate;

z: distance from the midplane in the thickness direction.

In order to consider strain resulting from thermal expansion, one can add the term $-\left\{\alpha\right\}^{(k)}\Delta T$ to the last equation.

The stress-strain relation for the principal material orientations is given by the following equation, relative to each lamina k [42]:

$$\begin{Bmatrix} \sigma_{11} \\ \sigma_{22} \\ \sigma_{12} \end{Bmatrix}^{(k)} = \begin{bmatrix} Q_{11} & Q_{12} & 0 \\ Q_{12} & Q_{22} & 0 \\ 0 & 0 & Q_{66} \end{bmatrix}^{(k)} \begin{Bmatrix} \varepsilon_{11} \\ \varepsilon_{22} \\ \gamma_{12} \end{Bmatrix}^{(k)} \tag{2.3}$$

$$Q_{11} = \frac{E_1}{1 - v_{12}v_{21}} \qquad Q_{22} = \frac{E_2}{1 - v_{12}v_{21}} \qquad Q_{12} = \frac{v_{12}E_2}{1 - v_{12}v_{21}} = \frac{v_{21}E_1}{1 - v_{12}v_{21}} \qquad Q_{66} = G_{12} \tag{2.4}$$

It becomes apparent that each lamina has its own stiffness matrix $[Q]$, dependent on the properties of each lamina. The equation analogous to the last, for the O_{xyz} global system can be obtained through the stiffness matrix in the global coordinate system $\left[\overline{Q}\right]$ and the transformation matrix $[T]$:

$$\left[\overline{Q}\right] = [T]^{-1}[Q][T]^{-T} \tag{2.5}$$

The resultant membrane forces and moment resultants per unit width, represented in Figure 2.10, are given by the following matrix equations [12]:

$$\begin{bmatrix} N_{xx} \\ N_{yy} \\ N_{xy} \end{bmatrix} = [A] \begin{bmatrix} \varepsilon^0_{xx} \\ \varepsilon^0_{yy} \\ \gamma^0_{xx} \end{bmatrix} + [B] \begin{bmatrix} k_{xx} \\ k_{yy} \\ k_{xy} \end{bmatrix} \tag{2.6}$$

$$\begin{bmatrix} M_{xx} \\ M_{yy} \\ M_{xy} \end{bmatrix} = [B] \begin{bmatrix} \varepsilon^0_{xx} \\ \varepsilon^0_{yy} \\ \gamma^0_{xx} \end{bmatrix} + [D] \begin{bmatrix} k_{xx} \\ k_{yy} \\ k_{xy} \end{bmatrix} \tag{2.7}$$

where,

N_{xx}, N_{yy}: normal force resultant in the x and yy directions, respectively;

N_{xy}: shear force resultant;

M_{xx}, M_{yy}: bending moment resultant in the yz and xz planes, respectively;

M_{xy}: twisting moment resultant;

$[A]$: extensional stiffness matrix for the laminate, in N/m;

$[B]$: coupling stiffness matrix, in N;

$[D]$: bending stiffness matrix for the laminate, in N m;

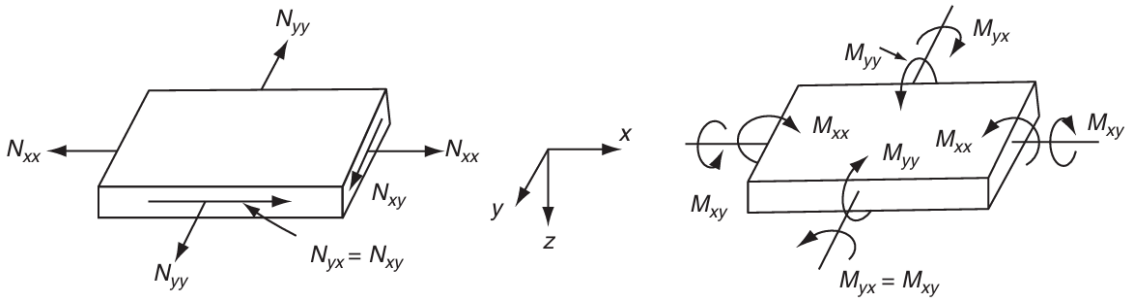

Figure 2.10: In-plane, bending, and twisting loads applied on a laminate [12].

The terms of the $[A]$, $[B]$ and $[D]$ matrices are given by the following equation [42]:

$$\begin{bmatrix} A_{ij} \\ B_{ij} \\ D_{ij} \end{bmatrix} = \sum_{k=1}^{n} \int_{t_{k-1}}^{t_k} \begin{bmatrix} 1 \\ z \\ z^2 \end{bmatrix} \overline{Q}_{ij}^{k} \, \mathrm{d}z \qquad i, j = 1, 2, \text{ or } 6 \tag{2.8}$$

The [A], [B] and [D] matrices in the above relation have a lot of significance in designing the laminates of a composite structure. By looking at these matrices the designer can determine if the type of ply stacking and the nature of any coupling between extension, shear, bending and twisting [41].

The transverse shear forces, along the thickness direction (z), can be determined according to First-order Shear Deformation Theory [42].

$$\begin{Bmatrix} T_{xz} \\ T_{yz} \end{Bmatrix} = \begin{Bmatrix} \sum_{k=1}^{n} \int_{-t_k/2}^{t_k/2} \tau_{xz}(x, y, z, t) \, \mathrm{d}z \\ \sum_{k=1}^{n} \int_{-t_k/2}^{t_k/2} \tau_{yz}(x, y, z, t) \, \mathrm{d}z \end{Bmatrix} \tag{2.9}$$

2.6.2 Failure Criteria

The primary objective in designing a composite structure is to use materials efficiently while ensuring structural safety. Failure criteria allow designers to compare the stresses (or strains) resulting from applied loads with the allowable strength (or strain) capacity of the material. For isotropic materials, such as metals, the Tresca (maximum shear stress) and von Mises (maximum distortion energy) criteria provide accurate estimates of the material's strength limit. Composites, however, are anisotropic and exhibit multiple failure modes; therefore, specific failure theories are required [12].

For an orthotropic lamina in a plane stress state, four independent elastic constants (E_{11}, E_{22}, G_{12} and ν_{12}) define its elastic characteristics. The strength properties are characterised by five independent strength, or homologous strain values [12]:

X_t: Tensile strength in 0° direction;

X_c: Compressive strength in 0° direction;

Y_t: Tensile strength in 90° direction;

Y_c: Compressive strength in 90° direction;

S: in-plane shear strength;

The classical failure criteria covered in this chapter are the Maximum Stress, Maximum Strain, and Tsai–Wu theories. All of these can be expressed in terms of the basic strength parameters introduced previously.

2.6.2.1 Maximum Stress Theory

Maximum stress theory defines that failure occurs when any stress in the principal material directions is equal or greater than the corresponding allowable strength [12]. The material does not fail as long as:

$$\begin{aligned} -X_c < \sigma_{11} < X_t, \\ -Y_c < \sigma_{22} < Y_t, \\ -S < \tau_{12} < S. \end{aligned} \tag{2.10}$$

The maximum stress criterion is more appropriate for the brittle failure modes and does not consider any interaction under general stress states [11].

2.6.2.2 Maximum Strain Theory

According to the maximum strain theory, failure occurs when at least one strain component along the principal material axes exceeds the corresponding ultimate strain in that direction.

$$\begin{aligned} -\varepsilon_c < \sigma_{11} < \varepsilon_t, \\ -\varepsilon_c < \sigma_{22} < \varepsilon_t, \\ -\gamma < \tau_{12} < \gamma. \end{aligned} \tag{2.11}$$

Unlike maximum stress, the maximum strain criterion allows for some interaction of stress components due to Poisson's effect [11, 12].

2.6.2.3 Tsai-Wu Failure Theory

The Tsai–Wu failure criterion originates from the von Mises yield criterion for isotropic materials, having been modified to account for orthotropic or transversely isotropic laminae. It distinguishes between tensile and compressive strengths and considers the interaction among normal stresses, representing a significant advancement over the earliest criteria [11].

Under plane stress conditions, the Tsai–Wu failure theory predicts failure in an orthotropic lamina when the following equality is satisfied [12]:

$$F_1\sigma_{11} + F_2\sigma_{22} + F_6\tau_{12} + F_{11}\sigma_{11}^2 + F_{22}\sigma_{22}^2 + F_{66}\tau_{12}^2 + 2F_{12}\sigma_{11}\sigma_{22} = 1 \tag{2.12}$$

where the F factors are called strength coefficients and are given by

$$\begin{aligned} F_1 &= \frac{1}{X_t} - \frac{1}{X_c} \\ F_2 &= \frac{1}{Y_t} - \frac{1}{Y_c} \\ F_6 &= 0 \\ F_{11} &= \frac{1}{X_t X_c} \\ F_{22} &= \frac{1}{Y_t Y_c} \\ F_{66} &= \frac{1}{S^2} \end{aligned} \tag{2.13}$$

and F_{12} is a strength interaction term that requires a suitable biaxial test to determine experimentally. Reliable biaxial tests can be difficult to perform; for this reason an appropriate range of values for F_{12} has been recommended [12].

$$-\frac{1}{2}\sqrt{F_{11}F_{22}} \leq F_{12} \leq 0 \tag{2.14}$$

In the absence of experimental data, the lower limit of Equation 2.14 can be used for F_{12} [43].

2.6.2.4 Other Failure Criteria

Other failure mode theories also exist for predicting the failure of composite structures, some of which are highly detailed and complex. These theories define independent sets of failure modes that account for the behaviour of the matrix, fibre, and interface.

The Hashin failure criterion identifies multiple failure modes, distinguishing between tensile and compressive failures, as well as between matrix and fibre failures. The Puck failure criterion introduces the concept of a fracture plane; in addition to providing the allowable stress level, it also offers valuable insight into the fracture mode and the expected fracture angle. More advanced approaches, such as recent three-dimensional failure criteria, provide an even more accurate description of composite failure, albeit with increased complexity [11].

2.6.2.5 First and Last Ply Failure

Common fibre-reinforced composite laminates do not exhibit extensive plastic yielding like metals, although they are not brittle materials in a classical sense. Total failure of a laminate typically occurs in a non-linear fashion due to sequential ply failures. Considering this paradigm, two options emerge as design limit modelling: First and Last Ply Failure (FPF and LPF) and the choice depends on the situation at hand. The first option leads to a more conservative model, and in many laminated constructions, the ultimate failure occurs soon after the FPF, and therefore, this

approach is justified. For other laminates, it may not be the case, and there can be a significant margin between first and last ply failure. A FPF approach in this case may be too conservative [12].

The LPF approach introduces complexity in the model, with the introduction of damage algorithms. Most last ply failure models work by degrading the properties of the lamina at the ply-level, assigning reduced stiffness and strength to the failed ply and subsequently recalculating the properties of the laminate, until the failure of the last remaining ply [12, 44].

Considering the design of a structural battery case, a first-ply failure approach, combined with an adequate failure criterion, may be more reasonable as a conservative approach.

2.7 Finite Element Method

The present work does not intend to describe the fundamental formulation of the finite element method in a mathematical sense, as it does not significantly contribute to the comprehension of the work. Alternatively, it aims to explain it in broader terms, without entering too much into complex mathematical formulations, only when necessary.

Simple engineering problems,those involving basic geometries, materials, loads, and boundary conditions, can be solved analytically using the appropriate governing physical equations (partial differential equations) along with suitable simplifying assumptions. However, real-world engineering problems are often too complex to be defined and solved analytically to their exact solution. In the words of Reddy [45]: *"While the derivation of the governing equations for most problems is not unduly difficult, their solution by exact methods of analysis is a formidable task. In such cases, approximate methods of analysis provide alternative means of finding solutions."*.

The Finite Element Method is the most widely used of such numerical methods, it allows to solve a broad spectrum of physics phenomena, including Solid Mechanics (static, dynamic, buckling or modal), Fluid Mechanics, Heat Transfer and others. The advancement of computers and the rapid increase in computational power in recent years allowed the Finite Element Method (FEM) to become the predominant tool at both academic and industrial levels [46].

The core approximation technique, and the main strength, of the finite element method is the process of **discretisation**, illustrated in Figure 2.11. In this process, a geometrically complex domain is represented as a collection of geometrically simple subdomains, called *finite elements*. These elements are connected through *nodes*, and the collection of nodes and elements that approximate the geometry is called the *mesh*. Discretisation is effective because the equilibrium equations need only to be satisfied over a finite number of elements, instead of across the entire continuous domain. This way, a continuous differential problem is transformed into a simpler, discrete problem [45].

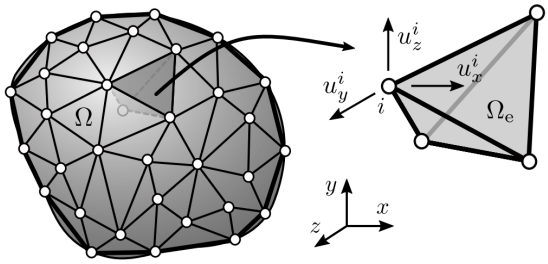

Figure 2.11: Finite element discretisation of a 3D domain into 4 node tetrahedral elements [46]

There are numerous types of finite elements available, and selecting the adequate one is crucial. The choice depends on the specific scenario and the underlying assumptions and simplifications made by the user.

Once the geometry is meshed, physical properties (such as material stiffness), external loads, and boundary conditions (defining how the system is constrained or interacts with its environment) are applied. This stage is referred to as *pre-processing*. The FEM then assembles a system of equations that approximates the behaviour of the whole domain based on the behaviour of each individual element.

The values at the nodes are obtained by satisfying the governing equations, often in a weighted-integral sense, over each element. Thus, the finite element method can be regarded as an element-wise application of the Rayleigh-Ritz or weighted residual methods, such as the Galerkin Method. Over each finite element, *interpolation functions*, often polynomial in form, describe the field variables solved at the nodes (displacements or derived quantities such as stress or strains in mechanical analyses) in the areas inside of each element [45].

FEM is a robust method, and modern software handles the bulk of the computational workload. However, it is the duty of the engineer to properly define the problem, from the real physical phenomena to a suitable approximation along with its underlying assumptions. Ensure a good discretisation of the geometry with a high-quality mesh, select the best simulation type and parameters, and finally carry out the post-processing, including the analysis and validation of the results.

2.7.1 Linear Static Analysis

Linear static analysis represents the most fundamental form of finite element simulation for structural problems, providing a first approximation of the behaviour of a structure under load.

The basic finite element equation can be expressed in a condensed form as:

$$[K]\{u\} = \{f\} \tag{2.15}$$

Where $[K]$ is the global stiffness matrix, which is an assembly of all individual element stiffness matrices of the discretised model. $\{u\}$ the global nodal displacement vector, and $\{f\}$ is the vector of loads applied to the structure.

The simple formulation of this type of analysis comes with its benefits, however, it also contains the following assumptions [47]:

- **Time-invariant (static) loading:** Loads are applied maintaining equilibrium, such that inertial and damping (dynamic) effects are disregarded.
- **Linear elastic materials:** Stress is directly proportional to strain according to Hooke's law, no plastic, yielding, damage or progressive failure behaviour is considered.
- **Small deformations:** Displacements and rotations are sufficiently small so that geometric nonlinearity can be neglected.
- **Constant stiffness matrix:** The structural stiffness does not vary with deformation or loading and so is constant throughout the simulation.
- **Linear boundary conditions:** Supports and constraints behave ideally, without nonlinear phenomena. Contact interfaces are simplified, with no varying contact area/reaction force, no separation or sliding.

2.7.2 Nonlinear Static Analysis

Nonlinear static analysis extends beyond the simplifying assumptions of linear static analysis by accounting for nonlinearities that may significantly influence structural behaviour.

Sources of nonlinearity can be [48]:

- **Geometric Nonlinearity:** In analyses involving geometric nonlinearity, changes in geometry as the structure deforms are considered in formulating the constitutive and equilibrium equations. Geometric nonlinearity can be modelled through two distinct types of analyses: Small Displacement Analysis or Large Displacement Analysis.
- **Material Nonlinearity:** Material nonlinearity involves the nonlinear behaviour of a material based on current deformation, deformation history, rate of deformation, temperature, pressure, etc.
- **Constraint and Contact Nonlinearity:** Constraint nonlinearity in a system can occur if kinematic constraints are present in the model. The kinematic degrees of freedom of a model can be constrained by imposing restrictions on its movement. In the case of contact, the constraint condition is based on inequalities and such a constraint generally does not allow penetration between any two bodies in contact.
- **Follower Loads:** Applied loads can depend upon the deformation of the structure when large deformations are involved. Geometrically, the applied loads can deviate from their initial direction based on how the model deforms at the location of application of load.

Many engineering analyses require the use of large deformation analysis based on geometric nonlinearity, such as metal forming or tyre analysis. Small deformation analysis is required in certain cases, such as analyses involving shells. Such applications involve small deformation, except for finite displacement or rotation. As a rule of thumb guideline, small displacement analysis should be limited to strains of a maximum of 5% in both translation and rotation. Large Displacement Nonlinear Static Analysis is the more accurate, though more numerically expensive alternative. Small Displacement Analyses can be more advantageous depending on the problem at hand [48].

Nonlinear Static Analysis is still a variant of static analysis; static inherently implies that a process occurring in real-time is being simulated infinitely slowly, ignoring inertia and momentum effects. However, the stiffness matrix is not constant throughout the analysis, the equilibrium equation is updated and must be satisfied at each step [48]. Though the simulation happens in steps, these do not constitute time integration, which is a particular trait to dynamic or transient analyses.

In nonlinear static analysis, the solution process must be carried out incrementally, since the response of the structure depends on its load history. At each load step, the equilibrium equations are solved iteratively using Newton's Method, with convergence being monitored through specific criteria. While the mathematical details of the iterative scheme are not necessary for the scope of this report, it is important to note that this approach ensures robustness and accuracy in capturing the complex behaviour of nonlinear systems.

Concluding, these reasons make nonlinear static analysis a more computationally demanding but also a more realistic tool for capturing the true response of structures under complex loading scenarios.

2.7.3 Linear Steady State Heat Transfer Analysis

Heat transfer finite element analysis is a numerical method used to study how thermal energy is distributed within a component or system. In this type of analysis, the objective is to solve for the unknown temperature fields and heat fluxes that develop under prescribed thermal loading conditions. Temperature is interpreted as a measure of the thermal energy stored within the material, while fluxes represent the rate and direction of thermal energy transfer [49].

Physical heat transfer phenomena present in finite element heat transfer analysis include:

- Conduction: thermal energy exchange through molecular motion;
- Convection: heat transfer between solids and surrounding fluids;
- Radiation: heat transfer through electromagnetic waves (only available in Nonlinear Steady State or Nonlinear Transient Heat Transfer Analysis).

The concise finite element formulation is as follows [49]:

$$(K_C + H)T = f \tag{2.16}$$

where K_C is the conductivity matrix, H is the boundary convection matrix, T are unknown nodal temperatures, and f is the thermal loading vector. The thermal loading vector can be expressed as:

$$f = f_B + f_H + f_Q \tag{2.17}$$

where f_B is the power vector due to heat flux, f_H is the boundary vector due to convection, and f_Q is the power vector due to internal heat generation. Thermal loading is defined as energy flow into and out of the system [49].

In the linear steady-state heat transfer formulation, the matrix on the left-hand side of Equation 2.16 is singular unless temperature boundary conditions are specified. The equilibrium equation is solved for the unknown temperatures, using a Gauss elimination method that exploits sparseness and symmetry for computational efficiency. Once the unknown temperatures at the nodal points of the elements are calculated, the temperature gradient ∇T can be calculated according to element shape functions [49].

Element fluxes can then be calculated using:

$$q'' = K_C (\nabla T) \tag{2.18}$$

where K_C is the conductivity of the material, expressed as a matrix.

To facilitate understanding, the fundamental governing equations and variables of heat transfer analysis can be directly compared to those used in structural FEM, presented earlier. The following Table 2.4 presents this analogy, presenting the correspondence between structural and thermal finite element formulations.

Table 2.4: Heat Transfer and Structural Analysis Analogy [49]

-	**Heat Transfer**	**Structural**
T / (K or $°C$)	Temperature	Displacement
∇T / -	Temperature gradient	Strain
q'' / W/m^2	Flux	Stress
K_C / -	Conductivity matrix	Stiffness matrix
H / -	Boundary convection matrix	Elastic foundation stiffness matrix
f / -	Thermal loading vector	Load vector
$\dot{q}$ / W/m^3	Volumetric heat generation in element	Gravity load

In a linear steady-state heat transfer analysis, material properties such as conductivity and convection coefficients are assumed to be constant and linear [49].

When using shell elements in heat transfer simulations, these are treated as membranes. In this formulation, composite properties are homogenised, resulting in only one degree of freedom per grid point (temperature). Consequently, the temperature distribution through the thickness of the shell is not resolved; instead, only the nodal temperature is obtained. Similarly, the heat flux in composite plates or shell elements is evaluated using the homogenised conductivity of the entire element [49].

For these reasons, it is often advantageous to discretise the model with solid elements, which allow a more detailed and realistic representation of the through-thickness temperature distribution, rather than relying solely on surface-based or 2D shell elements.

2.7.4 Linear Transient Heat Transfer Analysis

Linear transient heat transfer analysis calculates the temperature distribution in a system over time; its transient formulation enables the capture of the thermal behaviour of a system over time and the study of its evolution. On the contrary, steady-state analysis, as seen before, aims to find the state of equilibrium of the system. The thermal loads applied to the system can either be time-dependent or time-invariant [50].

For linear transient heat transfer analysis, the simple finite element formulation can be expressed as [50]:

$$C\dot{T} + (K_C + H)T = f \tag{2.19}$$

where C is the heat capacity matrix, K_C is the conductivity matrix, H is the boundary convection matrix, $\dot{T}$ is the derivative of the nodal temperature matrix with respect to time, T is the unknown nodal temperature matrix, and f is the thermal loading vector. The thermal loading vector is expressed as in the above-presented Equation 2.17.

The governing differential equation is solved to obtain the nodal temperatures T at the specified time steps. Compared to the Linear Steady-State Heat Transfer Analysis formulation, an additional term $C\dot{T}$ appears, which accounts for the transient nature of the problem [50].

In linear transient heat transfer analysis, the Newmark time integration scheme (implicit) is employed in combination with Automatic Time Stepping. The time stepping is controlled by evaluating the Local Truncation Error (LTE), which is expressed as [50]:

$$\varepsilon = \frac{h}{9.09}\sqrt{\frac{\Delta\dot{T}^T C \Delta\dot{T}}{T^T C T}} \tag{2.20}$$

where h is the time step, T is the nodal temperature vector, and C is the heat capacity matrix. Based on the magnitude of the truncation error relative to a prescribed tolerance, the time step size is automatically adjusted to ensure accuracy and stability.

In the transient heat transfer formulation, the governing Equation 2.19 remains solvable even in the absence of defined temperature boundary conditions. For example, if system initial temperature fields are defined, these will be used to evaluate the temporal evolution of the thermal response of the system throughout the simulation.

The Nonlinear Transient Heat Transfer Analysis adopts the same formulation but extends its capabilities by including additional effects, such as thermal radiation [51].

2.8 Dynamic Explicit Analysis

Dynamic problems refer to the analysis of systems or structures subjected to time-dependent loads or motion. This type of analysis evaluates the evolution of the system's response over time, accounting for the combined effects of inertia, damping, and external excitations. The dynamic behaviour of a discrete linear system with n degrees of freedom in the form of a generic system of differential equations is presented in Equation 2.21 [52]. It represents the physical phenomena that numerical dynamic finite element analyses aim to replicate.

$$[M]\{\ddot{u}(t)\} + [C]\{\dot{u}(t)\} + [K]\{u(t)\} = \{F(t)\} \tag{2.21}$$

where $[M]$, $[C]$ and $[K]$ represent, respectively, the mass matrix, the damping matrix and the stiffness matrix. The vectors $\{\ddot{u}(t)\}$, $\{\dot{u}(t)\}$ and $\{u(t)\}$ represent, respectively, the acceleration, velocity and displacement vectors; and $\{F(t)\}$ is the external forces vector [52].

The above-represented equation is solved for the unknown time-dependent quantities $\{\ddot{u}(t)\}$, $\{\dot{u}(t)\}$ and $\{u(t)\}$. From these variables, it is possible to derive other physical quantities such as strain, stress, and reaction forces [52]. The initial conditions necessary to solve the equations are the initial displacement and velocity, $\{u(t=0)\} = \{u_0\}$ and $\{\dot{u}(t=0)\} = \{\dot{u}_0\}$, respectively [52].

For simple harmonic analyses, the solution can be obtained in an analytical approach. Numerical methods rely on an approach based on a process of time discretisation to result in a suitable approximation of the solution.

2.8.1 Time Discretisation

Time discretisation is a method that enables numerical methods to transform an initial continuous problem in time to a discrete problem that is solved at regular intervals. The methods of direct numerical integration to numerically determine the system's response are based on the following assumptions [52]:

- Determination of the unknown time-dependent variables following the equation of motion only at discrete instants t_i, separated by time intervals Δt, thus not for the entire range of the continuous variable of time t.
- Establishment of a variation of displacement $\{u(t)\}$, velocity $\{\dot{u}(t)\}$ or acceleration $\{\ddot{u}(t)\}$ within each time interval. This variation is defined by the integration method, either implicit or explicit, as will be seen shortly.

The procedure, therefore, consists of dividing the response time T into n regular intervals $\Delta t = \frac{T}{n}$ and determining the solution at each discrete instant t_i [52].

The choice of time integration algorithms is fundamental, as each entails trade-offs in stability, accuracy, and applicability. Time integration algorithms are split into implicit and explicit integration methods depending on their fundamental characteristics [53, 54].

To explore the characteristics of implicit and explicit time integration schemes, consider the following example.

The simplest *explicit* integration method is the Forward Euler Method, presented in a general form for a coordinate y, in the following Equation 2.22,

$$y^{n+1} = y^n + \Delta t f\left(t^n, y^n\right) \tag{2.22}$$

where the time step is $\Delta t = t^{n+1} - t^n$ and $f(t,y)$ is the function defining the time derivative of y [53]. This method defines the coordinate y^{n+1} at the time instant $t = t^n + \Delta t$ solely based on the equation of dynamic equilibrium at the instant $t = t^n$; this is the reason for the designation "explicit" [52].

In contrast, the simplest *implicit* integration rule is the Backward Euler Method, presented in Equation 2.23 [53].

$$y^{n+1} = y^n + \Delta t f\left(t^{n+1}, y^{n+1}\right) \tag{2.23}$$

which requires the solution of the following *implicit* algebraic equation,

$$y^{n+1} - \Delta t f\left(t^{n+1}, y^{n+1}\right) = y^n \tag{2.24}$$

Now, for this method, the y^{n+1} solution at the time instant $t = t^n + \Delta t$ is obtained from the equation of dynamic equilibrium at the same time instant $t = t^{n+1}$. It constitutes, therefore, an "implicit" integration method [52].

Both methods appear at first glance to be similar and yield a result that is formally the same in terms of accuracy. However, explicit methods are limited by a stability constraint on its time step size. They are categorised as "conditionally stable". Implicit integration schemes, on the contrary, are unconditionally stable, which means that it can take an arbitrarily large time step size and remain numerically stable, though accuracy can be affected [53]. That being said, implicit methods may require convergence checks, as convergence of the algorithms is not guaranteed, while explicit methods ensure the convergence of the algorithm [53].

Implicit integration methods require the solution of large systems of nonlinear equations at every time step, commonly through Newton or quasi-Newton iterative methods. In the process of solving the nonlinear systems, the repetitive solution of linear systems are required, this fact can result in simulations that are both memory and CPU-intensive. Explicit methods do not require the solution of large systems of linear equations and therefore their computation requirements can be much smaller. To be cost-competitive with explicit methods, the implicit method must take a correspondingly large time step. Even if the accuracy requirements allows for a large enough time step, the radius of convergence for the iterative solver may limit the time step and therefore restrict the efficiency of the implicit formulation [53]. On the other hand, for problems of larger time magnitude, explicit methods can become impractical, as their stability conditions often require

very small time steps, leading to a high number of increments to reach the solution. This can make the simulation exceedingly lengthy

Taking into account the characteristics of each type of simulation, it can be concluded that implicit integration methods are more suited to problems of longer temporal scales. Explicit finite element methods are, in turn, more suited to solve large-scale, short-duration problems where transient phenomena are critical, such as strong shocks generated by high-velocity impacts and explosives [53] (Figure 2.12). Explicit methods are widely used for applications such as crash tests, impact, drop tests, detonation and ballistics problems.

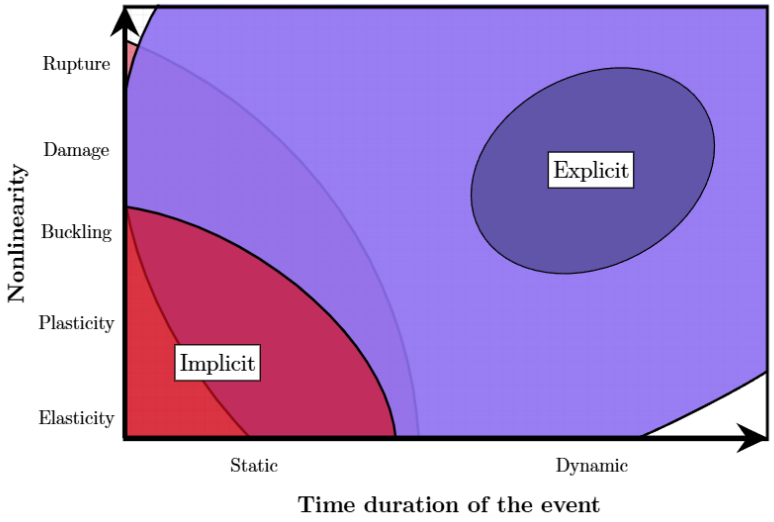

Figure 2.12: Applicability of implicit and explicit analyses (Adapted from [55])

Additionally, the absence of equation solvers in explicit methods means that adding complicated nonlinear physics is comparatively easy since there is no need to form a stiffness matrix [53]. Making explicit integration methods more suited for cases involving multiple nonlinearities, including complex contacts, material or geometrical behaviours.

2.8.2 Central Difference Integration

Many integration methods exist for explicit finite element methods and have been used in practical cases. The *central difference method* is by far the most popular one, and is the method used in Altair OptiStruct® [53].

It is based on the central difference approximation of the first derivative of a function, derived using a Taylor series; it is [53]:

$$\frac{df(t)}{dt} = \frac{f(t+\Delta t/2) - f(t-\Delta t/2)}{\Delta t} - \frac{1}{24}\frac{d^3 f(t)}{dt^3}(\Delta t)^2 + O((\Delta t)^3) \tag{2.25}$$

Computing the function at a midpoint, time-advanced solution at $t = t + \Delta t/2$ [53],

$$f\left(\frac{t+\Delta t}{2}\right) = f\left(\frac{t-\Delta t}{2}\right) + \frac{df(t)}{dt}\Delta t + \frac{1}{24}\frac{d^3 f(t)}{dt^3}(\Delta t)^3 + O((\Delta t)^4) \tag{2.26}$$

The resulting truncation error is [53]:

$$e^T(\Delta t) = \frac{1}{24}\frac{d^3 f(t)}{dt^3}(\Delta t)^3 \tag{2.27}$$

In the subsequent formulation, the central difference method is presented by the reference paper [53] using a notation convention widely adopted in the shock physics community. The discrete times of the numerical integration are denoted by t^n, where the superscript n indicates the integration step. The step size between two consecutive times t^{n-1} and t^n is defined as $\Delta t^n = t^n - t^{n-1}$.

The sequence of times can therefore be written as [53]:

$$t^n = t^0 + \sum_{i=1}^{n} \Delta t^i \tag{2.28}$$

which means that the current time t^n is obtained by summing all previous time increments from the initial instant. For convenience and without loss of generality, the starting time is taken as $t^0 = 0$ [53].

The coordinates (displacements) are explicitly integrated using the velocities [53],

$$\{u\}^{n+1} = \{u\}^n + \Delta t^{n+1}\{v\}^{n+1/2} \tag{2.29}$$

It is important to note that the velocity is located at the middle of the time step, which is expressed as $t^{n+1/2} = t^n + \Delta t^{n+1}/2$ and the velocity is written as $v^{n+1/2}$. Here, the displacement u is evaluated at integer time levels n while the velocity v is at half-integer time steps $n+1/2$, the velocity is often referred to as being *staggered* with respect to the coordinates in time [53].

The velocity is integrated from the acceleration [53].

$$\{v\}^{n+1/2} = \{v\}^{n-1/2} + \Delta t^{n+1/2}\{a\}^n \tag{2.30}$$

where $\Delta t^{n+1/2}$ is:

$$\Delta t^{n+1/2} = t^{n+1/2} - t^{n-1/2} = \frac{t^{n+1} + t^n}{2} \tag{2.31}$$

Combining the position and velocity updates, the central difference method is summarised as [53]:

$$\begin{cases} \{v\}^{n+1/2} = \{v\}^{n-1/2} + \Delta t^{n+1/2}\{a\}^n\left(\{u\}^n, \{v\}^{n-1/2}, t^n\right) \\ \{u\}^{n+1} = \{u\}^n + \Delta t^{n+1}\{v\}^{n+1/2} \end{cases} \tag{2.32}$$

where the arguments to the acceleration have been added to explicitly spell out its allowable dependencies [53].

To summarise, the acceleration is computed directly from the equilibrium equation, which is defined, in a solver-centred approach, in the following Equation 2.33 [54],

$$[M]\{a\}^n = \{f_e(\{u\}^n, t^n)\} + \{f_d(\{v\}^n, t^n)\} + \{f_c(\{u\}^n, t^n)\} + \{f_h(\{u\}^n, t^n)\} - \{f_i(\{u\}^n, t^n)\} \tag{2.33}$$

where,

- $[M]$: Lumped mass matrix;
- $\{f_e\}, \{f_d\}, \{f_c\}, \{f_h\}$ and $\{f_i\}$: External force, damping force, contact force, hourglass force and element internal force vectors, respectively;
- $\{a\}^n$: Acceleration vector at time instant t^n.

Then the velocity is updated according to Equation 2.30, finally the displacement u^{n+1} is obtained according to Equation 2.29.

The finite differences algorithm is therefore cyclic and adheres to the characteristics of explicit time integration methods explained in the last subsection.

2.8.3 Stability Condition

As discussed earlier, explicit integration methods are limited by a stability constraint.

Stability, in the roughest sense, requires that the numerical solution remains bounded for all time, assuming that the exact solution is bounded. Stability is completely divorced from any considerations of accuracy, it is entirely possible to setup an algorithm that will produce a stable, but inaccurate solution [53].

The stability condition is directly related to the highest natural frequency of the system, which in turn influences the maximum step size of the explicit integration algorithm that ensures numerical stability. The condition is as follows: *"The maximum time step size is roughly equal to the length of time a sound wave takes to traverse the smallest element in the mesh"*. This means that during a time step, a travelling shock wave should only pass through no more than one element. Typical step size for problems involving common structural materials is measured in microseconds [53]. Mathematically, the stability condition is represented as follows [52–54]:

$$\Delta t \leq \Delta t_{\text{crit}} = \frac{2}{\omega_{\max}} \tag{2.34}$$

where Δt_{crit} is the critical step size and $\omega_{\max}$ is the highest natural frequency of the system.

In OptiStruct®, the time step is calculated automatically by default depending on the verification of the condition in Equation 2.34. The verification of this condition involves the characteristic dimension of the critical element, the material properties, and the speed of sound through the system. For instance, the critical time step for solid and shell elements are obtained in the following way [54]:

Solid Elements

For solid elements, the critical time step size is computed from:

$$\Delta t_{\text{crit}} = \min\left(\frac{l}{Q+(Q^2+c^2)^{1/2}}\right) \tag{2.35}$$

where c is the adiabatic speed of sound through the solid element and Q is a function of the bulk viscosity coefficients C_0 and C_1 as follows:

$$Q = C_1 c + C_0 l \max(0, -\dot{\varepsilon_{kk}}) \tag{2.36}$$

The element characteristic length calculation depends on the element in question. Altair OptiStruct® 's documentation provides information on all types of available elements [54]. The solid elements more frequently utilised are illustrated in Figure 2.13.

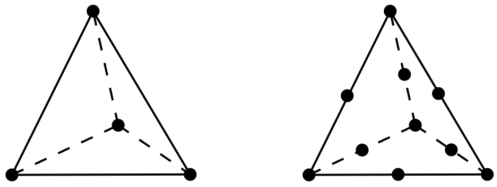

(a) Tetrahedral elements (TETRA4 and TETRA10)

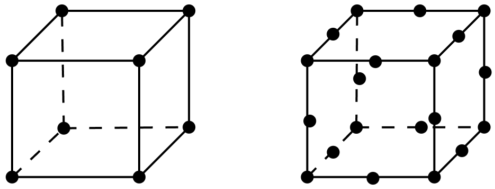

(b) Hexahedral elements (HEX8 and HEX20)

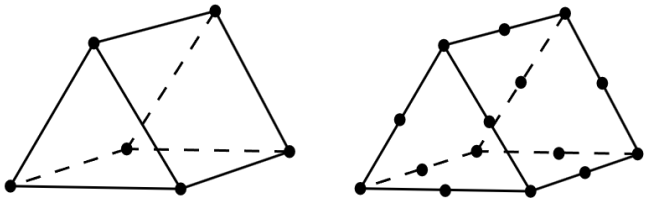

(c) Pentahedral elements (PENTA6 and PENTA15)

Figure 2.13: First and second-order solid elements common in HyperMesh®

Shell Elements

For shell elements, the time step size is determined by [54]:

$$\Delta t = \min\left(\frac{L}{c}\right) \tag{2.37}$$

where c is the speed of sound calculated as:

$$c = \sqrt{\frac{E}{\rho\,(1-\nu^2)}} \tag{2.38}$$

where E, ρ, ν and L are Young's modulus, material density, Poisson's ratio and L is the characteristic length, respectively.

- Quadrilateral elements (Figure 2.14): $L = \frac{A}{\max(L_1, L_2, L_3, L_4)}$

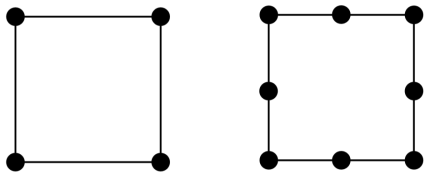

Figure 2.14: First and second-order quadrilateral shell elements (QUAD4 and QUAD8 in HyperMesh®)

- Triangular elements (Figure 2.15): $L = \frac{2 \times A}{\max(L_1, L_2, L_3)}$

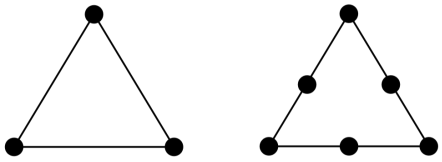

Figure 2.15: First and second-order triangular shell elements (TRIA3 and TRIA6 in HyperMesh®)

Therefore, the construction of a consistent and well-defined mesh is of fundamental importance to guarantee a sufficiently large and non-restrictive critical time step.

It is important to note that the critical time step is not a rigid value but is updated throughout the analysis as the elements deform under load.

2.8.4 Mass Scaling and Hourglass Control

Mass scaling is a numerical technique used in explicit time integration to artificially increase the critical time step by adjusting the mass matrix, typically through density scaling. This reduces computational time but must be applied with caution, as it modifies the physical response and is unsuitable for problems dominated by wave propagation, such as high-speed impact. Its application should therefore be limited and verified during post-processing to ensure the validity of results [53, 54].

Explicit analysis is commonly performed with first-order reduced integration elements, which are efficient but inherently susceptible to hourglass modes. Hourglass modes are non-physical deformation patterns that can appear in under-integrated elements. These modes let the element distort without any strain energy, which results in a "soft" behaviour that does not resist deformation. Hourglass control is therefore applied to suppress these non-physical zero-energy deformations, although excessive control may introduce artificial stiffness and distort the results [54].

2.9 Composite Numerical Modeling in Altair OptiStruct®

Altair OptiStruct®, HyperMesh® and HyperView® are all softwares under the HyperWorks® umbrella, a design and simulation platform that integrates optimisation and multiphysics simulation. Altair HyperMesh® is a pre-processing software used to prepare finite element models; OptiStruct® is a solver primarily used for structural analysis and optimisation; and HyperView® serves as a post-processing tool. The Altair suite provides a robust and integrated environment for the analysis of composite structures

OptiStruct®'s finite element formulation for composite laminate structures is derived from the Classical Lamination Theory, and for transverse shear forces, First Order Shear Deformation Theory is used, both formulations described in Section 2.6 [56].

Modelling laminate composites for FEA requires more information than isotropic models; the following information needs to be defined [41]:

- Part Geometry;
- Ply Geometry;
- Material Data;
- Mesh Data;
- Material Alignment;
- Lay-up sequence;
- Z-Offset Information;
- Drape Information.

Composite structures can be modelled in three distinct ways, using either 2D shell or solid elements, with most components represented through shell elements. The first modelling approach is the **Composite Ply-by-Ply Solid Modelling**. Solid modelling is the most accurate technique and the only one capable of capturing through-the-thickness effects, such as delamination. However, this accuracy comes at the cost of increased computational effort. Ply-by-ply solid modelling requires one solid element layer per ply, resulting in a considerable number of elements in the model [41].

The alternative methods available in OptiStruct are **Composite Zone-Based Shell Modelling** and **Composite Ply-Based Shell Modelling**. Both approaches rely on surface geometry meshed with 2D shell elements, but differ in the way the lamination is defined [41]. In a brief way:

- **Zone-Based Modeling**: it is the traditional approach to build composite models. It requires a property definition for each laminate zone within a composite structure, therefore, for each ply drop or addition location, another property needs to be defined. Plies that extend through multiple laminate zones must be redefined in each zone. This particularity results in inefficient data handling and makes subsequent modifications to the laminate stacking more difficult. Zone properties are defined in OptiStruct® through the `PCOMP` and `PCOMPG` property cards [41].
- **Ply-Based Modeling**: it is a relatively recent technique to build composite models. This method attempts to mimic the composite manufacturing process of cutting and stacking

plies "on top" of each other to construct a composite structure. In the ply-based modeling approach, plies are defined as physical entities of a given material with thickness and shape, then they are stacked to form a laminate. In this way, a ply is defined only once. Composite ply-based modeling techniques offer significant advantages for composite design optimisation, as it enables design updates to the composite model via modification of ply shapes and addition/subtraction of plies. Ply-based properties are defined in Optistuct® through the **PCOMPP** property card [41]. For the present work, the Ply-Based Shell Modeling approach was selected.

Composites shell element-based models are usually defined using the **MAT8** material type. This material card is used to define the material properties of linear temperature-independent orthotropic materials for 2D elements. The MAT8 material data entries directly correspond to the plane-stress state, classical lamination theory, as introduced in Equation 2.3.

An important aspect of composite design is the definition of the element normal and material orientation. The laminate plies are stacked in the direction of the element normal, as illustrated in Figure 2.16, so the orientation of the normal direction in the model needs to be correctly defined.

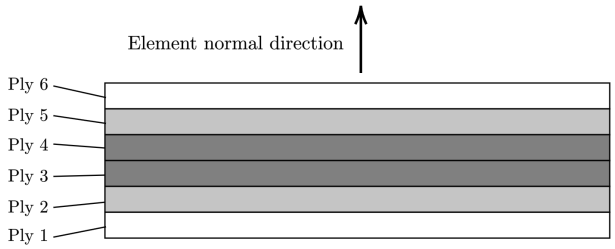

Figure 2.16: Ply stacking sequence with respect to the element normal [57]

The element coordinate system is highly dependent on the node numbering of each element. For composite elements, it is necessary to define a dedicated coordinate system, which serves as a reference for ply angle orientation. Furthermore, the material orientation is essential for defining the orthotropic material properties [41]. Figure 2.17 illustrates the process of element material orientation.

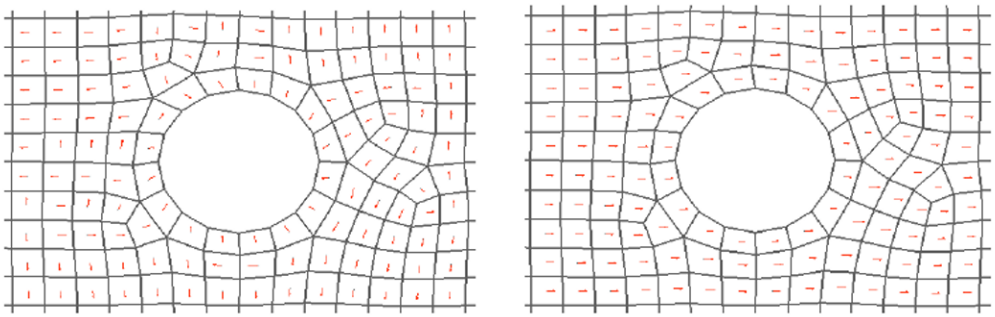

Figure 2.17: Alignment of elements according to the laminate main direction, before and after orientation [57]

OptiStruct's composite modelling and post-processing capabilities include the calculation of composite failure indices using various failure theories, ranging from simple maximum stress and strain, and Tsai–Wu criteria, defined in Subsection 2.6.2, to more advanced models such as the Puck and Hashin theories.

2.10 OptiStruct Composite Optimisation

This section delves into the theoretical basis of the methods of composite design optimisation implemented in this project. It begins with an overview of the concept of optimisation-driven design, followed by a theoretical overview of optimisation. Finally, the three-step methodology adopted in this project is presented, along with an explanation of Altair OptiStruct's optimisation capabilities.

2.10.1 Optimisation-Assisted Composite Design

The traditional design approach follows a linear process where the design of the component is followed by physical or numerical testing. This often leads to multiple back-and-forth iterations between design and analysis, which could be costly and time consuming.

The approach followed in part of this work will take advantage of numerical optimisation methods, integrating them early in the process of design and development, running in parallel to design activities. This methodology will streamline the development phase, reducing design iterations and ensuring the satisfaction of the performance targets with an optimised design. Such optimisation methods are a powerful tool for engineers, as they enable them to make informed decisions based on objective data rather than trial and error. This enhances the efficiency of the design process and can lead to innovative solutions that may not be apparent through conventional routes.

Figure 2.18 compares the traditional design method with the optimisation-driven approach used in this work.

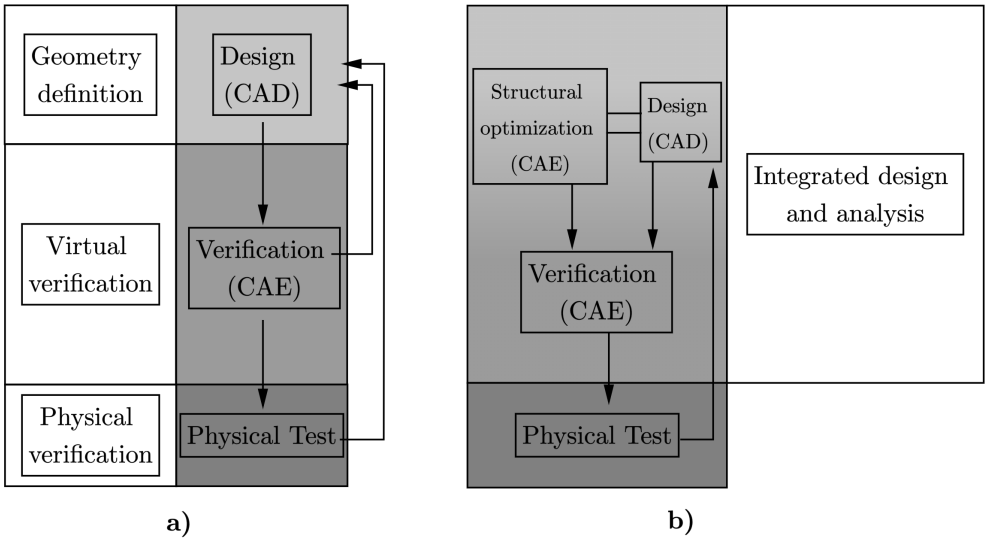

Figure 2.18: a) Traditional Design b) Optimisation-driven design (Adapted from [41])

2.10.2 Optimisation

Optimisation is an area of applied mathematics that, in the context of mechanical design, can be described as the process of identifying the most effective design of a component to ensure it meets its intended function and performance requirements.

Mathematically, an optimisation problem consists in minimising or maximising an objective function, subject to design constraints, by varying its inputs, known as design variables. The domain of possible values for these variables defines the design space. This corresponds to a non-linear programming problem of the following form [58] :

$$\begin{aligned} &\text{Minimise (or maximise) } f(x); \\ &\text{Subject to: } g_i(x) \leq 0,\ i = 1\ ...m \\ &\qquad\qquad h_j(x) = 0\ j = 1\ ...p \end{aligned} \tag{2.39}$$

$x = (x_1,\ ...,x_n)$ represents the vector of design variables;

$f(x)$ represents the objective function;

$g_i(x)$ represents the inequality constraint functions;

$h_j(x)$ represents the equality constraint functions.

The optimisation is an iterative process carried out by the solver OptiStruct®. It is considered successful when the algorithm converges to a solution that minimises the objective function while satisfying all constraints. This solution is called a feasible design. OptiStruct's optimisation algorithms are based on the **Gradient Descent Method**, which seeks the minimum of a function using

its gradient vector. The gradient descent method algorithm can be plainly described as follows [59]:

1. Start from an initial point x_0;
2. Evaluate the function $f(x_i)$ and the gradient of the function $\nabla f(x_i)$ at point x_i;
3. Determine the next point using the negative gradient direction: $x_{i+1} = x_i - \alpha \nabla f(x_i)$;
4. Repeat steps 2 and 3 until the function converges to a minimum.

Figure 2.19 illustrates the process of convergence in an optimisation algorithm.

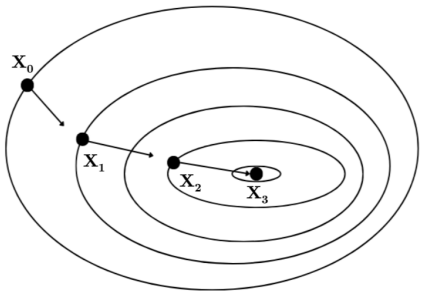

Figure 2.19: Visual representation of convergence (Adapted from [59])

The result computed is a local minimum. The most significant changes typically occur in the initial optimisation steps and, as a result, only a modest number of iterations are necessary in practical applications [59]. Consequently, it is considered good practice to start with a thoughtful and feasible initial design.

2.10.3 Methodology

The composite optimisation method developed by Altair® is divided into three phases: **Free-size Optimisation**, **Ply-Bundle Sizing Optimisation** and **Stacking Sequence Optimisation**.

2.10.3.1 Free Size Optimisation

Free-Size Optimisation is a concept-level optimisation process that alters the thickness of each ply on an element-by-element basis. In simpler terms, it aims to answer the question: *"What are the most efficient ply shapes for the loaded structure ?"*. The outcome of this phase is the definition of the thicknesses and ply shapes for each fibre orientation that result in the most efficient part. The majority of the optimisation effort is done in this phase, while the latter stages focus on fine-tuning and manufacturability [41, 59].

In this process, the design variables are the thicknesses of each ply for every element. Composite free-size optimisation is based on the concept of *super-plies*, which are bundles of all plies with the same fibre orientation. One super-ply with a large initial thickness should be created for

each fibre orientation, as the software mainly only removes material. During the optimisation process, OptiStruct® allows the thickness of each super-ply to vary freely within the lower and upper bounds defined by the user. By varying the thicknesses independently across all elements, both the total laminate thickness and the optimal composition of the composite laminate are simultaneously tailored across the structure [41, 59].

For both free-size and subsequent sizing optimisation, **SMEAR** technology should be used to ensure that the laminate behaviour remains independent of the stacking sequence. In terms of the classical lamination theory, this translates to the following conditions on the stiffness matrices $[A]$, $[B]$, and $[D]$ [41, 59]:

- $[A]_{\texttt{smear}} \rightarrow$ Stacking sequence independent
- $[B]_{\texttt{smear}} = 0$ (Symmetric)
- $[D]_{\texttt{smear}} = [A]_{\texttt{smear}}(T^2/12) \rightarrow$ Stacking sequence independent

For each ply angle, the tailored patch shapes correspond to super-ply bundles, which are generally split into four levels of resolution. Consequently, for each ply defined in the initial model, four plies with decreasing levels of material are created during the free-size optimisation process. The first discretised ply for each orientation always includes the entire model, including all elements. Users can specify a different number of ply bundles per orientation to tune the complexity of the design. Figure 2.20 illustrates the process of ply shape generation.

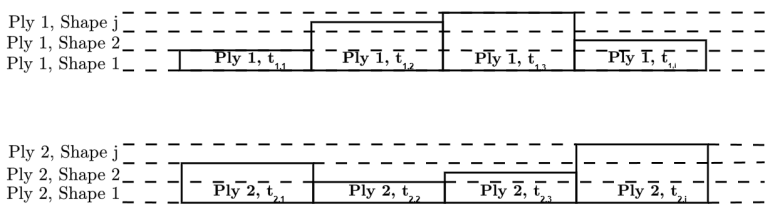

Figure 2.20: Free-size ply shape generation (Adapted from [41])

The manufacturing process of laminated composites is a central consideration in composite optimisation. To achieve a manufacturable design concept, manufacturing requirements must be incorporated as early as the concept design stage [41]. Design constraints such as lower and upper bounds for laminate thickness, minimum ply shape dimension (*Mindim*), and balancing of fibre orientations are important tools to introduce the manufacturing demands into free-size optimisation. Thickness limits help ensure a minimum manufacturable thickness across the entire structure. *Mindim* commands ensure that the resulting plies are close to manufacturable, while balance commands are used to enforce symmetry in the laminate, particularly important for the $\pm 45°$ fibre orientations.

2.10.3.2 Size Optimisation

Size Optimisation, or Ply-Bundle Sizing Optimisation, is a fine-tuning step that optimises the thickness of tailored plies. At this point, both the part thickness and the ply shapes that define the constant thickness zones are established. However, the exact number of each ply shape required to meet the strength and manufacturing targets needs to be determined through size optimisation [41].

Nevertheless, before any sizing optimisation, the user should review and edit the ply shapes resulting from free-size optimisation. The purpose of this intermediate phase is to guarantee that every ply has an efficient, manufacturable geometry, free from discontinuities or small, impractical patches. Incorporating this production-oriented perspective is crucial to achieving a final optimised design that closely resembles a feasible, real-world product.

Following the manual adjustment of ply shapes, it is recommended to re-optimise their thickness, in a similar way to the free-size phase; this process is known as **continuous sizing**. The resulting thicknesses are then discretised into several manufacturable plies through a process called **discrete sizing**, which is the real fine-tuning ply-bundle size optimisation. Thus, size optimisation can be divided into two steps: continuous and discrete sizing. Continuous sizing is necessary because the manual modification of plies could lead to substantial changes in ply shape, which can significantly alter the behaviour of the laminate compared to the original free-size results [41].

The design variables in size optimisation are the ply shapes. The result of this second optimisation procedure is a laminate design similar to free-size optimisation but comprising the optimum number of manufacturable plies for each orientation [41]. However, even after completing the composite size optimisation, the final design is not fully defined. The exact stacking sequence for the plies is still unknown and will be addressed in the next step, composite shuffling optimisation.

2.10.3.3 Composite Shuffling Optimisation

Shuffling Optimisation is a composite-specific process that reorganises the plies resulting from the sizing optimisation to determine the optimal stacking sequence. It is the final phase of the three-step composite optimisation methodology [41].

In preceding phases, the stacking sequence was not considered. In this final step, the solver iteratively rearranges the plies defined in the previous optimisation step until all manufacturing targets are satisfied. It is important to note that, during shuffling, the solver does not modify the thickness, mass, or shape of the plies. Among the manufacturing constraints that can be imposed are: positive/negative ply orientation pairings, the maximum number of consecutive plies for each orientation, and core/cover lay-ups [41].

Figure 2.21 summarises Altair's three-step composite optimisation methodology.

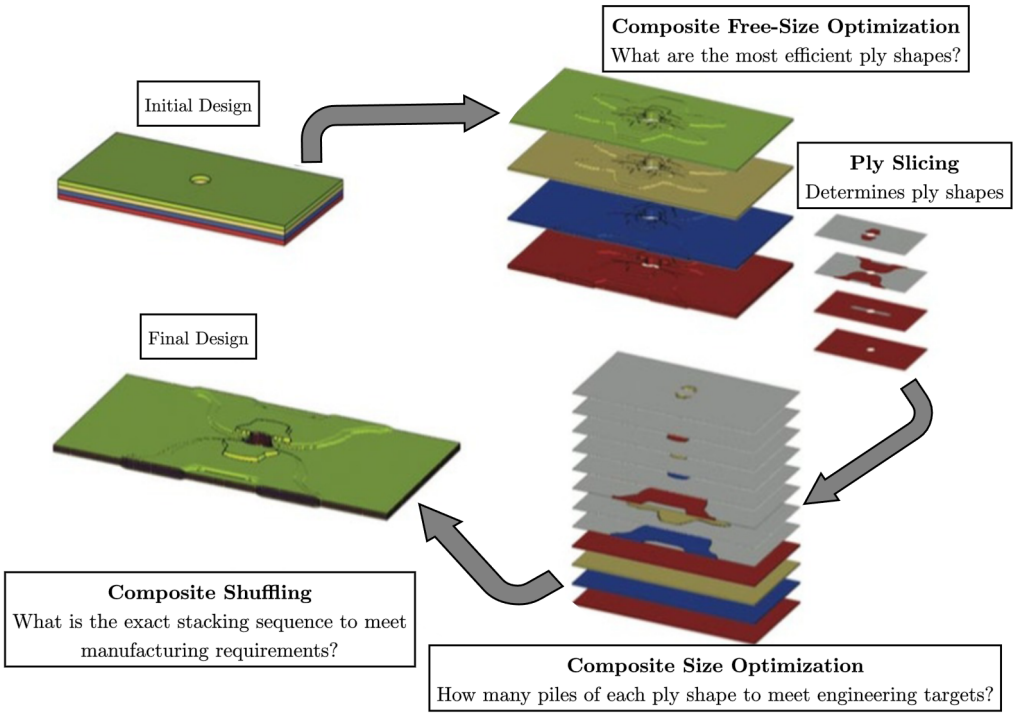

Figure 2.21: Altair's three-step optimisation methodology [41]

The resulting design from the complete composite optimisation process is an efficient structure, closely resembling the final part and ready for manufacturing. However, the design is not final. A concluding design verification must be performed, which aims to verify if the structure meets all structural and manufacturing requirements.

Chapter 3

Preliminary Analysis of the Stark VARG EX/MX Battery Enclosure

This chapter presents a preliminary study on the carbon fibre composite design of the battery enclosure for the Stark Future EX and MX electric motocross motorcycles. It begins with the motivation and context of this supporting work, which, while not the main focus of this thesis, contributes to its broader objectives. The study setup and results are then described, followed by a brief note on the conclusion of the collaboration.

3.1 Context and Motivation

3.1.1 Initial Circumstances

Following several months of generally unfruitful conversations with Famel, an opportunity emerged to collaborate with Stark Future, a promising new brand with an innovative line of high-performance electric motocross and enduro motorcycles. The collaboration's objective was to design a composite battery case for the current and/or future models within Stark Future's lineup.

An initial online meeting was promptly arranged, followed by an in-person discussion with one of Stark Future's Chief Engineers at Adamastor's facilities. The online meeting allowed Stark Future and Adamastor to present their ongoing projects and perspectives regarding a potential partnership. The following meeting with Stark Future's Chief Engineer delved into technical aspects, a full overview of their current battery solution was made, and preliminary ideas for composite-based alternatives were explored.

Both meetings were constructive and showed potential for collaboration. Nevertheless, developing a composite solution for the existing VARG EX/MX battery case presents a number of challenges, which will be addressed in the following subsection.

3.1.2 Stark Future VARG EX/MX Battery

The Stark Future VARG EX and MX are high-performance electric motorcycles based on the same platform. Both share a very similar architecture and only differ in some details. The MX is the motocross variant, whereas the EX is the road-legal enduro version, equipped with the necessary features for the road. The battery design for the MX and EX electric motorcycles is, in broad terms, identical.

As of March 2025, the VARG EX, being the most recent model, benefited from an upgrade in battery capacity from 6.5 kWh to 7.2 kWh. Still, this enhancement did not involve any changes to the geometry of the battery case. The reason for the upgrade will be explained in the next section. Figure 3.1 shows the Stark Future VARG EX alongside its battery.

(a) Stark VARG EX (b) Stark VARG Battery

Figure 3.1: Stark Future VARG EX and its Battery [1]

The Stark Future battery casing is described by the company as: *"A patented "Flying V" honeycomb magnesium battery (that) connects every cell directly to the casing, (...)"* [1]. The design of the battery case is very innovative. It consists of two magnesium alloy half-cases, sealed and bolted along the midplane. Manufacturing is carried out using a process of Magnesium Injection Moulding, with subsequent CNC machining for finer details. The choice of a magnesium alloy offers advantages such as high specific strength, low weight, and excellent thermal conductivity. However, magnesium is a notoriously expensive and challenging material to work with due to its reactivity and flammability.

The battery case is considered semi-structural, meaning that it contributes to the overall stiffness and integrity of the motorcycle while not being a primary load-bearing component. Thus, the mechanical performance of the battery case is an important factor to consider.

Nevertheless, the most striking detail of their battery design is the placement of the cells. Each cell is directly connected to the magnesium casing, supported by a circular "honeycomb" structure integrated in the inside face of the casing. This honeycomb structure is shown in Figure 3.2. According to Stark Future, this innovative design choice allows the battery to achieve better cooling, higher strength, and a lower weight [1]. Electrical insulation between the cells and the magnesium case is achieved through a specialised surface coating. Ensuring proper insulation and

grounding is crucial for high-power battery systems, both to prevent short circuits and to guarantee operational safety

Figure 3.2: Stark Future battery "honeycomb" structure (From the YouTube video [60])

The Stark VARG EX and MX, in their Alpha power configuration, are capable of producing around 60 hp continuously and an impressive 80 hp in short bursts. These power figures are thermally demanding on the battery pack, making thermal management a critical aspect of the design. The magnesium case is passively air-cooled, without the use of fans. As such, heat dissipation occurs primarily through conduction across the metallic casing and natural or forced convection with the surrounding air. The case is also rated IP69K dust and waterproof, thanks to a pressure relief system.

3.1.3 Collaboration Objectives

As previously stated in this chapter, the goal of the partnership was to develop a functional prototype of the Stark VARG battery enclosure using composite materials. Uniting Stark's requirements and Adamastor's targets for the design of this prototype, the following objectives could be defined. The design should:

- Maintain or improve the structural integrity of the original design;
- Reduce the mass of the battery compared to the magnesium version;
- Be flame-resistant in accordance with international standards, such as the UL94 V-0 Standard for Safety of Flammability;
- Retain its water and dust proof capabilities;
- Ensure an adequate thermal management, without the risk of overheating or thermal runaway;
- Ensure electric insulation, grounding and cell contact safety, as in the original design;
- Aim for the use of sustainable composite material solutions such as natural fibres, bio-resins or recyclable thermoplastics;

- Strive for an economically viable solution.

To satisfy these requirements, an optimisation-driven approach will be employed, leveraging the flexibility and unique characteristics of composite materials, as well as Adamastor's expertise in composite structural design. However, the innovative architecture of Stark's battery case introduces specific challenges for the development of the composite prototype.

The first, and arguably one of the biggest obstacles to face in the design of the composite prototype, is replicating the internal circular "honeycomb" structure that fixes the cells in place. Given that the manufacturing process of laminated composites is an additive process followed by a cure, it is virtually impossible to create such a detailed, tight pattern of geometry with precision through the laminating and cure process alone. This constraint narrows the viable options to two primary solutions: create a thick composite laminate and machine the geometry post-cure, or fabricate the honeycomb structure from a secondary material and bond it to the composite enclosure using structural adhesives. While both options are feasible, they introduce challenges, such as the difficulty in machining cured composites or the tight tolerances required for accurate placement and bonding.

A second significant challenge is ensuring correct thermal dissipation and regulation within the composite battery enclosure. The Stark VARG motorcycles are powerful, and thus, put the battery pack and cells in considerable energetic and thermal strain. Additionally, polymer matrix fibre-reinforced composites are notoriously poor thermal conductors, compared to metallic materials. In the case of an intense use of the bike, namely at its peaks of power, intense heat is generated in the battery cells. If the battery case cannot relieve this thermal stress efficiently, high temperatures could form in the cells, which can damage them, their longevity and performance. This difficulty could be surpassed through the design of an active cooling solution or through the incorporation of metallic inserts to improve heat conduction. Nonetheless, both solutions come with inherent drawbacks, such as added complexity, cost, or structural trade-offs.

Other, lesser but not insignificant, challenges include: achieving a structurally robust yet lighter solution than the original magnesium alloy design; ensuring internal electrical insulation and grounding; implementing sustainable composite solutions that offer good mechanical performance and durability, and cost-effectiveness, to name a few.

3.1.4 Initial Design Strategies

After a thorough analysis of the design constraint discussed in the previous subsection, the following solutions were identified as possible avenues for the development of the composite prototype:

1. Manufacture the circular "honeycomb" from a thick laminate of glass or flax fibres within the battery enclosure, followed by precision machining. Glass or flax fibres would be used for their electrical insulation properties.

2. A similar solution to the previous, however, the enclosure would be entirely made from carbon fibre composite. After machining, a coating would be added to the battery enclosure to ensure electrical insulation.

3. Fabricate the honeycomb structure from a different material than the composite enclosure, bonding it with structural adhesives either before or after the main laminate is cured. A precise positioning method would be required. Materials considered for the internal structure are: light metal alloys (e.g., aluminium) or metal-filled polymers, chosen for their enhanced thermal conductivity and heat-spreading characteristics.

All proposed strategies would also aim to integrate sustainable composite materials and metallic inserts to facilitate thermal conduction.

The in-person meeting showed promise for a productive and successful collaboration for both involved parties. Back-and-forth email conversations followed; however, no technical information on the battery case was made available by Stark Future, such as CAD models, technical drawings or load cases. As a result, and to avoid further project delays, an independent case study was initiated for two main reasons: to explore the mechanical and thermal behaviour of a simplified composite laminate design under typical battery load and temperature conditions; and to demonstrate early progress and technical commitment in the hope of encouraging further collaboration.

This independent effort began with a simple reverse engineering of the current VARG EX/MX battery enclosure, based on information disclosed in the meetings and readily available on the internet, mainly through Stark Future's official media platforms [1, 60]. The goal of this reverse engineering was not to replicate the exact geometry, but to approximate the design as closely as possible using concrete data. A CAD model that reflects the key dimensions and features of the real enclosure, and this model was used to create a simple constant-thickness laminate version of the battery case in Altair HyperMesh®.

From this model, a series of simplified finite element analyses (FEA) were performed. These included static structural assessments, initial laminate lay-up optimisation, and preliminary thermal analyses. It is important to emphasise that this initial study was not intended to satisfy all the prototype's requirements. Rather, it was done as an initial exploratory exercise to assess the feasibility and potential of composite lay-up optimisation, and to understand the thermal performance of a basic composite enclosure. This foundation would serve as the basis for further updates and refinement, which will be discussed in the following sections.

3.2 Reverse Engineering of the Battery Design

As mentioned previously, the approach described in this section does not constitute a precise reverse engineering methodology. The objective was to approximate the geometry of the Stark VARG EX/MX battery enclosure as accurately as possible, using the available information and with a solid foundation. While not all sources of information can be listed in this document, the main references were:

1. The official Stark Future website [1];
2. Two videos published by the official Stark Future account on YouTube, one presenting the MX motorcycle and another detailing the battery production process [60, 61];
3. Technical and contextual details shared during the meetings.

3.2.1 Battery Cells and Capacity

The starting point for the reverse engineering of the battery enclosure is the identification of the individual battery cells. In the YouTube video showcasing the production process of the battery, a close-up at timestamp 33 seconds reveals the inscription ***"INR-21700-P42A"*** on the cells [61]. This code refers to a 21700-type lithium-ion cell manufactured by Molicel^{TM}. These are high-performance rechargeable cells with higher capacity and larger dimensions compared to standard AA batteries.

The battery has undergone two capacity upgrades since the initial unveiling of the Stark VARG MX in late 2021. The initial version featured a 6 kWh capacity, which was increased to 6.5 kWh, and the most recent version, incorporated into the new EX model, now offers 7.2 kWh. According to publicly available information, the battery architecture consists of 400 21700-type cells arranged in a 100 series, 4 parallel configuration (100s4p). From the data of the individual cell, it is possible to verify if the capacity claimed by Stark Future aligns with the specifications of the battery cell found. The following references support the information presented: [1, 60–62].

By performing simple battery capacity calculations using the datasheet of the INR-21700-P42A cell, provided in Appendix A; the claimed battery capacity can be verified.

Battery capacity with INR-21700-P42A Li-ion cells

$$\begin{aligned} &\text{100 cells in series at nominal voltage: } 100 \times 3{,}6 \text{ V} = 360 \text{ V} \\ &\text{4 sets in parallel with typical capacity: } 4 \times 4.2 \text{ Ah} = 16.8 \text{ Ah} \\ &\text{Total expected capacity: } 360 \times 16.8 = 6048 \text{ Wh} \approx 6.0 \text{ kWh} \end{aligned} \tag{3.1}$$

Therefore, these simple hand calculations further confirm the use of Molicel's 21700 cells in the Stark VARG battery pack. An interesting observation arises if the same calculations are performed using the specifications of more recent and higher-performance Molicel cells, namely the **INR-21700-P45B** and **INR-21700-P50B**. The datasheets for these cells are also provided in Appendix A.

Battery capacity with INR-21700-P45B Li-ion cells

$$\begin{aligned} &\text{100 cells in series at nominal voltage: } 100 \times 3{,}6 \text{ V} = 360 \text{ V} \\ &\text{4 sets in parallel with typical capacity: } 4 \times 4.5 \text{ Ah} = 18 \text{ Ah} \\ &\text{Total expected capacity: } 360 \times 18 = 6480 \text{ Wh} \approx 6.5 \text{ kWh} \end{aligned} \tag{3.2}$$

Battery capacity with INR-21700-P50B Li-ion cells

$$\begin{aligned} \text{100 cells in series at nominal voltage: } & 100 \times 3{,}6 \text{ V} = 360 \text{ V} \\ \text{4 sets in parallel with typical capacity: } & 4 \times 5 \text{ Ah} = 20 \text{ Ah} \\ \text{Total expected capacity: } & 360 \times 20 = 7200 \text{ Wh} \approx 7.2 \text{ kWh} \end{aligned} \tag{3.3}$$

Thus, it is possible to conclude that the battery capacity updates result from updating the P42A cells with the more recent P45B and P50B models. This also confirms why the geometry and overall dimensions of the battery enclosure remain unchanged. From this point forward, the **INR-21700-P50B** cell will be used as the reference for all calculations and numerical analyses.

3.2.2 Creation of the geometry

With the battery cells now confirmed, the foundation on which the geometry is deduced was established. By definition, 21700 cells are cylindrical with a nominal diameter of 21 mm and a height of 70 mm. According to the Molicel INR-21700-P50B datasheet, in Appendix A, the limit dimensions for these cells are: a maximum diameter of 21.55 mm and a maximum length of 70.15 mm. Additionally, a thin plastic cap is placed under each cell before positioning within the enclosure, with an estimated thickness of 0.3 mm. Considering also a 0.5 mm diameter clearance gap, a total diameter of 22.65 mm is considered for the dimension of the honeycomb circular holes.

Each half-case contains 200 battery cells arranged in a “honeycomb” pattern, in orientations in multiples of 60°. According to Stark Future’s Chief Engineer, the minimum spacing between adjacent cell holes is 0.4 mm, also, larger gaps are included at regular intervals to accommodate packaging and wiring. Following the pattern defined, and meticulously comparing all the details of the geometry with the known dimensions of the cells, the outline of the half-case geometry was created. Figure 3.3 shows the outline of the battery, including a zoomed inset on the honeycomb cell pattern with dimensional detail.

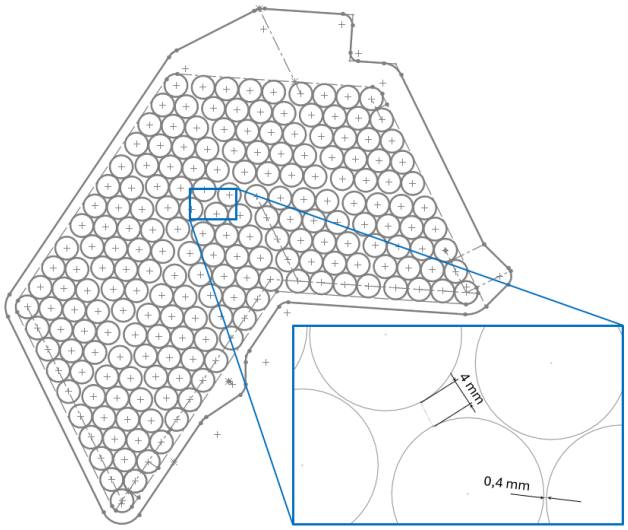

Figure 3.3: Outline of the geometry of the Stark VARG battery enclosure with a zoomed inset on the “honeycomb” geometry

The next logical step was to create the 3D geometry based on the previously described outline. All relevant features were carefully replicated, including fixing points, considering the dimensions of the motorcycle and information shared during the meetings, the appropriate wall thickness derived from the claimed half-case weight of 1.4 kg, draft angles, and cooling fins. The aim was to reproduce the real product as faithfully as possible, which is essential for ensuring the validity of the analyses presented in the following sections.

The final CAD model of the reverse-engineered battery enclosure is presented in Figures 3.4 and 3.5.

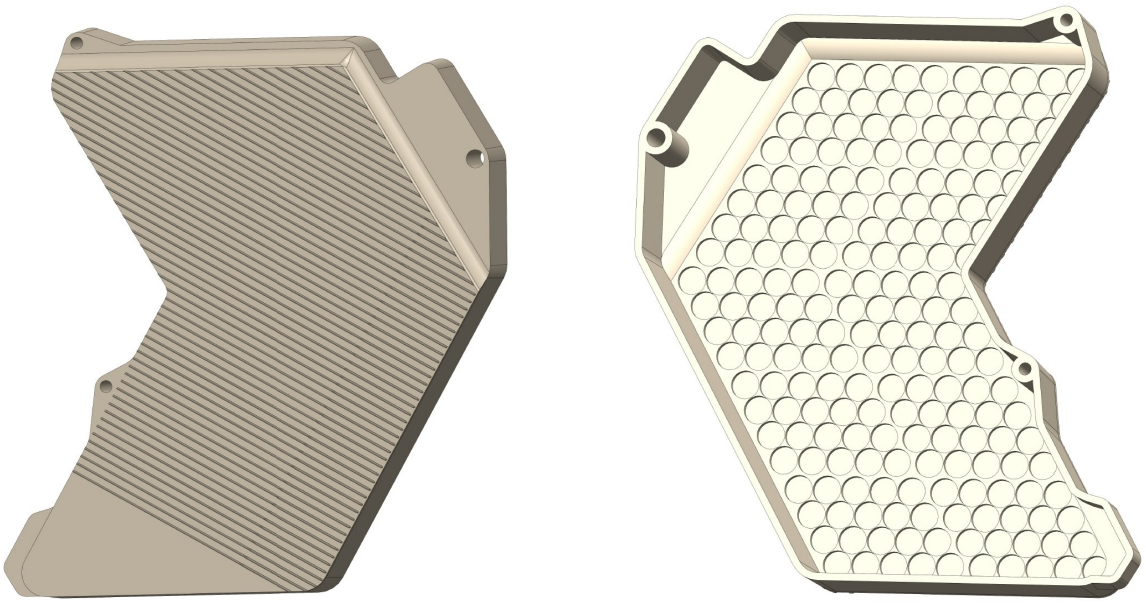

(a) Outside view (b) Inside view

Figure 3.4: Outside and inside views of the CAD model of the half enclosure

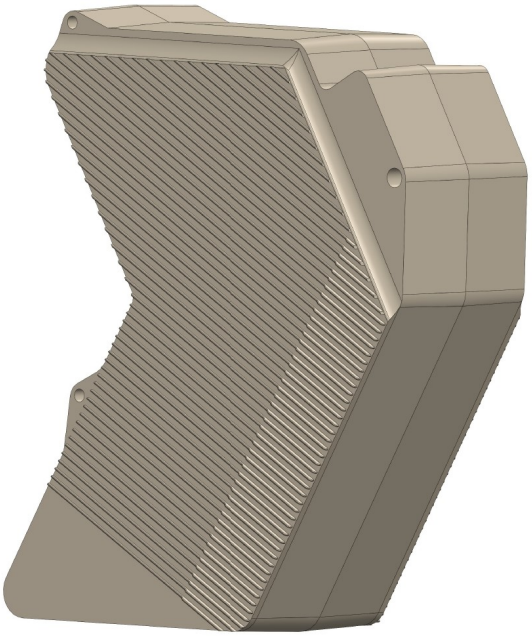

Figure 3.5: CAD model of the full enclosure

3.3 Structural Simulations

This section will delve into linear static finite element simulations performed on a composite version of the reverse-engineered Stark VARG battery enclosure. These simulations constitute simple initial structural analyses to evaluate the performance and feasibility of a simple, thin, symmetric composite laminate design with the overall geometry of the real enclosure, without the "honeycomb" geometry. They work as a starting point for the following composite layup optimisation. Simple load and boundary conditions and simplifying assumptions were made; these and other simulation setup details will be briefly explained in the following subsection.

3.3.1 Simulation Setup

The configuration of the initial static analyses was maintained throughout subsequent optimisation stages, as the loading conditions acting on the composite enclosure remained unchanged. Therefore, the following description provides the foundation of the preliminary finite element work.

The first step in the finite element setup involved preparing the geometry for meshing. This included defeaturing, simplification, and cleanup of the raw CAD model, which contained complex geometries not relevant to the overall structural response. The internal "honeycomb" structure and external heat-dissipating fins were removed, as they overly complicated the model, and in the case of the fins does not significantly affect the stiffness. The external surface of the enclosure was extracted and used as the base for a 2D shell model in HyperMesh®. Using the software's

topology-editing tools, further refinements such as fillet removal, line suppression, and surface splitting were applied. The resulting simplified half-enclosure surface is shown in Figure 3.6.

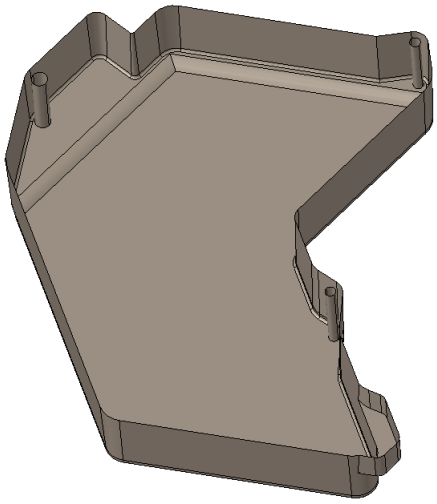

Figure 3.6: Two-dimensional external surface of the battery half-enclosure after topology alterations in HyperMesh®

The unit system adopted for the finite element analyses is presented in Table 3.1.

Table 3.1: Unit system chosen for finite element analysis

Quantities	**Unit**
Mass	g
Length	mm
Time	ms
Force	N
Pressure	MPa
Energy	N mm

The prepared surface was then discretised using second-order triangular shell elements (`TRIA6`) due to their adaptability to complex geometries and good numerical performance. Mesh quality was carefully assessed and improved using HyperMesh's mesh-editing tools. The element size was optimised to remain within the Student Version limitations. Only half of the enclosure was meshed to exploit symmetry. The mesh was then mirrored across the symmetry plane to obtain the complete model (Figure 3.7).

Figure 3.7: Discretised enclosure model in HyperMesh®

Two static structural analyses were performed. The main difference between them is the addition of filleted edges to the enclosure geometry in the second analysis. This was a detail change in the enclosure design to take into account manufacturing constraints for a composite enclosure. The corresponding mesh statistics are summarised in Tables 3.2 and 3.3.

Table 3.2: Analysis 1 mesh statistics

Element Type		Quantity
2D Shell	`TRIA6`	46 514
Total Nodes		93 024

Table 3.3: Analysis 2 (Fillet) mesh statistics

Element Type		Quantity
2D Shell	`QUAD8`	125
	`TRIA6`	44 086
Total Elements		44 211
Total Nodes		88 543

For these preliminary studies, a carbon fibre reinforced epoxy prepreg developed for high-performance automotive applications, including battery enclosures, was selected. The chosen material, supplied by Toray®, belongs to the TC346 series. Specifically, the variant used is a 200 g/m^2 2×2 twill weave reinforced with 6K intermediate modulus carbon fibres, with a resin content of 42 %.

The TC346 prepreg is optimised for structural performance at elevated temperatures, exhibiting high compression, shear, and toughness characteristics. Moreover, it offers excellent flame-retardant properties, meeting the UL 94 V-0 classification for a 2 mm thick test coupon, thereby aligning with the safety requirements typically imposed on electric vehicle enclosures.

The mechanical and thermal properties of the Toray TC346 Intermediate Modulus 6K Carbon 200 gsm 2×2 Twill 42 % RC prepreg are summarised in Table 3.4.

Table 3.4: Properties of Toray 346 Intermediate Modulus 6K Carbon 200gsm 2x2 Twill 42% RC prepreg composite material [63, 64]

TC 346 Intermediate Modulus 6K Carbon 200gsm 2x2 Twill 42% RC *		
Property	**Value**	**Method**
Onset Glass Transition Temperature T_g / °C	208	After cure of 2h at 180°C (ASTM D7028)
Nominal Laminate Density ρ / g/cm^3	1.5410	Assuming 0% void content, from Toray's Ply Thickness Calculator [64]
Nominal Cured Ply Thickness / mm	0.224	Assuming 0% void content, from Toray's Ply Thickness Calculator [64]
Flame-Retardancy / mm	2	Laminate thickness to comply with UL94 V-0 standard
Mechanical Properties for Composite Modeling		
Longitudinal Young's Modulus E_1 / GPa	72.1	BS EN ISO 527-4
Transverse Young's Modulus E_2 / GPa	72.7	BS EN ISO 527-4
In-Plane Shear Modulus G_{12} / GPa	4.70	ASTM D 3518 M
In-Plane Poisson's Ratio ν_{12} / -	0.04	BS EN ISO 527-4
Longitudinal Tensile Strength X_t / MPa	1034	BS EN ISO 527-4
Longitudinal Compressive Strength X_c / MPa	910	prEN 2850
Transverse Tensile Strength Y_t / MPa	956	BS EN ISO 527-4
Transverse Compressive Strength Y_c / MPa	866	prEN 2850
In-Plane Shear Strength S / MPa	148	ASTM D 3518 M

* IM7 carbon fibres; 2-hour cure at 180°C (dwell) with a 2°C/min ramp rate (heat-up), under 90 psi in an autoclave.
Mechanical properties represent the average of two batches tested at room temperature dry (RTD), with a fibre volume fraction of 52.6%.

The next step involved defining the laminate for the composite model. As discussed in Chapter 2, a ply-based modelling approach was adopted due to its numerous advantages. The material orientations and stacking sequence were established accordingly.

For this preliminary study, a 9-ply symmetric, quasi-isotropic lay-up was selected, with the stacking sequence [0/45/90/-45/0/-45/90/45/0]. Assuming a nominal cured ply thickness of 0.224 mm, the total laminate thickness reached approximately 2 mm, ensuring compliance with the UL 94 V-0 flame-retardancy standard. The laminate definition implemented in HyperMesh® is illustrated in Figure 3.8.

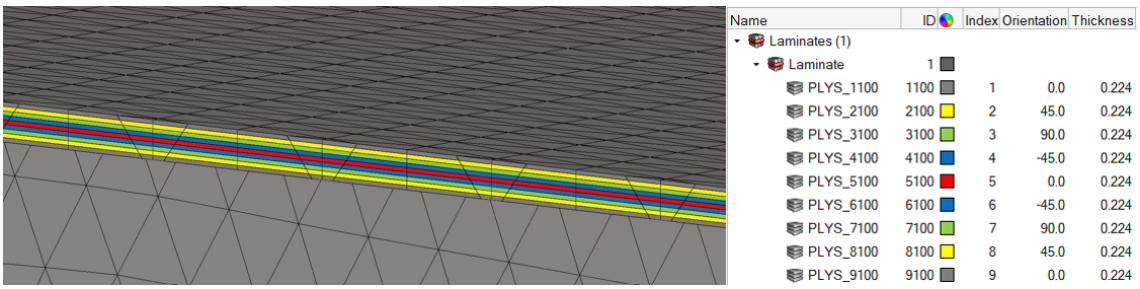

Figure 3.8: Laminate definition in HyperMesh®

The fixing and supporting points connecting the enclosure to the motorcycle chassis were identified during the reverse-engineering phase and modelled accordingly. Their locations were validated using official Stark Future documentation and reference material. In the finite element model, the nodes within the supporting holes were constrained in all six degrees of freedom ($U_1 = U_2 = U_3 = U_4 = U_5 = U_6 = 0$). The constrained regions are shown in Figure 3.9.

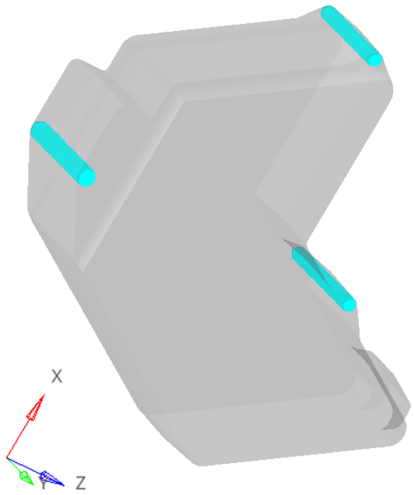

Figure 3.9: Constrained boundary conditions highlighted in HyperMesh®

The loading conditions were defined following an approach inspired by the UN ECE R100.03 regulation, which specifies mechanical shock testing for electric powertrain vehicles. Although primarily applicable to four-wheeled vehicles, this framework provided a solid reference for defining equivalent load cases. The regulation describes a sequence of short acceleration and deceleration events, as illustrated in Figure 3.10.

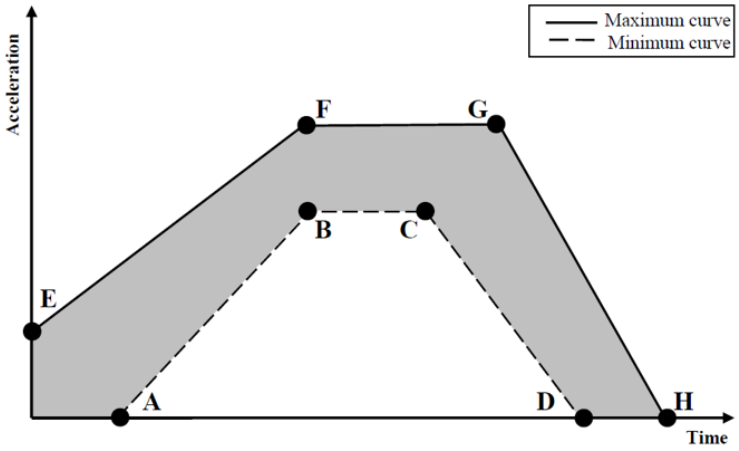

Point	Time (ms)	Acceleration (g)	
		Longitudinal	Transverse
A	20	0	0
B	50	20	8
C	65	20	8
D	100	0	0
E	0	10	4.5
F	50	28	15
G	80	28	15
H	120	0	0

Figure 3.10: Mechanical Shock procedure for electric vehicles [65]

To simplify the analysis, the dynamic shock loading was replaced by equivalent quasi-static load cases, computed based on the accelerations described in the regulation. The battery pack mass was estimated at 32 kg, in line with publicly available data for the Stark VARG EX/MX

models. Considering that 400 Molicel 21700 cells contribute to about 28.4 kg, the remaining 3.6 kg allocation for the enclosure and auxiliary electronics is reasonable.

Three static load subcases were therefore defined, applying forces distributed over the enclosure faces in the outward direction:

- **20g lateral load** – simulating a sudden side impact;
- **40g frontal load** – simulating a frontal collision;
- **20g downward load** – simulating an impact from a landing or jump.

These conditions replicate the extreme accelerations experienced during motocross operation. Figure 3.11 illustrates the three loading subcases applied in the model, highlighting the regions where the distributed forces were applied.

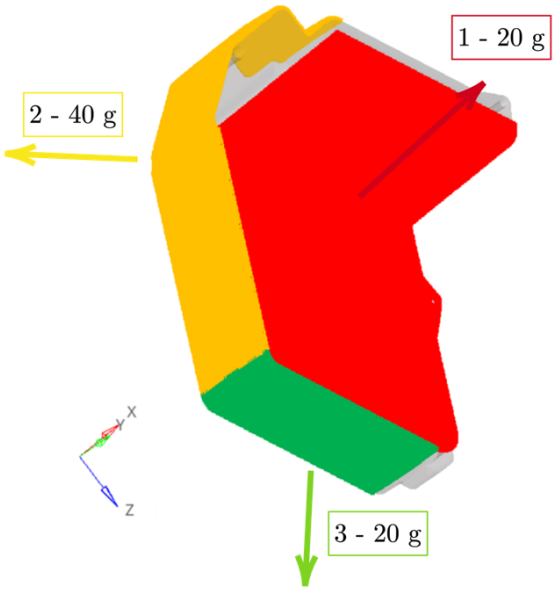

Figure 3.11: Three subcase loading conditions

The equivalent quasi-static forces were computed from the system mass and acceleration as follows:

Equivalent 20g static force

$$F = m \times a = m \times 20 \times g = 32 \times 20 \times 9.81 = 6278.4 \text{ N} \tag{3.4}$$

Equivalent 40g static force

$$F = m \times a = m \times 40 \times g = 32 \times 40 \times 9.81 = 12556.8 \text{ N} \tag{3.5}$$

3.3.2 Simulation Procedure and Results

The finite element model was analysed through a linear static structural simulation. A second model, differing only by the inclusion of filleted edges to reflect composite manufacturing constraints, was analysed using the same approach and serves as the baseline for subsequent optimisation studies.

Post-processing focused on four key physical quantities: total displacement, major principal stress, maximum shear stress, and the Tsai–Wu failure index. The Tsai–Wu criterion was selected for its simplicity, improved predictive capability compared to maximum stress or strain criteria, and its suitability for orthotropic composite materials.

The results of both analyses are summarised in Table 3.5.

Table 3.5: Results from initial linear static FEA for three load cases, comparing the baseline design (Analysis 1) and a filleted version (Analysis 2)

	Analysis 1	**Analysis 2**
Subcase 1 - 20g lateral		
Max. Displacement / mm	14.6	14.7
Max. Principal Stress σ_{P1} / MPa	930.8	956.0
Max. Shear Stress $\tau_{\max}$ / MPa	374.5	404.1
Tsai-Wu Failure Index	1.5	1.3
Subcase 2 - 40g front		
Max. Displacement / mm	8.6	9.0
Max. Principal Stress σ_{P1} / MPa	287.5	299.8
Max. Shear Stress $\tau_{\max}$ / MPa	141.6	172.1
Tsai-Wu Failure Index	0.1	0.2
Subcase 3 - 20g down		
Max. Displacement / mm	7.5	7.8
Max. Principal Stress σ_{P1} / MPa	293.4	476.2
Max. Shear Stress $\tau_{\max}$ / MPa	147.6	184.4
Tsai-Wu Failure Index	0.3	0.4

It was found that the most critical loading scenario was not the 40g frontal case, but rather the lateral impact condition. This behaviour results from the enclosure's geometry, which exposes a larger surface area laterally, leading to higher global deformation, and from stress concentrations induced by the V-shaped geometry of the structure. The introduction of filleted edges slightly exacerbated stress concentration in this region, though by only a few percent.

The lateral loading subcase also produced Tsai–Wu indices exceeding the critical value of 1, indicating local laminate failure. Conversely, the frontal and downward subcases remained well within allowable stress limits, showing no indication of failure. Overall, the addition of filleted edges did not significantly affect the enclosure's global stiffness or failure response.

To maintain clarity, only the Tsai–Wu failure index contour plots are presented, as they best represent the enclosure's mechanical integrity. Figures 3.12 to 3.14 illustrate the resulting failure index distributions for each loading case.

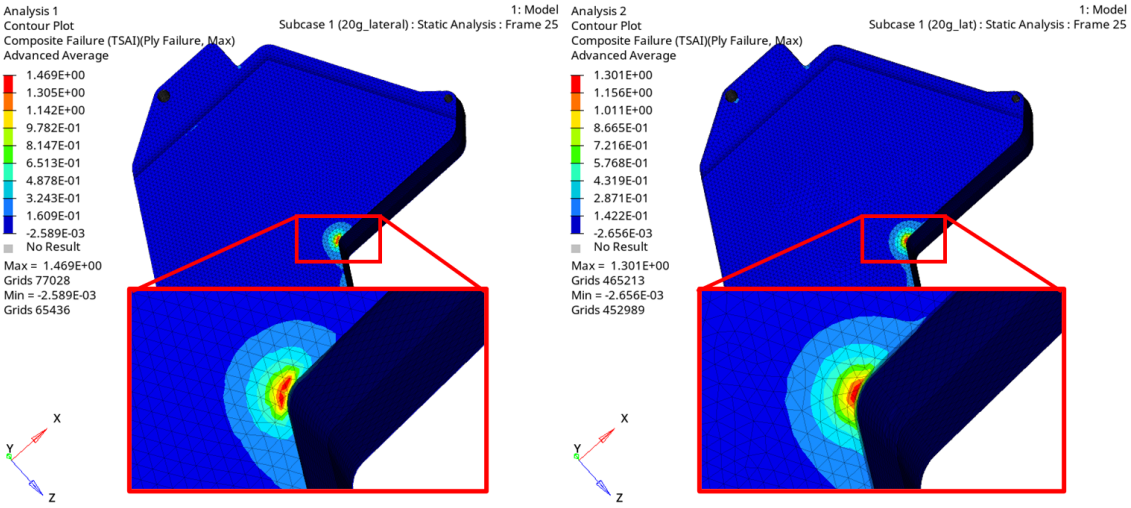

Figure 3.12: Tsai–Wu failure index contour plots, Load Subcase 1 (Analysis 1 on the left, Analysis 2 on the right)

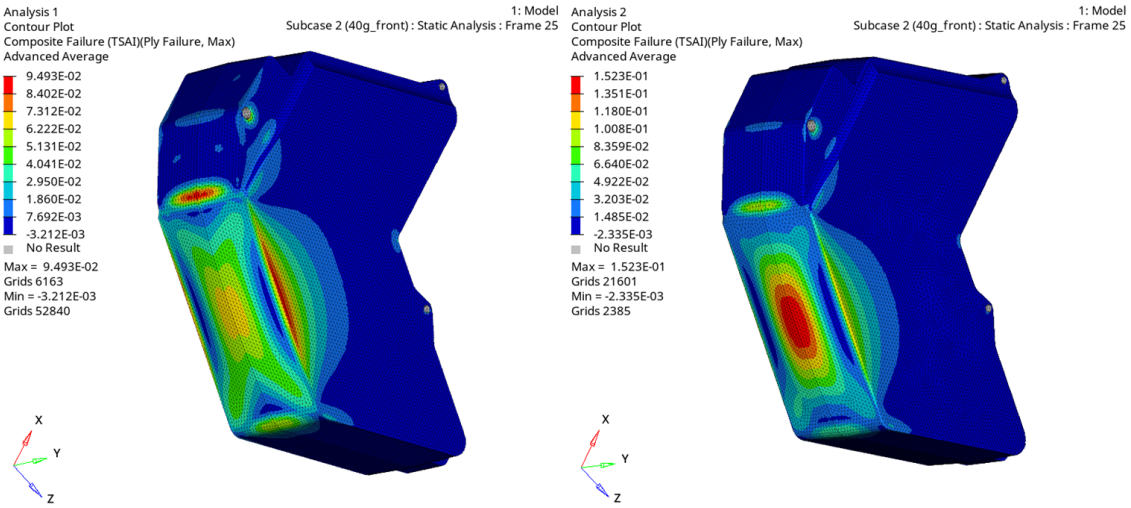

Figure 3.13: Tsai–Wu failure index contour plots, Load Subcase 2 (Analysis 1 on the left, Analysis 2 on the right)

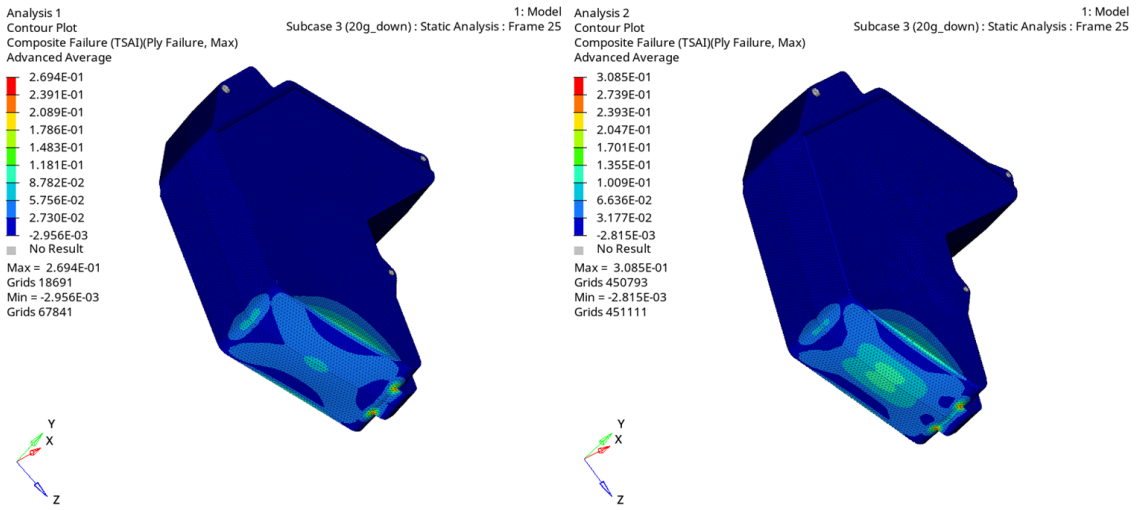

Figure 3.14: Tsai–Wu failure index contour plots, Load Subcase 3 (Analysis 1 on the left, Analysis 2 on the right)

3.4 Composite Lay-up Optimisation

This section presents the composite lay-up optimisation procedure developed for this project. The theoretical background of the optimisation framework was previously discussed in Chapter 2, Section 2.10.

The optimisation process was designed in three consecutive steps. However, only the first two were carried out, as justified later in this section. Each step includes a description of the optimisation setup and parameters, followed by an analysis of the obtained results. The optimisation sequence presented herein corresponds to the configuration that yielded the most promising results among the different setups tested.

The primary goal of optimising the Stark enclosure lay-up is to evaluate the potential of composite material tailoring to achieve a lighter and mechanically superior structure compared to the current magnesium alloy enclosure used in Stark Future motorcycles.

3.5 Free Size Optimisation

As outlined in the theoretical background, this first optimisation phase aims to determine the most efficient thickness distribution and ply shapes for each fibre orientation.

3.5.1 Parameters

The same model, boundary conditions, and loading configurations defined for Analysis 2 were employed, corresponding to the enclosure geometry with filleted edges for manufacturability.

In this stage, the concept of super-plies is applied. To enable the free-size algorithm to effectively remove material and determine optimal thickness distributions, the initial laminate ply thickness was increased from the nominal 0.224 mm to 1.00 mm, resulting in a total laminate thickness of 9.00 mm. The laminate definition used as input is summarised in Table 3.6.

Table 3.6: Laminate input for optimisation

Ply ID	**Material**	**Orientation / °**	**Thickness / mm**	**Shape**
1	TC346	0	1.00	Base
2	TC346	45	1.00	Base
3	TC346	90	1.00	Base
4	TC346	-45	1.00	Base
5	TC346	0	1.00	Base
6	TC346	-45	1.00	Base
7	TC346	90	1.00	Base
8	TC346	45	1.00	Base
9	TC346	0	1.00	Base
		Total:	9.00	

As the model is completely defined, the next step, and the fundamental step of optimisation, is defining the input parameters, which are provided in Table 3.7.

Table 3.7: Free size optimisation input parameters

Free size optimisation parameters	
Objective:	**min**(Compliance) **max**(Stiffness)
Constraints	
Stress:	$\sigma_{P1} < 900$ MPa
Mass:	$m < 1900$ g
Design Variable Constraints	
Laminate thickness:	$1.8 < t < 4.0$ mm
Ply minimum dimension (`MINDIM`):	100 mm
Symmetric plies:	Yes
Balance ply orientations:	-45° / 45°
Number of ply bundles:	2
Run parameters	
Maximum number of iterations:	200
Step size:	0.5
Convergence tolerance:	5×10^{-3}

The objective function was set to minimise compliance, equivalent to maximising stiffness. This choice emphasises the priority of the design which is its mechanical performance. The mechanical compliance of the enclosure is measured by the software for each loading subcase. The weight of each subcase was set as equal.

Constraints were imposed to ensure both mechanical integrity and lightweight design, with a principal stress limit of 900 MPa and a total mass cap of 1.9 kg, corresponding to approximately a 32% reduction relative to the 2.8 kg magnesium alloy enclosure.

Manufacturing constraints were also incorporated: bounds on laminate thickness, a minimum ply dimension to prevent overly thin geometries, laminate symmetry, and balanced ±45° orientations. Each super-ply was limited to two levels of refinement to prevent unnecessary complexity in the resulting design.

Default solver parameters were retained for the optimisation algorithm.

3.5.2 Result

The free-size optimisation completed in 21 minutes and 43 seconds over six design iterations, converging to a feasible solution with all constraints satisfied. The convergence history of the objective function is presented in Figure 3.15.

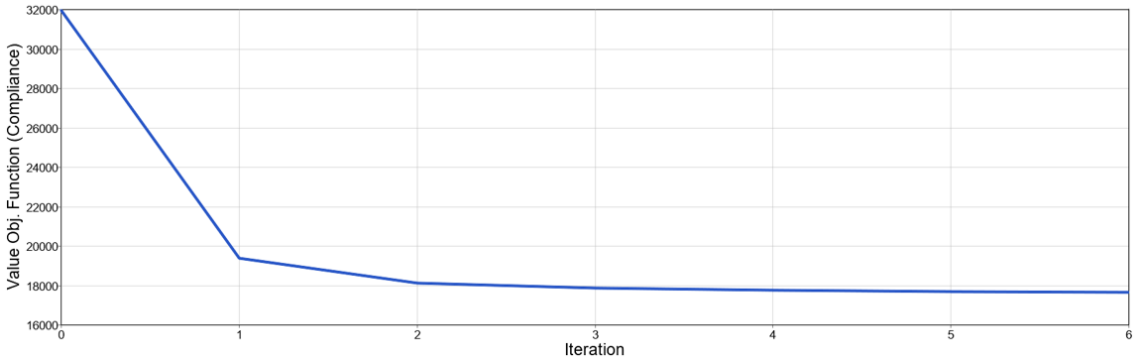

Figure 3.15: Free size optimisation objective function convergence plot

The resulting laminate configuration is summarised in Table 3.8. Each of the nine initial plies was divided into two, a base ply covering the full geometry and a reinforcement ply localised in critical regions, resulting in a total of 18 plies.

Table 3.8: Laminate after free size optimisation

Ply ID	Material	Orientation / °	Thickness / mm	Shape
1	TC346	0	0.272	Base
2	TC346	0	0.198	Reinforcement
3	TC346	45	0.279	Base
4	TC346	45	0.253	Reinforcement
5	TC346	90	0.273	Base
6	TC346	90	0.197	Reinforcement
7	TC346	-45	0.280	Base
8	TC346	-45	0.253	Reinforcement
9	TC346	0	0.272	Base
10	TC346	0	0.198	Reinforcement
11	TC346	-45	0.280	Base
12	TC346	-45	0.253	Reinforcement
13	TC346	90	0.273	Base
14	TC346	90	0.197	Reinforcement
15	TC346	45	0.280	Base
16	TC346	45	0.253	Reinforcement
17	TC346	0	0.272	Base
18	TC346	0	0.198	Reinforcement

The resulting thickness distribution across the enclosure is shown in Figure 3.16.

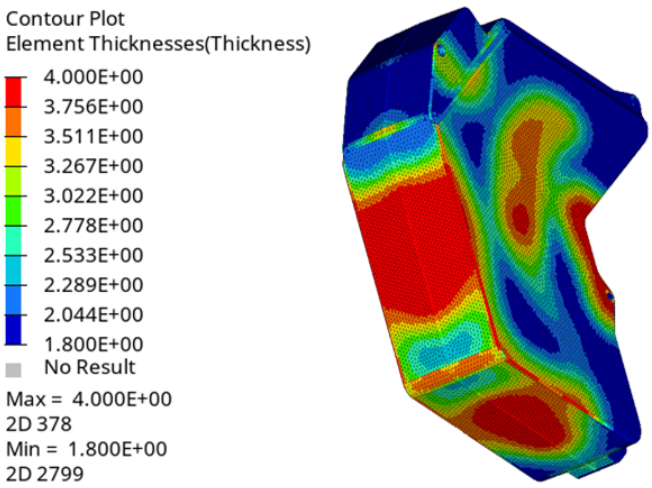

Figure 3.16: Thickness distribution after free-size optimisation

All reinforcement plies exhibit similar overall geometries, with minor dimensional variations depending on orientation. Figure 3.17 illustrates an example of the resulting ply shapes for a base ply and a reinforcement ply.

(a) 0° base ply (b) 45° reinforcement ply

Figure 3.17: Resulting ply shapes after free-size optimisation

The absolute thickness values obtained in this phase are not physically realistic, as they represent the relative optimal material distribution per orientation. The following optimisation step refines these results into a manufacturable laminate lay-up.

3.6 Size Optimisation

At this stage, both the part thickness distribution and the ply shapes defining the constant-thickness regions are established. However, the exact number of plies required for each orientation to meet the structural and manufacturing requirements must still be determined through a size optimisation process. This stage aims to define the optimal number of manufacturable plies for each fibre orientation while ensuring that all design constraints are respected.

A detail presented in the theoretical overview of the optimisation process was not done in this case, which is the manual redesign of the ply shapes given by the free size algorithm. This decision is justified by the exploratory nature of the work: the optimisation is not intended to produce a manufacturable component, but rather to assess the potential benefits of composite optimisation applied to this design. Therefore, only one size optimisation step was executed.

3.6.1 Parameters

The optimisation parameters for the size optimisation step are provided in Table 3.9.

Table 3.9: Size optimisation input parameters

Size optimisation parameters	
Objective:	**min**(Compliance) **max**(Stiffness)
Constraints	
Stress:	$\sigma_{P1} < 900$ MPa
Mass:	$m < 1900$ g
Design Variable Constraints	
Laminate thickness:	$2 < t < 4.0$ mm
Balance ply orientations:	-45° / 45°
Manufacturable ply thickness:	0.224 mm
Run parameters	
Maximum number of iterations:	30
Step size:	0.5
Convergence tolerance:	5×10^{-3}

The main optimisation parameters were maintained to preserve the same design intent as in the free-size stage, achieving a lightweight yet structurally efficient enclosure. The objective, mass, and stress constraints remained identical to the previous analysis.

A minimum laminate thickness of 2 mm was introduced to comply with the UL 94 V-0 flammability certification applicable to the TC346 prepreg. The ply thickness value was set according to Toray's ply thickness calculator [64], ensuring manufacturability. The balance constraint for the ±45° plies was kept to maintain laminate symmetry. All other algorithmic parameters were kept at their default settings, with a limit of 30 iterations.

3.6.2 Results

The size optimisation procedure concluded after 16 minutes and 11 seconds, converging after only two iterations to a feasible design that satisfied all imposed constraints. The convergence plots for the objective function and total mass are presented in Figures 3.18 and 3.19, respectively.

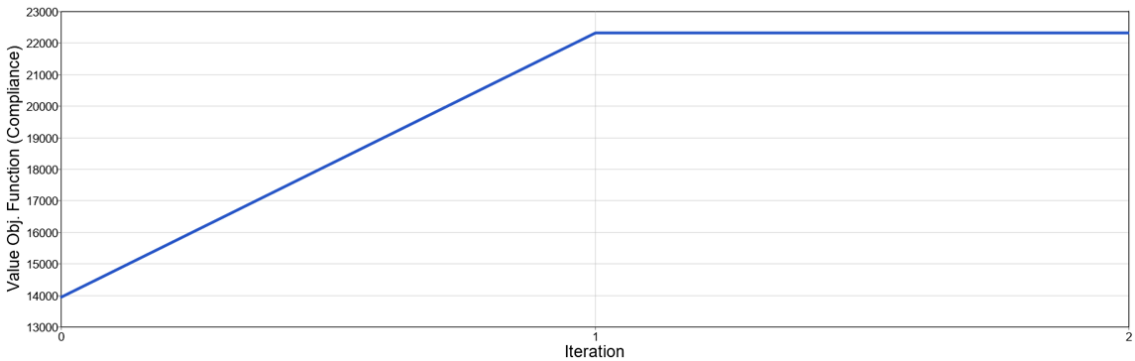

Figure 3.18: Size optimisation objective function convergence plot

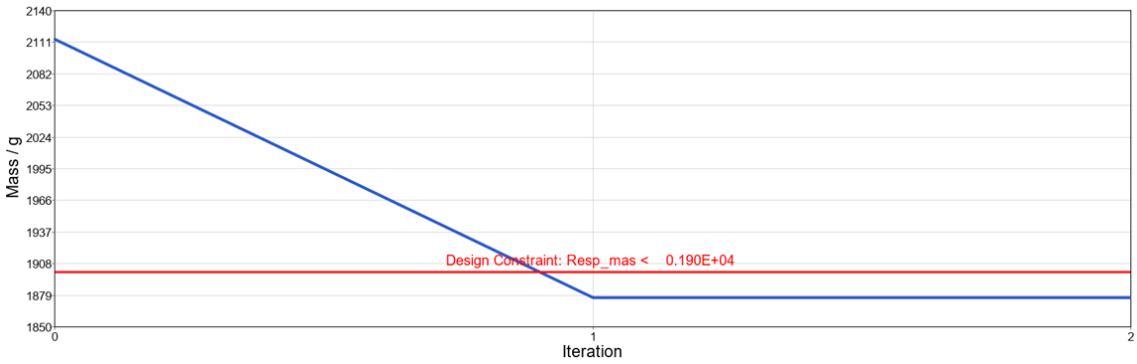

Figure 3.19: Mass constraint convergence plot

The optimised design achieved a final mass of 1877 grams, corresponding to approximately 940 grams per symmetrical half of the enclosure. The final laminate configuration is summarised in Table 3.10.

Table 3.10: Laminate after size optimisation

Ply ID	**Material**	**Orientation / °**	**Thickness / mm**	**Shape**
1	TC346	0	0.224	Base
2	TC346	0	0.224	Reinforcement
3	TC346	45	0.224	Base
4	TC346	90	0.224	Base
5	TC346	90	0.224	Reinforcement
6	TC346	-45	0.224	Base
7	TC346	0	0.224	Base
8	TC346	0	0.224	Reinforcement
9	TC346	-45	0.224	Base
10	TC346	90	0.224	Base
11	TC346	90	0.224	Reinforcement
12	TC346	45	0.224	Base
13	TC346	0	0.224	Base
14	TC346	0	0.224	Reinforcement

The resulting laminate consists of 14 plies of equal thickness, distributed between 9 base plies covering the entire surface and 5 reinforcement plies in critical regions. The overall thickness distribution of the optimised enclosure is shown in Figure 3.20.

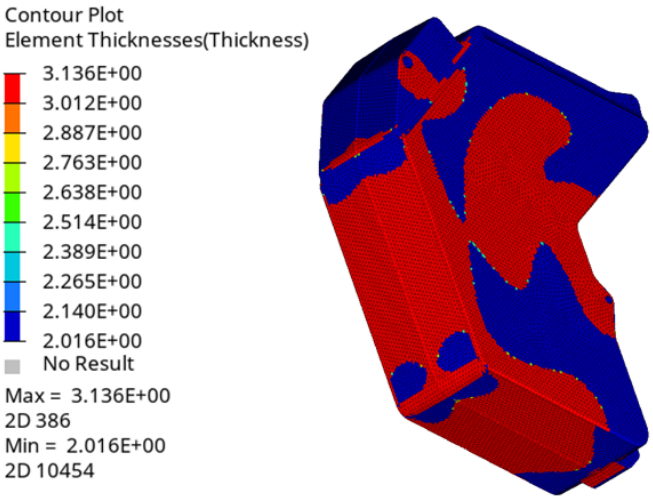

Figure 3.20: Element thickness plot after size optimisation

The thickness plot indicates two main thickness levels: 2.016 mm in areas covered solely by base plies and 3.136 mm in the reinforced zones, corresponding to the most critical regions under the applied loading conditions. Figure 3.21 illustrates the thickness distribution filtered by ply orientation. Reinforcements are only present in the 0° and 90° orientations, while the ±45° plies are limited to the base geometry.

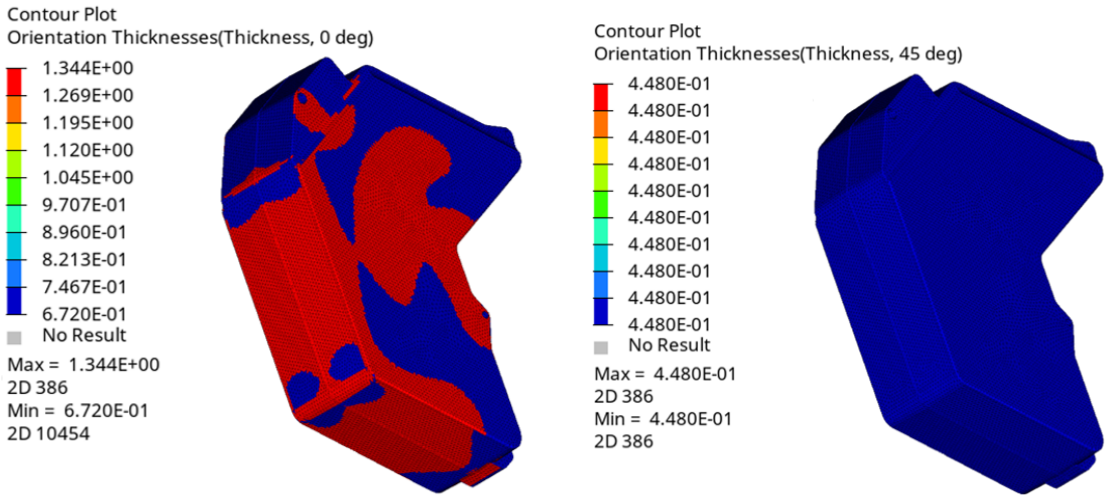

(a) 0° and 90° (b) -45° and 45°

Figure 3.21: Element thickness plot after size optimisation, by orientation

As observed, all reinforcement plies share an equal geometry, resulting in only two distinct ply shapes in the final laminate: a base and a reinforcement ply, shown in Figure 3.22. The overall ply shape distribution shows minimal variation compared to the free-size optimisation stage, which aligns with theoretical expectations.

(a) 0° base ply (b) 0° reinforcement ply

Figure 3.22: Ply shapes resulting from size optimisation

To assess the mechanical performance of the optimised design and verify constraint compliance, a direct comparison was made between the initial model (Analysis 2) and the final optimised configuration across all load subcases. The results, summarised in Table 3.11, show a substantial improvement in all key performance metrics.

Table 3.11: Comparison of results between the optimised and original design

	Original Design	**Optimised Design**	**Diff %**
Subcase 1 - 20g lateral			
Max. Displacement / mm	14.7	5.0	**-66%**
Max. Principal Stress σ_{P1} / MPa	956.0	450.9	**-53%**
Max. Shear Stress τ_{max} / MPa	404.1	245.0	**-39%**
Tsai-Wu Failure Index	1.3	0.4	**-72%**
Subcase 2 - 40g front			
Max. Displacement / mm	9.0	2.9	**-67%**
Max. Principal Stress σ_{P1} / MPa	299.8	194.6	**-35%**
Max. Shear Stress τ_{max} / MPa	172.1	107.3	**-38%**
Tsai-Wu Failure Index	0.2	0.05	**-66%**
Subcase 3 - 20g down			
Max. Displacement / mm	7.8	2.9	**-63%**
Max. Principal Stress σ_{P1} / MPa	476.2	201.6	**-58%**
Max. Shear Stress τ_{max} / MPa	184.4	88.85	**-52%**
Tsai-Wu Failure Index	0.3	0.06	**-82%**

Figure 3.23 presents the Tsai–Wu failure index distribution for the optimised design under the three loading subcases, with the critical lateral load case shown on the right.

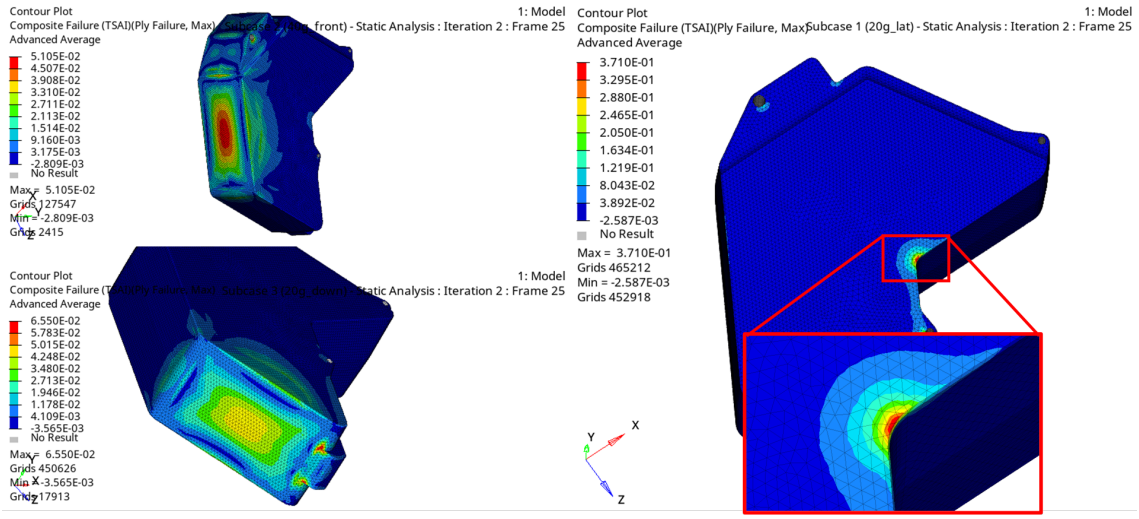

Figure 3.23: Tsai-Wu failure index contour plot result of the optimised design

The results demonstrate a clear enhancement in mechanical performance. Displacement and stress values decreased significantly, and the failure index dropped by more than half in all loading cases. Notably, the critical subcase, which previously exhibited failure, now presents a maximum Tsai–Wu index of approximately 0.4, well below the failure threshold.

Overall, the optimisation yielded a highly efficient design: approximately 33% lighter than the current magnesium enclosure and only around 340 grams heavier than the initial composite configuration, while delivering more than double the stiffness. A direct comparison between the mechanical compliance of the initial design (objective function value) and the final compliance shows a 2.3 times increase in stiffness.

$$\frac{\text{Initial compliance}}{\text{Optimised compliance}} = \frac{31960}{13946} \approx 2.3 \tag{3.6}$$

These compliance values represent a combined measure of the enclosure's stiffness across all loading subcases. While not individually representative of each load case, they still provide an insightful global metric to evaluate the overall performance of the design.

The results obtained from the mechanical analyses exceeded the stress constraint by a significant margin, suggesting that a subsequent optimisation phase with stricter constraints could lead to an even lighter design, while still fulfilling the extreme loading conditions imposed.

Ultimately, the third optimisation step, shuffling optimisation, was not carried out. This step only alters the stacking sequence of the plies without changing their number or thickness, serving mainly to satisfy manufacturing constraints. As the primary goal of this study was to evaluate the optimisation potential of a composite enclosure, performing this step would not have brought meaningful improvements to the design metrics.

3.7 Final Considerations

Although the exploration of a potential collaboration between Stark Future and Adamastor for the development of a composite enclosure for the EX/MX motorcycles was brief, allowing only a preliminary feasibility study, the work conducted provided valuable insight into the potential of a composite solution. The results, particularly from the laminate optimisation process, clearly demonstrated the significant performance and weight-saving advantages of a carbon fibre composite enclosure compared to the existing magnesium alloy one. Composite optimisation has proven to be an extremely powerful design approach.

In addition to the structural and design optimisation studies presented in this chapter, a number of preliminary thermal simulations were also performed. However, upon review of their setup and modelling assumptions, these were found to lack sufficient accuracy to be included in this report. Despite this, they served as a crucial learning experience for the thermal analyses developed later for the Famel prototype project, presented in Chapter 6.

From both the author's and Adamastor's perspective, the study carried out showed strong promise and represented a valuable opportunity to acquire data and practical experience, should Stark Future decide to pursue a composite-based enclosure in the future. Unfortunately, the collaboration was unexpectedly and silently discontinued from their side. Nevertheless, given the amount and quality of the work produced, and its direct relevance to subsequent projects, it was deemed appropriate to include it here. The knowledge gained throughout this study proved essential to the development of the Famel prototype design, both in methodology and technical understanding.

Chapter 4

Design of the Famel E-XF Battery Enclosure Prototype

The present and subsequent chapters of this dissertation delve into what constituted the original theme of the thesis project. This being the design, numerical validation, production and testing of a carbon fibre composite battery enclosure for the upcoming Famel E-XF electric motorcycle. This chapter is focused on the design process followed by the numerical modelling and finite element analysis validation of the composite enclosure prototype according to a vehicle safety regulation framework. Nevertheless, a brief context and a clear setting of the objectives is necessary.

4.1 Context and Objectives

The author and Adamastor experienced a prolonged wait for the necessary data to initiate design work due to multiple delays, issues between the E-XF motorcycle battery design supplier and the motorcycle maker, and communication lapses from Famel. Effectively, this "gridlock situation" ended in the first week of June, time when Famel shared the information that will be later described. This implied that the prototype project faced a tight deadline to meet the requirements for academic completion and presentation. Nevertheless, it was executed to the highest possible standard, with a strong emphasis on maintaining the quality of the final product.

The objective of the work carried out is to define and follow a design methodology for the creation of a functional prototype of a battery enclosure for the Famel E-XF electric motorcycle, made from carbon fibre composite material. The methodology, which will be described shortly, culminates in the production and experimental testing of the prototype. Acting out a clearly defined prototype design methodology, even when based on limited initial information, goes beyond producing a "work in progress" physical product. It enables the identification of missing or undefined requirements, provides valuable insights into the product's functional and structural needs, and ultimately guides and accelerates the development towards the final design. This is the main focus of the project, given that the information about the battery is limited and subject to change in the near future, due to the state of infancy of the battery and related components in the motorcycle.

The final product of this project will be an early prototype but will pave the way for the subsequent versions of the composite enclosure.

As a target for durability and safety in the design of the prototype, the UN ECE R136 technical regulation for the safety of electric two-wheel vehicles and their components is used. This regulation is briefly described in Section 2.5.

4.1.1 Famel E-XF Battery

The battery solution for the upcoming Famel E-XF electric motorcycle consists in the use of Li-ion batteries (up to two units per motorcycle), with a simple and compact battery + enclosure design that makes it possible to extract and later reposition in the motorcycle. These swappable batteries could be either charged separately or combined with the motorcycle. This is a concept present in other motorcycle in the same niche in the market, as seen in Section 2.2.

The following list gathers all the information shared by Famel for the design of the enclosure:

- The internal space to accommodate the battery unit and related components is $234.9 \times 115 \times 277$ mm. This and the overall enclosure design were shared, in the form that can be seen in Figure 4.1.

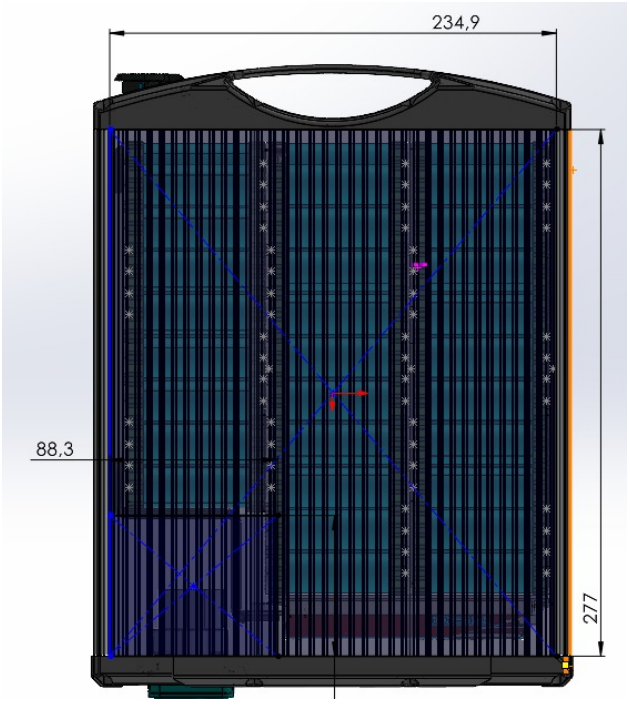

Figure 4.1: Enclosure geometry, as shared by Famel (Dimensions in mm)

- The battery unit and associated components weight approximately 14 kg, and were considered as such.

- When mounted to the motorcycle, the battery + enclosure assembly are snugly encapsulated by aluminium surfaces on all sides, ensuring complete immobilisation. No other details or mention of additional fixing or supports were mentioned by Famel.
- The enclosure solution designed by the battery supplier weighs approximately 4 kg. For a later term of comparison.
- For thermal designing purposes, the battery is considered to dissipate 500 W of heat, and the maximum allowable temperature for the battery cells is defined as 60 °C. No other information or details about the thermal behaviour of the battery pack were given;
- It was mentioned by Famel that the battery + enclosure assembly will be cooled down by forced convection when the motorcycle is in motion. However, no real detailed explanation of the system or the real-world conditions of cooling was given.

To add to this, Famel expressed its desire for the enclosure to be made from carbon fibre composite, mainly for its premium status appeal for their product, with the idea to be an option for the costumer when ordering its motorcycle.

Combining all the available information enumerated above with the author's and Adamastor's targets for the project and safety legislation required for swappable battery packs for electric motorcycles in Portugal's market, the following objective could be defined.

The enclosure prototype should:

- Be made from carbon fibre composites;
- Be as close to a functional prototype as possible, with the available information shared by Famel;
- Adhere to the UN regulation for safety of electric powertrain components for for L-Category vehicles (UN ECE R136), on the grounds of mechanical, drop test, fire-resistance and other areas;
- Ensure that Famel's requirements are met;
- Provide a degree of battery protection from external elements such as water and dust;
- Be lighter than the enclosure designed by the battery supplier;
- Strive for an economically viable solution.

4.2 Methodology

In this section, the methodology employed for the completion of this project's objectives will be layed-out. With the previous section, the reader is now aware of the context that surrounded this

project and the objectives that were set for the prototype design, and so, will be able to better understand the steps and choices present in the work methodology.

However, before the exposition of the structure of the work, it is important to mention the software employed:

- For the creation of any three-dimensional geometry included in this project, such as the enclosure designs, the Computer-Aided Design (CAD) software SolidWorks® was employed. It was also employed for minor tasks related to the geometry analysis and validation for the production of the final prototype enclosure.
- As for Computer-Aided Engineering tasks, Altair's HyperWorks® software suite was employed. The functions encompassed pre-processing and simulation setup with the software HyperMesh® and post-processing with HyperView®. All finite element analyses were solved with Altair's OptiStruct® mechanical solver. Linear and Non-linear Structural Static, Explicit Dynamic and Linear Transient Thermal Analyses were explored.

The strategy followed from the initial design, through the numerical validation to the final design is illustrated in Figure 4.2.

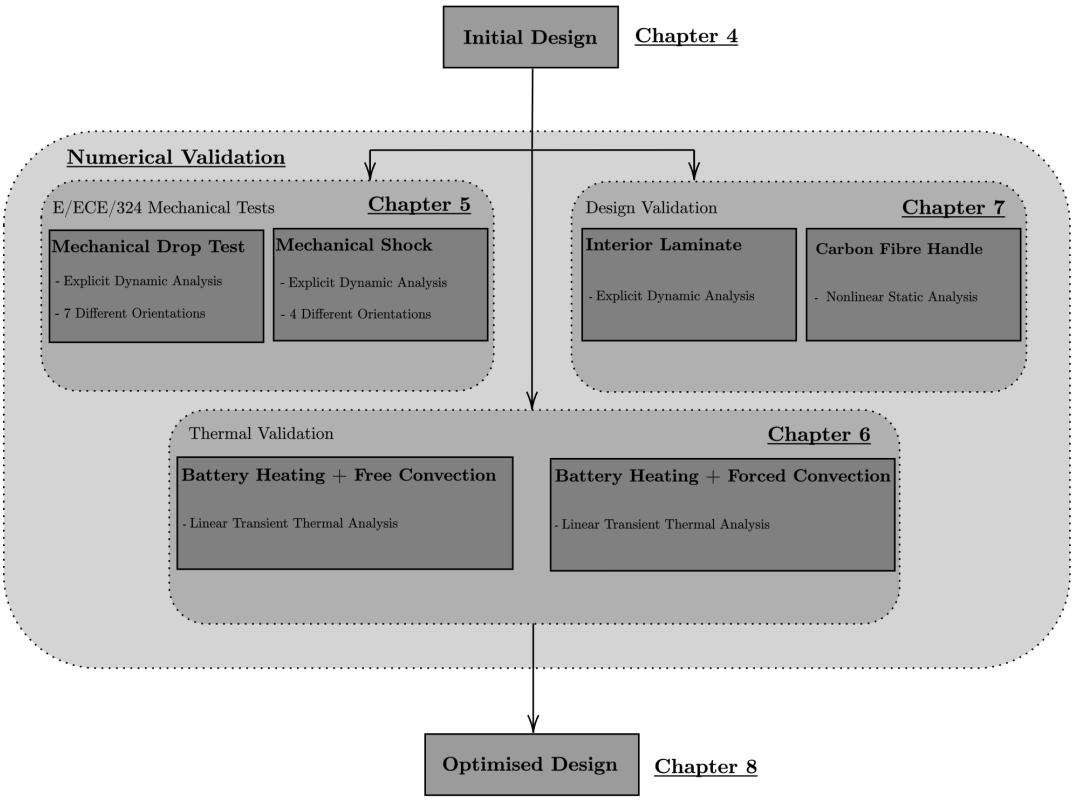

Figure 4.2: Structure of the Numerical Validation part of the work

The enclosure design and numerical validation are the basis of the whole process, and so is fundamental to have a robust strategy.

The first step is straightforward and consists of creating a good, simple initial design that is a good base from which to optimise in some details later. The main focus of the numerical validation methodology is for the enclosure design to adhere to the UN regulation on the safety of electric motorcycle components (UN ECE R136). The regulation is extensive in its definition of testing requirements, not all of which affect the enclosure directly, and are more targeted for the battery and its electrical safety, so were disregarded. One test could not be taken into account due to the lack of information given on fixing conditions of the battery enclosure to the motorcycle, the vibration test. The mounting points and respective boundary conditions are a fundamental part of any vibration or modal analysis; with a lack of data from Famel, it was impossible to validate the enclosure in this specific area of design. The fire resistance test, was also not considered, given its complexity to simulate and reproduce experimentally. Nevertheless, an alternative to it was found and will be explained in this section.

Summarising, only the Mechanical Drop and Mechanical Shock tests (Annex 8C and 8D, respectively) were considered as benchmarks for the design of the battery enclosure prototype. These mechanical resistance tests directly depend on the integrity of the enclosure and clearly define all testing conditions. Both tests were numerically simulated via Explicit Dynamic Analyses. To ensure that all critical testing conditions were accounted for, multiple simulations, encompassing several possible critical conditions, were explored. Resulting in seven variations of the Mechanical Drop Test and four variations of the Mechanical Shock Test.

The enclosure design was also tested for its thermal performance. Two cases meant to simulate critical working conditions were formulated, Battery Heating + Free Convection and Battery Heating + Forced Convection. Both were later used to assess the thermal performance of the composite enclosure and identify some areas of improvement for future designs.

The final focus of the Numerical Validation part of the work aimed to validate important details of the design. Finite Element Analyses were setup to assess the performance of two areas of the enclosure, the interior laminate and the carbon fibre handle.

Gathering all the results from the numerical simulations performed to the initial enclosure design, areas with room for improvement were identified and modified. This process resulted in a refined, optimised enclosure design. This optimised enclosure prototype was the starting point of the later part of the project.

The strategy followed from the final part of the project is illustrated in Figure 4.3.

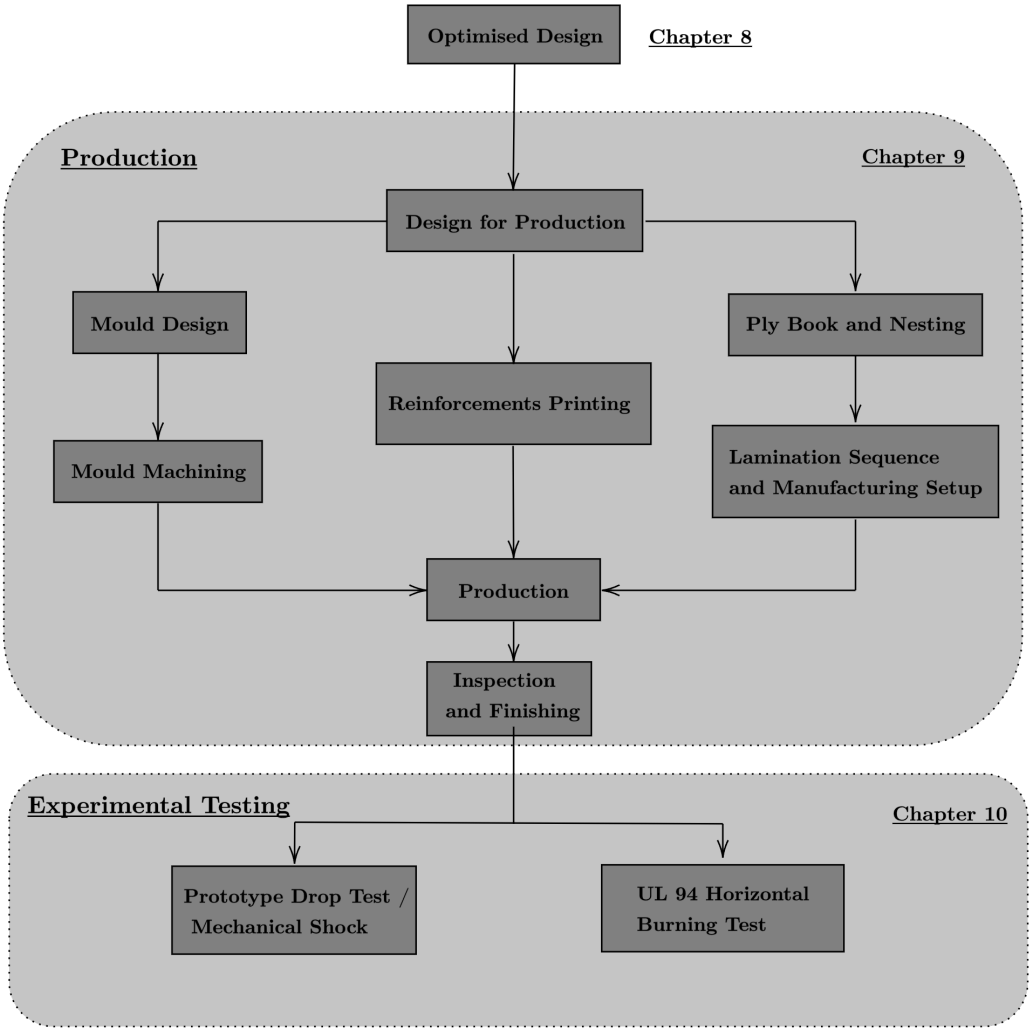

Figure 4.3: Structure of the Production and Experimental part of the work

As the diagram above describes, the optimised design is slightly altered to the final design. This final design includes the features necessary for a working prototype, such as inserts, holes and bonding flanges between parts connected by structural adhesive. The final design also accounts for the final ply layup, with junctions between internal and external laminates, and inclusion of the core and reinforcements inside the laminate.

From the final design of the prototype, ready for production, a typical composite component production sequence is employed. Necessary tasks include the design and production of moulds and reinforcements; CNC Machining of the moulds and core material; Ply layup documentation and Nesting; and the definition of the lamination procedure and setup of the conditions of production such as the autoclave cycle. These tasks can be considered as preparation work for the effective production of the carbon fibre composite component.

When every detail of production is defined and the necessary moulds, core and reinforcements are produced, production can be completed. After production, an inspection of the produced laminated composite parts is necessary to verify dimensional accuracy, fibre alignment, and the

absence of critical defects such as voids or delaminations.

At last, the final tasks of the project are the experimental testing of the prototype, either performing a Drop Test or a Mechanical Shock Test as according to the UN regulation. The choice between both experimental tests will be based on the results of the numerical validation simulations; the test that is revealed to be critical will be the one chosen. As stated, an alternative for the Fire Resistance test was found in the UL 94 HB (Horizontal Burning) Test. This test, contrary to the Fire Resistance Test found in the UN regulation, does not aim to expose the enclosure + battery assembly to fire, but instead aims to characterise the composite material from which the enclosure is made. Ensuring that the external material is resistant to fire, at least to a certain degree, it is possible to conclude on the fire resistance of the prototype battery enclosure. This choice results in a simpler and more economically viable strategy for the testing of the fire resistance of the prototype.

4.3 Initial Design

The design of an initial solution for the enclosure prototype was created based on the information that was given by Famel, this being the visual information presented in Figure 4.1. The aim was to replicate the overall external geometry present in the image and ensure an internal space that fits the dimensions of the battery.

The geometry of the component was reconstructed through a simple reverse engineering approach, whereby the known reference dimensions (the dimensions of the battery) were used to deduce the unknown measurements of the enclosure present in Figure 4.1. This resulted in a close replica of the expected dimensions for the prototype battery enclosure as a CAD 3D model.

The reverse-engineered enclosure geometry is presented in Figure 4.4.

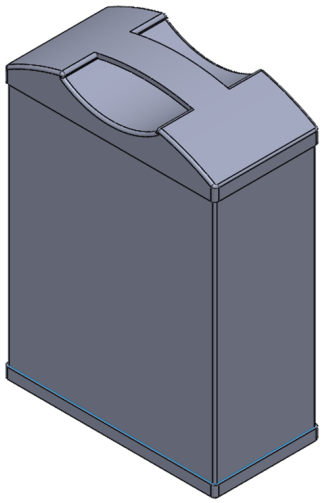

Figure 4.4: Reverse-engineered CAD geometry of the enclosure provided

From this point, the search for a viable enclosure solution made from carbon fibre composite material was initiated. A strong guideline for this initial design was the methodology presented in Section 4.2. This initial idea should aim to include the necessary features aimed at impact absorption and fire safety, to pass the stringent mechanical and fire resistance tests, set up numerically or experimentally.

4.3.1 Carbon Fibre Pre-preg Material

A fundamental choice for any design in the constituent material of the component, in the present case the main material of the enclosure is a carbon fibre composite material.

To be precise, the realm of choices only includes composite pre-preg materials. The manufacturing method available for this prototype, considering the possibilities of Adamastor and its main method of production of composite parts, is manual lay-up of pre-impregnated fibres followed by cure in an autoclave. This is the most sensible choice for the production of such a small volume of prototype components of simple and small geometry.

Considering the materials available either at Adamastor's facilities or possible to purchase from Toray, Adamastor's composite material supplier, in the available time, the following four pre-preg families were considered: E731, E750, E745 and TC346. The materials datasheets can be seen in Appendix B.

A short description of the characteristics of all pre-preg types:

- **E731**: A toughened epoxy pre-preg formulated for enhanced resin clarity, particularly to avoid white-spots—ideal for cosmetic components in high-performance automotive applications. Its mechanical properties, though good compared to aluminium, for example, are the lowest of this selection. However, it is the cheapest material, by a considerable margin [66].

- **E750**: A toughened epoxy pre-preg developed for structural automotive and motorsport applications. This material has high mechanical properties, and is around 40% more expensive than an equivalent E731 pre-preg [67].

- **E745**: A toughened epoxy pre-preg designed for impact-resistant structural uses, suitable for mechanically demanding applications. It has excellent mechanical properties; however, it also has a very high price, which is around 140% more than an equivalent E731 pre-preg [68].

- **TC346**: A high-temperature epoxy component pre-preg intended for structural use in Formula 1 and high-performance automotive, offering elevated thermal performance and post-curable properties. This material is probably the best choice due to its blend of excellent mechanical, thermal and fire-resistance properties. This pre-preg is used in composite battery enclosures in the automotive industry and meets UL94 V-0 flame-retardancy tests. Unfortunately, it is also the most expensive material presented in this work, more expensive than an

equivalent E745 pre-preg [63]. To add to that, it is the only material that is not available at Adamastor's location and is only available upon ordering from the supplier.

To keep the already expensive price of a carbon fibre composite component as low as possible, considering its enhanced visual appearance and good mechanical properties, an E731 pre-preg was chosen. The full identification of the material chosen is E731-00 HS2238 Carbon TR30S T 245gsm 2 x 2 Twill 3K 42% RC. The properties of the chosen carbon fibre composite pre-preg material are listed in Table 4.1

Table 4.1: Properties of E731-00 HS2238 Carbon TR30S T 245gsm 2 x 2 Twill 3K 42% RC prepreg composite material [64, 66]

E731-00 HS2238 Carbon TR30S T 245gsm 2 x 2 Twill 3K 42% RC *		
Property	**Value**	**Method**
Onset Glass Transition Temperature T_g / °C	140	After cure of 1h at 125°C
Nominal Laminate Density ρ / g/cm^3	1.5089	Assuming 0% void content, from Toray's Ply Thickness Calculator [64]
Nominal Cured Ply Thickness / mm	0.280	Assuming 0% void content, from Toray's Ply Thickness Calculator [64]
Mechanical Properties for Composite Modeling		
Longitudinal Young's Modulus E_1 / GPa	55.9	ISO 527-4
Transverse Young's Modulus E_2 / GPa	57.7	ISO 527-4
In-Plane Shear Modulus G_{12} / GPa	4.07	prEN 6031
In-Plane Poisson's Ratio ν_{12} / -	0.05	ISO 527-4
Longitudinal Tensile Strength X_t / MPa	705	ISO 527-4
Longitudinal Compressive Strength X_c / MPa	643	prEN 2850
Transverse Tensile Strength Y_t / MPa	662	ISO 527-4
Transverse Compressive Strength Y_c / MPa	664	prEN 2850
In-Plane Shear Strength S / MPa	119	prEN 6031
Interlaminar Shear Strength S_B / MPa	61.8	ASTM D 2344

* 1-hour cure at 125°C (dwell) with a 2°C/min ramp rate (heat-up) in an autoclave, pressure not indicated.

4.3.2 Honeycomb Material

The use of honeycomb material in the design of the prototype enclosure is heavily inspired by the information found in the state of the art (Chapter 2). As found in the author's review, several studies reveal multiple benefits in the use of closed-cell thin-walled honeycomb material structures inserted in a composite laminate for the design of battery packs.

For this reason, the introduction of honeycomb structures was chosen in the design of this prototype enclosure. These structures aim to:

- Serve as a structure from which a constant thickness carbon fibre laminate can follow the external geometry of the CAD design in Figure 4.4;
- Serve as an impact energy absorption structure to protect the battery cells in cases such as a fall from a moderate height or a crash;

- Serve as a fire wall to protect the battery of fire in the case of exposure to flames from an external source to the enclosure;
- Serve as a vibration absorber to avoid excessive vibration of the battery, in cases such as motorcycle riding.

As described, this structure is beneficial in a lot of different ways and is well supported by academic studies.

Two main types of honeycomb material are commonly found in the market and differ in their constituent material: Nomex® and Aluminium Honeycomb Structures.

Nomex® and aluminium honeycombs are both widely used lightweight core materials, each offering distinct advantages. Nomex® cores provide excellent specific stiffness and are inherently non-metallic, but they are considerably more expensive and limited in the range of cell sizes commercially available. Aluminium honeycomb, on the other hand, combines lower cost with higher mechanical resistance and slightly superior heat dissipation. Although it is heavier than Nomex, the difference is negligible in this context, as both materials are exceptionally lightweight. For these reasons, aluminium honeycomb was selected as the core material.

The honeycomb that was chosen is the 6.4mm Cell Aluminium Honeycomb from the supplier Easy Composites®, made from 3003 aluminium alloy. Its properties can be found in the following Table 4.2 and the respective datasheet is provided in Appendix C.

Table 4.2: Properties of 6.4mm Cell 3003 Aluminium Series Honeycomb from Easy Composites

6.4mm Cell 3003 Aluminium Series Honeycomb	
Property	**Value**
Nominal Density / kg/m^3	83.3
Foil Thickness / micron	70
Corrosion Treated	Yes
Maximum Service Temperature / °C	120
Mechanical Properties	
Compressive Strength - Bare / MPa	4.31
Compressive Strength - Stabilised / MPa	4.52
Crush Strength / MPa	1.62
Compressive Modulus in the Thickness Direction / MPa	1310
Plate Shear Strength in the Ribbon Direction / MPa	2.48
Plate Shear Modulus in the Ribbon Direction / MPa	448.16
Plate Shear Strength in the Transverse Direction / MPa	1.45
Plate Shear Modulus in the Transverse Direction / MPa	241.32

4.3.3 Design

From the reverse-engineered CAD model presented earlier, the model, including the aluminium honeycomb structures, was created, ensuring the necessary internal space and that the design is later possible to manufacture.

Figure 4.5 reveals the 3D model of the enclosure, both in a section cut and an exploded view.

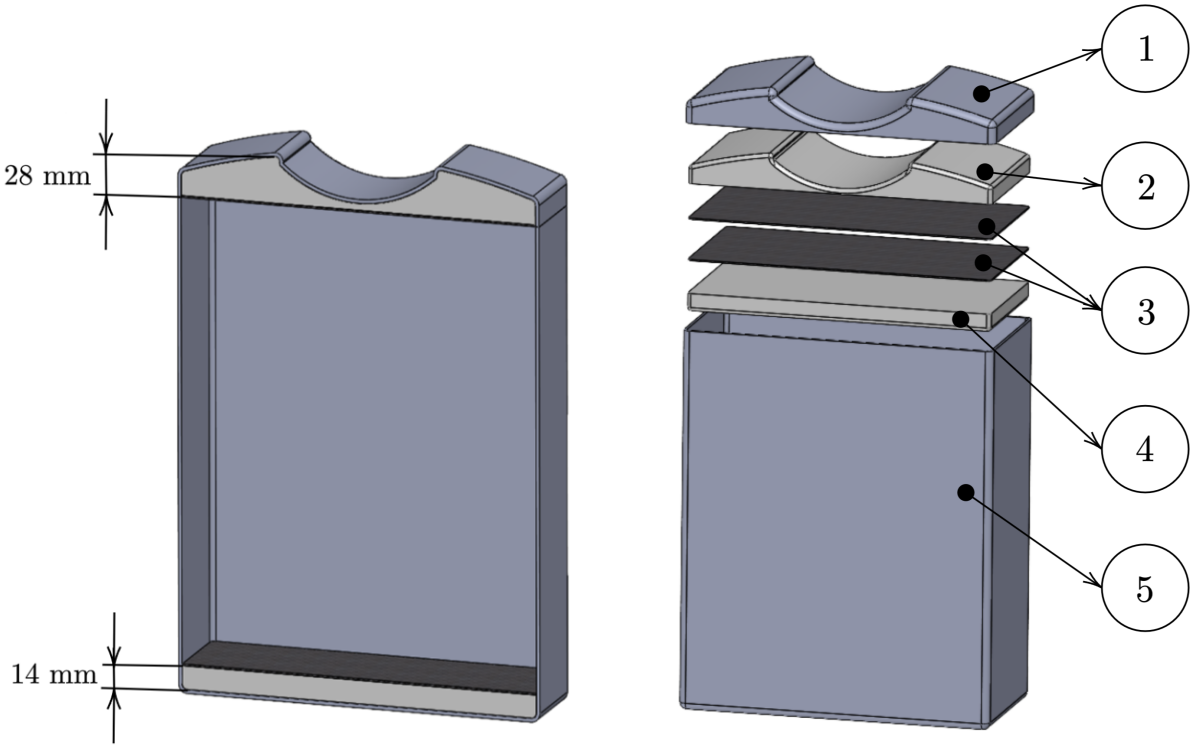

(a) Section Cut (b) Exploded View

Figure 4.5: Initial Enclosure Prototype Design CAD Model

Explaining in more detail all the components of the design, Figure 4.5b shows:

1. Top External Laminate: functions as a lid and is made from a laminate of E731 pre-preg as described above. The laminate is quasi-isotropic and symmetric; it is comprised of 8 plies in a $[45/0/-45/90]_S$ sequence with a resulting calculated cured thickness of 2.24 mm [64]. The resulting component has a weight estimated as 154 grams.

2. Top Honeycomb Core: made from 6.4 mm cell 3003 Aluminium Series Honeycomb. With a peak thickness of 28 mm and estimated to weigh 57 grams. It has an approximate thickness of 14.5 mm on the sides, is 27.5 mm thick at its peaks and 4 mm thick in its thinest part, in the middle.

3. Internal Laminates: positioned under the top and above the bottom honeycomb structures. They represent the laminate that surrounds the honeycomb structures in the inside of the enclosure. Though not represented here, they are to be seamlessly connected to the outside

laminate, such manufacturing details are not represented in this initial CAD design. The laminate is comprised of 4 plies in the same sequence as the external laminates [45/0/-45/90], resulting in a calculated thickness of 1.12 mm [64]. Each laminate is estimated to weigh 46 grams

4. Bottom Honeycomb Core: made from the same 6.4 mm cell 3003 Aluminium Series Honeycomb, with a thickness of 14 mm and weighs around 31 grams. It has a constant thickness of 14 mm.

5. Bottom External Laminate: functions as the main component of the enclosure. It is made from the same material and laminate as the Top External Laminate, and is calculated to weigh around 790 grams.

Adding the weight of all components of the enclosure, the total weight is estimated to be close to 1.1 kg. This means a 72.5 % reduction from the shared weight of 4 kg for the enclosure designed by Famel's supplier, all of this also increasing the stiffness, mechanical resistance of the design and adding impact absorbing structures. The resulting expected weight of the battery + enclosure assembly is around 15.1 kg.

The overall maximum dimensions of the enclosure are: 326 mm in height, 240 mm in length, and 120 mm in width.

The design accounts for fire resistance, first in the honeycomb structure in a lesser way, but mainly in a constant and relatively thick external laminate. A target of 2 mm was chosen, as it is the same benchmark for UL 94 fire resistance of the pre-preg TC346. While E731 does not come with UL 94 fire resistance, it is an objective of this project to test this material experimentally, in light of the UL 94 regulation.

The section cut in Figure 4.5a reveals two sandwich structures, one on top and another at the bottom of the enclosure. These structures, as described above, ensure energy absorption in case of impact when the enclosure falls in its vertical orientation. It can be important to limit the damage to the battery pack, as this can be the difference between the battery continuing to operate or failing after a fall, ultimately reducing both waste and unnecessary costs.

While this initial design does not have detailed manufacturing constraints in its thought process, as the ply design and layup is not yet defined; it already aims to reduce the number of moulds needed for production of the prototype. Parallel to this design, an alternative design that needed three moulds was disregarded due to the added complexity in production. Chapter 9 will delve into the final design and production constraints and will describe all the layup details that are not explained here.

Chapter 5

Mechanical Validation of the Enclosure Design in FEA

This chapter presents a comprehensive overview of the mechanical finite element analyses conducted to validate the structural performance of the Famel E-XF battery enclosure design. It begins by outlining the strategy established for the mechanical validation procedure, followed by a detailed description of the numerical finite element model and the corresponding simulation parameters. Finally, the results obtained from the analyses are thoroughly examined and discussed.

5.1 Methodology

This section aims to provide a clear, more in-depth, description of the methodology followed for the mechanical validation of the prototype enclosure, according to the test procedures defined in the UN ECE R136 regulation for the safety of electric motorcycle components.

As mentioned in Section 4.2, the mechanical tests to be simulated numerically are the Mechanical Drop and Mechanical Shock tests from Annex 8C and 8D of the regulation, respectively.

5.1.1 Mechanical Drop Test

As defined in the regulation, the battery, along with its enclosure and affiliated components, is dropped from a height of 1 meter, measured from the bottom of its geometry, to a smooth, horizontal concrete pad or other flooring type with equivalent hardness [36]. All intricacies of the test procedure are aimed to be taken into account in the setup of the corresponding analyses. In addition to the complete report of this, all assumptions and considerations necessary to replicate this testing procedure by numerical means will be explained later in this chapter.

Nevertheless, a detail from the description of the testing procedure requires the definition of a strategy to correctly replicate the testing procedure. As described in the regulation document: "*The removed REESS shall be dropped six times from different orientations as decided by the Technical Service. The manufacturer may decide to use a different removed REESS for each drop.*" [36]. The document does not explicitly specify the orientations from which the tested product is dropped.

Thus, it is at the discretion of the technical service representative. To account for this subjective choice of orientation for each repetition of the drop test, a strategy is needed to find all possible orientations that may be structurally critical for the battery enclosure in the testing conditions.

A 7 orientation strategy was devised, aimed to encompass first, the impact of the main faces of the enclosure, in a face-to-face contact. Then, the impact of the edges and vertices of the enclosure geometry that were deemed to be critical, with the ground, was considered. This results in a strategy that includes all worst-case scenarios for the impact of the enclosure.

The sequence of drop test orientations is illustrated in Figure 5.1 and further explained in Table 5.1.

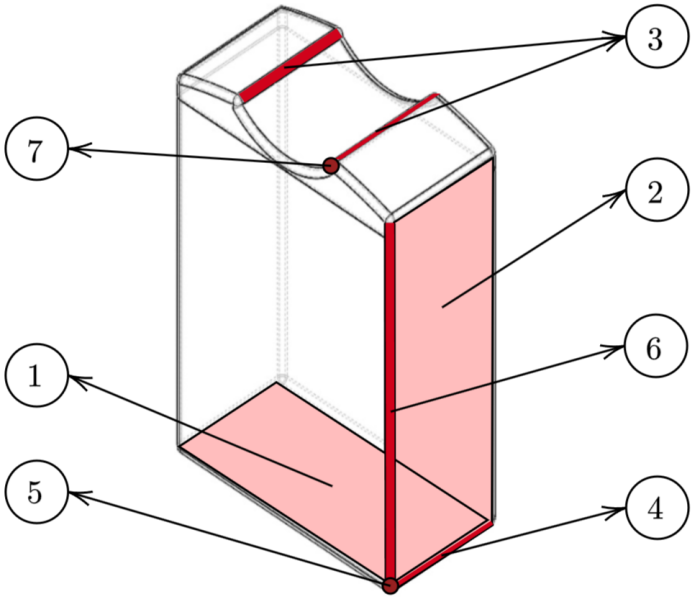

Figure 5.1: 7 orientation drop test procedure highlighted in zones of contact

Table 5.1: 7 orientation drop test procedure description

Orientation nº	Type of Contact	Angle of Contact	Aim
1	Enclosure surface to rigid floor	0°, parallel surfaces	Evaluate the crash absorption characteristic of the honeycomb structure in a head-on vertical drop.
2	Enclosure surface to rigid floor	0°, parallel surfaces	Evaluate the behaviour of the enclosure in a head-on vertical drop in a zone without crash absorption structures.
3	2 enclosure edges to rigid floor	0°, edges parallel to the floor surface	Evaluate the crash absorption characteristic of the honeycomb structure in a head-on vertical drop.
4	Enclosure edge to rigid floor	-45° rotation in the $x-y$ plane	Evaluate an impact in the smallest edge of the battery enclosure
5	Enclosure vertex to rigid floor	45° rotation $x-y$ and $y-z$ planes	Evaluate an impact in a vertex of the battery enclosure
6	Enclosure edge to rigid floor	45° between surface nº2 in Figure 5.1 and floor	Evaluate an impact in an edge of the battery enclosure without protection structures
7	Enclosure vertex to rigid floor	-	Evaluate the impact in a top vertex of the enclosure geometry

5.1.2 Mechanical Shock Test

The Mechanical Shock Test procedure is described in the UN regulation document as follows: "*The tested-device shall be secured to the testing machine by means of a rigid mount which will support all mounting surfaces of the tested-device.*

A gross mass of 12 kg or more shall be subjected to a half-sine shock of peak acceleration of 500 m/s^2 and pulse duration of 11 milliseconds.

For both the tested-device shall be subjected to three shocks in the positive direction followed by three shocks in the negative direction of each three mutually perpendicular mounting positions of the tested-device for a total of 18 shocks." [36].

The description of the testing procedure is clearly defined. As for the Mechanical Drop Test, all details of the procedure will be taken into account in the simulation setup and will be described later in this chapter, along with all assumptions and considerations.

The direction of application of the transient shock load encompasses three mutually perpendicular mounting positions. As the battery + enclosure assembly is considered to be fixed in its vertical position, the pulse shocks are applied to the three orthogonal directions x, y and z represented in Figure 5.2, both in the positive and negative directions.

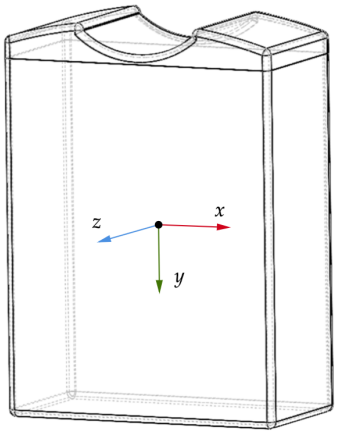

Figure 5.2: Coordinate system considered for the testing simulation procedure

Due to the symmetry of the battery enclosure in both $y-z$ and $x-y$ planes, the 18-shock procedure can be simplified to only 4 shocks, which are going to be designated: **X**, **Y+**, **Y-** and **Z**. Each shock pulse orientation will have its own simulation along with specified boundary and load conditions, as will be presented later in this chapter.

Due to their inherently transient nature and the involvement of nonlinear effects such as contact interactions and high-strain material responses, the Mechanical Drop Test and Mechanical Shock Test were modelled by way of explicit dynamic analyses, as theoretically justified in Chapter 2.

5.1.3 Limitations and Considerations

This section will delve into the limitations integral to this project and assumptions that were necessary to make in order to achieve the defined objectives.

As described in Section 4.1, the information regarding the battery + affiliated components system is very limited. Due to this, a choice had to be made between two approaches. First is creating a simplified three-dimensional model of the battery, making assumptions about some of its characteristics, including mechanical properties, resistance and contact interface with the enclosure. The alternative approach is replacing a battery model with its fundamental quantities, such as weight, inertia, and modelling its interaction with the enclosure as best as possible with the available tools in HyperMesh's. Considering that the aim of the project is the design of the enclosure and the added complexity that the former approach entails, the simpler approach was selected. The battery weight, inertia and interaction with the composite enclosure were included in the FEM models, these matters will be explained later in this chapter.

Although the battery enclosure exhibits clear symmetry in both the $y-z$ and $x-y$ planes, which would theoretically allow analysing only half of the structure to reduce computational cost, the full geometry was modelled. This choice is justified by the aim to capture the complete stress and strain distribution, its propagation throughout the enclosure, and the resulting global deformation behaviour. Additionally, the initial stages of the numerical validation of the prototype enclosure aimed to include a process of composite lay-up optimisation, as seen in Chapter 3. The

consideration of the entire enclosure geometry in the process of lay-up optimisation would simplify the obtention of manufacturable ply shapes in its later stages. Unfortunately, this idea was left behind due to the incompatibility of the OptiStruct composite lay-up optimisation algorithm with the explicit dynamic analyses needed to capture all physical phenomena involved in the mechanical testing procedures.

Concerning the dynamic explicit analyses, as will be described later in the section on the pre-processing, the behaviour of all the materials of the model was kept as simple, linear elastic formulations. Plastic deformation, brittle ply/laminate failure, delamination and other real-life material mechanisms were not taken into account. Although these are important behaviours to model in mechanical problems like the ones at hand, they are very complex to include in finite element analyses, and would come at a heavy time and computational cost. Given the time established for the course of this project, it was found that the effort necessary to include these details would not be compatible with the deadline of the work.

Still, concerning the intricacies of the numerical analyses, the choice not to include scaling was made. The use of these tools depends on a case-by-case basis, and can be omitted so long as the run and results of the analyses are not affected by the problems such tools aim to tackle. Adding to this, all simulations used the default settings on element formulation and hourglass control, which resulted in the use of reduced integration elements and measures to limit the unrealistic hourglass deformation modes. The necessary review of the analysis data to justify the omission of mass scaling and the use of reduced integration and hourglass control will be presented later in this chapter.

Rayleigh damping was not introduced in the finite element model, as the simulated events are short-duration impact phenomena where material damping plays a negligible role in the overall structural response. In this context, the enclosure behaves in a purely elastic manner according to the material definitions, and any energy dissipation in the system occurs only through numerical effects such as hourglass control or bulk viscosity. For such transient events, adding artificial damping would risk overdamping the response and distorting the physical accuracy of the results.

Additionally, the mesh density was limited to a maximum of 100,000 nodes, a numerical restriction imposed by the student version of the Altair HyperWorks® software suite. Nevertheless, this limitation did not compromise the validity of the analyses, as will be demonstrated through the mesh convergence study presented ahead.

Other limitations of the numerical validation for mechanical resistance include the use of a simplified enclosure design that does not yet include some manufacturing details, such as transition, overlap or joint regions between laminates. These features will be added to the final design before production. In this preliminary phase of the design, only the overall geometry and laminate and their performance were evaluated. For the connection and bonding between different components of the enclosure, connectors particular for this kind of task were used. This will be described in detail in the next section of the report.

Finally, due to the evident lack of detailed information regarding the motorcycle, namely the positioning and fixation methods of the battery and its enclosure, it was unfortunately not possible

to formulate and assess a realistic load case scenario involving the assembly, which would have allowed for a more accurate evaluation of the prototype's performance and resistance under real-world operating conditions.

5.1.4 Unwritten Work

Although not directly relevant for the results presented in this chapter, a significant amount of preliminary effort was dedicated to identifying the assumptions and computational tools that most accurately represent the problems under study. The methodology adopted was inherently exploratory, consisting of a systematic variation of modelling approaches, simulation parameters, and boundary conditions, combined with continuous evaluation of their effectiveness. This process was complemented by an extensive review of relevant literature and technical documentation to ensure that the selected configurations were both robust and justified.

Several classes of numerical simulations were investigated in succession: beginning with linear static analysis, then progressing to nonlinear static analysis, and ultimately converging on explicit dynamic analysis as the most suitable framework for the intended validation tasks. Along this path, multiple boundary condition strategies and load application methods were examined, including different representations of rigid bodies, gravitational and acceleration-based loads, imposed velocities, as well as various contact formulations ranging from node-to-surface (`N2S`) to surface-to-surface (`S2S`).

5.2 Numerical Modelling

This section focuses on the finite element model developed for the mechanical validation stage of the project, encompassing the whole pre-processing phase, while explaining all of its intricacies and justifications behind them. The matters described here apply to both the Mechanical Drop and the Mechanical Shock Test. To save time and effort, a base finite element model was created for both analyses, as a lot is common between them. Geometry, mesh, materials, laminates, connectors, and more remain the same from analysis to analysis. Differences that occur at boundary conditions and loads will be described in separate sections corresponding to the Mechanical Shock and Mechanical Drop Test simulations.

5.2.1 Geometry

First, it is necessary to address the unit system chosen in both the CAD software SolidWorks® and in HyperMesh®, to define and analyse the simulations. The unit system is provided in Table 5.2. Evidently, not all units are directly provided in the table, but all relevant units of measurement can be expressed from these fundamental units.

Table 5.2: Unit system chosen for finite element analysis

Quantities	Unit
Mass	g
Length	mm
Time	ms
Force	N
Pressure	MPa
Energy	N mm

The initial tasks in the finite element pre-processing software consist of importing and preparing the geometry to make it suitable for the meshing discretisation process. From the CAD geometry previously presented in Figure 4.5, the external surface of the enclosure's outer shell as well as the surface of the internal laminate components, were extracted. This is necessary since these components need to be meshed as shell elements to later be defined as a composite laminate in HyperMesh®. The resulting surfaces, combined with the solid geometry of the honeycomb core structures, were then imported to HyperMesh®.

Next, a process of geometry and topology alterations was realised to clean up, or modify, any complex features in the model that could hamper the discretisation process and are not of significant importance for the accuracy or overall resistance of the enclosure. One of such processes was the suppression of unnecessary surface edges. In the process of meshing, the software uses surface edges to guide the creation of elements, placing nodes in these edges. In the occurrence of a multitude of edges in a small zone, such as the vertices of filleted edges, the software may create low-quality, distorted elements that will negatively impact the performance of the model. Suppressing some edges that are not necessary for the software to correctly follow the surface geometry will solve this problem. Figure 5.3 shows this process of edge suppression in the enclosure surface geometry.

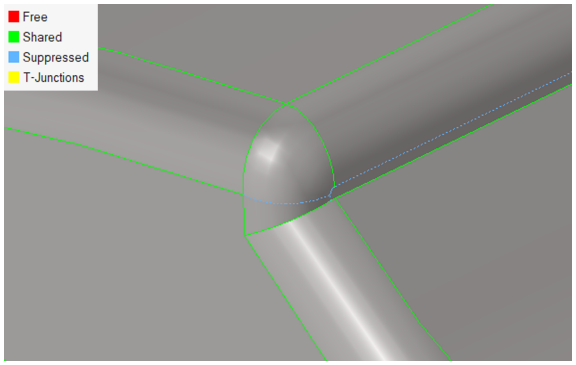

Figure 5.3: Surface topology alterations by edge suppression in the enclosure model (suppressed edges in blue)

Another important geometry cleanup process realised is fillet defeature to the honeycomb core geometries, both top and bottom. This process is presented in Figure 5.4.

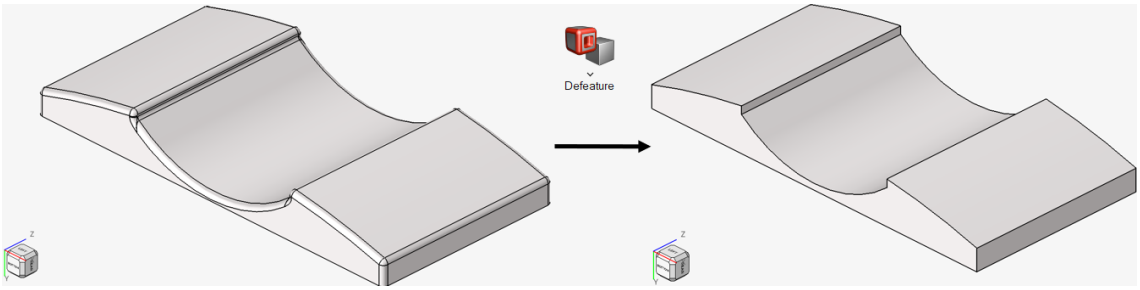

Figure 5.4: Fillet defeature process to honeycomb core geometry

The fillet defeaturing process is crucial to an efficient discretisation of the honeycomb core geometries, as it greatly simplifies the process by enabling the use of the automatic 3D solid mesh mapping tool in the software. It results in a high-quality mesh of hexahedral elements, as opposed to tetrahedral elements, which perform worse and would require a more time-consuming process that would result in a lower-quality mesh.

5.2.2 Mesh

Before describing the process of meshing and the final discretised enclosure model, a brief overview of element quality and mesh metrics will be provided.

5.2.2.1 Mesh Metrics

In finite element analysis, the accuracy and reliability of the results often depend on a critical factor: mesh quality. A well-constructed mesh is an important factor in ensuring simulations run smoothly and deliver reliable results. Conversely, a poorly designed mesh can lead to inaccurate predictions, unnecessary computational costs, and overlooked design flaws [69].

Mesh quality in FEA refers to measuring how well a mesh represents a model's geometry and how effectively it supports accurate and stable simulations. In simpler terms, it's an evaluation of the shape, size, and distribution of the mesh elements within a simulation model [69].

When generating a finite element mesh, several key principles must be considered to ensure accuracy and computational efficiency. A balanced element distribution is essential: while uniform meshing promotes consistency in stress and strain calculations, regions with stress concentrations, sharp corners, or steep gradients require local refinement to capture critical effects. Element aspect ratios should ideally remain close to unity (square in 2D or cubic in 3D) to minimise numerical errors, though exceptions exist; for instance, thin-walled structures or boundary layer regions may necessitate high-aspect-ratio elements to properly follow the geometry. Furthermore, smooth transitions in element size are preferred over abrupt changes, as they reduce numerical artefacts and maintain solution accuracy. Finally, the mesh must accurately represent the geometry without resorting to excessive refinement, striking a balance between fidelity and computational cost [69].

For reference, the following metrics to ensure a quality mesh were considered:

- The **aspect ratio** is a measure of the proportionality of an element's dimensions. For 2D elements, it is typically calculated as the ratio of the longest edge to the shortest edge. In 3D elements, the aspect ratio considers the ratio of element lengths along different axes, making it more complex. **Ideal Range**: An aspect ratio < 5 is optimal [69].
- The **Jacobian** matrix evaluates the mapping of the element from its natural (idealised) coordinates to the actual coordinates in the mesh. **Ideal Range**: While a Jacobian value close to 1 is generally ideal, acceptable values can vary depending on the solver and analysis type. For some applications, values below 0.6 may still be acceptable, so a threshold of 0.7 will be considered [69].
- The **Quality Index** value is a function of twelve criteria with user-defined weight factors. The default weight values were found to be a good reference for this case. Each criterion has five rating levels. The elements that pass a criterion are assigned a penalty value of 0.0 to 1.0 for that criterion. The elements that fail a criterion are assigned a penalty of 1.0 to 10.0 as a linear function of how far the element is from satisfying the criterion. Each element is assigned the corresponding element Q.I. colour [70]. All of this means that higher compound Q.I. values indicate worse quality, so a **low value of Q.I. is an objective**. Figure 5.5 illustrates the five Q.I. rating levels.

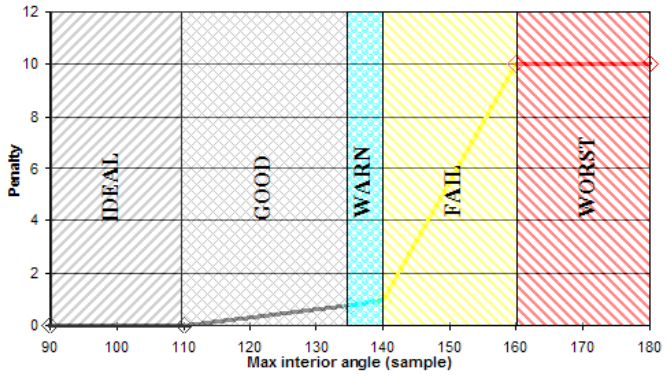

Figure 5.5: Criterion Levels in HyperMesh® [70]

Where possible, the use of structured meshes with hexahedral elements (3D) or quadrangular elements (2D) is recommended, as they generally offer better accuracy and efficiency compared to unstructured tetrahedral or triangular meshes [69]. Also, taking advantage of symmetry in a model is important to save effort but also to ensure a symmetric behaviour. For symmetric structures, the mesh should also be generated symmetrically; otherwise, even with symmetric loads and boundary conditions, the analysis may yield artificially asymmetric results.

5.2.2.2 Meshed Enclosure Model

The discretisation process was divided in two main sequences. First, the two-dimensional shell mesh was created for the outer surface and the inner surfaces of the enclosure model. A process of

Freeform 2D mesh was used, which consists of a semi-manual definition of meshing parameters. The elements were selected to be first order to comply with the requirements of the OptiStruct ® Explicit Solver, which only utilises first-order elements for its explicit dynamic solver. Average element size was selected as 3 mm, and the density of nodes on critical edge and vertex zones was refined to ensure result accuracy and to follow the surface geometry with good detail. This process is shown ahead. The inherent symmetry of the model was used to great effect by meshing part of the model, then replicating it through mesh mirror processes, ensuring that nodes are equivalenced at the symmetry planes. Secondly, the solid element discretisation of the internal core components was carried out through automatic mapping, resulting in a well-structured first-order hexaheadral and pentahedral elements. Default mesh parameters were found to lead to excellent results, and the average size was set to 4 mm. Figures 5.6 and 5.7 present the discretised components from the enclosure model, separately.

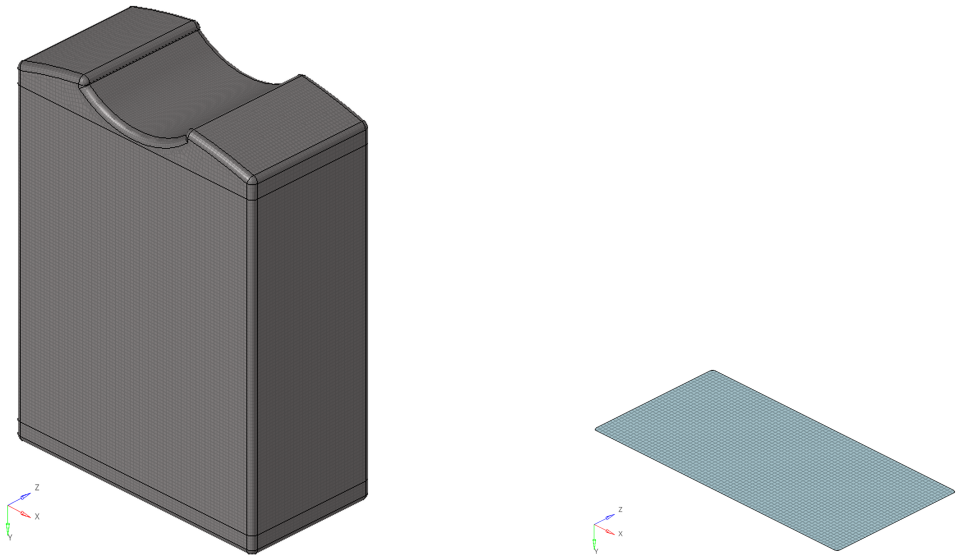

(a) External meshed surface (b) Internal meshed surface

Figure 5.6: Components discretised with shell elements

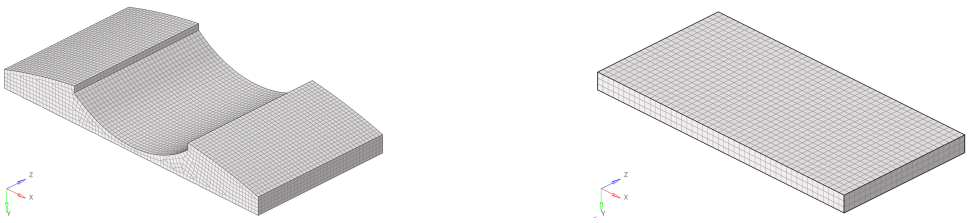

(a) Meshed top honeycomb core (b) Bottom honeycomb core

Figure 5.7: Components discretised with solid elements

Figure 5.8 shows two details of the resulting mesh.

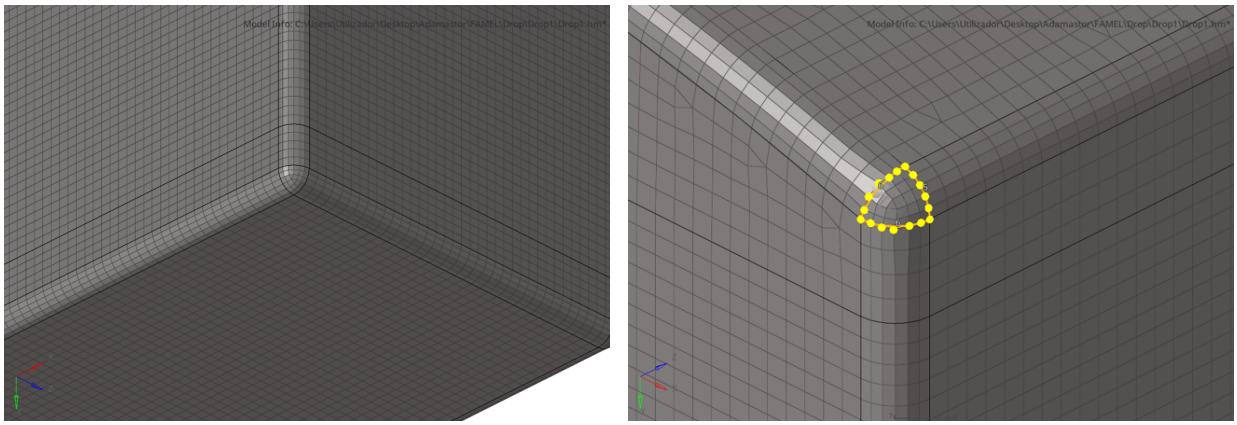

(a) Close-up view of the external meshed surface (b) Nodal density refinement tool

Figure 5.8: Details in the external enclosure mesh

As mentioned, great care was given to ensure a correct refinement of the edges and corners of the enclosure model, the nodal density refinement at the edges is shown in Figure 5.8b. A good compromise between element quantity and aspect ratio was obtained.

Table 5.3 lists the statistics of the final mesh.

Table 5.3: Mesh Statistics

Element Type		**Quantity**
2D Shell	`QUAD4`	44 646
	`TRIA3`	220
3D Solid	`HEX8`	19583
	`PENTA6`	1178
Total Elements		65 627
Total Nodes		70 428

As an indication, information on the type of element formulation will be given without going into excessive detail. To learn more about the element formulations available in HyperMesh®, refer to Altair®'s documentation that is cited in this paragraph. As referred to previously, the default settings regarding the explicit reduced integration element formulations were used. This means that the elements in the mesh are almost all in a reduced integration formulation. `QUAD4` elements in the model are Belytschko-Wong-Chiang with full projection reduced integration elements (`BWC`), `TRIA6` elements are by definition integrated by a single Gauss integration point, so reduced integration is not applicable. `HEX8` elements are formulated as Uniform Reduced Integration elements (`URI`), one-point integration is used. And `PENTA6` are defined in a Selective Reduced Integration (`SRI`) formulation [54, 71, 72]. The hourglass control will be explained later.

Concluding, the resulting mesh is well structured, prioritises better-performing quadrilateral elements in surfaces and hexahedral elements in solids, and uses triangular and pentahedral elements for smooth mesh transitions. However, the quality of elements is still not verified.

5.2.2.3 Mesh Quality Assessment

Figures 5.9 and 5.10 provide the mesh quality metrics of the discretised exterior surface of the enclosure in the 3 criteria considered: Aspect ratio, Jacobian matrix and Quality Index.

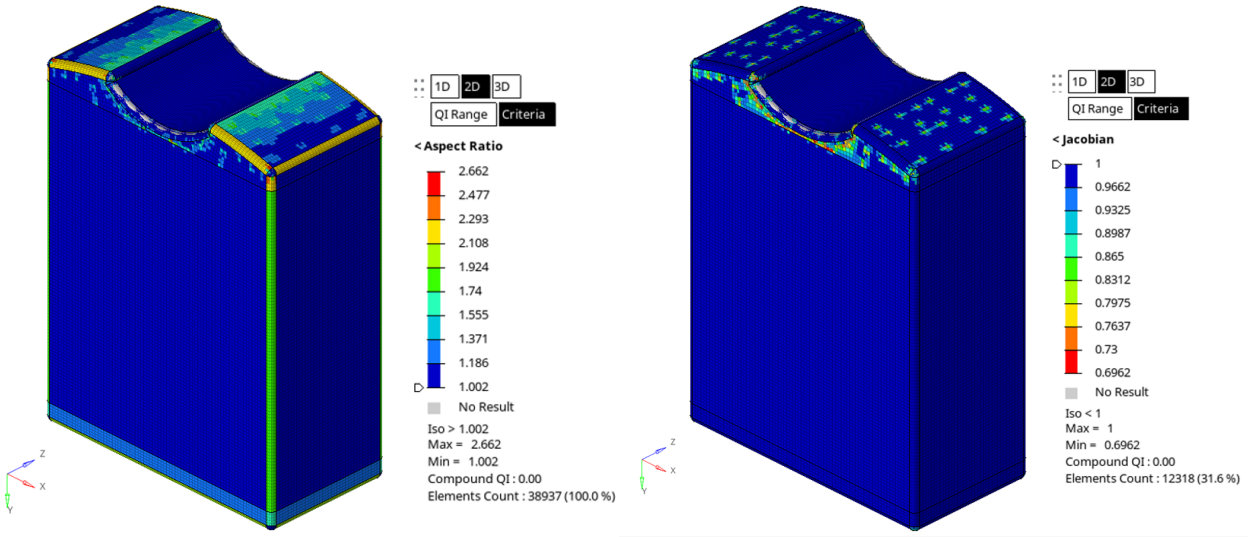

(a) Aspect Ratio (b) Jacobian Matrix

Figure 5.9: Quality metrics of exterior shell mesh

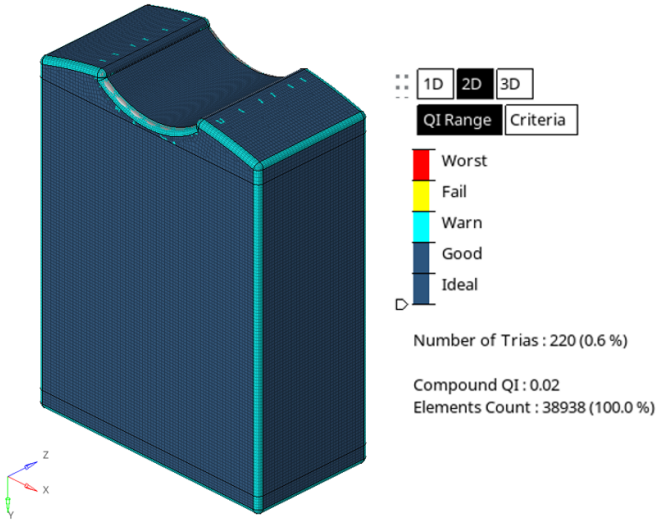

Figure 5.10: Quality Index of exterior shell mesh

The element quality visualisation tool in HyperMesh® demonstrates that the exterior shell mesh is up to the quality standards set. The aspect ratio values fall well within the maximum acceptable value of 5, even in the corners and edges of the model. The minimum value of the Jacobian matrix index falls at the threshold value, which was considered acceptable. Though the edges of the model are of teal colour in Figure 5.10, which refers to a *Warn* criteria, it happens due to the elongated nature of the elements at the edges, since the values of aspect ratio are moderate, it is found to be acceptable for this work. To add to this, the overall compound Q.I. is extremely small, which indicates an overall excellent mesh quality.

Figure 5.11 validates the quality of discretisation of the interior surfaces of the model, with a superb compound Q.I. of 0.0. All other quality criteria are excellent since

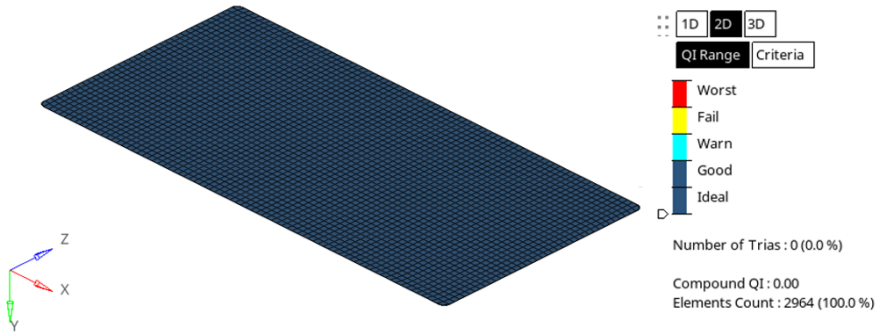

Figure 5.11: Quality Index of interior shell mesh

As for the solid mesh for the discretisation of the core, crash-absorption structures, they also verify the quality standards. Figure 5.12 provides the results of the element quality visualisation tool used for the meshed honeycomb core components.

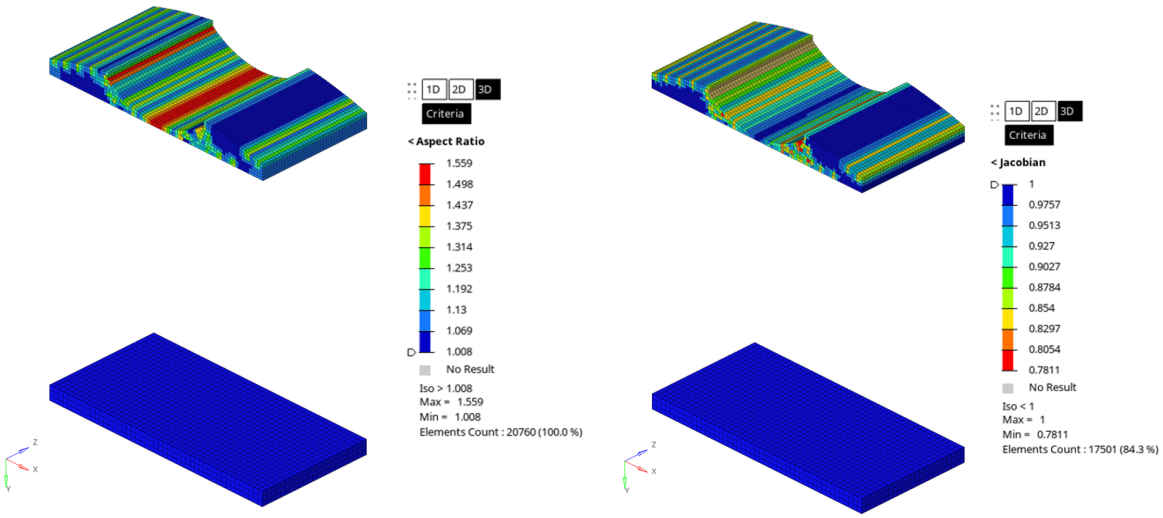

(a) Aspect Ratio (b) Jacobian Matrix

Figure 5.12: Quality metrics of honeycomb core solid mesh

5.2.3 Laminate

With the model correctly meshed, it is time to define its materials. As the main material of the prototype enclosure is a composite laminate, its process of definition is complex and differentiates itself from simple isotropic materials. The laminate modelling followed a composite ply-based approach, and its methodology is described in Section 2.9.

The composite material laminates were explained in Section 4.3, so the work now consists of translating these ideas into the finite element software. The ply-based approach mimics the manufacturing process of the components in the software, so a good understanding of it is necessary to correctly define the material model. As the manufacturing process will consist of a ply lamination directly on a mould, the first ply will be the one visible on the exterior of the enclosure. This means the lamination will be in the exterior-to-interior direction, inward. This is the direction that is defined as the normal laminate direction in HyperMesh®. The normal laminate direction can be seen in Figure 5.13, in a section view of the model as to verify the normals of the external and internal directions. The red colour means that the normal vector of the corresponding element is pointing out of the surface, the blue colour means that the normal vector of the corresponding element is pointing into the surface.

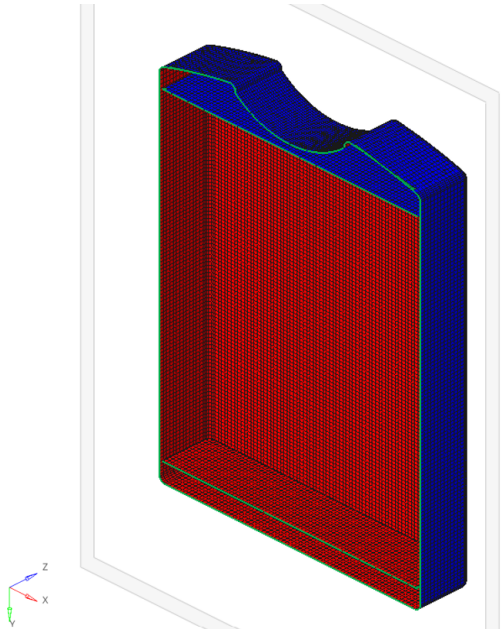

Figure 5.13: Element normals of the enclosure model

The next step was to impose a material direction, to define the reference direction from which each ply of carbon fibre pre-impregnated is orientated. The material direction can be visualised in HyperMesh® (Figure 5.14), with the red arrows indicating the 0° direction.

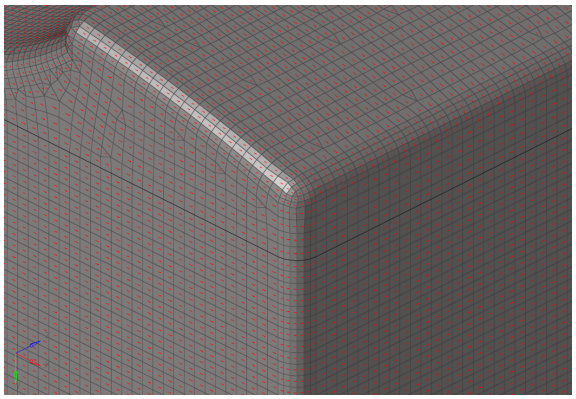

Figure 5.14: Material orientation of the enclosure model

The carbon fibre prepreg material E731-00 HS2238 Carbon TR30S T 245gsm 2 x 2 Twill 3K 42% RC was defined as a `MAT8` material card in the software; its mechanical properties, listed in Table 4.1 were converted into the correct unit system (Table 5.2) and included in the software. Then, both external and internal laminates were created ply by ply, with careful consideration of the stacking sequence in the normal direction of the laminate. As described in Section 4.3, the external laminate is comprised of 8 plies in a $[45/0/-45/90]_S$ sequence and the internal laminate is comprised of 4 plies in a [45/0/-45/90] sequence. Table 5.4 presents the full enclosure laminate information, and Figure 5.15 shows a close-up of the laminate in HyperMesh®.

Table 5.4: Laminate specifications for the enclosure model

	Ply	Orientation / °	Thickness / mm	Material
External laminate				
1	Ply1_45	45	0.28	E731 prepreg
2	Ply1_0	0	0.28	E731 prepreg
3	Ply1_−45	-45	0.28	E731 prepreg
4	Ply1_90	90	0.28	E731 prepreg
5	Ply2_90	90	0.28	E731 prepreg
6	Ply2_−45	-45	0.28	E731 prepreg
7	Ply2_0	0	0.28	E731 prepreg
8	Ply2_45	45	0.28	E731 prepreg
		Total:	2.24	
Internal laminate				
1	Ply90	90	0.28	E731 prepreg
2	Ply-45	-45	0.28	E731 prepreg
3	Ply0	0	0.28	E731 prepreg
4	Ply45	45	0.28	E731 prepreg
		Total:	1.12	

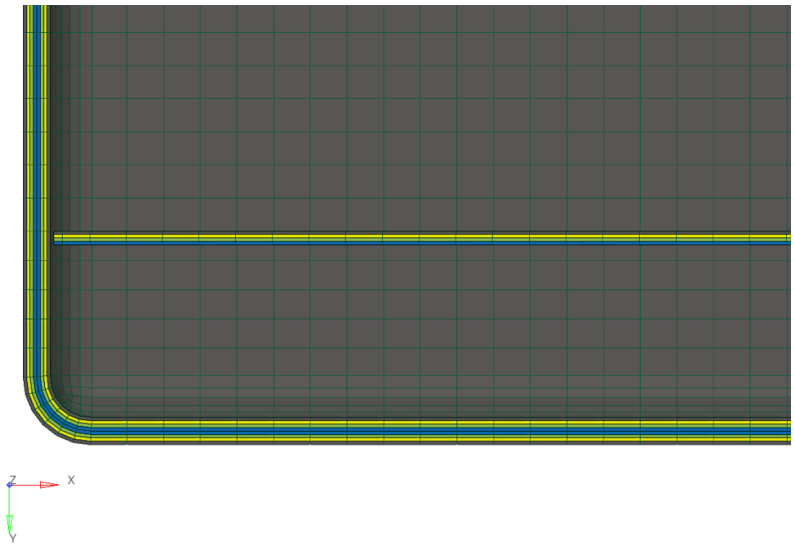

Figure 5.15: Laminate in HyperMesh®

5.2.4 Honeycomb Structure

For the numerical modelling of the aluminium honeycomb, an approach based on the recommendations of Hexcell, one of the main suppliers of honeycomb structures worldwide, was considered. Their technology manual [73] gives guidelines on how to properly model the behaviour of a honeycomb structure in FEA. Given the complex geometry and height of the honeycomb structures in the enclosure design, the honeycomb will be discretised by solid 3D elements, without creating the thin wall geometry. Hexcell does not recommend modelling the individual cells for normal engineering analyses since it greatly increases the complexity of the model. A particular set of conditions in the definition of the material attributed to the honeycomb model will be able to simulate the honeycomb behaviour [73].

These considerations presented by Hexcell are [73]:

$$E_x \approx E_y \approx 0$$

$$\mu_{xy} \approx \mu_{xz} \approx \mu_{yz} \approx 0$$

$$G_{xy} \approx 0$$

$$G_{xz} = G_L = \text{shear modulus in ribbon direction}$$

$$G_{yz} = G_W = \text{shear modulus in transverse direction}$$

$$E_z = E_C = \text{compressive modulus of core material}$$

Figure 5.16 illustrates the reference directions of honeycomb structures, the x axis is aligned with the ribbon direction where the structure has double wall thickness due to the manufacturing process, and the y axis is aligned with the transverse direction.

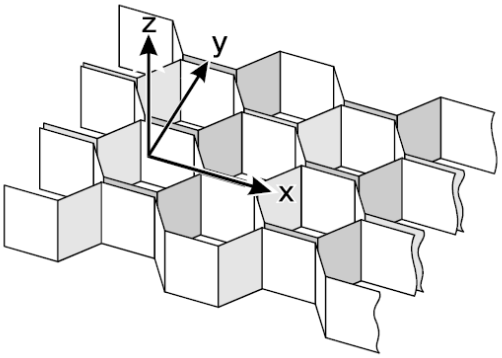

Figure 5.16: Reference directions of honeycomb structures [73]

The above-described simplistic approach has proven to give good engineering solutions for practical applications [73]. Considering the properties present in Table 4.2, it results in the following honeycomb properties to include in the numerical model: $E_z = 1310$ MPa, $G_{xz} = 448.16$ MPa and $G_{yz} = 241.32$ MPa.

To add to this, the Malek and Gibson [74] analytical model for honeycombs with double thickness vertical walls was used for the following modulus properties: E_x, E_y and G_{xy}. Values for these properties add physical accuracy and are needed to avoid singularities in the FEA model. The analytical expressions are:

$$l_b = l - t\tan\left(\frac{\pi}{4} - \frac{\theta}{2}\right), \tag{5.1}$$

$$h_b = h - t\tan\left(\frac{\pi}{4} - \frac{\theta}{2}\right) \tag{5.2}$$

$$E_x^* = E_{Al}\left(\frac{t}{l_b}\right)^3 \frac{\cos\theta}{\left(\frac{h}{l}+\sin\theta\right)\sin^2\theta}\left[\frac{1}{1+(2.4+1.5\nu_{Al}+\cot^2\theta)\left(\frac{t}{l_b}\right)^2}\right] \tag{5.3}$$

$$E_y^* = E_{Al}\left(\frac{t}{l_b}\right)^3 \frac{\left(\frac{h}{l}+\sin\theta\right)}{\cos^3\theta}\left[\frac{1}{1+\left(2.4+1.5\nu_{Al}+\tan^2\theta+\frac{(h_b/l_b)}{\cos^2\theta}\right)\left(\frac{t}{l_b}\right)^2}\right] \tag{5.4}$$

$$C = 1+2\left(\frac{h_b}{l_b}\right)+\left(\frac{t}{l_b}\right)^2\left[\frac{(2.4+1.5\nu_{Al})}{(h_b/l_b)}\left(4+\frac{h}{l}+\sin\theta\right)+\frac{(h/l+\sin\theta)}{(h_b/l_b)^2}\left[(h/l+\sin\theta)\tan^2\theta+\sin\theta\right]\right. \tag{5.5}$$

$$G_{12}^* = E_s\left(\frac{t}{l_b}\right)^3 \frac{\left(\frac{h}{l}+\sin\theta\right)}{\left(\frac{h_b}{l_b}\right)^2\cos\theta}\left(\frac{1}{C}\right) \tag{5.6}$$

with,

- l and h are the length of the inclined and vertical cell walls, respectively;

- t is the wall thickness;

- θ is the honeycomb wall angle as in Figure 5.17;
- E_{Al} and ν_{Al} are the Young's modulus and the Poisson ratio of the honeycomb material, respectively.

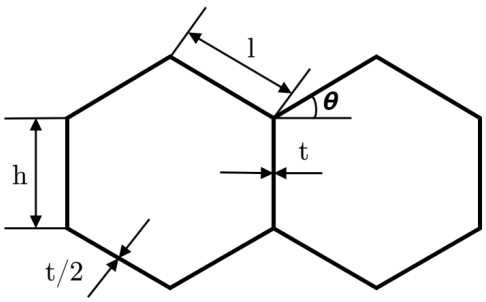

Figure 5.17: Honeycomb Dimensions

Considering a perfectly hexagonal honeycomb cell of size 6.4 mm, the dimensions are: $l = h = 3.695$ mm, $t = 0.07$ mm, $\theta = 30$. And 3003 Aluminium properties are: $E_{Al} = 69.5$ GPa and $\nu_{Al} = 0.33$. This results in the following honeycomb properties to include in the numerical model: $l_b = h_b = 3.654$ mm, $E_x = 1.125$ MPa, $E_y = 1.126$ MPa, $C = 3.006$ and $G_{xy} = 0.281$ MPa.

The aforementioned mechanical properties were defined for the honeycomb structure components in HyperMesh® by way of the creation of a specially defined orthotropic material. The `MAT9OR` orthotropic material card was utilised, combined with a Cartesian coordinate system, indicating the reference direction of the material properties, which differ from the global axis system of the model. Figure 5.18 shows the honeycomb structures and its material coordinate system.

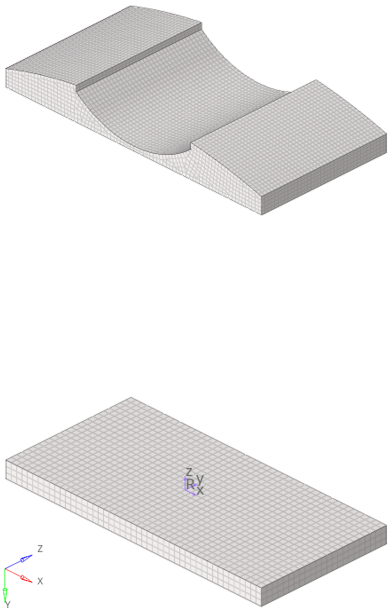

Figure 5.18: Honeycomb structures and its material coordinate system in purple

5.2.5 Connectors

This work encompassed the discretisation and mechanical properties of all physical components of the enclosure finite element model. However, the mechanical relationship between them remains undetermined; for that task, connectors were used.

To simulate an accurate assembly model, it is essential to define how the different bodies interact with each other. The real-world connection between the honeycomb core and the laminated composite material around it consists of a thin epoxy resin adhesive film. This adhesive is cured under heat and pressure, allowing it to flow slightly into the top of the honeycomb cells and form a fillet around each cell wall. This process creates a continuous bondline across the interface, ensuring load transfer and structural integrity of the sandwich structure. So the connection in the finite element software should aim to emulate this continuous linkage around all surfaces of the core geometry.

In HyperMesh®, connectors are geometric entities that define how different parts of a model are fastened together, representing the physical connection between components. They are later realised into FE elements that capture the mechanical and structural behaviour of the joint in the simulation [75]. Area and line-type connectors were utilised for the mechanical linking of the honeycomb solid component and the laminated composite surfaces. These commands work by connecting areas of surfaces or lines, respectively, of the meshed bodies node to node by rigid `RBE2` elements. These elements are one-dimensional, rigid rod-type elements that link one independent node to one or multiple dependent nodes. The motion of the independent node governs the motion of the dependent nodes completely through the rigid link; no relative displacement or rotation is possible [75].

Connectors, and consequently `RBE2` elements, were created around the entire geometry of the honeycomb core components, linking them to the meshed bodies of the laminated surfaces. This approach ensures a full kinematic connection between core and facesheet, meaning that all displacements, rotations, and loads are completely transferred between the two components, accurately replicating the real-world adhesive bond.

Particular care was taken in correctly defining which components were set as independent (masters) and which as dependent (slaves). Since the dependent nodes of an `RBE2` element are fully governed by the motion of their master node, loads and constraints can only be applied to the independent component in the simulation setup. Additionally, attention was given to avoid creating nodal over-constraints, as a single node cannot be simultaneously dependent on two masters without leading to an ill-defined system of equations, potentially causing singularities and rendering the simulation unsolvable. Knowing this, all connectors of this model are defined to have the laminate surface components as master components and the core structures as slave components. This modelling choice is coherent with the physical behaviour of the structure, as in reality the laminates are the first elements to interact with external loads and constraints, while the core functions primarily as a load-transmitting and energy-absorbing medium.

The resulting model contains 31 connectors encompassing all bonding surfaces, which are realised by 2892 `RBE2` rigid 1D elements. Figure 5.19 presents the defined connectors in green with `RBE2` rigid elements in red or blue.

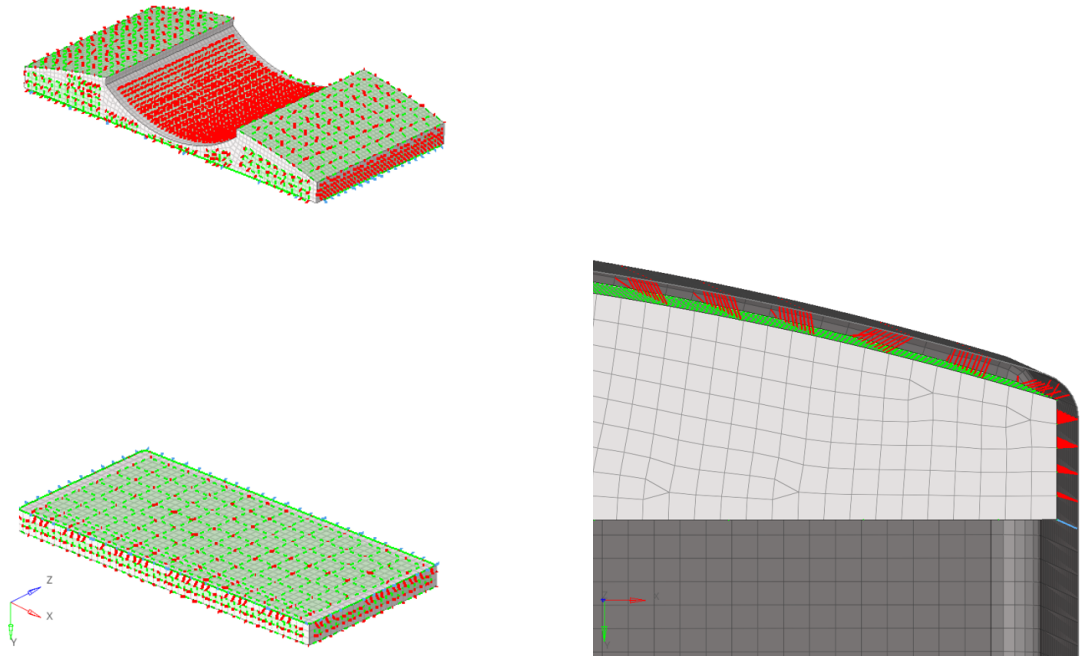

(a) Overall (b) Close-up

Figure 5.19: Connectors in the HyperMesh® enclosure model

5.2.6 Battery Model

As was briefly explained in Subsection 5.1.3, a simple battery model approach was chosen to represent it in the form of its fundamental quantities, such as weight, inertia and interaction with the enclosure components.

The solution found to simulate the battery's fundamental quantities goes as follows:

1. Creation of a concentrated mass/inertia `CONM2` element at the position of the would-be centroid of the rectangular cuboid-shaped battery. To this HyperMesh® zero-dimensional element, the mass and the 3D inertia tensor of the battery are characterised.

2. Creation of a local coordinate axis system at the same position as the `CONM2` element, coincident with the principal axes of the cuboid-shaped battery geometry, with origin at the battery centroid. Define the inertia and mass quantities according to this axis system.

3. Connection of the simplified battery geometrical model to the enclosure surfaces, according to the correct orientation for the respective mechanical drop/shock test, using `RBE3` load distribution 1D interpolation constraint elements.

To provide a detailed explanation of `CONM2` and `RBE3` elements:

`CONM2` elements in HyperMesh® define a concentrated mass and associated inertia tensor at a single node, representing a point mass in the model. The mass and inertia properties can be referenced to either the global coordinate system or a user-defined local axis system, allowing precise control of their orientation. They are commonly used to represent components without the need to create a detailed mesh, reducing model complexity [76].

In contrast to `RBE2`, `RBE3` elements are conceptually similar but fundamentally different in behaviour. Instead of rigidly linking nodes, they interpolate the motion of a dependent node (centre of the battery) as a weighted average of the motions of several independent nodes (enclosure surfaces that would be in contact with the battery), distributing forces back to them without adding artificial stiffness to the structure. The unique behaviour of `RBE3` elements means they are typically used to distribute loads applied on the dependent node amongst the selected independent nodes. This makes `RBE3` ideal for realistic load transfer and mass distribution without over-constraining the model, justifying its use for the task of load transmission in the model [77, 78].

In the creation of this simplified battery model, several simplifying assumptions were made. The centre of gravity of the battery was assumed to coincide with its geometric centre, and its total mass was considered as continuously distributed throughout its volume. The inertial properties were defined in their simplest form, aligned with the principal axes, to simplify their specification. A dedicated local coordinate system was created for this purpose, and the software automatically performs the necessary transformations to the global reference frame during the simulation process. With this in mind, consider the moment inertia tensor of a solid rectangular cuboid, given in its principal axis system, with dimensions w (x-direction), h (y-direction), d (z-direction), and mass m. This is illustrated in Figure 5.20 and mathematically represented in Equation 5.7.

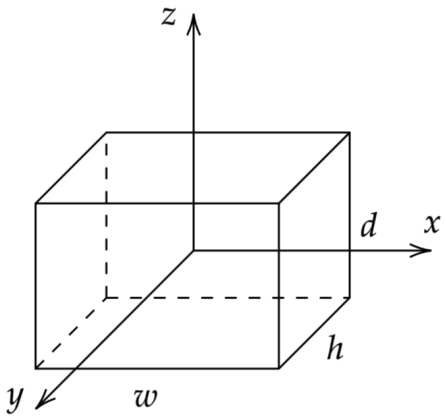

Figure 5.20: Rectangular cuboid and its principal Cartesian system

$$[I] = \begin{bmatrix} \frac{1}{12}m\left(h^2+d^2\right) & 0 & 0 \\ 0 & \frac{1}{12}m\left(w^2+d^2\right) & 0 \\ 0 & 0 & \frac{1}{12}m\left(w^2+h^2\right) \end{bmatrix} \left[\text{g mm}^2\right] \tag{5.7}$$

Solving for the quantities given of 14 kg weight and $234.9 \times 277 \times 115$ mm battery dimensions, we have the following momentum inertia tensor in the chosen unit system:

$$[I] = \begin{bmatrix} 1.049 \times 10^8 & 0 & 0 \\ 0 & 1.539 \times 10^8 & 0 \\ 0 & 0 & 7.980 \times 10^7 \end{bmatrix} \left[\text{g mm}^2\right] \tag{5.8}$$

This tensor, as for the 14 kg mass of the battery, were defined in the software. Then, the `RBE3` element connecting the `CONM2` element to the enclosure components was created. The node-to-node connections of the `RBE3` elements were carefully defined to replicate the most realistic possible load distribution, taking into account the conditions of the real drop and shock tests. Since different load orientations were considered in the testing methodology, a distinct `RBE3` configuration was created for each simulation setup. This ensured that the concentrated mass and inertia represented by the `CONM2` element were correctly coupled to the relevant regions of the structure, faithfully reproducing the expected load paths. The resulting configurations will be illustrated in the following Figures 5.21 and 5.22.

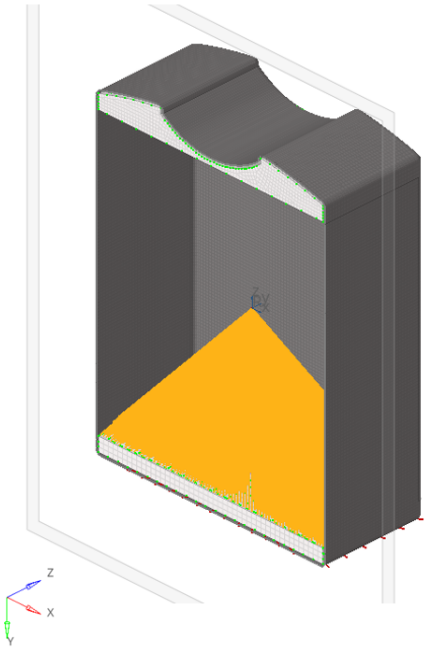

Figure 5.21: `CONM2`, `RBE3` element and respective axis system (Drop test orientation n°1)

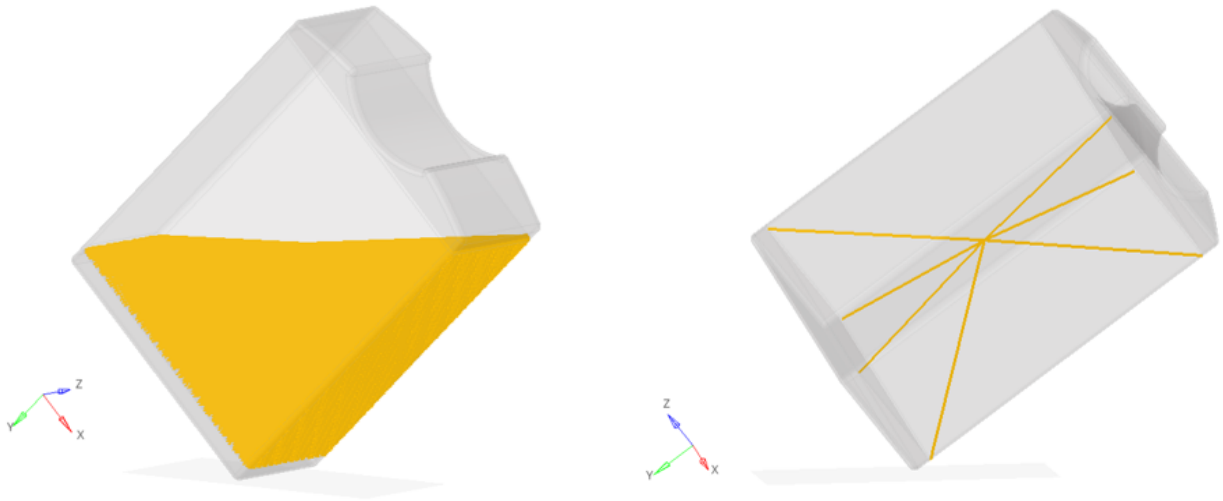

(a) Orientation nº4 (b) Orientation nº5

Figure 5.22: RBE3 elements for drop test orientation nº4 and 5

5.2.7 Contact Definition

In the finite element method, contacts are used to prevent components that do not share the same nodes (no connectivity) from penetrating or sliding through each other, ensuring a physically realistic interaction between bodies. Contact pressure resists penetration, while frictional shear resists sliding. However, contact analysis is inherently challenging due to large and sudden changes in contact stiffness, discontinuities, and its highly nonlinear nature, which often leads to increased computational effort [55].

In HyperMesh®, contacts are formulated using penalty methods, which simulate contact forces through equivalent spring elements. When a secondary node penetrates the main contact surface, an elastic spring is virtually activated between the two, generating a restorative force proportional to the penetration depth. This force acts to push the secondary node back, effectively eliminating interpenetration and ensuring that the contact behaviour remains physically realistic [55].

To simulate the contact of the enclosure with the ground in drop test simulations and with the wall support in mechanical shock test simulations, respectively, perfectly rigid walls were created. These walls were chosen to be rigid to simplify their creation and to ensure that the simulation does not become too computationally expensive. The walls are created in the finite element software as planar surfaces that are coarsely meshed and made rigid by way of `RBE2` elements that link all the nodes of the meshed wall to a fully constrained node in all translations and rotations. The totally constrained elements making the walls are, in this way, left out of the calculations of the solver, further optimising the computational needs of the solver. As every particular simulation differs in the orientation of load, differently positioned walls were created for each simulation. For all walls created, a small gap was added between the enclosure model surface and the wall to ensure that the simulation begin with the contact open, with a quick approximation phase of the enclosure to

the wall at the start of each simulation. This detail is crucial for the realistic behaviour of the load applied to the model, which will be delved into later. An iteration of wall model is represented in Figure 5.23

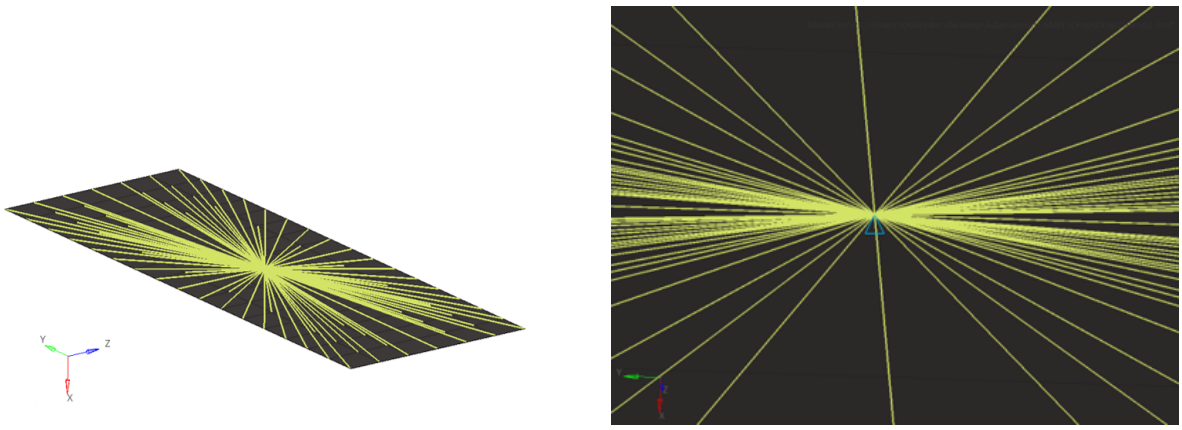

(a) Wall model

(b) Node `SPC` constraint

Figure 5.23: Wall model with `RBE2` element in green

The contact definition chosen consists of a surface-to-surface (`S2S`) discretisation with a `SLIDE` type property. The `SLIDE` property allows for relative tangential motion of both contact surfaces with a user-defined friction model and coefficient. For this work, a frictionless approach was chosen ($\mu = 0$), as the main motion of contact is normal and not tangential in both drop and shock tests, the study of the effect of friction was found to be of secondary importance. The `S2S` contact discretisation was chosen over the more common node-to-surface (`N2S`) discretisation due to its better capture of the physical contact phenomena, verified both in Altair's educational programs and by user experience. `S2S` formulations result in more consistent and realistic contact pressure distributions than their `N2S` counterpart, independently of the mesh in the contact area. However, `S2S` is more computationally expensive, still better results were found to be worth the added expense.

Figure 5.24 provides a close-up view of the contact surfaces defined in HyperMesh®.

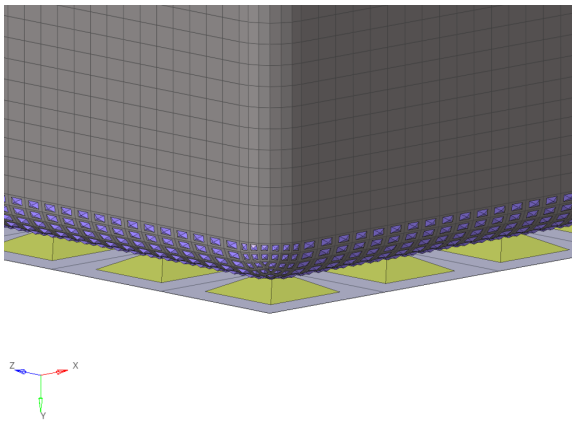

Figure 5.24: Contact surfaces in HyperMesh®

5.2.8 Drop Test Boundary Conditions and Loads

The present subsection will delve into the boundary conditions and loads added to the model that are specific to the Mechanical Drop Test simulations. As previously mentioned, a base finite element model was created due to both simulation types sharing most a lot between them, which gains time and is convenient down the line.

To correctly simulate the drop test scenario in finite element form, a basic approach was chosen. No loads are directly applied to the enclosure model to replicate the loading scenario of the impact of the enclosure from a height of one meter. As a replacement, the kinematics of the enclosure at the point of impact are recreated, and the finite element software defines the loads through its nonlinear contact formulation. This contact is deeply tied to the boundary conditions of the simulation, as will be explained hereafter.

The terminal velocity that the enclosure reaches in the instant before impact can be easily determined through simple calculations, assuming the principle of conservation of energy. For a conservative system, with the enclosure stationary at one meter height before its fall $v_0 = 0$ we have:

$$T_f = V_i \tag{5.9}$$

where T_f is the kinetic energy at the point of impact (final instant) and V_i is the gravitational potential energy of the stationary enclosure (initial instant). The terminal velocity v_f is defined as follows:

$$\frac{1}{2}mv^2 = mgh \Rightarrow v_f = \sqrt{2gh} = \sqrt{2 \times 9.81 \times 1} \approx 4.43 \text{ m/s} \tag{5.10}$$

This velocity was applied to the finite element enclosure model through a velocity initial condition. This was done by using a `TIC` entry in HyperMesh®. `TIC` defines values for the initial conditions of variables used in Explicit Analysis. Both displacement and velocity values can be specified at independent degrees of freedom [79]. The same initial velocity condition is applied to all nodes that comprise the enclosure model geometry, ensuring the rigid free-fall movement desired for this simulation. The resulting velocity vector was decomposed into its x, y and z values to achieve a total linear velocity of 4.43 m/s in the specified orientation for each drop test simulation. Figure 5.25 shows the velocity vector direction for each orientation of drop test.

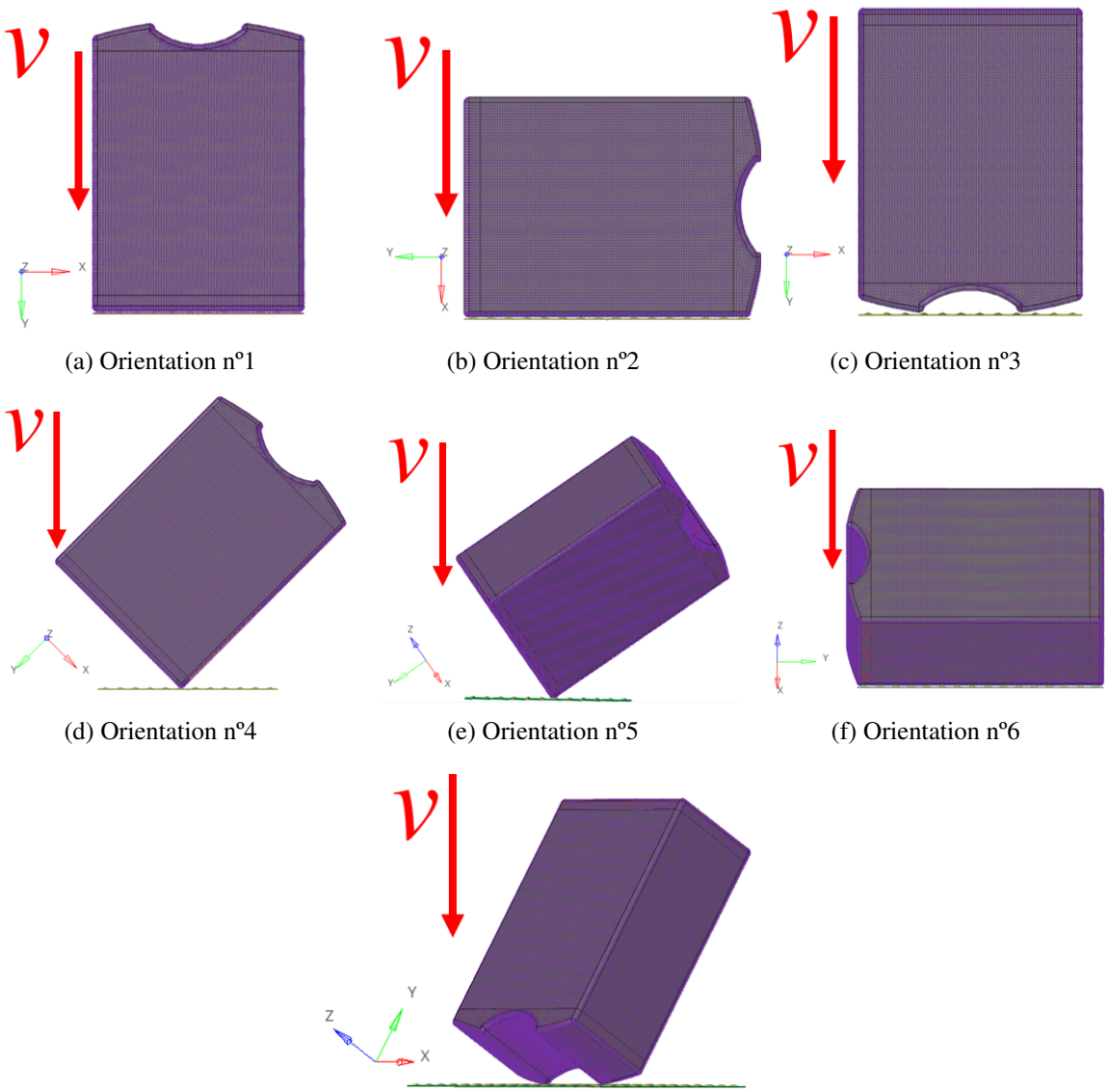

(a) Orientation nº1 (b) Orientation nº2 (c) Orientation nº3

(d) Orientation nº4 (e) Orientation nº5 (f) Orientation nº6

(g) Orientation nº7

Figure 5.25: Resultant velocity direction in each drop test orientation

The main boundary condition of the model consists of the rigid wall model and its contact interaction with the geometry in study; its implementation into the FEA software is explained in detail in the previous subsection. The enclosure model is not constrained in any other way during the simulation, ensuring the correct free-fall behaviour of the enclosure.

5.2.9 Drop Test Explicit Analysis Parameters

The main parameters selected for all mechanical drop test simulations are listed in Table 5.5, and then some details will be explained.

Table 5.5: Drop test explicit dynamic analysis settings

Drop Test Analysis Settings	
Explicit time step control type:	Critical element
Maximum time step (DT) / ms:	Program controlled
Time step safety factor (DTFAC):	0.9
Minimum time step (DTMIN) / ms:	Default (0.0)
End time (TTERM) / ms:	4.0
Increment result output (NLOUT):	30
Initial conditions (IC):	TIC(V) initial velocity

The termination time best suited for the drop test explicit analyses was found to be 4 milliseconds. Although it may seem very short, the proximity of the rigid wall to the enclosure in the analysis setup, combined with the high initial condition velocity makes it possible to analyse the impact of the enclosure, the following rebound and shockwave propagation. The scope of the drop test analysis does not aim to include secondary impacts of the enclosure with the ground since they are less straining and therefore, not critical. This end-time was found by trial and error in a preliminary analysis, and results in a good balance between results and solver run time.

As for the time step control, the minimum time step value was left at its default value, which is zero. This choice is in parallel to the decision not to use mass scaling features to control the minimum time step, which was described earlier in this chapter. The relevance of this choice will be explored in the results study.

The maximum time step is controlled by the solver OptiStruct® in the way thoroughly described in Subsection 2.8.3. For each simulation and time step, the value of maximum time step is computed as in Equations 2.35 or 2.37, for solid or shell elements, respectively. To this value, a safety factor of 0.9 was introduced in the analysis settings to ensure stability. Data from the results of all seven analyses reveal that the explicit algorithm time step was constant to all drop orientations and throughout the duration of the analyses. The value is 1.419×10^{-4} milliseconds and refers to element number 79541. As will be seen, it resulted in simulations with a normal solver run time, considering the size of the model.

The result outputs in explicit analysis (NLOUT) is defined by the user. A value of 30 result outputs was chosen to ensure a proper investigation of the behaviour of the model throughout the wall approximation, contact and rebound phases of the analysis.

As previously mentioned, hourglass control features were utilised to minimise the occurence of hourglass deformation modes in the reduced integration elements that were used, as part of the default element formulation for explicit analysis settings in OptiStruct®. For hourglass control of shell elements, Flanagan-Belytschko-stiffness form is used for QUAD4 elements, and for solid elements, Puso enhanced assumed strain-stiffness form is used. The default hourglass control parameters for both types were found to be applicable for this simulation task [54].

5.2.10 Mechanical Shock Test Boundary Conditions and Loads

The mechanical shock test load definition is more straightforward than the drop test. The regulation on which this test is based clearly specifies the acceleration profile, its transient nature, and its time duration. The regulation describes *"a half-sine shock of peak acceleration of 500 m/s^2 and pulse duration of 11 milliseconds"*. To complement this shock pulse, an additional 2 ms step of zero acceleration was introduced immediately after the half-sine pulse. This resting phase allows the structure to freely respond after the application of the shock, ensuring that the subsequent energy propagation dynamic behaviour is captured in the analysis. It also provides a reference period where no external load is applied, enabling verification that the simulation exhibits realistic behaviour and returns to equilibrium as expected. The resulting load definition is therefore a two-phase transient curve, consisting of the half-sine acceleration pulse followed by a short load-free interval. Converting the units to the system chosen for this finite element model (mm/ms^2), the shock can be mathematically expressed as follows:

$$a(t) = \begin{cases} 0.5 \sin\left(\frac{\pi t}{11}\right), & 0 \leq t \leq 11\,\text{ms (phase I)} \\ 0, & 11 \leq t \leq 13\,\text{ms (phase II)} \end{cases} \tag{5.11}$$

Its graphical representation is given in Figure 5.26

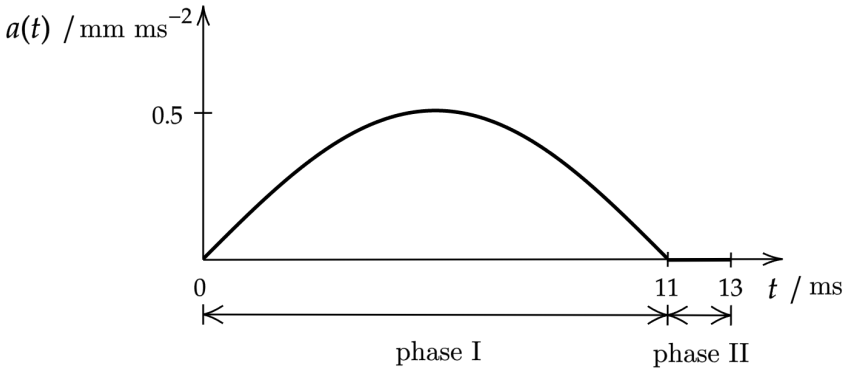

Figure 5.26: Acceleration shock defined

The acceleration loads were reproduced in HyperMesh® by defining a time-dependent dynamic load using the `TLOAD1` entry, which was associated with a `GRAV` body acceleration applied to the entire enclosure model. The gravitational acceleration scale factor was set to 0.5, and a two-phase time-history curve was linked to this load, consisting of a half-sine pulse with a peak value of 1 followed by a short resting interval. The curve in HyperMesh® is provided in Figure 5.27. This procedure ensures that the transient loading conditions implemented in the solver exactly replicate the mathematically defined excitation described earlier. The direction of application of the acceleration load was chosen according to the 4 orientation procedure in x, $y-$, $y+$ and z directions.

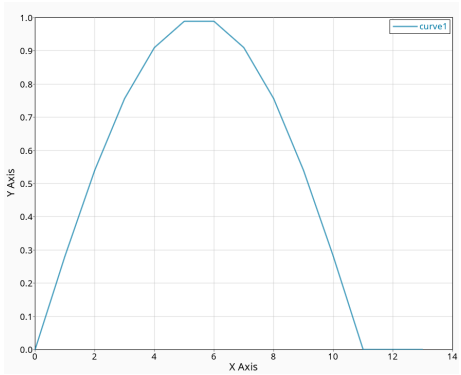

Figure 5.27: TABLED1 curve in HyperMesh®

Regarding the boundary conditions, the same fundamental setup as in the drop test was adopted, consisting of the rigid walls previously described in Subsection 5.2.7. For each simulation case, only the wall opposing the direction of the applied acceleration was modelled. This wall represents the actual support surface on which the enclosure would collide under the corresponding loading condition. Including additional surrounding walls would have increased the computational cost while contributing only marginally to the enclosure's structural response, as the contact with those surfaces plays a secondary role in the overall load transfer.

5.2.11 Mechanical Shock Test Analysis Parameters

The main parameters selected for all mechanical shock test simulations are listed in Table 5.6.

Table 5.6: Mechanical shock test explicit dynamic analysis settings

Mechanical Shock Test Analysis Settings	
Explicit time step control type:	Critical element
Maximum time step (DT) / ms:	Program controlled
Time step safety factor (DTFAC):	0.9
Minimum time step (DTMIN) / ms:	Default (0.0)
End time (TTERM) / ms:	13.0
Increment result output (NLOUT):	30

As can be observed, the overall explicit analysis settings remain largely consistent with those used for the drop test. The primary difference lies in the simulation end time, which was set to 13 milliseconds in order to fully capture the two-phase load curve. This naturally leads to longer computation times. Furthermore, no initial conditions were applied to the load step, since the loading is explicitly defined as an acceleration input. The same output frequency of 30 result increments was found to provide sufficient resolution for post-processing. Finally, as this simulation employs the same mesh as the drop test, the resulting time step is identical and is governed by the same critical element.

5.3 Computation and Energy Checks

To ensure the reliability and physical validity of explicit dynamic analyses, it is essential to carry out thorough computation and energy checks. As stated in Altair's explicit computation checks guideline [80], even if the run does not fail, it needs to be verified that three fundamental conservation laws are respected. In other words, the simulation must conserve mass, momentum, and energy to be considered physically consistent. Performing these checks is therefore a crucial step in the validation of the model results, as they help detect modeling errors that could otherwise go unnoticed. A qualitative evaluation of the results plays an important role in identifying potential issues early in the analysis process [80].

Energy Balance Verification

Energy balance checks are one of the most reliable indicators of the correctness of an explicit simulation. According to Altair's guideline, the sum of all internal, kinetic, hourglass, contact, and other energy components must correspond to the variation of the external work [80]:

$$E_{int} + E_{kin} + E_{hrgls} + E_{cont} + ... = \Delta W_{ext} \tag{5.12}$$

Ideally, taking into account the external works, the total energy of the system should remain constant throughout the analysis or decrease slightly due to numerical dissipation. A slight increase may be observed at the end of computation, during the initial loading cycles or during spring-back events, but significant energy growth is indicative of instabilities or modelling errors [80]

Particular attention should be given to the hourglass energy, which represents the work done by the artificial forces introduced to resist hourglass modes in under-integrated elements. As a general guideline, the hourglass energy should remain below 10 % of the total energy, and preferably below 5 %, which is an indication of a numerically stable and physically meaningful solution. If this criterion is not satisfied, a mesh refinement or the adoption of physical hourglass control methods is recommended [80].

Likewise, contact energy, which is not strictly physical, should remain within reasonable limits. A combined contribution of hourglass and contact energies below approximately 15 % of the total energy is considered acceptable for most analyses [80]. In mathematical form:

$$\frac{E_{hrgls} + E_{cont}}{E_{total}} \leq 15\% \tag{5.13}$$

Finally, it is good practice to verify whether the computed energy values are consistent with the expected physical behaviour. This can be done by performing hand calculations for specific quantities, such as estimating the kinetic energy from the known mass and velocity of the moving structure, thereby providing an independent validation of the numerical results.

Time Step Evolution

The evolution of the explicit time step throughout the simulation is another important indicator of stability. As highlighted by Altair's guideline, transient reductions in the time step followed by

a quick recovery are not necessarily problematic. However, large oscillations from one cycle to another may indicate an excessively stiff interface or other numerical issues. Most importantly, a persistently low time step is a clear sign of instability and should be investigated. In such cases, it is advisable to identify the node or element controlling the time step and determine the reason for its reduction. A stable time step is generally considered a strong indicator of a well-posed and numerically robust simulation [80].

Visual Inspection of Deformed Parts

Beyond numerical metrics, a qualitative visual inspection of the simulation results is essential. The deformed shape of the structure, when viewed through post-processing animations, should be physically plausible and smooth. It is important to check that [80]:

- No nodes or elements are "flying of" the structure unexpectedly.
- The deformation pattern is smooth and consistent with the applied loads.
- Adjacent elements maintain a sufficiently small chord angle, avoiding excessive distortion.
- No element intersections or penetrations occur unless they are expected and properly modelled.

This visual assessment ensures that the simulation accurately reproduces a realistic structural response and that no numerical artefacts compromise the results.

Verification of Physical Quantities

Finally, the obtained field results, such as contact forces, von Mises stresses, nodal velocities, and accelerations, should be examined carefully. Unrealistic values,such as abnormally high von Mises stresses on the order of gigapascals for a polymeric component, may indicate modelling errors or unit inconsistencies. Ensuring unit consistency across the entire model is one of the first and most critical checks when confronted with implausible numerical results [80].

5.4 Result Analysis Methodology

After a thorough description of the finite element model of each type of numerical simulation realised for the mechanical resistance validation of the prototype enclosure according to the UN ECE R136 regulation for L-category vehicles, this and the following sections concern the exposition of results and its study. For information on the analysis, such as modelling and parameters, refer to Section 5.2.

As previously stated, a seven-simulation strategy was employed to study the behaviour and resistance of the enclosure model in a one-meter drop test to a rigid surface. Additionally, a four-simulation strategy was devised to simulate the second mechanical resistance test of the regulation, the mechanical shock test. Although this methodology ensures a comprehensive study of the enclosure in all possible critical impact orientations, it also results in a very extensive amount of information to review and analyse. A complete and detailed description of each simulation result

would be an excessively long process, and hard to read. To remedy this, the exposition and study of the results will be done in a simplified way while ensuring a complete overview of each notable detail of each simulation.

The following sections are organised as follows: first, a detailed analysis of a representative drop test simulation is presented, including a step-by-step verification of computational and energy checks to ensure the quality and validity of the results. This is followed by a detailed examination of the deformation behaviour of the model under load, concluding with the assessment of its stress state. All subsequent simulations, comprising six differently oriented drop test cases and three mechanical shock simulations, are first subjected to the same rigorous validation process, in which the results are checked for consistency through the evaluation of the time step evolution, energy balance, and energy component histories, as outlined in the previous subsection. These checks ensure that the solutions obtained are numerically stable and physically meaningful before proceeding to interpret the structural response.

Once validated, only the most relevant and noteworthy results for each simulation are discussed in detail, with a summary stress result table provided for clarity and comparison. It is essential to highlight that this simulation methodology is designed to identify the critical loading scenarios for the battery enclosure, that is, the conditions under which the enclosure is most mechanically solicited, so that the design can subsequently be optimised to improve its structural resistance and impact performance, ultimately ensuring enhanced protection for the internal battery components.

The deformation and stress results are analysed in terms of global displacements, von Mises stress for solid regions, principal stress P_1, maximum shear stress, and composite failure strain for the laminated surfaces. Additionally, the contact conditions (open/closed areas) are examined to understand the contact behaviour during impact. Where relevant, the overall structural response is qualitatively compared with the expected real-world behaviour of a battery enclosure assembly under equivalent testing conditions, providing further confidence in the fidelity of the simulation results. Unfortunately, composite failure criteria are not available in HyperMesh Explicit®, which limits the assessment to strain- and stress-based indicators rather than full progressive failure analysis.

Since all simulations share an identical modelling setup, including geometry, mesh, material definitions, boundary conditions, and loading profile, the only variable between cases is the orientation of the enclosure relative to the applied load. As a result, no additional influencing factors are introduced between simulations, ensuring that the observed differences in structural response are exclusively attributable to orientation effects. This consistency enables a direct and meaningful comparison of results across all simulated orientations, allowing for an objective identification of the most critical loading scenarios.

5.5 Drop Test Analysis Results

5.5.1 Drop Orientation nº1

The mechanical drop test simulation of the enclosure in the first orientation had a run time of 14 minutes and 26 seconds. The run procedure was smooth and without time step fluctuations, the critical time step remained the same throughout the simulation run time and equal to 1.491×10^{-4} ms. As will be seen, all drop test simulations resulted in elapsed computation times around 15 minutes, a typical duration for medium-scale simplified drop test simulations such as this one. Additionally, the same time step behaviour was verified for all simulations, this validates the choice of excluding mass scaling features from these simulations.

5.5.1.1 Computational Checks

The explicit analysis energy evolution graph is provided in Figure 5.28. It is important to note that the energy scale is in N mm and that the time scale is in milliseconds.

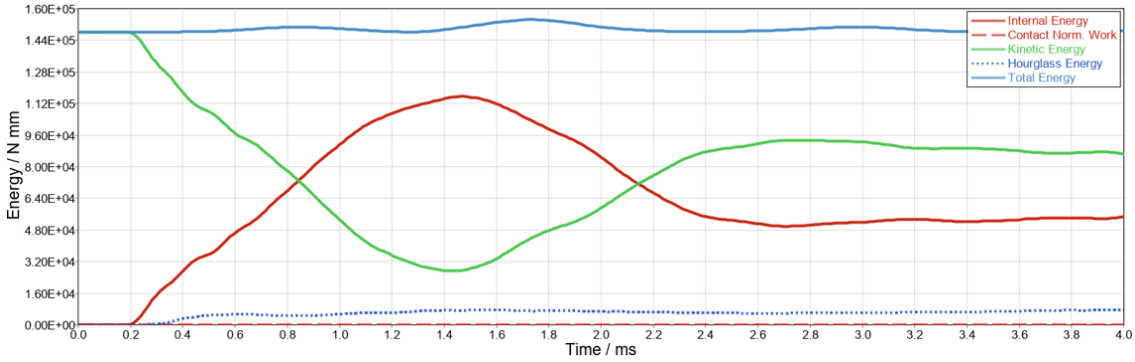

Figure 5.28: Drop nº1 explicit simulation energy plot

From the overall shape of the energy curves and a posterior data analysis of the `.out` file of the simulation, it is possible to confirm that the expected evolution of a drop test can be verified. First and most fundamentally, the principle of energy conservation is verified, the total energy of the system maintains a approximately constant value of 1.482×10^5 N mm, which equates to 148.2 J. This is true as no external work is applied to the system; only the initial motion of the system is defined, and contact boundaries, which do not result in energy transfer to the complete system. The data analysis of energy values for each time step revealed a negligible variation of 0.44 % of the total energy. Furthermore, this value, which is equal to the initial kinematic energy of the system, is also verified by simple hand calculations. Consider the initial condition of velocity $v_0 = 4.43$ m/s and a combined enclosure and battery mass of $14 + 1.1 = 15.1$ kg:

$$T = \frac{1}{2}mv^2 = \frac{1}{2} \times 15.1 \times 4.43^2 = 148.2 \text{ J} \tag{5.14}$$

As can be observed, at the initial instant $t = 0$ ms, all energy quantities start at their minimum values except for the kinetic energy, which is at its maximum. This behaviour is physically consistent, as the enclosure–battery assembly is still in free motion toward the rigid wall, and no contact has yet occurred. Shortly after, at approximately $t = 0.2$ ms, impact takes place, initiating the conversion of kinetic energy into strain energy, referred to as internal energy in the post-processing software. At $t = 1.5$ ms, the system reaches maximum contact and deformation, resulting in a minimum of kinetic energy and a peak in internal energy. From this point onward, the assembly begins to rebound from the rigid wall, causing kinetic energy to rise again while internal energy decreases correspondingly. The contact phase between the enclosure and the wall ends at approximately $t = 2.9$ ms, as indicated by the stabilisation of both kinetic and internal energy curves.

The maximum internal energy achieved is 115.6 J, corresponding to approximately 78% of the total initial kinetic energy. This significant energy absorption highlights the effectiveness of the prototype design, where the integrated honeycomb structures play a crucial role in dissipating impact energy and protecting the internal battery components. It is important to note, however, that the numerical model exhibits a greater fraction of energy recovery (rebound) compared to real-world behaviour, which is expected to involve more plastic deformation and permanent energy dissipation, particularly in the honeycomb structures. Despite this, the obtained maximum internal energy value remains a meaningful metric for comparing the energy absorption performance of the honeycomb structures under different drop orientations in subsequent simulations.

Regarding the energy computational checks referenced in Section 5.3, the evolution and proportion of hourglass energy throughout the simulation remained well within the recommended threshold, with a maximum value of only 5.13% of the total energy, comfortably below the 10% guideline for stable solutions. Furthermore, the combined contribution of contact and hourglass energy, defined in Equation 5.13, also stayed well under the 15% limit, again peaking at 5.13%. This indicates that contact energy was very low and only present during the brief instants of contact between the enclosure and the rigid wall, which is expected for this type of simulation.

As will be discussed in the following section, the deformation behaviour of the system closely matched the expected physical response, and all resulting physical quantities were consistent and physically reasonable. Taken together, these verifications confirm that the simulation results meet the quality criteria recommended by Altair's explicit computation check guidelines, supporting their reliability for subsequent analysis and design evaluation.

5.5.1.2 Deformation

The enclosure overall behaviour throughout the simulation can be seen in Figure 5.29. The rigid wall surface is perpendicular to the view presented below and is visible as an orange line. In terms of contacts, the drop simulations all present a three-stage behaviour: approximation to the surface, contact with deformation and rebound.

The deformation of the composite enclosure throughout the explicit analysis is illustrated in Figure 5.30, where section views of the internal cavity of the enclosure are presented. The expected displacement behaviour of the model was obtained, confirming the validity of the simulation setup.

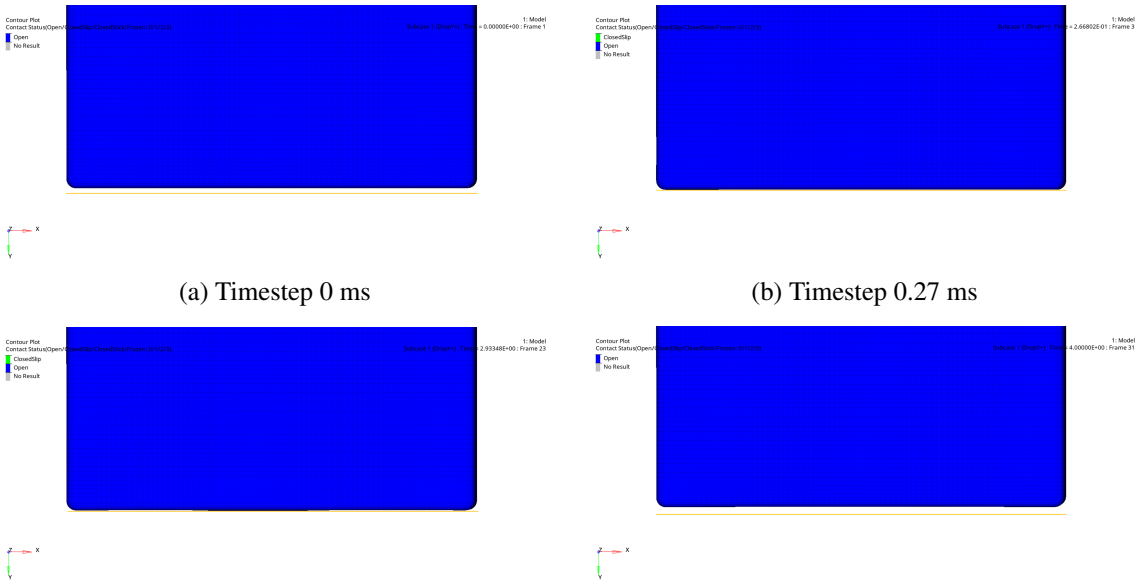

(a) Timestep 0 ms

(b) Timestep 0.27 ms

(c) Timestep 2.9 ms

(d) Timestep 4 ms

Figure 5.29: Drop n°1 contact progression

It is important to note that the entire enclosure moves approximately 3 mm as a rigid body before contacting the rigid surface. Consequently, all reported displacements must be interpreted relatively, discounting this initial rigid-body motion. Furthermore, all deformed configurations shown are represented at true scale, without exaggeration or inverse deformation.

At the beginning of the simulation, shown in Figure 5.30a, the system is still in free fall, moving as a unified rigid body without internal deformation, until the first contact occurs at approximately 0.2 ms. Figure 5.30b depicts the structure during the initial contact phase, while deformation is still developing and the internal energy has not yet reached its peak value. A global downward displacement of both the inner laminate surface and the honeycomb core can be observed, mainly driven by the momentum of the battery model, which is still being decelerated.

The maximum deformation of the enclosure is shown in Figure 5.30c, corresponding to the instant of peak internal energy absorption from the 14 kg battery. At this stage, a generalised deformation of approximately 2.5 mm is observed, with localised peak displacements reaching 3.4 mm. These peaks are largely attributed to localised load transfer through the RBE2 connectors between the components, and a representative global deformation value of about 3 mm can be considered more accurate for the overall behaviour.

Figures 5.30d and 5.30e represent the unloading phase, during which the enclosure restitutes internal energy back into kinetic energy. In Figure 5.30d, the enclosure is still in contact with the rigid surface, whereas in Figure 5.30e, the final instant of the simulation, the enclosure has already detached from the surface and has gained upward velocity. The deformation magnitudes in these latter stages are lower than those observed at the peak deformation, consistent with the recovery of elastic energy. It should be emphasised, however, that these late instances do not fully replicate real-life behaviour. Given that the model assumes purely elastic material properties, it exhibits

greater energy restitution and rebound compared to what would be observed in reality, where plastic deformation and damage would dissipate more energy and thus provide a more effective cushioning effect for the internal battery components.

Finally, Figure 5.30e also reveals two secondary peaks in the displacement history, which correspond to a natural vibration response of the enclosure structure, a shockwave triggered by the initial impact event. Overall, the deformations are confined to the components at the bottom of the enclosure, as expected for a bottom impact scenario, confirming that the structural response is physically consistent.

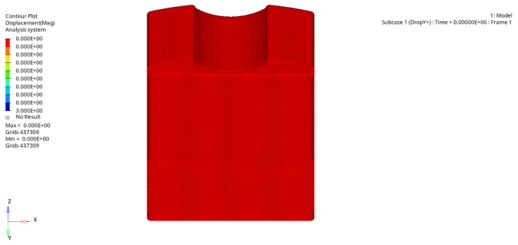

(a) Timestep 0 ms

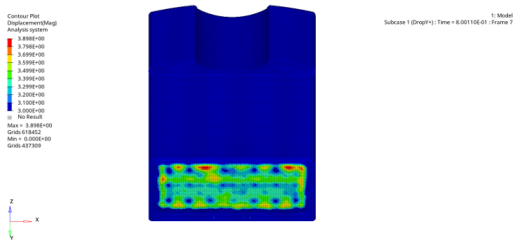

(b) Timestep 0.8 ms

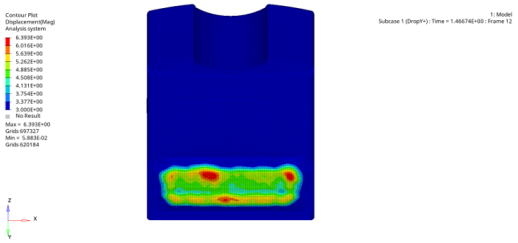

(c) Timestep 1.5 ms

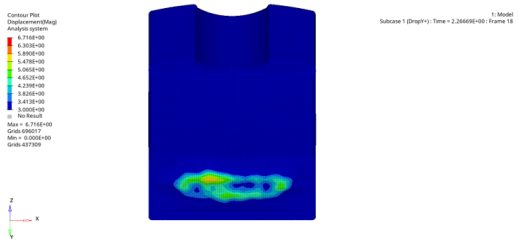

(d) Timestep 2.3 ms

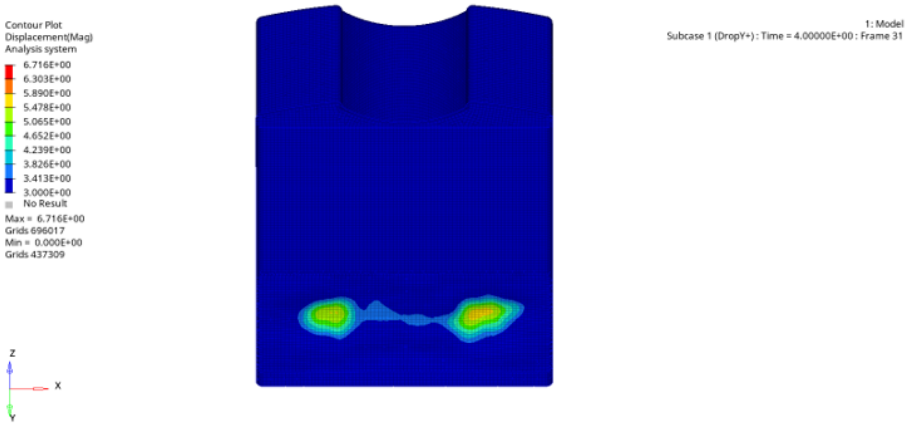

(e) Timestep 4 ms

Figure 5.30: Internal displacement progression

Figure 5.31 presents the maximum displacement and state of deformation of both the internal components of the enclosure model and of the isolated honeycomb structure.

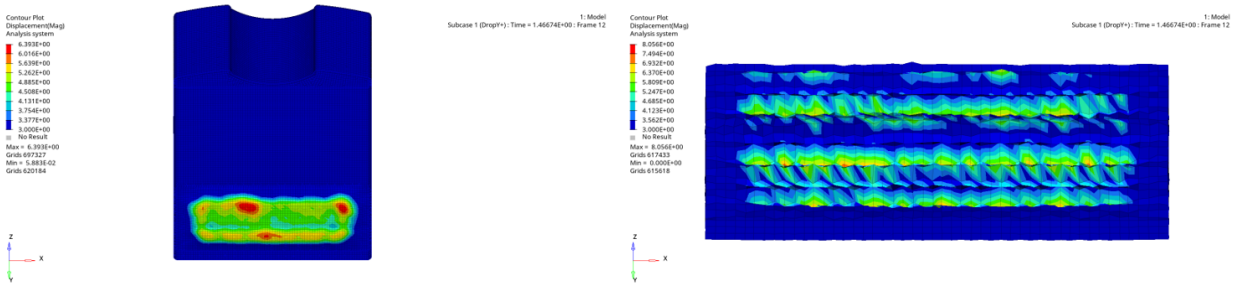

(a) Composite surface (b) Inferior honeycomb structure

Figure 5.31: Peak internal displacement by components

It is interesting to observe the deformation of the honeycomb structure due to the inertial effect of the battery model in movement. This deformation in generalised across the whole length and width of the core, as expected. However, due to the localised effect of the connectors realised as small rigid elements that link the internal laminate surface to the honeycomb structure, the visible deformation behaviour is concentrated at the positions of these rigid elements. This results in a high deformation in parallel lines close together, as opposed to a more planar deformation. This can be seen as a small limitation of this enclosure model, however, it still gives insightful information, from which the real behaviour can be extrapolated. An overall 3 mm crush of the honeycomb structure is expected, given the green colour dominated the visual representation of displacement in Figure 5.31b.

5.5.1.3 Stress

Figure 5.32 provides the peak stress states in both the external and internal laminate composite surfaces of the enclosure model, in terms of principal stress values (P_1 major stress in HyperView®).

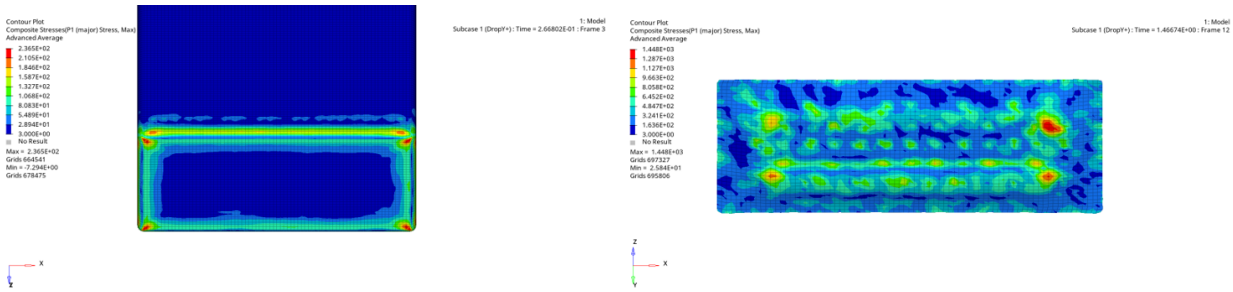

(a) External surface (b) Internal surface

Figure 5.32: Peak stress state in composite components

The stress quantity selected as most representative of the overall stress state in the laminate composite is the principal stress, specifically the first principal stress. This choice is justified as the principal stresses provide a direct indication of the maximum normal stress experienced by the

composite material, which is of primary interest when assessing the likelihood of fibre-dominated failure modes. Principal stress evaluation also facilitates a clearer interpretation of the stress field, as it is independent of the orientation of the global coordinate system and directly aligned with the material directions where the maximum tensile or compressive effects occur.

For completeness, additional stress measures are also reported, including maximum shear stress. The maximum values of these quantities, along with the principal stresses, are summarised in the tables immediately following this section, enabling a comprehensive understanding of the stress state across the entire model.

Figure 5.32a represents the maximum stress state in the external surface of the composite enclosure, and is due to the contact pressure between it and the rigid wall surface. The maximum stress evidences no expected failure of the external laminate due to the contact, specially fibre-dominated failure modes. As will be seen in Table 5.7, maximum shear stress values surpass the allowable in very concentrated zones of the exterior laminate, indicating that this external laminate impact may result in shear-driven matrix cracks and gradual stiffness degradation in individual plies but no catastrophic failure of the entire laminate.

As for the internal laminate surface, directly in contact with the battery, and the first line of protection of the battery, this vertical drop constitutes the critical loading conditions. Very high values of principal stress appear throughout the internal surface geometry, with generalised values around 900 MPa, above the allowable tensile and compressive stress. Concentrated values of principal stress reach values close to 1500 MPa, although those are mainly due to stress concentrations from the connectors and peaks of stress due to shockwaves. Additionally, maximum shear stress values also reach very high values, way above the allowable threshold. This stress state in the internal laminate indicates failure of the entire laminate in the case of a vertical drop of the battery and enclosure assembly. This is an expected behaviour, taking into account the dimensions and weight of the battery components.

Figure 5.33 shows the stress and strain state of the protective honeycomb structure, through the visualisation of Von Mises stress and strain.

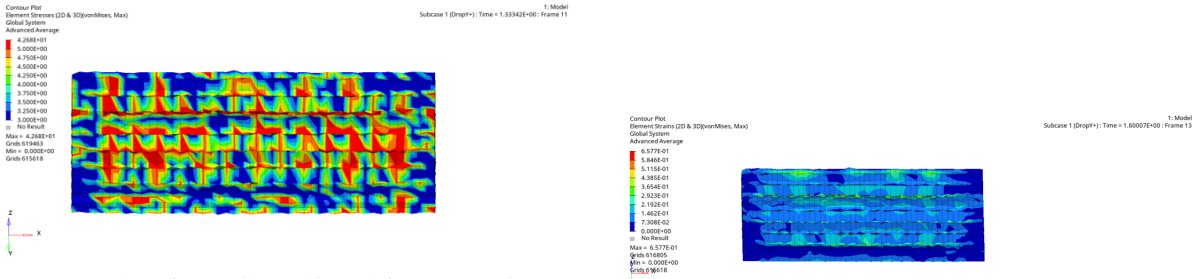

(a) External surface (Filtered in red for $\sigma_{VM} > 5$ MPa)

(b) Internal surface

Figure 5.33: Peak stress and strain state in honeycomb structure

The high stress and strain state observed in the honeycomb structure is indicative of the overall compressive crushing behaviour that is expected to occur under such loading conditions. Very high

levels of both stress and strain are observed throughout the geometry of the core, most notably in Figure 5.33a, where regions exceeding 5 MPa, higher than the nominal compressive strength of the honeycomb material (4.5 MPa), are represented in red. The prevalence of red zones visually dominates the stress plot, strongly suggesting that this drop test scenario would lead to significant and permanent plastic deformation of the core structure.

This crushing of the honeycomb is not detrimental to the design but, rather, a desirable outcome. The progressive collapse of the core dissipates a large fraction of the kinetic energy from the impact, effectively absorbing and dampening the shock transmitted to the surrounding laminate facesheets and, ultimately, to the internal battery pack. In doing so, the honeycomb acts as a sacrificial energy-absorbing layer, ensuring that the internal components remain within safe stress and displacement limits and are protected against potentially damaging impact loads. This observation is consistent with the internal energy results, which show that approximately 78 % of the initial kinetic energy is converted into strain energy, largely through core crushing.

Complementary maximum stress values are given in the following Table 5.7, separated by components. Only values considered physically meaningful are presented, with unrealistic peaks caused by localised numerical concentrations deliberately excluded, in order to provide a fair and representative assessment of the structural response.

Table 5.7: Maximum meaningful values of stress and strain state, by component (Orientation nº1)

Physical quantity	**Approx. Meaningful Value**	**Note**
External Laminate		
P_1 (major) principal stress (σ_{P1}) / MPa	≈ 240	
P_3 (minor) principal stress (σ_{P3}) /MPa	≈ 210	-
Maximum shear stress (τ_{max}) / MPa	≈ 140	
Internal Laminate		
P_1 (major) principal stress (σ_{P1}) / MPa	> 900	
P_3 (minor) principal stress (σ_{P3}) /MPa	> 700	Critical loading condition
Maximum shear stress (τ_{max}) / MPa	> 600	
Honeycomb structure		
Von Mises stress (σ_{VM}) / MPa	≈ 30	Critical loading condition
Von Mises strain (ε_{VM}) / %	≈ 66	

Overall, the deformation and strain behaviour of the model was realistic and aligned with the expected physical response of the enclosure under such loading conditions, and all resulting values were consistent and physically meaningful.

5.5.2 Drop Orientation nº2

The second drop test simulated resulted in a run time of 15 minutes and 34 seconds. The run procedure was smooth with no timestep fluctuations. Critical time step: 1.491×10^{-4} ms.

5.5.2.1 Computational Checks

The explicit analysis energy evolution graph is provided in Figure 5.34.

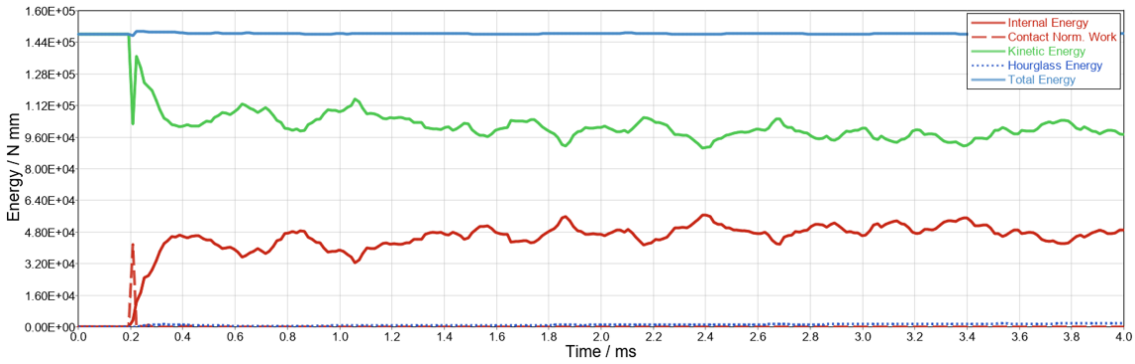

Figure 5.34: Drop nº2 explicit simulation energy graph

Although the principle of conservation of energy is overall verified in this simulation, the energy history highlights a limitation of the defined model in accurately replicating a side impact event. The total energy remains nearly constant throughout the entire simulation, with a maximum fluctuation of only 0.09 %, and its magnitude matches the initial kinetic energy value computed analytically, confirming the validity of the global energy balance. Contact is initiated at approximately 0.2 ms and ends very shortly after, around 0.7 ms, resulting in an almost instantaneous impact event. An expected trade-off between kinetic and internal energy is observed, with both curves mirroring each other. However, at the onset of contact ($\approx$ 0.2 ms), a sharp spike of contact energy is registered, indicating that a portion of the kinetic energy is dissipated as contact energy rather than being converted into internal strain energy. This is not representative of realistic impact behaviour and leads to a local violation of Equation 5.13, which otherwise remains satisfied throughout the remainder of the simulation.

Furthermore, the resulting internal strain energy fraction is significantly lower when compared with the first drop test presented, suggesting that very little deformation energy is absorbed by the enclosure and its internal components. This behaviour can be attributed to the modelling approach adopted for linking the battery mass and inertia to the enclosure using an RBE3 distributing element. In this configuration, the nodes of the enclosure surface in contact with the rigid plane are also connected to rigid elements, preventing localised deformation and causing the kinetic energy to propagate through the model as a high-frequency displacement and stress wave. While free-vibration phenomena do occur in reality, they do not represent the dominant structural behaviour expected in a side drop event. This modelling limitation makes it impossible to draw meaningful conclusions about the state of the battery in this drop case. Even the structural performance of the external surface of the enclosure itself cannot be confidently assessed under this simulation setup.

Finally, the hourglass energy remained well within the acceptable 10 % threshold, with a maximum contribution of 1.18 %, confirming the numerical stability of the mesh. Nevertheless, due to the modelling limitations previously discussed, this simulation cannot be used to reliably assess the structural integrity of the battery itself under a side drop impact. However, it still provides valuable information regarding the overall behaviour of the enclosure, such as the distribution of contact stresses, the internal laminate stress state, and the loading experienced by the honeycomb

core. These results can be used to qualitatively evaluate whether the enclosure and its internal components remain within acceptable stress levels, even if a full verification of battery integrity is not possible.

To accurately replicate side impacts, the model would need to be updated with a more realistic representation of the battery, ideally as a solid with appropriate internal components, material properties, and a more realistic contact definition between the battery and the enclosure surface. Due to the lack of detailed information from Famel regarding the battery and the very strict time limitations of this study, such an update was not feasible, and therefore, only the performance of the enclosure is evaluated in this scenario.

5.5.2.2 Deformation and Stress

The referred shockwave propagation is presented in Figure 5.35 in terms of nodal displacement at each time step. Displacement is given in millimetres.

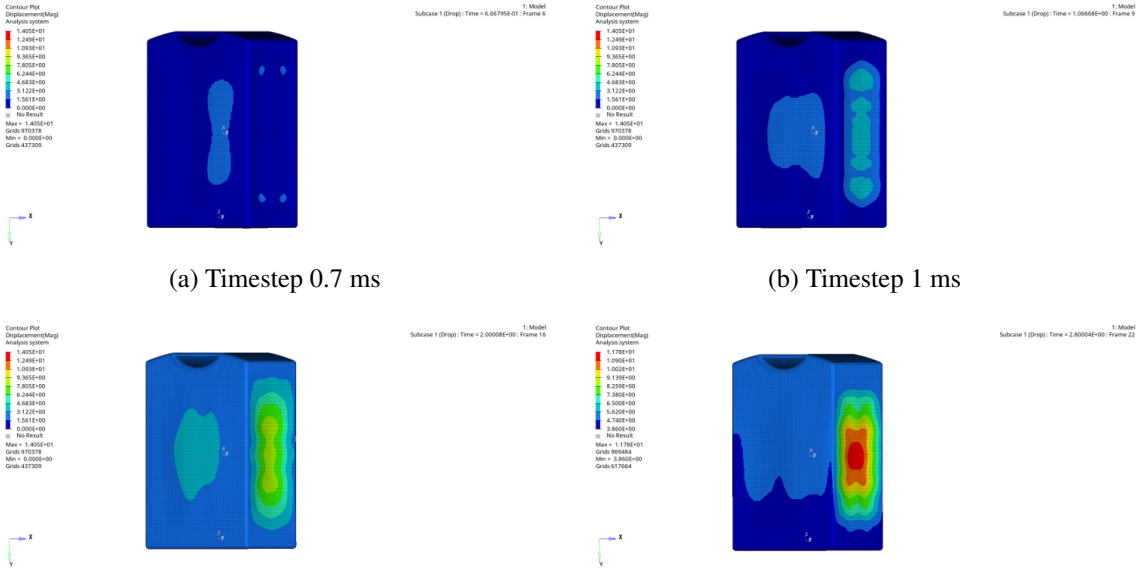

(a) Timestep 0.7 ms

(b) Timestep 1 ms

(c) Timestep 2 ms

(d) Timestep 2.8 ms

Figure 5.35: Drop nº2 shock wave progression

Deformation and stress states in the model are not critical in all enclosure model components, and so, will only be swiftly presented. Stress values originated by the contact pressure on the external composite surface remain within the elastic range, overall. The internal laminates and honeycomb structures remain largely intact during and after the impact. Only small zones of higher stress values are present on the side of the enclosure that is impacted. In this drop test orientation, the honeycomb structures do not directly contribute to the protection of the battery pack.

Table 5.8 presents overall stress values, by component.

Table 5.8: Maximum meaningful values of stress and strain state, by component (Orientation nº2)

Physical quantity	Approx. Meaningful Value	Note
External Laminate		
P_1 (major) principal stress (σ_{P1}) / MPa	≈ 400	
P_3 (minor) principal stress (σ_{P3}) /MPa	≈ 320	-
Maximum shear stress (τ_{max}) / MPa	≈ 250	
Internal Laminate		
P_1 (major) principal stress (σ_{P1}) / MPa	≈ 250	
P_3 (minor) principal stress (σ_{P3}) /MPa	≈ 180	-
Maximum shear stress (τ_{max}) / MPa	≈ 100	
Honeycomb structure		
Von Mises stress (σ_{VM}) / MPa	≈ 5	-
Von Mises strain (ε_{VM}) / %	≈ 2	

5.5.3 Drop Orientation nº3

The third drop test simulated resulted in a run time of 14 minutes and 52 seconds. The run procedure was smooth with no timestep fluctuations. Critical time step: 1.491×10^{-4} ms.

5.5.3.1 Computational Checks

The explicit analysis energy evolution graph is provided in Figure 5.36.

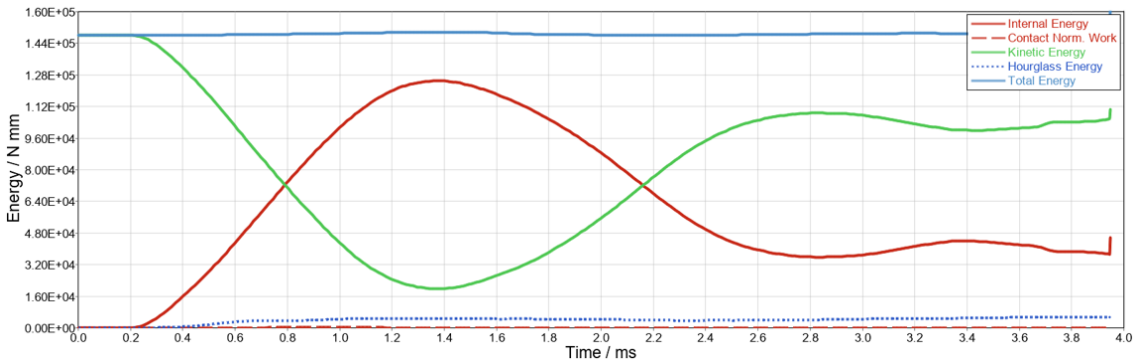

Figure 5.36: Drop nº3 explicit simulation energy graph

This drop test simulation is very similar to the first presented, both in terms of energy plot data and physical behaviour and results. For a detailed overview, refer to Subsection 5.5.1. The energy evolution plot shows the same overall behaviour as drop test orientation nº1, with total energy remaining essentially constant (maximum variation of 0.2 %) and consistent with the initial kinetic energy. Contact occurs between 0.2 ms and 2.5 ms, with a peak of strain energy around 1.4 ms. The maximum internal energy is slightly higher than in the first drop test, reaching 125 J (approximately 83 % of the initial kinetic energy), which underlines the effectiveness of the larger top honeycomb structure. The computational validity criteria are met throughout the analysis, with a peak hourglass and Equation 5.13 value of 3.76 %. A small energy jump occurs only at the final

timestep, which, as discussed in Section 5.3, can happen at the end of an explicit analysis and does not compromise the validity of the results. Overall, the deformation behaviour closely matches expectations, and all resulting quantities are physically consistent.

5.5.3.2 Deformation and Stress

Figure 5.37 illustrates the maximum contact area between the top geometry of the enclosure and the rigid wall.

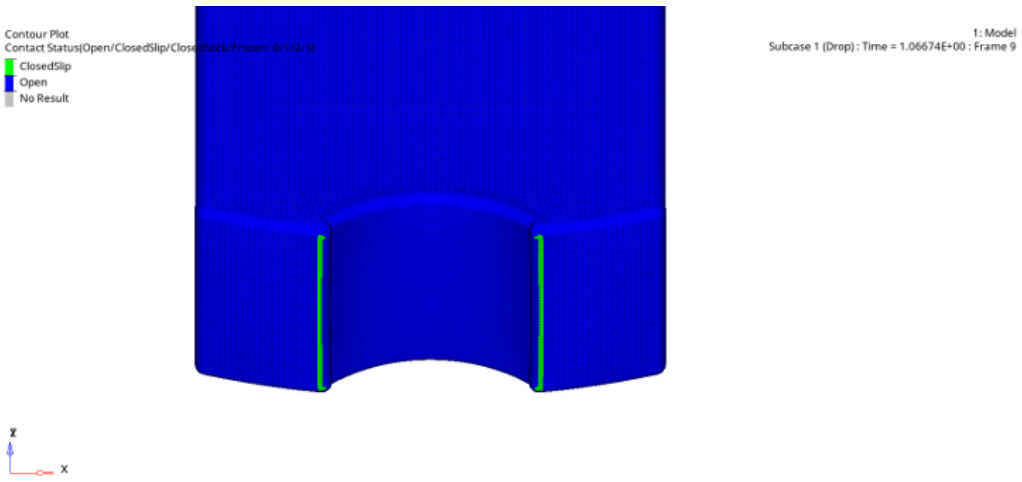

Figure 5.37: Drop nº3 contact zone

Due to the different shape of the enclosure top cover, a vertical drop along the y reference direction of the model results in two line contacts, opposed to one planar face-to-surface contact. This, of course, will result in higher, more concentrated contact stresses, as is shown in Figure 5.38.

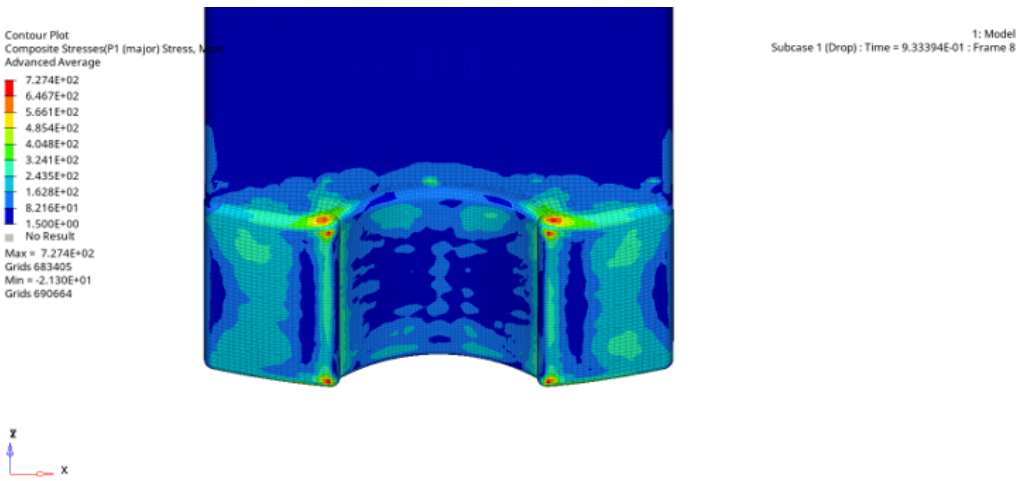

Figure 5.38: Drop nº3 external laminate stress state

The maximum principal stress distribution indicates that the vertices of the enclosure are the most susceptible regions to failure, making them critical areas in the overall design. This behaviour justifies the dedicated analysis of vertex impacts, which will be addressed in drop orientations nº5 and nº7. The maximum principal stress values remain within the same order of magnitude as the laminate allowable limits, suggesting that the design performs adequately under this loading condition. However, as shown later in Table 5.9, the maximum in-plane shear stress values exceed the corresponding allowable value. This result suggests the potential onset of local ply failure, either through fibre-dominated mechanisms or shear-driven matrix cracking.

Figures 5.39 and 5.40 illustrate the maximum deformation states of the honeycomb core and the internal components, providing further insight into the global and local deformation modes.

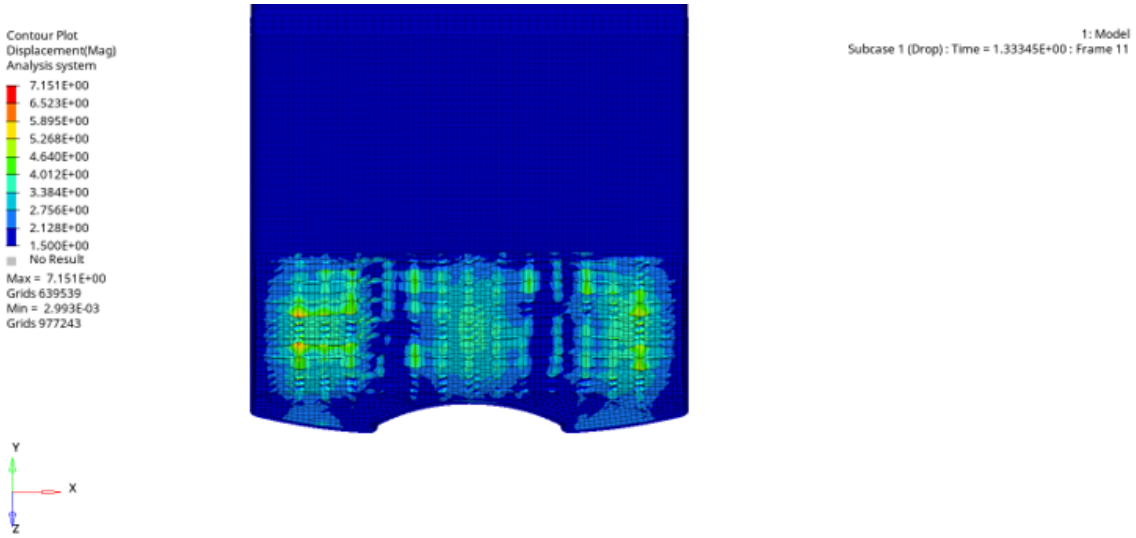

Figure 5.39: Drop nº3 honeycomb structure deformation

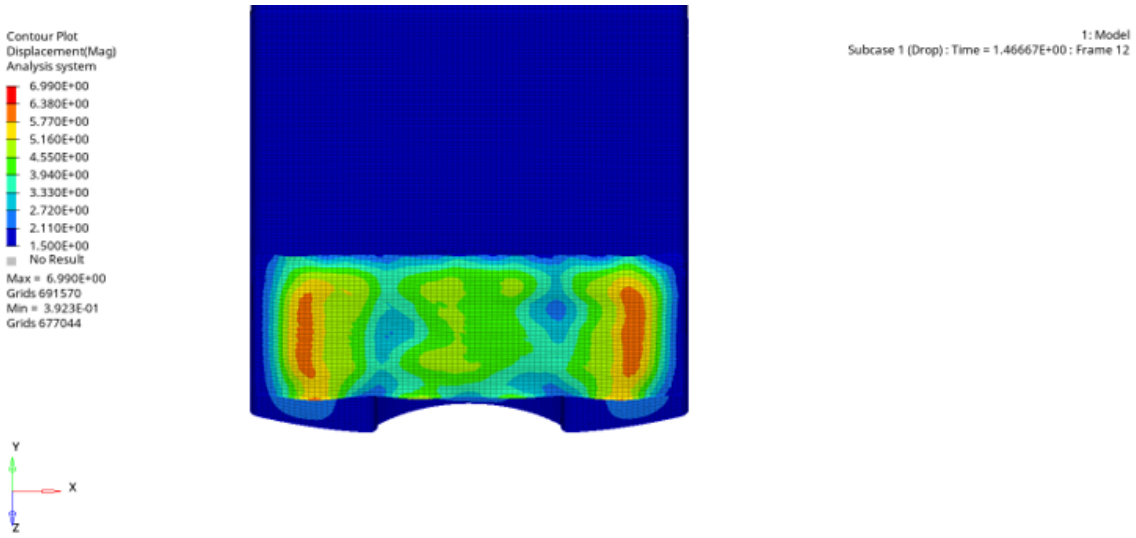

Figure 5.40: Drop nº3 internal laminate deformation

Once again, the expected behaviour is observed, closely matching the response obtained in the first drop test. The overall displacement values are slightly higher, which can be attributed to the larger size of the core structures, allowing for greater vertical deflection as the energy-absorbing components undergo crushing. The results of this drop test are consistent with the previous case regarding the mechanical integrity of both the honeycomb core and the internal laminates. The simulation indicates permanent plastic deformation of the honeycomb structures and partial, potentially even total, failure of the internal laminates, fulfilling their purpose of dissipating energy and protecting the battery components from excessive loads.

Table 5.9: Maximum meaningful values of stress and strain state, by component (Orientation nº3)

Physical quantity	Approx. Meaningful Value	Note
External Laminate		
P_1 (major) principal stress (σ_{P1}) / MPa	≈ 730	
P_3 (minor) principal stress (σ_{P3}) /MPa	≈ 600	-
Maximum shear stress (τ_{max}) / MPa	≈ 480	
Internal Laminate		
P_1 (major) principal stress (σ_{P1}) / MPa	≈ 1100	
P_3 (minor) principal stress (σ_{P3}) /MPa	≈ 570	Critical loading condition
Maximum shear stress (τ_{max}) / MPa	≈ 700	
Honeycomb structure		
Von Mises stress (σ_{VM}) / MPa	≈ 40	Critical loading condition
Von Mises strain (ε_{VM}) / %	≈ 76	

5.5.4 Drop Orientation nº4

The fourth drop test simulated resulted in a run time of 15 minutes and 16 seconds. The run procedure was smooth with no timestep fluctuations. Critical time step: 1.491×10^{-4} ms.

5.5.4.1 Computational Checks

The explicit analysis energy evolution graph is provided in Figure 5.41.

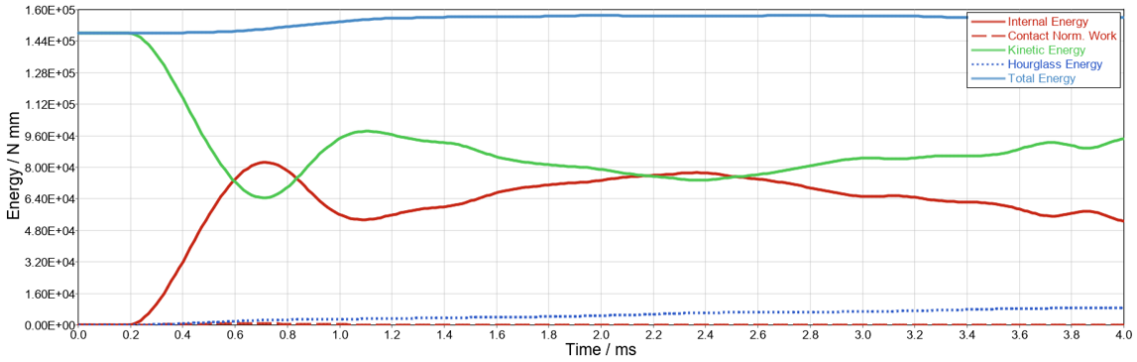

Figure 5.41: Drop nº4 explicit simulation energy graph

The overall energy plot is in line with what is expected for drop tests, as we have come to see. For a detailed overview of a drop test graph, refer to Subsection 5.5.1. Contact occurs, once again, at around 0.2 ms and ends at approximately 1.2 ms, with a peak of strain energy at ≈ 0.7 ms. The maximum internal energy is lower than in the previous drop tests, with a value of 82.6 J ($\approx 56\%$ of E_t), which is consistent with the fact that the contact now occurs at an edge. This reduces the ability of the energy-absorbing core to perform its intended function. The hourglass and contact energy fraction criteria are satisfied throughout the analysis, with peak values of 5.65%.

From 1.2 ms onward, it would be expected that the internal and kinetic energy curves stabilise. However, this is not observed in the energy plot. Instead, a mirrored increase in internal energy and decrease in kinetic energy is visible, caused by a large shockwave generated at the moment of impact and propagating through the enclosure. This free vibration persists until the end of the simulation at 4 ms and is clearly noticeable in the energy history. Subsequent strain and stress evaluations confirm that these oscillations do not compromise the mechanical integrity of the enclosure. The effect of this shockwave is likely amplified by the absence of Rayleigh damping in the material definition, which would otherwise help attenuate such high-frequency vibrations. Figure 5.42 illustrates the peak displacement associated with this shockwave, with displacement values presented relative to the rigid-body motion of the assembly prior to impact.

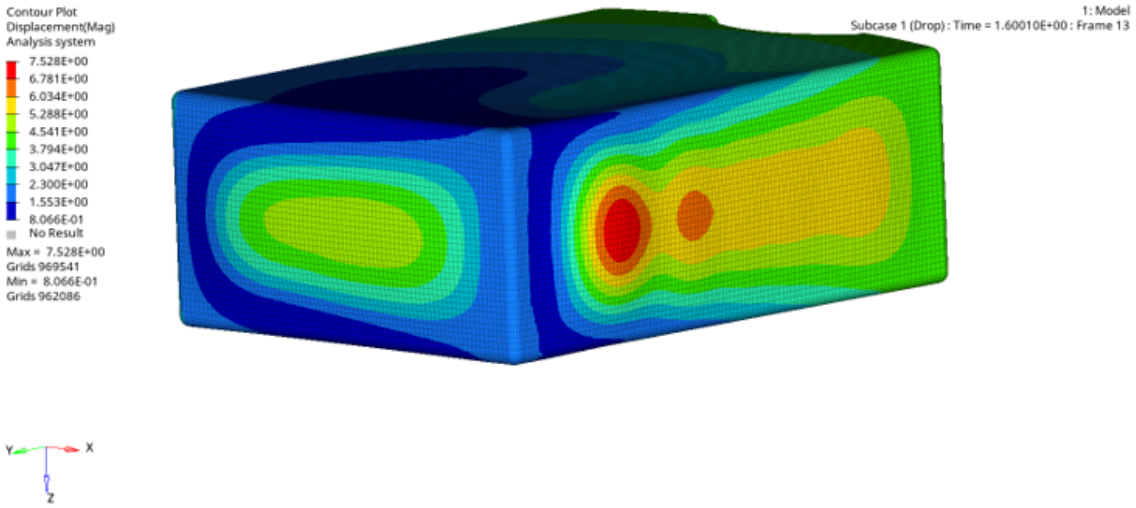

Figure 5.42: Drop nº4 shock wave

However, the variation of total energy between the first and last time step is around 5%. Its initial value matches the expected analytical kinetic energy. Since the timestep evolution showed no anomalies, mass scaling was not applied; contact settings behaved as expected (no contact energy spikes were observed), and the overall deformation behaviour of the enclosure system was physically reasonable. This energy growth is attributed to the high element strains and large deformations occurring during the analysis. Because this drop is concentrated on an edge rather than a face, the deformation becomes more localised and severe, leading to elevated element distortion and an artificial increase in total energy. As will be shown in the subsequent results, the model

behaviour is consistent, the deformation patterns make physical sense, and the results are therefore deemed acceptable for design evaluation

Figure 5.43 shows the plot of element strain in the contact area, at its peak deformation.

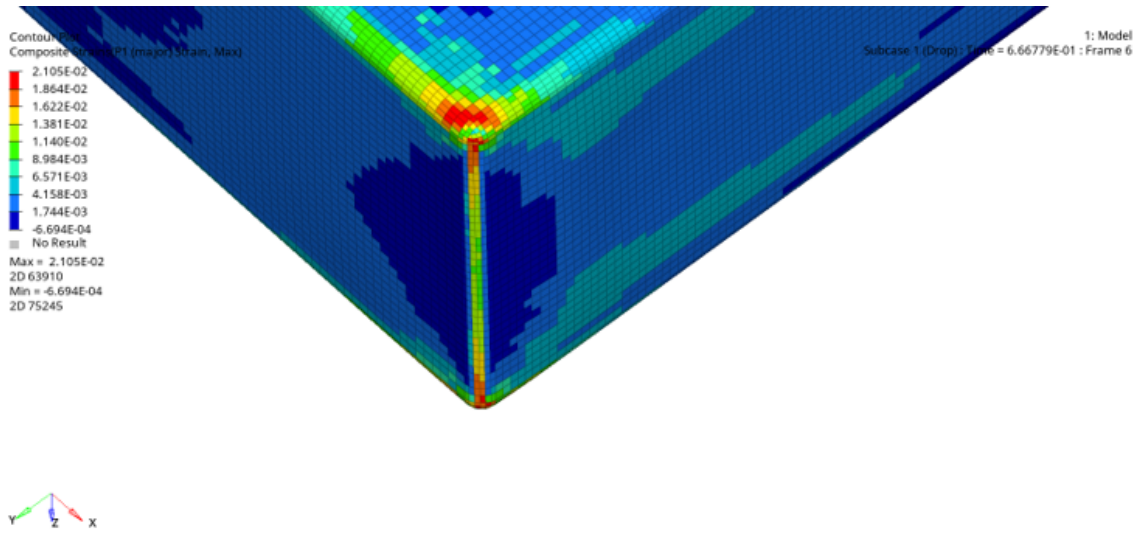

Figure 5.43: Drop n°4 element strain

5.5.4.2 Deformation and Stress

Figure 5.44 illustrates the maximum line contact area between the bottom edge of the enclosure and the rigid wall.

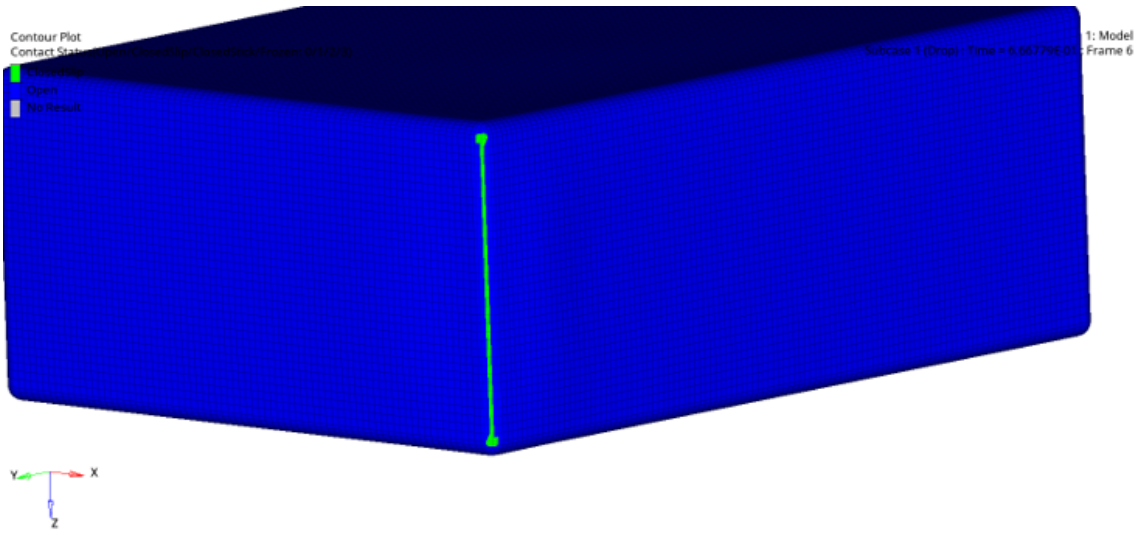

Figure 5.44: Drop n°4 contact zone

This contact, concentrated in a single line, results in a very high stress and strain state in the thin region of direct contact, but even more so in the vertices close to the contact. This very structurally demanding state suggests localised ply and even laminate failure. Figure 5.45 provides the peak local contact stress state in the external laminate.

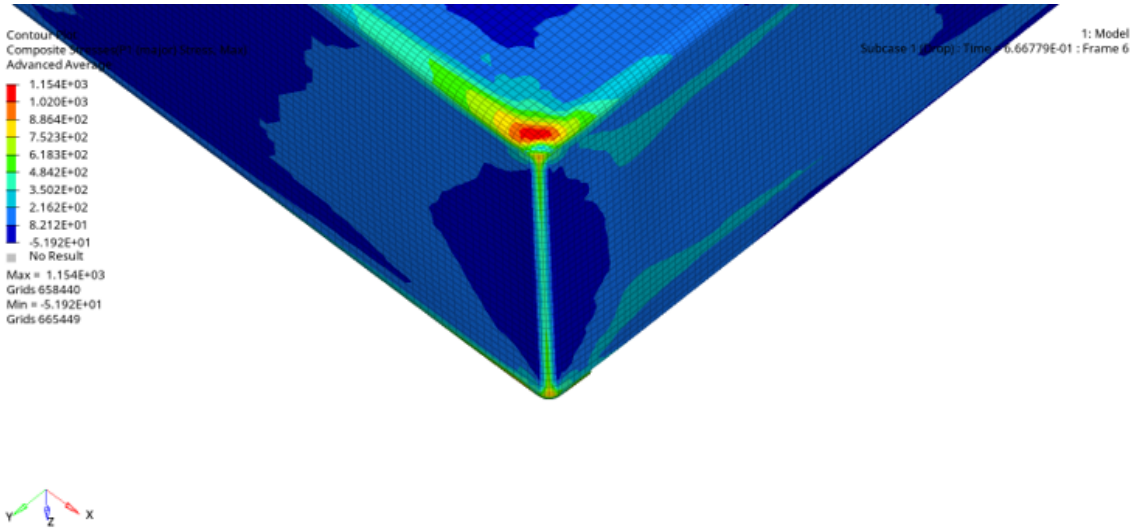

Figure 5.45: Drop n°4 external laminate stress

The following Figures 5.46, 5.47 and 5.48 provide the peak strain and stress state of the interior enclosure components after impact.

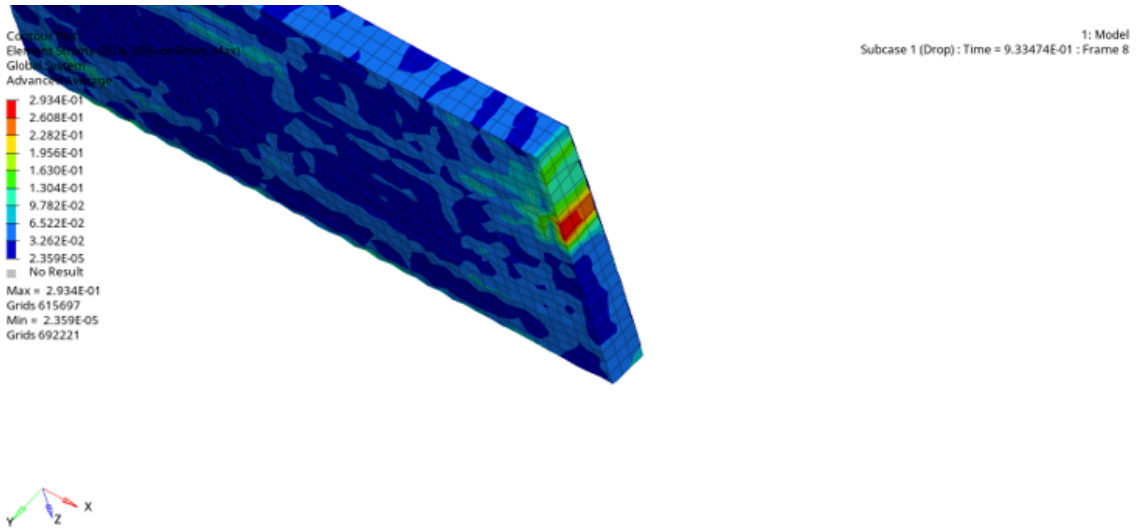

Figure 5.46: Drop n°4 honeycomb structure strain

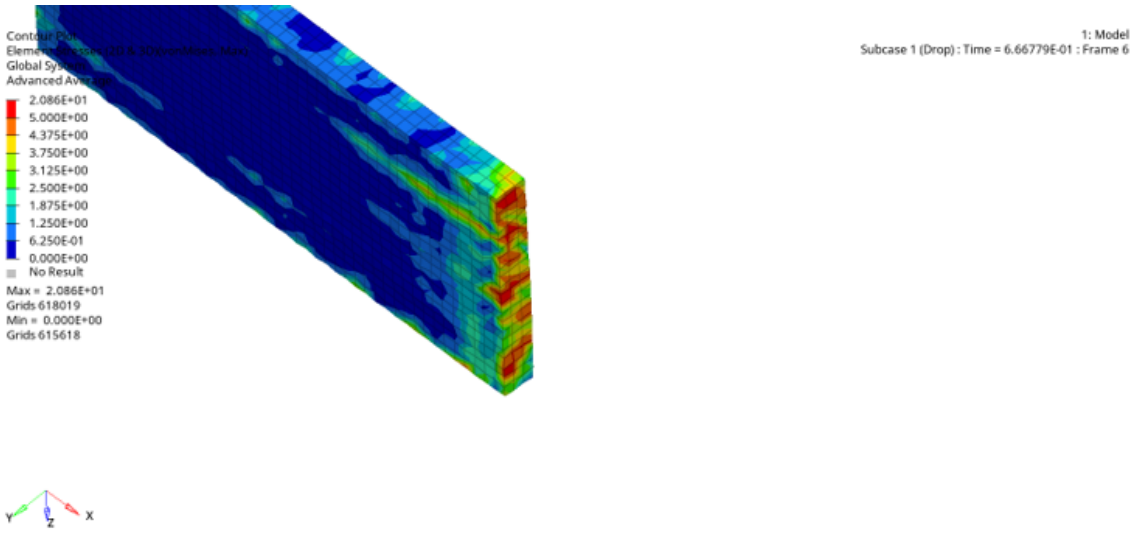

Figure 5.47: Drop nº4 honeycomb structure stress (Filtered in red for $\sigma_{VM} > 5$ MPa)

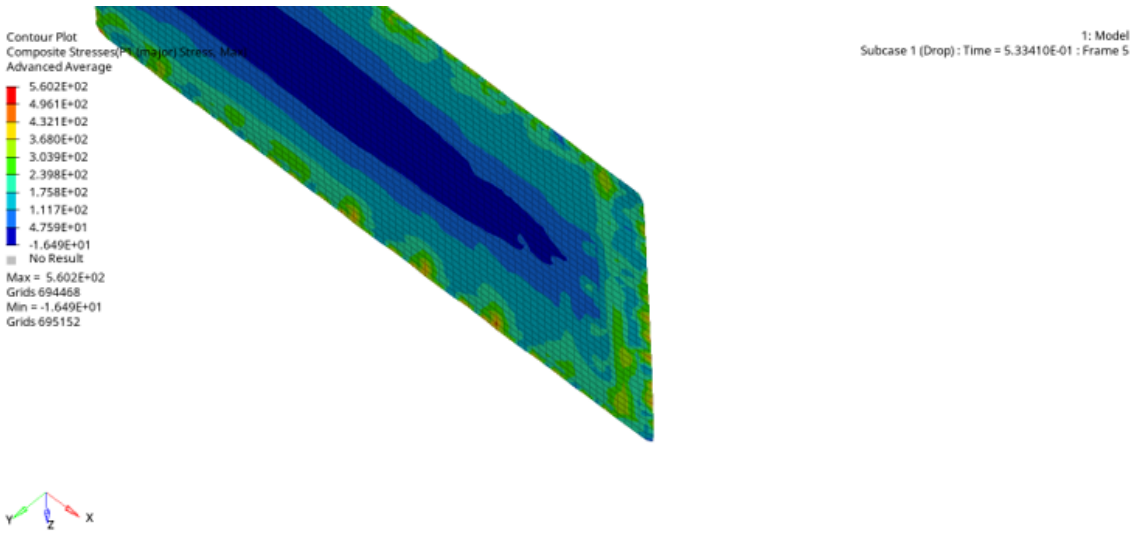

Figure 5.48: Drop nº4 internal laminate stress

The expected behaviour is clearly observed in this simulation. This drop test configuration is highly demanding on all components of the enclosure near the impact region. The internal laminate and honeycomb core perform their impact-absorbing function, albeit under a side-impact condition rather than a perfectly parallel collision with the ground. As a result, the overall level of protection offered to the battery components is quantitatively lower. Nevertheless, the results indicate that both the internal laminate and the honeycomb core undergo permanent deformation in the regions closest to the contact area, as evidenced by the peak internal energy values and the post-processing plots presented above.

Complementary maximum stress values are given in the following Table 5.10, separated by components.

Table 5.10: Maximum meaningful values of stress and strain state, by component (Orientation nº4)

Physical quantity	Approx. Meaningful Value	Note
External Laminate		
P_1 (major) principal stress (σ_{P1}) / MPa	≈ 1150	
P_3 (minor) principal stress (σ_{P3}) /MPa	≈ 700	Critical loading condition
Maximum shear stress (τ_{max}) / MPa	≈ 900	
Internal Laminate		
P_1 (major) principal stress (σ_{P1}) / MPa	≈ 850	
P_3 (minor) principal stress (σ_{P3}) /MPa	≈ 400	Critical loading condition
Maximum shear stress (τ_{max}) / MPa	≈ 550	
Honeycomb structure		
Von Mises stress (σ_{VM}) / MPa	≈ 20	-
Von Mises strain (ε_{VM}) / %	≈ 27	

5.5.5 Drop Orientation nº5

The fifth drop test simulated resulted in a run time of 15 minutes and 16 seconds. The run procedure was smooth with no timestep fluctuations. Critical time step: 1.491×10^{-4} ms.

5.5.5.1 Computational Checks

The explicit analysis energy evolution graph is provided in Figure 5.49.

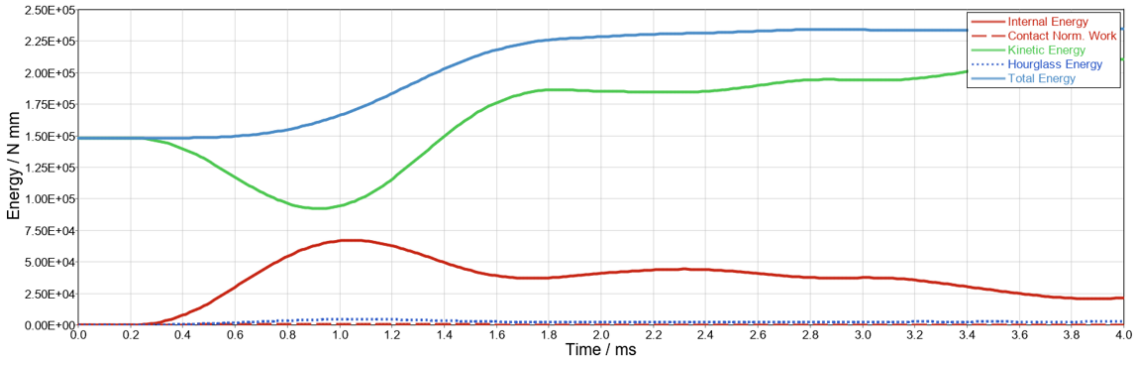

Figure 5.49: Drop nº5 explicit simulation energy graph

This highly demanding drop test orientation simulates a direct impact of the enclosure on one of its vertices. The same total energy increase observed in drop test nº4 is present here, but in a much more pronounced manner. The most plausible explanation for this increase lies in the very high element strains and large deformations experienced by the external surface of the enclosure and the internal components, such as the honeycomb structure. This leads to the formation of ill-deformed elements even in instances where no external loads are applied. This phenomenon is evidenced in Figure 5.52. In particular, Figures 5.50 and 5.51 highlight the extreme deformation experienced by the impacted vertex.

The time-step evolution was verified and showed no anomalies, mass scaling was not applied, and the contact settings behaved as expected, with no spikes in contact energy being observed. Furthermore, the overall deformation behaviour of the enclosure system remained physically reasonable. The results obtained, as will be presented in the following sections, are consistent and sensible when compared to the expected real-world response.

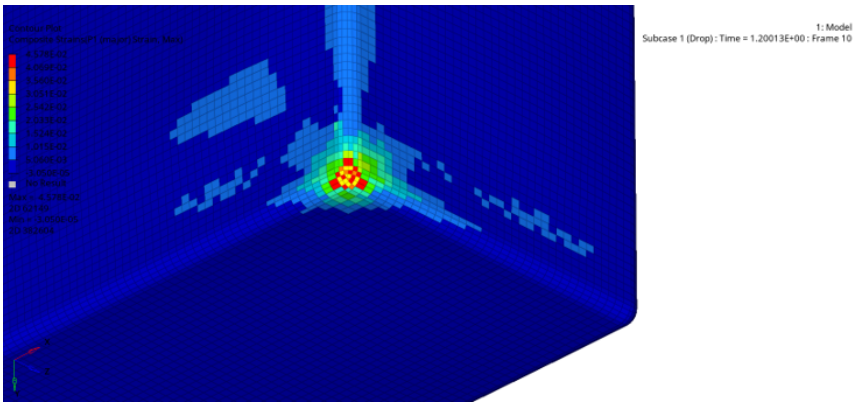

Figure 5.50: Drop nº5 high element strain

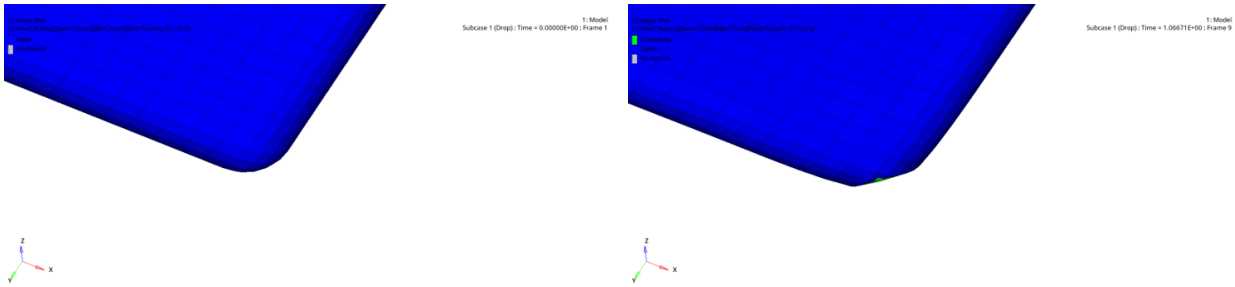

(a) Timestep 0 ms

(b) Timestep 1.1 ms

Figure 5.51: Drop nº5 enclosure vertex deformation

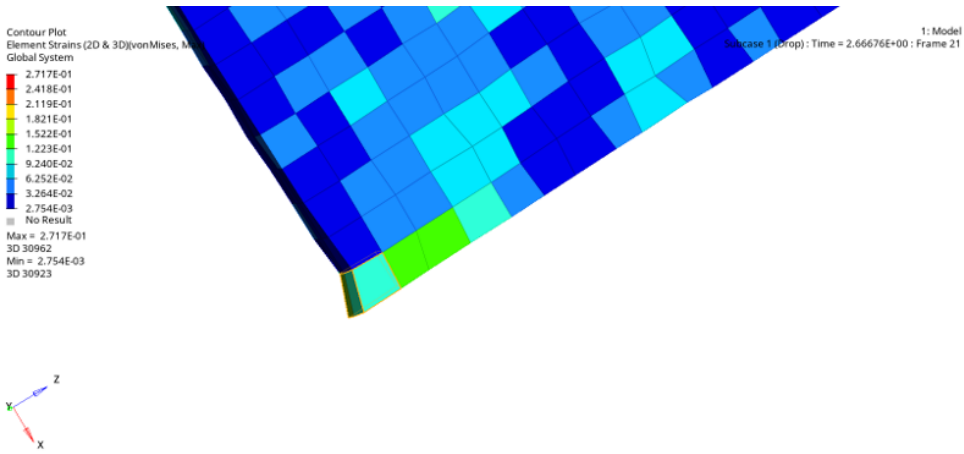

Figure 5.52: Drop nº5 ill-deformed elements at the edge of the honeycomb structure

Contact begins at approximately 0.2 ms and ends at around 1.9 ms, with the peak of internal energy reached at $\approx$ 1.0 ms. The maximum internal energy accounts for 67.1 Joules of energy absorbed, corresponding to roughly 45% of the initial kinetic energy. The hourglass and contact energy fraction criteria are satisfied throughout the simulation, with peak values of 2.72% and 3.17 %, respectively.

5.5.5.2 Deformation and Stress

Figure 5.53 shows the concentrated contact zone.

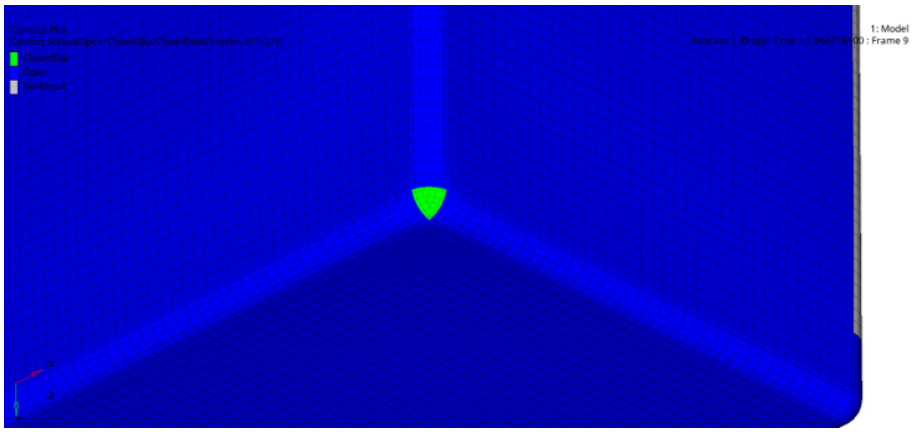

Figure 5.53: Drop nº5 contact zone

The following Figures 5.54 and 5.55 show the extreme strain and stress state of the external surface at the point of contact. Total laminate failure, at the very reduced zone of impact seems inevitable.

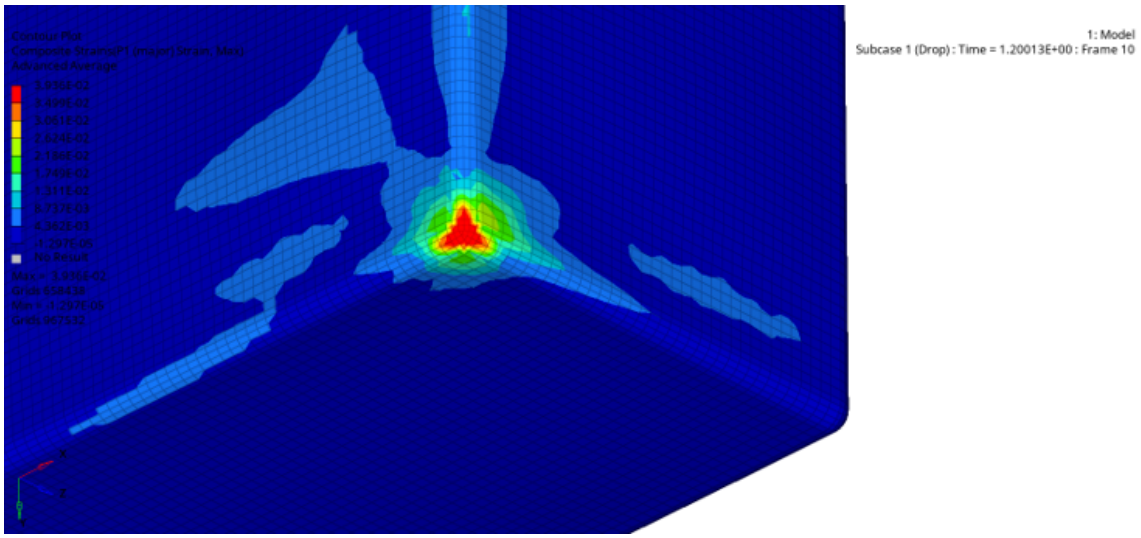

Figure 5.54: Drop nº5 external laminate strain

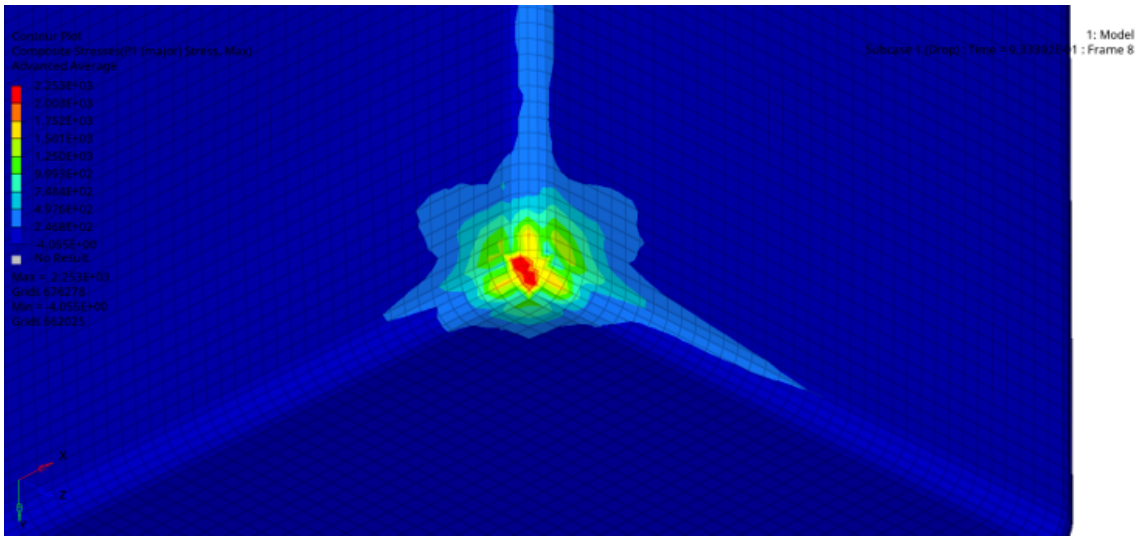

Figure 5.55: Drop nº5 external laminate stress

The internal laminate and honeycomb structure on the other hand do not exhibit such extreme values of strain and stress. Permanent deformation of the honeycomb core is expected in the very closest zone to the vertex of impact and the integrity of the internal laminate seems to be retained through the process, at least at the laminate level, ply failures may be present. This is visible in the following Figures 5.56, 5.57 and 5.58.

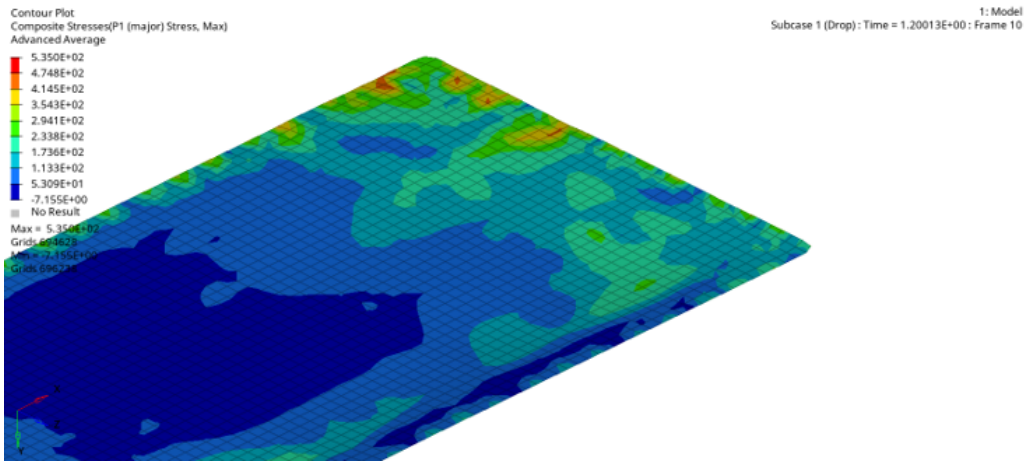

Figure 5.56: Drop nº5 internal surface stress

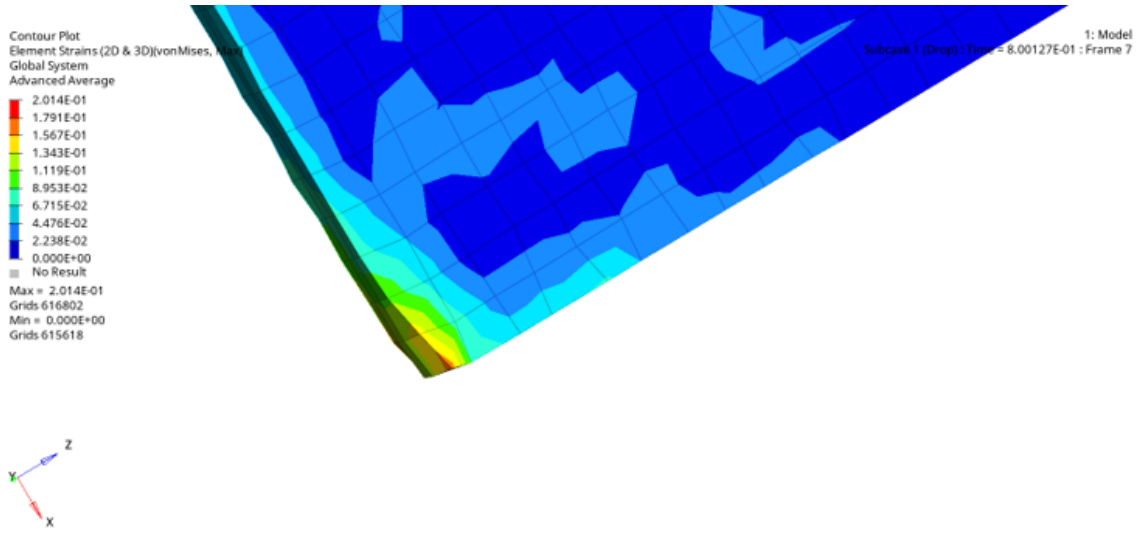

Figure 5.57: Drop nº5 inferior honeycomb strain

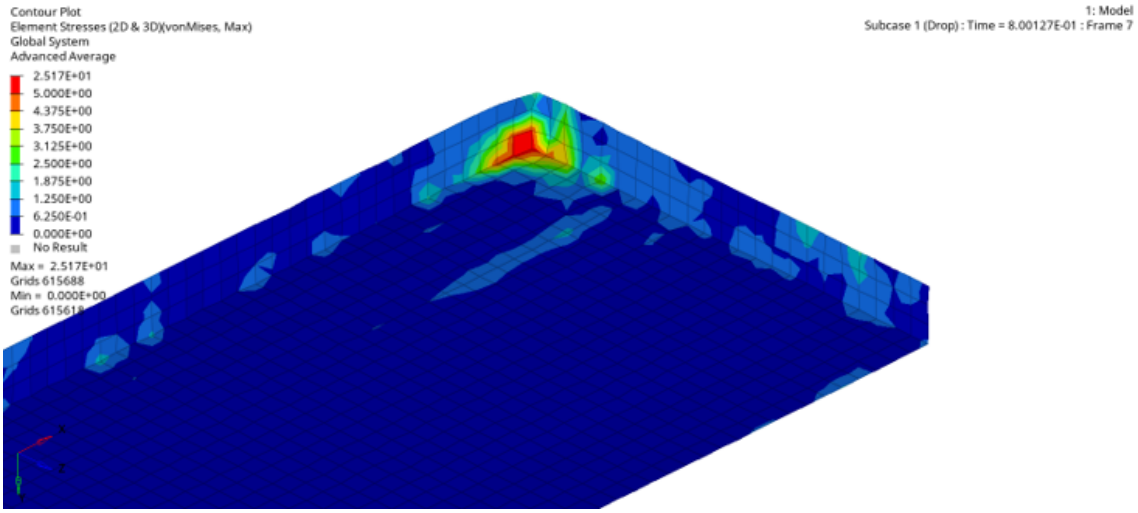

Figure 5.58: Drop nº5 inferior honeycomb stress

Complementary stress and strain values of this simulation are provided in Table 5.11.

Table 5.11: Maximum meaningful values of stress and strain state, by component (Orientation nº5)

Physical quantity	Approx. Meaningful Value	Note
External Laminate		
P_1 (major) principal stress (σ_{P1}) / MPa	$\approx$ 2250	
P_3 (minor) principal stress (σ_{P3}) /MPa	$\approx$ 1785	Critical loading condition
Maximum shear stress (τ_{max}) / MPa	$\approx$ 2335	
Internal Laminate		
P_1 (major) principal stress (σ_{P1}) / MPa	$\approx$ 400	
P_3 (minor) principal stress (σ_{P3}) /MPa	$\approx$ 250	-
Maximum shear stress (τ_{max}) / MPa	$\approx$ 500	
Honeycomb structure		
Von Mises stress (σ_{VM}) / MPa	$\approx$ 25	-
Von Mises strain (ε_{VM}) / %	$\approx$ 20	

It is evident that a vertex impact is the critical impact scenario for the external laminate of the enclosure.

5.5.6 Drop Orientation nº6

The sixth drop test resulted in a run time of 16 minutes and 17 seconds. The run procedure was smooth with no timestep fluctuations. Critical time step: 1.491×10^{-4} ms.

5.5.6.1 Computational Checks

The explicit analysis energy evolution graph is provided in Figure 5.59.

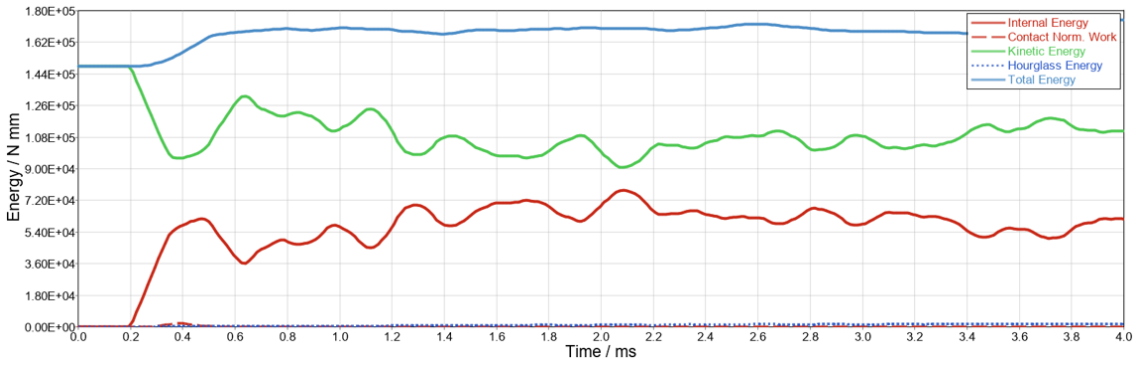

Figure 5.59: Drop nº6 explicit simulation energy graph

A combination of the behaviours observed in the second and fourth drop test simulations is present in this case. For detailed analyses of these behaviours, refer to Subsections 5.5.2 and 5.5.4, respectively. As in the second drop simulation, the nodes of the enclosure edge in contact with the rigid plane are also connected to rigid elements, which prevents localised deformation and causes the kinetic energy to propagate through the model as a high-frequency displacement and stress wave. This behaviour results in limited kinetic energy absorption by structural deformation.

The contact event is very short, and the honeycomb structures and internal laminate are almost unaffected, remaining structurally safe. In a real scenario, such an edge drop could be particularly damaging for the battery, but given the current model definition, the response of the battery cannot be fully evaluated.

Similarly to the fourth drop case, the contact occurs at an edge, resulting in highly concentrated and elevated stress levels in the impacted region. Nonetheless, when compared with other drop test orientations, this case does not constitute a critical scenario for the overall integrity of the enclosure. A noticeable increase in total energy is observed, attributable to the high strain in the impacted elements, but this time without any significant contact energy spikes. The initial value of total energy matches the expected value.

All computational validity criteria are satisfied, with a maximum hourglass energy fraction of 1.04% and a combined hourglass + contact energy fraction of 1.55%. Conclusively, although this drop case is not among the most critical scenarios, the resulting stress fields in the contact area provide valuable insights into the local response of the structure under such loading.

5.5.6.2 Deformation and Stress

The maximum principal stress plot due to contact is provided in Figure 5.60 and additional strain and stress values are listed in Table 5.12.

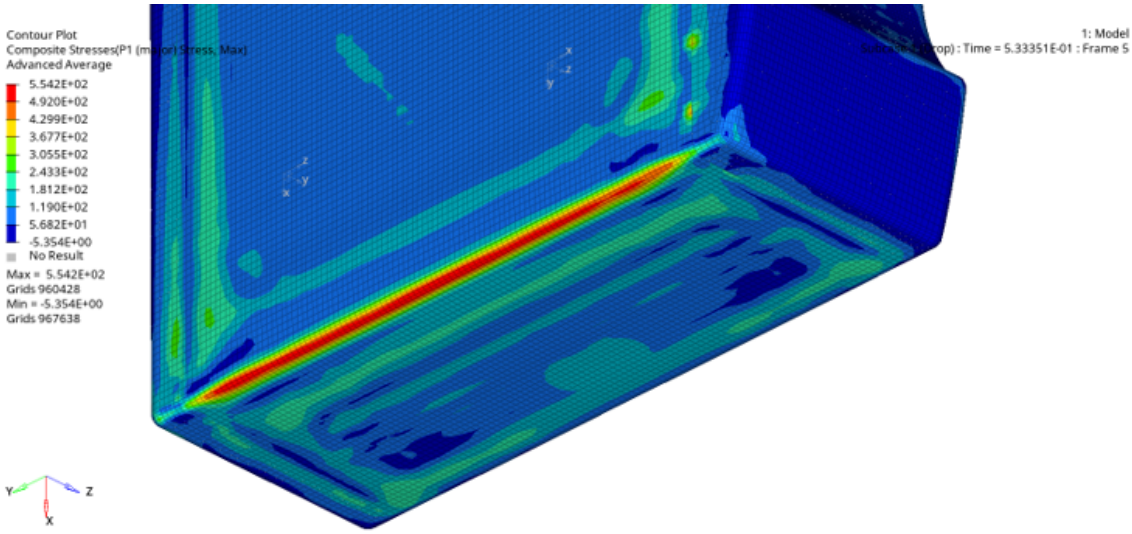

Figure 5.60: Drop nº6 external laminate stress

Table 5.12: Maximum meaningful values of stress and strain state, by component (Orientation nº6)

Physical quantity	Approx. Meaningful Value	Note
External Laminate		
P_1 (major) principal stress (σ_{P1}) / MPa	≈ 700	
P_3 (minor) principal stress (σ_{P3}) /MPa	≈ 400	-
Maximum shear stress (τ_{max}) / MPa	≈ 400	
Internal Laminate		
P_1 (major) principal stress (σ_{P1}) / MPa	≈ 400	
P_3 (minor) principal stress (σ_{P3}) /MPa	≈ 340	-
Maximum shear stress (τ_{max}) / MPa	≈ 400	
Honeycomb structure		
Von Mises stress (σ_{VM}) / MPa	≈ 4	-
Von Mises strain (ε_{VM}) / %	≈ 10	

5.5.7 Drop Orientation nº7

The seventh and final drop test simulation resulted in a run time of 14 minutes and 49 seconds. The run procedure was smooth with no timestep fluctuations. Critical time step: 1.491×10^{-4} ms.

5.5.7.1 Computational checks

The explicit analysis energy evolution graph is provided in Figure 5.61.

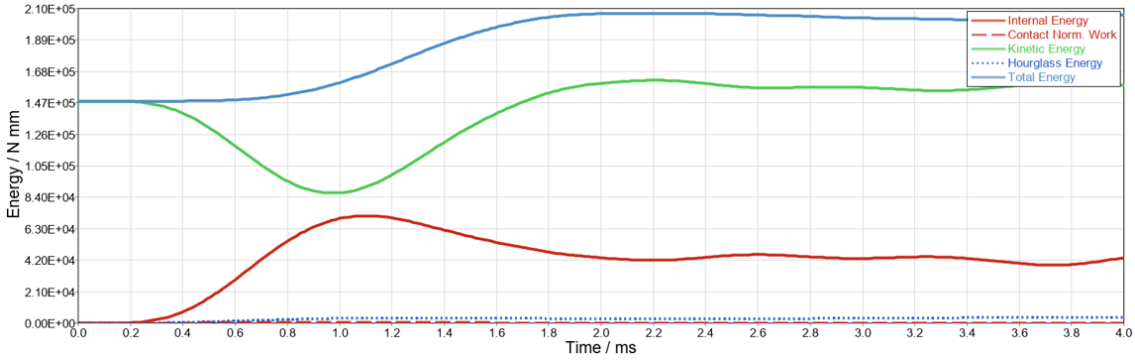

Figure 5.61: Drop nº7 explicit simulation energy graph

As can be seen in a direct comparison of this drop test simulation nº7 with nº5, both the energy plot and the results are very similar. No in-depth description of the phenomena will be presented here; for a detailed explanation, refer to Subsection 5.5.5.

In summary, a considerable surge in total energy is observed, for the same reasons outlined for drop n°5. The contact initiates at approximately 0.2 ms, proceeds through one vertex, then two vertices, and finally ends at the vertex opposite to the initial point of contact at around 2.1 ms. Figures 5.62 and 5.63 clearly illustrate the very high strain and deformation concentrated on the impacted vertices. The internal energy peak is slightly greater than that of drop n°5, with a value of 71.6 J (around 48% of the initial kinetic energy). This higher value can be attributed to the larger top honeycomb structure, which offers a greater capacity for deformation and energy absorption, thereby contributing to the protection of the battery components.

All other computational validity criteria are satisfied, with a maximum hourglass energy fraction of 2.05% and a maximum combined hourglass + contact energy fraction of 2.4%. The mechanical behaviour of the model in this case is physically consistent and, for this reason, the results will be considered valid for the assessment of the enclosure's performance.

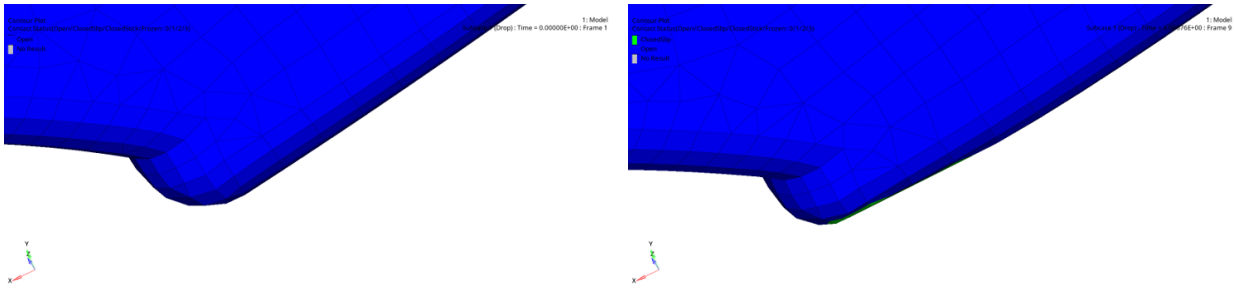

(a) Timestep 0 ms (b) Timestep 1.1 ms

Figure 5.62: Drop n°7 enclosure vertex deformation

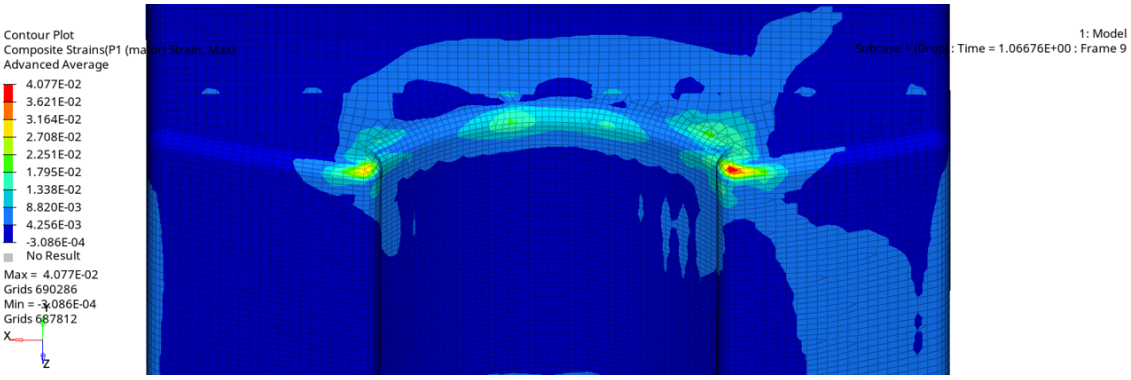

Figure 5.63: Drop n°7 external laminate strain

5.5.7.2 Deformation and Stress

The peak contact area is provided in Figure 5.64, and the first and last contact instances in Figure 5.65.

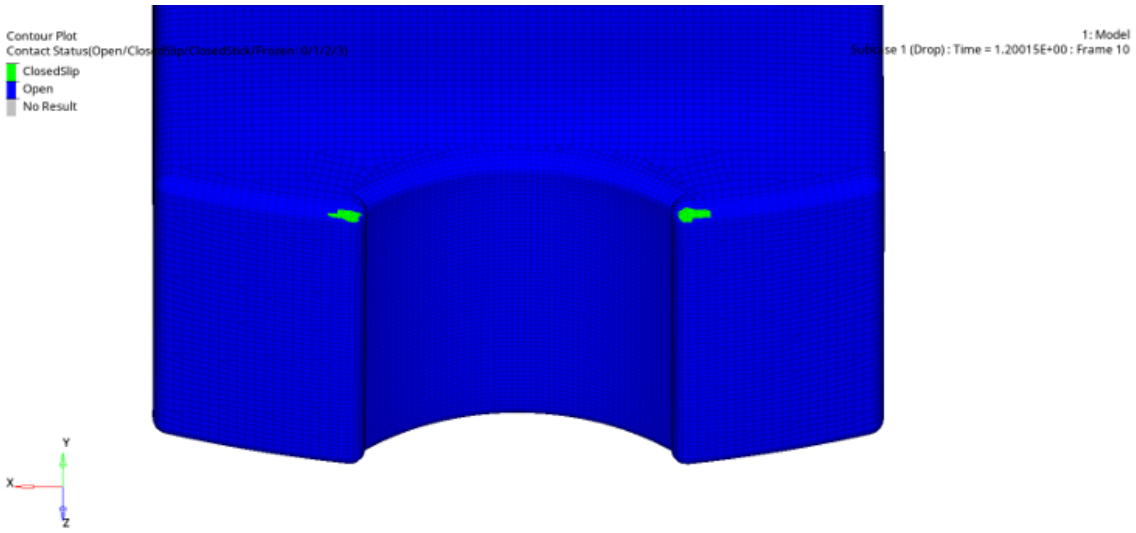

Figure 5.64: Drop nº7 peak contact zone

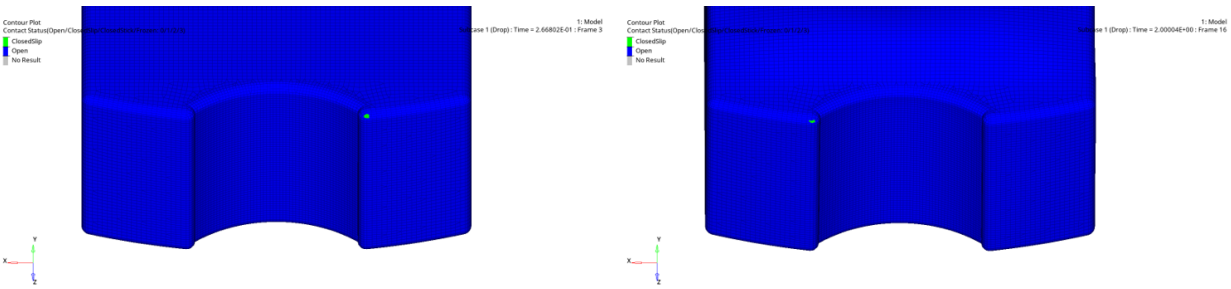

(a) Timestep 0.26 ms

(b) Timestep 2 ms

Figure 5.65: Drop nº7 first and last contact instances

Figure 5.66 presents results consistent with those observed in drop test nº5, with extreme stress levels indicating total laminate failure in localized regions of high stress concentration.

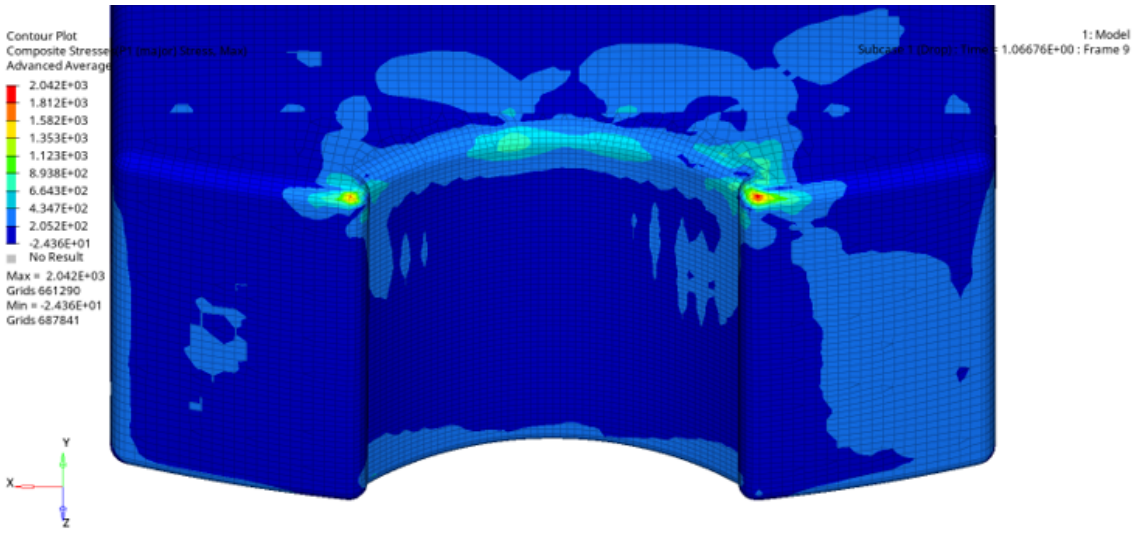

Figure 5.66: Drop nº7 external laminate stress

Figures 5.67, 5.68 and 5.69 highlight the crushing of the honeycomb core in the areas closest to the impact vertex, while the internal laminate largely preserves its integrity at the global level. Nevertheless, the presence of localised ply failures cannot be ruled out.

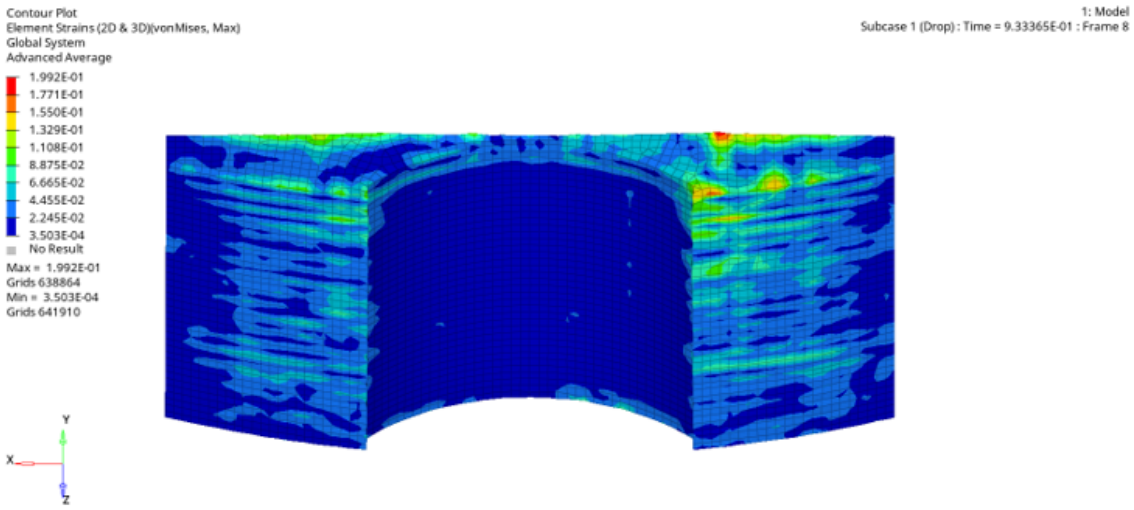

Figure 5.67: Drop nº7 superior honeycomb strain

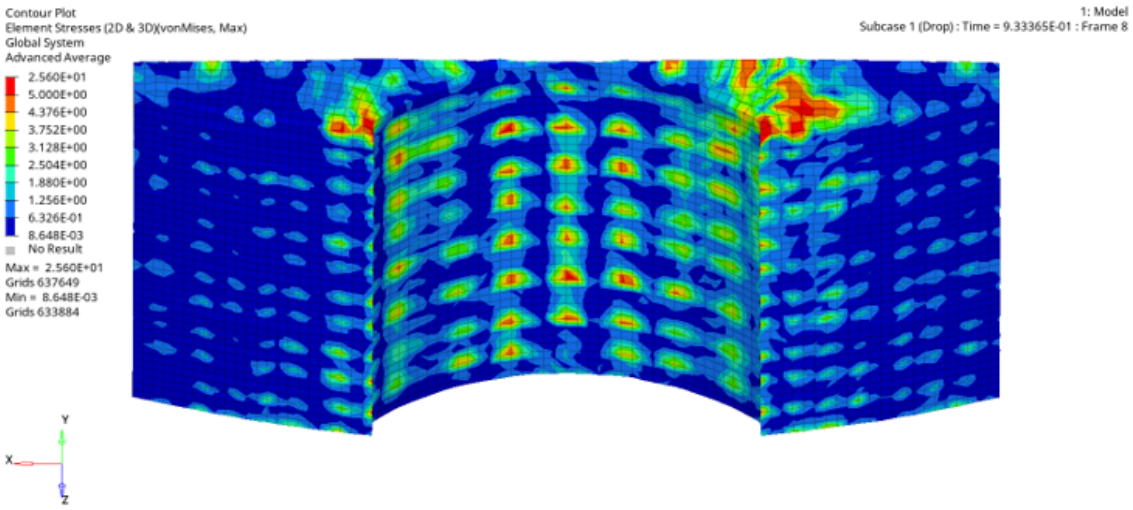

Figure 5.68: Drop nº7 superior honeycomb stress (Filtered in red for $\sigma_{VM} > 5$ MPa)

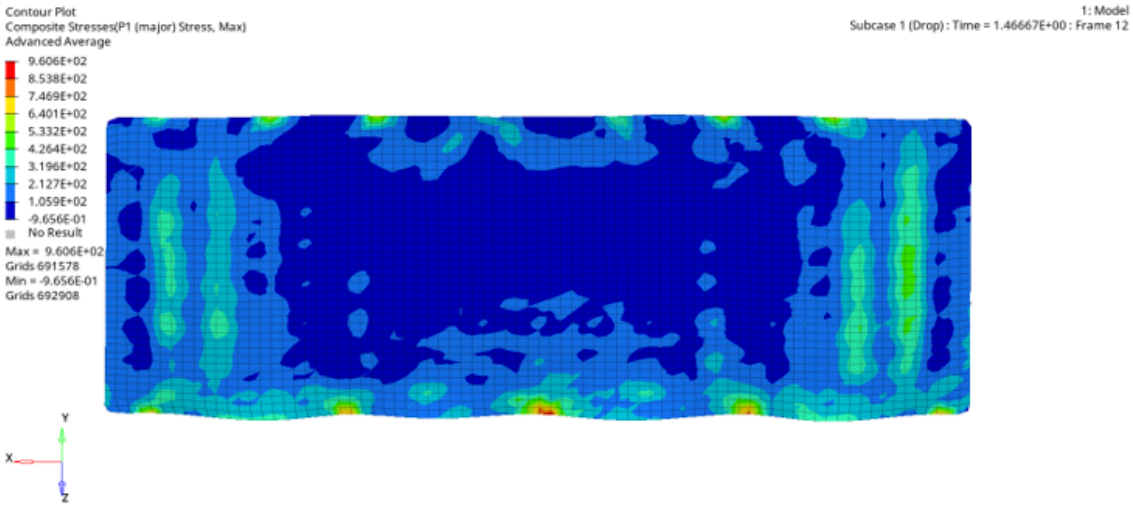

Figure 5.69: Drop nº7 internal surface stress

Complementary stress and strain data for this simulation are summarised in Table 5.13.

Table 5.13: Maximum meaningful values of stress and strain state, by component (Orientation n°7)

Physical quantity	**Approx. Meaningful Value**	**Note**
External Laminate		
P_1 (major) principal stress (σ_{P1}) / MPa	≈ 2040	
P_3 (minor) principal stress (σ_{P3}) /MPa	≈ 1234	Critical loading condition
Maximum shear stress (τ_{max}) / MPa	≈ 1500	
Internal Laminate		
P_1 (major) principal stress (σ_{P1}) / MPa	≈ 575	
P_3 (minor) principal stress (σ_{P3}) /MPa	≈ 200	-
Maximum shear stress (τ_{max}) / MPa	≈ 500	
Honeycomb structure		
Von Mises stress (σ_{VM}) / MPa	≈ 30	-
Von Mises strain (ε_{VM}) / %	≈ 20	

5.5.8 Conclusion of Drop Test Simulations

Although the present model could be further improved, for instance, by refining the mesh, explicitly modelling the battery modules, among other enhancements, the significant effort required to perform a complete remeshing, model reconstruction, and re-execution of all drop tests was beyond the available project timeline.

The results obtained were therefore deemed acceptable within the context of this study. They provided valuable insights into the structural behaviour of the battery enclosure under impact loading and enabled the identification of the most critical loading scenarios, namely those indicating failure of the external composite material and crushing of the honeycomb structures. These phenomena confirm the intended energy absorption and dissipation mechanisms, demonstrating the structure's ability to protect the internal battery components under severe impact conditions.

As will be seen in the following sections, these critical load conditions derived from the drop test simulations will serve as a basis for performing optimised design iterations, ensuring improved crashworthiness and structural performance of the enclosure.

5.6 Shock Test Analysis Results

As previously described, a four-simulation strategy was devised to replicate the second mechanical resistance test defined in the regulation, the mechanical shock test. For a detailed description of the model setup, boundary conditions, and simulation parameters, refer to Section 5.2.

As will become evident from the results presented in this section, the shock loading conditions do not represent the most critical scenarios for the enclosure design. In fact, the resulting solicitations of the battery case and its components are significantly lower than those observed in the drop test simulations. Nevertheless, these results will be analysed to confirm this behaviour and to provide a complete overview of the enclosure's performance under regulatory mechanical testing.

Given the strong similarities between the results, the four simulations are grouped into two sets: one comprising the **Y+** and **Y-** shock directions, and the other comprising the **X** and **Z** directions. This approach avoids redundancy and facilitates a clearer comparison of the observed behaviours.

In line with the methodology adopted for the drop test analyses, the results are first subjected to computational and energy check verifications to ensure their numerical validity. A concise evaluation of the deformation and stress responses of the model follows this. These include global displacements, von Mises stresses in the solid regions, maximum principal stress P_1, maximum in-plane shear stress, and composite failure strain for the laminated surfaces of the enclosure model.

5.6.1 Y+ and Y+ Shock Analyses

The mechanical shock test simulations with **Y+** and **Y-** loads resulted in a run time of 1 hour 13 minutes and 41 seconds, and 37 minutes and 12 seconds, respectively. Despite both simulations being very similar, the latter had a shorter run time due to more CPU cores being allocated for the computational task. The run procedure was smooth and without time step fluctuations, the time step remained the same throughout the simulation run time and equal to 1.491×10^{-4}ms, equal to drop tests due to the fact that the run time is dependent on the same critical mesh element. Shock test simulations resulted in longer run times simply due to the longer simulation end time of 13 ms, as opposed to 4 ms for drop tests.

5.6.1.1 Computational Checks

The explicit analysis energy evolution plots of **Y+** and **Y-** simulations are provided in Figures 5.70 and 5.71. Note that the energy values are provided in N mm and time in ms.

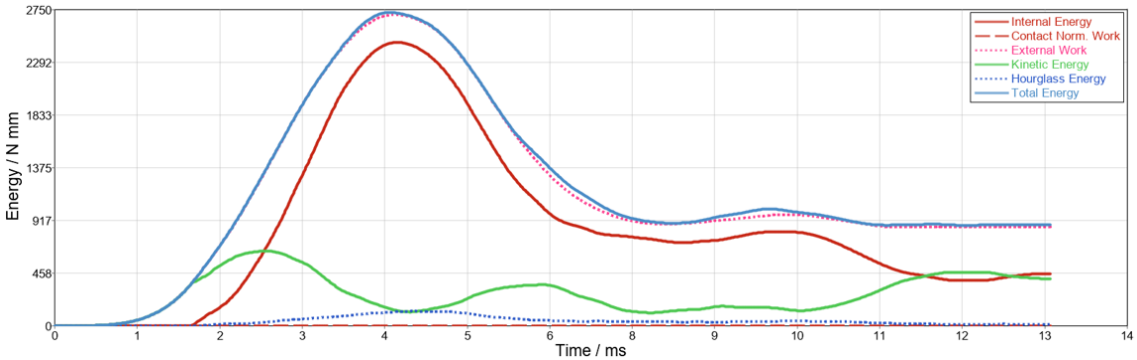

Figure 5.70: **Y+** shock explicit simulation energy graph

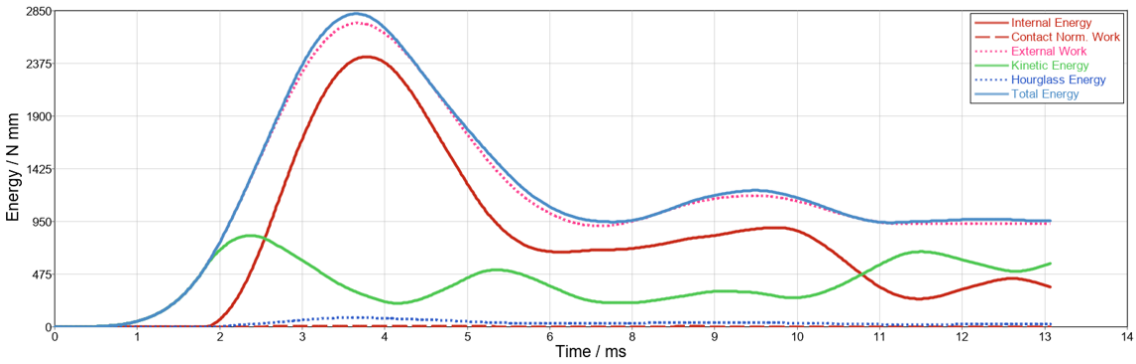

Figure 5.71: **Y-** shock explicit simulation energy graph

From the overall shape of the energy curves (and confirmed by inspection of the simulation `.out` file), the expected energy evolution is observed; the two shock simulations produce very similar energy histories and therefore warrant the same interpretation. First and foremost, the global energy accounting is correct: unlike the drop tests, these shock simulations include an active external work input, so the relevant conservation check is that the total energy E_t follows the external work E_{ext} (i.e. $E_t - E_{\text{ext}} \approx 0$) at all time steps. The half-sine acceleration pulse (11 ms duration) is clearly visible in the external work curve; after 11 ms the external work becomes constant and the total energy stabilises accordingly.

Prior to contact, the assembly undergoes a small rigid-body motion of approximately 0.15 mm. This offset was intentionally included so the initial contact is open and numerical problems are avoided. Contact with the rigid wall begins at about 1.8 ms and persists until roughly 12 ms. At contact initiation, the internal (strain) energy rises from zero, and during the active pulse, most of the applied external energy is converted into strain energy in the enclosure. The peak internal energy is small, about 2.4 J, reached near 4 ms and is mirrored only by a very small fraction of kinetic energy associated with residual vibration of the system.

With respect to the numerical validity checks, Section 5.3, the simulations meet Altair's recommended criteria: hourglass energy remains low (peak $\approx 5\%$ for the **Y+** case and $< 4\%$ for **Y–**), and the combined hourglass + contact contribution is similarly small, indicating that contact energy is negligible in both simulations.

Taken together, the energy histories, timestep behaviour and low hourglass/contact contributions indicate numerically stable and physically plausible simulations. As will be discussed right ahead, the deformation response likewise matched the expected physical behaviour, and all reported physical quantities were consistent and physically reasonable. These verifications satisfy Altair®'s explicit computation check guidelines and support the reliability of the results for subsequent analysis and design evaluation.

5.6.1.2 Deformation and Stress

The following Figures 5.72 to 5.76 present the maximum deformation, strain, and stress states of the enclosure model for both simulations.

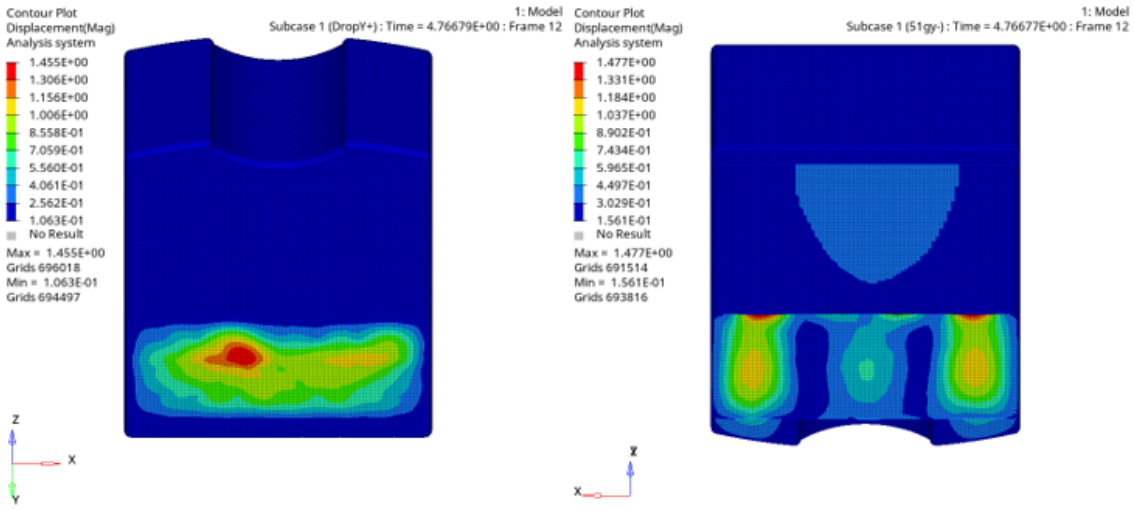

Figure 5.72: Nodal displacement at instant of peak deformation (**Y+** simulation to the left and **Y-** to the right)

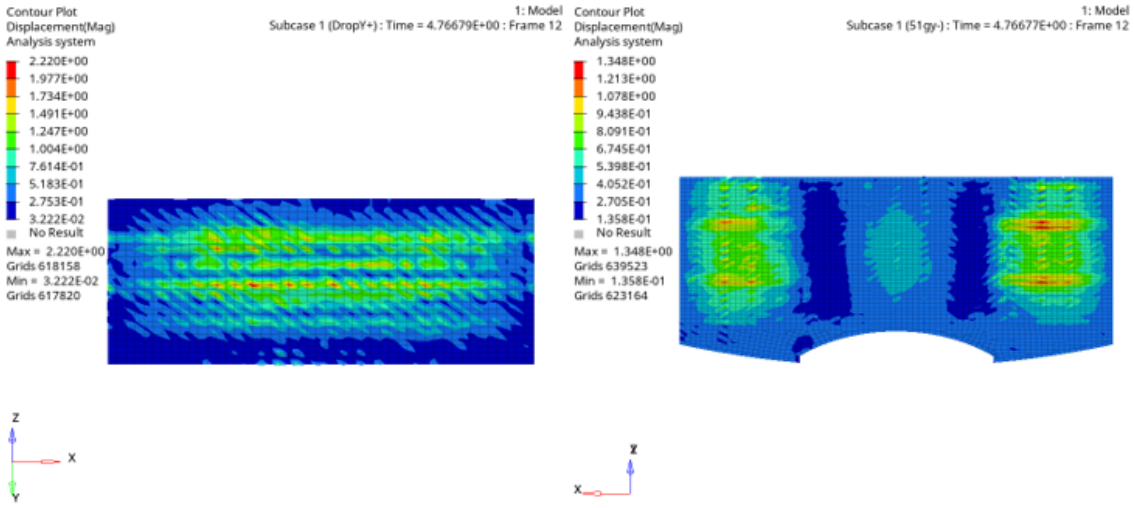

Figure 5.73: Nodal displacement in honeycomb cores at instant of peak deformation (**Y+** simulation to the left and **Y-** to the right)

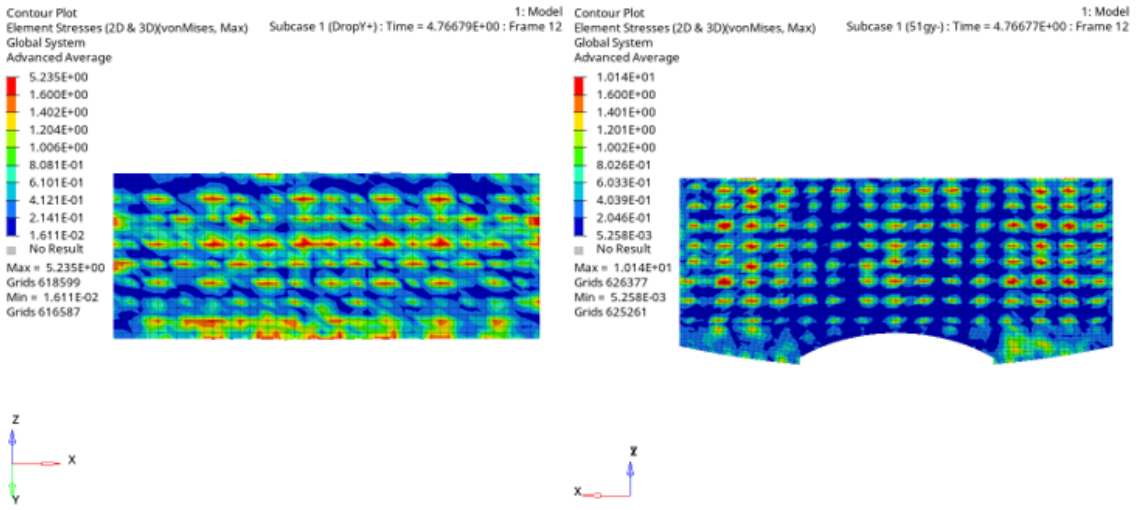

Figure 5.74: P_1 principal stress in honeycomb cores at instant of peak deformation, filtered in red for $\sigma_{VM} > 1.6$ MPa (**Y+** simulation to the left and **Y-** to the right)

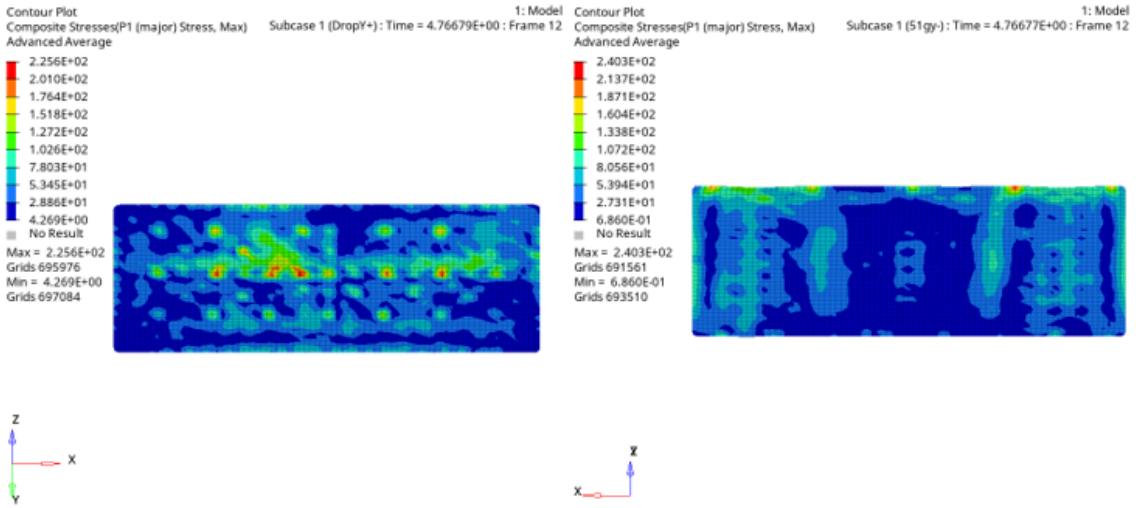

Figure 5.75: P_1 principal stress in internal laminate at instant of peak deformation (**Y+** simulation to the left and **Y-** to the right)

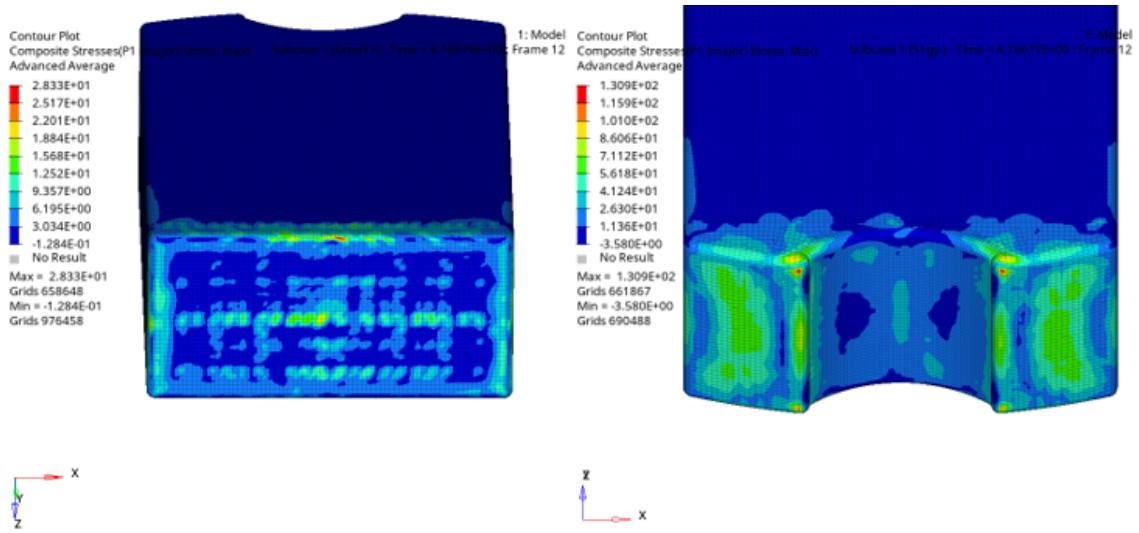

Figure 5.76: P_1 principal stress in external laminate at instant of peak deformation (**Y+** simulation to the left and **Y-** to the right)

Tables 5.14 and 5.15 provide additional stress and strain results.

Table 5.14: Maximum meaningful values of stress and strain state, by component (Mechanical Shock **Y+**)

Physical quantity	**Approx. Meaningful Value**	**Note**
External Laminate		
P_1 (major) principal stress (σ_{P1}) / MPa	≈ 30	
P_3 (minor) principal stress (σ_{P3}) /MPa	≈ 15	-
Maximum shear stress (τ_{max}) / MPa	≈ 30	
Internal Laminate		
P_1 (major) principal stress (σ_{P1}) / MPa	≈ 100	
P_3 (minor) principal stress (σ_{P3}) /MPa	≈ 60	-
Maximum shear stress (τ_{max}) / MPa	≈ 50	
Honeycomb structure		
Von Mises stress (σ_{VM}) / MPa	< Crush Strength	-
Von Mises strain (ε_{VM}) / %	≈ 8	

Table 5.15: Maximum meaningful values of stress and strain state, by component (Mechanical Shock **Y-**)

Physical quantity	**Approx. Meaningful Value**	**Note**
External Laminate		
P_1 (major) principal stress (σ_{P1}) / MPa	≈ 130	
P_3 (minor) principal stress (σ_{P3}) /MPa	≈ 85	-
Maximum shear stress (τ_{max}) / MPa	≈ 75	
Internal Laminate		
P_1 (major) principal stress (σ_{P1}) / MPa	≈ 100	
P_3 (minor) principal stress (σ_{P3}) /MPa	≈ 40	-
Maximum shear stress (τ_{max}) / MPa	≈ 60	
Honeycomb structure		
Von Mises stress (σ_{VM}) / MPa	< Crush Strength	-
Von Mises strain (ε_{VM}) / %	≈ 6	

All results clearly demonstrate that the deformation, strain, and stress levels are very low and remain well within the allowable elastic range of the materials. These shock tests, therefore, do not compromise the structural integrity of the enclosure or the safety of the battery components.

5.6.2 X and Z Shock Analyses

The mechanical shock test simulations with **X** and **Z** loads resulted in a run time of 1 hour 16 minutes and 2 seconds, and 53 minutes and 47 seconds, respectively.

The explicit analysis energy evolution plots of Y+ and Y- simulations are provided in Figures 5.77 and 5.78.

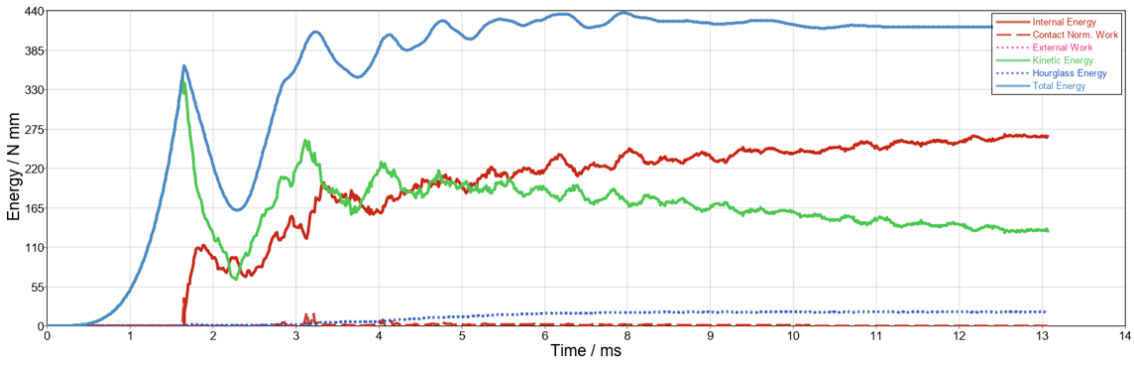

Figure 5.77: **X** shock explicit simulation energy graph

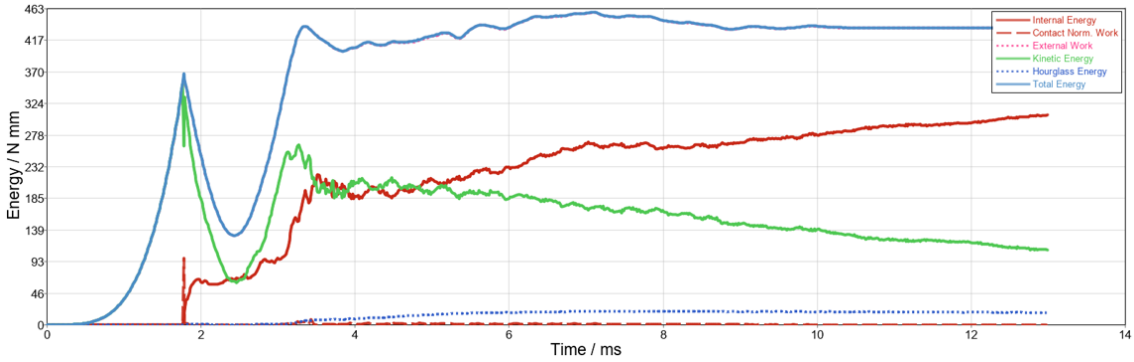

Figure 5.78: **Z** shock explicit simulation energy graph

The analysis of simulations X and Z shows a behaviour fully consistent with that observed in Drop Tests nº2 and 6, which was expected given the similar enclosure contact conditions. The erratic energy plot response can be attributed to the modelling approach adopted to link the battery mass and inertia to the enclosure via an RBE3 distributing element. In this configuration, the enclosure nodes in contact with the external surface are also connected to rigid elements, which suppresses localised deformation and leads to the propagation of kinetic energy through the model as a high-frequency displacement and stress wave.

The principle of conservation of energy is verified, as the total energy curve closely follows the external work, though in an unrealistic way. Most of the total energy is converted into kinetic energy, in line with the fact that contact is dominated by rigid-to-rigid interaction. The primary deformation and stress response is driven by high-frequency vibration rather than by plastic deformation. A marked spike of contact energy is observed at ≈ 1.8 ms, followed by sustained contact until ≈ 11.5 ms.

From a computational check standpoint, the hourglass contribution remains below 5 %. However, the energy condition defined in Equation 5.13 is not satisfied at the instant of contact for simulation **Z** (≈ 27 %) and approaches the threshold for simulation **X** (≈ 10 %), which indicates that the model has limitations for representing side-impact shock events realistically.

Overall, both simulations indicate that the mechanical shock loads considered are not critical for the enclosure design. The maximum displacements remain below 1 mm, the honeycomb and internal laminates are practically unaffected, and stress levels are well below the elastic limit.

Therefore, the analysis of the energy plots indicates that the results of these simulations are not particularly realistic or representative. Furthermore, as already observed in the **Y+** and **Y–** cases, the mechanical shock tests impose significantly lower mechanical solicitations on the enclosure compared to the drop test simulations. For these reasons, there is no real need to evaluate the results of the **X** and **Z** shock simulations in detail, and attention can be focused on the critical loading conditions provided by the drop test simulations, which will serve as the basis for the subsequent optimisation phase.

Chapter 6

Thermal Validation of the Enclosure Design in FEA

This chapter provides a comprehensive overview of the thermal finite element analyses performed to assess and validate the thermal performance of the Famel E-XF battery enclosure design. It begins by outlining the methodology and strategy adopted for the thermal study, followed by a detailed description of the numerical finite element model and the associated simulation parameters. Finally, the obtained results are presented and critically discussed, with the key findings and considerations summarised at the end of the chapter.

6.1 Methodology

This section aims to provide an explanation of the methodology that was initially planned for the thermal validation of the enclosure prototype, and the real path that was done. Compared to the mechanical validation of the enclosure, described in Chapter 5, the thermal study of the enclosure prototype was very much limited on what could be possible to do considering the information that was given to the author.

As stated in Chapter 4, Subsection 4.1.1, where all the information shared by the collaborator for the development of the prototype, all the information regarding thermal conditions is:

- The battery is considered to dissipate 500 W of heat (No further information was given, so it is taken as the peak thermal dissipation);
- The maximum allowable temperature for the cells is 60°C;
- The battery + enclosure assembly will be cooled down by forced convection when the motorcycle is in motion. (It was assumed that when the motorcycle is still, the heat from the battery is dissipated via free conduction. No explanation of the cooling system was given or any cooling conditions).

With this in mind, the initial plan aimed to simulate four operating conditions, accounting for heat dissipation inside the enclosure and convection to the outside air. Both free convection (motorcycle stationary) and forced convection (motorcycle in motion) were considered.

The methodology was designed to cover a representative range of scenarios: on one hand, moderate and elevated ambient temperatures to replicate demanding summer heat conditions; on the other, both stationary and moving cases of the motorcycle while the battery operates at peak dissipation. For the moving condition, a speed of 40 km/h was selected as a representative average value for the purpose of this work.

The following four-simulation strategy was, therefore, defined:

1. Free convection to outside still air at 25 °C
2. Forced convection to outside moving air at a speed of 40 km/h and temperature of 25 °C
3. Free convection to outside still air at 40 °C
4. Forced convection to outside moving air at a speed of 40 km/h and temperature of 40 °C

Unfortunately, only the first and second simulation cases were carried out. As will be described later, the results obtained for these two cases (both at 25 °C) were sufficient to exclude any practical interest in performing simulations with an external air temperature of 40 °C. The reasoning behind this conclusion will be explored and justified in detail later in this chapter.

Taking this into account, the methodology effectively applied in this work consisted of the following two-case simulation strategy:

1. **Battery Heating + Free Convection**:
    - Constant battery heat dissipation of 500 W;
    - Free convection to the surrounding outside air enveloping the battery–enclosure assembly at 25 °C;
    - Initial uniform temperature of 25 °C.
2. **Battery Heating + Forced Convection**:
    - Constant battery heat dissipation of 500 W;
    - Forced convection to the surrounding outside air enveloping the battery–enclosure assembly at 25 °C, considering a flow velocity of 40 km/h;
    - Initial uniform temperature of 25 °C.

The detailed modelling assumptions and boundary conditions for both cases will be discussed in the following sections, which describe the finite element model developed for this analysis.

From the results of these simulations, several aspects are to be analysed. The first step is to verify whether the internal surface temperature of the enclosure approaches or exceeds the maximum tolerable limit for the battery cells, set at 60 °C. If this critical temperature is not reached, the

thermal adequacy of the enclosure would be considered validated as designed. On the contrary, if the limit is reached or surpassed, the following aspects would require careful evaluation:

- The transient evolution of temperature over time;
- The time required to reach the critical temperature;
- The spatial distribution of hot spots within the model and the regions where maximum temperatures occur;
- The steady-state temperature values achieved once equilibrium is reached.

Based on these analyses, conclusions can then be drawn regarding potential improvements to the enclosure design. Specifically, regarding if additional cooling strategies, either passive or active would be necessary to ensure safe operating conditions for the battery system.

6.2 Limitations and Considerations

The thermal validation stage of this work was subject to several limitations.

First, no detailed battery model was available, nor specific information such as the cell type, discharge rate, or *C*-rate. The methodology was therefore developed using a simplified representation of the battery, based on the overall heat dissipation data provided. This constraint was inherent to the project, as the information shared by Famel was limited, and the approach taken represents the most comprehensive strategy that could be realistically implemented.

Second, radiative heat transfer was not considered in the simulations. However, as the battery enclosure is designed to operate inside the motorcycle, where radiation effects are expected to be minimal compared to conduction and convection, this simplification is not expected to significantly influence the results.

Third, the thermal properties of all materials were derived from academic studies and reference books. This approach was necessary because reliable and concrete data on the thermal behaviour of carbon fibre/epoxy composites and aluminium honeycomb closed-cell structures is scarce. The exact sources will be clearly presented and justified in the following section to ensure transparency and traceability of the assumptions made.

Finally, limitations related to the finite element model must also be acknowledged. The version of Altair HyperWorks® used imposes a maximum of 100,000 nodes, which required the model to be meshed within this constraint. As a consequence, the thin laminate regions of the enclosure were discretised with only one solid element through the thickness, and exclusively first-order elements were employed. While these measures allowed the simulations to be executed successfully, they also imposed restrictions on the resolution of the results.

In summary, the methodology and modelling strategies adopted were the best possible within the given constraints. Although these limitations reduce the level of detail of the thermal validation, they do not compromise the ability of this work to assess the thermal adequacy of the battery enclosure design.

6.3 Numerical Modelling

This section presents the finite element model developed for the thermal validation stage of the project, covering all aspects of the pre-processing phase. As in the mechanical validation stage, both thermal simulations were based on a common finite element model, sharing geometry, mesh, material definitions, thermal contacts, and heat flux loads. The only differences arise from the convection parameters, which will be detailed separately for each case.

Compared to Chapter 5, the description provided here will be more concise, as thermal validation was not a central focus of the project and was subject to certain limitations. Nevertheless, all essential modelling aspects are addressed to ensure clarity and completeness of the analysis.

6.3.1 Geometry

First, regarding the unit system adopted for both the CAD and finite element models, it is the same as in the mechanical validation phase, as summarised in Table 5.2. All physical quantities were converted to the correct unit system before being defined in the model. For clarity, however, this document will continue to present values in more familiar units.

The initial step was the creation of a CAD model in SolidWorks®. As discussed in the state-of-the-art (Subsection 2.7.3), the particularities of heat transfer analysis in HyperMesh® make the use of solid elements advantageous whenever possible. For this reason, the CAD geometry was modelled exclusively with solid bodies, including the thin laminate regions of the enclosure. The resulting geometry was then imported into the finite element pre-processor. Figure 6.1 illustrates the solid CAD model created in SolidWorks®.

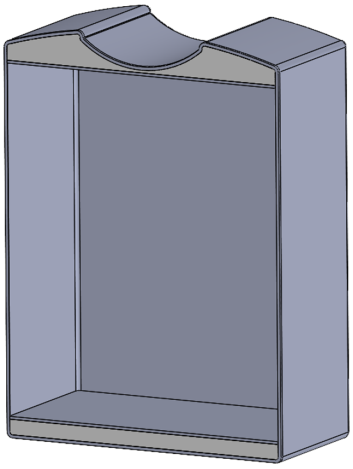

Figure 6.1: Solid CAD enclosure model for thermal analysis in SolidWorks® (Section view)

Subsequently, a topology clean-up and simplification stage was carried out to facilitate the discretisation of the geometry into 3D solid elements. This process involved suppressing unnecessary edges, splitting complex bodies into more regular sub-parts, and exploiting model symmetry. These steps streamlined the meshing process and reduced the likelihood of computational errors. The resulting 3D topology visualisation in HyperMesh® is shown in Figure 6.2.

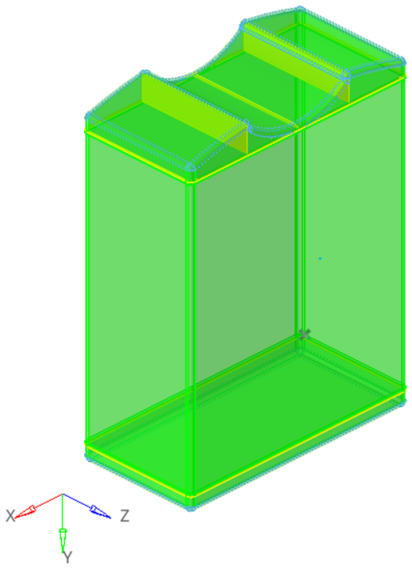

Figure 6.2: 3D topology visualisation tool applied to the model

6.3.2 Mesh

The enclosure model was then discretised using solid elements. The external laminate component was meshed with the Thin Solids BatchMesh function, applying one element through the thickness and combining hexahedral and pentahedral elements. The lower honeycomb structure, due to its regular geometry, was efficiently meshed using automatic mapping, yielding a structured `HEX` and `PENTA` mesh. The upper honeycomb structure, by contrast, required a tetrahedral mesh because of its more intricate geometry. This meshing process was performed in several steps to prevent errors and ensure element quality. Finally, model symmetry was exploited by meshing only half of the geometry and replicating it through mesh mirroring, with proper equivalencing of nodes along the symmetry planes.

Overall, the meshing process proved to be significantly more reliant on automated procedures compared to shell-based models, leaving less margin for manual optimisation. As a result, generating an acceptable 3D solid mesh for this case was a laborious task.

Figures 6.3 and 6.4 present the discretised components from the enclosure model, separately.

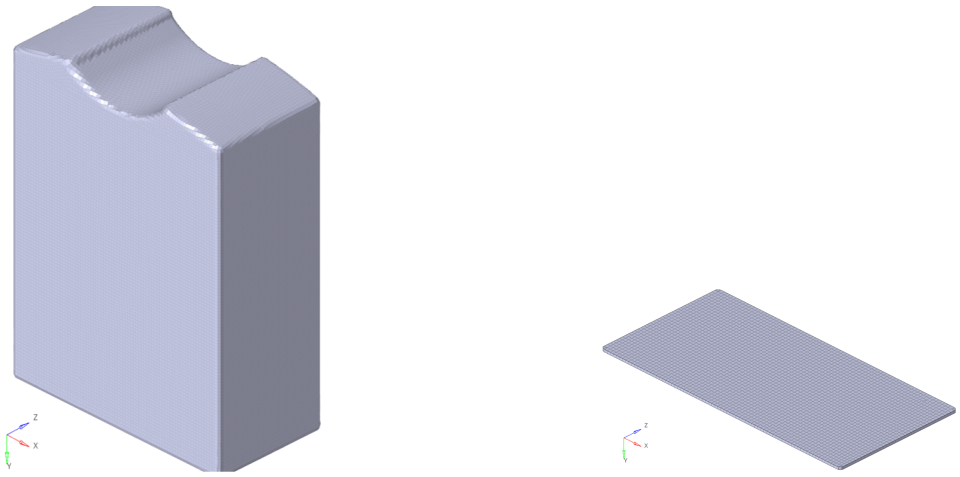

(a) External meshed surface (b) Internal meshed surface

Figure 6.3: Laminate components discretised with solid elements

(a) Meshed top honeycomb core (b) Bottom honeycomb core

Figure 6.4: Honeycomb components discretised with solid elements

Table 6.1 lists the statistics of the mesh.

Table 6.1: Thermal model mesh Statistics

Element Type		**Quantity**
3D Solid	HEX8	46 494
	TETRA4	43 390
	PENTA6	316
Total Elements		90 200
Total Nodes		95 900

The finite element model developed for the thermal validation of the enclosure was discretised exclusively with first-order solid elements, with priority given to structured hexahedral and pentahedral elements wherever possible, namely in the thin laminate regions and the lower honeycomb structure. Due to software limitations in the Altair HyperWorks® version employed (maximum of 100,000 nodes), the model was created at the fringe of the allowed capacity. For this reason, only one element through the thickness of the thin laminate body was defined, and first-order elements

were used throughout; otherwise, it would not have been possible to execute the simulations within the imposed constraints.

The following Figures 6.5 and 6.6 provide the Jacobian matrix and Aspect ratio quality metrics for the mesh created for thermal validation of the enclosure.

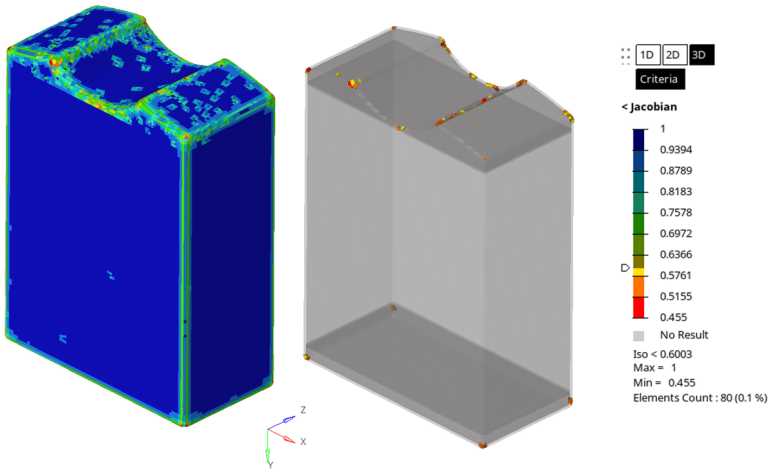

Figure 6.5: Jacobian matrix mesh quality metric (elements under 0.6 isolated to the right)

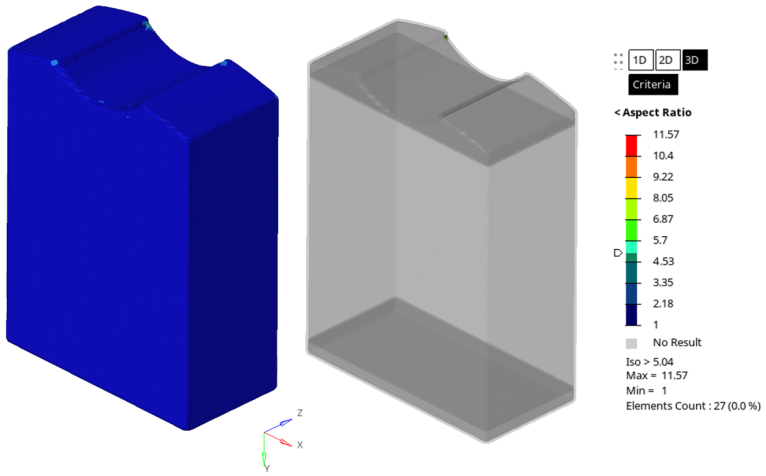

Figure 6.6: Aspect ratio mesh quality metric (elements over 5 isolated to the right)

The resulting mesh and elements were optimised to comply with the quality metrics defined in Subsection 5.2.2, and in general, these metrics were successfully met. As can be observed from the quality check legends presented in Figures 6.5 and 6.6, only a negligible fraction of elements fall below the acceptable thresholds. Specifically, only 80 elements (approximately 0.1%) presented a Jacobian matrix index lower than 0.6, and just 27 elements (less than 0.1%) exceeded the maximum allowable aspect ratio of 5. Considering these values, the mesh was found to be of acceptable quality for the purposes of the present work.

6.3.3 Carbon Fibre Composite Material

Carbon fibre composite laminates are inherently anisotropic in their thermal conduction behaviour. In woven configurations such as 2×2 twill fabrics, the material can be considered orthotropic, exhibiting approximately equal in-plane conductivity in both principal directions, while showing significantly lower conductivity through the thickness. This is a direct consequence of the fibre architecture, where fibres are mainly oriented in-plane, and only the polymer matrix and limited fibre intersections contribute to heat transfer across the laminate thickness.

The high thermal conductivity of carbon fibres, typically around 24 W/(m·K), contrasts sharply with the much lower values of polymeric matrices, generally between 0.17 and 0.79 W/(m·K) [81]. As a result, fibre orientation, weave configuration, and fibre volume fraction have a strong influence on the overall heat transfer capability of composite materials. Unidirectional laminates tend to present higher thermal conductivity along the fibre direction due to the absence of fibre crossings, whereas woven fabrics, although more isotropic in-plane, exhibit lower overall conductivity. Through the thickness, heat transfer is dominated by the matrix material and interlaminar interfaces, which act as barriers to conduction and significantly reduce the effective thermal conductivity of the laminate [81, 82].

Each composite laminate presents distinct thermal conduction properties that depend on a multitude of factors, such as fibre type, orientation, weave pattern, fibre volume fraction, and matrix characteristics. Consequently, identifying accurate thermal properties for a given composite system can be a challenging task. For the purposes of this project, the material properties defined for the finite element model were selected based on relevant academic literature. In particular, two key studies were evaluated: *"Thermal properties of carbon fibre–epoxy composites with different fabric weaves"* [81], and *"Measurement of the anisotropic thermal conductivity of carbon-fiber/epoxy composites based on laser-induced temperature field: Experimental investigation and numerical analysis"* [82].

The first study experimentally characterised the thermal diffusivity and conductivity of carbon fibre–epoxy prepreg composites using the light flash method. Samples with different fibre configurations, including unidirectional, plain weave, and eight-harness satin weaves, were analysed to assess the influence of fibre architecture on the thermal behaviour. The results showed good agreement with other references in the literature, reporting a specific heat capacity (C_p) of approximately 850 J/(kg·K) at 25 °C for all three configurations. For the satin weave, the in-plane and through-thickness conductivities were found to be 3.2 W/(m·K) and 0.73 W/(m·K), respectively, while for the plain weave, they were 2.4 W/(m·K) and 0.6 W/(m·K).

In the second study, a hybrid numerical–experimental methodology was employed, combining thermographic measurements of a laser-induced temperature field with an inverse finite element approach to determine the thermal conductivity tensor of a plain weave carbon fibre/epoxy laminate. The specimens were manually laminated (fibre and resin not preinpregnated), consisting of 19 layers (7.8 mm total thickness), and exhibited a relatively low fibre volume fraction of 34%. The results yielded thermal conductivities of 6.8 W/(m·K) in the fibre direction and 0.32 W/(m·K)

through the thickness.

Ultimately, the results from [81] were selected for this work. The laminate characteristics in that study more closely resemble those of the enclosure under analysis, with comparable thickness (around 2 mm), similar manufacturing method (prepreg-based), and a fibre volume fraction of 48.9%. Furthermore, the purely experimental methodology and the good correlation with values reported in the literature reinforce the adequacy of adopting these results as the basis for defining the thermal properties of the composite laminate used in the present thermal analyses.

To define the laminate material in HyperMesh®, a `MAT5` entry was employed. This card specifies the thermal properties of anisotropic materials in the finite element model. The required parameters include the thermal conductivity matrix $[K]$, defined as:

$$[K] = \begin{bmatrix} k_{xx} & k_{xy} & k_{xz} \\ k_{xy} & k_{yy} & k_{yz} \\ k_{xz} & k_{yz} & k_{zz} \end{bmatrix} \tag{6.1}$$

together with the specific heat capacity C_p and the density ρ [83].

Based on the results from [81], and considering that a twill weave prepreg typically exhibits conduction properties intermediate between satin and plain weaves due to its balanced fibre crossings, the following values were adopted for the thermal model:

- $k_{xx} = \frac{2.4+3.2}{2} = 2.8$ W/(m K);
- $k_{yy} = \frac{2.4+3.2}{2} = 2.8$ W/(m K);
- $k_{zz} = \frac{0.6+0.73}{2} = 0.665$ W/(m K);
- $k_{xy} = k_{xz} = k_{yz} \approx 0$;
- $C_p = 850$ J/(Kg K)
- $\rho = 1.5089$ g/cm^3

The off-diagonal terms (k_{xy}, k_{xz}, k_{yz}) were assumed negligible, as in woven composites, these are typically close to zero unless significant off-axis fibre orientations or strong anisotropy are present. In a symmetric and balanced laminate, such as a quasi-isotropic layup, heat transfer occurs predominantly along the fibre and through-thickness directions.

Three `MAT5` materials were created to account for different laminate orientations relative to the global coordinate system. These are represented in red, green, and blue in Figure 6.7.

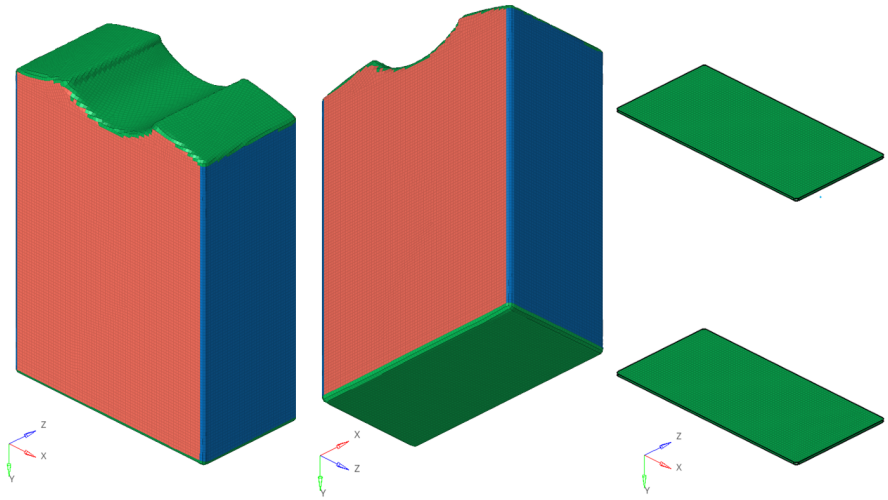

Figure 6.7: `MAT5` materials created for the carbon fibre laminate material of the model enclosure

It was assumed that the thermal properties of all materials in the model remain constant with temperature. Although this assumption does not strictly reflect real behaviour, literature indicates that the variation of thermal properties in carbon fibre composites and closed-cell honeycomb structures is minimal. Therefore, this simplification reduces model complexity without significantly affecting the accuracy of the results.

6.3.4 Honeycomb Structure Material

The modelling of the aluminium honeycomb structure's thermal behaviour was, similarly to its mechanical behaviour, based on analytical models and data available in the literature. The main references consulted include the paper *"Thermal Transport and Fire Retardance Properties of Cellular Aluminium Alloys"* by Lu and Chen [32], and the foundational book that underpins the analytical approach of that study, *"Cellular Solids: Structure and Properties"* by Gibson and Ashby [84].

The literature indicates that heat transfer in closed-cell metallic structures is primarily governed by solid conduction along the cell walls, while the contribution of thermal radiation remains negligible even at elevated temperatures (up to 600 °C). Moreover, gaseous conduction within the cells contributes only about 10^{-2} W/(m K) to the overall thermal conductivity, and can thus be disregarded for metal foams. The apparent thermal conductivity of such structures depends strongly on the cell geometry, wall connectivity, and overall topology [32].

As with composite laminates, aluminium honeycomb structures exhibit anisotropic thermal behaviour. Therefore, a `MAT5` material definition was employed to represent their orthotropic conduction characteristics. Since the structure is symmetric and exhibits no significant coupling between orthogonal heat fluxes, the off-diagonal terms (k_{xy}, k_{xz}, k_{yz}) were considered negligible.

The analytical model presented by Lu and Chen [32], which is derived from the formulations in Gibson and Ashby [84], describes the effective thermal conductivity of regular double-wall honeycombs without defects as:

$$\begin{aligned} \rho_{\text{rel}} &= \frac{(1+h/l)t/l}{\cos\theta(h/l+\sin\theta)} \\ k_{xx} &= \frac{3}{8}\rho_{\text{rel}}k_s \\ k_{yy} &= \frac{9}{16}\rho_{\text{rel}}k_s \\ k_{zz} &= \rho_{\text{rel}}k_s \end{aligned} \tag{6.2}$$

where ρ_{rel} is the relative density of the honeycomb, k_s the thermal conductivity of the base material, and θ, l, h, and t are the geometric parameters defined in Figure 6.8. The x and y coordinates correspond to the in-plane directions of the honeycomb, while z represents the through-thickness direction.

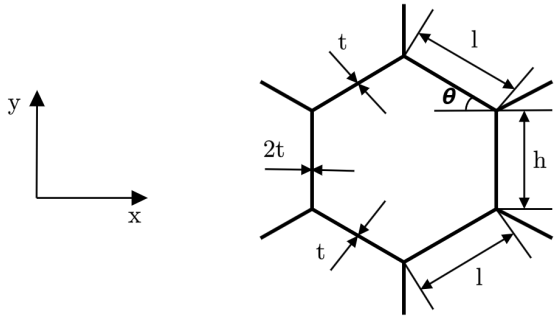

Figure 6.8: Unit cell of a hexagonal honeycomb with non-uniform thickness cell walls, dimensions and axis orientation (Adapted from [32])

According to Gibson and Ashby [84], even in low-density cellular structures, the specific heat capacity C_p remains approximately equal to that of the constituent material, as the mass contribution of the enclosed air is negligible. Considering this assumption, the geometric parameters adopted ($\theta = 30$ °, $t = 0.07$ mm, $l = h = 3.695$ mm), the properties of aluminium 3003 [85, 86], and the density of the honeycomb material ($\rho = 83.3$ kg/m^3), the thermal properties defined for the honeycomb `MAT5` material were:

- $\rho_{\text{rel}} = \frac{(1+1)\times 0.07/3.695}{\cos(30°)(1+\sin(30°))} = 0.0292$
- $k_{xx} = \frac{9}{16} \times 0.0292 \times 190 = 3.117$ W/(m K);
- $k_{yy} = 0.0292 \times 190 = 5.542$ W/(m K);
- $k_{zz} = \frac{3}{8} \times 0.0292 \times 190 = 2.078$ W/(m K);
- $k_{xy} = k_{xz} = k_{yz} \approx 0$;
- $C_p = 893$ J/(Kg K);
- $\rho = 83.3$ Kg/m^3.

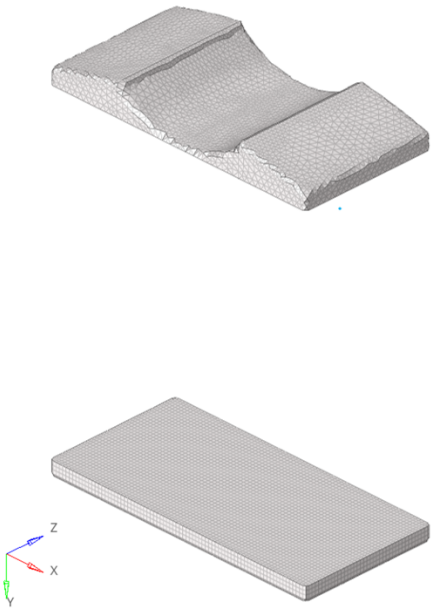

Figure 6.9: Honeycomb structures and global axis system in HyperMesh®

6.3.5 Thermal Contact

The thermal model of the enclosure comprises multiple components and materials. To enable heat transfer between these components, appropriate thermal contacts must be defined. In this model, the thermal contact was established between the carbon fibre composite laminates and the aluminium honeycomb structures, as illustrated in Figure 6.10.

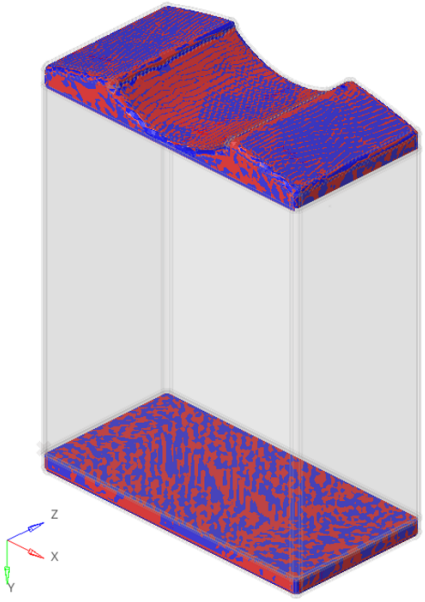

Figure 6.10: Visualisation of the thermal contact in HyperMesh®

Thermal contacts in HyperMesh® are defined in a similar manner to mechanical contacts, using a `CONTACT` entry paired with a `PCONT` property definition.

The parameter governing the efficiency of heat transfer across a contact interface is the thermal conductance, h_t, or equivalently, the thermal resistance of the contact, R_t [87]. These parameters quantify how effectively heat flows between two contacting surfaces.

The thermal conductance between contacting bodies is expressed as the ratio between the heat flux $\dot{q}$ transmitted through the interface and the corresponding temperature difference across it:

$$h_t = \frac{\dot{q}}{\Delta T} \text{ [W/(m}^2\text{·K)]} \tag{6.3}$$

The thermal resistance represents the inverse of the thermal conductance, and can be written as:

$$R_t = \frac{1}{h_t} = \frac{\Delta T}{\dot{q}} \tag{6.4}$$

The value of thermal conductance adopted in this work was selected based on evidence from the academic literature. Specifically, it was obtained from the study presented in the chapter *"Investigation of the Improvement of the Thermal Contact Conductance between a Baseplate and a Honeycomb Platform Using Various Interstitial Materials"*, part of the book *"Thermal Conductivity 14"* by Wild and Bouchez [88].

This study reports a series of experimental tests conducted on a representative satellite baseplate–honeycomb platform assembly to assess improvements in interface temperature differentials achieved through the use of various interstitial fillers. The results indicated that, for the contact between an aluminium honeycomb and a carbon fibre composite skin, the effective thermal conductance was approximately 270 W/(m^2·K).

Consequently, this value was adopted as the contact conductance for the closed interface between the honeycomb core and the composite laminates, implemented in the model through the `PCONTHT` conductance entry.

6.3.6 Convection

This subsection will delve into the modelling of the thermal convection heat transfer between the enclosure and the surrounding air. As stated earlier, two distinct cases are considered: Free convection to air at 25 °C and Forced Convection to moving air at a flow velocity of 40 km/h, and 25 °C, each will be treated separately. Both convection definitions are based on the analytical convection heat transfer equation as follows:

$$\dot{q} = h\Delta T \tag{6.5}$$

This equation is also the basis of the convection modelling method in OptiStruct®. Knowing the adequate convection coefficient h, and assigning it to its associated geometry, a simplified, physically correct convection heat transfer behaviour can be modelled for the enclosure.

The calculation of convection coefficients will be based on the analytical methodology learnt in the Heat Transfer course, namely its extensive formulary and book [89, 90].

6.3.6.1 Free Convection

The enclosure geometry was divided into three zones depending on its value of convection coefficient h. Each zone is identified in Figure 6.11 and is considered to be a flat surface for the purpose of calculation of h. Further considerations for the determination of convection coefficients are that the surface geometry is at a constant temperature of 60 °C, the maximum heat allowed for the validation of the enclosure, an arbitrary value is necessary to proceed to the calculations, the consideration of 60 °C was found to be meaningful for this work.

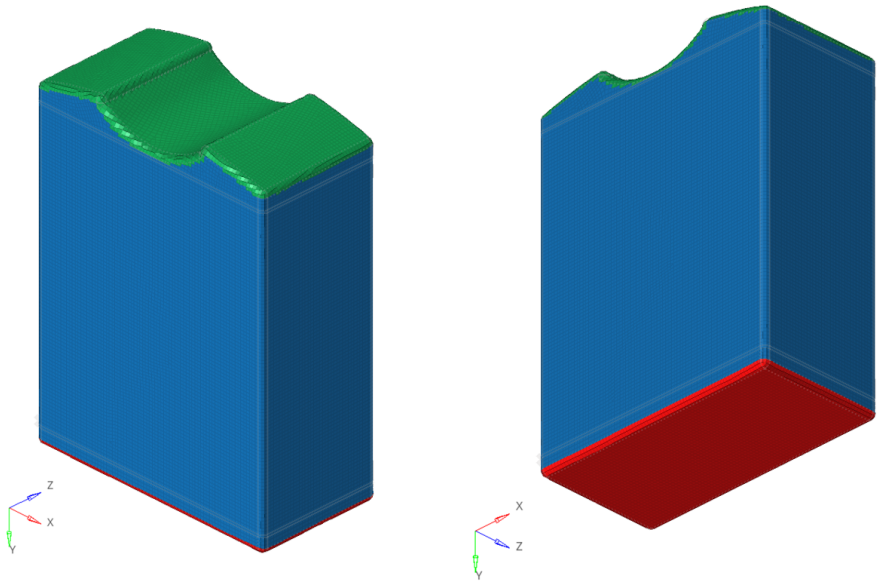

Figure 6.11: Free convection zones considered, colour-coded

First, let's define the surface-air physical properties that are equal in all convection areas:

1. Air temperature: $T_\infty = 25°$ C;
2. Surface temperature: $T_s = 60°$ C;
3. Boundary temperature: $T_{\text{filme}} = \frac{60+25}{2} = 42.5°$ C (used to obtain the following properties);
4. Air conductivity: $k_{\text{air}} = 0.027$ W/(m K);
5. Air kinematic viscosity: $\nu_{air} = 17.0.71 \times 10^{-6}$ m^2/s;
6. Air's Prandtl: 0.7015;
7. $\beta = 3.168 \times 10^{-3}$ K^{-1}

Blue area

The characteristic length of this area is its height of approximate value: $L = 300$ mm. Grashof's number is defined as:

$$Gr_L = \frac{g\beta(T_{\text{surf}} - T_\infty)L^3}{\nu^2} = \frac{9.81 \times 3.168 \times 10^{-3} \times (60-25) \times 0.3^3}{(17.071 \times 10^{-6})^2} = 1.01 \times 10^8 \tag{6.6}$$

Rayleigh's number results in:

$$Ra_L = Gr_L Pr = 1.01 \times 10^8 = 7.06 \times 10^7 \tag{6.7}$$

As Rayleigh's number finds itself in the $10^4 - 10^9$ range, Nusselt's number is:

$$Nu = \frac{hL}{k} = 0.59 Ra_L^{\frac{1}{4}} = 0.59 \times \left(7.06 \times 10^7\right)^{\frac{1}{4}} = 54.098 \tag{6.8}$$

Reworking the equation, the convection coefficient comes to:

$$h = \frac{k_{\text{air}} Nu}{L} = 4.87 \text{ W/(m}^2 \text{ K)} \tag{6.9}$$

Green area

The green area is a situation of horizontal hot surface that dissipates heat to colder air above it. Its characteristic value is the ratio of the surface area by its perimeter. Both values were obtained from the CAD model of the enclosure in SolidWorks®.

$$L = \frac{A}{p} = \frac{32954.6 \text{ mm}^2}{744.95 \text{ mm}} = 44.237 \times 10^{-3} \text{ m} \tag{6.10}$$

Its Grashof's number is then:

$$Gr_L = \frac{9.81 \times 3.168 \times 10^{-3} \times (60-25) \times \left(44.237 \times 10^{-3}\right)^3}{(17.071 \times 10^{-6})^2} = 323122.49 \tag{6.11}$$

Rayleigh's number:

$$Ra_L = 323122.49 \times 0.701 = 226509.9 \tag{6.12}$$

As it falls in the $10^4 - 10^7$ range, with a Prandtl number above 0.7 ($Pr \geq 0.7$), Nusselt's number is given by:

$$Nu = 0.54 \times Ra_L^{\frac{1}{4}} = 11.7805 \tag{6.13}$$

Which gives a convection coefficient of:

$$h = \frac{k_{\text{air}} Nu}{L} = 7.1902 \text{ W/(m}^2 \text{ K)} \tag{6.14}$$

Red area

This calculation closely resembles the last, however, the horizontal surface is above the surrounding air. Its characteristic value is:

$$L = \frac{A}{p} = \frac{30685.11}{708.72} = 43.33 \times 10^{-3} \text{ m} \tag{6.15}$$

Its value of Grashof's number is:

$$Gr_L = \frac{9.81 \times 3.168 \times 10^{-3} \times (60 - 25) \times \left(43.33 \times 10^{-3}\right)^3}{\left(17.071 \times 10^{-6}\right)^2} = 303582.9 \tag{6.16}$$

Rayleigh's number is:

$$Ra_L = 212813 \tag{6.17}$$

As it falls in the $10^4 - 10^7$ range, with a Prandtl number above 0.7 ($Pr \geq 0.7$), Nusselt's number is given by:

$$Nu = 0.52 \times Ra_L^{\frac{1}{5}} = 6.048 \tag{6.18}$$

Which gives a convection coefficient of:

$$h = \frac{k_{\text{air}} Nu}{L} = 3.77 \text{ W/(m}^2 \text{ K)} \tag{6.19}$$

So a lower value than the superior horizontal surface, which dissipates to the air above.

6.3.6.2 Forced Convection

For the definition of the convection conditions to moving air (Forced convection), the same methodology was employed. The only difference lies in the analytical equations used to obtain the resulting convection coefficients.

Here, three areas of the enclosure, that differ from the free convection case, were defined. These areas depend on the orientation of the air flow around the enclosure. The orientation of flow was chosen to be parallel to the length of the enclosure, a situation that should result in higher heat dissipation than, for example, a perpendicular flow. The convection zones and the orientation of air flow are represented in Figure 6.12.

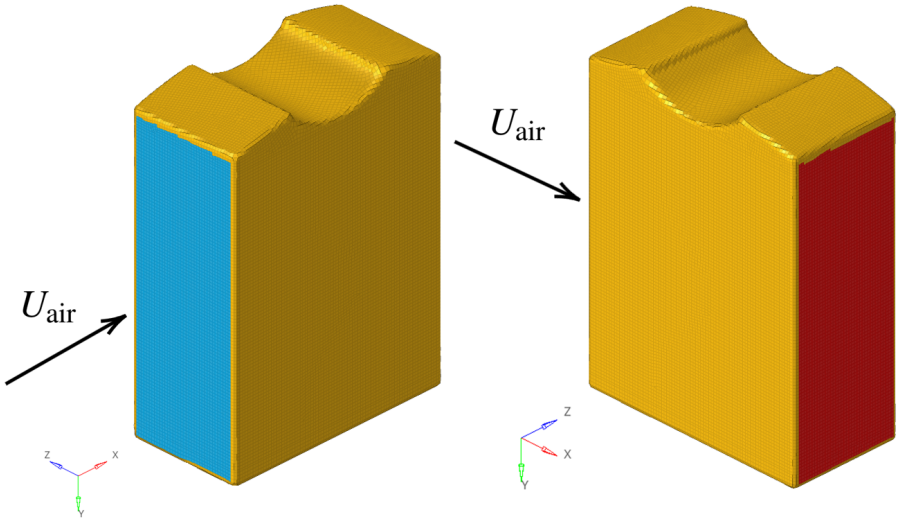

Figure 6.12: Forced convection zones considered, colour-coded with air direction identified

The surface-air physical properties that are equal in all convection areas are:

1. Air temperature: $T_\infty = 25°$ C (used to find the properties);
2. Surface temperature: $T_s = 60°$ C;
3. Air conductivity: $k_{\text{air}} = 0.026$ W/(m K);
4. Air kinematic viscosity: $\nu_{air} = 15.575 \times 10^{-6}$ m^2/s;
5. Air's Prandtl: 0.7125;
6. Flow velocity: $U_{\text{air}} = 40$ km/h ≈ 11.1 m/s.

Yellow area

The characteristic length of this area is: $L = 0.3$ m.
Reynolds number is defined as:

$$Re = \frac{U_{\text{air}} L}{\nu} = \frac{11.1 \times 0.3}{15.575 \times 10^{-6}} = 213804.2 \tag{6.20}$$

Considering turbulent flow and using the average Nusselt's number,

$$\overline{Nu_L} = \frac{\overline{h}L}{k_{\text{air}}} = 0.037 Re_L^{\frac{4}{5}} Pr^{\frac{1}{3}} = 606.936 \tag{6.21}$$

Reworking the equation, we have:

$$h = \frac{k_{\text{air}} \overline{Nu_L}}{L} = 52.6 \text{ W/(m}^2 \text{ K)} \tag{6.22}$$

Blue area

This convection case is one of a vertical wall perpendicular to the air flow. Its characteristic length its width: $L \approx 0.115$ m. In this case the air properties are at the temperature of the boundary: $T_{\text{filme}} = 42.5°\text{C}$ ($Pr = 0.701$, $\nu_{\text{air}} = 17.071 \times 10^{-6}$ m^2/s).

The Reynolds number of the air flow is:

$$Re = \frac{U_{\text{air}} L}{\nu} = \frac{11.1 \times 0.115}{17.071 \times 10^{-6}} = 74775.9 \tag{6.23}$$

In this convection case the empirical equation is:

$$\overline{Nu_L} = \frac{\overline{h} L}{k_{\text{air}}} = C Re_L^m Pr^{\frac{1}{3}} \tag{6.24}$$

as the dissipation surface is ahead of the flow, the coefficient values are: $C = 0.667$ and $m = 0.5$. This results in:

$$\overline{Nu_L} = 0.667 \times (74775.9)^{0.5} \times 0.701^{\frac{1}{3}} = 162.024 \tag{6.25}$$

which results in a convection coefficient of:

$$h = 38.040 \text{ W/(m}^2 \text{ K)} \tag{6.26}$$

Red area

This zone is defined similarly to the last, with the same characteristic length and Reynolds number. The corresponding equation is:

$$\overline{Nu_L} = C Re_L^m Pr^{\frac{1}{3}} \tag{6.27}$$

with coefficients values of: $C = 0.191$ and $m = 0.667$.

This results in a Nusselt's number of:

$$\overline{Nu_L} = 0.191 \times (74775.9)^{0.667} \times 0.701^{\frac{1}{3}} = 302.277 \tag{6.28}$$

And a resulting convection coefficient of:

$$h = 70.96 \text{ W/(m}^2 \text{ K)} \tag{6.29}$$

All of these convection coefficients were defined for their corresponding areas using `MAT4` materials, created only for the convection definition, that were associated with convection properties `PCONV`.

6.3.7 Heat Flux Load

A constant heat flux load is applied to the internal faces of the enclosure through a `HEATFLUX` load entry in HyperMesh®. This heat generation is constant through the analysis and equal to the maximum heat dissipation claimed by Famel, of 500 W.

Heat flux is the rate at which thermal energy, or heat, is transferred through a unit area of a surface per unit time. The internal enclosure area, calculated directly from its CAD model, is equal to 247871.6 mm^2, the resulting heat flux is then:

$$\dot{q} = \frac{Q}{A} = \frac{500}{247871.6} = 2.017 \times 10^{-3} \text{ W/mm}^2 \tag{6.30}$$

The element surfaces where the heat flux is applied can be visualised in the following Figure 6.13.

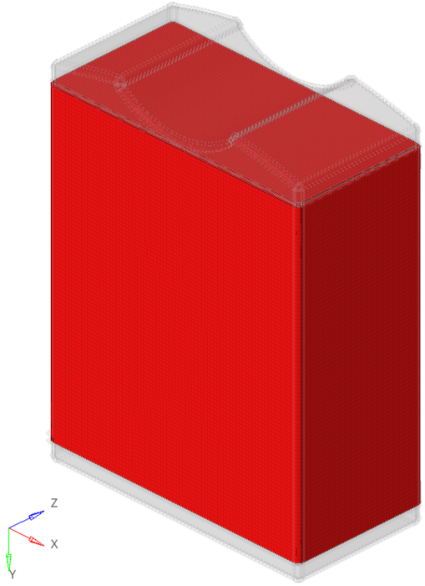

Figure 6.13: Heat flux load visualisation in HyperMesh®

6.3.8 Linear Transient Heat Transfer Analyses Parameters

The main simulation parameters defined for both heat transfer analyses (**Battery Heating + Free/Forced Convection**) are presented in Table 6.2.

Table 6.2: Battery Heating + Free Convection analysis settings

Battery Heating + Free Convection Analysis Settings	
Implicit time step control type:	Newmark integration scheme
Number of time steps (`N`):	60
Time step (`DT`) / ms:	3×10^4 (= 30 s)
End time / ms:	1.8×10^6 (= 30 min)
Result outputs:	60
Initial conditions (`IC`):	`T1` = 25°C system temperature

Both the free and forced convection simulations share the same global simulation parameters, differing only in the convection boundary conditions applied. The time control parameters were manually defined by the user, as required in a linear transient heat transfer analysis.

The choice of time step and number of increments was guided by the objective of simulating up to conditions close to the steady state while maintaining adequate temporal resolution of the transient results. Thus, a total of 60 increments of 30 seconds each were defined, with result outputs generated at every time step, leading to a total simulation time of 30 minutes. The theoretical background related to time integration schemes in transient heat transfer analyses was discussed previously in Chapter 2.

It is worth noting that, despite the relatively long simulated time, the computational cost of these analyses remained low, with total simulation run times under one minute.

The initial temperature conditions were defined by assigning uniform nodal temperatures of 25 °C throughout the entire enclosure finite element model, ensuring a consistent thermal state at the start of the simulation.

6.4 Thermal Analysis Results

Following the thorough description of the thermal validation methodology, the finite element model, and the analysis parameters of each numerical simulation, now come the study of the results. Each simulation's results will be analysed individually, and at the end, the key takeaways of the thermal study will be discussed.

6.4.1 Battery Heating + Free Convection

This simulation had a total run time of 23 seconds and completed smoothly without any numerical instabilities or convergence issues.

Figure 6.14 presents the temperature evolution at selected nodal points of the enclosure throughout the simulation, providing an overview of the transient thermal behaviour.

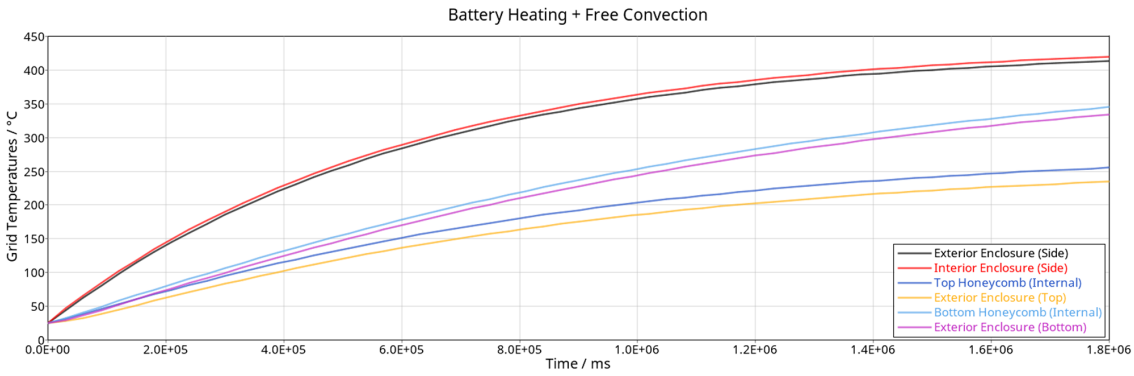

Figure 6.14: Temperature evolution of key points of the enclosure

Figures 6.15 and 6.16 illustrate the nodal temperature contour plots at two key moments: the instant when the internal temperature of the enclosure exceeds 60 °C, and the final timestep of the simulation, respectively.

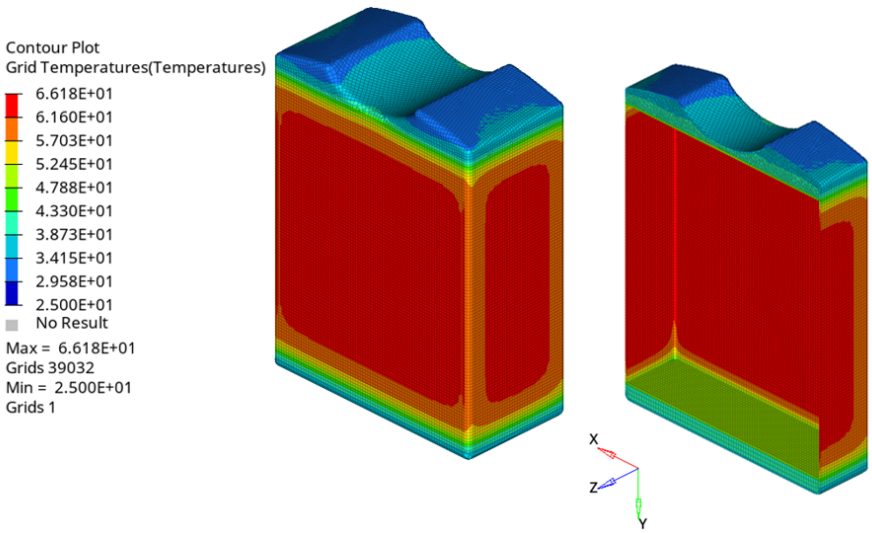

Figure 6.15: Temperature contour plot of the enclosure at timestep $t = 6.0 \times 10^4$ ms (60 seconds)

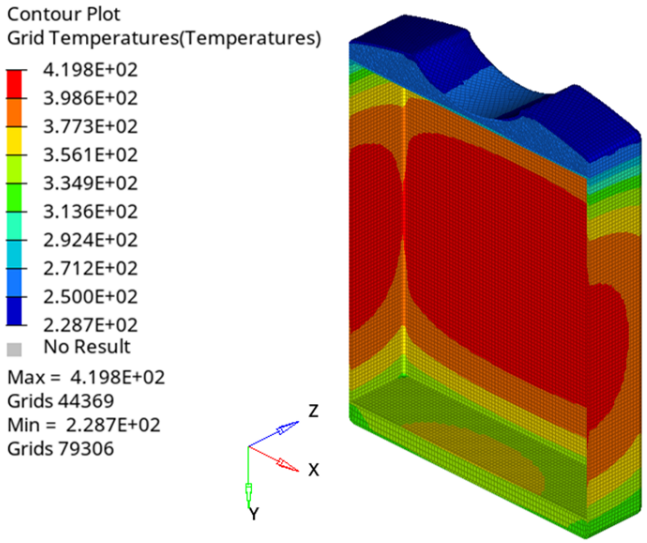

Figure 6.16: Temperature contour plot of the enclosure at the final timestep $t = 1.8 \times 10^6$ ms (30 minutes)

The results show very high temperature levels across the entire enclosure, with particularly elevated values observed at the side walls, where only a thin laminate skin is present. Internal and external wall temperatures in these regions exceed 400 °C and are closely matched. After 60 seconds of continuous heat dissipation, the internal temperature surpasses 60 °C, confirming a rapid temperature increase under the imposed conditions.

These results highlight the low thermal conductivity of both the carbon fibre laminate and the aluminium honeycomb core. Temperature curves for points located further from the heat input exhibit similar temporal behaviour but lower magnitudes, all remaining above 200 °C. The honeycomb structure effectively acts as a thermal barrier, limiting heat transfer through the top and bottom walls.

Although the simulation duration of 30 minutes does not fully reach steady-state, the temperature trends indicate that the system approaches thermal equilibrium. The high thermal resistance of the materials and the low external convection coefficient result in limited heat dissipation to the environment, explaining the elevated temperatures observed.

The distribution of temperatures within the laminate and honeycomb layers confirms that the thermal contacts were properly defined, reproducing the expected heat flow paths through the structure.

Given the unexpectedly high temperature values, several verification steps were conducted, including checks of the applied heat flux, units, and boundary conditions, as well as sensitivity tests with increased convection coefficients. The results were found to be consistent across all checks.

To further validate the numerical results, an analytical calculation was performed, as presented below.

Temperature analytical calculations

Considering a single vertical wall representative of the side of the enclosure, the same heat flux and boundary conditions from the simulation are applied:

- $\dot{q} = 2017$ W/m^2
- $k = 0.665$ W/(m·K) (through-thickness direction)
- $t = 2.24$ mm (laminate thickness)
- $T_\infty = 25$ °C
- $h = 5$ W/(m^2·K) (average value in the model)

From Fourier's law of heat conduction:

$$\dot{q} = k\frac{dT}{dx} \mapsto 2017 = 0.665\frac{dT}{dx} \tag{6.31}$$

Solving for the temperature gradient:

$$\frac{dT}{dx} = -3033.08 \tag{6.32}$$

Integrating across the wall thickness gives the temperature difference between the inner and outer surfaces:

$$\Delta T = -3033.08 \times \Delta x \mapsto \Delta T = 6.794 \text{ °C} \tag{6.33}$$

From the convection equation:

$$\dot{q} = h\Delta T \tag{6.34}$$

The corresponding wall surface temperatures are obtained as follows, considering an ambient air temperature of 25 °C:

$$\Delta T = T_{sup} - T_\infty = \frac{2017}{5} = 403.4 \text{ °C} \tag{6.35}$$

Thus, the wall temperatures are:

$$T_{ext} = 428.4 \text{ °C } T_{int} = 428.4 + 6.794 = 435.2 \text{ °C} \tag{6.36}$$

The analytical results closely match the numerical simulation, confirming the validity of the thermal model.

To visualise the overall heat flow distribution, Figure 6.17 shows the element heat flux contour at the final timestep of the simulation.

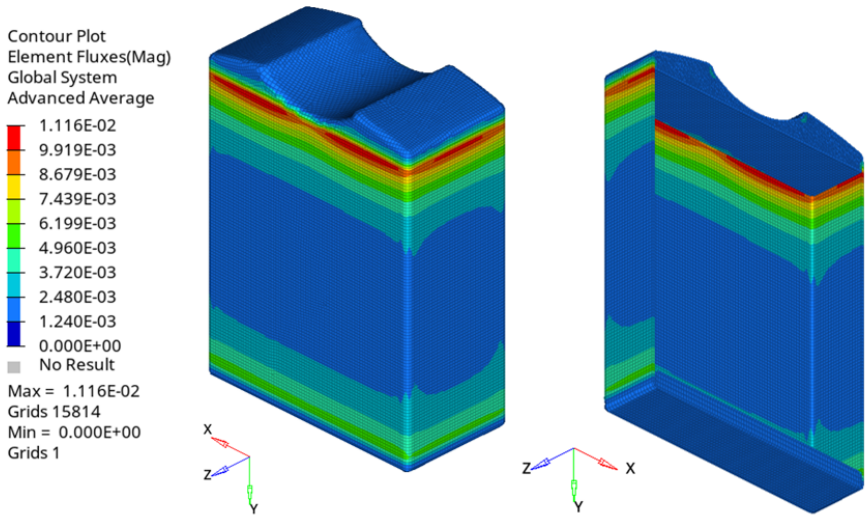

Figure 6.17: Element fluxes contour plot of the enclosure at the final timestep $t = 1.8 \times 10^6$ ms (30 minutes)

6.4.2 Battery Heating + Forced Convection

This simulation had a comparable run time of 22 seconds and completed without convergence issues.

Similarly to the previous case, Figure 6.18 presents the temperature evolution at selected nodal points of the enclosure throughout the simulation.

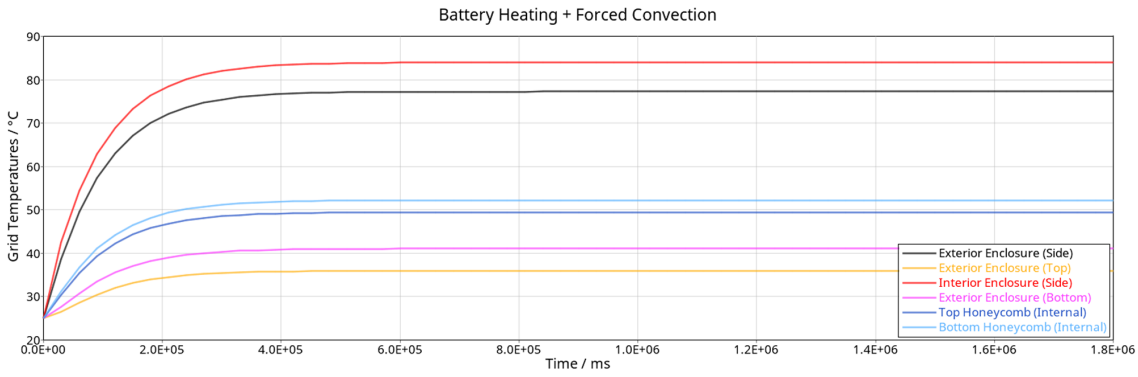

Figure 6.18: Temperature evolution of key points of the enclosure

Figures 6.19 and 6.20 show the temperature contour plots at the instant when the internal temperature of the enclosure exceeds 60 °C and at the final timestep of the simulation, respectively.

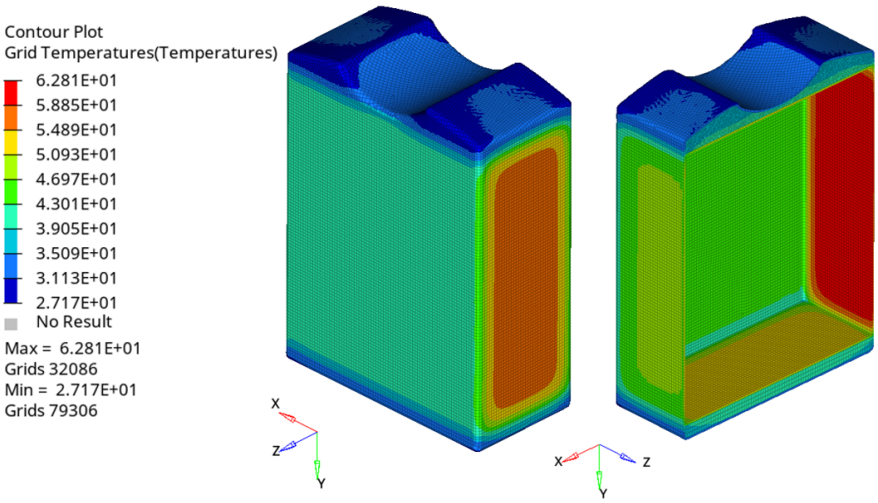

Figure 6.19: Temperature contour plot of the enclosure at timestep $t = 9.0 \times 10^4$ ms (90 seconds)

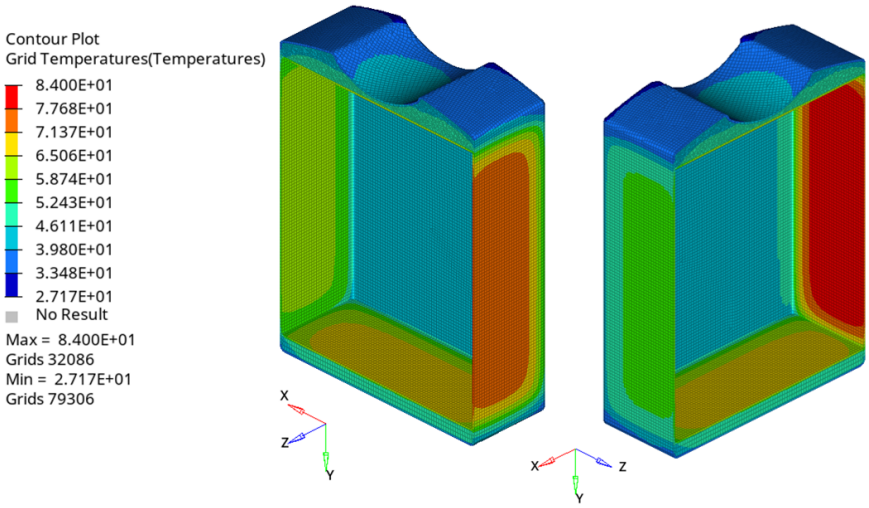

Figure 6.20: Temperature contour plot of the enclosure at the final timestep $t = 1.8 \times 10^6$ ms (30 minutes)

The results demonstrate the effectiveness of forced convection in reducing the enclosure temperature under continuous battery heat generation, with an external airflow of 40 km/h. Under identical heat dissipation power, the maximum temperature in the internal laminate decreases significantly, reaching approximately 80 °C.

All temperature curves reach steady-state conditions after roughly 7 minutes, showing stable final values. The temperature difference between the internal and external surfaces is more pronounced than in the free convection case, indicating improved heat transfer to the surrounding air.

Slightly higher temperatures are observed on one side of the enclosure, perpendicular to the x-axis, which results from the asymmetric airflow and lower convection efficiency on that face.

The internal surface reaches 60 °C after approximately 90 seconds, an improvement compared to the free convection case, although still above the defined acceptable temperature threshold for the enclosure.

Finally, Figure 6.21 illustrates the element heat flux distribution at the final timestep, highlighting the global heat flow behaviour throughout the structure.

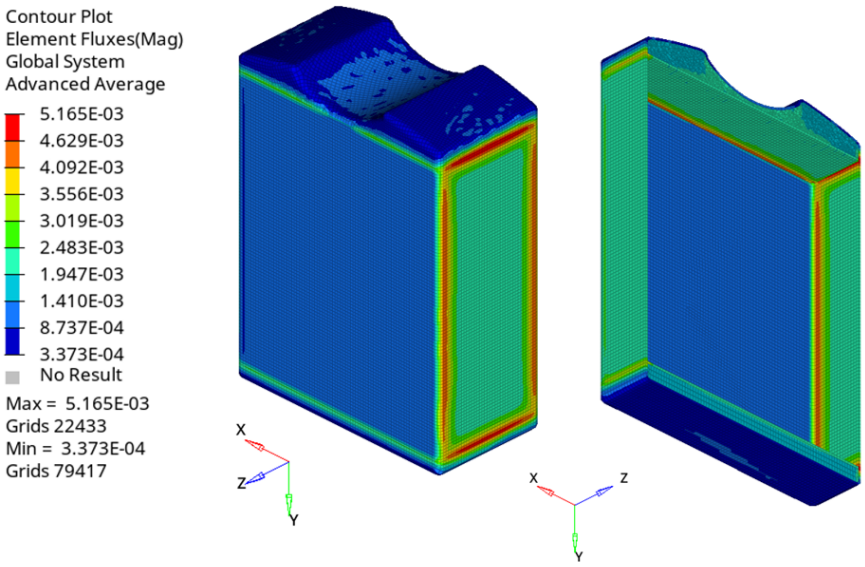

Figure 6.21: Element fluxes contour plot of the enclosure at the final timestep $t = 1.8 \times 10^6$ ms (30 minutes)

6.4.3 Result Takeaways

The results indicate that thermal simulations with higher values of external air temperature are unnecessary to assess the thermal performance of the enclosure, as it is already evident that its thermal management capabilities are insufficient and require improvement.

The results from the forced convection analyses demonstrate that forced air cooling has potential to regulate the temperature of the battery; however, it alone is not enough to ensure adequate thermal control. Even with an air velocity of 40 km/h, a relatively high value that represents a best-case scenario akin to the battery being directly exposed to ambient airflow, the internal temperature still exceeds acceptable levels. In reality, the battery is expected to be enclosed within the motorcycle structure, which would further limit airflow and significantly reduce the cooling effect.

To better contextualise these findings, a comparative simulation was carried out using the same model as the free convection case, but with aluminium thermal properties replacing those of the carbon fibre composite. The temperature contour of this model is presented in Figure 6.22.

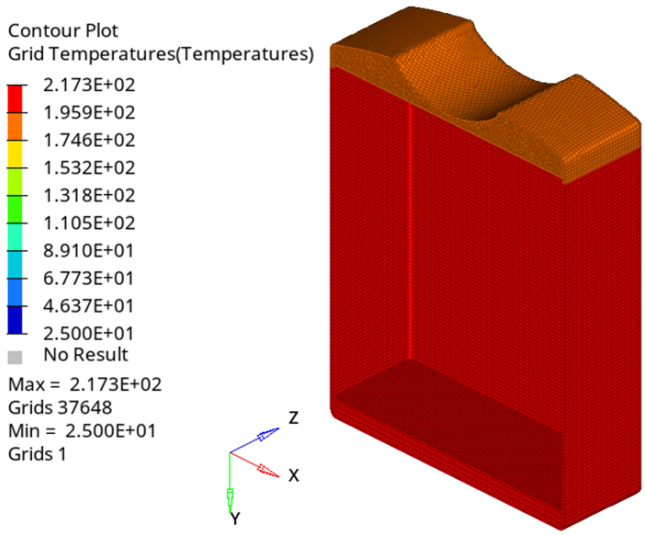

Figure 6.22: Temperature contour plot of aluminium enclosure model at the final timestep $t = 1.8 \times 10^6$ ms (30 minutes)

The results clearly show that a more thermally conductive material such as aluminium enables faster heat transfer and reduces peak temperatures. Nonetheless, even in this case, the maximum temperature remains above 200 °C. This reinforces the conclusion that the main limitation lies not in the conduction through the materials, but in convection as the sole mechanism of heat dissipation to the environment.

Maintaining appropriate battery cell temperatures is critical for performance, safety, and longevity. Elevated temperatures accelerate cell degradation, reduce charge efficiency, and can lead to irreversible damage or, in extreme cases, thermal runaway. Therefore, the implementation of effective thermal control systems is indispensable.

From the results obtained, it can be concluded that dedicated thermal management strategies must be considered for this battery enclosure. These may include both *passive* and *active* approaches. Passive methods could involve improving material conductivity, integrating thermal interface materials, or designing the structure to promote natural heat dissipation. Active solutions may include liquid cooling systems, internal air channels, or embedded heat pipes to control the internal temperature distribution more effectively. Given the poor thermal conductivity of both the laminated carbon fibre and the aluminium honeycomb core, relying solely on external airflow for cooling is unlikely to yield satisfactory results. An internal cooling approach, possibly integrated directly within the battery module, would likely offer greater efficiency. Additionally, implementing an energy management strategy that limits peak power usage or operating time under maximum load conditions could help regulate internal heat generation and extend battery lifespan.

It should also be noted that the available information regarding the battery system was extremely limited. Despite repeated requests for detailed data, including the type of cells, internal architecture, material composition, C-rate, discharge profiles, and integration details within the motorcycle, no meaningful information was provided. This lack of data significantly restricted

the scope and accuracy of the thermal analysis. As seen in the literature, notably in the study *"A Numerical Thermal Analysis of a Battery Pack in an Electric Motorbike Application"* by Shahjalal et al. [91], such parameters are essential to achieve realistic and representative thermal models.

In conclusion, the analyses presented were developed to the fullest extent possible with the limited data available. Although they offer valuable insights into the general thermal behaviour of the enclosure, the results should be interpreted with caution and viewed critically. The study highlights the urgent need for further investigation supported by detailed battery specifications and experimental validation to define an effective thermal management solution for this system.

Chapter 7

Design Validation of the Enclosure

The present chapter will delve into two independent validations of elements of the enclosure design presented and analysed under testing conditions in previous chapters. Both will be adequately presented, with a contextualisation and presentation of the finite element models created for each, followed by the analysis parameters and finishing with a study of the results.

7.1 Internal laminate study

7.1.1 Methodology

The first topic addressed in this chapter is the evaluation of different internal laminate configurations of the enclosure. For this purpose, the loading conditions of drop test n°1, which was previously identified as one of the most critical for the internal laminate, were repeated using exactly the same analysis setup, parameters, and pre-processing conditions. For an in-depth explanation of the finite element model and analysis parameters, refer to Chapter 5, Section 5.2.

The sole modification consisted of varying the internal laminate layup, testing two alternative configurations with 6 and 8 carbon-fibre plies in a similar quasi-isotropic layup. So, the three different internal laminate layups that are part of this analysis are :

- The original 4-ply internal layup with a resulting thickness of 1.12 mm: [45/0/-45/90];
- An alternative 6-ply internal layup with a resulting thickness of 1.68 mm: [+45/0/-45/-45/0/+45];
- An alternative 8-ply internal layup with a resulting thickness of 2.24 mm: [45/0/-45/90/90/-45/0/45]. This laminate is the same as the one used in the external laminate of the enclosure.

The objective of increasing the number of plies in the internal laminate is to enhance its structural resistance slightly, given that this component is one of the most highly solicited during the drop tests, and to further improve the enclosure's protective capacity for the battery. Laminates with more than eight plies were not considered, as this would represent an excessive material usage and would require additional space within the enclosure. Such a modification would either

reduce the size of the honeycomb cores or necessitate an overall increase in enclosure dimensions, both of which were deemed undesirable for the design

The results of these two simulations are subsequently compared with those of the original drop test nº1, allowing for the selection of the most suitable internal laminate configuration for the final design. The comparative assessment considers the maximum strain energy of each case, employed as an approximate indicator of crash energy absorption potential, as well as global displacements, stress distributions, and the associated weight of the laminate configurations. A detailed assessment of computational quality indicators and energy plot evolution was deemed unnecessary in this case, as all three simulations exhibit nearly identical behaviours. The variation in internal laminate configuration did not produce any significant influence on the energy plots or computational checks.

7.1.2 Result study

Table 7.1 provides a comparison between the 3 simulations in terms of peak internal energy.

Table 7.1: Energy absorption metrics for different internal laminates

	Peak E_{int} / J	**Var. (%)**	**% of $E_{\text{kin}}^{\text{max}}$**
Internal laminate			
4 plies	115.6		$\approx 78\%$
6 plies	120.0	$\approx +3.8\%$	$\approx 81\%$
8 plies	123.7	$\approx +7.0\%$	$\approx 83.5\%$

It can be verified that, as expected, an increase in internal laminate material results in a greater capacity to transform the impact energy from the drop test into internal strain energy. In particular, an 8-ply internal laminate shows a consequent increase of 7%, translating into an 83.5 % proportion of the kinetic energy of the assembly before impact.

Figures 7.1, 7.2, and 7.3 show the displacement, principal stress and shear stress state comparison of all three simulations at the instant of peak model deformation ($t = 1.5$ ms). The data is then organised and evaluated in Table 7.2.

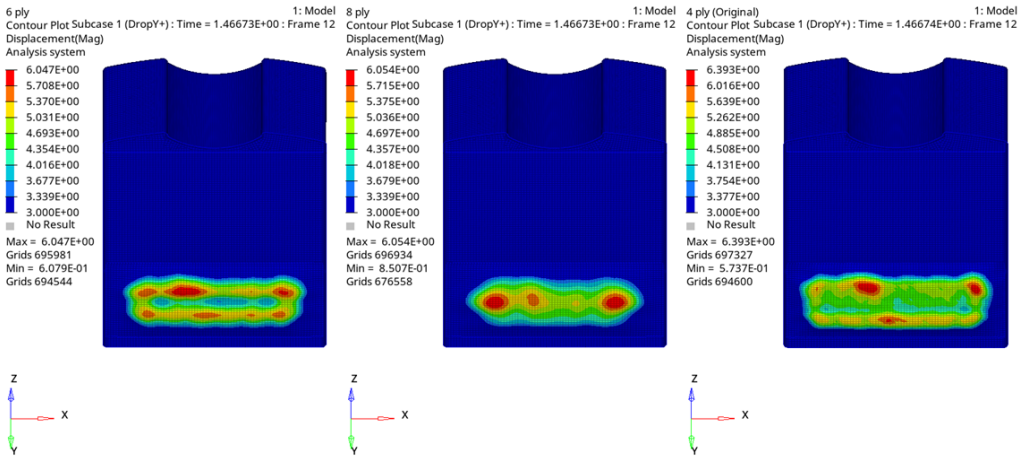

Figure 7.1: Deformation contour of the enclosure components, 6-ply, 8-ply and 4-ply internal laminates, from left to right, respectively

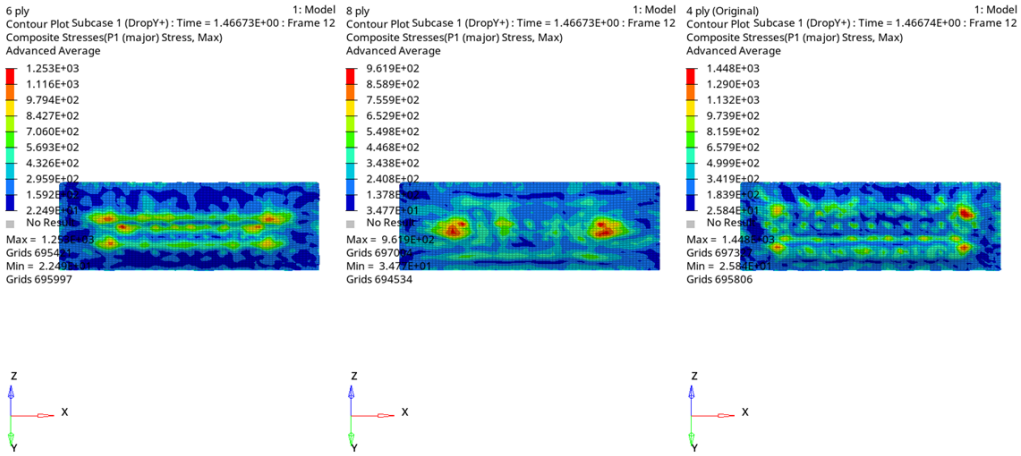

Figure 7.2: P_1 principal stress contour of the internal laminate, 6-ply, 8-ply and 4-ply internal laminates, from left to right, respectively

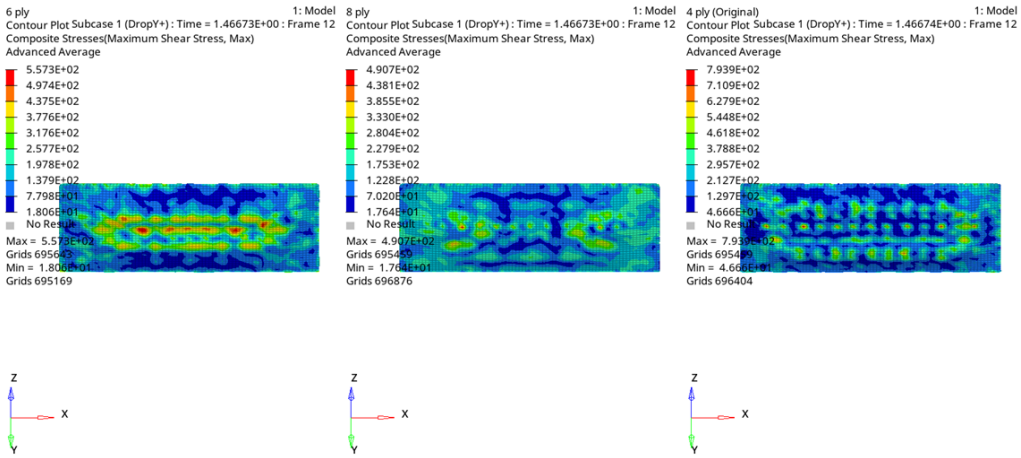

Figure 7.3: Maximum shear stress contour of the internal laminate, 6-ply, 8-ply and 4-ply internal laminates, from left to right, respectively

Table 7.2: Comparison of post-processing results of different internal laminates

		4 plies	**6 plies**		**8 plies**	
Deformation	Generalised / mm	2.5	2.2	(-12 %)	2.2	(-12 %)
	Peak / mm	3.4	3.05	(-10 %)	3.05	(-10 %)
Peak Stress	P_1 (major) principal stress (σ_{P1}) / MPa	1448	1253	(-13.5 %)	961.9	(-33 %)
	Maximum shear stress (τ_{max}) / MPa	793.9	557.3	(-30 %)	490.7	(-38 %)

As observed from the results, the overall behaviour of the system remains consistent with that of the original drop test simulation. The downward displacement pattern is preserved across all three cases, with the magnitudes of maximum displacement showing a clear trend. While the 4-ply laminate exhibits the highest displacement, both the 6-ply and 8-ply configurations present nearly identical maximum and generalised displacement values. These represent an approximate reduction of 10 % relative to the 4-ply case, a modest but meaningful improvement in structural stiffness and deformation control.

In terms of stress state, it is important to note that no post-processing considerations were applied to exclude local stress concentrations caused by modelling limitations. Instead, the absolute maximum values were taken for a direct and fair comparison between simulations. The results clearly demonstrate that increasing the number of plies in the internal laminate substantially reduces the stress levels. In particular, the 8-ply laminate shows a reduction of approximately 30 % in maximum principal stress and 40 % in maximum shear stress, representing a significant improvement in the mechanical resistance of the enclosure.

Table 7.3 compares the resulting enclosure and assembly (battery + enclosure) weight, considering each internal laminate variant.

Table 7.3: Comparison of the resulting enclosure mass for different internal laminates

Enclosure mass		
4 plies:	1.104 kg	-
6 plies:	1.150 kg	(+4.13 %)
8 plies:	1.173 kg	(+6.19 %)
Assembly mass		
4 plies:	15.104 kg	-
6 plies:	15.150 kg	(+0.30 %)
8 plies:	15.173 kg	(+0.45 %)

As it is logical, the above mass values consider the top and bottom laminates of the enclosure. The added material from the 6 and 8-ply internal laminates slightly increases the overall mass of the enclosure. Considering the enclosure alone, it results in a 4 % and 6 % increase, respectively. Nevertheless, the most meaningful comparison arises when the total weight of the assembly battery + enclosure is considered. Even with the added 8 plies of carbon fibre material for the heaviest case (8-ply internal laminate, 4 plies added for top and bottom, each), only a very small increase of 0.45 % is verified, a difference that is almost indetectable.

Concluding, taking into account the significant improvement in mechanical performance combined with an almost negligible weight penalty, an 8-ply internal laminate design was chosen for the final enclosure design.

7.2 Enclosure Handle Validation

This section presents the validation of the handle design developed for the battery enclosure prototype. It encompasses all stages of the process, from the initial design concept to the setup of a meaningful finite element analysis and the discussion of the resulting outcomes..

7.2.1 Handle Design

The battery enclosure design presented in Chapter 4 does not include any handle or feature to aid in carrying the battery enclosure. This was a deliberate decision, as the handle was conceived and designed only after the structural validation of the enclosure itself. This approach ensured that no redesigns would be required and, additionally, that the correct final mass of the battery assembly could be considered for the handle's design and validation.

Several handle concepts were evaluated, ranging from simple textile solutions to rigid structural alternatives. Ultimately, a lightweight, thin carbon-fibre handle was considered for validation. This choice aligns with the overall aesthetics of the enclosure, which is itself made of carbon fibre, and capitalises on Adamastor's expertise in composite materials, allowing the handle to be manufactured entirely in-house without the need for external suppliers. As will be seen, it is not the choice made for the final design, that being said, the validation of the composite handle was a valuable study.

To balance cost, weight, and performance, a thin but effective laminate configuration was adopted for the handle design. A five-ply symmetric layup of the same Toray E731 carbon fibre prepreg material, [45/0/90/0/-45], was chosen, combining aesthetic appeal with structural performance. The $\pm 45°$ plies provide interlaminar shear resistance and contribute to its characteristic composite appearance, while the 0° and 90° plies, in twill weave, deliver stiffness and bending load-bearing capability. This results in a balanced, efficient, and purposeful layup, suitable for the expected loading conditions during handling.

The handle is designed to be attached to the enclosure using bolted connections through two clearance holes located at each extremity of the handle, ensuring secure fastening, ease of assembly and replaceability. The final handle design is illustrated in Figure 7.4.

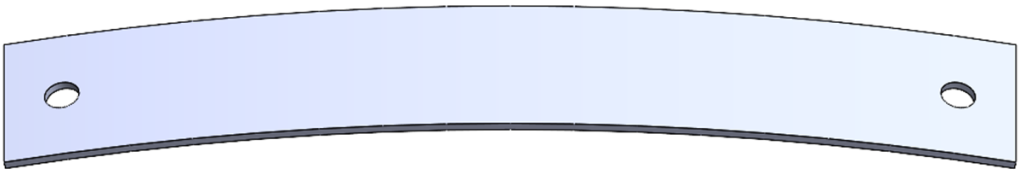

Figure 7.4: Simple handle CAD design in SolidWorks ®

To validate the performance of this handle, a finite element analysis was conducted, simulating conditions of lifting the battery enclosure with a single hand placed on the handle. The modelling approach, analysis parameters, and validation criteria are detailed in the following subsection.

7.2.2 Handle FEA Validation Setup

The process of creating the finite element model and analysis for the handle follows the same methodology previously described in Section 5.2. Consequently, the description presented in this chapter is intentionally more concise, focusing only on the aspects specific to the handle validation.

The same unit system previously adopted, as presented in Table 5.2, was used for this analysis.

In order to simplify and optimise the analysis with respect to computational cost, the inherent symmetry of the handle geometry was exploited. By taking advantage of this symmetry, it was possible to model and analyse only half of the handle, while still obtaining a representative stress and deformation response. This approach significantly reduces the number of elements in the finite element model, resulting in faster computation without compromising the accuracy of the results.

Accordingly, only half of the handle's surface geometry was imported into HyperMesh®. No modifications to the geometry were necessary, as the original CAD surface already met the meshing standards.

The meshing process consisted in an automatic Freeform 2D mesh with better-performing second-order shell elements. The element size was selected as 0.5 mm, ensuring a fine discretisation of the geometry with an excellent node density around the circular hole (Figure 7.6). Figure 7.5 shows the discretised handle geometry, and Table 7.4 lists the statistics of the mesh.

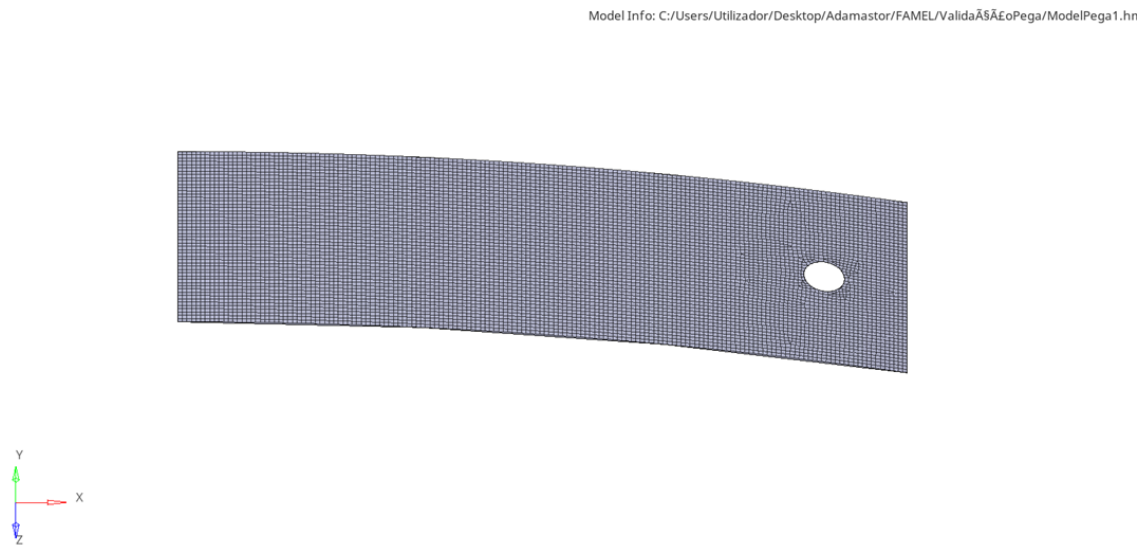

Figure 7.5: Discretised handle geometry

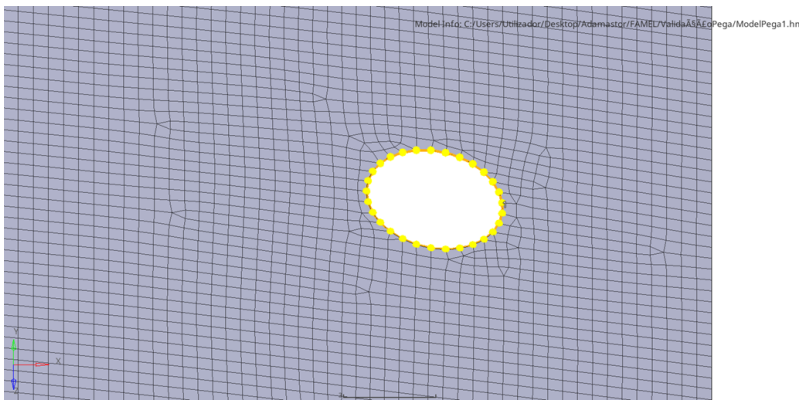

Figure 7.6: Nodal density around hole geometry

Table 7.4: Handle model mesh Statistics

Element Type		**Quantity**
2D Shell	QUAD8	8353
	TRIA6	25
Total Elements		8378
Total Nodes		25 563

The resulting mesh demonstrates an excellent detail discretisation, a continuous structure with good uniformity, and an overall reliance on `QUAD8` second-order elements, with a sensible use of `TRIA6` elements for mesh transition.

The following Figures 7.7, 7.8 and 7.9 provide the mesh quality metrics of the handle model in the same 3 criteria considered before: Quality Index, Jacobian matrix and Aspect Ratio.

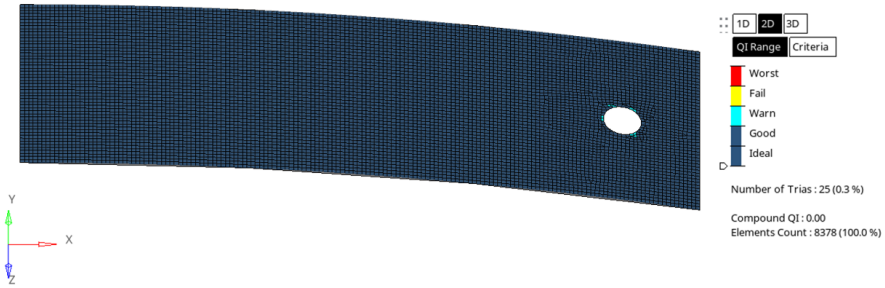

Figure 7.7: Quality Index (Q.I.) plot of handle mesh

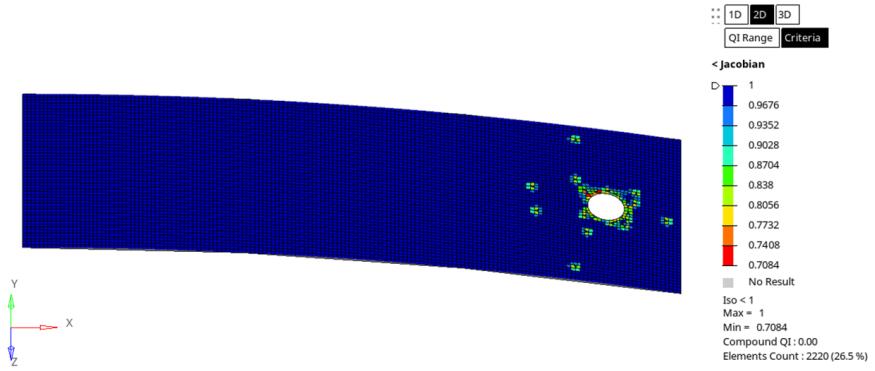

Figure 7.8: Jacobian matrix plot of handle mesh

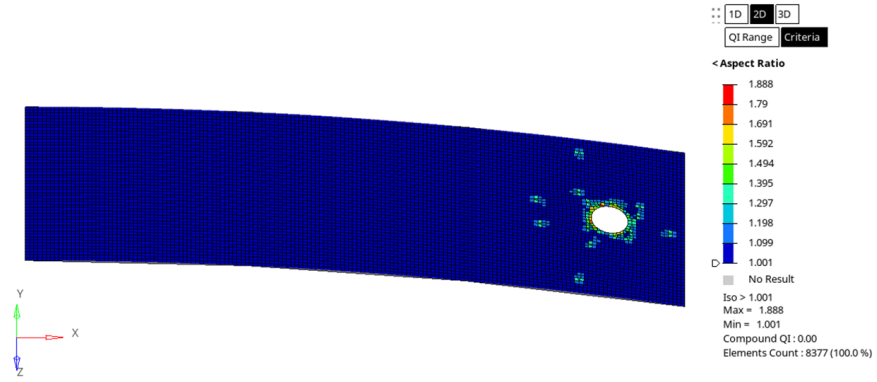

Figure 7.9: Aspect ratio plot of handle mesh

The element quality visualisation tool in HyperMesh® demonstrates that the handle shell mesh is up to the quality standards set in Subsection 5.2.2. All mesh quality metrics are met, and the excellent compound Q.I. value of 0.0 highlights the quality of the discretisation.

With the mesh created and validated, the materials and laminate were defined. The process was the same as seen earlier, the material, its orientation and normal, and the laminate were defined in the pre-processing software. Table 7.5 presents the handle laminate specification, and Figure 7.10 shows a close-up of the laminate in HyperMesh®.

Table 7.5: Handle laminate specifications

	Ply	Orientation / °	Thickness / mm	Material
Laminate				
1	ply1	45	0.28	E731 prepreg
2	ply2	0	0.28	E731 prepreg
3	ply3	90	0.28	E731 prepreg
4	ply4	0	0.28	E731 prepreg
5	ply5	-45	0.28	E731 prepreg
		Total:	1.40	

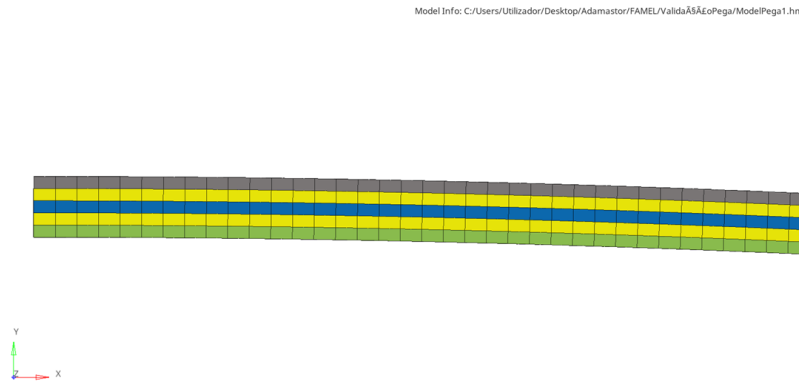

Figure 7.10: Handle laminate in HyperMesh®.

The load and boundary conditions defined to replicate the handling conditions of the enclosure and battery assembly to the composite handle model are illustrated in Figure 7.11.

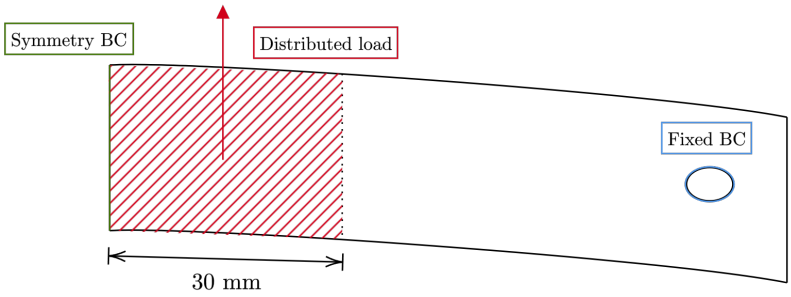

Figure 7.11: Schematic representation of the loads and boundary conditions applied

First, to replicate the fixing conditions in a simple yet effective manner, the nodes along the clearance hole were constrained through the use of `RBE2` rigid elements. A single independent node was created at the geometric centre of the clearance hole and fully constrained in all six degrees of freedom ($U_1 = U_2 = U_3 = U_4 = U_5 = U_6 = 0$). The `RBE2` element rigidly connects this independent node to all dependent nodes located on the edge of the clearance hole, thereby ensuring that no relative motion or rotation can occur at the hole boundary. This modelling approach is a computationally efficient way of reproducing the behaviour of a fully bolted connection, where the handle is securely fastened to the enclosure.

Figure 7.12 provides a visualisation of the clearance hole boundary conditions.

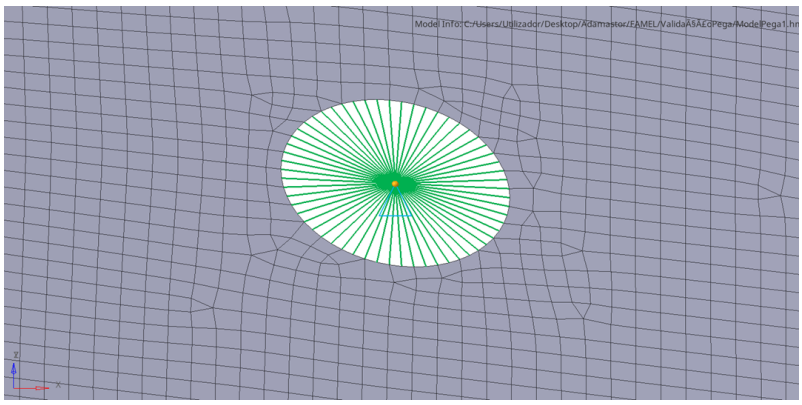

Figure 7.12: Close up of the boundary conditions in the handle clearance hole

Subsequently, the vertical load representing the force applied by a hand lifting the battery enclosure was applied as a distributed load. This load was uniformly distributed across the entire width of the handle and over a length of 30 mm, which approximately corresponds to half of the support area provided by four fingers during normal handling. The magnitude of this load was calculated as half of the total weight of the battery–enclosure assembly, in accordance with the

symmetry assumption adopted in the model, where only one half of the handle is simulated. The total load to be distributed is then, considering a weight of battery-enclosure assembly of 15.2 kg:

$$W(1/2 \text{ enclosure}) = \frac{1}{2} \times 15.2 \times 9.81 = 74.556 \text{ N} \tag{7.1}$$

Finally, to correctly represent the symmetry of the model and avoid introducing spurious deformations, symmetry boundary conditions were imposed along the plane of symmetry. Since the handle was cut along the y–z plane, with the edge of symmetry aligned with the z-axis, the following constraints were applied to all nodes lying on this edge: zero displacement in the x-direction ($U_1 = 0$), and zero rotations about the x- and z-axes ($U_4 = U_6 = 0$). These conditions effectively mirror the structural response of the half-handle about the plane of symmetry, reproducing the behaviour of the complete handle under loading while halving the computational cost of the analysis.

Figure 7.13 provides a visualisation of the applied symmetry conditions and distributed load to the handle model.

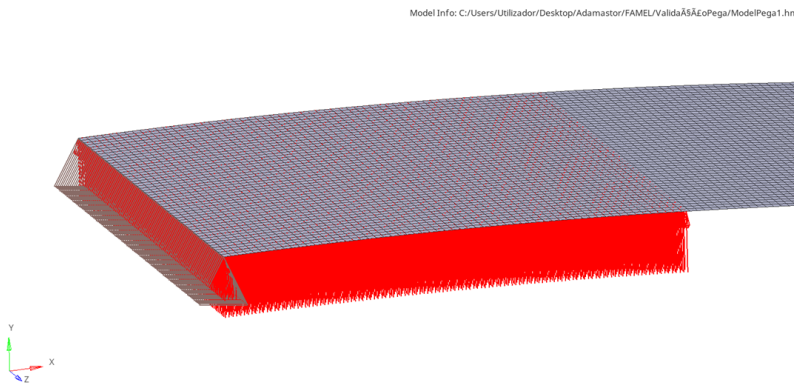

Figure 7.13: Distributed load and symmetry boundary conditions applied to the model

For this simulation, a nonlinear static analysis was utilised, as the applied loading is quasi-static. This approach allows the solver to account for possible geometric nonlinearities that can occur in thin composite shell structures, ensuring a more accurate prediction of displacements and stresses. A small-displacement formulation was adopted to reduce computational cost, and the 5 % rule of thumb strain criterion will later be verified to confirm its validity. If exceeded, the setup can be easily adapted to a large-displacement formulation.

To evaluate the structural integrity of the laminate, the Tsai–Wu failure criterion was applied, as this criterion is particularly suited for multidirectional laminates such as the layup defined for this component.

7.2.3 Analysis Results

First thing worth verifying from the results of the analysis is the overall deformation behaviour of the handle under load. It is particularly important in a case such as this one, where only half of the geometry was modelled, a verification of the overall physical behaviour allows to ensure the correct choice of symmetry boundary conditions. The deformation behaviour of the handle in post-processing can be visualised in Figure 7.14, a scale of 2 and symmetry was applied to the handle along its symmetry edge to aid in the analysis.

Figure 7.14: Deformation behaviour of the handle under analysis (Scale:2.0)

The handle exhibits the correct deformation behaviour, ensuring accurate load calculation and continuity along its symmetry edge. For all following post-processing images, the model is represented in true scale.

Figure 7.15 provides the displacement contour plot of the model.

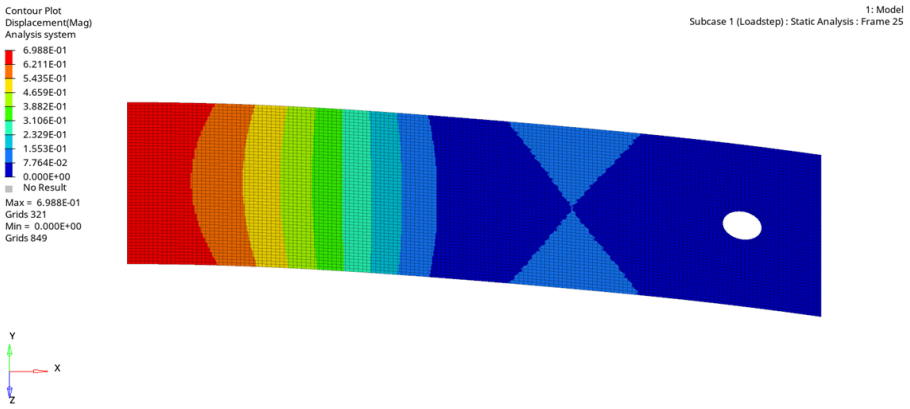

Figure 7.15: Displacement contour of the handle under analysis

The handle shows a very low peak displacement, localised at the middle of the complete handle or at the edge of the half-handle geometry, confirming the overall stiffness of the carbon fibre handle. Figure 7.16 provides the principal composite strain contour plot of the handle under load.

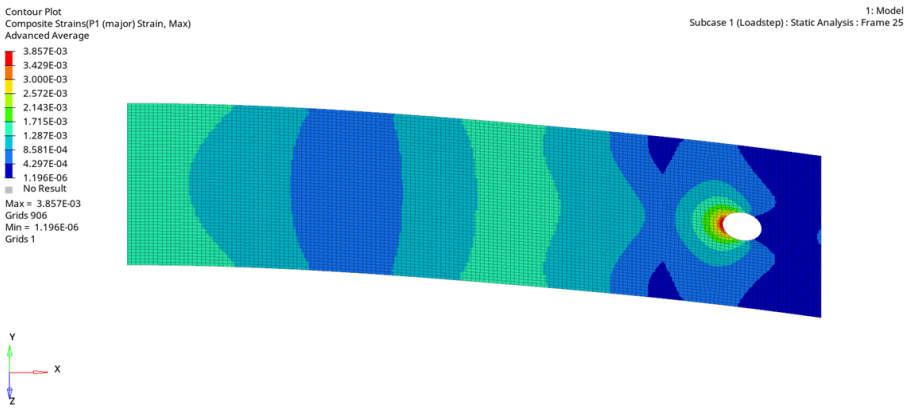

Figure 7.16: P_1 (major) principal strain countour plot of the model under analysis

It can be seen that there is a concentration of strain around the constrained hole of the handle, which is expected since such geometries are notable stress and strain concentration regions. Also, the maximum principal strain value of around 0.4 % validates the choice of a Small Displacement Nonlinear Static Analysis.

The following Figures 7.17 and 7.18 provide the plot of Tsai-Wu and Bond Failure indices.

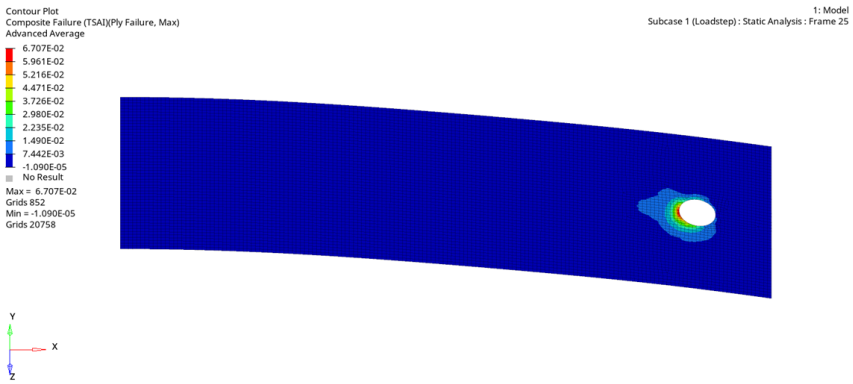

Figure 7.17: Tsai-Wu composite failure index contour plot of the handle under analysis

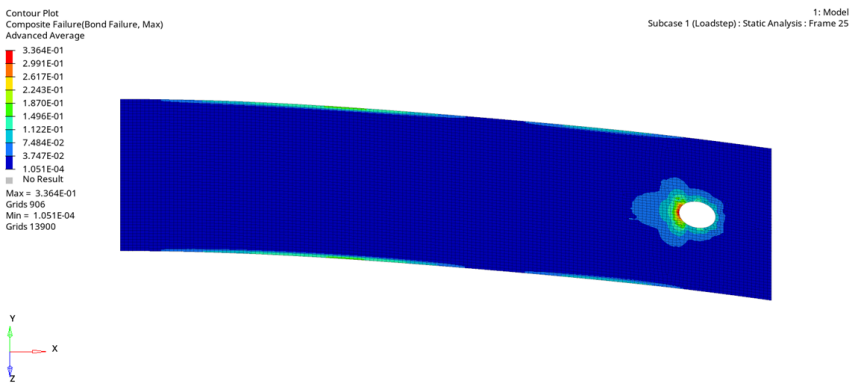

Figure 7.18: Composite bond failure index contour plot results

Failure indices are the most effective means of assessing the structural state of composite components, making their evaluation essential. The Tsai–Wu failure index, which indicates the likelihood of ply-level failure, was used in the present study. The contour plot above shows very low index values, with a maximum of 0.067, concentrated around the most critical location at the edge of the fastening hole. Considering that failure is only expected when the index approaches unity, this result demonstrates a very comfortable safety margin.

In parallel, bond failure indices were also examined. These indices represent the risk of delamination between plies and are directly associated with interlaminar shear stresses exceeding the bonding material's shear strength. Unlike ply failure mechanisms such as fibre breakage or matrix cracking, bond failure is a distinct interlaminar phenomenon. The contour plot highlights the same critical region near the fastening hole, with a maximum value of approximately 0.34, again well below the threshold for failure. Additional values around 0.2 are observed on either side of the handle, in the curved transition zones where bending produces elevated shear stresses. Although these areas indicate geometrically sensitive regions for potential delamination, the results confirm that under the present loading conditions, the structure remains far from critical.

Figure 7.19 provides the major principal stress plot results.

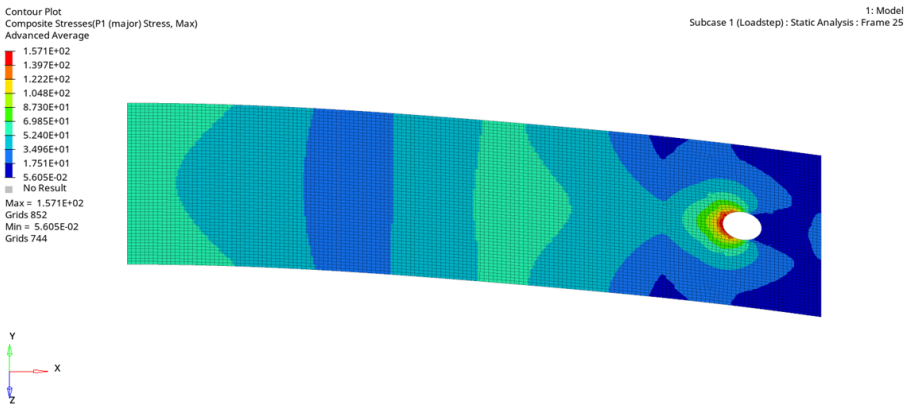

Figure 7.19: Maximum P_1 principal composite stress contour plot results

The resulting maximum value is well under the acceptable range, which translates to a very high safety factor value of:

$$S.F.\,(\sigma_{P1}) = \frac{705}{157.1} \approx 4.5$$

.

The following Figure 7.20 shows the maximum shear stress plot of the handle under loading conditions.

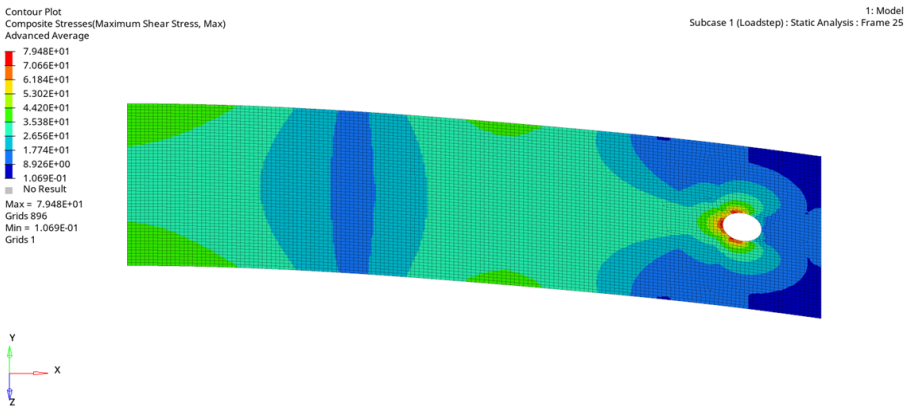

Figure 7.20: Maximum shear stress contour plot results

Here again, it is verified that the shear stress values remain below the elastic threshold and are concentrated around the hole. In this case, however, the margin is more limited, with a resulting safety factor of :

$$S.F.\,(\tau_{\max}) = \frac{119}{79.48} \approx 1.5$$

This value is generally acceptable in the design of composite structures, though it would be preferable to achieve a higher safety margin to further enhance reliability.

The following Figures 7.21 and 7.22 provide the interlaminar shear stress contour plots, $1Z$ and $2Z$, respectively.

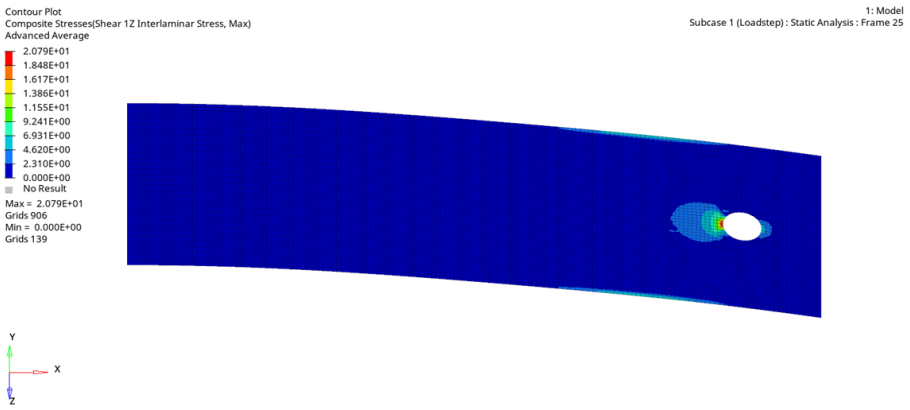

Figure 7.21: Maximum $1Z$ interlaminar shear stress contour plot results

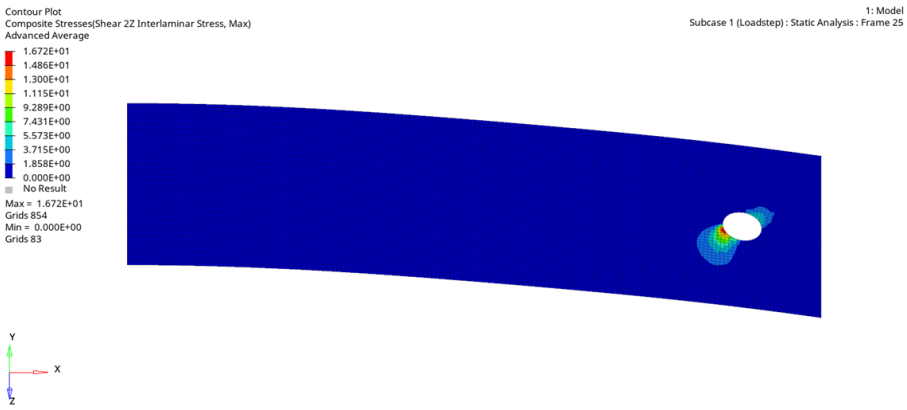

Figure 7.22: Maximum $2Z$ interlaminar shear stress contour plot results

Once again, interlaminar shear stress values show similar plots and values well inside the safety range with a resulting factor of:

$$S.F.\,(\tau_{1Z}) = \frac{61.8}{20.79} \approx 3$$

This safety factor refers to interlaminar shear stress $1Z$, the lowest safety factor of both maximum interlaminar stresses.

7.2.4 Handle Validation Conclusion

The validation results show that the handle exhibits very low deformation values and are fully consistent with the expected realistic behaviour of such a component. The results also confirm the adequacy of employing a small-displacement nonlinear static analysis, which proved well-suited for this type of structural assessment.

Failure indices indicate that the handle should perform effectively under the intended loading conditions. Likewise, the stress analysis confirmed that all values remain below critical thresholds with adequate safety margins. The only point requiring attention is the shear stress response, which approaches the limit more closely, resulting in a safety factor of approximately 1.5. While this value is generally acceptable for advanced composite applications, it may be prudent to introduce a modest reinforcement, either by adding plies in the vicinity of the clearance holes or by slightly increasing the overall laminate thickness, to achieve a higher safety margin, closer to 2.0, as recommended in the literature [11].

In conclusion, the carbon fibre composite handle design can be considered validated. Although a minor optimisation around the hole region could further strengthen the designs. Though this optimisation avenue will not be necessary, as will be seen later.

Chapter 8

Optimised Design of the Prototype Enclosure

After analysing the mechanical performance of the initial prototype battery enclosure and identifying the critical load cases affecting its structural integrity, this chapter presents an optimised enclosure design. It begins with a review of the critical areas identified in the initial configuration, followed by the presentation of the proposed design improvements.

8.1 Review of the Critical Areas of Design

As discussed in Chapter 5, the drop test impact load cases were identified as the most demanding conditions for the external composite laminate. The results revealed particularly high stress and strain levels in the regions affected by the battery assembly's impact with the ground, especially when the contact area was reduced, as occurs in drops involving an edge or a vertex of the enclosure. In these scenarios, the initial design of the enclosure is expected to experience complete laminate failure and fracture. Situations in which the outer shell fails entirely, leaving the battery and its components exposed to the environment, must therefore be strictly avoided.

To mitigate these weaknesses, a design optimisation process was carried out, involving targeted design modifications to strengthen critical regions of the enclosure and improve its impact resistance. The main objective was to locally increase the laminate thickness in the areas where failure was predicted to occur in the original design, thereby enhancing stiffness and energy absorption capability. The addition of material in these critical regions is expected to improve the overall impact resistance of the enclosure, ensuring that even under the most severe impact conditions, only partial ply failure occurs, rather than complete laminate rupture, thus maintaining the protection of the internal components from external exposure.

It should be clarified that the "optimisation" referred to in this context does not correspond to a numerical layup optimisation process, such as the composite layup optimisation methodology described in Chapter 2. Such a method was not deemed advantageous in this case for several reasons. First, a minimum laminate thickness of 2 mm was required throughout the enclosure to

guarantee a basic level of fire resistance, ensuring that the material would take longer to ignite when exposed to flames. Moreover, traditional laminate optimisation techniques typically aim to minimise weight or maximise stiffness through the addition of high-cost carbon fibre reinforcements in selected regions. The solution proposed here, while also aiming to improve stiffness and impact resistance, was developed to achieve these objectives through a more cost-effective approach, as will be detailed later in this chapter.

The drop test orientations identified as critical for the external composite laminate were orientations 3, 4, 5, and 7, all of which correspond to impacts on reduced contact areas such as edges or vertices. Based on the results obtained for maximum shear stress and P_1 major principal stress at the instants of peak material solicitation, contour plots were filtered to distinguish between safe and critical regions, based on the allowable stress values of the E731 carbon fibre prepreg material, in Table 4.1. In these plots, areas where the laminate is not expected to fail are represented in greyscale, while the regions with higher probability of failure are highlighted in colour. This visual distinction enables clear identification of the areas requiring structural reinforcement.

Figures 8.1, 8.2, 8.3, and 8.4 present the filtered contour plots that illustrate the critical areas of the enclosure corresponding to drop orientations 4, 5, 7, and 3, respectively.

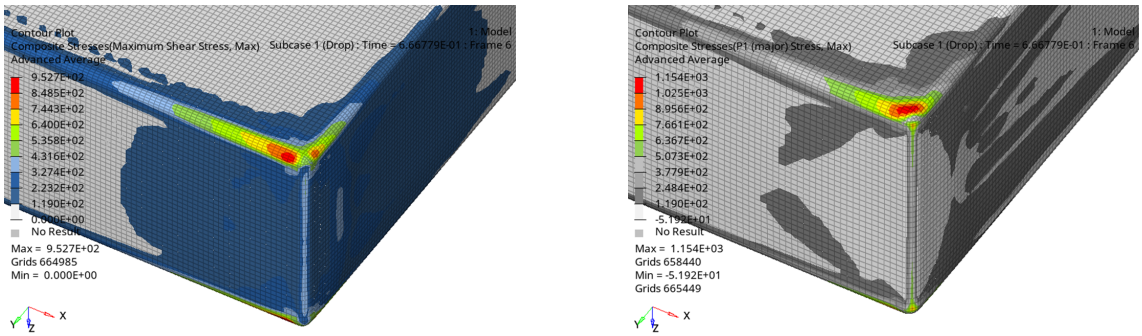

(a) Maximum shear stress (b) P_1 major principal stress

Figure 8.1: Filtered contour plots results from drop test orientation n°4

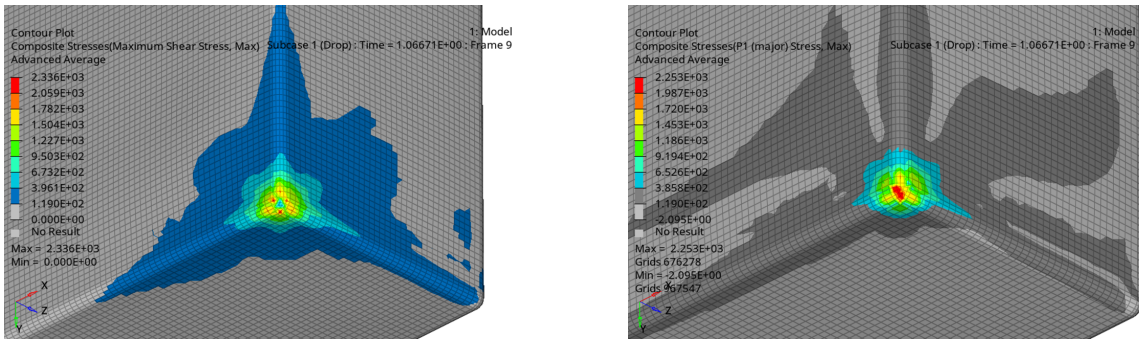

(a) Maximum shear stress (b) P_1 major principal stress

Figure 8.2: Filtered contour plots results from drop test orientation n°5

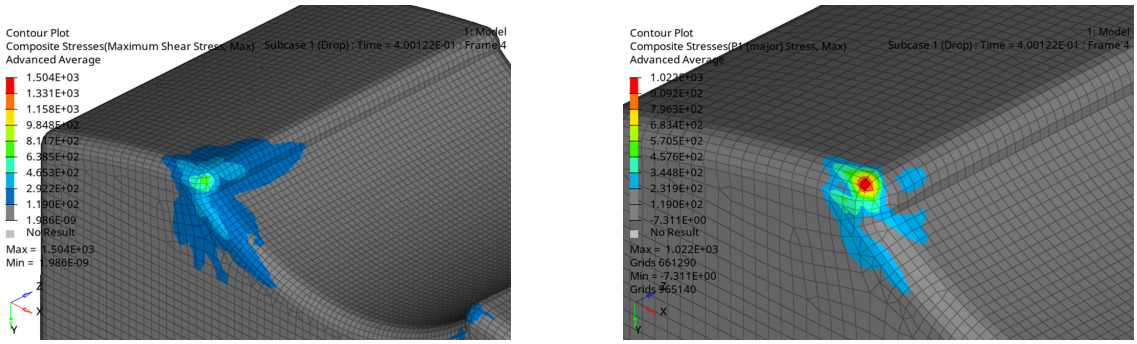

(a) Maximum shear stress (b) P_1 major principal stress

Figure 8.3: Filtered contour plots results from drop test orientation nº7

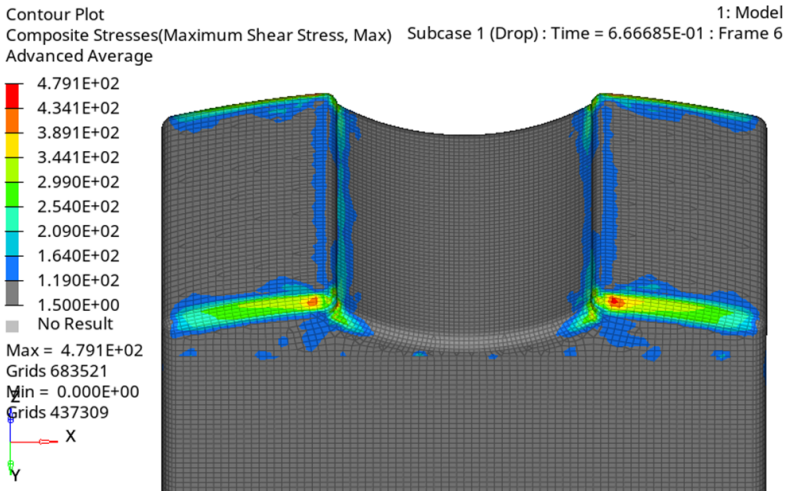

Figure 8.4: Maximum shear stress filtered contour plot results from drop test orientation nº3

The results presented indicate that, under the most critical drop test conditions, the highest stress values, exceeding the material's allowable limits, are concentrated primarily around the enclosure's edges and vertices, following its geometric contours.

From these contour plots, the dimensions of the critical regions were determined. Considering the available internal space within the original enclosure design suitable for incorporating local laminate reinforcements, the zones highlighted in Figure 8.5 were identified as the most appropriate areas to reinforce. These regions define the overall outline of the reinforcement layout adopted for the optimised design.

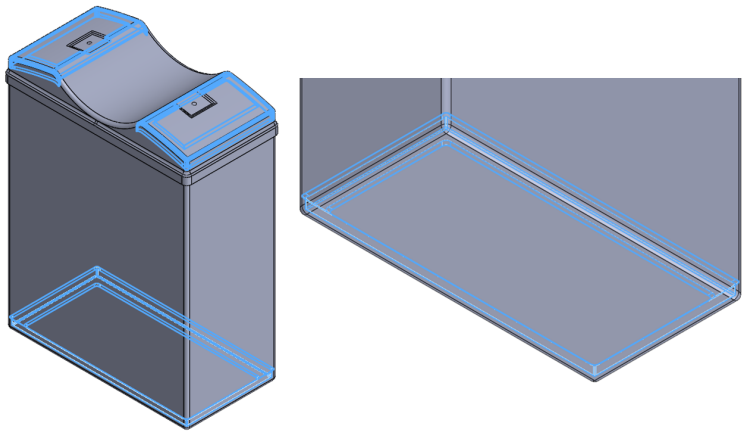

Figure 8.5: Outline of reinforcements defined for the optimised enclosure design

Since the central portion of the enclosure closely envelops the battery, no additional space is available in this region to introduce reinforcements within the laminate. Therefore, the upper and lower edge zones of the enclosure were selected for reinforcement. These are also the areas most likely to experience impact in realistic drop or fall scenarios. Moreover, the top and bottom regions of the enclosure offer sufficient volume to accommodate thicker laminate sections by slightly reducing the space initially allocated for the aluminium honeycomb core, without significantly affecting its structural or energy-absorbing function. The concept, geometry, and integration of these reinforcements within the laminate and overall enclosure design are detailed in the following subsection.

8.2 Optimised Design

The reinforcements were designed in SolidWorks® and subsequently integrated into the final CAD model.

Figure 8.6 presents the optimised prototype of the enclosure in an exploded view, showing the external laminate reinforcements with the honeycomb structures.

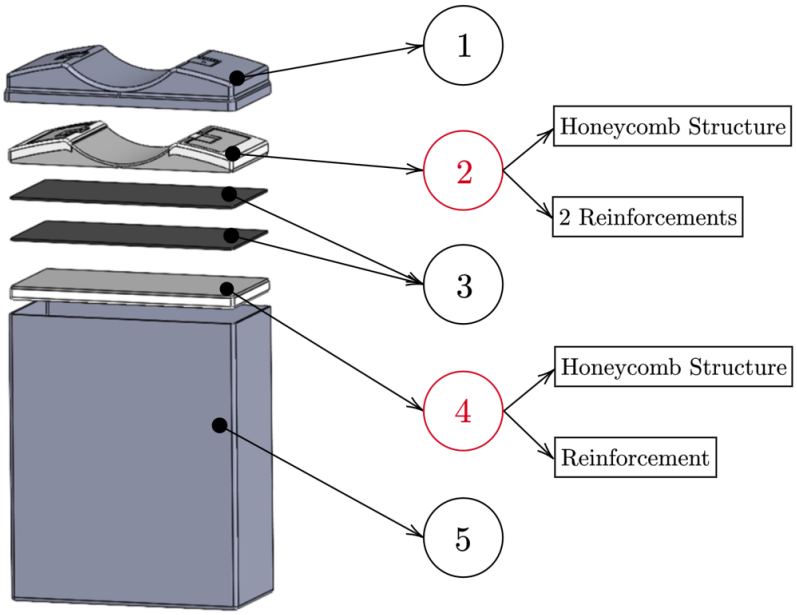

Figure 8.6: Optimised enclosure prototype design with the reinforcement integrated into it, along with the honeycomb structures

It should be noted that some additional details in the upper portion of the enclosure were not present in the initial design. These will be discussed in the next chapter, within the **Design for Production** phase.

To better understand the configuration of the optimised design in Figure 8.6, each component is described as follows:

1. **Top External Laminate:** identical to the component in the initial design, functioning as the top lid. It is manufactured from the same quasi-isotropic, symmetric laminate of E731 prepreg ($[45/0/\text{-}45/90]_S$), resulting in a total thickness of approximately 2.24 mm.

2. **Top Honeycomb Core and Reinforcements:** although represented under the same index, these are distinct components. The honeycomb structure is produced from the same 6.4 mm cell 3003 Aluminium Series Honeycomb material.

   Two identical reinforcements were designed to follow the edge geometry of the top portion of the enclosure, precisely positioned at the mid-plane of the symmetric external laminate. Thus, half of the laminate plies are laid above and half below the reinforcement— , four plies on each side. Each reinforcement is 2 mm thick and manufactured by 3D printing using a high-performance filament: Nylon (Poliamide) reinforced with glass fibre (PA6 + GF). The resulting laminate thickness in the reinforced zones is approximately 4.24 mm.

   This material offers excellent impact resistance and an advantageous balance between hardness and mechanical strength. Furthermore, it provides high thermal resistance, making it particularly suitable for this application [92].

The reinforcement concept, developed to optimise impact resistance, draws inspiration from the design philosophy employed in crash-critical structures of the Adamastor Furia supercar. In that context, thick 3D-printed inserts are embedded within composite laminates, functioning as lightweight, stiff, and crash-absorbing sandwich cores, at a lower cost compared to adding additional layers of carbon fibre reinforcement.

The reinforcement geometry was designed to integrate seamlessly with the enclosure, maintaining proper offsets between the honeycomb core and the outer laminate. As a result, the reinforcement remains fully embedded and invisible in the finished prototype.

To incorporate these reinforcements, slight modifications were made to the honeycomb geometry, removing the material volume corresponding to the reinforcement interface with the bottom laminate.

Figure 8.7 shows the reinforcement geometry in white, representing the PA6 + GF components.

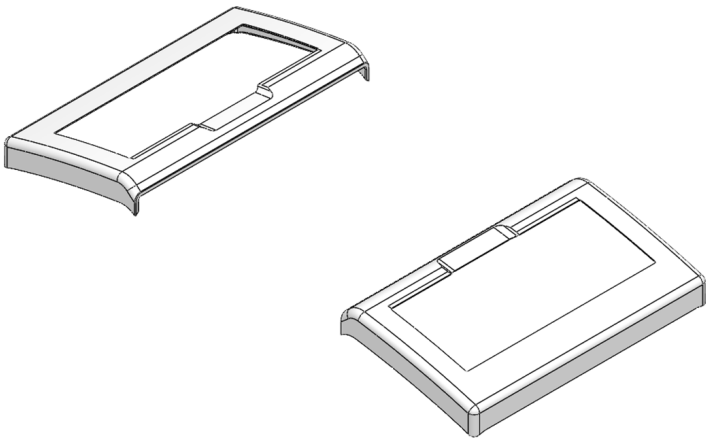

Figure 8.7: Top reinforcement CAD model

3. **Internal Laminates:** analogous to those of the initial design. In this optimised version, however, the internal laminate adopts the same 8-ply stacking sequence as the external laminate ($[45/0/\text{-}45/90]_S$), as defined in Chapter 7, Section 7.1, resulting in a thickness of approximately 2.24 mm.

4. **Bottom Honeycomb Core and Reinforcement:** again, distinct components represented under the same index. The honeycomb core is the same 6.4 mm cell 3003 Aluminium Series Honeycomb.

   The bottom reinforcement follows the enclosure's lower edge geometry and follows the same design logic as the upper one: a 2 mm thick PA6 + GF insert integrated within the external laminate. The CAD model of the bottom reinforcement is shown in Figure 8.8.

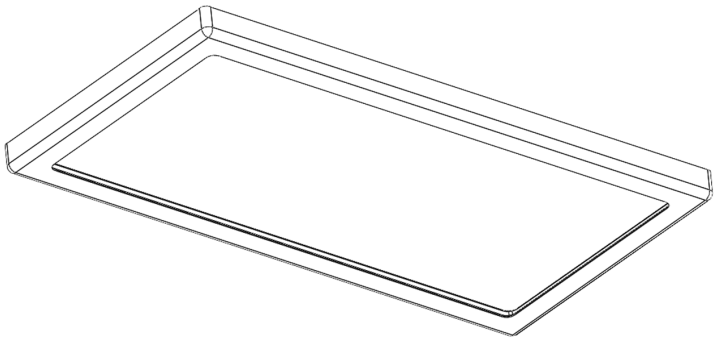

Figure 8.8: Bottom reinforcement CAD model

5. **Bottom External Laminate:** equivalent to the component in the initial design, acting as the main structural part of the enclosure. It is made from the same laminate material as the top component, with the bottom reinforcements integrated within it.

To better illustrate the integration of the 3D-printed reinforcements into the enclosure laminate, Figure 8.9 presents the carbon fibre plies represented as lines corresponding to the mid-plane of each ply. The plies located above the reinforcement are coloured black, while those below are represented in blue.

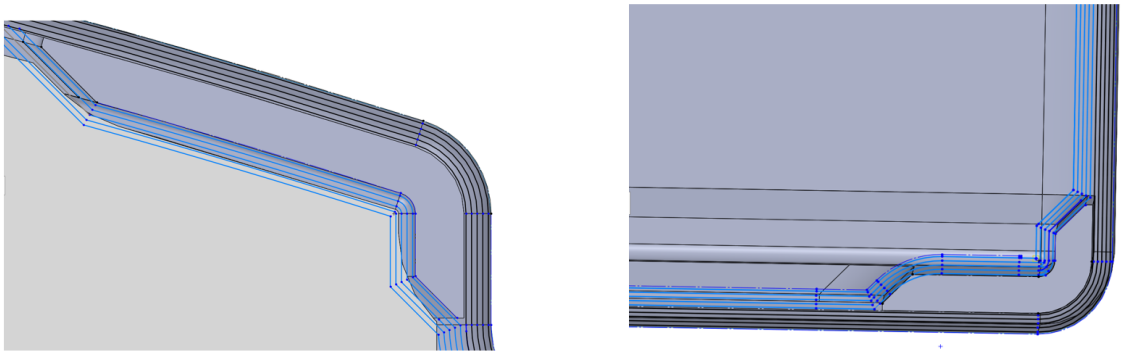

(a) Top reinforcement

(b) Bottom reinforcement

Figure 8.9: Illustration of the integration of the reinforcements into the external enclosure laminate

This representation clearly shows that the reinforcements act as thin cores within the laminate, functioning similarly to sandwich structures that significantly increase stiffness and impact resistance.

The reinforcement geometry was specifically designed with 45° edge transitions between the two laminate halves, ensuring a smooth connection and avoiding the creation of voids or resin-rich zones that could weaken the laminate or promote delamination.

The use of 3D printing for the reinforcements is particularly suitable for the prototype phase of this project, as it allows for the rapid production of complex geometries and precise integration within the laminate. However, if the enclosure design proceeds to mass production, an alternative

manufacturing approach should be considered to ensure feasibility in terms of cost and production time. In that scenario, the reinforcement material may also need to be revised to align with industrial manufacturing constraints.

Chapter 9

Production of the Enclosure Prototype

This chapter presents the complete production process of the prototype, detailing all stages of manufacturing. It begins with a description of the final prototype design taken into production, outlining the modifications made to the optimised design, the encountered challenges, and the reasons that led to the redesign. Subsequently, the design, machining, and preparation of the moulds used in production are discussed, followed by a brief overview of the manufacturing of the 3D-printed internal components of the enclosure. Finally, a complete description of the manual prepreg layup process is provided, covering ply nesting preparation, cutting, layup sequence, autoclave curing, and the final finishing operations leading to the completed prototype.

The author would like to acknowledge the invaluable support of the entire Adamastor team, whose contributions were essential throughout the preparation and execution of the production process. While the author was responsible for all aspects of the design work, under the guidance and collaboration of several team members, the definition of machining sequences, CNC machining operations, preparation of 3D-printed components, and the nesting and ply cutting stages were carried out by different members of the team. The author was present during every step of the process, both to learn and to provide input when relevant. The manual operations of mould preparation and ply layup were performed by experienced Adamastor technicians, as these require specific practical expertise. Nonetheless, the author actively participated in these stages, assisting with ply cutting, layup sequence definition, and general support tasks.

Although not everything proceeded according to plan, due to both minor errors and unforeseen setbacks, the overall process was successfully completed, culminating in the fabrication of the composite enclosure prototype.

9.1 Design for Production

9.1.1 Design changes

9.1.1.1 New Battery

After completing the optimised design, several minor modifications were introduced to incorporate final functional features, such as the connection system between the top lid and the main body of the enclosure, as well as the integration of the handle previously validated in Chapter 7. The updated design was then submitted to Famel for verification, ensuring compliance with their functional requirements and compatibility with the prototype electric motorcycle, particularly regarding the maximum external dimensions, which had not been specified.

Following this review, Famel requested a last-minute modification related to the battery for which the enclosure was designed. The initial design had been developed for a battery and associated components with dimensions of $277 \times 234.9 \times 115$ mm^3, whereas the new specified internal volume was $280 \times 224 \times 136$ mm^3. This represented an approximate 14% increase in the required internal volume compared to the original design.

Additionally, Famel requested that the total height of the enclosure be reduced by 12 to 15 mm, as measured from the top of the handle, resulting in a target total height between 316 and 319 mm, ignoring the handle. The other external dimensions, length and width, were deemed acceptable. This height reduction posed a significant challenge, as it could only be achieved by decreasing the thickness of the aluminium honeycomb crash-absorbing structures. Preliminary design adjustments indicated that accommodating both the increased internal height (by 3 mm) and the reduced overall height (by 12 mm) would require a total reduction of 15 mm in the honeycomb thickness, effectively halving it and compromising its intended protective function.

To identify a viable solution that maintained the structural integrity and functionality of the enclosure, the new battery unit was temporarily provided by Famel for direct measurement and evaluation. This allowed for a reassessment of the internal space requirements and the development of a design revision capable of housing the updated battery while preserving the effectiveness of the crash-absorbing structures. The battery provided by Famel is shown in Figure 9.1.

Figure 9.1: Battery provided by Famel for dimensional verification

Ultimately, the measured dimensions revealed that Famel's initial height estimate had been overstated, allowing for a design solution that met all functional and dimensional requirements without compromising the integrity of the protective structures. The dimensions of the battery are: $244 \times 223 \times 136$, and a solution to leave space for the cables and external connector was found in a support for the battery. This will be explained ahead.

9.1.1.2 Aluminium Honeycomb Machining

Another design aspect that required careful reconsideration was the creation of the honeycomb structures, particularly the top honeycomb, which presented a complex three-dimensional geometry. Two possible manufacturing approaches were evaluated. The first involved forming the shape directly from a thick, constant-area honeycomb panel. However, this method posed significant risks of crushing and local buckling of the thin cell walls, compromising both dimensional accuracy and mechanical performance. The second approach involved CNC machining the honeycomb to achieve the desired geometry.

Machining such a fragile aluminium structure presents considerable challenges, including severe defects caused by crushing, melting of thin cell walls due to tool friction, difficulties in properly fixing the material to the CNC bed, and the general complexity of accurately shaping the structure. To assess the feasibility of this option, an extensive review of specialised tooling solutions for honeycomb machining was performed [93, 94], along with fixation methods [95] and material preparation techniques designed to improve machinability. Among these, the use of sacrificial or soluble cores, such as AquaCore™ and AquaPour™ materials, was considered. These materials can be cast into the honeycomb cells to provide temporary support, machined as if solid, and subsequently dissolved in water [96].

Further investigation included the analysis of alternative machining methods and experimental research on improved parameters and techniques, such as ice fixation and machining parameter optimisation, as discussed in the following studies [97–100]. These methods can offer improved

dimensional control but also introduce new complications related to temperature control, material handling, and equipment safety. For instance, techniques involving ice or paraffin fixation would require maintaining low temperatures to prevent premature melting, potentially leading to water ingress, contamination, and damage to the CNC machine or cutting tools.

Ultimately, although CNC machining of aluminium honeycomb was initially considered, the combination of factors, including the lack of appropriate tooling, reliable fixation methods, and the limitations of a three-axis CNC machine primarily intended for epoxy mould machining, rendered the process unfeasible within the project's timeframe. Given the potential material waste, experimental uncertainty, and risk to equipment, an alternative manufacturing approach for the top honeycomb structure was therefore adopted.

9.1.1.3 E731 Prepreg carbon fibre

The prepreg material initially considered during the design phase was the Toray® E731 series, with the following full designation: **E731-00 HS2238 Carbon TR30S 245 gsm 2 × 2 Twill 3K 42% RC**.

However, the material available at Adamastor's facilities at the time of production was a slightly different variant: **E731-00 HS0838 Carbon TR30S 205 gsm 2 × 2 Twill 3K 40% RC**. Although both may appear identical, they differ in some aspects. They share the same Mitsubishi TR30S 3K fibres, the same E731 resin system, and a nearly identical resin content (42% vs. 40%), but the areal weight of the reinforcement fabric differs slightly, from 245 gsm to 205 gsm. This change implies that each ply of the 205 gsm prepreg contains less fibre material, resulting in thinner cured plies. According to Toray's Ply Thickness Calculator, the cured ply thickness for the 205 gsm prepreg is approximately 0.219 mm, compared to 0.28 mm for the 245 gsm version.

Since both materials use the same fibres and resin, laminates with equal total thickness are expected to exhibit identical mechanical and thermal properties. To validate this, E731 specimens were manufactured under the same autoclave curing conditions as the enclosure, for UL 94 fire resistance testing (Chapter 10). Laminates with 8, 10, and 12 plies were produced, and their cured thicknesses were precisely measured. It was found that a 10-ply laminate of the 205 gsm prepreg achieved a total thickness equivalent to the 8-ply laminate originally designed, with an average cured ply thickness of 0.23 mm.

Consequently, all 8-ply laminates defined in the design phase were adapted to 10-ply laminates using the 205 gsm prepreg. The resulting laminates remain quasi-isotropic, with a final thickness of approximately 2.3 mm instead of 2.24 mm, maintaining equivalent mechanical properties and overall design integrity.

9.1.2 Final Design

Figure 9.2 presents the final prototype design in an exploded view.

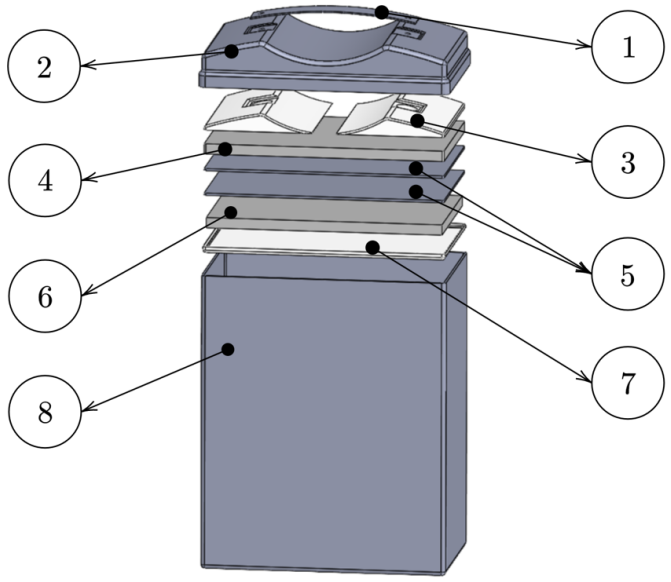

Figure 9.2: Exploded view of the final enclosure prototype design

Each component is described below according to its index:

1. **Enclosure Handle**: Designed to allow transportation of the enclosure, its geometry derives from the composite handle validated in Chapter 7. Although the use of a carbon-fibre handle was initially considered, this component was not produced. A fabric or leather handle is currently planned to reduce tooling and material costs.

2. **Enclosure Lid Laminate**: Manufactured from Toray® E731 205 gsm carbon fibre prepreg in a 10-ply $[45/0/90/\text{-}45/90]_S$ symmetric quasi-isotropic layup, with a total thickness of 2.3 mm and an estimated weight of 208 g. Together with the 3D-printed core, honeycomb layer, and internal laminate, it forms the upper part of the enclosure. The CAD model is shown in Figure 9.3.

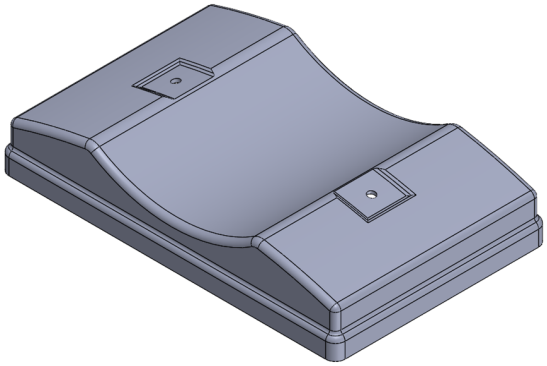

Figure 9.3: Enclosure lid in SolidWorks®

3. **3D-Printed Core**: Consists of two identical parts printed in nylon (PA6) reinforced with glass fibre (GF). The core supports the honeycomb structure and preserves the lid's geometry, maintaining a constant offset relative to the inner laminate surface. It also includes holes for assembly features discussed in the next section. Although the filament density is comparable to that of carbon composites, its weight depends on printing parameters and was not estimated. The CAD model is shown in Figure 9.4.

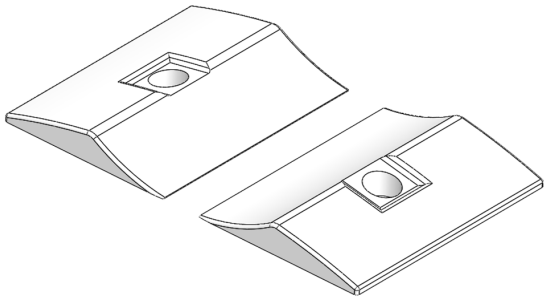

Figure 9.4: 3D-printed core in SolidWorks®

4. **Top Honeycomb Structure**: A 10 mm thick rectangular panel of 3003 aluminium honeycomb with 6.4 mm cell size, estimated to weigh 27 g. Its CAD model is presented in Figure 9.5.

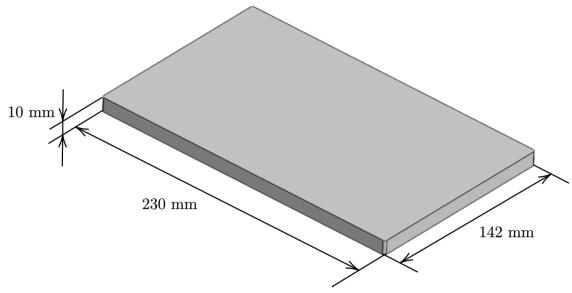

Figure 9.5: Top honeycomb structure in SolidWorks®

5. **Internal Laminates**: Located on the top and bottom honeycomb structures, these laminates form the inner surfaces of the enclosure. They are produced using the same 10-ply, 2.3 mm-thick E731 laminate as the external shell, with an estimated weight of approximately 110 g.

6. **Bottom Honeycomb Structure**: Identical to the top honeycomb layer (Index 4).

7. **Bottom Laminate Reinforcement**: Designed according to the same philosophy as in Chapter 8, this 2 mm-thick PA6 + GF insert follows the entire bottom surface and corners, ensuring a flat base for integration with the honeycomb structure. It is integrated within the external laminate. The CAD model is shown in Figure 9.6.

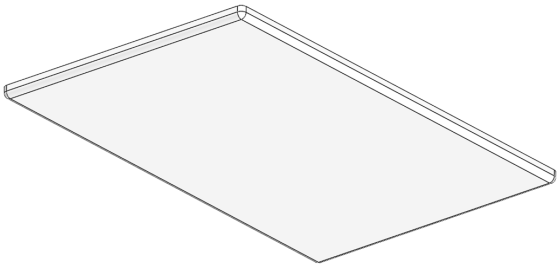

Figure 9.6: Bottom reinforcement SolidWorks® CAD model

8. **Enclosure Container Laminate**: Forms the main body of the enclosure, housing the battery pack and internal components. It is made from the same 10-ply laminate as the lid, with the bottom reinforcement integrated within its laminate midplane. The CAD model is shown in Figure 9.7.

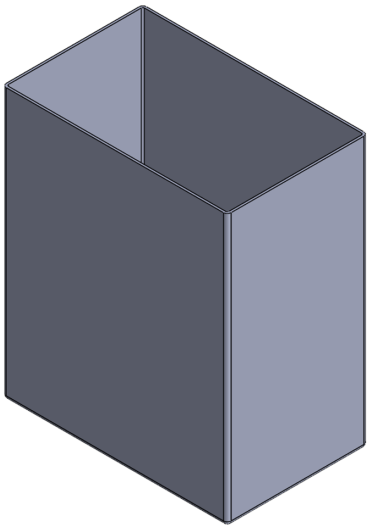

Figure 9.7: SolidWorks® CAD model of the bottom laminate of the enclosure

The CAD model of the assembled battery enclosure prototype is shown in Figure 9.8, along with its overall external dimensions. With a height of 317 mm (excluding the handle shown in the image), the final design complies with the dimensional requirements specified by Famel.

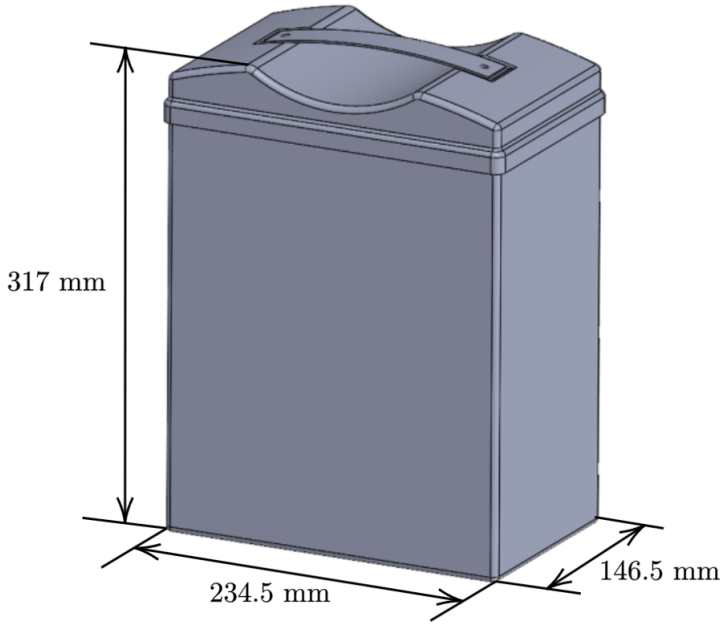

Figure 9.8: Assembled enclosure prototype CAD model with global dimensions

Figure 9.9 presents a midplane sectional view of the enclosure prototype, both with and without the battery and its supporting structure, illustrating the internal geometry and available space.

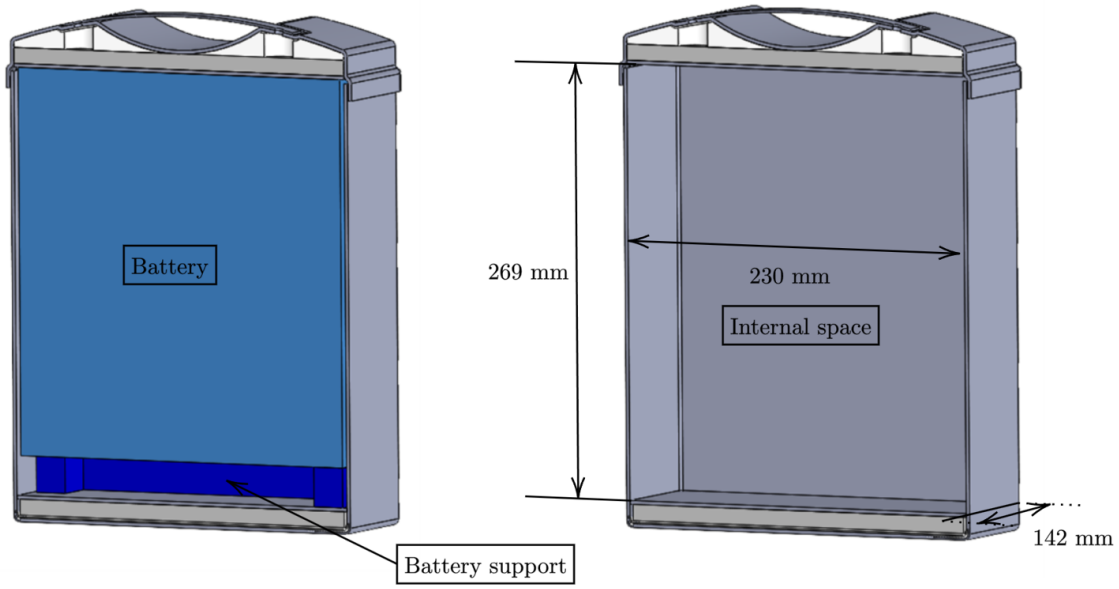

Figure 9.9: Sectional view of the assembled enclosure prototype showing internal dimensions

The internal geometry of the enclosure provides a clearance of approximately 3 mm in all directions to ensure proper accommodation of the battery and its components. The battery support illustrated in Figure 9.9 is not part of the enclosure itself but serves as a conceptual representation of a potential supporting component. As shown in Figure 9.1, sufficient space must be reserved for battery cabling, and an external connector. The final production version of the enclosure must therefore integrate a dedicated support for this connector.

The connector, together with the battery's associated components and cable management system, was not specified or adequately described by Famel. Due to the lack of this essential information, the corresponding design work could not be developed within this project. Consequently, this area remains undefined and is expected to be addressed by Famel in future iterations, based on the present prototype. The integration of these elements will likely affect the lower section of the enclosure and may require adjustments to its protective structures.

The total estimated weight of all components is approximately 1.332 kg, excluding the mass of the additively manufactured parts produced using glass fibre–reinforced nylon (PA6 + GF) filament. The exact weight of these components depends strongly on the printing parameters, particularly the infill structure of the 3D-printed core, which is expected to include an internal lattice to minimise material use, printing time, and weight while maintaining structural strength. Threaded metal inserts, discussed later, will also contribute slightly to the total mass.

The increase in mass compared to the initial design (1.1 kg) results mainly from the additional material required to accommodate the updated battery geometry and the reinforcement of the internal laminates. The prototype will be weighed after production for validation and comparison with design estimates.

Regarding the design challenges encountered, the final version effectively addresses manufacturability issues associated with the honeycomb structures while maintaining the same external appearance. The characteristic curved top lid, designed for hand clearance, was achieved through the introduction of 3D-printed cores, and the protective zones were retained with a simplified geometry that is significantly easier to produce. The honeycomb material, supplied pre-manufactured with a nominal thickness of 10 mm, only required manual cutting to the specified rectangular dimensions before integration into the laminate. Although this thickness is slightly reduced compared to the original concept, it represents a practical compromise between impact protection and the strict height limitations imposed by the design envelope.

Finally, the laminate layup was revised to $[45/0/90/\text{-}45/90]_S$, corresponding to the addition of two 90° plies to the original 8-ply configuration. This maintains laminate symmetry while increasing strength along the principal load direction, enhancing performance in vertical drop scenarios.

9.1.3 Design Details

The first relevant detail of the prototype enclosure concerns the connection method between the top lid and the main body. For this purpose, a structural adhesive bond was selected. Considering

the use of composite materials, adhesive bonding offers a highly effective, reliable, and straightforward means of joining components. It enables a continuous load path, distributes stresses uniformly across the bonded area, and eliminates the need for mechanical fasteners that could introduce local stress concentrations or require additional inserts. The connection was implemented through a bonding flange, designed to ensure a flat and parallel interface between the two components, as shown in Figure 9.10.

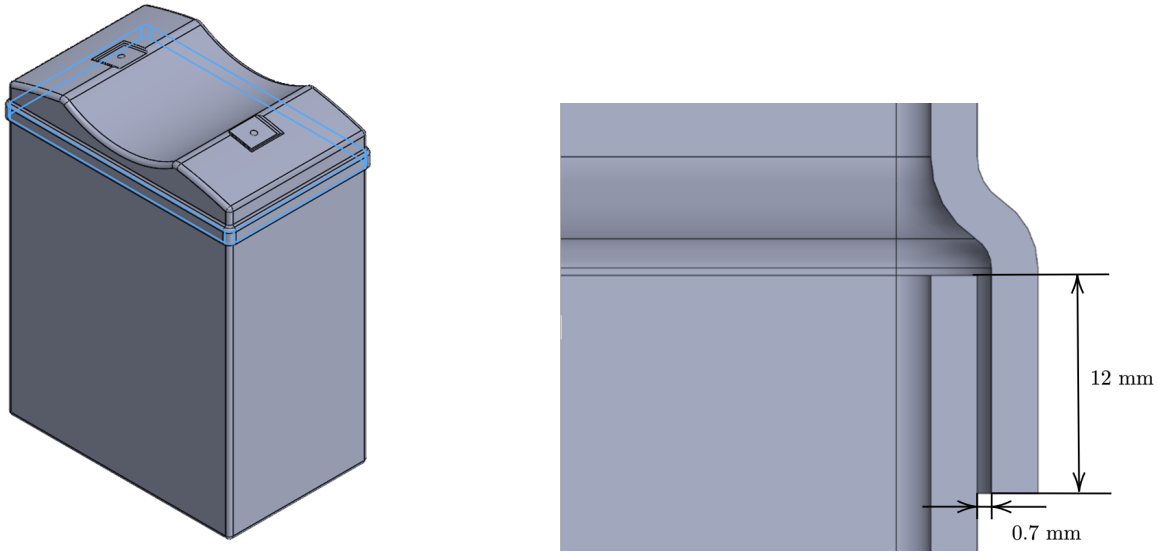

(a) Adhesive area highlighted (b) Adhesive flange

Figure 9.10: Adhesive flange feature for connection between the top and bottom parts of the enclosure

The bonding flange follows the entire perimeter of the enclosure, with a constant width of 12 mm. To ensure adequate adhesive performance, particular attention was given to achieving a high-quality surface finish, good parallelism, and a controlled adhesive gap. These aspects are guaranteed by the enclosure container mould design and by specific measures adopted during the top lid manufacturing process, as described later in this chapter.

The selection of an adhesive connection for this prototype was primarily driven by practical and time-related considerations. Adhesive bonding represents the simplest and most convenient approach at this stage, requiring minimal additional design complexity and making use of structural adhesives already available at Adamastor's facilities. While it is acknowledged that this solution limits serviceability, as the lid cannot be removed without damaging the bonded area, it ensures a strong and reliable structural connection within the time constraints of the project.

Alternative joining methods, such as mechanical fastening or hybrid adhesive–mechanical solutions, would require the design and integration of dedicated inserts, precise tolerances, and potentially external manufacturing support. These tasks, while standard in composite structures, would significantly extend the development timeline and increase production costs. Therefore, the adhesive bond was adopted as a preliminary solution for this prototype, prioritising manufacturing feasibility and structural integrity over disassembly convenience. Future iterations of the enclosure

should focus on developing an integrated mechanical joining system that enables safe opening and closing of the enclosure, while maintaining structural performance.

A constant adhesive gap of 0.7 mm was designed for the bonding interface. Structural adhesives typically achieve optimal performance at reduced thicknesses in the range of 0.2–0.5 mm [101]. However, to accommodate minor dimensional deviations inherent to the manufacturing process and ensure complete adhesive coverage, a slightly larger nominal gap of 0.7 mm was defined.

The adhesive selected for the connection is SikaPower®-740 (ADEKIT A140-1 / H9940-1), a high-performance, two-component epoxy adhesive specifically formulated for structural bonding of composite materials. The datasheet is provided in Appendix D.

To preliminarily validate the suitability of the adhesive joint, a simplified hand calculation was carried out, estimating the mean shear stress in the bond under a representative loading case. An effective adhesive width of 10 mm (slightly reduced from the 12 mm flange width) was considered, along with a 3g vertical loading condition, intended to simulate a severe acceleration scenario during handling of the battery enclosure.

Given:

- Flange perimeter: $p = 730.24$ mm
- Effective adhesive width: $b = 10$ mm
- Adhesive area: $A = p \times b = 7302.4$ mm^2
- Lap shear strength at 23°C (after 16h cure at 70°C, composite–composite joint): $\tau_{\max} = 17$ MPa [102]
- Enclosure + battery mass: $m = 15.3$ kg
- Applied load (3g vertical case): $F = m \times 3g = 15.3 \times 3 \times 9.81 = 453.2$ N

The mean shear stress in the adhesive is:

$$\tau_{\text{mean}} = \frac{F}{A} = \frac{453.2}{7302.4} = 0.0621 \text{ MPa} \tag{9.1}$$

The corresponding safety factor is therefore:

$$S.F. = \frac{\tau_{\max}}{\tau_{\text{mean}}} = \frac{17}{0.0621} \approx 274 \tag{9.2}$$

This result clearly indicates that the adhesive connection is highly overdimensioned for the expected service loads, providing a substantial safety margin. Therefore, no further detailed modelling of the adhesive layer was deemed necessary.

The following Figure 9.11 illustrates the laminate configuration of the enclosure lid. Each ply is represented by a line at its mid-plane, with colour coding applied to facilitate visual interpretation.

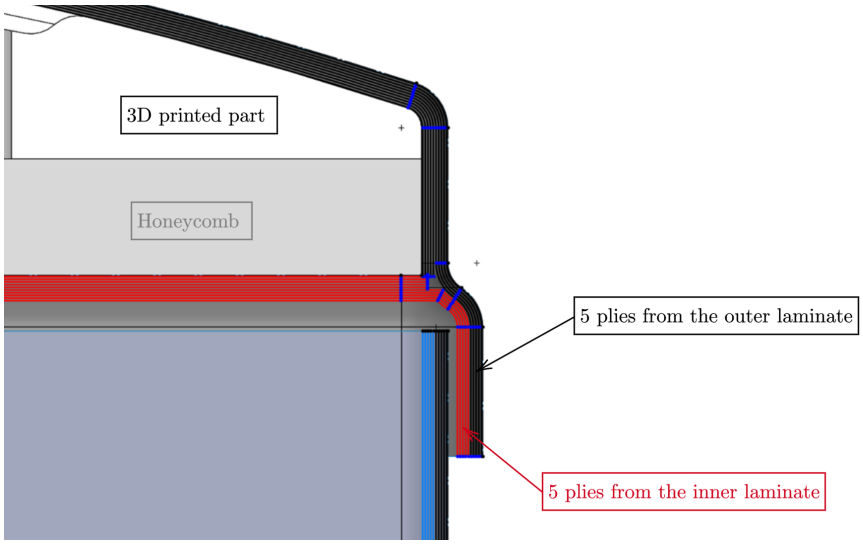

Figure 9.11: Laminate design detail nº1

The schematic representation shows the printed and honeycomb cores of the enclosure lid, as well as the junction region that connects the internal and external laminates. At the flange geometry, the laminate is split into two five-ply sublaminates, one internal and one external, ensuring adequate adhesion and structural continuity between both laminate sides.

Figure 9.12 presents a similar laminate design detail, this time at the bottom section of the enclosure.

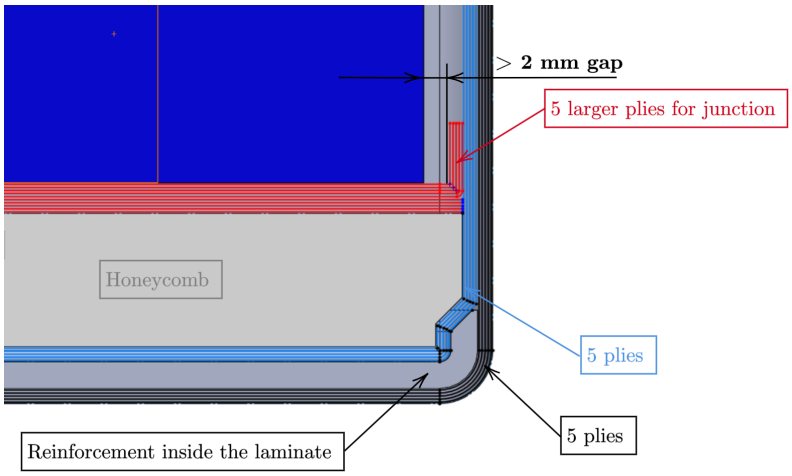

Figure 9.12: Laminate design detail nº2

This figure shows a sectional view highlighting the integration of the local reinforcement with the honeycomb core. A slight geometric deformation of the honeycomb is visible, which is expected during the vacuum bagging process. Since the offset induced by the reinforcement is minimal, it does not compromise the structural integrity of the honeycomb. The junction between the internal and external laminates is also shown. The designed clearances in the internal enclosure allow for a small local increase in thickness. In practice, the transition region would be more

gradual, achieved through progressive ply drop-offs to reduce the junction's thickness. The detail shown in Figure 9.12 is therefore a schematic representation.

bigHead® fasteners are metallic anchoring elements designed to provide secure load transfer between composite components and external attachments. Two M5 BigHead threaded collars (sighted holes) were integrated into the composite enclosure to enable fastening of the handle. bigHeads can be adhesively bonded to composite surfaces (post-process) or, preferably, co-cured within the laminate (co-process), offering superior mechanical interlocking and load transfer. The integration methods are illustrated in Figure 9.13.

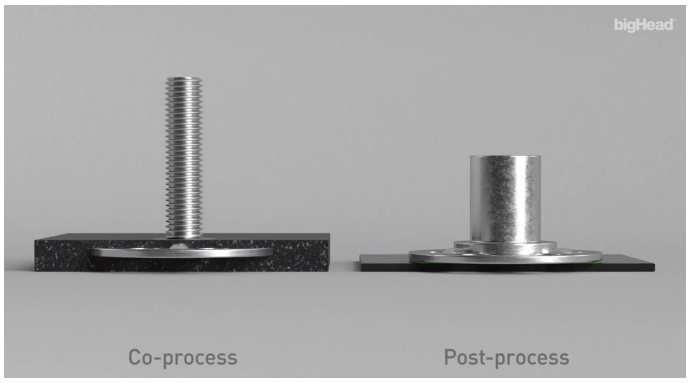

Figure 9.13: bigHead® components integration into composite laminates [103]

In this design, the bigHeads are co-cured within the laminate, following the co-process configuration. Five plies are placed above the bigHead®, each with a clearance hole, followed by another five plies below it, as represented in Figure 9.14.

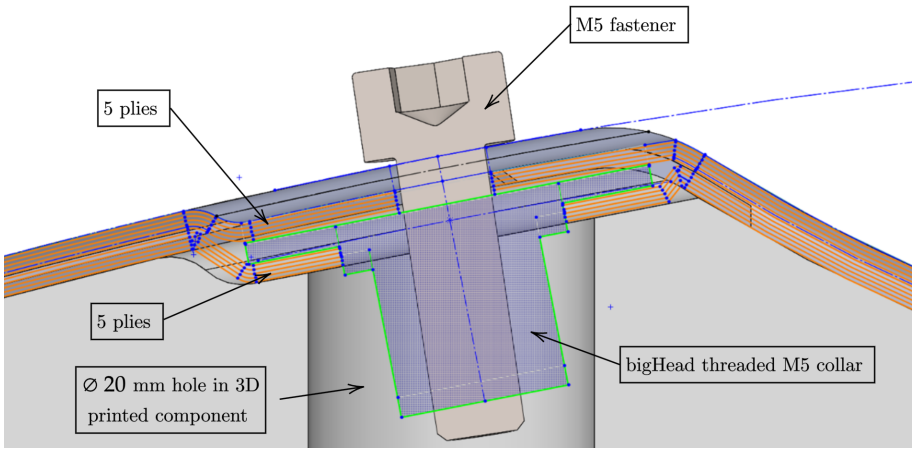

Figure 9.14: Laminate design detail n°3

This configuration ensures that the threaded insert is embedded at the mid-plane of the carbon fibre laminate, achieving firm and reliable integration. The printed core geometry accommodates both the bigHead® insert and the handle support. This feature also facilitates production, allowing the insert to be accurately positioned within the mould, as detailed later in this chapter.

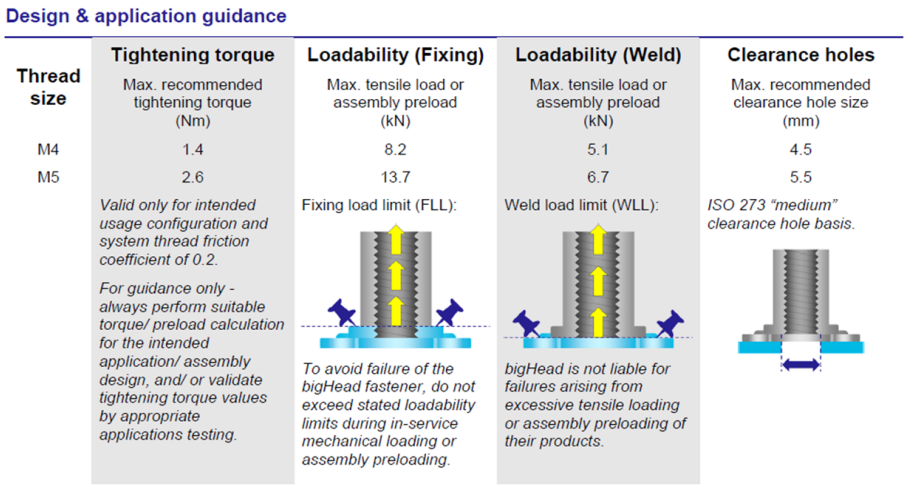

Figure 9.15: bigHead® design and application guidance [104]

According to the manufacturer's datasheet, bigHead fasteners are robust components. When co-cured within the stiff carbon fibre laminate, they do not represent a critical region of the design. Adamastor's prior experience with these components supports this assumption. For this reason, the handle assembly was validated, while the bigHead fasteners themselves were not (see Chapter 7).

9.2 Moulds

This section presents the tasks related to the design and fabrication of the moulds required for the production of the prototype enclosure.

9.2.1 Design

The moulds were designed directly from the CAD models of the enclosure components using SolidWorks®. Figure 9.16 illustrates the three moulds developed in preparation for production. The wireframe volumes represent the material stock required for each mould, and their respective dimensions are also indicated.

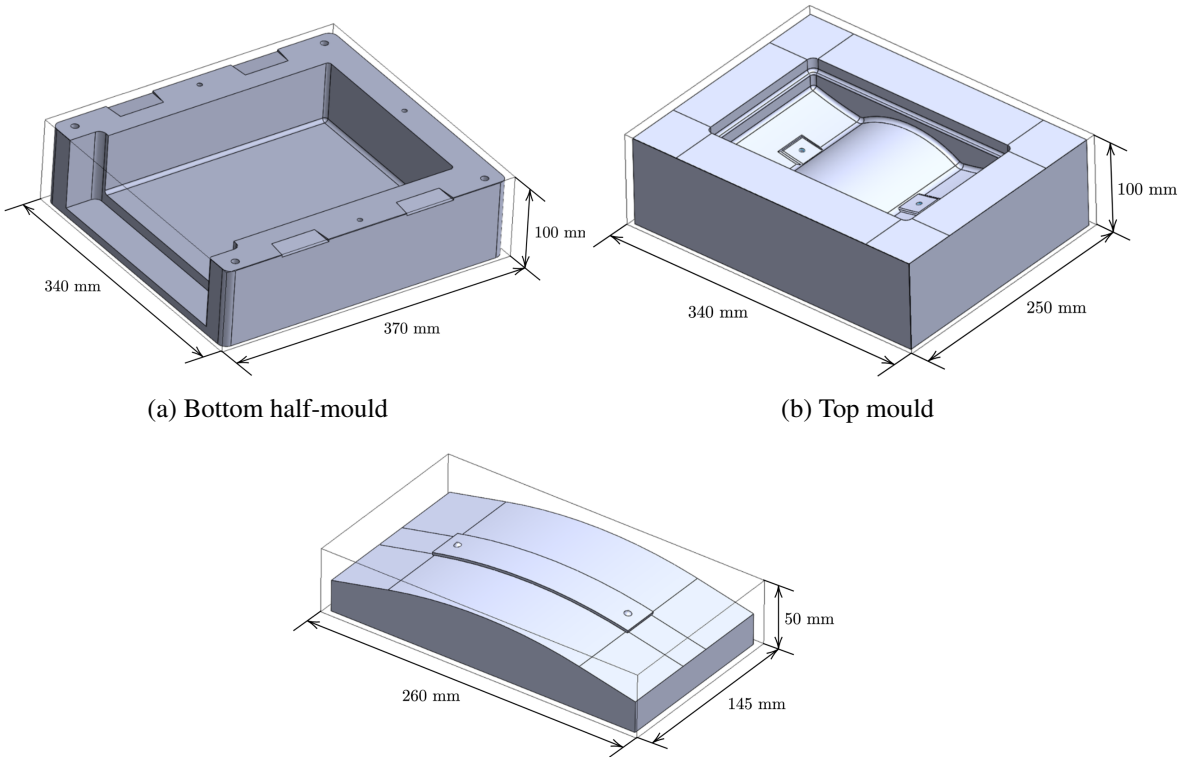

(a) Bottom half-mould

(b) Top mould

(c) Composite handle mould

Figure 9.16: Mould designs in SolidWorks®, stock dimensions in wireframe representation

Each mould incorporates specific design features, which will be justified in the following paragraphs. The stock blocks were modelled with an offset of approximately 5 mm from the mould geometry, except on the bottom surface. This allowance ensures sufficient machining depth and guarantees that all mould features are accurately produced during the machining process.

Although three moulds were initially designed, one of them, intended for the carbon fibre handle, was ultimately not manufactured, following the decision to replace the composite handle with a fabric alternative. Nevertheless, since the handle mould design was completed, it is still presented and described in this section for completeness.

Excluding the handle mould, the production of the composite enclosure requires three moulds: two identical half-moulds for the bottom laminate (enclosure container) and one mould for the top lid. Figures 9.17 and 9.18 show detailed views of the bottom half-mould design. The second figure depicts the two half-moulds assembled as intended during the lamination process.

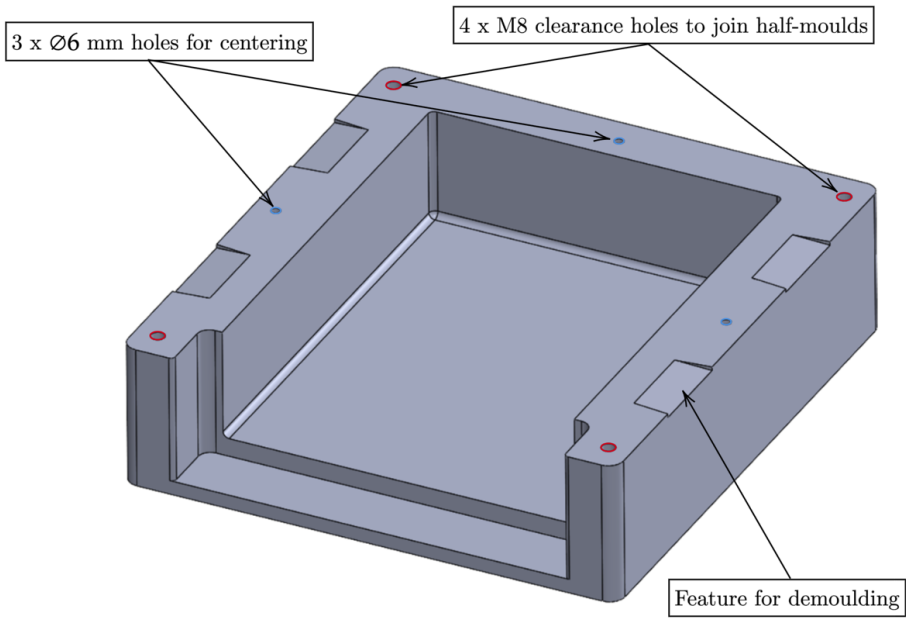

Figure 9.17: Features in the design of the bottom half-mould

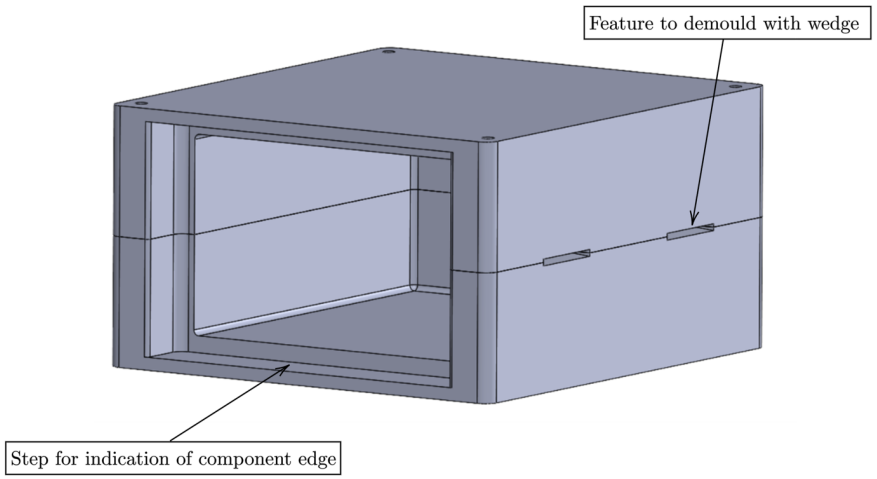

Figure 9.18: Features in the design of the bottom half-mould (assembled)

Each half-mould includes four M8 clearance holes used to secure the two halves together during lamination. Assembly is achieved using threaded studs, washers, and hexagonal nuts, with rounded head nuts selected to reduce the risk of tearing the vacuum bag during manufacturing. To ensure accurate alignment and geometric continuity between both halves, three Ø6 mm blind holes were added for centering pins. The design also allows the operator to hand-laminate the prepreg plies within the mould cavity without needing to separate the mould halves. Furthermore, the moulds include a clearly defined component edge to assist in the trimming of excess material after curing, as well as wedging features that facilitate the separation of the mould halves and safe demoulding of the part after autoclave curing.

Figure 9.19 also present details of the top lid mould. At each bigHead® fastener location, a 1 mm deep, 60° conical depression will be machined to mark the exact position of the insert. This reference will later serve to drill the necessary to position the bigHead® accurately during lay-up.

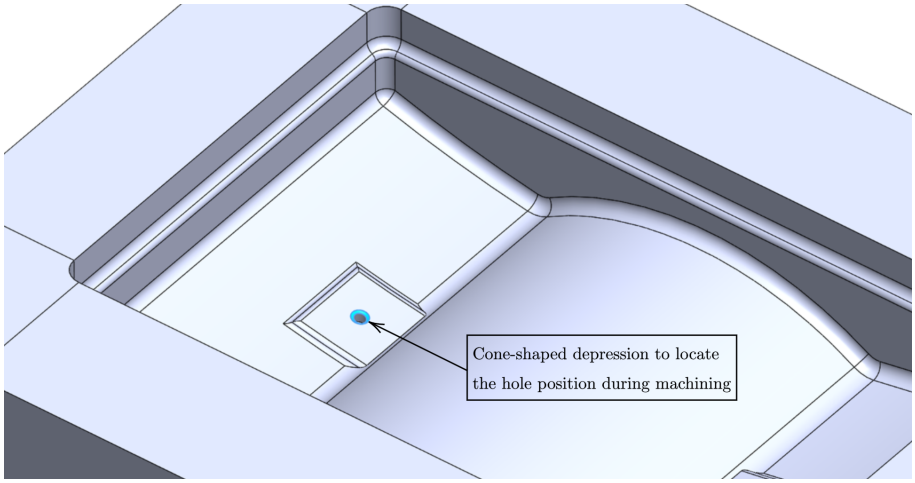

Figure 9.19: Hole positioning feature in the top mould

Figure 9.20 displays two design details of the handle mould.

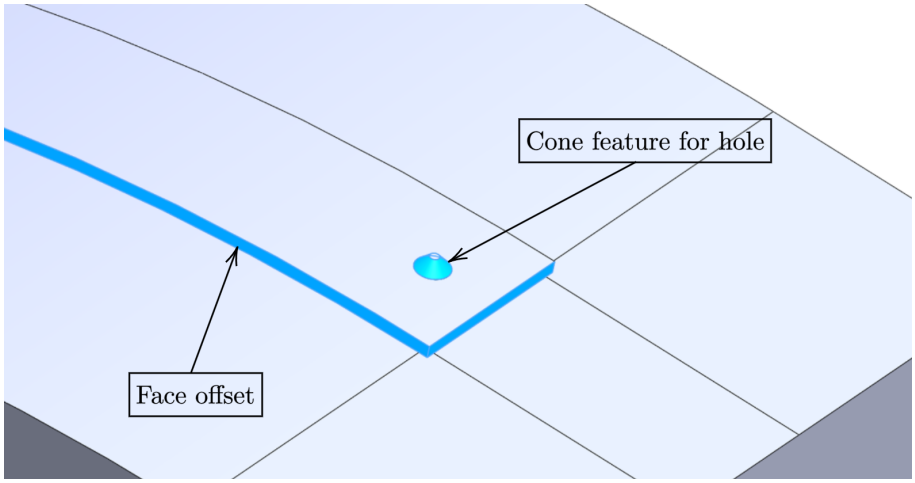

Figure 9.20: Features in the handle mould

This mould was designed as an open tool, enabling easy lay-up of the composite plies. A protruding cone with the clearance hole dimensions at its base was added to facilitate hole placement and creation during manual lamination. Additionally, the base surface where the handle rests was elevated relative to the surrounding area. Adding to this, an offset in length and width accounts for the saw blade thickness used to trim excess material after curing, ensuring that the final component meets the target dimensions.

Figure 9.21 presents the draft angle analysis performed on the three mould designs.

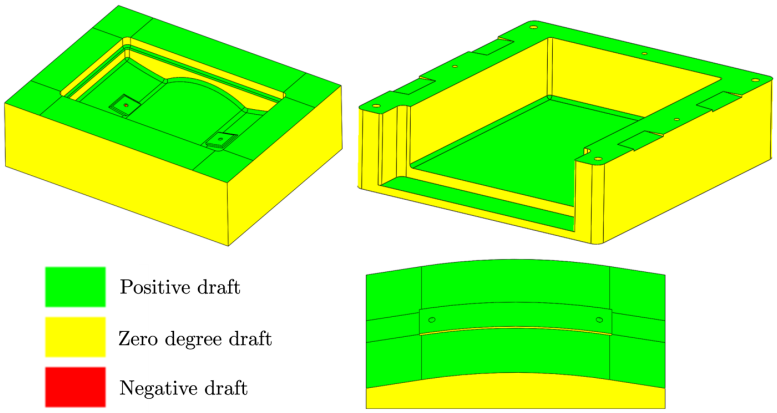

Figure 9.21: Draft angle analysis on the three mould designs

To ensure proper demoulding of the composite parts, none of the mould geometries include negative draft surfaces. However, several surfaces present neutral (0°) draft angles, which could lead to increased resistance during demoulding.

This potential issue is mitigated in the bottom mould, which is split into two separate halves—significantly reducing the effort required to release the cured component.

For the top mould, demoulding may be somewhat more challenging due to its single-piece configuration; nonetheless, the moderate size and height of the lid component indicate that the process should remain manageable.

9.2.2 Preparation of Stock

The stock material for the moulds was produced using high-temperature epoxy tooling boards, supplied in panels of 1564×610 mm^2 with a thickness of 50 mm.

To achieve the required 100 mm stock thickness for both the top mould and the bottom half-moulds, the boards were cut to size and subsequently bonded in pairs. The procedure is described below.

First, the available tooling board area was optimised for cutting, in order to obtain the required 50 mm thick blocks with minimal waste. The resulting cutting layout is shown in Figure 9.22, which achieved approximately 75% material utilisation.

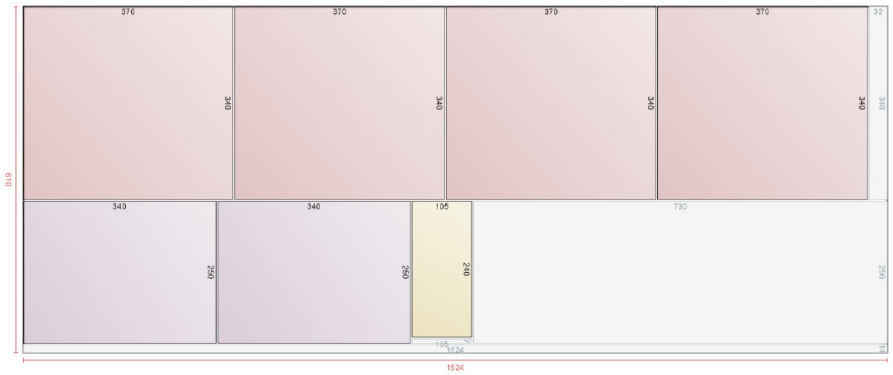

Figure 9.22: Epoxy tooling board stock optimisation

After cutting, the individual epoxy blocks were bonded together using a two-part epoxy adhesive (epoxy and catalyst mixed in a 5:1 ratio) to form the final stock height of 100 mm. To eliminate air entrapment and ensure full adhesion between layers, the bonded blocks were vacuum bagged and left to cure under vacuum pressure for over 24 hours. Figures 9.23 and 9.24 illustrate this preparation process.

Figure 9.23: Epoxy adhesive application to the epoxy blocks

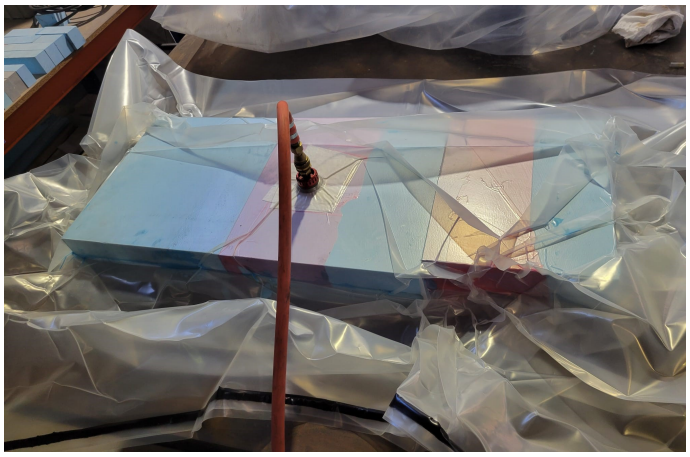

Figure 9.24: Stock vacuum bagging process

9.2.3 CNC Machining

This subsection briefly describes the machining process. For complete details on the CNC setup and machining parameters, refer to Annex E, where the full setup sheets for both machining processes are provided. The CAM setup of each operation was performed using Autodesk Fusion® software. It should be noted that this task was not executed by the author.

Table 9.1 summarises some parameters of the CNC program for the bottom half-mould.

Table 9.1: Bottom half-mould CNC machining statistics

Half-mould CNC machining statistics	
Number of operations:	11
Number of tool changes:	2
Estimated cycle time	3 h 54 min 43 sec

A total of 11 operations were defined, employing three different tools (Ø16 mm flat end mill, Ø8 mm R4 ball end mill, and Ø6 mm R3 ball end mill), requiring two tool changes. The estimated machining time for one half-mould was 3 h 54 min 43 s, considering an average tool change time of 20 s.

Figure 9.25 illustrates the bottom half-mould at the end of the Fusion CAM simulation.

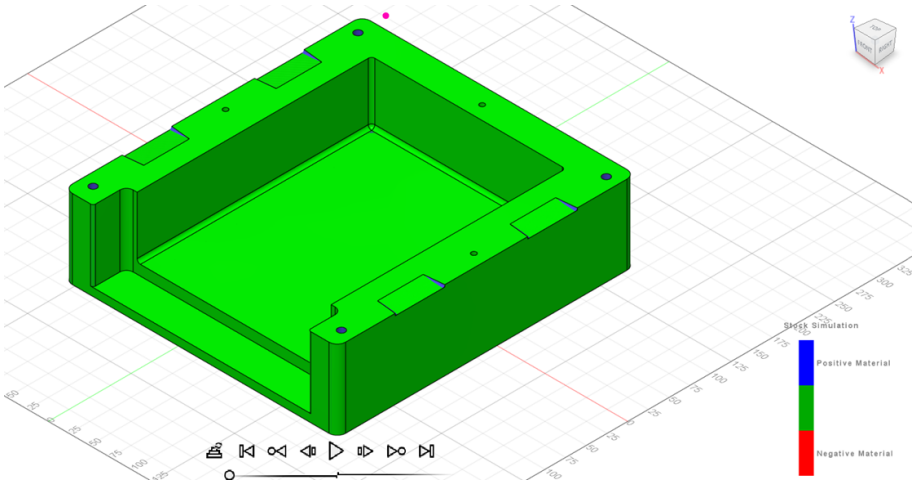

Figure 9.25: Bottom half-mould at the end of CAM simulation

Table 9.2 presents the machining parameters for the top mould.

Table 9.2: Top mould CNC machining statistics

Top mould CNC machining statistics	
Number of operations:	5
Number of tool changes:	1
Estimated cycle time	3 h 09 min 41 sec

Five operations were defined using two different tools (Ø16 mm flat end mill and Ø8 mm R4 ball end mill), requiring a single tool change. The estimated machining time for this mould was 3 h 09 min 41 s. Considering the total of three moulds, the cumulative expected machining time was approximately 11 h. In practice, machining extended over several days due to operational constraints.

Figure 9.26 shows the top mould after the CAM simulation.

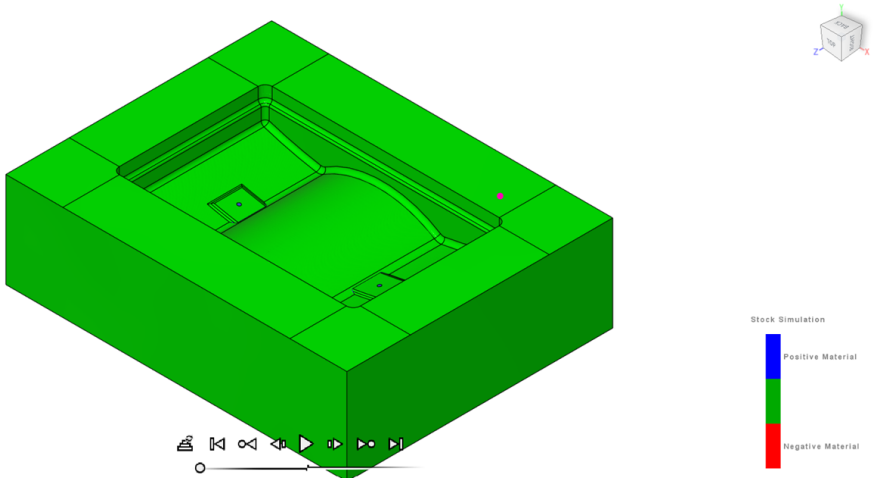

Figure 9.26: Top mould at the end of CAM simulation

Figures 9.27a and 9.27b show two relevant CAM simulation details: a small portion of unmachined material, to be corrected during mould finishing, and the conical depression used to locate the bigHead® inserts.

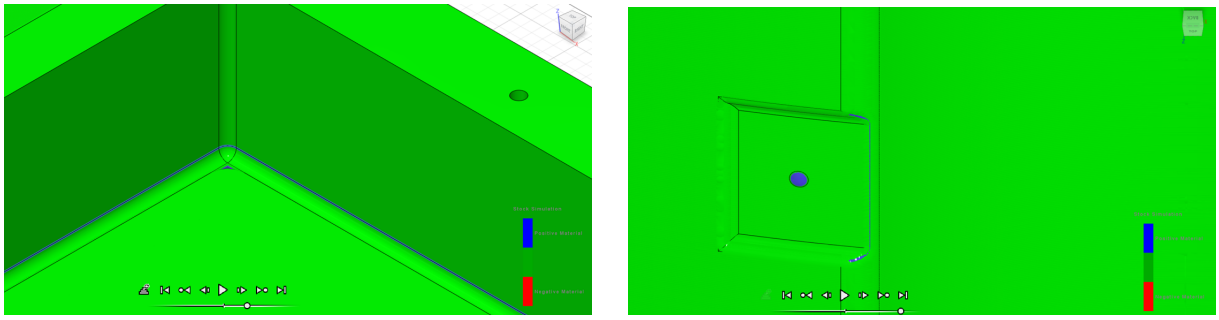

(a) Unmachined material region (b) Insert location feature

Figure 9.27: Details from the CAM machining program

The machining operations were carried out using Adamastor's in-house 3-axis CNC machine, shown in Figure 9.28.

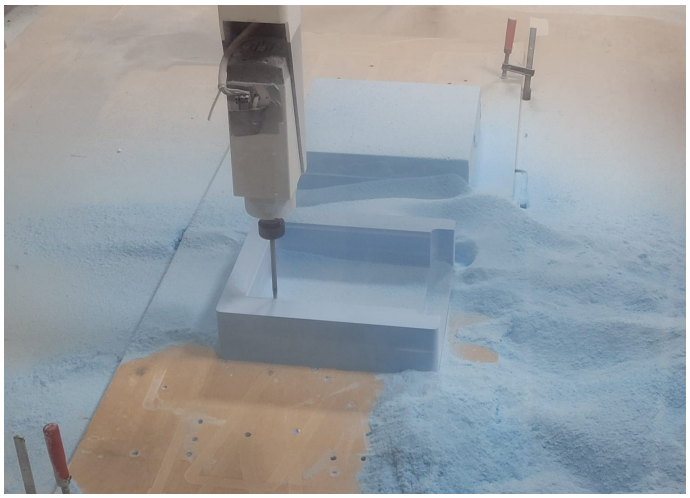

Figure 9.28: CNC machining of the bottom half-moulds

Figure 9.29 presents the machined moulds immediately after the CNC process.

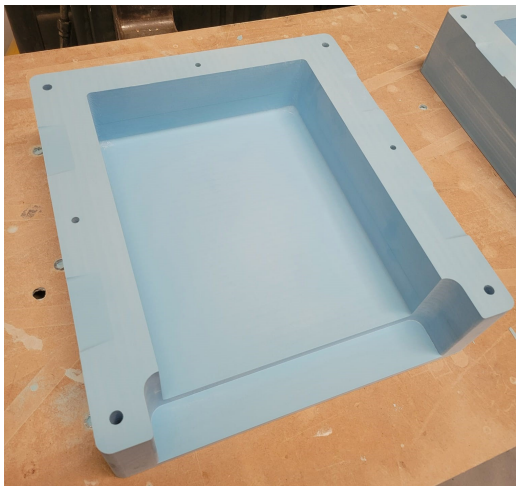

(a) Bottom half-mould

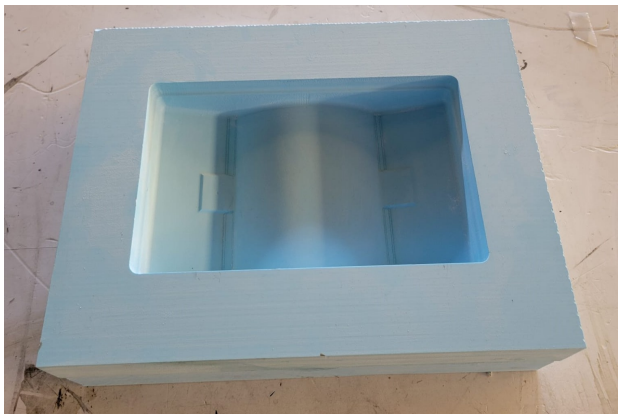

(b) Top mould

Figure 9.29: Moulds after machining

9.2.4 Preparation

After removal from the CNC machine, the moulds required surface finishing before use in lamination. As indicated in Figure 9.27a, certain regions, particularly near the mould vertices, could not be fully machined due to tool path limitations. This residual material can also be seen in Figure 9.30a. Additionally, minor surface irregularities, such as visible tool marks and shallow grooves, resulted from tool vibration and cutting passes, particularly in curved fillet regions (Figure 9.30).

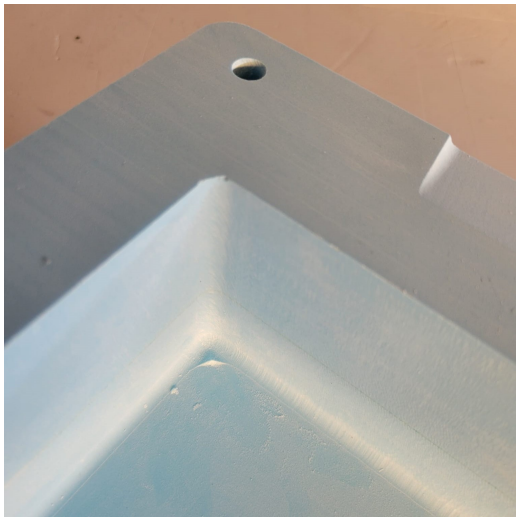

(a) Unmachined region in bottom mould

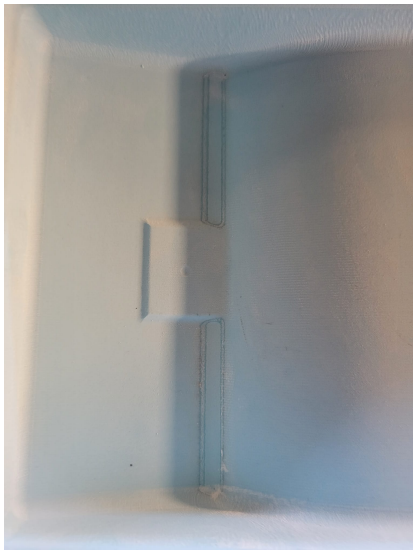

(b) Surface marks on top mould

Figure 9.30: Close-up views of the moulds after machining

Since any surface defect would be directly transferred to the composite component, a meticulous sanding and polishing process was required. The moulds were first manually sanded to remove machining marks, followed by fine wet sanding to achieve a smooth and continuous surface. Subsequently, four layers of a mould sealer (Sealer Mikon® 398 MC) were applied, allowing 15–20 minutes of curing between each layer and a longer final cure. Before lamination, a release agent (Release Agent Mikon® W 64 +) was applied to ensure proper demoulding. Careful mould preparation was essential, as surface quality directly influences the final composite finish.

Figure 9.31 shows the bottom half-moulds after the sealer application.

Figure 9.31: Bottom half-moulds after application of mould sealer

As previously mentioned, the positioning of the bigHead inserts required a precise method to ensure proper alignment during manufacturing. This was achieved by manually drilling holes at the exact locations defined during the CNC process, as shown in Figure 9.32a. A modified M5 screw was then threaded into the bigHead insert and used to position it accurately within the mould cavity during lamination, as illustrated in Figure 9.32b.

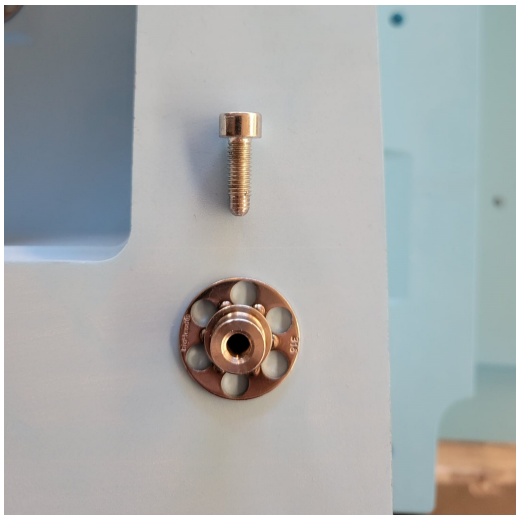

(a) Modified M5 bolt and bigHead insert

(b) Blind holes in the top mould

Figure 9.32: Top mould insert positioning solution

9.3 3D Printing

The 3D printing of the cores and reinforcement components was carried out at Adamastor's facilities using their in-house additive manufacturing equipment. The author designed the geometry of the printed parts, although the printing parameters and setup were defined and executed by Adamastor's team.

The additive manufacturing process used for these components was **Fused Filament Fabrication (FFF)**, also known by its trademarked name **Fused Deposition Modelling (FDM)**. This technique builds parts layer by layer through the extrusion of a thermoplastic filament.

The printed components, immediately after manufacturing, are shown in Figure 9.33.

Figure 9.33: Cores and reinforcement after additive manufacturing

Due to a limited quantity of PA6 glass fibre reinforced filament, only the top cores were produced with this material. The bottom reinforcement was therefore printed using an alternative high-performance filament composed of PA6 with 20% carbon fibre. The filaments used are **Fiberon® PA6-CF20 filament** and **Innovatefil® Nylstrong PA6-GF25 filament** [92, 105].

The bottom reinforcement component was printed with 100% infill to ensure sufficient stiffness, given its low thickness. The top cores were printed with five outer walls and a 20% infill density, forming a central pattern structure inside. This configuration was selected to optimise printing time, reduce material usage, and balance weight with mechanical resistance.

After printing, the components were carefully sanded to remove any excess filament and to achieve smoother surfaces. The sanded cores are presented in Figure 9.34.

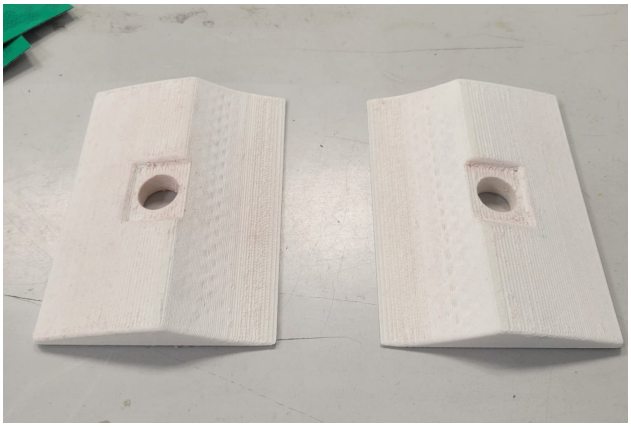

Figure 9.34: Sanded printed cores

9.4 Lamination Process

This section delves into the lamination process, from its preparation and the strategy defined for each top and bottom components, to a description of the process itself, highlighting some details of importance.

The lamination process was carried out using prepreg materials. This manufacturing route was selected as it allows for improved process control and simplifies production preparation, particularly important in a component that integrates inserts and cores. Prepregs ensure that resin and catalyst levels, as well as the fibre resin content, are precisely controlled by the material manufacturer, allowing for high fibre volume fractions with minimal voids. In addition, prepreg material was already available and suited for use in prototype development. The main drawbacks of this method include the higher cost, the need for autoclave curing, and the requirement for tooling and core materials capable of withstanding the elevated processing temperatures and pressures.

9.4.1 Preparation and Process Definition

9.4.1.1 Bottom Mould

The process of layup for the bottom enclosure component, the enclosure container, was based on an organised ply design and nesting defined in a plybook. Using the tool Nesting Center [106], the geometry of the mould was analysed, and each ply was planned to ensure proper conformity and continuity of fibres over the component's geometry.

Four different ply shapes were created, each one repeated several times for different fibre orientations, resulting in a total of 30 individual pieces of fabric.

The lamination layout strategy was defined with several factors in mind, ensuring manufacturability and laminate quality. Due to the box-like geometry, each continuous ply was divided into sub-plies to conform to the mould without wrinkles or fibre distortion. One elongated ply covers three adjacent faces, while smaller plies complete the remaining sides. Controlled overlaps were applied and alternated between layers to avoid aligned seams, creating weak lines in the laminate. Consecutive orientations were rotated by 90° to balance the laminate and improve adhesion between sub-plies. Corner areas were reinforced to prevent bridging and ensure uniform thickness.

Figure 9.35 presents the ply nesting layout developed for the bottom enclosure component, achieving an approximate material efficiency of 88.3%. The complete nesting details, along with the full ply list, are provided in Appendix F.

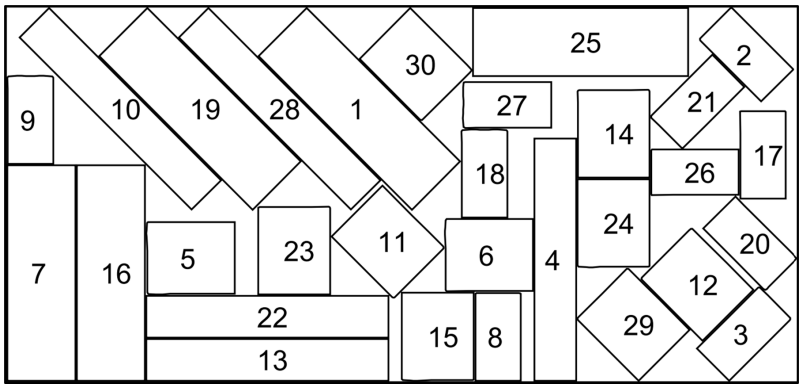

Figure 9.35: Nesting layout for the bottom component

The sequence of tasks followed during the lamination of the bottom enclosure component is summarised below. The order of ply application was defined directly from the plybook (Appendix F), with each ply identified by its unique ID. Accordingly, the first ply to be laminated is designated **LAM001-P001**, followed by **LAM001-P002**, and so forth.

Bottom Component Lamination

1. **Lamination of first ply (45°)**
2. **Debulking (vacuum bag)**
3. **Lamination up to 5th ply (0°, 90°, –45°, 90°)**
4. **Placement of 3D printed reinforcement**
5. **Debulking**
6. **Lamination up to 10th ply (90°, –45°, 90°, 0°, 45°)**
7. **Vacuum bagging**
8. **First autoclave cycle (1h @ 125°C, 6 bar)**
9. **Placement of honeycomb core**
10. Lamination of 5 plies (45°, 0°, 90°, –45°, 90°)
11. **Lamination of 5 extended plies (90°, –45°, 90°, 0°, 45°)**
12. **Vacuum bagging**
13. **Second autoclave cycle (1h @ 125°C, 1 bar)**

9.4.1.2 Top Mould

The lamination of the enclosure's top component followed the same principles of ply segmentation adopted for the bottom mould. This approach ensured good drapability, minimised wrinkling or deformation, and alternated the orientation of overlap zones to avoid the alignment of cut lines between consecutive plies. Two distinct ply geometries, referred to as the "Horizontal" and "Vertical" configurations, were alternated throughout the process. These configurations and their intended layout over the mould are illustrated in Figures 9.36 and 9.37.

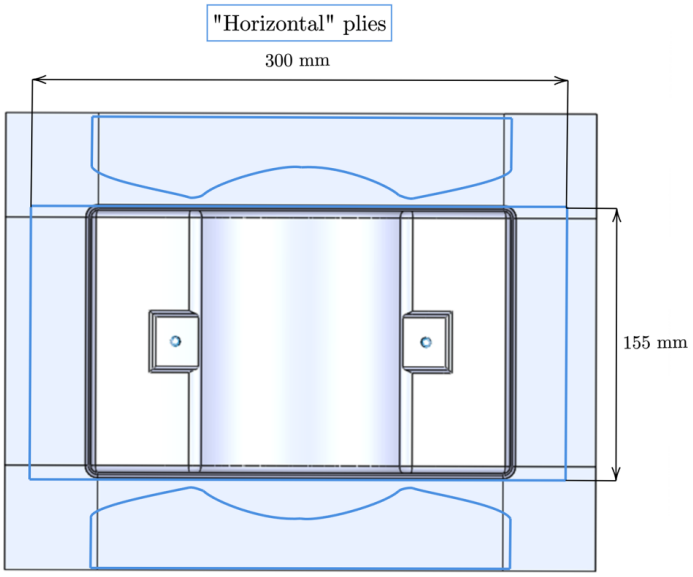

Figure 9.36: "Horizontal" ply configuration

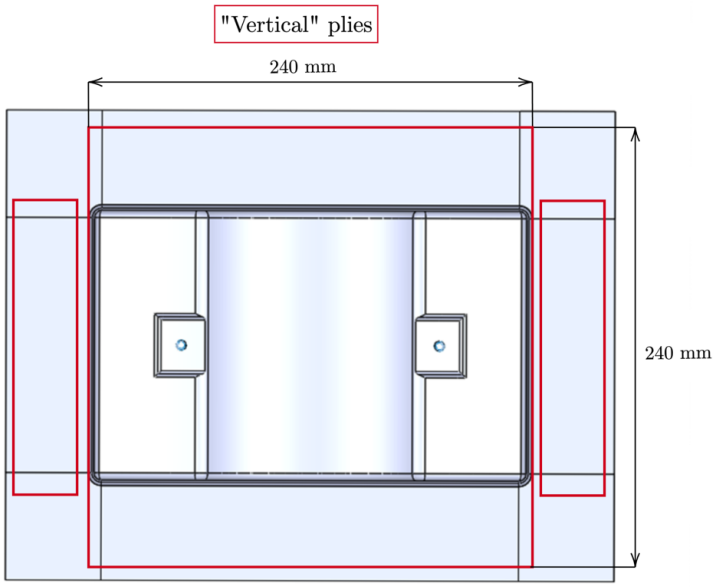

Figure 9.37: “Vertical” ply configuration

Each ply was slightly oversized to ensure complete coverage of the mould surface. The excess material was trimmed after curing and, when possible, reused for local reinforcements.

To assist in defining the sequence of fibre orientations and alternating ply configurations that result in the final laminate stacking of $[45°/0°/90°/–45°/90°]_S$, the layup plan shown in Figure 9.38 was prepared.

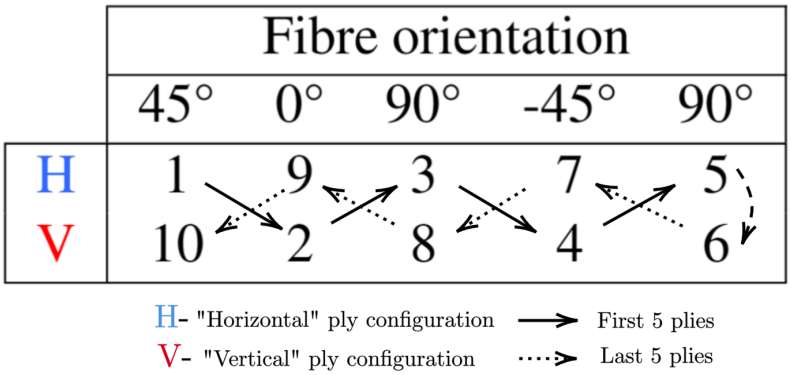

Figure 9.38: Layup sequence of the top laminate

The complete lamination sequence is summarised below.

Top Component Lamination

1. **Lamination of first ply (45°)**
2. **Debulking**
3. **Lamination up to 5th ply (0°, 90°, –45°, 90°)**
4. **Debulking**
5. **Clearance hole for insert**
6. **bigHead insert positioning**
7. **Lamination up to 10th ply (90°, –45°, 90°, 0°, 45°), integrating the insert**
8. **Vacuum bagging**
9. **First autoclave cycle (1h @ 125°C, 6 bar)**
10. **Remove bolts for bigHead placement**
11. **Placement of printed cores**
12. **Placement of honeycomb core**
13. **Lamination of 5 plies (45°, 0°, 90°, –45°, 90°)**
14. **Lamination of 5 extended plies (90°, –45°, 90°, 0°, 45°)**
15. **Vacuum bagging**
16. **Second autoclave cycle (1h @ 125°C, 1 bar)**

9.4.1.3 Internal Laminate

The internal laminate required only two ply geometries: shorter plies (230×142 mm), and longer plies (260×180 mm), which overlap with the external laminates to form the junction regions.

9.4.1.4 Material Cutting

Due to an equipment malfunction during prototype manufacturing, the prepreg plies could not be CNC-cut as planned. Instead, the material was manually cut, which proved feasible given the manageable thickness of the prepreg.

Templates were first produced according to the defined ply shapes and nesting plan. The thawed prepreg sheets were then cut manually with a sharp blade following these templates. Figure 9.39 presents the four templates used for the bottom laminate component.

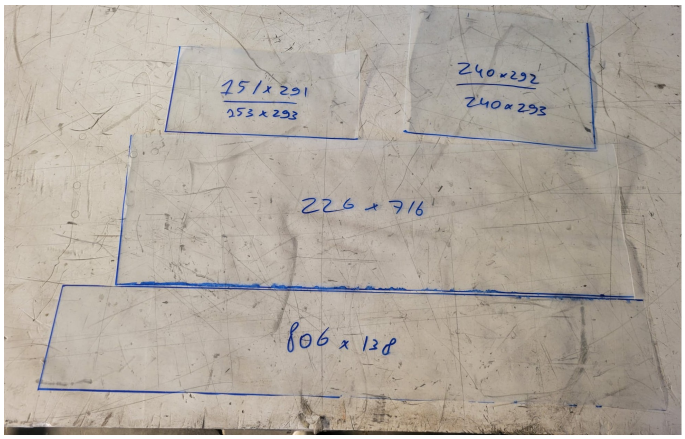

Figure 9.39: Ply shape templates for the bottom laminate

Complex ply shapes used in the top laminate were also cut manually, based on mould geometry templates. Figure 9.40 shows examples of these plies after cutting.

Figure 9.40: Cut plies from the “Horizontal” configuration

The honeycomb cores were cut in the same manner, using dedicated templates. A change from the planned 6.4 mm cell aluminium honeycomb to a 3.2 mm cell version was made due to material availability. This substitution offers a small strength improvement, with only a minor weight penalty. The prepared honeycomb panels are shown in Figure 9.41.

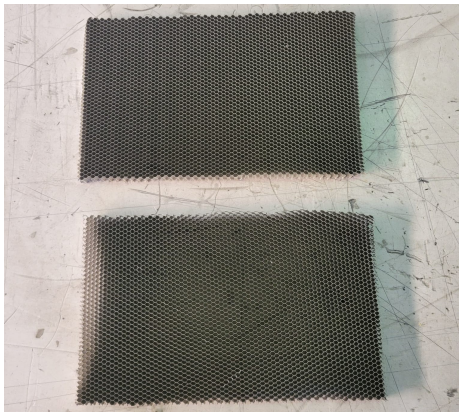

Figure 9.41: Prepared honeycomb panels

9.4.2 First Lamination

From this stage onwards, the manufacturing process is described with focus on relevant operational details. Figure 9.42 shows the moulds prepared for production, as well as the prepreg plies already cut and ready for lamination.

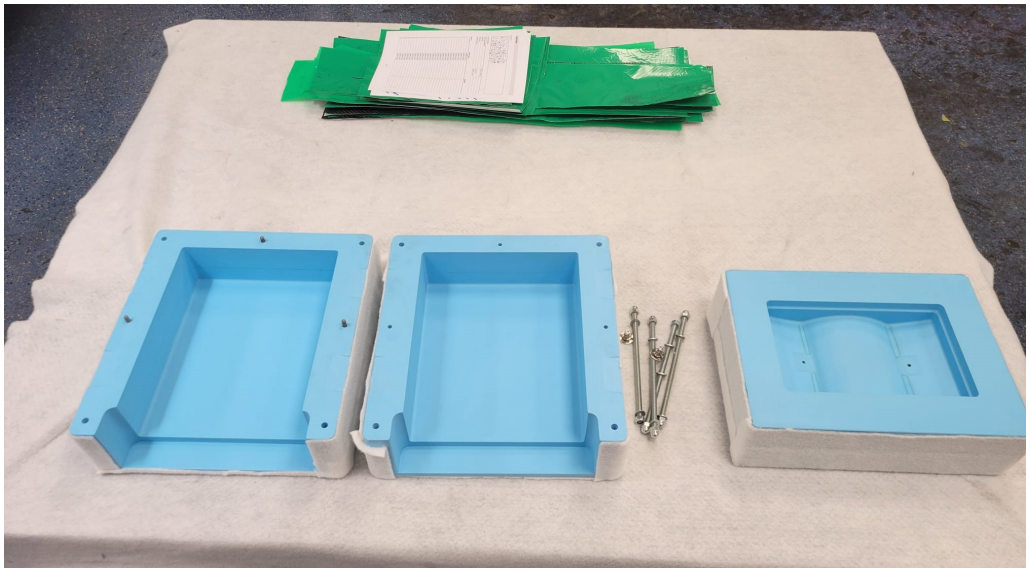

Figure 9.42: Moulds and prepreg materials ready for manufacturing

The two half-moulds were assembled, and the lamination process initiated. Following the placement of the first plies forming the external surface of the components, a debulking operation was performed for both moulds. This process ensures that the initial plies conform properly to the mould geometry, promoting good compaction and facilitating the subsequent lamination stages. After the application of release film, breather cloth, and vacuum bag, vacuum pressure was maintained for approximately 20 minutes. Figure 9.43 shows the first plies applied to the bottom mould after the debulking process. The step feature on the mould demonstrates its utility in clearly marking the edge of the component during material application.

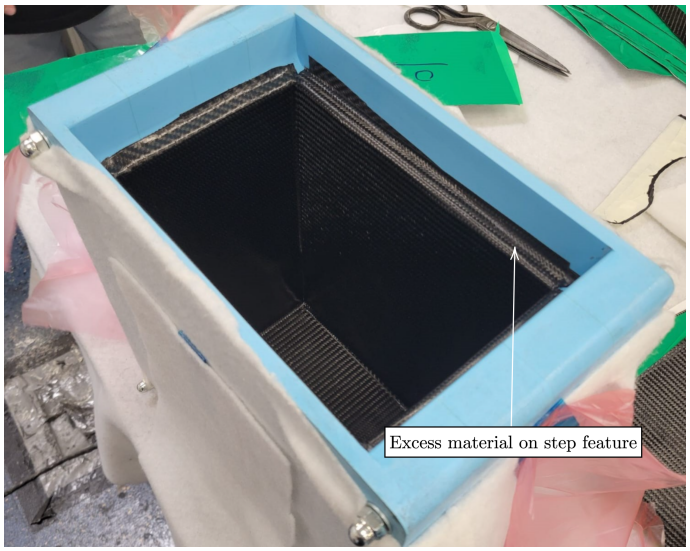

Figure 9.43: First plies conformed to the bottom mould after debulking

The lamination continued up to the fifth ply, after which a second debulking process was carried out using the same consumables. In the case of the bottom mould, the 3D printed reinforcement was placed prior to debulking. Figure 9.44 shows both moulds during this second debulking stage.

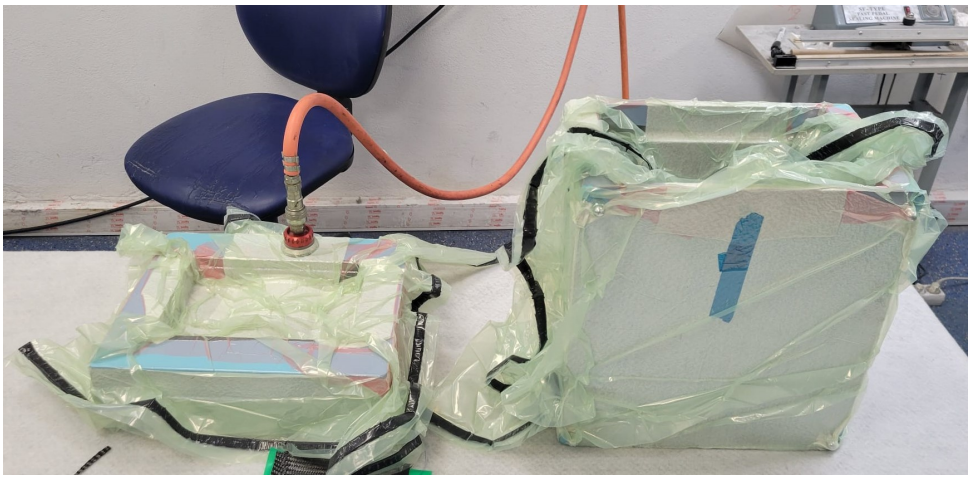

Figure 9.44: Mould during the second debulking process

As illustrated in Figure 9.45, besides ensuring correct lamination and removal of trapped air, the debulking process also contributed to the accurate positioning of the reinforcement on top of the initial plies.

Figure 9.45: Bottom mould with reinforcement positioned

The lamination of the following plies proceeded thereafter. The process was straightforward for the bottom mould, given its simpler and larger geometry. The top mould, however, required more effort due to its complexity. In particular, the lamination of plies in the "vertical" configuration (Figure 9.37) proved more challenging. Local trimming of the prepreg material was necessary to achieve proper conformity to the mould without wrinkling. The cuts made in the plies can are illustrated in Figure 9.46.

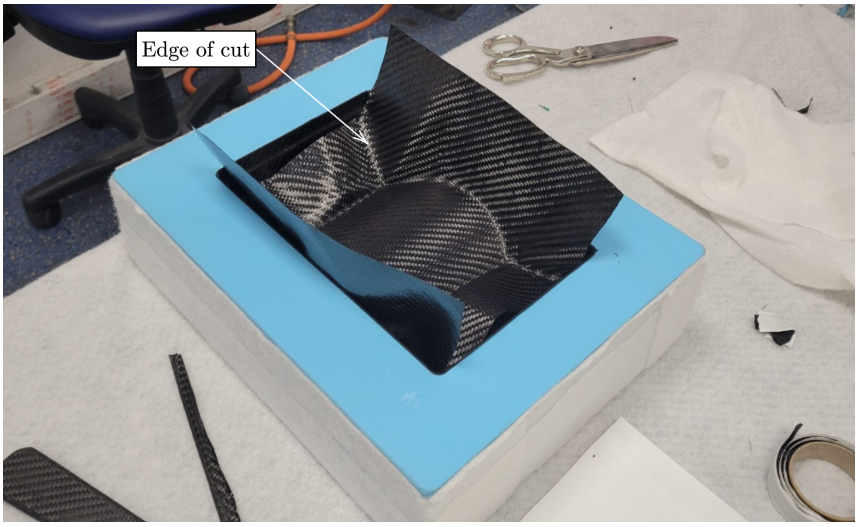

Figure 9.46: Prepreg cuts for conformation on the top mould

Additional local carbon fibre reinforcements were applied around the bigHead insert and along the edge of the lid. These reinforcements ensured proper integration of the insert into the laminate and strengthened the edges, where ply cut lines were concentrated, preventing the formation of weak zones. These improvements were implemented based on the technicians' experience. Figure 9.47 presents these details.

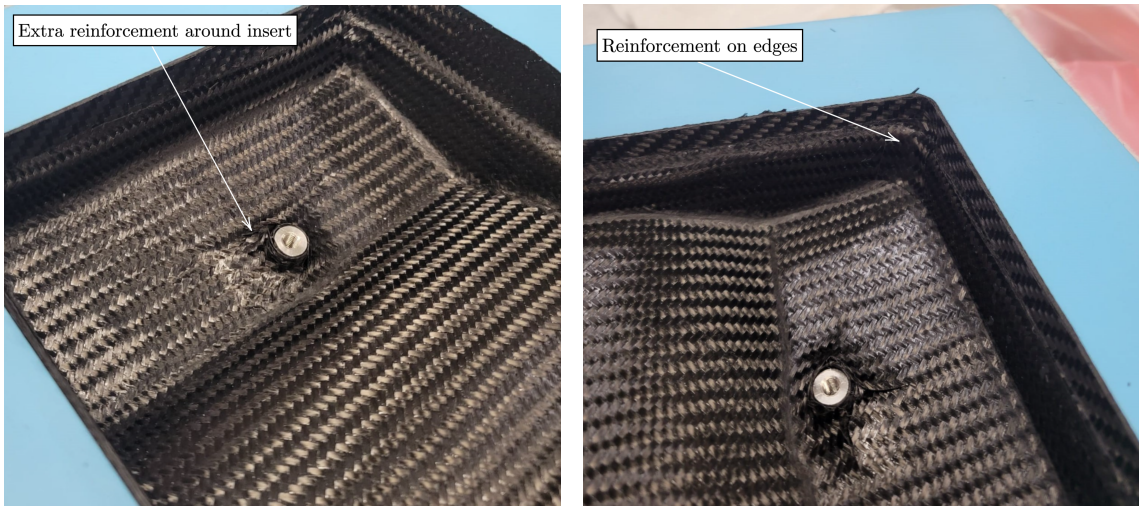

(a) Insert reinforcement (b) Edge reinforcement

Figure 9.47: Lamination details in the top mould

Once all prepreg plies forming the outer laminates of the enclosure components were laid up, vacuum bagging was performed. This stage requires greater attention compared to a debulking cycle. All areas covered with prepreg material must be fully covered with release film, followed by breather cloth. The breather cloth must be properly distributed across the mould to ensure continuous air evacuation paths during vacuum application. Figure 9.48 illustrates the correct application of these consumables in the bottom mould.

After putting the mould into the sealed plastic bag for vacuum, as the vacuum is pulling down, the bag should be manipulated into all of the contours and corners of the components geometry to avoid bridging and ensure that an even pressure is applied over the entire part.

(a) Release film (b) Breather cloth

Figure 9.48: Application of release film and breather cloth in the vacuum bagging process

Once the assembly was sealed within the vacuum bag, the bag was manually conformed to all contours and corners of the component's geometry to prevent bridging and to ensure uniform pressure distribution. For the top mould, an additional step was performed to prevent resin infiltration into the threads of the bolt and bigHead insert. The bolts were coated with a release wax, and additional breather cloth was placed above the bolt area to prevent potential tearing of the vacuum bag during autoclave curing. This configuration is shown in Figure 9.49.

Figure 9.49: Vacuum bagging detail in the top mould

Once vacuum was fully applied, the line was disconnected from the quick-release valve and a vacuum gauge was attached to verify system tightness. The gauge behaviour was monitored to detect any pressure loss, in a verification process known as the "drop test", which is a standard pre-cure validation step. Figure 9.50 shows the vacuum gauge setup during this procedure.

Figure 9.50: Vacuum gauge during the "drop test" procedure

9.4.3 First Autoclave Cycle

After ensuring an adequate vacuum bagging process, the moulds were placed in the autoclave for curing. Each mould was connected to its corresponding vacuum line, and the system was verified to ensure proper operation. Due to its larger dimensions, the bottom mould was equipped with two vacuum valves, while the smaller top mould used one. Thermocouples were inserted into both moulds to monitor the part temperature throughout the curing process. Figure 9.51 shows both moulds positioned inside the autoclave, ready for the first cure cycle.

Figure 9.51: Moulds in the autoclave before the first autoclave cycle

The autoclave provided real-time readings of temperature and pressure, which were used to record the cure cycle data. The curing process was controlled by a timer that started once the thermocouple indicated that the part had reached the target curing temperature. Figure 9.52 shows the main instruments used during this process.

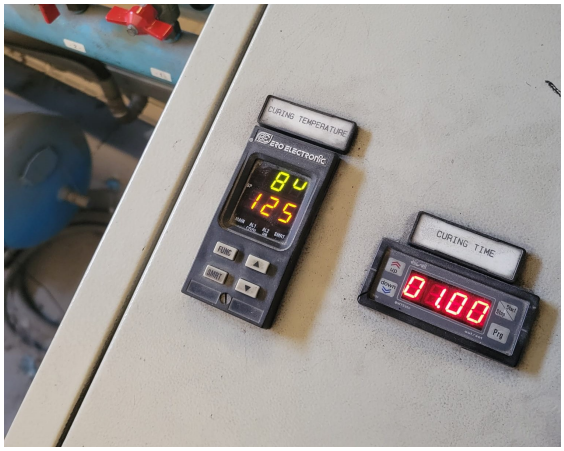

(a) Part temperature reading and cure timer

(b) Autoclave temperature (top) and pressure (bottom) gauges

Figure 9.52: Autoclave process readings

The first autoclave cycle followed the recommended curing procedure from the Toray E731 prepreg datasheet (Appendix B). The selected cure parameters consisted of a dwell at 125°C for one hour under 6 bar of pressure. Although the datasheet does not specify the recommended pressure for cure, 6 bar was chosen based on other Toray prepreg systems. Additionally, higher pressure levels are generally beneficial for laminate consolidation and mechanical performance. Figure 9.53 shows both the theoretical and recorded temperature profiles of the cycle. The heating and cooling phases were planned at a rate of 2°C/min; however, the autoclave's real heating capability was approximately 1°C/min, resulting in a slightly longer total cycle duration.

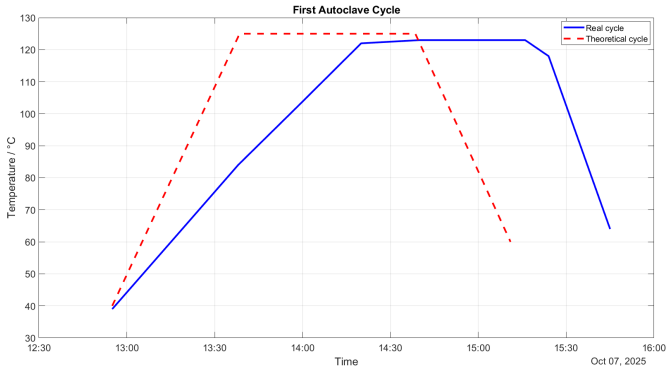

Figure 9.53: First autoclave cycle

Pressure was gradually increased in parallel with the autoclave temperature ramp-up until reaching the specified curing pressure of 6 bar. The curing process proceeded smoothly and without incident.

Following completion of the cycle, the components were allowed to cool down gradually inside the autoclave. Subsequent inspection of the laminates confirmed good consolidation and uniform resin cure in both components.

9.4.4 Second Lamination

During the placement of the 3D printed cores into the top lid mould, a minor issue was encountered. The filleted edges of the printed cores were not sufficiently curved, preventing a perfect fit. The cores were manually sanded and reshaped until they conformed to the mould geometry. Although this design inaccuracy did not cause major issues, it was noted for correction in future iterations of the enclosure. The remainder of the core geometry functioned as intended, particularly the insert holes designed for integration of the bigHead inserts. Once the cores were properly positioned, the honeycomb core was placed on top. The printed cores were designed to create a flat surface that supported the honeycomb material without deformation. Figure 9.54 shows the adjusted printed components and the mould with both the cores and honeycomb in position

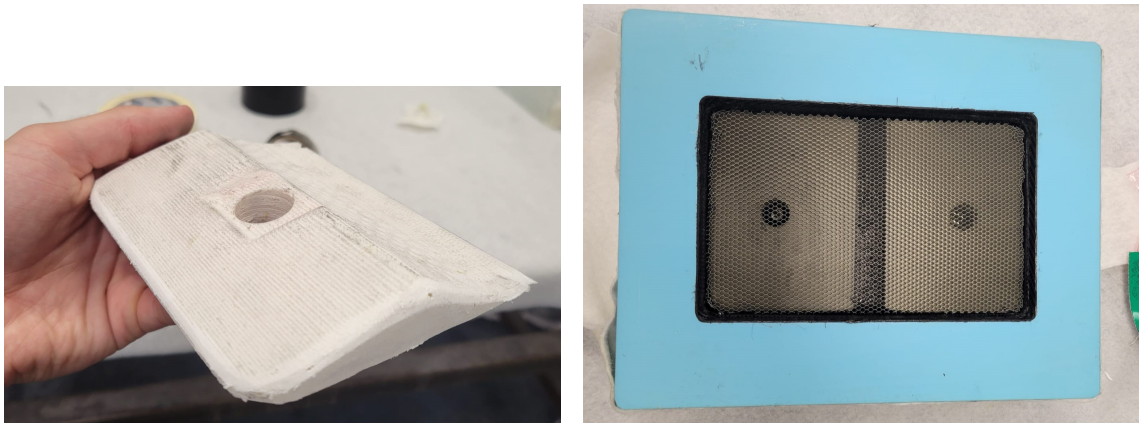

(a) 3D printed cores after sanding

(b) Top mould with cores and honeycomb material

Figure 9.54: Details of manufacturing of the top enclosure component

The honeycomb was also placed in the bottom laminate, followed by the lamination of 10 prepreg plies according to the previously defined stacking sequence.

Additional details worth mentioning include the trimming of the extended plies forming the junction between the internal and external laminates. This was necessary to ensure proper ply conformity without folds or wrinkles, and to create a gradual ply drop-off region, as shown in Figure 9.55a. Furthermore, a layer of peel ply was applied on the assembly flanges to facilitate post-processing operations such as sanding and polishing, ensuring a clean and reactive bonding surface. This detail is shown in Figure 9.55b.

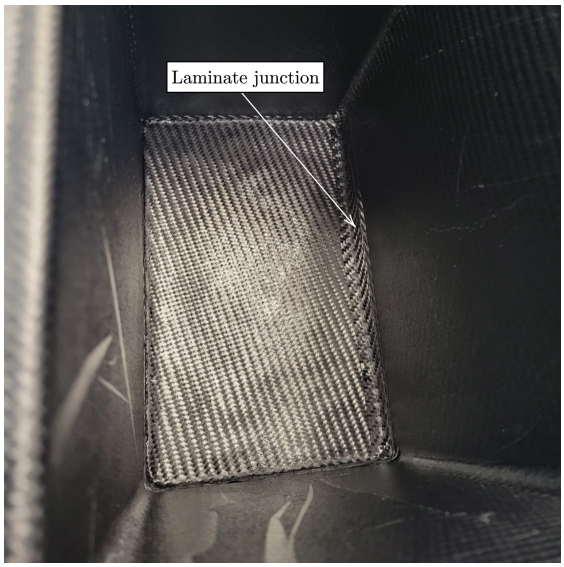

(a) Bottom component during lamination of the final plies

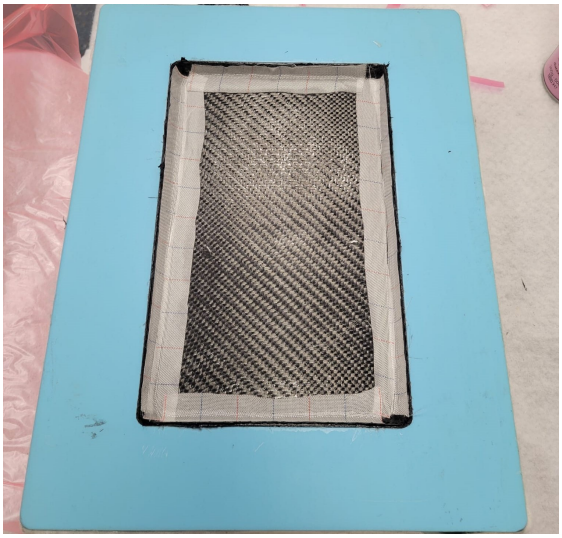

(b) Peel ply applied to the adhesion flanges

Figure 9.55: Additional manufacturing details

A final vacuum bagging process was then performed following the same procedure previously described.

9.4.5 Second Autoclave Cycle

After completion of the second lamination, the components were prepared for the final autoclave cure. Figure 9.56 shows both moulds inside the autoclave before and after this second cycle.

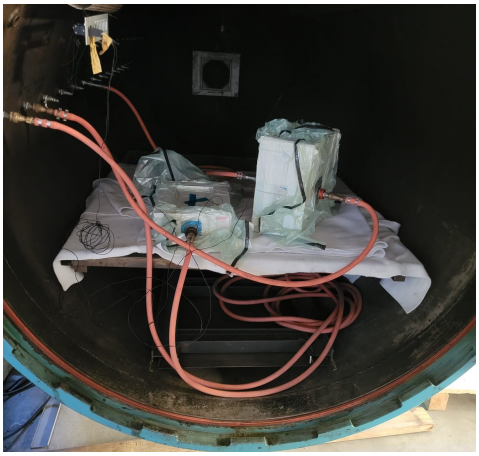

(a) Moulds in the autoclave before the second autoclave cycle

(b) Moulds after the second cure

Figure 9.56: Second autoclave cure process

A two-step cure strategy was adopted to prevent honeycomb core crushing. Performing a single high-pressure cure (>1.5 bar) would risk permanent deformation of the core and render the components unusable. Therefore, the first cycle was defined at high pressure to ensure optimal consolidation of the external laminates, followed by a second, low-pressure cycle for the internal laminates. This approach provided an effective compromise between mechanical performance and structural integrity.

The second autoclave cycle consisted of a one-hour dwell at 125°C under 1 bar pressure, with the same heating and cooling rates applied previously. The theoretical and real temperature profiles of this cycle are presented in Figure 9.57.

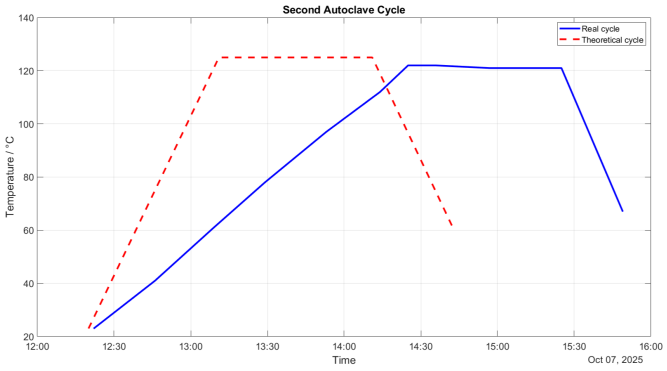

Figure 9.57: Second autoclave cycle

9.4.6 Demoulding and Finishing

Once the curing process was completed, the carbon fibre components were demoulded. The bottom component was easily extracted due to the mould's geometry, whereas the top component required greater care during demoulding. Both parts were successfully released and are shown in Figures 9.58a and 9.58b.

(a) Bottom and top components after demoulding

(b) Top component after demoulding

Figure 9.58: Second autoclave cure process

The components were visually inspected for surface defects and porosity. Only minor superficial imperfections were identified, confirming good overall laminate quality. Several post-processing steps remain, including trimming of excess material, edge sanding, and the application of a protective varnish to achieve an enhanced "exposed carbon" aesthetic finish. Figures 9.59 and 9.60 show the assembled composite prototype and its components following the trimming process.

Figure 9.59: Enclosure after removal of excess material

(a) Top component

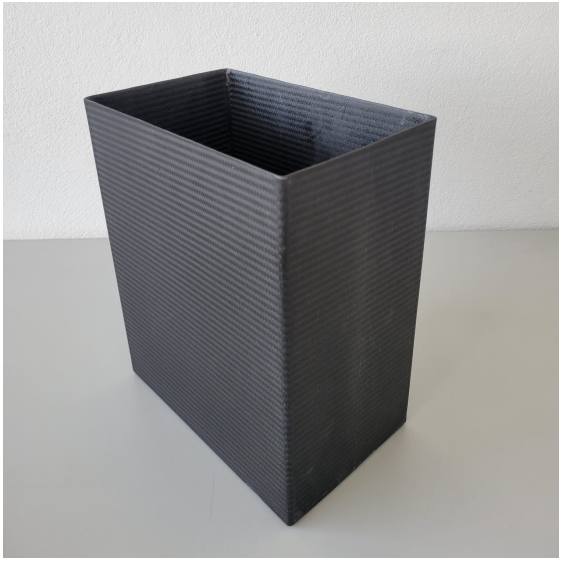

(b) Bottom component

Figure 9.60: Enclosure components after trimming process

At this stage, only exterior finishing steps remain to be completed.

The final weight of the prototype enclosure is 1.53 kg, approximately 200 grams higher than the estimated value for the final design. Assuming the 3D printed parts account for roughly 200 grams, the discrepancy falls within acceptable tolerance. Overall, the prototype achieves an approximate 60% weight reduction compared with the previous Famel enclosure design (claimed to be 4 kg). Figure 9.61 shows the prototype placed on a scale, confirming its final weight.

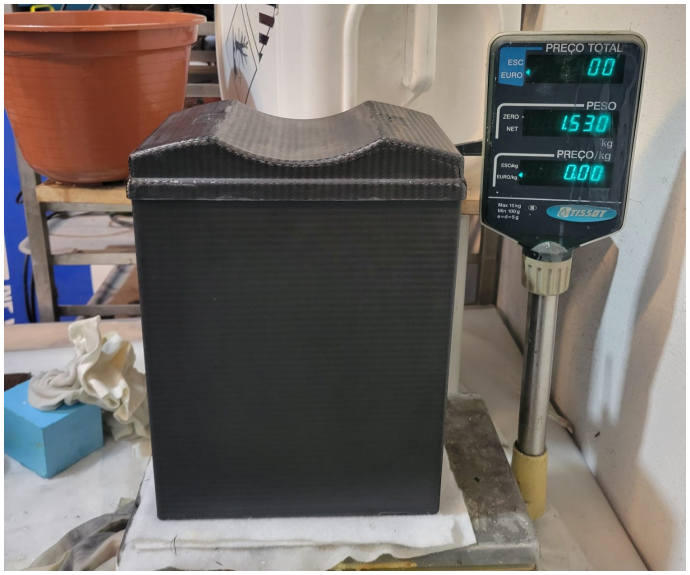

Figure 9.61: Enclosure weight measurement

Chapter 10

Carbon Fibre Composite Material Flammability Testing

This chapter presents the experimental flammability testing of carbon fibre composites according to the UL 94 *Standard for Safety of Flammability of Plastic Materials for Parts in Devices and Appliances*. The standard was introduced in Chapter 2, Section 2.5. The chapter begins with a brief description of the specimen production process, followed by the testing procedure and corresponding results.

10.1 Specimen Production

The specimens were produced at Adamastor by the author, with the assistance of the company's technicians. The process followed a conventional prepreg–autoclave manufacturing route, described concisely below.

Three different prepreg materials were used:

- E731-00 HS0838 Carbon TR30S 205 gsm 2×2 Twill 3K 40% RC
- E750-00 HS0838 Carbon TR30S 205 gsm 2×2 Twill 3K 40% RC
- E745-00 IM0123-A Carbon IM7 280 gsm 5HS 6K 42% RC

These materials will be referred to as E731, E745, and E750, respectively. The selected materials included the prepreg used for the enclosure prototype (E731) and two other prepregs available at Adamastor. The primary goal was to characterise the flammability behaviour of the prototype's prepreg to validate the design, while also extending the company's knowledge of the other materials.

The initial plan was to manufacture eight specimens from each prepreg, using an eight-ply layup, consistent with the original laminate design of the enclosure. However, as discussed in Chapter 9, additional specimens were produced using 10 and 12 plies of E731 prepreg to determine the number of plies required to match the thickness of an eight-ply laminate made from the E731

245 gsm prepreg. The thickness of each specimen was then measured to determine the cured ply thickness.

Since flammability performance is mainly influenced by the material's chemical composition and total thickness, the laminates were manufactured with a simple [0º] layup. This approach simplified production and minimised waste compared to reproducing the quasi-isotropic laminate of the enclosure, while still yielding representative results.

Lamination began with the manual placement of rectangular prepreg plies on a flat aluminium surface that had been cleaned, abraded, and coated with release agent. The laminate size was selected to allow the production of eight specimens per material. As the UL 94 test requires six specimens per laminate, two additional ones were produced as a safety margin. Four laminates were prepared: three with eight plies (E731, E745, and E750) and one E731 laminate with 10 plies on one half and 12 plies on the other. Figure 10.1 shows the lamination process.

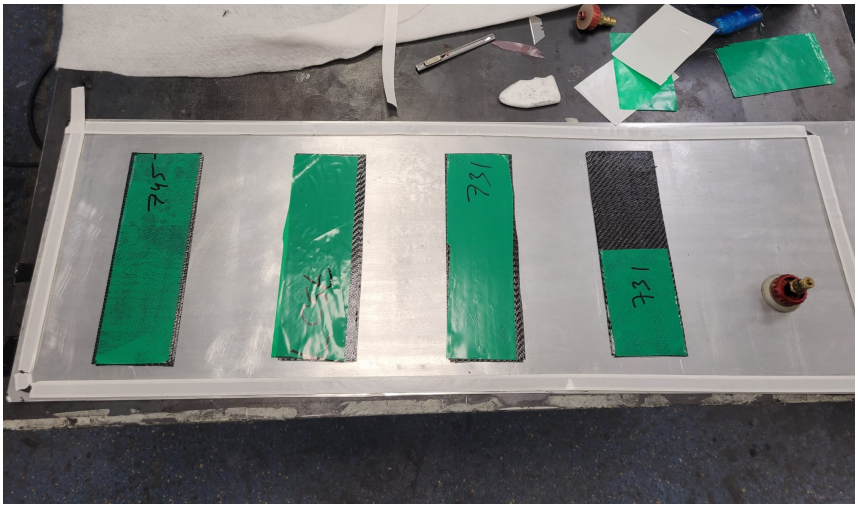

Figure 10.1: Lamination of plies for specimen production

Each laminate was debulked at its midpoint before completing the remaining plies. A final vacuum bagging process was then performed, as shown in Figure 10.2.

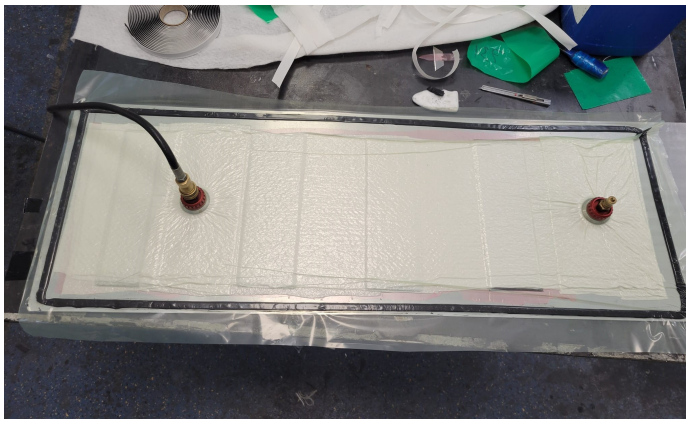

Figure 10.2: Vacuum bagging of specimen laminates

The vacuum integrity was verified using a “drop test” prior to autoclave curing. The laminates were then placed in the autoclave, as shown in Figure 10.3, and cured following the parameters recommended in the Toray E731 datasheet (Appendix B). The cure cycle consisted of a dwell at 125°C for one hour under 6 bar pressure, identical to the defined conditions for the enclosure’s outer laminate.

Figure 10.3: Specimen laminates inside the autoclave before cure

The curing process proceeded without issues, resulting in laminates with good compaction and surface quality (Figure 10.4).

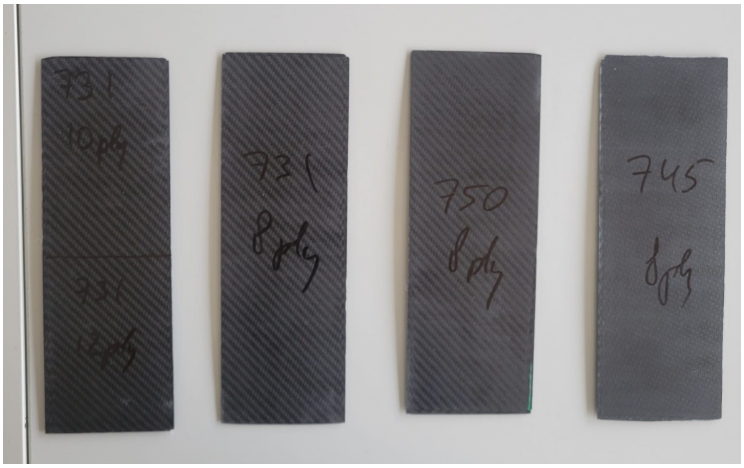

Figure 10.4: Cured specimen laminates

After curing, the laminates were CNC-cut into eight specimens each (with the E731 10-ply and 12-ply laminates yielding four specimens each). CNC cutting ensured compliance with the tight dimensional tolerances required by the standard. Figure 10.5a shows the cutting process, and Figure 10.5b illustrates a finished E731 specimen.

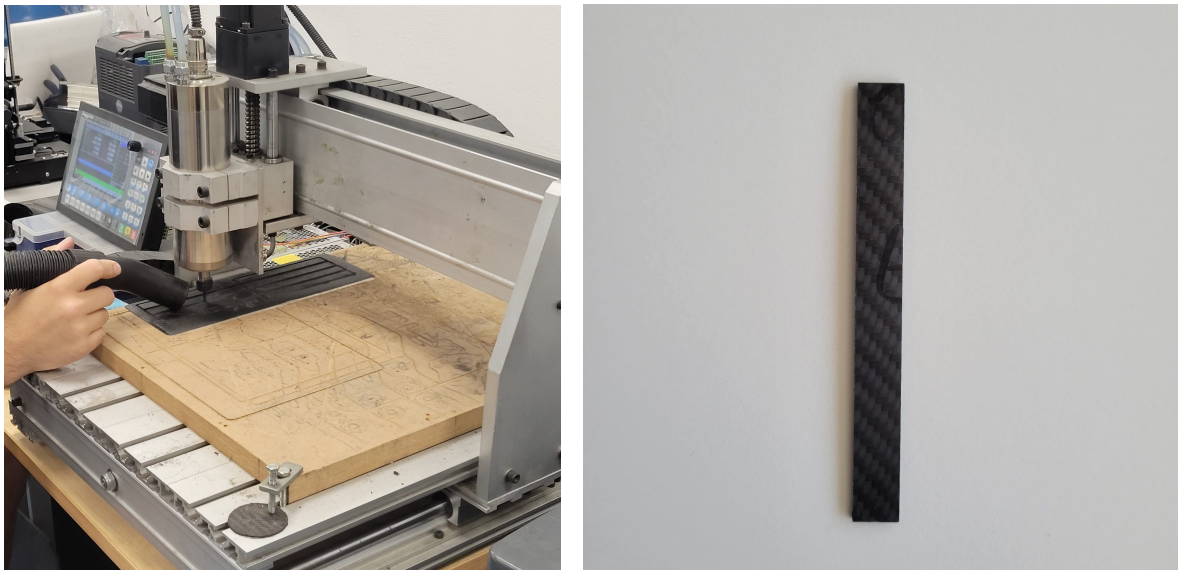

(a) CNC cutting of the specimens (b) E731 Specimen

Figure 10.5: Specimen preparation

Dimensional verification of the E731 specimens was carried out using a calliper, and the results are presented in Table 10.1.

Table 10.1: E731 prepreg specimens dimensions and mean ply thickness

Specimen nº	**Dimensions (Length / Width / Thickness) / mm**	**Mean Dimensions / mm**
E731 8ply		
1	$125.29 \times 13.33 \times 1.90$	$125.26 \times 13.34 \times 1.87$
2	$125.25 \times 13.35 \times 1.87$	
3	$125.25 \times 13.29 \times 1.86$	
4	$125.25 \times 13.25 \times 1.89$	
5	$125.22 \times 13.38 \times 1.85$	
6	$125.29 \times 13.43 \times 1.87$	
7	$125.28 \times 13.36 \times 1.88$	
8	$125.23 \times 13.29 \times 1.85$	
	Mean ply thickness:	$\approx$ **0.23**
E731 10ply		
1	$125.32 \times 13.38 \times 2.32$	$125.30 \times 13.34 \times 2.3$
2	$125.25 \times 13.28 \times 2.28$	
3	$125.28 \times 13.34 \times 2.31$	
4	$125.37 \times 13.38 \times 2.30$	
	Mean ply thickness:	$\approx$ **0.23**
E731 12ply		
1	$125.34 \times 13.36 \times 2.81$	$125.32 \times 13.38 \times 2.80$
2	$125.33 \times 13.48 \times 2.80$	
3	$125.26 \times 13.23 \times 2.79$	
4	$125.35 \times 13.46 \times 2.81$	
	Mean ply thickness:	$\approx$ **0.23**

All specimens complied with the dimensional specifications of the UL 94 standard (125 ±5 mm in length and 13.0 ±0.5 mm in width). Regarding thickness, measurements for the 8-, 10-, and 12-ply E731 laminates indicated a cured ply thickness of approximately 0.23 mm. This value closely matches the theoretical ply thickness of 0.219 mm provided by Toray's calculator [64]. Consequently, a 10-ply laminate of E731 205 gsm prepreg achieves a total thickness of about 2.3 mm, comparable to the 2.24 mm of the originally specified E731 245 gsm laminate for the enclosure. This equivalence justified the transition to a 10-ply laminate in the final prototype design without compromising its structural intent. Moreover, the variation in laminate thickness among the specimens enables assessing the influence of thickness on the flammability behaviour of E731 carbon fibre prepreg.

Following the cutting process, a manufacturing error was detected in the E750 8-ply laminate, resulting in several defective specimens. The remaining usable material was salvaged into 5-ply specimens, which were still tested for reference. As thicker laminates generally exhibit improved flammability performance, successful testing of the thinner E750 laminate can be considered a conservative indication of compliance for an equivalent 8-ply configuration.

10.2 UL 94 Horizontal Burning Test

10.2.1 Description and Preliminary Measures

The flammability tests were conducted at INEGI's fire laboratory by certified laboratory technicians. The specimens were grouped into five sets according to material and thickness:

- Sample 1 – E731, 8 plies;
- Sample 2 – E731, 10 plies;
- Sample 3 – E731, 12 plies;
- Sample 4 – E745, 8 plies;
- Sample 5 – E750, 5 plies.

The testing followed the UL 94 Horizontal Burning Test, Edition 7 (2023). The equipment used included:

- UL chamber (Figure 10.6);
- Chronometer;
- Ruler;
- Digital calliper;
- Balance.

Figure 10.6: UL chamber used during testing

Before testing, all specimens were conditioned for 48 hours at 23 ±2°C and 50 ±10% relative humidity, as specified by ASTM D618 (ISO 291). Each specimen was marked at 25 mm and 100 mm from the ignited end, measured, and weighed. The corresponding dimensions are provided in Table 10.2, confirming that all specimens conformed to the standard's dimensional tolerances.

Table 10.2: Specimen measurements made by Inegi

Specimens	Length / mm	Width / mm	Thickness / mm	Mass / g
Sample 1 – 731 8ply				
LFF.2025.321.01	125	13	2.0	4.6
LFF.2025.321.02	125	13	2.0	4.6
LFF.2025.321.03	125	13	2.0	4.5
Sample 2 – 731 10ply				
LFF.2025.322.01	125	13	2.5	5.8
LFF.2025.322.02	125	13	2.5	5.7
LFF.2025.322.03	125	13	2.5	5.7
Sample 3 – 731 12ply				
LFF.2025.323.01	125	13	2.9	6.9
LFF.2025.323.02	125	13	2.9	7.0
LFF.2025.323.03	125	13	2.9	6.8
Sample 4 – 745 8ply				
LFF.2025.324.01	125	13	2.8	6.4
LFF.2025.324.02	125	13	2.8	6.4
LFF.2025.324.03	125	13	2.8	6.4
Sample 5 – 750 5ply				
LFF.2025.325.01	125	13	1.4	2.9
LFF.2025.325.02	125	13	1.4	2.9
LFF.2025.325.03	125	13	1.4	2.9

During the test, the specimen was positioned horizontally, and the free end was exposed to a blue flame, 20 mm high, at a 45° angle. The flame was applied for 30 ±1 seconds or until the combustion front reached the 25 mm mark, whichever occurred first. After removing the flame, the burning progression was recorded until the flame self-extinguished or reached the 100 mm reference mark.

According to the UL 94 HB classification criteria, a material is classed as HB if:

- Its burning rate does not exceed 40 mm/min over a 75 mm span for specimens 3.0–13 mm thick, or
- Its burning rate does not exceed 75 mm/min over a 75 mm span for specimens less than 3.0 mm thick, or
- It ceases burning before reaching the 100 mm mark.

Figures 10.7 and 10.8 show a specimen during and after flame exposure.

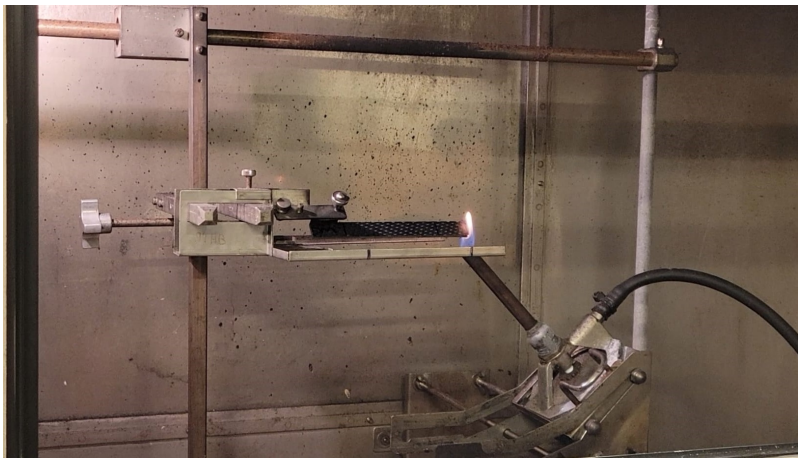

Figure 10.7: Specimen during testing conditions, exposed to the flame

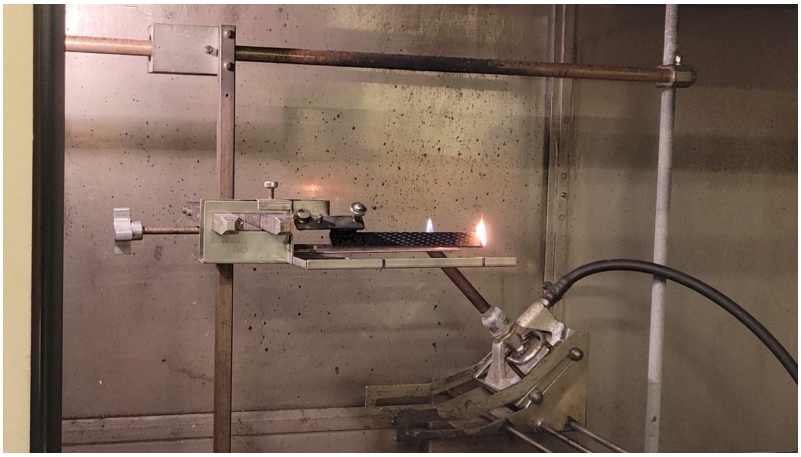

Figure 10.8: Specimen during testing conditions, flame removed

10.2.2 Results

Flame propagation was recorded for all specimens, and the main results are summarised in Table 10.3.

Table 10.3: Horizontal burning test results

Test specimen reference	**First measurement point**	**Measured values**		**Linear Burning Rate / mm/min**	**Compliance**
		Burning Distance / mm	**Burning Time / s**		**Pass/Fail**
Sample 1 - 731 8ply					
LFF.2025.321.01	Not reached	-	-	-	Pass
LFF.2025.321.02	Not reached	-	-	-	Pass
LFF.2025.321.03	Not reached	-	-	-	Pass
Sample 2 - 731 10ply					
LFF.2025.322.01	Not reached	-	-	-	Pass
LFF.2025.322.02	Not reached	-	-	-	Pass
LFF.2025.322.03	Not reached	-	-	-	Pass
Sample 3 - 731 12ply					
LFF.2025.323.01	Not reached	-	-	-	Pass
LFF.2025.323.02	Not reached	-	-	-	Pass
LFF.2025.323.03	Not reached	-	-	-	Pass
Sample 4 - 745 8ply					
LFF.2025.324.01	Not reached	-	-	-	Pass
LFF.2025.324.02	Not reached	-	-	-	Pass
LFF.2025.324.03	Not reached	-	-	-	Pass
Sample 5 - 750 5ply					
LFF.2025.325.01	Not reached	-	-	-	Pass
LFF.2025.325.02	Not reached	-	-	-	Pass
LFF.2025.325.03	Not reached	-	-		Pass

Considering the above test results, all material samples meet the burn-rate requirement of the standard UL94, for specimens having a thickness less than 3.0 mm, and are classed HB.

Across all tests, the behaviour was consistent: the specimen tips ignited during the 30-second flame exposure but self-extinguished within a few seconds after flame removal, before the combustion front reached the 25 mm mark. Therefore, no measurable burning rate was recorded, and all materials easily passed the horizontal burning test. Figure 10.9 illustrates a specimen after testing.

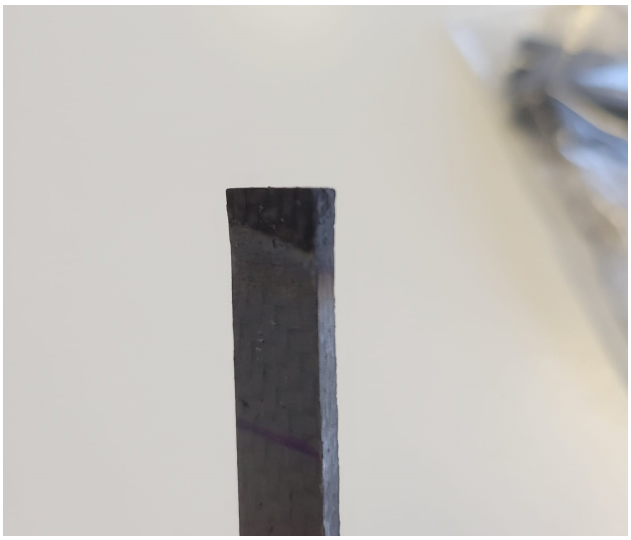

Figure 10.9: Specimen after testing

All prepregs, with their different combinations of resin and fiber performed really well in these testing conditions. Some details could be taken from the test. Like thickness plays a big role in the capacity for the material to catch fire (flame resisitance) and the time that the specimen then takes to self estinguish. Thicker laminates take longer to catch fire and when they catch fire they take longer to estinguish themselves.

All three prepregs, despite differences in fibre type and resin formulation, demonstrated excellent flame resistance under these test conditions. The results also confirm that laminate thickness plays a significant role: thicker laminates were more resistant to ignition and, once ignited, required slightly more time to self-extinguish.

The successful performance of all materials, particularly the E731 prepreg used in the enclosure prototype, highlights the material's potential for flame retardancy and suitability for the intended application. This outcome reinforces the safety and robustness of the prototype design.

Chapter 11

Conclusion

11.1 Project Overview and Reflections

The main objective, to devise and implement a complete methodology for the design and development of a composite battery enclosure leading to a physical prototype, was fully achieved. Nevertheless, the project faced several constraints, particularly limited technical support from both collaborating companies. On Stark Future's side, the collaboration did not materialise beyond the initial phase. On Famel's side, access to key technical data regarding the motorcycle and battery system was scarce, which restricted the project's capacity to achieve full functional integration of the prototype with the real vehicle. Time was also a significant limitation, as the effective work could only begin in June, leaving a very condensed timeframe for the project's execution.

Despite these challenges, the work conducted with Stark Future represented a valuable learning phase. It allowed the acquisition of essential knowledge of composite modelling, finite element analysis, and optimisation tools that were later applied successfully in the Famel project. Furthermore, it demonstrated the feasibility and benefits of transitioning from a lightweight metallic enclosure, such as magnesium, to a composite-based structure. The optimisation studies carried out for the Stark VARG enclosure revealed that a carbon fibre composite enclosure could achieve a weight reduction of approximately 30% compared to the magnesium design, while maintaining excellent stiffness and mechanical integrity.

Regarding the Famel E-XF project, even with the functional and time constraints, all objectives initially set for this dissertation were fulfilled. The methodology was fully developed and executed, covering conceptual design, mechanical and thermal numerical validation, optimisation, prototype production, and experimental testing. The framework was firmly grounded in relevant safety and homologation standards, ensuring that all design and validation steps were aligned with regulatory requirements.

The mechanical and thermal validation phases required the development of detailed finite element models designed to replicate the testing procedures defined in the UN ECE R136 regulation and to meet the specific requirements established by Famel. Although these simulations could not fully reproduce real test conditions—mainly due to the limited timeframe available and the

incomplete technical information concerning the battery system—they provided valuable insights into the structural and thermal performance of the enclosure. In particular, the mechanical validation phase resulted in an optimised design concept aimed at enhancing the enclosure's capacity to protect the battery modules under mechanical loads, while preserving structural efficiency and maintaining a lightweight configuration.

The production phase represented one of the greatest challenges and, simultaneously, one of the most valuable learning experiences of this dissertation. It tested the feasibility of the design under real manufacturing constraints and provided extensive hands-on experience in composite fabrication processes. This stage also required close teamwork and continuous knowledge transfer from Adamastor's technical team to the author. Despite the complexity of the task, the manufacturing of a full-scale carbon fibre composite prototype was successfully completed. The resulting enclosure achieved an overall weight reduction of approximately 60% compared with the previous Famel enclosure design, confirming the significant potential of composite materials for electric motorcycle applications.

On the experimental validation side, due to time limitations, only the UL 94 flammability test on composite specimens could be conducted. Nevertheless, this represented an important step in the validation of the prototype's safety performance. The results confirmed that all tested materials successfully passed the UL 94 HB horizontal burning test, demonstrating acceptable flame retardancy characteristics and providing valuable data for future developments.

11.2 Future Work

Several opportunities for continuation and improvement have been identified.

First, numerical model refinement is essential. Future work should include mesh convergence and sensitivity studies to ensure numerical accuracy and robustness of the finite element results.

Further development of the Stark VARG composite enclosure concept is also recommended. The initial studies showed great potential for a lightweight and high-performance enclosure design, but further optimisation is required to balance performance, manufacturability, and cost-effectiveness. A refined design could offer a strong alternative to metallic enclosures in future Stark motorcycle models.

Regarding the Famel E-XF prototype, several developments are suggested to move closer to a functional, production-ready design. These include improving the integration of the enclosure with the motorcycle by incorporating components such as charging connectors, which were not made available by Famel during this project. Additionally, a detailed study of the enclosure's vibration behaviour should be conducted, as this analysis could not be performed within the scope and timeframe of the present work. The current bonded configuration could also be reconsidered in favour of a more modular fastening system, allowing access to the internal battery pack for maintenance or replacement. Such an approach would simplify servicing, reduce repair costs, and increase the product's overall practicality and sustainability.

Another key step would be to deepen the thermal validation of the composite enclosure. A more comprehensive thermal study should be conducted using real operating data from Famel's battery system. This would allow testing and evaluation of passive and active thermal management solutions, which could then be integrated and validated experimentally.

Future research should also explore alternative manufacturing methods aimed at cost reduction and sustainability. A comparative analysis of production processes, such as resin infusion, combined with a Life Cycle Assessment (LCA), could quantify both the economic and environmental benefits of composite enclosures. The potential use of bio-based or recyclable composite materials should also be investigated, considering natural or hybrid fibres and thermoplastic or bio-resin matrices.

Establishing quality control procedures for composite manufacturing is another important step, ensuring repeatability, performance, and compliance with homologation standards. Furthermore, future work should address the transition from prototype to scalable production, taking into account expected production volumes and cost targets. Design choices suitable for small-batch prototyping, such as 3D printed inserts, could be replaced with more industrially viable polymeric alternatives for serial production.

Finally, additional validation efforts are recommended. The final prototype should undergo further mechanical and thermal finite element analyses, followed by experimental mechanical drop tests according to the UN ECE R136 procedures. In terms of fire safety, further UL 94 testing is advised, including the UL 94 V (Vertical Burning) classification, to fully characterise the material's flame-retardant behaviour. If the selected materials do not comply with the stricter vertical test, fire-approved and self-extinguishing materials such as Toray TC346 could be considered. Should homologation be pursued, the full regulatory testing procedure must be conducted, including all associated battery components.

References

[1] Stark Future. *Stark VARG EX – The Fastest Electric Off-Road Bike in the World*. https://starkfuture.com/pt-PT/products/stark-varg-ex. Accessed: 2025-05-22. 2025.

[2] Seyed Mahdi Miraftabzadeh, Michela Longo, and Federica Foiadelli. "Mobility and Future Trends". In: *Emerging Battery Technologies to Boost the Clean Energy Transition*. Springer, 2024, pp. 3–11. DOI: 10.1007/978-3-031-48359-2_1. URL: https://link.springer.com/chapter/10.1007/978-3-031-48359-2_1.

[3] Marc Dijk, Renato J. Orsato, and René Kemp. "The emergence of an electric mobility trajectory". In: *Energy Policy* 52 (2012), pp. 135–145. ISSN: 0301-4215. DOI: 10.1016/j.enpol.2012.04.024. URL: https://www.sciencedirect.com/science/article/pii/S0301421512003242.

[4] Remco Hoogma et al. *Experimenting for Sustainable Transport: The Approach of Strategic Niche Management*. London: Spon Press, 2002. ISBN: 9780415271172. DOI: 10.4324/9780203994061. URL: https://www.taylorfrancis.com/books/oa-mono/10.4324/9780203994061.

[5] *Global Electric Mobility Market Report and Forecast 2024-2032*. Dec. 2023. URL: https://www.researchandmarkets.com/reports/5921482/global-electric-mobility-market-report-forecast.

[6] Automobile Association of Portugal (ACAP). *Automotive Sector Statistics in Portugal*. Accessed: February 19, 2025. 2025. URL: https://acap.pt/pt/estatisticas/graficos.

[7] Irvylle Cavalcante et al. "Dataset on Electric Road Mobility: Historical and Evolution Scenarios until 2050". In: *Scientific Data* 11 (Sept. 2024), p. 1019. DOI: 10.1038/s41597-024-03801-3. URL: https://www.nature.com/articles/s41597-024-03801-3.

[8] Associação Automóvel de Portugal (ACAP). *Mercado de Ciclomotores, Motociclos, Triciclos e Quadriciclos em Portugal - Dezembro 2024*. Accessed: 2025-03-06. 2024. URL: https://www.acap.pt/pt/noticia/1130/mercado-de-ciclomotores-motociclos-triciclos-e-quadriciclos-em-portugal-dezembro-2024.

[9] Statista. *Electric motorcycle sales in Europe by key country*. Accessed: 2025-03-06. 2025. URL: https://www.statista.com/statistics/1223205/europe-electric-motorcycle-sales-by-key-country/.

[10] Fan Zhang et al. “The battery-swapping revolution: Exploring user preferences in electric micro-mobility sector”. In: *Transportation Research Part A: Policy and Practice* 194 (2025), p. 104416. ISSN: 0965-8564. DOI: https://doi.org/10.1016/j.tra.2025.104416. URL: https://www.sciencedirect.com/science/article/pii/S0965856425000448.

[11] Albertino Arteiro. *Advanced Materials: Course Materials and Semi-Products*. FEUP, 2021.

[12] P. K. Mallick. *Fiber-Reinforced Composites: Materials, Manufacturing, and Design*. Boca Raton: CRC Press, 2007. DOI: 10.1201/9781420005981.

[13] Seçkin Erden and Kingsley Ho. “3 - Fiber reinforced composites”. In: *Fiber Technology for Fiber-Reinforced Composites*. Ed. by M. Özgür Seydibeyoğlu, Amar K. Mohanty, and Manjusri Misra. Woodhead Publishing Series in Composites Science and Engineering. Woodhead Publishing, 2017, pp. 51–79. ISBN: 978-0-08-101871-2. DOI: https://doi.org/10.1016/B978-0-08-101871-2.00003-5. URL: https://www.sciencedirect.com/science/article/pii/B9780081018712000035.

[14] Hexcel Corporation. *HexPly® Prepreg Technology*. Tech. rep. Publication No. FGU 017c. Hexcel Corporation, 2013.

[15] X. Huang. “Fabrication and Properties of Carbon Fibers”. In: *Materials (Basel)* 2.4 (2009), pp. 2369–2403. DOI: 10.3390/ma2042369.

[16] Siti Madiha Muhammad Amir et al. “16 - Nondestructive testing method for Kevlar and natural fiber and their hybrid composites”. In: *Durability and Life Prediction in Biocomposites, Fibre-Reinforced Composites and Hybrid Composites*. Ed. by Mohammad Jawaid, Mohamed Thariq, and Naheed Saba. Woodhead Publishing Series in Composites Science and Engineering. Woodhead Publishing, 2019, pp. 367–388. ISBN: 978-0-08-102290-0. DOI: https://doi.org/10.1016/B978-0-08-102290-0.00016-7. URL: https://www.sciencedirect.com/science/article/pii/B9780081022900000167.

[17] Saptarshi Maiti et al. “Sustainable Fiber-Reinforced Composites: A Review”. In: *Advanced Sustainable Systems* (Sept. 2022). DOI: 10.1002/adsu.202200258. URL: https://doi.org/10.1002/adsu.202200258.

[18] Eco-Technilin. *Lineo Flax Prepreg*. Accessed: 2025-02-26. 2025. URL: https://pdf.nauticexpo.com/pdf/eco-technilin/lineo-flax-prepreg/39306-29802.html.

[19] Ansys Inc. *Ansys CES EduPack 2024 R2*. Software database. Material property data accessed via Ansys CES EduPack 2024 R2 software. 2024.

[20] Easy Composites. *Technical Data Sheet - FlaxPreg T-UD 100*. Accessed: 2025-02-26. 2025. URL: https://media.easycomposites.co.uk/datasheets/Technical%20Data%20Sheet%20FlaxPreg%20T-UD%20100.pdf.

[21] Ru-Min Wang, Shui-Rong Zheng, and Ya-Ping Zheng. *Polymer Matrix Composites and Technology*. Cambridge, UK and Beijing, China: Woodhead Publishing and Science Press, 2011. ISBN: 978-1-84569-727-3. URL: https://www.woodheadpublishing.com/.

[22] Gurit. *Guide to Composites*. Version v5. 2022.

[23] Sunarto Kaleg et al. “Addressing Fire Safety, Ground Impact Resistance, and Thermal Management in Composite EV Battery Enclosures: A Review”. In: *Automotive Experiences* 7 (Dec. 2024), pp. 460–485. DOI: 10.31603/ae.12540.

[24] Carl-Christoph Höhne et al. “New approach for electric vehicle composite battery housings: Electromagnetic shielding and flame retardancy of PUR/UP-based sheet moulding compound”. In: *Composites Part A: Applied Science and Manufacturing* 167 (2023), p. 107404. ISSN: 1359-835X. DOI: https://doi.org/10.1016/j.compositesa.2022.107404. URL: https://www.sciencedirect.com/science/article/pii/S1359835X22005851.

[25] B. Azzopardi et al. “Recent Advances in Battery Pack Polymer Composites”. In: *Energies* 16.17 (2023), p. 6223. DOI: 10.3390/en16176223. URL: https://doi.org/10.3390/en16176223.

[26] R. K. Chidambaram, P. Pedapati, P. R. Kanna, et al. “Structural assessment of electric two-wheeler battery enclosure: thermal and structural study”. In: *Journal of Thermal Analysis and Calorimetry* (2024). DOI: 10.1007/s10973-024-13458-0. URL: https://doi.org/10.1007/s10973-024-13458-0.

[27] C. Schludi and J. Joos. “Lightweight and Safe Composite Battery Housings”. In: *Lightweight Design Worldwide* 12 (2019), pp. 44–47. DOI: 10.1007/s41777-019-0061-0. URL: https://doi.org/10.1007/s41777-019-0061-0.

[28] Amar K. Mohanty et al. “Sustainable composites for lightweight and flame retardant parts for electric vehicles to boost climate benefits: A perspective”. In: *Composites Part C: Open Access* 12 (2023), p. 100380. ISSN: 2666-6820. DOI: https://doi.org/10.1016/j.jcomc.2023.100380. URL: https://www.sciencedirect.com/science/article/pii/S2666682023000361.

[29] Parvez Alam et al. “The fatigue of carbon fibre reinforced plastics - A review”. In: *Composites Part B: Engineering* 166 (2019), pp. 555–579. ISSN: 1359-8368. DOI: https://doi.org/10.1016/j.compositesb.2019.02.016. URL: https://www.sciencedirect.com/science/article/pii/S1359836818321784.

[30] Weiwei Wang et al. “Design optimization of a novel negative Poisson’s ratio non-module battery pack system considering crashworthiness and heat dissipation”. In: *Composite Structures* 275 (2021). Accessed: Feb. 2025, p. 114458. ISSN: 0263-8223. DOI: https://doi.org/10.1016/j.compstruct.2021.114458. URL: https://www.sciencedirect.com/science/article/pii/S026382232100920X.

[31] Proto Labs. *UL 94 Classification and Flame-Retardant Plastic Materials*. https://www.protolabs.com/resources/blog/flame-retardant-thermoplastics-and-ul-classifications. Published June 12, 2025. 2025.

[32] T.J. Lu and C. Chen. “Thermal transport and fire retardance properties of cellular aluminium alloys”. In: *Acta Materialia* 47.5 (1999), pp. 1469–1485. ISSN: 1359-6454. DOI: https://doi.org/10.1016/S1359-6454(99)00037-3. URL: https://www.sciencedirect.com/science/article/pii/S1359645499000373.

[33] S. Nikbakt, S. Kamarian, and M. Shakeri. “A review on optimization of composite structures Part I: Laminated composites”. In: *Composite Structures* 195 (2018). Accessed: Feb. 2025, pp. 158–185. ISSN: 0263-8223. DOI: https://doi.org/10.1016/j.compstruct.2018.03.063. URL: https://www.sciencedirect.com/science/article/pii/S0263822317336279.

[34] Li Shui et al. “Design optimization of battery pack enclosure for electric vehicle”. In: *Structural and Multidisciplinary Optimization* 58.1 (2018). Accessed: Feb. 2025, pp. 331–347. DOI: 10.1007/s00158-018-1901-y. URL: https://doi.org/10.1007/s00158-018-1901-y.

[35] Yihui Zhang et al. "Multi-objective optimization of lithium-ion battery pack casing for electric vehicles: Key role of materials design and their influence". In: *International Journal of Energy Research* 44.12 (2020). Accessed: Feb. 2025, pp. 9414–9437. DOI: 10.1002/er.4965. URL: https://doi.org/10.1002/er.4965.

[36] United Nations Economic Commission for Europe (UNECE). *Agreement Concerning the Adoption of Uniform Technical Prescriptions for Wheeled Vehicles, Equipment and Parts — Addendum 135: Regulation No. 136. Uniform provisions concerning the approval of vehicles of category L with regard to specific requirements for the electric power train*. https://unece.org/fileadmin/DAM/trans/main/wp29/wp29regs/2016/R136e.pdf. ECE/TRANS/505/Rev.2/Add.135, entered into force on 20 January 2016. 2016.

[37] Ennovation Technology. *Battery Homologation for Electric Vehicles – How Does the Process Work?* https://ennovationtech.eu/en/battery-homologation-for-electric-vehicles-how-does-the-process-work/. Accessed: April 2025. May 2024.

[38] *UL 94: Test for Flammability of Plastic Materials for Parts in Devices and Appliances*. Edition of May 22, 2001. Northbrook, Illinois, USA: Underwriters Laboratories Inc., May 2001.

[39] R. M. Jones. *Mechanics of Composite Materials*. 2nd. CRC Press, 1999. DOI: 10.1201/9781498711067. URL: https://doi.org/10.1201/9781498711067.

[40] Mahmood M. Shokrieh and S. Masoud Kamali Shahri. "6 - Modeling residual stresses in composite materials". In: *Residual Stresses in Composite Materials (Second Edition)*. Ed. by Mahmood M. Shokrieh. Second Edition. Woodhead Publishing Series in Composites Science and Engineering. Woodhead Publishing, 2021, pp. 193–213. ISBN: 978-0-12-818817-0. DOI: https://doi.org/10.1016/B978-0-12-818817-0.00006-8. URL: https://www.sciencedirect.com/science/article/pii/B9780128188170000068.

[41] Dr. Matthias Goelke. *Composites with Altair OptiStruct*. Online. On behalf of the Altair University Team. 2021. URL: https://www.advanced-eng.cz/wp-content/uploads/2021/06/2021_ebook-Composite_with_Altair_OptiStruct.pdf.

[42] Pedro Leal Ribeiro. *Plates and Shells: Orthotropic, Laminated and Non-Homogeneous Plates*. Master in Mechanical Engineering, Version: 3 April 2024. 2024.

[43] Shuguang Li et al. "The Tsai-Wu failure criterion rationalised in the context of UD composites". In: *Composites Part A: Applied Science and Manufacturing* 102 (2017), pp. 207–217. ISSN: 1359-835X. DOI: https://doi.org/10.1016/j.compositesa.2017.08.007. URL: https://www.sciencedirect.com/science/article/pii/S1359835X17303068.

[44] Ravi Joshi, P. Pal, and S.K. Duggal. "Ply-by-ply failure analysis of laminates using finite element method". In: *European Journal of Mechanics - A/Solids* 81 (2020), p. 103964. ISSN: 0997-7538. DOI: https://doi.org/10.1016/j.euromechsol.2020.103964. URL: https://www.sciencedirect.com/science/article/pii/S0997753819308642.

[45] J. N. Reddy. *An Introduction to the Finite Element Method*. 3rd. New York: McGraw-Hill Education, 2006. ISBN: 9780072466850.

[46] Francisco M. A. Pires, António M. C. Carneiro, and Igor A. R. Lopes. *Finite Element Method*. Lecture slides, Master in Mechanical Engineering, Faculdade de Engenharia da Universidade do Porto. 4th year – 1st semester. 2024.

[47] Altair Engineering. *Linear Static Analysis – OptiStruct User Guide*. https://help.altair.com/hwsolvers/os/topics/solvers/os/analysis_linear_static_c.htm. 2025.

[48] Altair Engineering. *Nonlinear Static Analysis – OptiStruct User Guide*. https://help.altair.com/hwsolvers/os/topics/solvers/os/analysis_nonlinear_quasi_static_c.htm. 2025.

[49] Altair Engineering. *Linear Steady-State Heat Transfer Analysis – OptiStruct Documentation*. https://help.altair.com/hwsolvers/os/topics/solvers/os/analysis_linear_steady_state_heat_transfer_c.htm. 2025.

[50] Altair Engineering. *Linear Transient Heat Transfer Analysis – OptiStruct Documentation*. https://help.altair.com/hwsolvers/os/topics/solvers/os/analysis_linear_transient_heat_transfer_c.htm. 2025.

[51] Altair Engineering. *Nonlinear Transient Heat Transfer Analysis – OptiStruct Documentation*. https://help.altair.com/hwsolvers/os/topics/solvers/os/analysis_nonlinear_transient_heat_transfer_c.htm. 2025.

[52] José Dias Rodrigues. *Apontamentos de Vibrações de Sistemas Mecânicos*. Didactic support material for the curricular unit of Mechanical Vibrations, Master in Mechanical Engineering, Faculdade de Engenharia da Universidade do Porto. 2021.

[53] David J. Benson. "Explicit Finite Element Methods for Large Deformation Problems in Solid Mechanics". In: *Encyclopedia of Computational Mechanics Second Edition*. John Wiley Sons, Ltd, 2017, pp. 1–43. ISBN: 9781119176817. DOI: https://doi.org/10.1002/9781119176817.ecm2072. eprint: https://onlinelibrary.wiley.com/doi/pdf/10.1002/9781119176817.ecm2072. URL: https://onlinelibrary.wiley.com/doi/abs/10.1002/9781119176817.ecm2072.

[54] Altair Engineering. *Nonlinear Explicit Analysis – OptiStruct 2025 User Guide*. https://help.altair.com/hwsolvers/os/topics/solvers/os/analysis_nonlinear_explicit_r.htm. 2025.

[55] Altair Engineering. *Non-Linear Analysis with OptiStruct (eLearning Course)*. Online course, Altair Learn. 2025. URL: https://learn.altair.com/courses/non-linear-analysis-with-optistruct-elearning.

[56] Altair Engineering. *Composite Stress Toolbox*. https://2022.help.altair.com/2022.1/hwdesktop/hm/topics/pre_processing/composites/composites_composite_stress_toolbox_1_r.htm. Accessed: 2025-05-03. 2022.

[57] Marius Müller. *Tutorial: Composite Optimization of a Skateboard using Altair HyperMesh™ and Altair OptiStruct™ 2019*. 2020.

[58] Carlos Alberto da Conceição António. *Optimization of mechanical systems - fundamentals and algorithms / Carlos Alberto da Conceição António*. eng. Porto: Universidade do Porto. Faculdade de Engenharia, 2021. ISBN: 978-989-53416-0-3.

[59] Altair Engineering. *Structural Optimization using OptiStruct*. Accessed: 2025-05-13. Altair Engineering, Inc. 2013. URL: https://www.researchgate.net/profile/Mohamed_Mourad_Lafifi/post/Optimization_algorithm_in_Optistruct/attachment/5d61722bcfe4a7968dc3e8f6/AS%3A795474491629568%401566667306073/download/OptiStruct_Optimization.pdf.

[60] Stark Future. *The World's Fastest Motocross Bike is now Electric - Stark VARG*. https://www.youtube.com/watch?v=ozEEvlgtTPE. Accessed: 2025-05-22. 2021.

[61] Stark Future. *Stark VARG battery production behind-the-scenes*. https://www.youtube.com/watch?v=UVSum5ZVvlc. Accessed: 2025-05-27. 2022.

[62] WD Racing. *Battery Stark VARG 6.5 kWh*. https://www.wdracing.eu/gb/34252-battery-stark-varg-65-kwh.html. Accessed: 2025-05-27. 2025.

[63] Toray Advanced Composites. *TC346 Epoxy Prepreg – Product Data Sheet*. Accessed: 2025-06-02. URL: https://www.toraytac.com/media/cd295b07-0837-4bb1-b511-0f3ca5a8d905/5AX7hA/TAC/Documents/Data_sheets/Thermoset/UD%20tapes%20and%20prepregs/TC346_Epoxy_PDS.pdf.

[64] Toray Advanced Composites. *Composite Property Calculator (CPT)*. Accessed: 2025-06-02. 2024. URL: https://www.toraytac.com/resources/Calculators/CPT.

[65] United Nations Economic Commission for Europe (UNECE). *Regulation No. 100: Uniform provisions concerning the approval of vehicles with regard to specific requirements for the electric power train (Revision 3, Addendum 99)*. Tech. rep. E/ECE/TRANS/505/Rev.3/Add.99. Entry into force: 23 March 2022. UNECE, Mar. 2022.

[66] Toray Advanced Composites. *E731 Epoxy Prepreg – Product Data Sheet*. Accessed: 2025-06-06. URL: https://www.toraytac.com/media/33851e2f-46f9-41fc-92ac-67caae1c49b8/5Q8-Yw/TAC/Documents/Data_sheets/Thermoset/UD%20tapes%20and%20prepregs/E731_Epoxy_PDS.pdf.

[67] Toray Advanced Composites. *E750 Epoxy Prepreg – Product Data Sheet*. 2021. URL: https://www.toraytac.com/media/d5776847-a3be-4cd7-a71e-965a3c926497/ZCvPpQ/TAC/Documents/Data_sheets/Thermoset/UD%20tapes%20and%20prepregs/E750_Epoxy_PDS.pdf.

[68] Toray Advanced Composites. *E745 Epoxy Prepreg – Product Data Sheet*. 2020. URL: https://www.toraytac.com/media/0aca2295-3458-437f-b756-729525495674/OIWeow/TAC/Documents/Data_sheets/Thermoset/UD%20tapes%20and%20prepregs/E745_Epoxy_PDS.pdf.

[69] Yurii Shumak. *The Fundamentals of Mesh Quality: Why It Matters*. https://sdcverifier.com/structural-engineering-101/the-fundamentals-of-mesh-quality/. 2025.

[70] Altair Engineering. *Review 2D Elements by Quality Index – HyperWorks Help Documentation*. https://help.altair.com/hwdesktop/hwx/topics/pre_processing/meshing/2d_element_quality_by_quality_index_review_t.htm. 2025.

[71] Altair Engineering. *PSHELL – Bulk Data Entry (Shell Element Properties) – OptiStruct Reference Guide*. https://help.altair.com/hwsolvers/os/topics/solvers/os/pshell_bulk_r.htm. 2025.

[72] Altair Engineering. *PSOLID – Bulk Data Entry (Solid Element Properties) – OptiStruct Reference Guide, version 2024.1*. https://2024.help.altair.com/2024.1/hwsolvers/os/topics/solvers/os/psolid_bulk_r.htm. 2025.

[73] Hexcel Composites. *HexWeb™ Honeycomb Sandwich Design Technology*. Tech. rep. Hexcel Composites, 2025. URL: http://www.hexcel.com/user_area/content_media/raw/Honeycomb_Sandwich_Design_Technology.pdf.

[74] Sardar Malek and Lorna J. Gibson. "Effective Elastic Properties of Periodic Hexagonal Honeycombs". In: *Mechanics of Materials* 91 (Dec. 2015), pp. 226–240. DOI: 10.1016/j.mechmat.2015.07.008. URL: http://hdl.handle.net/1721.1/112341.

[75] Altair Engineering. *Connectors – HyperMesh Help, HyperWorks 2025.1*. https://help.altair.com/hwdesktop/hwx/topics/pre_processing/connectors/connectors.htm. 2025.

[76] Altair Engineering. *CONM2 Bulk Data Entry – OptiStruct Reference Guide*. https://help.altair.com/hwsolvers/os/topics/solvers/os/conm2_bulk_r.htm. 2025.

[77] Altair Engineering. *RBE3 – HyperMesh Help Documentation*. https://help.altair.com/hwdesktop/hwx/topics/pre_processing/entities/rbe3_r.htm. 2025.

[78] Altair Support. *What is the difference between RBE-2 and RBE-3 elements?* https://support.altair.com/csm/en?id=community_question&sys_id=d9f99cb21be21954507ca6442a4bcbc1. 2025.

[79] Altair Engineering. *TIC – Bulk Data Entry (Initial Conditions) – OptiStruct Reference Guide*. https://help.altair.com/hwsolvers/os/topics/solvers/os/tic_bulk_r.htm. Accessed: 2025-09-08. 2025.

[80] Altair Engineering. *Computation Checks – Radioss Explicit Solver Documentation*. https://help.altair.com/hwsolvers/rad/topics/solvers/rad/computation_checks_r.htm. 2025.

[81] Ronald Joven et al. "Thermal properties of carbon fiber-epoxy composites with different fabric weaves". In: *International SAMPE Technical Conference* (Jan. 2012).

[82] Sebastian Pawlak et al. "Measurement of the anisotropic thermal conductivity of carbon-fiber/epoxy composites based on laser-induced temperature field: Experimental investigation and numerical analysis". In: *International Communications in Heat and Mass Transfer* 139 (2022), p. 106401. ISSN: 0735-1933. DOI: https://doi.org/10.1016/j.icheatmasstransfer.2022.106401. URL: https://www.sciencedirect.com/science/article/pii/S0735193322005231.

[83] Altair Engineering. *MAT5 – Bulk Data Entry (Thermal Material Properties) – OptiStruct Reference Guide*. https://2024.help.altair.com/2024.1/hwsolvers/os/topics/solvers/os/mat5_bulk_r.htm. 2025.

[84] Lorna J. Gibson and Michael F. Ashby. *Cellular Solids: Structure and Properties*. 2nd ed. Cambridge Solid State Science Series. Cambridge University Press, 1997.

[85] MatWeb. *Aluminum 3003-H18 Datasheet*. https://www.matweb.com/search/datasheet_print.aspx?matguid=91c99440833341fc8fbe1d26149bc35e. Accessed: 2025-09-15.

[86] Aalco Metals Limited. *Aluminium Alloy – Commercial Alloy – 3003 '0' Sheet Datasheet*. https://www.aalco.co.uk/datasheets/Aluminium-Alloy-3003-0-Sheet_59.ashx. 2018.

[87] Che-Wei Yeh et al. "Measurement of thermal contact resistance of aluminum honeycombs". In: *Experimental Thermal and Fluid Science* 27 (Mar. 2003), pp. 271–281. DOI: 10.1016/S0894-1777(02)00297-2.

[88] A. Wild and J.-P. Bouchez. "Investigation of the Improvement of the Thermal Contact Conductance between a Baseplate and a Honeycomb Platform Using Various Interstitial Materials". In: *Thermal Conductivity 14*. Ed. by P. G. Klemens and T. K. Chu. Boston, MA: Springer US, 1976, pp. 449–462. ISBN: 978-1-4899-3751-3. DOI: 10.1007/978-1-4899-3751-3_60. URL: https://doi.org/10.1007/978-1-4899-3751-3_60.

[89] Armando C. F. C. Oliveira. *Transferência de Calor: Um Guia para a Resolução de Problemas Práticos*. 1ª edição. Este livro é publicado eletronicamente. ISBN 978-989-33-2674-9. Portugal: Publicado pelo autor, 2022.

[90] Armando Carlos Figueiredo Coelho de Oliveira et al. *Heat Transfer: Course Materials and Semi-Products*. Portugal: FEUP, 2023.

[91] Mohammad Shahjalal et al. "A Numerical Thermal Analysis of a Battery Pack in an Electric Motorbike Application". In: *Designs* 6.4 (2022). ISSN: 2411-9660. DOI: 10.3390/designs6040060. URL: https://www.mdpi.com/2411-9660/6/4/60.

[92] Smart Materials 3D. *Nylstrong Filament*. Smart Materials 3D. 2025. URL: https://www.smartmaterials3d.com/en/nylstrong-filament.

[93] LMT Onsrud. *29-100 Solid Carbide Honeycomb Hogger, ZrN Coated*. https://www.onsrud.com/Series/29-100.asp. Accessed: 2025-10-04.

[94] CoreHog. *Composites – Honeycomb Tooling (Roughing Finishing Core Tools)*. https://www.corehog.com/products/milling/composites-honeycomb. Accessed: 2025-10-04.

[95] Park Aerospace Corp. *CoreFix – Structural Core Bonding System*. https://parkaerospace.com/aerospace-products/corefix. Accessed: 2025-10-05.

[96] Advanced Ceramics Manufacturing. *AquaCore™– Machinable Core Material*. https://acmtucson.com/acm_products/aquacore/. Accessed: 2025-10-05. 2025.

[97] Kunxian Qiu et al. "Study on the cutting force in machining of aluminum honeycomb core material". In: *Composite Structures* 164 (2017), pp. 58–67. ISSN: 0263-8223. DOI: https://doi.org/10.1016/j.compstruct.2016.12.060. URL: https://www.sciencedirect.com/science/article/pii/S0263822316320220.

[98] Fengbiao Wang et al. "Green machining of aluminum honeycomb treated using ice fixation in cryogenic". In: *The International Journal of Advanced Manufacturing Technology* 92 (Sept. 2017). DOI: 10.1007/s00170-017-0181-9.

[99] Shaowei Jiang et al. "Impact of cutting state variables on machining defects in milling of superalloy honeycomb core thin wall". In: *Journal of Manufacturing Processes* 120 (2024), pp. 123–134. ISSN: 1526-6125. DOI: https://doi.org/10.1016/j.jmapro.2024.04.035. URL: https://www.sciencedirect.com/science/article/pii/S1526612524003864.

[100] Y. Wang, Y. Gan, H. Liu, et al. "Surface Quality Improvement in Machining an Aluminum Honeycomb by Ice Fixation". In: *Chinese Journal of Mechanical Engineering* 33.20 (2020). DOI: 10.1186/s10033-020-00439-1. URL: https://doi.org/10.1186/s10033-020-00439-1.

[101] Sika. *Structural Bonding Solutions – High Performance Adhesives*. 2018.

[102] Sika Advanced Resins. *SikaPower®-740 (ADEKIT A140-1 / H9940-1) — Product Data Sheet*. https://www.amtcomposites.co.za/wp-content/uploads/2021/05/H9940-SikaPower-740-gb.pdf?srsltid=AfmBOoq61VuKq4qG3CUc5sZYvz24hwN8tqMH Version 01 /2023. June 2023.

[103] bigHead®. *Embedding and Surface Bonding of bigHead® Fasteners*. https://www.youtube.com/watch?v=7mFJZYk-YXc. 2025.

[104] bigHead Bonding Fasteners Ltd. *bigHead SF2-S23 Stainless Steel Collar — Technical Data Sheet*. https://bighead.co.uk/wp-content/uploads/dlm_uploads/2024/05/bigHead_SF2_S23_TDS.pdf. Version 2.0, April 2024. 2024.

[105] Polymaker. *Fiberon PA6-CF20 Technical Data Sheet*. https://fiberon.polymaker.com/wp-content/uploads/TDS_FIBERON-PA6-CF20_V1.0_EN.pdf. Accessed: 2025-10-06. 2024.

[106] Nesting Center. *Nesting Center – Online Nesting System for Material Cutting*. https://nestingcenter.com/. Accessed: 2025-10-06. 2025.

[107] Molicel. *INR21700 P42A Technical Datasheet*. https://www.molicel.com/wp-content/uploads/INR21700P42A-V4-80092.pdf. Accessed: 2025-05-27.

[108] Molicel. *INR21700 P45B Technical Datasheet*. https://www.molicel.com/wp-content/uploads/INR21700P45B_1.2_Product-Data-Sheet-of-INR-21700-P45B-80109.pdf. Accessed: 2025-05-27.

[109] Molicel. *INR21700 P50B Technical Datasheet*. https://www.molicel.com/wp-content/uploads/Product-Data-Sheet-of-INR-21700-P50B-80122.pdf. Accessed: 2025-05-27.

Appendix A

Molicel Lithium-ion Battery Cells

A.1 INR-21700-P42A

MOLICEL®

LITHIUM-ION RECHARGEABLE BATTERY

PRODUCT DATA SHEET

MODEL INR-21700-P42A

■ CELL CHARACTERISTICS

Capacity	Typical	4200 mAh 15.5 Wh
	Minimum	4000 mAh 14.7 Wh
Cell Voltage	Nominal	3.6 V
	Charge	4.2 V
	Discharge	2.5 V
Charge Current	Standard	4.2 A
Charge Time	Standard	1.5 hr
Discharge Current	Continuous	45 A
Typical Impedance	AC (1 KHz)	10 mΩ
	DC (10A/1s)	16 mΩ
Temperature	Charge	0°C to 45°C
	Discharge	-40°C to 60°C
Energy Density	Volumetric	615 Wh/l
	Gravimetric	230 Wh/kg

■ PHYSICAL CHARACTERISTICS

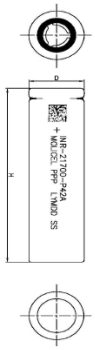

Shape	Cylindrical
Can	Steel
Diameter	21.7 mm (Max)
Height	70.2 mm (Max)
Weight	70 g (Max)

The information contained herein is for reference only and does not imply a performance guarantee or a product warranty. Specifications and characteristics are subject to change without prior notice.

For application specific information, please contact E-One Moli Energy Sales and Applications or the nearest MOLICEL® recognized agent.

■ Charge Characteristics

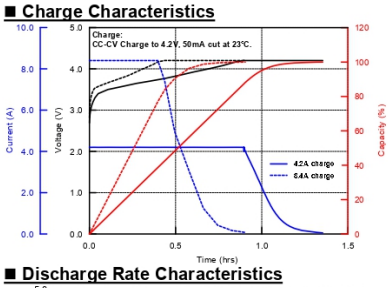

■ Discharge Rate Characteristics

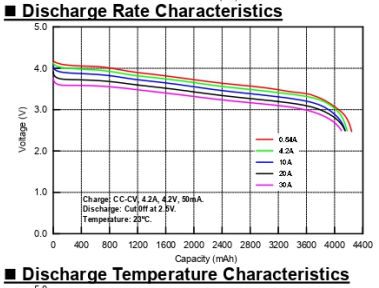

■ Discharge Temperature Characteristics

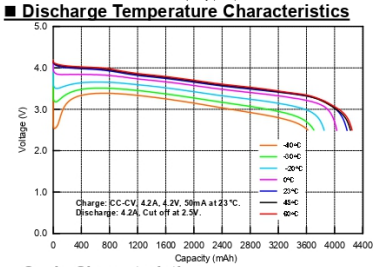

■ Cycle Characteristics

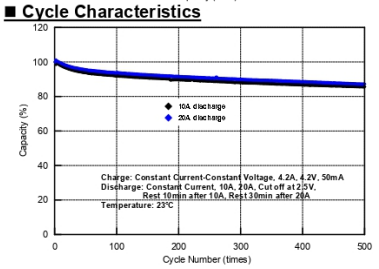

■ Taiwan Facility
10 Dali 2nd Rd., Shan-Hwa,
Tainan City, Taiwan, R.O.C.
Tel: 886-6-505-0666
Fax: 886-6-505-0777
mailto:service@molicel.com
http://www.molicel.com

■ Canada Facility
20 000 Stewart Crescent
Maple Ridge, BC, Canada, V2X 9E7
Tel: 1-604-466-6654
Fax: 1-604-466-6600
mailto:molicel@molicel.com
http://www.molicel.com

■ Headquarters
10F, 113, Sec.2, Zhung Shan N Rd.,
Taipei, Taiwan, R.O.C.
Tel: 886-2-2567-3500
Fax: 886-2-2567-6500

Figure A.1: Product data sheet of Molicel INR-21700-P42A [107]

A.2 INR-21700-P45B

MOLICEL®

LITHIUM-ION RECHARGEABLE BATTERY

PRODUCT DATA SHEET
MODEL INR-21700-P45B

■ **CELL CHARACTERISTICS**

Capacity	Typical	4500 mAh 16.2 Wh
	Minimum	4300 mAh 15.5 Wh
Cell Voltage	Nominal	3.6 V
	Charge	4.2 V
	Discharge	2.5 V
Charge Current	Standard	4.5 A
	Maximum	13.5 A (70°C cut-off)
Charge Time	Standard	1.5 hr
Discharge Current	Continuous	45 A (80°C cut-off)
Temperature	Charge	0°C to 60°C
	Discharge	-40°C to 60°C
Energy Density	Volumetric	643 Wh/l
	Gravimetric	242 Wh/kg
Typical Impedance	AC (30%SOC)	7 mΩ
	DC (50%SOC)	15 mΩ

■ **PHYSICAL CHARACTERISTICS**

Shape	Cylindrical
Can	Steel
Diameter	21.55 mm (Max)
Height	70.15 mm (Max)
Weight	70 g (Max)

■ **Charge Characteristics**

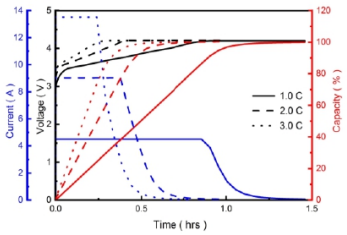

■ **Discharge Rate Characteristics**

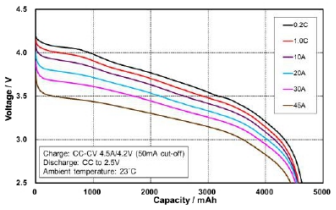

■ **Discharge Temperature Characteristics**

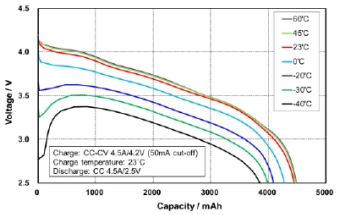

■ **Cycle Characteristics**

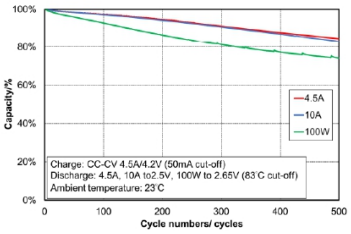

The information contained herein is for reference only and does not imply a performance guarantee or a product warranty. Specifications and characteristics are subject to change without prior notice.

For application specific information, please contact E-One Moli Energy Sales and Applications or the nearest MOLICEL® recognized agent.

Version 1.2

Taiwan Facility
10 Dali 2nd Rd., Shan-Hwa,
Tainan City, Taiwan, R.O.C.
Tel: 886-6-505-0666
Fax: 886-6-505-0777
Mail to:service@molicel.com
http://www.molicel.com

Canada Facility
20 000 Stewart Crescent
Maple Ridge, BC, Canada, V2X 9E7
Tel: 1-604-466-6654
Fax: 1-604-466-6600
Mail to:molicel@molienergy.com
http://www.molicel.com

Headquarters
10F, 113, Sec.2, Zhung Shan N Rd.,
Taipei, Taiwan, R.O.C.
Tel: 886-2-2567-3500
Fax: 886-2-2567-6500
Mail to:service@molicel.com
http://www.molicel.com

Figure A.2: Product data sheet of Molicel INR-21700-P45B [108]

A.3 INR-21700-P50B

MOLICEL®

LITHIUM-ION RECHARGEABLE BATTERY

PRODUCT DATA SHEET
MODEL INR-21700-P50B

■ **CELL CHARACTERISTICS**

Capacity	Typical	5000 mAh 18.0 Wh
	Minimum	4850 mAh 17.5 Wh
Cell Voltage	Nominal	3.6 V
	Charge	4.2 V
	Discharge	2.5 V
Charge Current (70°C cut-off)	Standard	5.0 A
	Maximum	25 A
Charge Time	Standard	1.5 hr
Discharge Current (80°C cut-off)	Continuous	60 A
Ambient Temperature	Charge	-20°C to 60°C
	Discharge	-40°C to 60°C
Energy Density	Volumetric	714 Wh/l
	Gravimetric	260 Wh/kg
Typical Impedance	AC (30%SOC)	6.5 mΩ
	DC (50%SOC)	12.8 mΩ

■ **PHYSICAL CHARACTERISTICS**

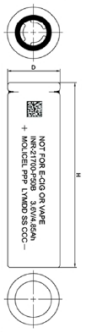

Shape	Cylindrical
Can	Steel
Diameter	21.55 mm (Max)
Height	70.15 mm (Max)
Weight	71 g (Max)

■ **Charge Characteristics**

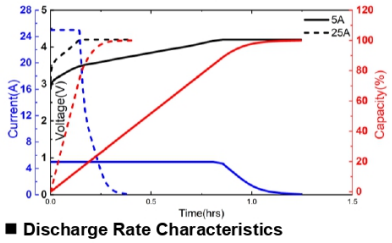

■ **Discharge Rate Characteristics**

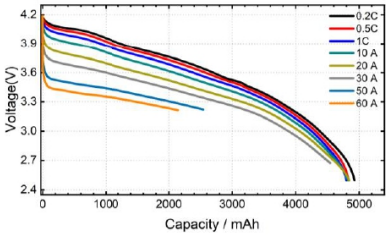

■ **Discharge Temperature Characteristics**

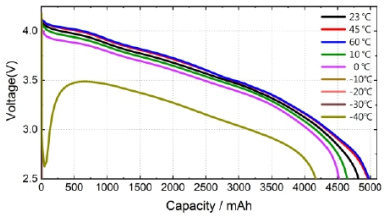

■ **Cycle Characteristics**

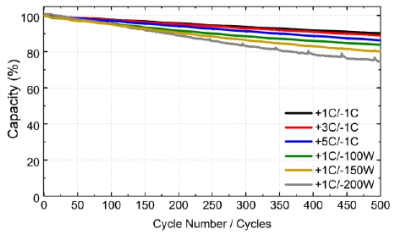

The information contained herein is for reference only and does not imply a performance guarantee or a product warranty. Specifications and characteristics are subject to change without prior notice.
This product is not designed or produced for use in any vape or e-cigarette devices.

For application specific information, please contact E-One Moli Energy Sales and Applications or the nearest MOLICEL® recognized agent.
Version 1.1

Taiwan Facility
10 Dali 2nd Rd., Shan-Hwa,
Tainan City, Taiwan, R.O.C.
Tel: 886-6-505-0666
Fax: 886-6-505-0777
Mail to:service@molicel.com
http://www.molicel.com

Canada Facility
20 000 Stewart Crescent
Maple Ridge, BC, Canada, V2X 9E7
Tel: 1-604-466-6654
Fax: 1-604-466-6600
Mail to:molicel@molienergy.com
http://www.molicel.com

Headquarters
10F, 113, Sec.2, Zhung Shan N Rd.,
Taipei, Taiwan, R.O.C.
Tel: 886-2-2567-3500
Fax: 886-2-2567-6500
Mail to:service@molicel.com
http://www.molicel.com

Figure A.3: Product data sheet of Molicel INR-21700-P50B [109]

Appendix B

Toray Carbon Fibre Composite Pre-pregs

B.1 Toray E731 pre-preg

Toray E731

TORAY
Toray Advanced Composites

PRODUCT DATA SHEET

DESCRIPTION

Toray E731 is a toughened epoxy resin system designed to deliver enhanced resin clarity for cosmetic components within high performance automotive. The resin formulation ensures that components are free from white-spots and exhibit high clarity.

FEATURES

- **Enhanced resin clarity—"white-spot" free**
- **Toughened system—good mechanical properties**
- **Controlled tack allows easy repositioning**
- **Medium temperature cures—100°C (212°F) to 125°C (257°F)**
- **T_g (DMTA onset) of 140°C (284°F) after 1 hour at 125°C autoclave cure**
- **14 days out life at 18°C (64°F)**
- **6 months storage life at -18°C (0°F)**

PRODUCT TYPE

100°C (212°F) to 125°C (257°F) Cure
Cosmetic High Clarity Toughened Epoxy Component Prepreg

TYPICAL NEAT RESIN PROPERTIES

Density	1.24 g/cm³ (77.4 lbs/ft³)
T_g (DMTA) after 1 hr at 125°C (257°F)	Onset: 140°C (284°F); Peak tan δ: 160°C (320°F)

TYPICAL APPLICATIONS

- Cosmetic and high clarity components
- Door panels, centre console, dashboard

KEY PROPERTIES

- Resin clarity
- Drapeable

SHELF LIFE

Out Life:	14 days at 18°C (64°F)
Storage Life:	6 months at -18°C (0°F)

Out life is the maximum time allowed at room temperature before cure.

To avoid moisture condensation
Following removal from cold storage, allow the prepreg to reach room temperature before opening the polythene bag. Typically, the thaw time for a full roll of material will be 4 to 6 hours.

Contact us for more information:
North America/Asia/Pacific
e explore@toraytac-usa.com
t +1 408 465 8500

Europe/Middle East/Africa
e explore@toraytac-europe.com
t +44 (0)1773 530899

Figure B.1: Page 1 of Toray's E731 pre-preg datasheet [66]

Toray E731

TORAY
Toray Advanced Composites

PRODUCT DATA SHEET

TYPICAL LAMINATE PROPERTIES

E731-00 HS2238 Carbon TR30S T 245gsm 2 x 2 Twill 3K 42% RC		
Property	**Method**	**Test Temperature RT**
Tensile Strength 0°	ISO 527-4	705 MPa
Tensile Modulus 0°	ISO 527-4	55.9 GPa
Tensile Strength 90°	ISO 527-4	662 MPa
Tensile Modulus 90°	ISO 527-4	57.7 GPa
Poisson's Ratio	ISO 527-4	0.05
Compression Strength 0°	prEN 2850	643 MPa
Compression Modulus 0°	prEN 2850	49.8 GPa
Compression Strength 90°	prEN 2850	664 MPa
Compression Modulus 90°	prEN 2850	49.7 GPa
In-Plane Shear Strength	prEN 6031	119 MPa
In-Plane Shear Modulus	prEN 6031	4.07 GPa
Poisson's Ratio	prEN 6031	0.8
Interlaminar Shear Strength 0°	ASTM D 2344	63.9 MPa
Interlaminar Shear Strength 90°	ASTM D 2344	61.8 MPa
Mode I Interlaminar Fracture Toughness (G_{Ic} Strain Energy Release Rate)	prEN 6033	318
Cured 1 hr at 125°C (257°F)		

REINFORCEMENTS AVAILABLE

Fiber Type	Weight (gsm)	Weave Style	Standard Resin Content w/o
Standard modulus 3K carbon	245	2 x 2 twill	42 (surface ply)
Standard modulus 6K carbon	400	2 x 2 twill	37 (bulk ply)
Standard modulus 12K carbon	650	2 x 2 twill	32 (heavier bulk ply)
Prepreg width is 1.25m; Other fabrics and resin weights available on request			

Figure B.2: Page 2 of Toray's E731 pre-preg datasheet [66]

Toray E731

'TORAY'
Toray Advanced Composites

PRODUCT DATA SHEET

RHEOLOGY

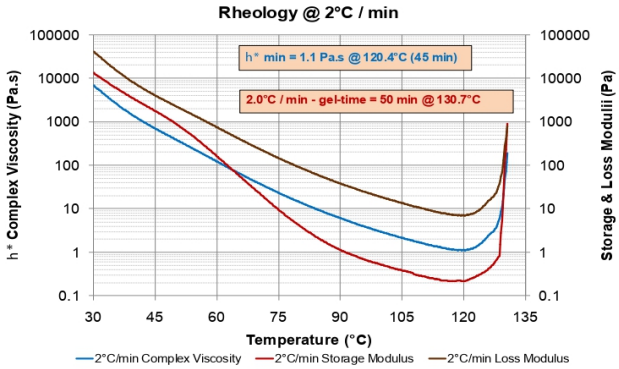

VISCOSITY

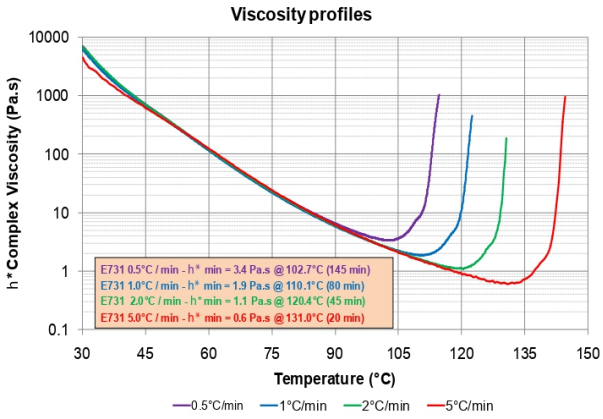

INITIAL MINIMUM CURE TIMES

Temperature	Time (hrs)
100°C (212°F)	4
110°C (230°F)	2
125°C (257°F)	1

Figure B.3: Page 3 of Toray's E731 pre-preg datasheet [66]

Toray E731

TORAY
Toray Advanced Composites

PRODUCT DATA SHEET

TYPICAL CURE PROFILES

125°C (257°F) Cure Temperatures		
Ramp	2.0°C (3.6°F)/min to 125°C (257°F)	Dwell for 1 hour
Ramp	2.0°C (3.6°F)/min to 50°C (122°F)	Followed by demold
Total time: 2 hours 30 minutes		

100°C (212°F) Cure Temperatures		
Ramp	2.0°C (3.6°F)/min to 100°C (212°F)	Dwell for 4 hours
Ramp	2.0°C (3.6°F)/min to 50°C (122°F)	Followed by demold
Total time: 5 hours		

INITIAL MINIMUM 125°C CURE SCHEDULE

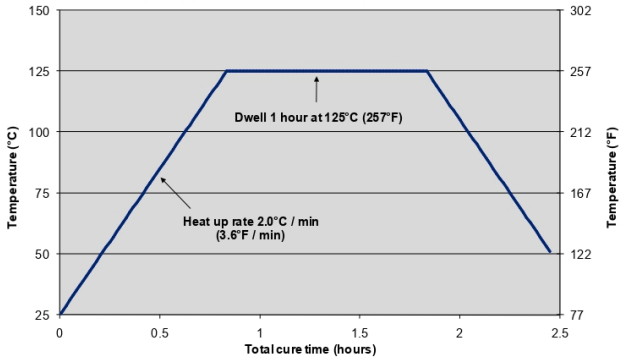

INITIAL MINIMUM -100°C CURE SCHEDULE

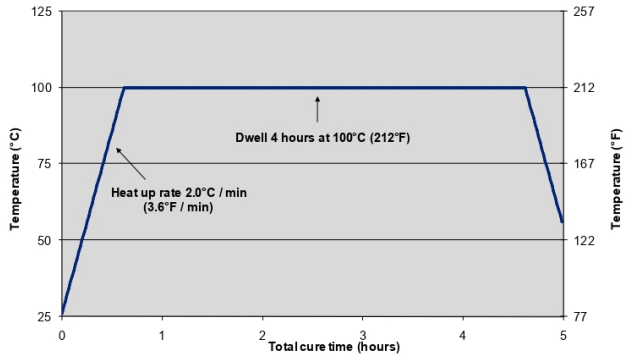

E731_PDS_v2_2019-07-14
Page 4/5

Figure B.4: Page 4 of Toray's E731 pre-preg datasheet [66]

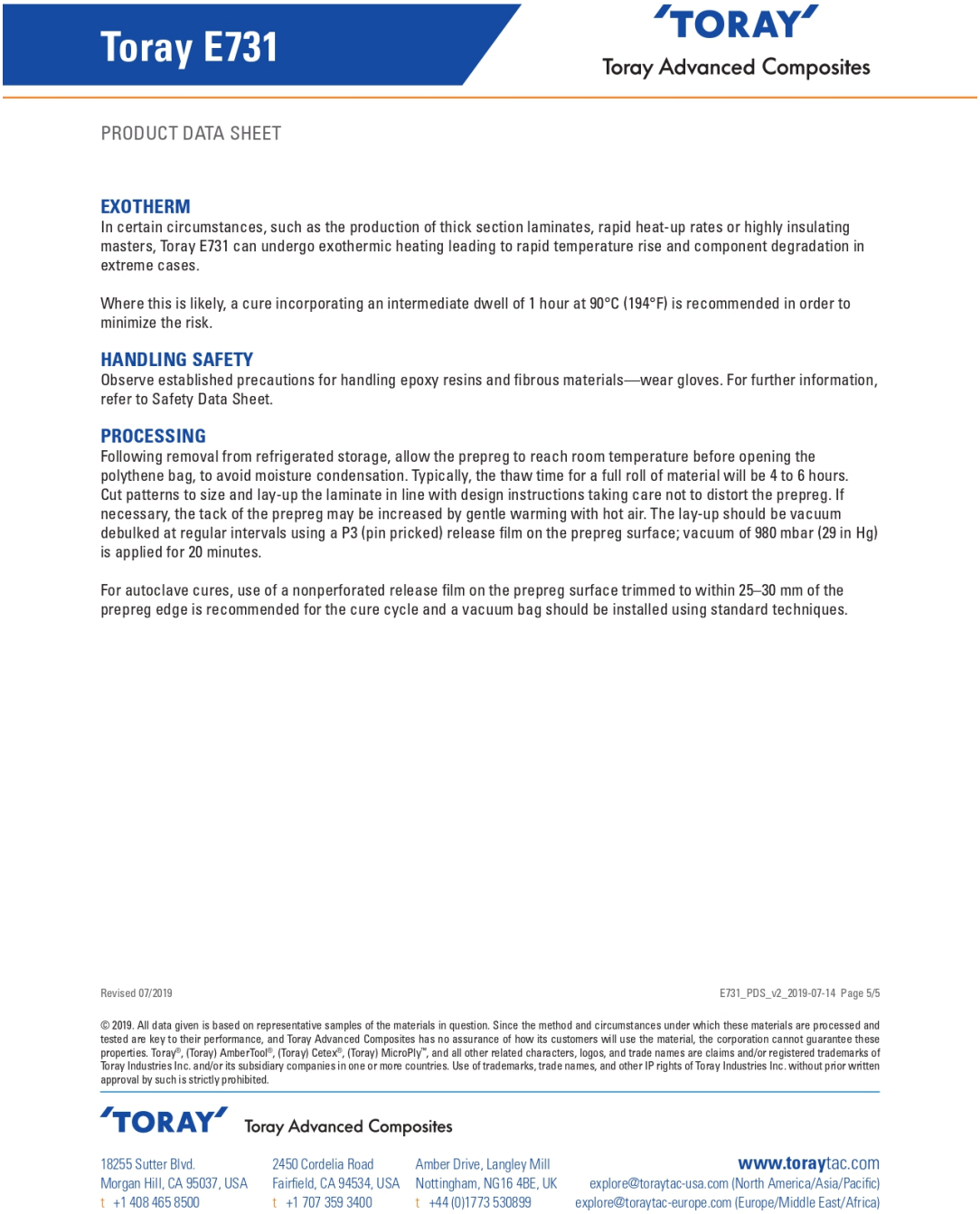

Toray E731

TORAY
Toray Advanced Composites

PRODUCT DATA SHEET

EXOTHERM
In certain circumstances, such as the production of thick section laminates, rapid heat-up rates or highly insulating masters, Toray E731 can undergo exothermic heating leading to rapid temperature rise and component degradation in extreme cases.

Where this is likely, a cure incorporating an intermediate dwell of 1 hour at 90°C (194°F) is recommended in order to minimize the risk.

HANDLING SAFETY
Observe established precautions for handling epoxy resins and fibrous materials—wear gloves. For further information, refer to Safety Data Sheet.

PROCESSING
Following removal from refrigerated storage, allow the prepreg to reach room temperature before opening the polythene bag, to avoid moisture condensation. Typically, the thaw time for a full roll of material will be 4 to 6 hours. Cut patterns to size and lay-up the laminate in line with design instructions taking care not to distort the prepreg. If necessary, the tack of the prepreg may be increased by gentle warming with hot air. The lay-up should be vacuum debulked at regular intervals using a P3 (pin pricked) release film on the prepreg surface; vacuum of 980 mbar (29 in Hg) is applied for 20 minutes.

For autoclave cures, use of a nonperforated release film on the prepreg surface trimmed to within 25–30 mm of the prepreg edge is recommended for the cure cycle and a vacuum bag should be installed using standard techniques.

Revised 07/2019 E731_PDS_v2_2019-07-14 Page 5/5

© 2019. All data given is based on representative samples of the materials in question. Since the method and circumstances under which these materials are processed and tested are key to their performance, and Toray Advanced Composites has no assurance of how its customers will use the material, the corporation cannot guarantee these properties. Toray®, (Toray) AmberTool®, (Toray) Cetex®, (Toray) MicroPly™, and all other related characters, logos, and trade names are claims and/or registered trademarks of Toray Industries Inc. and/or its subsidiary companies in one or more countries. Use of trademarks, trade names, and other IP rights of Toray Industries Inc. without prior written approval by such is strictly prohibited.

TORAY Toray Advanced Composites

18255 Sutter Blvd.
Morgan Hill, CA 95037, USA
t +1 408 465 8500

2450 Cordelia Road
Fairfield, CA 94534, USA
t +1 707 359 3400

Amber Drive, Langley Mill
Nottingham, NG16 4BE, UK
t +44 (0)1773 530899

www.toraytac.com
explore@toraytac-usa.com (North America/Asia/Pacific)
explore@toraytac-europe.com (Europe/Middle East/Africa)

Figure B.5: Page 5 of Toray's E731 pre-preg datasheet [66]

B.2 Toray E745 pre-preg

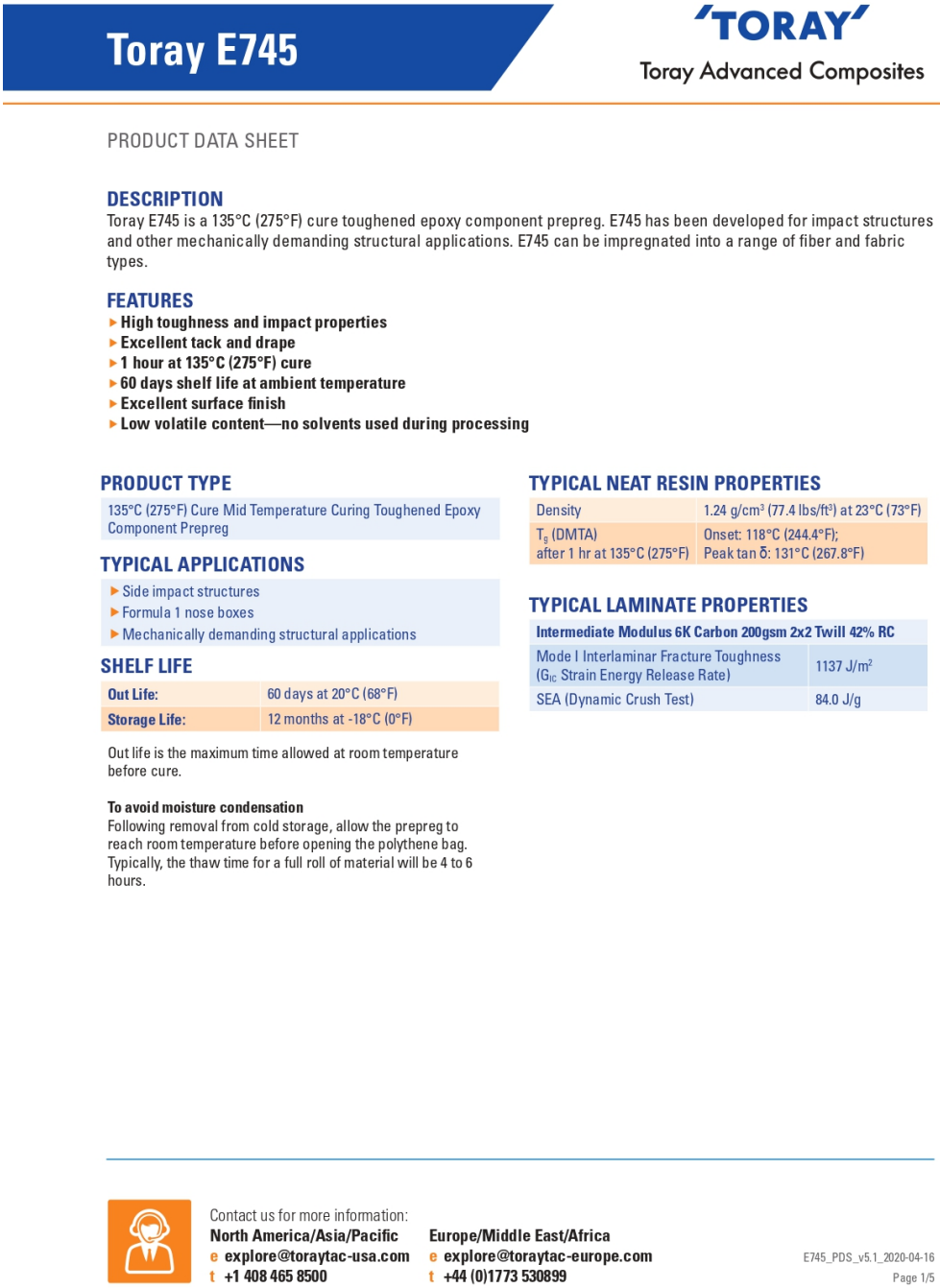

Toray E745

TORAY
Toray Advanced Composites

PRODUCT DATA SHEET

DESCRIPTION

Toray E745 is a 135°C (275°F) cure toughened epoxy component prepreg. E745 has been developed for impact structures and other mechanically demanding structural applications. E745 can be impregnated into a range of fiber and fabric types.

FEATURES

- **High toughness and impact properties**
- **Excellent tack and drape**
- **1 hour at 135°C (275°F) cure**
- **60 days shelf life at ambient temperature**
- **Excellent surface finish**
- **Low volatile content—no solvents used during processing**

PRODUCT TYPE

135°C (275°F) Cure Mid Temperature Curing Toughened Epoxy Component Prepreg

TYPICAL APPLICATIONS

- Side impact structures
- Formula 1 nose boxes
- Mechanically demanding structural applications

SHELF LIFE

Out Life:	60 days at 20°C (68°F)
Storage Life:	12 months at -18°C (0°F)

Out life is the maximum time allowed at room temperature before cure.

To avoid moisture condensation
Following removal from cold storage, allow the prepreg to reach room temperature before opening the polythene bag. Typically, the thaw time for a full roll of material will be 4 to 6 hours.

TYPICAL NEAT RESIN PROPERTIES

Density	1.24 g/cm³ (77.4 lbs/ft³) at 23°C (73°F)
T_g (DMTA) after 1 hr at 135°C (275°F)	Onset: 118°C (244.4°F); Peak tan δ: 131°C (267.8°F)

TYPICAL LAMINATE PROPERTIES

Intermediate Modulus 6K Carbon 200gsm 2x2 Twill 42% RC	
Mode I Interlaminar Fracture Toughness (G_{Ic} Strain Energy Release Rate)	1137 J/m²
SEA (Dynamic Crush Test)	84.0 J/g

Contact us for more information:
North America/Asia/Pacific
e explore@toraytac-usa.com
t +1 408 465 8500

Europe/Middle East/Africa
e explore@toraytac-europe.com
t +44 (0)1773 530899

Figure B.6: Page 1 of Toray's E745 pre-preg datasheet [68]

B.3 Toray E750 pre-preg

Toray E745

'TORAY'
Toray Advanced Composites

PRODUCT DATA SHEET

TYPICAL LAMINATE PROPERTIES

Intermediate Modulus 6K Carbon 200gsm 2x2 Twill 42% RC				
Property	**Condition**	**Method**	**Results**	
Tensile Strength 0°	RTD	ISO 527-4	1072 MPa	156 ksi
Tensile Modulus 0°	RTD	ISO 527-4	75.9 GPa	11.0 Msi
Poisson's Ratio	RTD	ISO 527-4	0.04	
Tensile Strength 90°	RTD	ISO 527-4	1130 MPa	164 ksi
Tensile Modulus 90°	RTD	ISO 527-4	78.9 GPa	11.4 Msi
Poisson's Ratio	RTD	ISO 527-4	0.04	
Compression Strength 0°	RTD	EN 2580	717 MPa	104 ksi
Compression Modulus 0°	RTD	EN 2580	70.6 GPa	10.2 Msi
Compression Strength 0°	RTD	EN 2580	707 MPa	103 ksi
Compression Modulus 90°	RTD	EN 2580	71.4 GPa	10.4 Msi
In-Plane Shear Strength	RTD	ISO 14129	124 MPa	18 ksi
In-Plane Shear Modulus	RTD	ISO 14129	3.9 GPa	0.6 Msi
Interlaminar Shear Strength 0°	RTD	ISO 14130	70 MPa	10 ksi
Interlaminar Shear Strength 90°	RTD	ISO 14130	69 MPa	10 ksi

Cured 1 hr at 135°C (275°F)
Results normalized to 55% Vf, otherwise results are at actual 49.3% Vf

RHEOLOGY

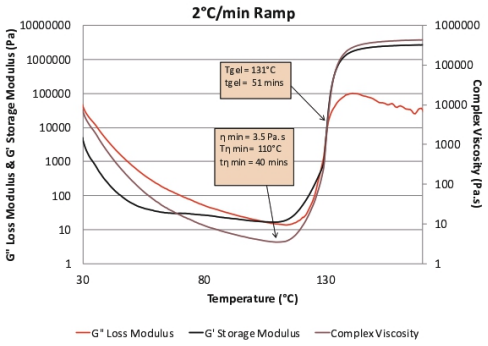

E745_PDS_v5.1_2020-04-16
Page 2/5

Figure B.7: Page 2 of Toray's E745 pre-preg datasheet [68]

B.4 Toray TC346 pre-preg

Toray E745

TORAY
Toray Advanced Composites

PRODUCT DATA SHEET

VISCOSITY

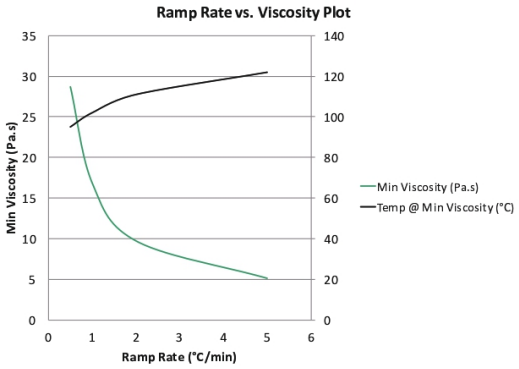

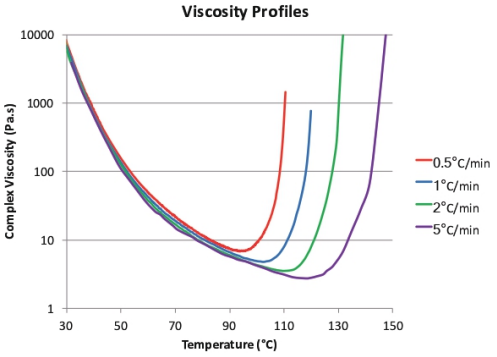

CURE PROPERTIES: VISCOSITY PROFILE (30°C TO 170°C OR 86°F TO 338°F)

Ramp rate [°C(°F)/min]	Minimum Viscosity (Pa.s)	Temperature at Minimum Viscosity
0.5 (1.0)	6.8	94°C (201°F)
1.0 (1.8)	4.74	102°C (216°F)
2.0 (3.6)	3.5	110°C (230°F)
5.0 (9.0)	2.73	118°C (244°F)

Figure B.8: Page 3 of Toray's E745 pre-preg datasheet [68]

Toray E745

'TORAY'
Toray Advanced Composites

PRODUCT DATA SHEET

RECOMMENDED CURE CYCLE

- Toray E745 can be successfully molded by vacuum bag, autoclave, or matched die molding techniques.
- Increase autoclave pressure to 1.4 bar (20 psi) with vacuum applied.
- Vent to atmosphere and raise pressure to 6.2 bar (90 psi) (or max allowed by the core material).
- Increase air temperature at 2°C (3.6°F)/min and hold for 1 hour at 135°C (275°F).
- Allow to cool to 60°C (140°F) before removal of pressure.

CURE SCHEDULE

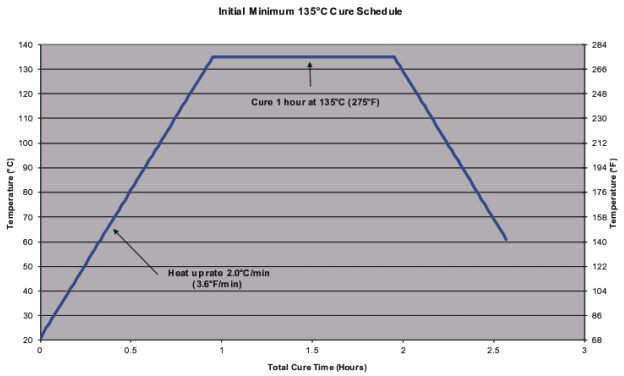

Figure B.9: Page 4 of Toray's E745 pre-preg datasheet [68]

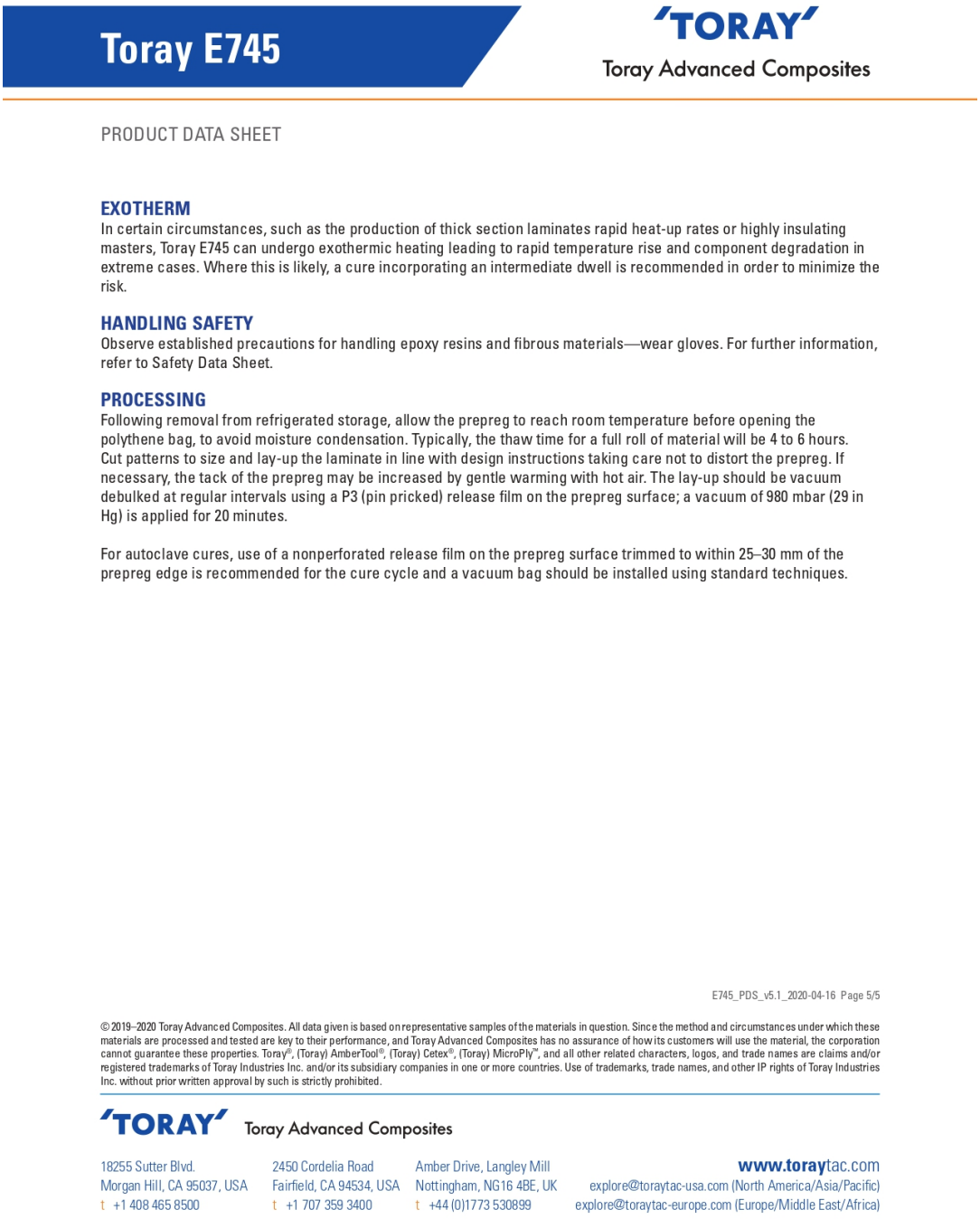

Toray E745

TORAY
Toray Advanced Composites

PRODUCT DATA SHEET

EXOTHERM
In certain circumstances, such as the production of thick section laminates rapid heat-up rates or highly insulating masters, Toray E745 can undergo exothermic heating leading to rapid temperature rise and component degradation in extreme cases. Where this is likely, a cure incorporating an intermediate dwell is recommended in order to minimize the risk.

HANDLING SAFETY
Observe established precautions for handling epoxy resins and fibrous materials—wear gloves. For further information, refer to Safety Data Sheet.

PROCESSING
Following removal from refrigerated storage, allow the prepreg to reach room temperature before opening the polythene bag, to avoid moisture condensation. Typically, the thaw time for a full roll of material will be 4 to 6 hours. Cut patterns to size and lay-up the laminate in line with design instructions taking care not to distort the prepreg. If necessary, the tack of the prepreg may be increased by gentle warming with hot air. The lay-up should be vacuum debulked at regular intervals using a P3 (pin pricked) release film on the prepreg surface; a vacuum of 980 mbar (29 in Hg) is applied for 20 minutes.

For autoclave cures, use of a nonperforated release film on the prepreg surface trimmed to within 25–30 mm of the prepreg edge is recommended for the cure cycle and a vacuum bag should be installed using standard techniques.

© 2019–2020 Toray Advanced Composites. All data given is based on representative samples of the materials in question. Since the method and circumstances under which these materials are processed and tested are key to their performance, and Toray Advanced Composites has no assurance of how its customers will use the material, the corporation cannot guarantee these properties. Toray®, (Toray) AmberTool®, (Toray) Cetex®, (Toray) MicroPly™, and all other related characters, logos, and trade names are claims and/or registered trademarks of Toray Industries Inc. and/or its subsidiary companies in one or more countries. Use of trademarks, trade names, and other IP rights of Toray Industries Inc. without prior written approval by such is strictly prohibited.

TORAY Toray Advanced Composites

18255 Sutter Blvd.
Morgan Hill, CA 95037, USA
t +1 408 465 8500

2450 Cordelia Road
Fairfield, CA 94534, USA
t +1 707 359 3400

Amber Drive, Langley Mill
Nottingham, NG16 4BE, UK
t +44 (0)1773 530899

www.toraytac.com
explore@toraytac-usa.com (North America/Asia/Pacific)
explore@toraytac-europe.com (Europe/Middle East/Africa)

Figure B.10: Page 5 of Toray's E745 pre-preg datasheet [68]

Toray E750

'TORAY'
Toray Advanced Composites

PRODUCT DATA SHEET

DESCRIPTION

Toray E750 is a toughened epoxy component prepreg developed for structural applications within Formula 1 and high performance automotive. Toray E750 allows curing from 80°C (176°F) to 180°C (356°F) and can be impregnated into a range of fiber and fabric types.

Toray E750 is compatible for co-cure with a range of Toray MicroPly™ film adhesive and syntactic core products.

FEATURES

- **Versatile cure schedules 80°C (176°F) to 180°C (356°F)**
- **Excellent translation of fiber properties**
- **Good impact resistance**
- **Excellent retention of properties at 120°C (248°F)**
- **Controlled flow**
- **Good drape and tack**
- **60 days out life at 18°C (64°F)**
- **12 months storage life at -18°C (0°F)**

PRODUCT TYPE

80°C (176°F) to 180°C (356°F) Cure Versatile Temperature Curing Toughened Epoxy Component Prepreg

TYPICAL APPLICATIONS

- Structural applications within Formula 1 and high performance automotive

SHELF LIFE

Out Life:	60 days at 18°C (64°F)
Storage Life:	12 months at -18°C (0°F)

Out life is the maximum time allowed at room temperature before cure.

To avoid moisture condensation
Following removal from cold storage, allow the prepreg to reach room temperature before opening the polythene bag. Typically, the thaw time for a full roll of material will be 4 to 6 hours.

TYPICAL NEAT RESIN PROPERTIES

Density	1.23 g/cm³ (76.8 lbs/ft³)
T_g (DMTA) after 1 hr at 135°C (275°F)	Onset: 148°C (298.4°F); Peak tan δ: 185°C (365°F)

Contact us for more information:
North America/Asia/Pacific
e explore@toraytac-usa.com
t +1 408 465 8500

Europe/Middle East/Africa
e explore@toraytac-europe.com
t +44 (0)1773 530899

Figure B.11: Page 1 of Toray's E750 pre-preg datasheet [67]

Toray E750

'TORAY'
Toray Advanced Composites

PRODUCT DATA SHEET

MECHANICAL PROPERTIES

Intermediate Modulus T800 6K Carbon 200gsm 2x2 Twill 42% RC			
Property	Method	Laminate Test Condition	
		RTD	ETD
Tensile Strength 0°	ISO 527-4	1079 MPa	1126 MPa
Tensile Modulus 0°	ISO 527-4	78.6 GPa	75.1 GPa
Poisson's Ratio 0°	ISO 527-4	0.04*	
Tensile Strength 90°	ISO 527-4	993 MPa	999 MPa
Tensile Modulus 90°	ISO 527-4	76.9 GPa	76.7 GPa
Poisson's Ratio 90°	ISO 527-4	0.04*	0.05*
Compression Strength 0°	prEN 2580	777 MPa	637 MPa
Compression Modulus 0°	prEN 2580	66.3 GPa	66.7 GPa
Compression Strength 90°	prEN 2580	758 MPa	622 MPa
Compression Modulus 90°	prEN 2580	67.4 GPa	67.4 GPa
In-Plane Shear Strength	prEN 6031	122 MPa*	92 MPa*
In-Plane Shear Modulus	prEN 6031	4.33 GPa*	3.34 GPa*
Poisson's Ratio ± 45°	prEN 6031	0.80*	
Interlaminar Shear Strength 0°	ASTM D 2344	76.8 MPa*	47.9 MPa*
Mode I Interlaminar Fracture Toughness (G_{Ic} Strain Energy Release Rate)	prEN 6033	525 J/m²*	-

Cured 1 hr at 135°C (275°F)
Room Temperature Dry (RTD) 22°C (71.6°F); Elevated Temperature Dry (ETD) 120°C (248°F); Test results normalized (55% Vf) except * actual data (52.93% Vf)

Figure B.12: Page 2 of Toray's E750 pre-preg datasheet [67]

Toray E750

'TORAY'
Toray Advanced Composites

PRODUCT DATA SHEET

Intermediate Modulus T1000 12K Carbon 280gsm 5HS 42% RC			
Property	Method	Laminate Test Condition	
		RTD	ETD
Tensile Strength 0°	ISO 527-4	1243 MPa	1302 MPa
Tensile Modulus 0°	ISO 527-4	77.2 GPa	75.6 GPa
Poisson's Ratio 0°	ISO 527-4	0.06*	0.05*
Tensile Strength 90°	ISO 527-4	1331 MPa	1269 MPa
Tensile Modulus 90°	ISO 527-4	77.7 GPa	75.9 GPa
Poisson's Ratio 90°	ISO 527-4	0.05*	0.06*
Compression Strength 0°	prEN 2580	664 MPa	548 MPa
Compression Modulus 0°	prEN 2580	70.6 GPa	68.2 GPa
Compression Strength 90°	prEN 2580	703 MPa	588 MPa
Compression Modulus 90°	prEN 2580	72.1 GPa	68.6 GPa
In-Plane Shear Strength	prEN 6031	113 MPa*	84 MPa*
In-Plane Shear Modulus	prEN 6031	4.30 GPa*	3.09 GPa*
Poisson's Ratio ± 45°	prEN 6031	0.8*	
Interlaminar Shear Strength 0°	ASTM D 2344	67.7 MPa*	47.3 MPa*
Mode I Interlaminar Fracture Toughness (G_{Ic} Strain Energy Release Rate)	prEN 6033	696 J/m²*	-

Cured 1 hr at 135°C (275°F)
Room Temperature Dry (RTD) 22°C (71.6°F); Elevated Temperature Dry (ETD) 120°C (248°F); Test results normalized (55% Vf) except * actual data (51.63% Vf)

Figure B.13: Page 3 of Toray's E750 pre-preg datasheet [67]

Toray E750

'TORAY'
Toray Advanced Composites

PRODUCT DATA SHEET

High Modulus M46J 6K Carbon 200gsm 2x2 Twill 42% RC			
Property	Method	Laminate Test Condition	
		RTD	ETD
Tensile Strength 0°	ISO 527-4	661 MPa	868 MPa
Tensile Modulus 0°	ISO 527-4	113.8 GPa	114.1 GPa
Poisson's Ratio 0°	ISO 527-4	0.03*	
Tensile Strength 90°	ISO 527-4	631 MPa	824 MPa
Tensile Modulus 90°	ISO 527-4	112.7 GPa	111.4 GPa
Poisson's Ratio 90°	ISO 527-4	0.02*	0.04*
Compression Strength 0°	prEN 2580	494 MPa	492 MPa
Compression Modulus 0°	prEN 2580	95.8 GPa	95.8 GPa
Compression Strength 90°	prEN 2580	505 MPa	470 MPa
Compression Modulus 90°	prEN 2580	96.4 GPa	96.4 GPa
In-Plane Shear Strength	prEN 6031	90 MPa*	71 MPa*
In-Plane Shear Modulus	prEN 6031	4.43 GPa*	3.4 GPa*
Poisson's Ratio	prEN 6031	0.9*	
Interlaminar Shear Strength 0°	ASTM D 2344	63.0 MPa*	41.5 MPa*
Mode I Interlaminar Fracture Toughness (G_{IC} Strain Energy Release Rate)	prEN 6033	471 J/m²*	-

Cured 1 hr at 135°C (275°F)
Room Temperature Dry (RTD) 22°C (71.6°F)
Elevated Temperature Dry (ETD) 120°C (248°F);
Test results normalized (55% Vf) except * actual data (53.18% Vf)

RHEOLOGY

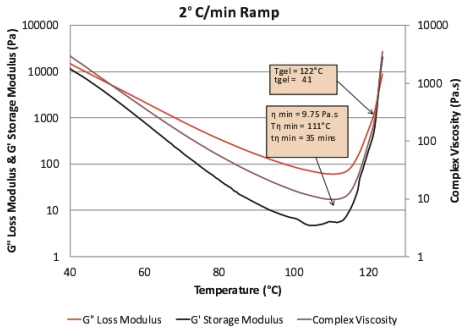

Figure B.14: Page 4 of Toray's E750 pre-preg datasheet [67]

Toray E750

'TORAY'
Toray Advanced Composites

PRODUCT DATA SHEET

VISCOSITY

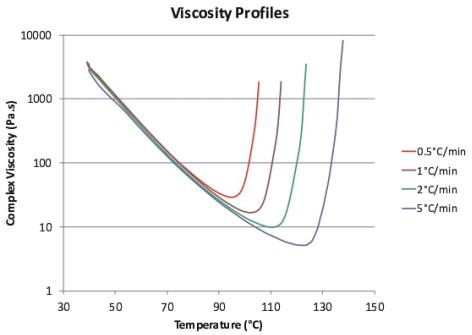

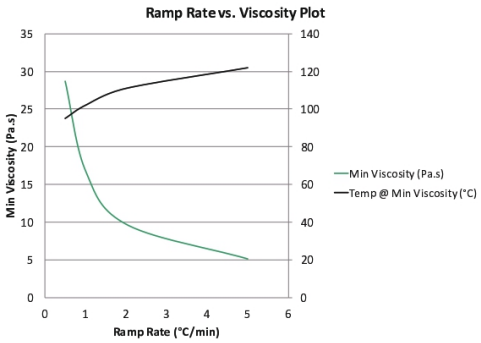

CURE PROPERTIES: VISCOSITY PROFILE 30°C TO 150°C

Ramp rate [°C (°F)/min]	Minimum Viscosity (Pa.s)	Temperature at Minimum Viscosity
0.5 (0.9)	28.73	95°C (203°F)
1.0 (1.8)	16.87	102°C (216°F)
2.0 (3.6)	9.75	111°C (231°F)
5.0 (9.0)	5.14	122°C (251°F)

Figure B.15: Page 5 of Toray's E750 pre-preg datasheet [67]

Toray E750

'TORAY'
Toray Advanced Composites

PRODUCT DATA SHEET

TYPICAL CURE PROFILES

135°C (275°F) Cure Temperatures		
Ramp	2.0°C (3.6°F)/min to 135°C (275°F)	Dwell for 1 hour
Cool	2.0°C (3.6°F)/min to below 60°C (140°F)	Followed by demold
Total time: 2 hours 35 minutes		

INITIAL MINIMUM CURE TIMES

Cure Cycle	T_g Onset (°C)	T_g Peak tan δ (°C)
16 hours at 80°C (176°F)	102°C	120°C
4 hours at 100°C (212°F)	119°C	148°C
1 hour at 135°C (275°F)	148°C	185°C
30 minutes at 150°C (302°F)	158°C	186°C
1 hour at 135°C (275°F) plus 2 hours at 180°C (356°F)	173°C	195°C

CURE SCHEDULE

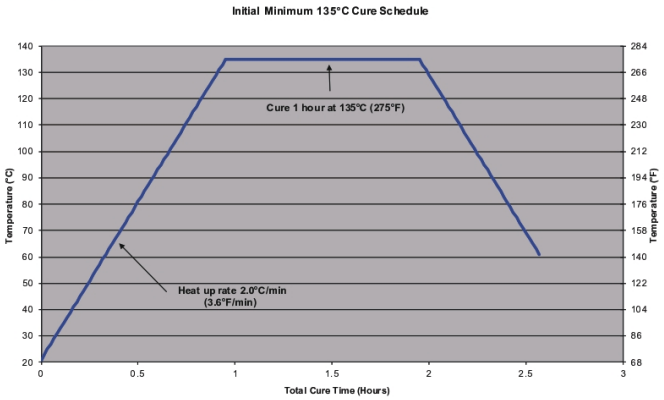

Figure B.16: Page 6 of Toray's E750 pre-preg datasheet [67]

Toray E750

'TORAY'
Toray Advanced Composites

PRODUCT DATA SHEET

EXOTHERM

In certain circumstances, such as the production of thick section laminates rapid heat-up rates or highly insulating masters, Toray E750 can undergo exothermic heating leading to rapid temperature rise and component degradation in extreme cases. Where this is likely, a cure incorporating an intermediate dwell is recommended in order to minimize the risk.

HANDLING SAFETY

Observe established precautions for handling epoxy resins and fibrous materials—wear gloves. For further information, refer to the Safety Data Sheet.

PROCESSING

Following removal from refrigerated storage, allow the prepreg to reach room temperature before opening the polythene bag, to avoid moisture condensation. Typically, the thaw time for a full roll of material will be 4 to 6 hours. Cut patterns to size and lay-up the laminate in line with design instructions taking care not to distort the prepreg. If necessary, the tack of the prepreg may be increased by gentle warming with hot air. The lay-up should be vacuum debulked at regular intervals using a P3 (pinpricked) release film on the prepreg surface; a vacuum of 980 mbar (29 inHg) is applied for 20 minutes.

For autoclave cures, use of a nonperforated release film on the prepreg surface trimmed to within 25–30 mm of the prepreg edge is recommended for the cure cycle and a vacuum bag should be installed using standard techniques.

© 2019–2021 Toray Advanced Composites. All data given is based on representative samples of the materials in question. Since the method and circumstances under which these materials are processed and tested are key to their performance, and Toray Advanced Composites has no assurance of how its customers will use the material, the corporation cannot guarantee these properties. Toray®, (Toray) AmberTool®, (Toray) Cetex®, (Toray) MicroPly™, and all other related characters, logos, and trade names are claims and/or registered trademarks of Toray Industries Inc. and/or its subsidiary companies in one or more countries. Use of trademarks, trade names, and other IP rights of Toray Industries Inc. without prior written approval by such is strictly prohibited.

'TORAY' Toray Advanced Composites

18255 Sutter Blvd.
Morgan Hill, CA 95037, USA
t +1 408 465 8500

2450 Cordelia Road
Fairfield, CA 94534, USA
t +1 707 359 3400

Amber Drive, Langley Mill
Nottingham, NG16 4BE, UK
t +44 (0)1773 530899

www.toraytac.com
explore@toraytac-usa.com (North America/Asia/Pacific)
explore@toraytac-europe.com (Europe/Middle East/Africa)

Figure B.17: Page 7 of Toray's E750 pre-preg datasheet [67]

Toray TC346

TORAY
Toray Advanced Composites

PRODUCT DATA SHEET

DESCRIPTION

Toray TC346 is a high temperature epoxy component prepreg developed for structural applications within Formula 1 and high performance automotive. Toray TC346 is designed to deliver enhanced compression properties to manufactured parts while maintaining a good fracture toughness. When exposed to elevated temperature environments, TC346 composites demonstrate excellent retention of mechanical performance.

Toray TC346 resin system meets UL94 V-0 flame-retardancy tests, further demonstrating how the system is ideally suited to satisfy the rigorous demands of the high performance automotive and motorsport markets.

FEATURES

- **T_g 208°C (406°F) after 180°C (356°F) cure cycle**
- **Structural system—mechanical performance optimized for compression, short-beam shear, fracture toughness**
- **Excellent retention of properties at elevated temperatures**
- **Toughened system—good interlaminar fracture toughness energy achieved without significant compromise of compression properties**
- **Flame-retardant test material: TC346 HM0545 200gsm 2x2 Twill HM63 12K 42% Resin Content**
  - **UL94 V-0 (2 mm thickness)**
- **Controlled tack level to aid laminating**
- **Controlled resin flow during recommended cure cycle**
- **21-day out life at 20°C (68°F)**
- **12-month storage life at -18°C (0°F)**

PRODUCT TYPE

135°C (275°F) to 180°C (356°F) Cure High Temperature Epoxy Component Prepreg

TYPICAL APPLICATIONS

- Structural applications within Formula 1and high performance automotive

SHELF LIFE

Out Life:	21 days at 20°C (68°F)
Storage Life:	12 months at -18°C (0°F)

Out life is the maximum time allowed at room temperature before cure.

To avoid moisture condensation
Following removal from cold storage, allow the prepreg to reach room temperature before opening the polythene bag. Typically, the thaw time for a full roll of material will be 4 to 6 hours.

TYPICAL NEAT RESIN PROPERTIES

Density (ASTM D792)	1.3 g/cm³ (81.2 lbs/ft³)
T_g (DMA) after 2 hrs at 180°C (356°F) (ASTM D7028)	Onset: 208°C (406°F); Peak tan δ: 228°C (442°F)
T_g (DMA) after 2 hrs at 200°C (392°F) post cure (ASTM D7028)	Onset: 221°C (430°F); Peak tan δ: 236°C (457°F)
T_g (DMA) after 3 hrs at 135°C (275°F) (ASTM D7028)	Onset: 156°C (313°F); Peak tan δ: 178°C (352°F)

SPECIFICATIONS

Flame-Retardancy	
UL94 V-0	2 mm thickness
Test material: TC346 HM0545 200gsm 2x2 Twill HM63 12K 42% Resin Content	

Contact us for more information:
North America/Asia/Pacific
e explore@toraytac-usa.com
t +1 408 465 8500

Europe/Middle East/Africa
e explore@toraytac-europe.com
t +44 (0)1773 530899

Figure B.18: Page 1 of Toray's TC346 pre-preg datasheet [63]

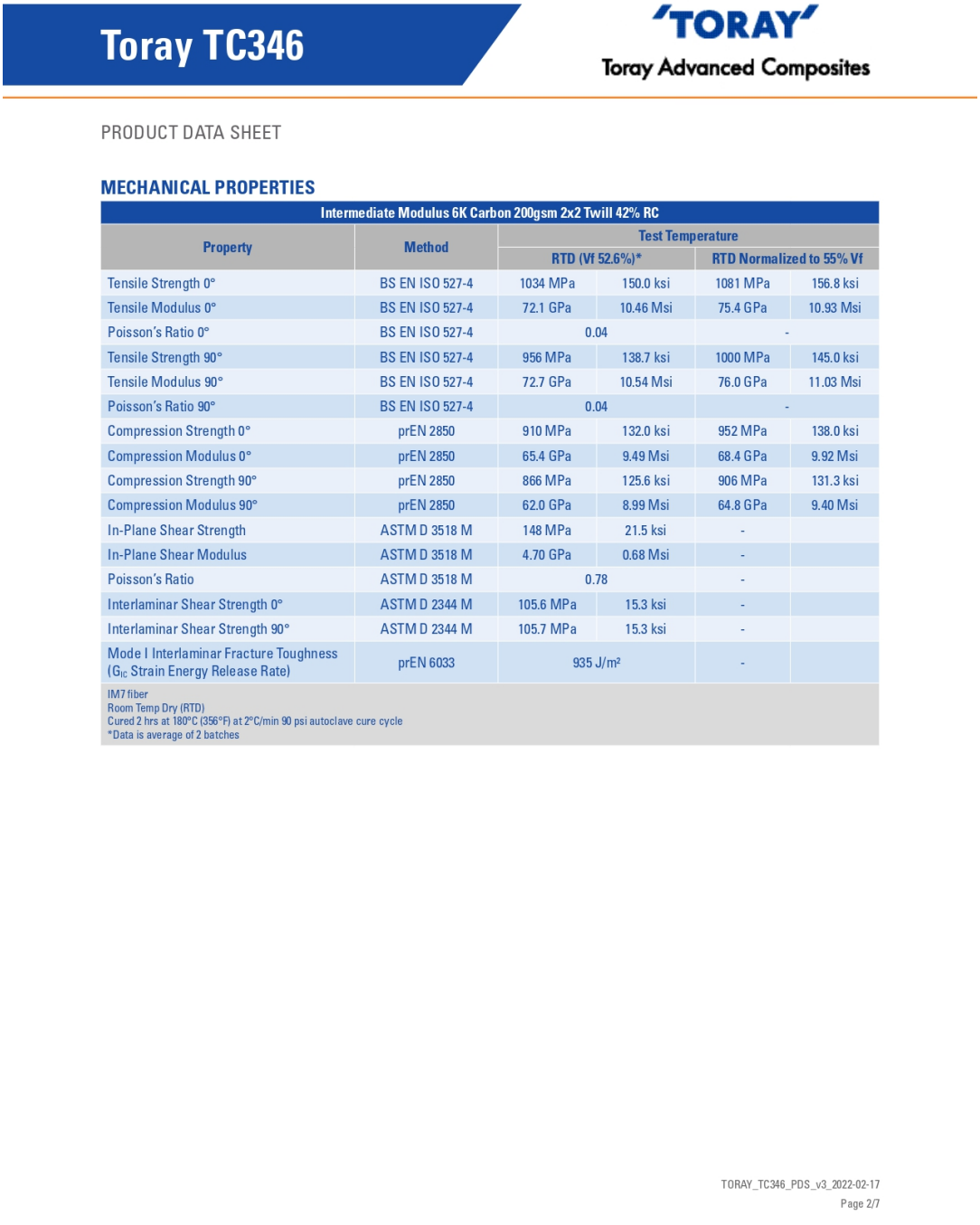

Toray TC346

TORAY
Toray Advanced Composites

PRODUCT DATA SHEET

MECHANICAL PROPERTIES

Intermediate Modulus 6K Carbon 200gsm 2x2 Twill 42% RC					
Property	Method	Test Temperature			
		RTD (Vf 52.6%)*		RTD Normalized to 55% Vf	
Tensile Strength 0°	BS EN ISO 527-4	1034 MPa	150.0 ksi	1081 MPa	156.8 ksi
Tensile Modulus 0°	BS EN ISO 527-4	72.1 GPa	10.46 Msi	75.4 GPa	10.93 Msi
Poisson's Ratio 0°	BS EN ISO 527-4	0.04		-	
Tensile Strength 90°	BS EN ISO 527-4	956 MPa	138.7 ksi	1000 MPa	145.0 ksi
Tensile Modulus 90°	BS EN ISO 527-4	72.7 GPa	10.54 Msi	76.0 GPa	11.03 Msi
Poisson's Ratio 90°	BS EN ISO 527-4	0.04		-	
Compression Strength 0°	prEN 2850	910 MPa	132.0 ksi	952 MPa	138.0 ksi
Compression Modulus 0°	prEN 2850	65.4 GPa	9.49 Msi	68.4 GPa	9.92 Msi
Compression Strength 90°	prEN 2850	866 MPa	125.6 ksi	906 MPa	131.3 ksi
Compression Modulus 90°	prEN 2850	62.0 GPa	8.99 Msi	64.8 GPa	9.40 Msi
In-Plane Shear Strength	ASTM D 3518 M	148 MPa	21.5 ksi	-	
In-Plane Shear Modulus	ASTM D 3518 M	4.70 GPa	0.68 Msi	-	
Poisson's Ratio	ASTM D 3518 M	0.78		-	
Interlaminar Shear Strength 0°	ASTM D 2344 M	105.6 MPa	15.3 ksi	-	
Interlaminar Shear Strength 90°	ASTM D 2344 M	105.7 MPa	15.3 ksi	-	
Mode I Interlaminar Fracture Toughness (G_{Ic} Strain Energy Release Rate)	prEN 6033	935 J/m²		-	

IM7 fiber
Room Temp Dry (RTD)
Cured 2 hrs at 180°C (356°F) at 2°C/min 90 psi autoclave cure cycle
*Data is average of 2 batches

Figure B.19: Page 2 of Toray's TC346 pre-preg datasheet [63]

Toray TC346

TORAY
Toray Advanced Composites

PRODUCT DATA SHEET

MECHANICAL PROPERTIES

High Modulus M46JB 12K Carbon 140gsm UD 34% RC					
Property	Method	Test Temperature			
		RTD (Vf 62.1%)		RTD Normalized to 60% Vf	
Tensile Strength 0°	BS EN ISO 527-5	1906 MPa	276.4 ksi	1842 MPa	267.1 ksi
Tensile Modulus 0°	BS EN ISO 527-5	258.9 GPa	37.55 Msi	250.1 GPa	36.28 Msi
Poisson's Ratio 0°	BS EN ISO 527-5	0.30		-	-
Tensile Strength 90°	BS EN ISO 527-5	35 MPa	5.1 ksi	-	-
Tensile Modulus 90°	BS EN ISO 527-5	7.4 GPa	1.07 Msi	-	-
Compression Strength 0°	prEN 2850 Type B	1057 MPa	153.3 ksi	1021 MPa	148.1 ksi
Compression Modulus 0°	prEN 2850 Type B	229.9 GPa	33.34 Msi	222.1 GPa	32.22 Msi
Compression Strength 90°	prEN 2850 Type B	256 MPa	37.1 ksi	-	-
Compression Modulus 90°	prEN 2850 Type B	7.7 GPa	1.12 Msi	-	-
In-Plane Shear Strength	ASTM D 3518 M	66 MPa	9.6 ksi	-	-
In-Plane Shear Modulus	ASTM D 3518 M	4.8 GPa	0.70 Msi	-	-
Poisson's Ratio	ASTM D 3518 M	0.80		-	-
Interlaminar Shear Strength 0°	ASTM D 2344 M	95.4 MPa	13.84 ksi	-	-
Flexural Strength 0°	BS EN ISO 14125	1650 MPa	239.3 ksi	1594 MPa	231.2 ksi
Flexural Modulus 0°	BS EN ISO 14125	234 GPa	33.9 Msi	226.1 GPa	32.8 Msi
Mode I Interlaminar Fracture Toughness (G_{Ic} Strain Energy Release Rate)	prEN 6033	193 J/m²		-	-

Room Temp Dry (RTD)
Cured 2 hrs at 180°C (356°F) at 2°C/min 90 psi autoclave cure cycle

Figure B.20: Page 3 of Toray's TC346 pre-preg datasheet [63]

Toray TC346

TORAY
Toray Advanced Composites

PRODUCT DATA SHEET

High Modulus M46JB 6K Carbon 200gsm 2x2 Twill 38% RC					
Property	Method	Test Temperature			
		RTD (Vf 55.65%)		RTD Normalized to 55% Vf	
Tensile Strength 0°	BS EN ISO 527-4	596 MPa	86.4 ksi	589 MPa	85.4 ksi
Tensile Modulus 0°	BS EN ISO 527-4	109.6 GPa	15.90 Msi	108.3 GPa	15.71 Msi
Poisson's Ratio 0°	BS EN ISO 527-4	0.01		-	-
Tensile Strength 90°	BS EN ISO 527-4	529 MPa	76.7 ksi	523 MPa	75.8 ksi
Tensile Modulus 90°	BS EN ISO 527-4	103.7 GPa	15.04 Msi	102.5 GPa	14.86 Msi
Poisson's Ratio 90°	BS EN ISO 527-4	0.02		-	-
Compression Strength 0°	prEN 2850 Type B	526 MPa	76.3 ksi	520 MPa	75.4 ksi
Compression Modulus 0°	prEN 2850 Type B	101.1 GPa	14.66 Msi	99.9 GPa	14.49 Msi
Compression Strength 90°	prEN 2850 Type B	493 MPa	71.5 ksi	487 MPa	70.7 ksi
Compression Modulus 90°	prEN 2850 Type B	97.1 GPa	14.08 Msi	96.0 GPa	13.92 Msi
In-Plane Shear Strength	ASTM D 3518 M	102 MPa	14.8 ksi	-	-
In-Plane Shear Modulus	ASTM D 3518 M	4.47 GPa	0.65 Msi	-	-
Poisson's Ratio	ASTM D 3518 M	0.90		-	-
Interlaminar Shear Strength 0°	ASTM D 2344 M	74.3 MPa	10.78 ksi	-	-
Interlaminar Shear Strength 90°	ASTM D 2344 M	75.6 MPa	10.96 ksi	-	-
Mode I Interlaminar Fracture Toughness (G_{Ic} Strain Energy Release Rate)	prEN 6033	503 J/m²		-	-

Room Temp Dry (RTD)
Cured 2 hrs at 180°C (356°F) at 2°C/min 90 psi autoclave cure cycle

RETENTION OF MECHANICAL PROPERTIES AT ELEVATED TEMPERATURES

Elevated Temperature Dry (ETD) Cured 2 Hrs at 180°C (356°F) at 2°C/min at 90 psi

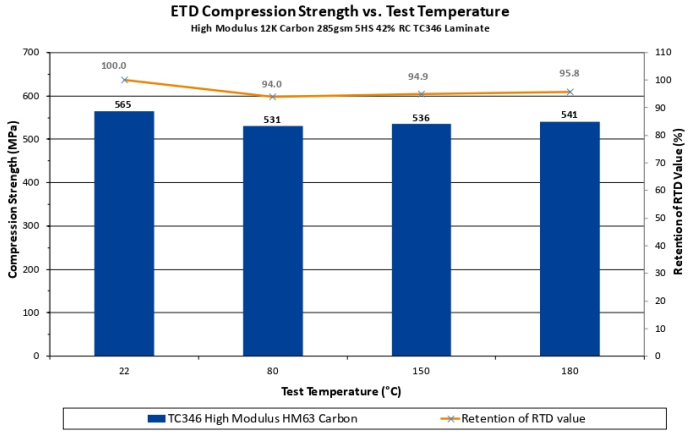

Figure B.21: Page 4 of Toray's TC346 pre-preg datasheet [63]

Toray TC346

TORAY
Toray Advanced Composites

PRODUCT DATA SHEET

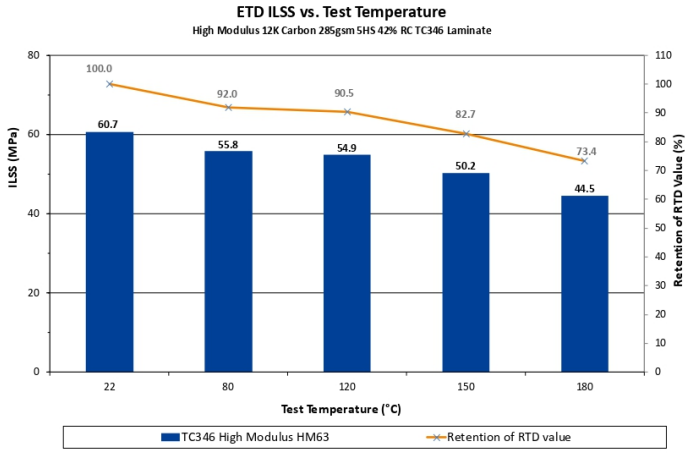

RHEOLOGY

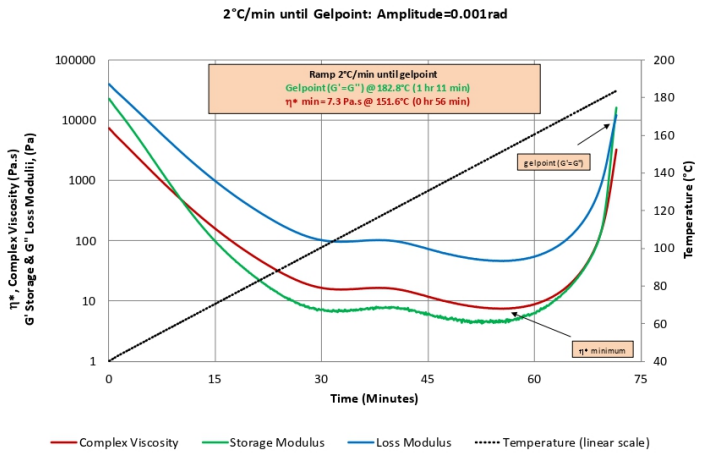

Figure B.22: Page 5 of Toray's TC346 pre-preg datasheet [63]

Toray TC346

Toray Advanced Composites

PRODUCT DATA SHEET

TYPICAL CURE PROFILE

180°C (356°F) Cure Temperature with 90 psi Pressure		
Ramp	2.0°C (3.6°F)/min to 180°C (356°F)	Dwell for 2 hrs
Cool	2.0°C (3.6°F)/min to 60°C (140°F)	Followed by demold
Total time: 4 hours 30 minutes		

CURE SCHEDULE

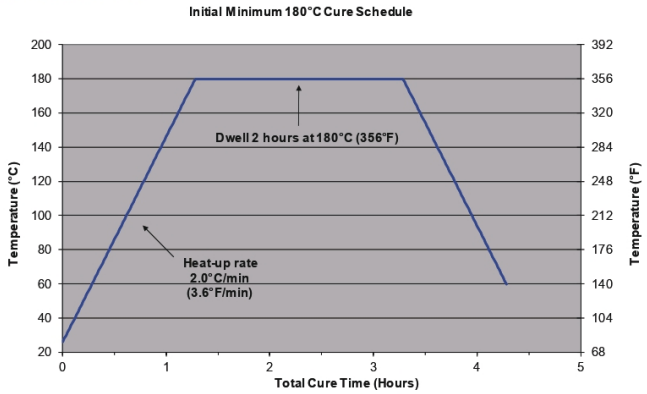

A 60-minute dwell at 107°C (225°F) may also be used.
An alternative cure cycle at 135°C (275°F) may be used followed by a 180°C (356°F) freestanding post cure.

135°C (275°F) Cure Temperature with 90 psi Pressure		
Ramp	2.0°C (3.6°F)/min to 135°C (275°F)	Dwell for 3 hrs
Cool	2.0°C (3.6°F)/min to 60°C (140°F)	Followed by demold
Followed by freestanding post cure for 2 hours at 180°C (356°F)		
Total time: 4 hours 40 minutes		

Alternative cure cycles and molding techniques may be employed. Please consult our technical support engineers for advice on your specific cure requirements.

Figure B.23: Page 6 of Toray's TC346 pre-preg datasheet [63]

Toray TC346

TORAY
Toray Advanced Composites

PRODUCT DATA SHEET

EXOTHERM

In certain circumstances, such as the production of thick section laminates rapid heat-up rates or highly insulating masters, Toray TC346 can undergo exothermic heating leading to rapid temperature rise and component degradation in extreme cases. Where this is likely, a cure incorporating an intermediate dwell is recommended in order to minimize the risk.

HANDLING SAFETY

Observe established precautions for handling epoxy resins and fibrous materials—wear gloves. For further information, refer to the Safety Data Sheet.

PROCESSING

Following removal from refrigerated storage, allow the prepreg to reach room temperature before opening the polythene bag, to avoid moisture condensation. Typically, the thaw time for a full roll of material will be 4 to 6 hours. Cut patterns to size and lay-up the laminate in line with design instructions taking care not to distort the prepreg. If necessary, the tack of the prepreg may be increased by gentle warming with hot air. The lay-up should be vacuum debulked at regular intervals using a P3 (pinpricked) release film on the prepreg surface; a vacuum of 948 mbar (28 in Hg) is applied for 10 minutes.

For autoclave cures, use of a nonperforated release film on the prepreg surface trimmed to within 25–30 mm of the prepreg edge is recommended for the cure cycle and a vacuum bag should be installed using standard techniques.

© 2019–2022 Toray Advanced Composites. All data given is based on representative samples of the materials in question. Since the method and circumstances under which these materials are processed and tested are key to their performance, and Toray Advanced Composites has no assurance of how its customers will use the material, the corporation cannot guarantee these properties. Toray®, (Toray) AmberTool®, (Toray) Cetex®, (Toray) MicroPly™, and all other related characters, logos, and trade names are claims and/or registered trademarks of Toray Industries Inc. and/or its subsidiary companies in one or more countries. Use of trademarks, trade names, and other IP rights of Toray Industries Inc. without prior written approval by such is strictly prohibited.

TORAY Toray Advanced Composites

18255 Sutter Blvd.
Morgan Hill, CA 95037, USA
t +1 408 465 8500

2450 Cordelia Road
Fairfield, CA 94534, USA
t +1 707 359 3400

Amber Drive, Langley Mill
Nottingham, NG16 4BE, UK
t +44 (0)1773 530899

www.toraytac.com
explore@toraytac-usa.com (North America/Asia/Pacific)
explore@toraytac-europe.com (Europe/Middle East/Africa)

Figure B.24: Page 7 of Toray's TC346 pre-preg datasheet [63]

Appendix C

Easy Composites 6.4 mm cell Aluminium Honeycomb

easycomposites™
share the knowledge

CORE MATERIAL
ALUMINIUM HONEYCOMB

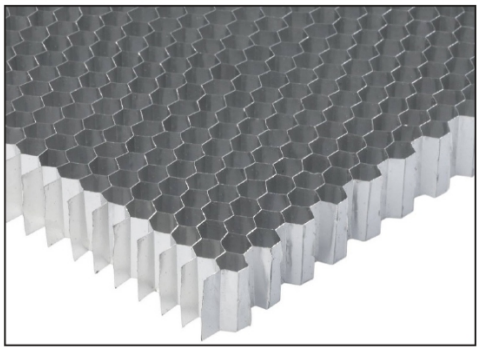

Product Description

High performance aluminium honeycomb core exactly as supplied to the world's top composites engineering, aerospace and motorsport manufacturers. Aluminium honeycomb core is one of the most widely used high performance honeycomb materials; chosen for its excellent strength to weight ratio (the best of all core materials) and bonding characteristics.

Aluminium honeycomb is used extensively in the motorsport, marine and aerospace industries and increasing now in construction industry where reducing weight whilst maintaining or improving the strength of a composite is of key importance.

In its un-expanded (block) form aluminium honeycomb is also very compact and easy to ship cost effectively and without risk of damage. Un-expanded blocks can be easily expanded into their full sheet form without the need for sophisticated equipment. Sheets are available in blocks which will expand to a full sheet size of 2500mm x 1250mm or to a smaller sheet size of 1250mm x 652mm.

Like all core materials aluminium honeycomb is designed to be sandwiched between two skins of material to create a sandwich panel. By creating distance between the two skins and ensuring that these skins cannot move relative to each other great mechanical advantage is gained making for very stiff panels with only minimal increase in weight.

Recommended Uses

Aluminium honeycomb is used in a wide range of applications, including:

- Motorsport (monocoques, splitters, floors, diffusers, crash cells)
- Aviation (bulkheads, dashboards, floors)
- Marine (decks, bulkheads, dashboards)
- Renewable energy (turbine housings, blade construction)
- Architectural (panels, doors, floors)
- Mass transit
- Crash attenuation (impact cells for crash tests, crumple zones)
- Air straighteners (wind tunnels)
- Laser cutting beds

Key Features

- High Shear Strength
- High Compressive Strength
- Low Density
- Corrison & Temperature Resistant
- Accurate Thickness Tolerance

Specification & Properties

The following table lists the specification and properties for the different cell sizes of honeycomb we supply.

Property	1/8" (3.2mm)	1/4" (6.4mm)	3/4" (19.1mm)
Nominal Density	72.1 kg/m^3	83.3kg/m^3	28.8kg/m^3
Aluminium Series	5052	3003	3003
Foil Thickness (micron)	35	70	50
Perforated?	No	Yes	Yes
Corrosion Treated	No	Yes	Yes
Comp Strength - Bare	539 psi	625 psi	115 psi
Comp Strength - Stabilised	559 psi	655 psi	125 psi
Crush Strength	255 psi	235 psi	40 psi
Plate Shear (L dir.) Strength	340 psi	360 psi	95 psi
Plate Shear (L dir.) Modulus	70 ksi	65 ksi	22 ksi
Plate Shear (W dir.) Strength	220 psi	210 psi	60 psi
Plate Shear (W dir.) Modulus	31 ksi	35 ksi	10 ksi
Max Service Temperature	120 °C	120 °C	120 °C

Expanding the Honeycomb

IMPORTANT - wear gloves before handling the block.

Commonly Aluminium Honeycomb is supplied as an unexpanded block. This is for two reasons, firstly because expanded honeycomb would be expensive to ship, and secondly because in its expanded un-stabilised form, the honeycomb is very susceptible to damage and would unlikely survive transport intact.

In large scale manufacturing, a specialist expanding machine is used to expand the honeycomb. However, for smaller applications and one off jobs, such machinery is prohibitively expensive and large thus an alternative method is needed.

Equipment needed

You will need 2 wooden battens, both as wide as the sheet you are expanding and stiff enough not to flex too much. 2" by 4" wooden battens are usually ideal and easily obtained. You will also need a bag of wood nails. They need to be long enough so that they can go through both the wooden batten and still protrude enough to go through the honeycomb.

For cutting honeycomb you need a steel ruler and a sharp Stanley type knife with a blade long enough to cut through the honeycomb to its full thickness in one go.

Figure C.1: Page 1 of Aluminium Honeycomb datasheet

Making tools to aid expansion

Take one of the battens and mark out a series of dots on the wood along the battens length spaced at approximately 50mm intervals.

Once marked, hammer the nails through the dots marked on the batten (taking care nothing is underneath!). The final result should be a batten with regular nails poking through.

Repeat for the second batten so you have two identical battens with nails sticking out.

You now just need a flat surface to work on and an assistant to help you expand the honeycomb.

Expanding the honeycomb

The first step is to lay the honeycomb onto a flat surface and by hand tease out gently the first few cells. Take care as you work across the sheet to ensure you do not pull too much out in one go as otherwise the honeycomb will kink making it harder to work.

The reason for expanding the first few cells by hand is to give the nails enough material to pull out the sheet without just ripping through the cells at the edge. The sheets are deliberately cut oversize to allow a little waste at each end due to expansion.

Repeat on the other side of the honeycomb.

At this stage you will need an assistant. Insert the batten tools into each side of the honeycomb. With one person holding each batten, slowly apply tension to expand the honeycomb.

If you find it is just ripping through the cells you have teased out by hand, then stop, pull out a few more cells by hand then start the process again. Expect the cells at the edge to distort and stretch as the sheet expands.

As you build up tension the honeycomb will begin to expand. Be careful you don't put on too much force and distort excessively the honeycomb as it expands. Gentle but firm is the method to use.

Continue to apply the tension to the battens to expand the whole sheet, taking care as it expands to keep the sheet as straight as possible. Once you are happy the honeycomb has been expanded sufficiently, then you can remove the battens and then use the honeycomb for your project.

Cutting the honeycomb

You will need a sharp Stanley type knife and a metal ruler. The blade needs to be long enough to cut the cell foils in one action for the chosen thickness of honeycomb.

The method is relatively simple. Measure the sheet out and use the metal rule as the cutting edge. Working from one side of the planned cut, individually cut through each cell foil from top to bottom using the knife. You need to ensure each foil is fully cut before moving onto the next one, so that when you try to separate the honeycomb, it comes apart neatly and doesn't catch or distort the cells.

Do not attempt to cut across the honeycomb in one go as it is easy to tear and distort the cells as you drag the knife blade across the honeycomb.

Disclaimer

This data is not to be used for specifications. Values listed are for typical properties and should not be considered minimum or maximum.

Our technical advice, whether verbal or in writing, is given in good faith but Easy Composites Ltd gives no warranty; express or implied, and all products are sold upon condition that purchasers will make their own tests to determine the quality and suitability of the product for their particular application and circumstances.

Easy Composites Ltd shall be in no way responsible for the proper use and service of the product, nor for the safeguarding of personnel or property, all of which is the duty of the user. Any information or suggestions are without warranty of any kind and purchasers are solely responsible for any loss arising from the use of such information or suggestions. No information or suggestions given by us shall be deemed to be a recommendation to use any product in conflict with any existing patent rights.

Before using any of our products, users should familiarise themselves with the relevant technical and safety datasheets provided by Easy Composites Ltd.

AeroFilm™ is a trademark of Easy Composites Ltd.

easycomposites™
share the knowledge

Easy Composites Ltd
Unit 39, Park Hall Business Village, Longton, Stoke on Trent, Staffordshire, ST3 5XA, United Kingdom.
Tel. +44 (0)1782 454499, Fax. +44 (0)1782 596868, Email sales@easycomposites.co.uk, Web www.easycomposites.co.uk

Figure C.2: Page 2 of Aluminium Honeycomb datasheet

Appendix D

SikaPower®-740 (ADEKIT A140-1 / H9940-1) Epoxy Adhesive

PRODUCT DATA SHEET

SikaPower®-740 (ADEKIT A140-1 / H9940-1)

TWO-COMPONENT EPOXY ADHESIVE
HIGH PERFORMANCES

DESCRIPTION

Bonding of car body, of metallic structures (racing vehicles)
Bonding in Aeronautic, bonding of inserts, of Composite structures.

PROPERTIES

- 2 component high performances room temperature curing Epoxy adhesive
- Non sagging pasty product suitable for vertical applications and to fill irregular joints
- Excellent mechanical performances
- Excellent strength to dynamic loads (vibrations and impacts)
- Product adapted to stringent ageing and aggressive environments

PHYSICAL PROPERTIES

Composition		RESIN (A)	HARDENER (B)	MIX	METHOD
Mix ratio by weight		100	90		
Mix ratio by volume at 25 °C		100	100		
Colour		Beige (BG) Black (BK)	Beige	Beige (BG) Black (BK)	
Density at 25 °C (KP)		1.38	1.22	-	LT-020
Density of cured product at 23 °C		-	-	1.30	ISO 2781
Viscosity at 25 °C	(Pa.s)	950 (KP)	380	370	LT-054 / 0.1 s^{-1}
Pot life at 25°C on 100g (KP)	(min)	-	-	25	LT-002
Open time on 7mm bead at 23°C	(min)	-	-	40	LT-006-B

(KP) Key properties. These values are enclosed in Certificate of Analysis.

MECHANICAL PROPERTIES (1)

Hardness	(Shore D)	80	ISO 868
Tensile strength	(MPa)	30	ISO 527-2
Elongation at break	(%)	4	ISO 527-2
Young Modulus	(MPa)	2500	ISO 527-2
Recommended application temperature	(°C)	15 to 30	
Working temperature (2)	(°C)	- 40 to 130	LT-006-B

(1) Cured 16 hours at 70 °C

(2) Working temperature is defined as the temperature at which product keeps 80 % of its initial Lap Shear Strength after 1000 hours ageing at this temperature, value on Aluminium, measured at 23 °C.

BUILDING TRUST

Figure D.1: Page 1 of SikaPower®-740 datasheet

HANDLING TIME (1)

At 23 °C	4h	LT-006-B
At 40 °C	1 h 30	
At 60 °C	30 min	

(1) Handling time is defined as the time needed to obtain Lap Shear Strength on Aluminium at 23 °C, of 1 MPa.

MECHANICAL PROPERTIES ON ASSEMBLIES (1)

	LAP SHEAR STRENGTH AT 23 °C (MPa)		METHOD
Aluminium 2017A (sandblasted)	**Initial**	**20 CF**	LT-006-B
	After wet cataplasm 7 days at 70 °C / 100 % RH	**16 CF**	
	After 21 cycles D3 (2)	**16 CF**	
Stainless Steel 304 (sandblasted)		**23 CF**	
Electro-galvanized Steel (sandblasted)		**21 CF**	
Electro-galvanized Steel (Acetone wiped)		**20 CF**	
ABS (sanded + Isopropanol)		**5 SF**	
PC (sanded + Isopropanol + Plastic primer (3))		**2 AF**	
PVC (sanded + Isopropanol)		**5 SF**	
PMMA (sanded + Isopropanol + plastic primer (3))		**3 AF**	
PA6E (sanded + Isopropanol)		**4.5 SF/AF**	
GFR Polyester (Isopropanol wiped)		**7 DF**	
GFR Epoxy (Isopropanol wiped)		**17 SCF**	

(1) Cured 16 hours at 70 °C

(2) Cycle D3 : 16 h at 40 °C/95 % RH + 3 h at -20 °C + 5 h at 70 °C/50 % ± 5 % RH, according to ISO 9142 standard

(3) Plastic sanded, Isopropanol wipe and coated with Sika Advanced Resins Plastic Primer 5069

CF : Cohesive Failure, AF : Adhesive Failure, SCF : Special Cohesive Failure, SF: Substrate Failure, DF: Delamination Failure, SCF : Special Cohesive Failure, according to EN ISO 10365 Standard

FLOATING ROLLER PEEL STRENGTH AT 23 °C

Aluminium 2017A (sandblasted)	(kN/m)	**6**	ISO 4578

Figure D.2: Page 2 of SikaPower®-740 datasheet

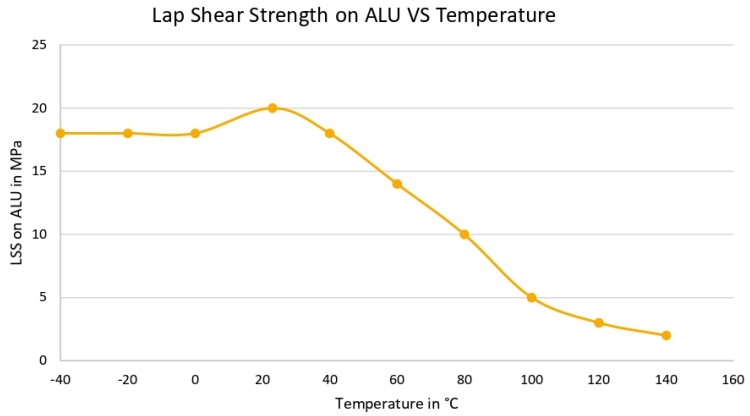

PROCESSING

- **Equipment: SikaPower®-740 BLACK (AB)** packaged in 50 ml and 400 ml cartridges and **SikaPower®-740 BEIGE (AB)** packaged in 400 ml cartridges require a manual or pneumatic gun. Please consult our technical department for applications needing a machine.
- **Substrate preparation**: The item to be bonded must be free of all dirt, oil or other foreign matter. A clean, dry surface is a must. **Consult our Technical Support about surface preparations**.

HANDLING PRECAUTIONS

Normal health and safety precautions should be observed when handling these products:

- Ensure good ventilation.
- Wear gloves, glasses and protective clothes.

For further information, please consult the Safety Data Sheet.

STORAGE CONDITIONS

Shelf life of **SikaPower®-740 (AB)** (cartridges) is **12 months** stored in a dry place and in its original unopened packaging at a temperature between 15 °C and 25 °C.

Shelf life of **SikaPower®-740 (A) (Resin) and SikaPower®-740 (B) (Hardener)** is **12 months** stored in a dry place and in their original unopened packaging at a temperature between 15 °C and 25 °C.

Figure D.3: Page 3 of SikaPower®-740 datasheet

PACKAGING

■ SikaPower®-740 BLACK (AB) / 50 ml	Box of 12 cartridges
■ SikaPower®-740 BLACK (AB) / 400 ml	Box of 12 cartridges
■ SikaPower®-740 BEIGE (AB) / 400 ml	Box of 12 cartridges
■ SikaPower®-740 (A) BLACK (Resin)	5 kg, 40 kg
■ SikaPower®-740 (A) BEIGE (Resin)	5 kg, 40 kg
■ SikaPower®-740 (B) (Hardener)	4.5 kg, 36 kg
■ SikaPower®-740 (AB) BLACK 6(0.5 + 0.45)	6 (0.5 kg (A) + 0.45 kg (B)) KIT

FURTHER INFORMATION

The information herein is offered for general guidance only. Advice on specific applications is available on request from the Technical Department of Sika Advanced Resins. Copies of the following publications are available on request: Safety Data Sheets.

VALUE BASES

All technical data stated in this Product Data Sheet are based on laboratory tests. Actual measured data may vary due to circumstances beyond our control.

HEALTH AND SAFETY INFORMATION

For information and advice regarding transportation, handling, storage and disposal of chemical products, users shall refer to the actual Safety Data Sheets containing physical, ecological, toxicological and other safety-related data.

LEGAL NOTICE

The information, and, in particular, the recommendations relating to the application and end-use of Sika products, are given in good faith based on Sika's current knowledge and experience of the products when properly stored, handled and applied under normal conditions in accordance with Sika's recommendations. In practice, the differences in materials, substrates and actual site conditions are such that no warranty in respect of merchantability or of fitness for a particular purpose, nor any liability arising out of any legal relationship whatsoever, can be inferred either from this information, or from any written recommendations, or from any other advice offered. The user of the product must test the product's suitability for the intended application and purpose. Sika reserves the right to change the properties of its products. The proprietary rights of third parties must be observed. All orders are accepted subject to our current terms of sale and delivery. Users must always refer to the most recent issue of the local Product Data Sheet for the product concerned, copies of which will be supplied on request.

Figure D.4: Page 4 of SikaPower®-740 datasheet

CONTACT

SIKA DEUTSCHLAND GmbH
Stuttgarter Straße 139
72574 Bad Urach – GERMANY
Tel.: (+49) 7 125 940 492
Fax. : (+49) 7 125 940 401
E-mail : tooling@de.sika.com
Website : www.sikaadvancedresins.de

SIKA AUTOMOTIVE FRANCE S.A.S.
ZI des Béthunes - 15, Rue de l'Equerre
95310 Saint-Ouen-l'Aumône
CS 40444
95005 CERGY PONTOISE Cedex – FRANCE
Tel.: (+33) 1 344 034 60
Fax: (+33) 1 342 197 87
E-mail: advanced.resins@fr.sika.com
Website : www.sikaadvancedresins.fr

AXSON TECHNOLOGIES SPAIN, S.L.
Polígon Industrial Congost - Guardaagulles, 8
08520 LES FRANQUESES DEL VALLES – SPAIN
Tel.: (+34) 932 25 16 20
E-mail: spain@axson.com
Website: www.sikaadvancedresins.es

AXSON ITALIA S.R.L
Via Morandi 15
21047 Saronno (Va) – ITALY
Tel.: (+39) 02 9670 2336
Fax: (+39) 02 9670 2369
E-mail: axson@axson.it
Website: www.sikaadvancedresins.it

AXSON UK Ltd
Unit 15 Studlands Park Ind. Estate
Newmarket Suffolk, CB8 7AU – UNITED KINGDOM
Tel.: (+44) 1638 660 062
Fax (+44) 1638 665 078
E-mail: sales.uk@axson.com
Website: www.sikaadvancedresins.uk

SIKA AUTOMOTIVE SLOVAKIA s.r.o.
Tovarenska 49
95301 ZLATE MORAVCE – SLOVAKIA
Tel: (+421) 376 422 526
Fax (+421) 376 422 527
E-mail: axson.sk@axson.com
Web site: www.sikaadvancedresins.sk

SIKA ADVANCED RESINS US
30800 Stephenson Highway
Madison Heights, Michigan 48071 – USA
Tel.: (+1) 248 588-2270
Fax: (+1) 248 577-0810
E-mail: axsonmh@axson.com
Web site: www.sikaadvancedresins.us

SIKA AUTOMOTIVE MEXICO S.A. DE C.V.
Ignacio Ramirez #20
Despacho 202 Col. Tabacalera
C.P. 06030 CDMX – MEXICO
Tel.: (+52) 55 5264 4922
Fax: (+52) 55 5264 4916
E-mail: marketing@axson.com.mx
Website: www.sikaadvancedresins.mx

SIKA AUTOMOTIVE SHANGHAI CO. Ltd
N°53 Tai Gu Road
Wai Gao Qiao
Free Trade Zone, Pudong
200131 Shanghai – CHINA
Tel.: (+86) 21 5868 3037
Fax: (+86) 21 5868 2601
E-mail: marketing.china@axson.com
Website: www.sikaadvancedresins .cn

SIKA JAPAN Ltd
2-5-12 Onishi Okazaki Aichi
444-0871 – JAPAN
Tel.: (+81) 564 26 2591
Fax: (+81) 564 26 2593
E-mail: sales.japan@axson.com
Website: www.sikaadvancedresins.jp

AXSON INDIA Pvt. Ltd.
Office n°8, Building Symphony C - 3rd Floor
Range Hills Road
Bhosale Nagar
PUNE 411 020 – INDIA
Tel: (+ 91) 20 25 56 07 10
Fax: (+ 91) 20 25 56 07 12
E-mail: info.india@axson.com
Website: www.sikaadvancedresins.in

Figure D.5: Page 5 of SikaPower®-740 datasheet

Appendix E

Machining Setup Sheet

E.1 Bottom Mould

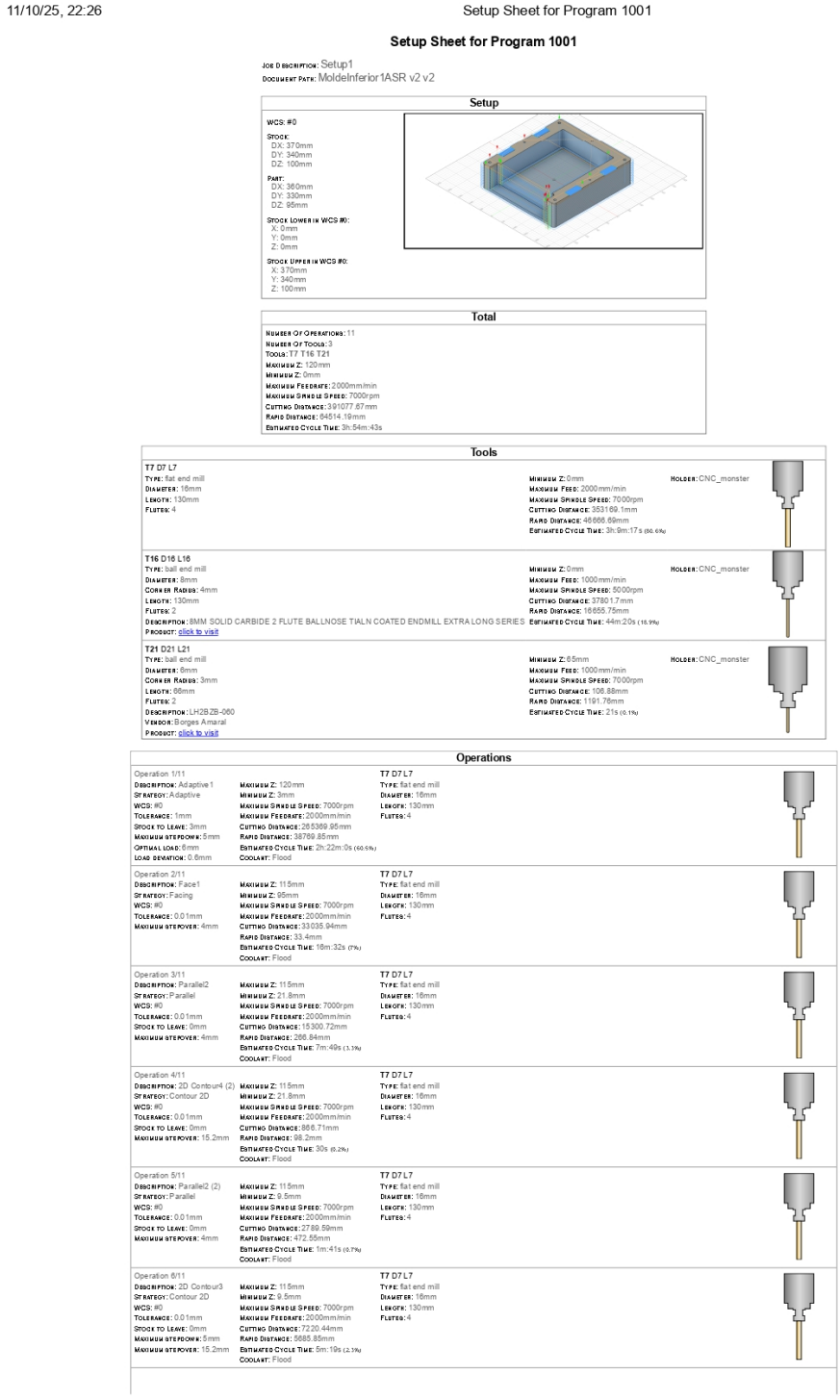

11/10/25, 22:26 Setup Sheet for Program 1001

Setup Sheet for Program 1001

Job Description: Setup1
Document Path: MoldeInferior1ASR v2 v2

Setup

WCS: #0
Stock:
DX: 370mm
DY: 340mm
DZ: 100mm
Part:
DX: 360mm
DY: 330mm
DZ: 95mm
Stock Lower in WCS #0:
X: 0mm
Y: 0mm
Z: 0mm
Stock Upper in WCS #0:
X: 370mm
Y: 340mm
Z: 100mm

Total

Number Of Operations: 11
Number Of Tools: 3
Tools: T7 T16 T21
Maximum Z: 120mm
Minimum Z: 0mm
Maximum Feedrate: 2000mm/min
Maximum Spindle Speed: 7000rpm
Cutting Distance: 391077.67mm
Rapid Distance: 64514.19mm
Estimated Cycle Time: 3h:54m:43s

Tools

T7 D7 L7
Type: flat end mill
Diameter: 16mm
Length: 130mm
Flutes: 4
Minimum Z: 0mm
Maximum Feed: 2000mm/min
Maximum Spindle Speed: 7000rpm
Cutting Distance: 353169.1mm
Rapid Distance: 46666.69mm
Estimated Cycle Time: 3h:9m:17s (80.6%)
Holder: CNC_monster

T16 D16 L16
Type: ball end mill
Diameter: 8mm
Corner Radius: 4mm
Length: 130mm
Flutes: 2
Description: 8MM SOLID CARBIDE 2 FLUTE BALLNOSE TIALN COATED ENDMILL EXTRA LONG SERIES
Product: click to visit
Minimum Z: 0mm
Maximum Feed: 1000mm/min
Maximum Spindle Speed: 5000rpm
Cutting Distance: 37801.7mm
Rapid Distance: 16655.75mm
Estimated Cycle Time: 44m:20s (16.9%)
Holder: CNC_monster

T21 D21 L21
Type: ball end mill
Diameter: 8mm
Corner Radius: 3mm
Length: 66mm
Flutes: 2
Description: LH2BZB-080
Vendor: Borges Amaral
Product: click to visit
Minimum Z: 65mm
Maximum Feed: 1000mm/min
Maximum Spindle Speed: 7000rpm
Cutting Distance: 106.88mm
Rapid Distance: 1191.76mm
Estimated Cycle Time: 21s (0.1%)
Holder: CNC_monster

Operations

Operation 1/11
Description: Adaptive1
Strategy: Adaptive
WCS: #0
Tolerance: 1mm
Stock to Leave: 3mm
Maximum Stepdown: 5mm
Optimal Load: 6mm
Load Deviation: 0.6mm
Maximum Z: 120mm
Minimum Z: 3mm
Maximum Spindle Speed: 7000rpm
Maximum Feedrate: 2000mm/min
Cutting Distance: 265369.95mm
Rapid Distance: 38789.85mm
Estimated Cycle Time: 2h:22m:0s (60.5%)
Coolant: Flood
T7 D7 L7
Type: flat end mill
Diameter: 16mm
Length: 130mm
Flutes: 4

Operation 2/11
Description: Face1
Strategy: Facing
WCS: #0
Tolerance: 0.01mm
Maximum Stepover: 4mm
Maximum Z: 115mm
Minimum Z: 95mm
Maximum Spindle Speed: 7000rpm
Maximum Feedrate: 2000mm/min
Cutting Distance: 33035.94mm
Rapid Distance: 33.4mm
Estimated Cycle Time: 16m:32s (7%)
Coolant: Flood
T7 D7 L7
Type: flat end mill
Diameter: 16mm
Length: 130mm
Flutes: 4

Operation 3/11
Description: Parallel2
Strategy: Parallel
WCS: #0
Tolerance: 0.01mm
Stock to Leave: 0mm
Maximum Stepover: 4mm
Maximum Z: 115mm
Minimum Z: 21.8mm
Maximum Spindle Speed: 7000rpm
Maximum Feedrate: 2000mm/min
Cutting Distance: 15300.72mm
Rapid Distance: 286.84mm
Estimated Cycle Time: 7m:49s (3.3%)
Coolant: Flood
T7 D7 L7
Type: flat end mill
Diameter: 16mm
Length: 130mm
Flutes: 4

Operation 4/11
Description: 2D Contour4 (2)
Strategy: Contour 2D
WCS: #0
Tolerance: 0.01mm
Stock to Leave: 0mm
Maximum Stepover: 15.2mm
Maximum Z: 115mm
Minimum Z: 21.8mm
Maximum Spindle Speed: 7000rpm
Maximum Feedrate: 2000mm/min
Cutting Distance: 866.71mm
Rapid Distance: 98.2mm
Estimated Cycle Time: 30s (0.2%)
Coolant: Flood
T7 D7 L7
Type: flat end mill
Diameter: 16mm
Length: 130mm
Flutes: 4

Operation 5/11
Description: Parallel2 (2)
Strategy: Parallel
WCS: #0
Tolerance: 0.01mm
Stock to Leave: 0mm
Maximum Stepover: 4mm
Maximum Z: 115mm
Minimum Z: 9.5mm
Maximum Spindle Speed: 7000rpm
Maximum Feedrate: 2000mm/min
Cutting Distance: 2789.99mm
Rapid Distance: 472.55mm
Estimated Cycle Time: 1m:41s (0.7%)
Coolant: Flood
T7 D7 L7
Type: flat end mill
Diameter: 16mm
Length: 130mm
Flutes: 4

Operation 6/11
Description: 2D Contour3
Strategy: Contour 2D
WCS: #0
Tolerance: 0.01mm
Stock to Leave: 0mm
Maximum Stepdown: 5mm
Maximum Stepover: 15.2mm
Maximum Z: 115mm
Minimum Z: 9.5mm
Maximum Spindle Speed: 7000rpm
Maximum Feedrate: 2000mm/min
Cutting Distance: 7220.44mm
Rapid Distance: 5685.85mm
Estimated Cycle Time: 5m:19s (2.3%)
Coolant: Flood
T7 D7 L7
Type: flat end mill
Diameter: 16mm
Length: 130mm
Flutes: 4

file:///C:/Users/Utilizador/Desktop/Adamastor/FAMEL/Programas maq/MoldeInferior1ASR v2 v2.html 1/2

Figure E.1: Page 1 of bottom mould CNC machining setup sheet

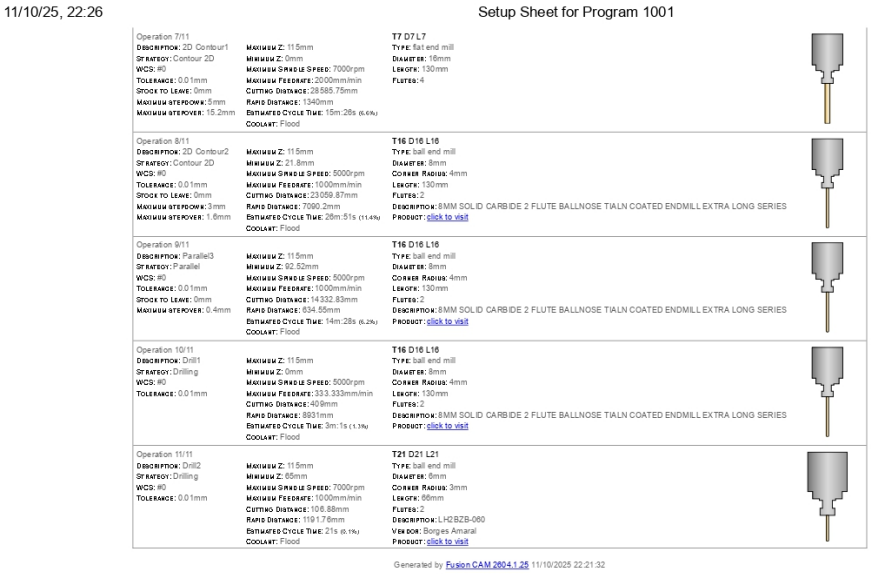

11/10/25, 22:26 Setup Sheet for Program 1001

Operation 7/11
Description: 2D Contour1
Strategy: Contour 2D
WCS: #0
Tolerance: 0.01mm
Stock to Leave: 0mm
Maximum stepdown: 5mm
Maximum stepover: 15.2mm

Maximum Z: 115mm
Minimum Z: 0mm
Maximum Spindle Speed: 7000rpm
Maximum Feedrate: 2000mm/min
Cutting Distance: 28585.75mm
Rapid Distance: 1340mm
Estimated Cycle Time: 15m:26s (6.6%)
Coolant: Flood

T7 D7 L7
Type: flat end mill
Diameter: 16mm
Length: 130mm
Flutes: 4

Operation 8/11
Description: 2D Contour2
Strategy: Contour 2D
WCS: #0
Tolerance: 0.01mm
Stock to Leave: 0mm
Maximum stepdown: 3mm
Maximum stepover: 1.6mm

Maximum Z: 115mm
Minimum Z: 21.8mm
Maximum Spindle Speed: 5000rpm
Maximum Feedrate: 1000mm/min
Cutting Distance: 23059.87mm
Rapid Distance: 7090.2mm
Estimated Cycle Time: 26m:51s (11.4%)
Coolant: Flood

T16 D16 L16
Type: ball end mill
Diameter: 8mm
Corner Radius: 4mm
Length: 130mm
Flutes: 2
Description: 8MM SOLID CARBIDE 2 FLUTE BALLNOSE TIALN COATED ENDMILL EXTRA LONG SERIES
Product: click to visit

Operation 9/11
Description: Parallel3
Strategy: Parallel
WCS: #0
Tolerance: 0.01mm
Stock to Leave: 0mm
Maximum stepover: 0.4mm

Maximum Z: 115mm
Minimum Z: 92.52mm
Maximum Spindle Speed: 5000rpm
Maximum Feedrate: 1000mm/min
Cutting Distance: 14332.83mm
Rapid Distance: 634.55mm
Estimated Cycle Time: 14m:28s (6.2%)
Coolant: Flood

T16 D16 L16
Type: ball end mill
Diameter: 8mm
Corner Radius: 4mm
Length: 130mm
Flutes: 2
Description: 8MM SOLID CARBIDE 2 FLUTE BALLNOSE TIALN COATED ENDMILL EXTRA LONG SERIES
Product: click to visit

Operation 10/11
Description: Drill1
Strategy: Drilling
WCS: #0
Tolerance: 0.01mm

Maximum Z: 115mm
Minimum Z: 0mm
Maximum Spindle Speed: 5000rpm
Maximum Feedrate: 333.333mm/min
Cutting Distance: 409mm
Rapid Distance: 8931mm
Estimated Cycle Time: 3m:1s (1.3%)
Coolant: Flood

T16 D16 L16
Type: ball end mill
Diameter: 8mm
Corner Radius: 4mm
Length: 130mm
Flutes: 2
Description: 8MM SOLID CARBIDE 2 FLUTE BALLNOSE TIALN COATED ENDMILL EXTRA LONG SERIES
Product: click to visit

Operation 11/11
Description: Drill2
Strategy: Drilling
WCS: #0
Tolerance: 0.01mm

Maximum Z: 115mm
Minimum Z: 65mm
Maximum Spindle Speed: 7000rpm
Maximum Feedrate: 1000mm/min
Cutting Distance: 106.88mm
Rapid Distance: 1191.76mm
Estimated Cycle Time: 21s (0.1%)
Coolant: Flood

T21 D21 L21
Type: ball end mill
Diameter: 6mm
Corner Radius: 3mm
Length: 86mm
Flutes: 2
Description: LH2BZB-060
Vendor: Borges Amaral
Product: click to visit

Generated by Fusion CAM 2604.1.25 11/10/2025 22:21:32

file:///C:/Users/Utilizador/Desktop/Adamastor/FAMEL/Programas maq/MoldeInferior1ASR v2 v2.html 2/2

Figure E.2: Page 2 of bottom mould CNC machining setup sheet

E.2 Top Mould

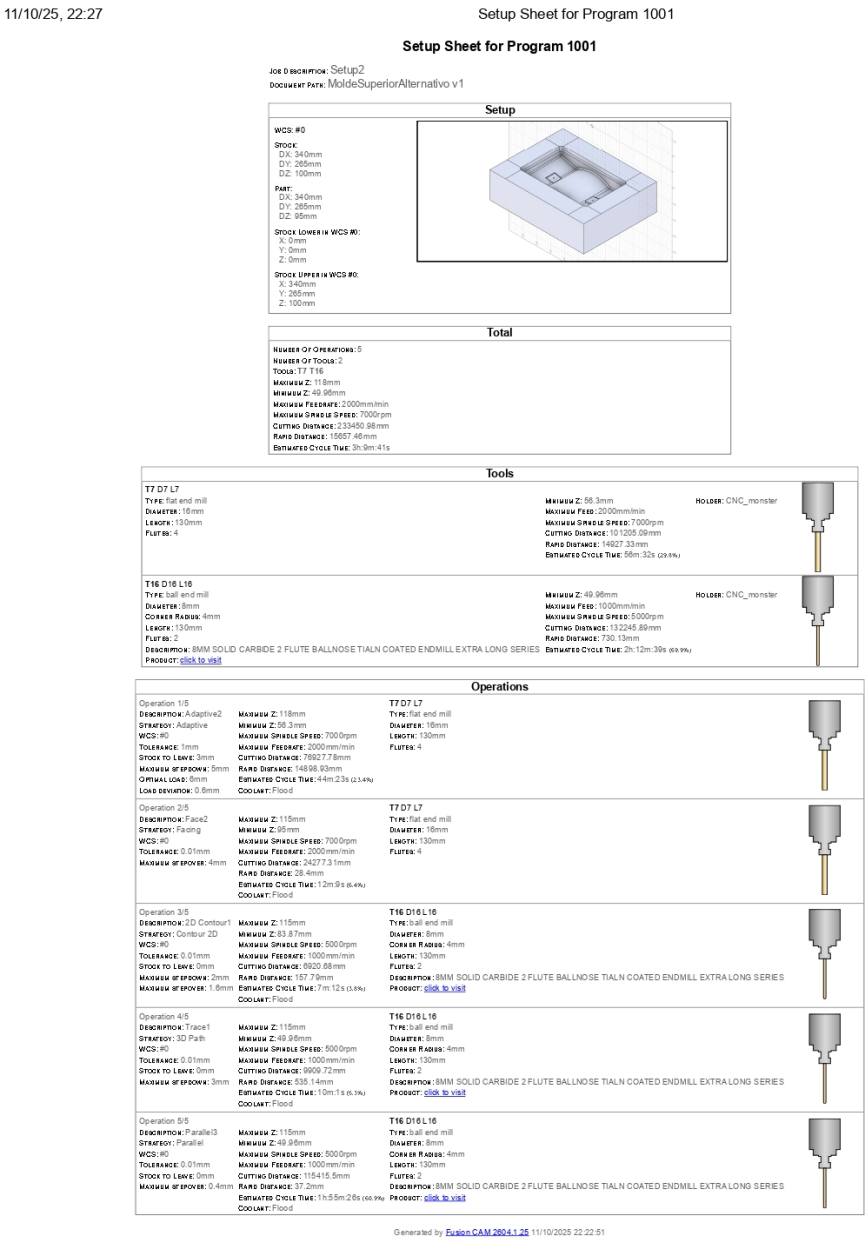

Figure E.3: Top mould CNC machining setup sheet

Appendix F

Nesting and Ply Report

10/14/2025

NESTING CENTER
https://nestingcenter.com

Nesting report

Summary

Number of sheets	1
Number of parts	30
Efficiency	33.48 %
Cutting length	38293.31 mm
Nested area	2.51 m²

Material list

Name	Length [mm]	Height [mm]	Quantity
6000 x 1250	6000	1250	1

Figure F.1: Nesting report page 1

Layouts

Layout 1

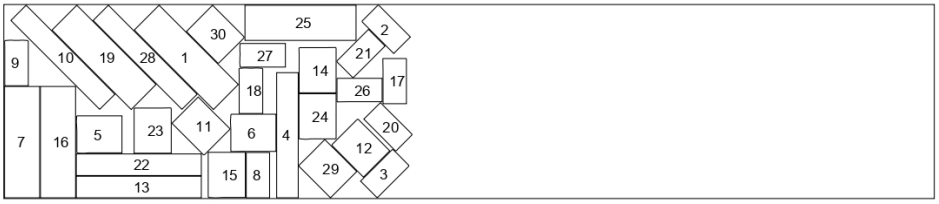

Layout details

Sheet dimensions	6000 x 1250 mm
Quantity	1
Efficiency	33.48 %
Cutting length	38293.31 mm

Part Id	Part name	Quantity
1	LAM001-P001	1
2	LAM001-P002	1
3	LAM001-P003	1
4	LAM001-P004	1
5	LAM001-P005	1
6	LAM001-P006	1
7	LAM001-P007	1
8	LAM001-P008	1
9	LAM001-P009	1
10	LAM001-P010	1
11	LAM001-P011	1
12	LAM001-P012	1
13	LAM001-P013	1
14	LAM001-P014	1
15	LAM001-P015	1
16	LAM001-P016	1
17	LAM001-P017	1
18	LAM001-P018	1
19	LAM001-P019	1
20	LAM001-P020	1
21	LAM001-P021	1
22	LAM001-P022	1
23	LAM001-P023	1
24	LAM001-P024	1
25	LAM001-P025	1
26	LAM001-P026	1
27	LAM001-P027	1
28	LAM001-P028	1

Figure F.2: Nesting report page 2

29	LAM001-P029	1
30	LAM001-P030	1

Figure F.3: Nesting report page 3

Parts list

Part Id	Part name	Quantity	Length [mm]	Height [mm]	Preview
1	LAM001-P001	1	671	671	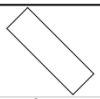
2	LAM001-P002	1	310	310	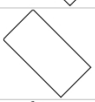
3	LAM001-P003	1	311	310	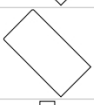
4	LAM001-P004	1	138	806	
5	LAM001-P005	1	294	241	
6	LAM001-P006	1	293	240	
7	LAM001-P007	1	226	716	
8	LAM001-P008	1	151	291	
9	LAM001-P009	1	153	293	
10	LAM001-P010	1	671	671	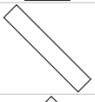
11	LAM001-P011	1	373	373	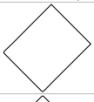
12	LAM001-P012	1	373	373	
13	LAM001-P013	1	806	138	
14	LAM001-P014	1	240	292	

Figure F.4: Nesting report page 4

15	LAM001-P015	1	240	293	
16	LAM001-P016	1	226	716	
17	LAM001-P017	1	151	291	
18	LAM001-P018	1	153	293	
19	LAM001-P019	1	671	671	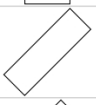
20	LAM001-P020	1	310	310	
21	LAM001-P021	1	310	311	
22	LAM001-P022	1	806	138	
23	LAM001-P023	1	240	292	
24	LAM001-P024	1	240	293	
25	LAM001-P025	1	716	226	
26	LAM001-P026	1	291	151	
27	LAM001-P027	1	293	153	
28	LAM001-P028	1	671	671	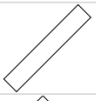
29	LAM001-P029	1	373	373	

Figure F.5: Nesting report page 5

30	LAM001-P030	1	373	373	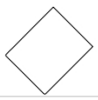

Figure F.6: Nesting report page 6